FOSSIL ENERGY

DOE/MC/22042-15
(DE89000774)

RESERVOIR CHARACTERIZATION FOR THE CO_2 ENHANCED OIL RECOVERY PROCESS

Final Report

By
Franklin M. Orr, Jr.

November 1989

Performed Under Contract No. AC21-85MC22042

Stanford University
Stanford, California

Bartlesville Project Office
U. S. DEPARTMENT OF ENERGY
Bartlesville, Oklahoma

DOE/MC/22042-15
Distribution Category UC-122

RESERVOIR CHARACTERIZATION FOR THE CO_2 ENHANCED OIL RECOVERY PROCESS

Final Report
By
Franklin M. Orr, Jr.

November 1989

Work Performed Under Contract No. AC21-85MC22042

Prepared for
U. S. Department of Energy
Assistant Secretary for Fossil Energy

Royal J. Watts, Project Manager
Morgantown Energy Technology Center
P. O. Box 880
Morgantown, WV 26505

Prepared by
Stanford University
Department of Petroleum Engineering
Stanford, CA 94305

Table of Contents

List of Tables

List of Figures

Acknowledgements

The research program described in this report was supported by the U. S. Department of Energy under Contract DE-AC21-85MC-22042 and by the Stanford University Miscible Flooding Industrial Affiliates: Amoco Production Company, Arco Oil and Gas Company, BP Exploration Inc., Chevron Oil Field Research Company, Conoco Inc., Intevep, S.A., Japan National Oil Corporation, Mobil Research and Development Corporation, Shell Development Company, Tenneco Inc., Texaco Inc. and Unocal Corporation. Additional financial assistance for laboratory equipment was also provided by the Mobil Foundation and by Arco Oil and Gas. Fellowship funds for graduate students whose work is described here were provided by the Mannon Fund, the National Science Foundation, the Steel Fund and the Terry Fund. We gratefully acknowledge all those sources of support.

Many of our fellow students and faculty in the School of Earth Sciences contributed to the ideas presented here. In the Petroleum Engineering Department, Khalid Aziz, Bill Brigham, Roland Horne, and Hank Ramey, and, of course, their students, engaged in endless discussions that helped guide us in many ways. We also benefited from the advice, questions, and comments of faculty and students in the Geophysics, Applied Earth Sciences, and Geology Departments. For example, our flow visualization experiments were digitized on image processing equipment of Amos Nur's Rock Physics group (with expert help from Brian Quinn). André Journel's Geostatistics group helped us represent heterogeneous porous media, and Simon Brassell's Organic Geochemistry group was very much involved in the mass spectrometry work to characterize crude oil compositions. Similar collaborations will continue to be required if we are to make progress toward understanding the complex flow behavior of enhanced oil recovery processes in heterogeneous reservoir rocks. Much of this report is about interactions of physical mechanisms. Our experience indicates that interactions between investigators with different scientific backgrounds adds much to the study of the interactions of the mechanisms. Finally, we are grateful to our colleagues in the Department of Energy (especially our Technical Project Officer, Royal Watts) and in the companies that support this work. We thank them for their interest, for taking time to listen to and talk to our students, and for offering many thoughtful comments and suggestions.

The assembly of this report was supervised by Jeanne Mankinen. Her care and attention to detail in all aspects of its preparation is evident throughout the final version. Ted Sumida's eye for inconsistencies in notation and grammatical indiscretions, Pat Ota's many hours of word processing, and Rosalee Benelli's typesetting expertise all deserve our thanks as well. That anything like a finished report emerged from the first drafts prepared by students and faculty is incontrovertible testimony to their efforts.

F. M. Orr, Jr.
Stanford, California
March, 1989

Abstract

This report summarizes progress in a research effort to quantify the effects of nonuniform flow on displacement performance in CO_2 floods. Results are reported in five areas:

(1) Phase behavior, fluid properties and characterization of crude oils

(2) Interactions of phase behavior and multiphase flow in one dimension

(3) Interaction of viscous instability and flow in heterogeneous porous media

(4) Detection of reservoir heterogeneity

(5) Representation of reservoir heterogeneity

In the first area, the development of a new experimental apparatus for simultaneous measurement of phase compositions, viscosities, and densities is described, and results of experiments to investigate extraction of hydrocarbons by CO_2, N_2 and C_1 are reported. Those results show that CO_2 is a much more effective extraction agent for hydrocarbon present in a Permian basin oil than nitrogen or methane at the same molar density. Also reported are results of crude oil analyses by supercritical fluid chromatography (SFC). The preliminary work performed to date suggests that crude oil characterizations can be obtained much more rapidly by SFC than by standard simulated distillation. Finally, results of initial experiments to investigate the use of mass spectrometry to determine how efficiently hydrocarbons of various molecular weights and types are extracted by dense CO_2 are reported.

In the second area, the method of characteristics is used to determine how phase behavior couples to multiphase flow in one dimension to determine displacement efficiency. The analytical solutions reported extend significantly understanding of the effects of phase behavior on dispacement performance. Three new solutions are reported. The first is an extension of existing theory to four-component systems. The four-component theory is used to resolve a long-standing controversy concerning the effect of dissolved methane on minimum miscibility pressure. Those calculations show that measured minimum miscibility pressures are insensitive to the presence of methane because it partitions so effectively into the vapor phase that all the methane has been displaced before the CO_2 arrives. Also analyzed is the flow of steam/oil/water mixtures with temperature variation. Solutions for a variety of physical situations indicate that front saturations and propagation velocities are quite sensitive to initial and injection temperatures and to the condensation of steam into higher density liquid water. The third solution examines the impact of heterogeneity on development of miscibility. Solutions are reported for binary and ternary mixtures flowing in a two-layer porous medium. The solutions indicate that crossflow generally aids recovery despite an interaction with phase behavior that increases the residual oil saturation in the high permeability layer. Also reported are results of an investigation of the interaction of phase behavior with dispersive mixing. Those calculations show that the sensitivity of the performance of a displacement to changes in the level of dispersion depends strongly on the size and shape of the two-phase region for ternary systems.

In the third area, partly-scaled experiments to study the effects of viscous instability in the presence of permeability variation are described. Displacement results for uniform porous media and for layered systems are reported. In addition, results of detailed simulations of the growth of viscous fingers in both homogeneous and heterogeneous porous media are described. Simulation predictions agree very well with experimental observations reported here and with those of other investigators. Calculations for heterogeneous permeability fields indicate that when local permeability in a heterogeneous permeability field is correlated over a significant fraction of the flow length, the pattern of finger growth is dominated by the permeability variation.

In the fourth area, use of a combination of pressure transient and well-to-well tracer tests to detect the presence of reservoir heterogeneities is discussed. Also presented is a technique

for calculation of the transient pressure response to large scale heterogeneities and an analysis of the pressure response of one- and two-dimensional composite reservoirs.

In the fifth area, the problem of representation of the effects of reservoir heterogeneity in simulations is considered. First, the use of fractional flow functions to represent effects of layering is discussed. The results show that fractional flow functions can be obtained, but they are scale dependent. Next, results of calculations of the effects of heterogeneity and capillary and viscous crossflow are reported. They show that for mild permeability variations, crossflow can mitigate effects of heterogeneity sufficiently that representation of the flow in terms of pseudorelative permeability functions is reasonable. Finally, calculation of tensor grid-block transmissibilities is described. The tensor transmissibilities allow consistent representation of the effects of permeability variations at scales smaller than a grid-block.

1. Introduction

Extensive laboratory testing and a considerable body of field experience indicate that CO_2 flood processes can displace oil effectively at both scales. The oil recovered at either scale results from a complex interplay of interacting and competing transport mechanisms: phase behavior, variations in fluid properties with phase compositions, diffusion and dispersion, viscous instability, density and capillary driven crossflow and, of course, reservoir heterogeneity. The scale dependence of process performance results from the fact that the length scales on which the various mechanisms have the largest impact change in different ways as the scale of the displacement changes. Quantification of that scale dependence is the central issue of current research on methods for more accurate prediction of CO_2 flood performance at field scale.

Unfortunately, fully detailed field-scale simulation of the combined effects of phase behavior and nonuniform flow caused by viscous instability, heterogeneity or both, is not possible using simulation techniques and computers currently available. Indeed, for the foreseeable future simulations will be conducted with grid blocks that are large compared to some of the scales of variation of rock properties and fluid compositions. Thus, large-scale simulation representations will rely on averages of process mechanisms operating at smaller scales. The objective of the research described in this report is to improve quantitative descriptions of the interplay of process mechanisms and scales, so that averaged representations can be developed that reflect those mechanisms with reasonable accuracy.

Because the overall problem is too complex to be attacked directly, we consider here a sequence of simpler problems that illustrate behavior in relevant limiting cases. In Chapter 2 we describe experimental equipment developed to study the phase behavior and fluid properties of mixtures that occur during miscible displacements. Results of phase composition and fluid property measurements that compare the efficiency of supercritical extraction of hydrocarbons by CO_2, methane and nitrogen are also reported. Those results indicate that CO_2 extracts larger amounts of hydrocarbons and also much heavier hydrocarbons than do methane or nitrogen.

Also described in Chapter 2 are investigations of the use of supercritical fluid chromatography using CO_2 as a carrier and crude oil composition analysis by mass spectrometry. Both techniques offer significant potential for improved characterization of crude oils for miscible flood applications.

In Chapter 3, the analytical theory of miscible flooding is examined in some detail. New solutions by the method of characteristics are presented for flow of two-phase four-component mixtures with volume change on mixing. That solution is used to show why displacement efficiency in one-dimensional flow is insensitive to the amount of methane dissolved in the oil. Also presented in Chapter 3 are two other analyses by the method of characteristics. The first is for displacement of oil and water by steam. That analysis includes effects of density changes with temperature variations. The second is a calculation of the interaction of viscous crossflow with phase behavior during two-phase flow in a two-layer porous medium. That calculation shows that crossflow can induce two-phase flow even for displacements that would be multicontact miscible in one-dimensional flow, but that for high permeability ratio, the negative effects of two-phase flow are more than offset by the benefits of transferring hydrocarbons into the high velocity layer. Chapter 3 concludes with a demonstration that the magnitude of the effect of the interaction of phase behavior with numerical dispersion depends on the size and shape of the two-phase region.

Interactions of viscous fingering with reservoir heterogeneity are considered in Chapter 4. A new numerical method, based on particle tracking with a random-walk representation of dispersion, is developed for simulation of finger growth. Predictions made with the method agree very well with previously published experimental data and with results of partly-scaled displacements, also described in Chapter 4. The numerical method is then used to explore how fingers develop and grow in heterogeneous porous media.

In Chapter 5, we examine the question of detection of reservoir heterogeneities by well-to-well tracer tests and by pressure transient well testing. We show first how the existence of significant permeability variation coupled to significant correlation of high and low permeability is manifested in both tracer and well tests. We also present a technique for calculation of the transient pressure response to large scale heterogeneities and demonstrate the impact for various example systems. Also presented is an analysis of the pressure response of one- and two-dimensional composite reservoirs, those in which different sections of the reservoir have contrasting properties.

In Chapter 6, the problem of representation of the effects of reservoir heterogeneity in simulations is considered. First, the use of fractional flow functions to represent effects of layering is discussed. The results show that fractional flow functions can be obtained, but they are scale dependent. Next, results of calculations of the effects of heterogeneity and capillary and viscous crossflow are reported. They show that for mild permeability variations, crossflow can mitigate effects of heterogeneity sufficiently that representation of the flow in terms of pseudorelative permeability functions is reasonable. Finally, calculation of tensor grid-block transmissibilities is described. The tensor transmissibilities allow consistent representation of the effects of permeability variations at scales smaller than a grid-block.

The experiments and calculations described deliberately isolate portions of the displacement process, so that the mechanisms of specific interactions can be understood and their magnitudes calculated. That approach is in recognition of the complexity of the displacement process. The overall goal of the research effort, of course, is improved accuracy in predictions of process performance. The research described in this report, therefore, is designed to provide the physical understanding upon which rational scaling of process mechanisms interacting on multiple scales must be based.

2. Phase Behavior, Fluid Properties and Characterization of Crude Oils.

High local displacement efficiency in a CO_2 or other miscible process depends on the transfer of components between phases. If the transfer is efficient, and the effects of dispersion and nonuniform flow negligible, local displacement efficiency may approach 100 percent. Thus, in nearly one-dimensional displacements, such as occur in a slim tube, for example, phase behavior dominates the displacement process. Hence phase behavior and accompanying fluid property data are an important part of any description of miscible flood processes. In Section 2.1 we describe the design of a new apparatus for phase behavior and fluid property measurements. In addition, we report results of measurements of supercritical extraction by CO_2, nitrogen (N_2) and methane (CH_4) at similar molar densities.

In Section 2.2 we report preliminary results of an investigation of the use of supercritical fluid chromatography to characterize crude oils. The experiments performed show clearly the effect of CO_2 density on extraction behavior. Moreover, they suggest that crude oil analysis can be performed more efficiently by SFC than by more conventional gas chromatography (GC).

In Section 2.3 we describe mass spectrometry (GC-MS) experiments to identify specific hydrocarbon molecules in hydrocarbon mixtures. These experiments are part of a long term campaign to understand how molecular structure affects extraction of a hydrocarbon by dense CO_2.

2.1 Supercritical Extraction, Phase Behavior and Fluid Properties

Gersem Andrade, Aaron N. Stessman and Milind D. Deo

The single most important factor that determines the local displacement efficiency in miscible flooding is the phase behavior between the crude and the injected fluid. The phase properties are also important in order to be able to predict the process performance. Miscible displacement processes may use carbon dioxide, nitrogen or methane. For all three fluids, efficient displacement results when the fluid is dense enough to extract hydrocarbons from the crude. Slim tube displacement experiments have demonstrated that the pressures required for high recovery are much higher for N_2 and CH_4 than for CO_2. This behavior is the result of the low critical temperatures of N_2 (126°K) and CH_4 (191°K). Typical reservoir temperatures are much higher reduced temperatures for N_2 and CH_4 than for CO_2, and hence high pressures are required to produce comparable molar densities. While it is known that high density is required for relatively efficient extraction, it is not clear whether N_2, CH_4 and CO_2 extract the same amounts or types of hydrocarbons when injected fluid has similar molar density. To examine the relationship between the extraction for the three fluid systems and to provide for the characterization of phase behavior and measurement of phase properties for a variety of systems of interest, a high-pressure, high-temperature, PVT apparatus was designed and assembled.

2.1.1 Equipment

Central to the PVT system is a PVT cell mounted in a temperature-controlled oven as shown in the schematic in Fig. 2.1-1. The cell is rated to a pressure of 10000 psia. A positive displacement pump and a microprocessor controlled constant flow rate pump are used to charge the PVT cell with a mixture of known composition using fluids from the supply vessels. Mercury is used as a transfer fluid, and the pressure of the system is monitored with a sensitive quartz transducer. A platinum resistance thermometer is used to measure the system

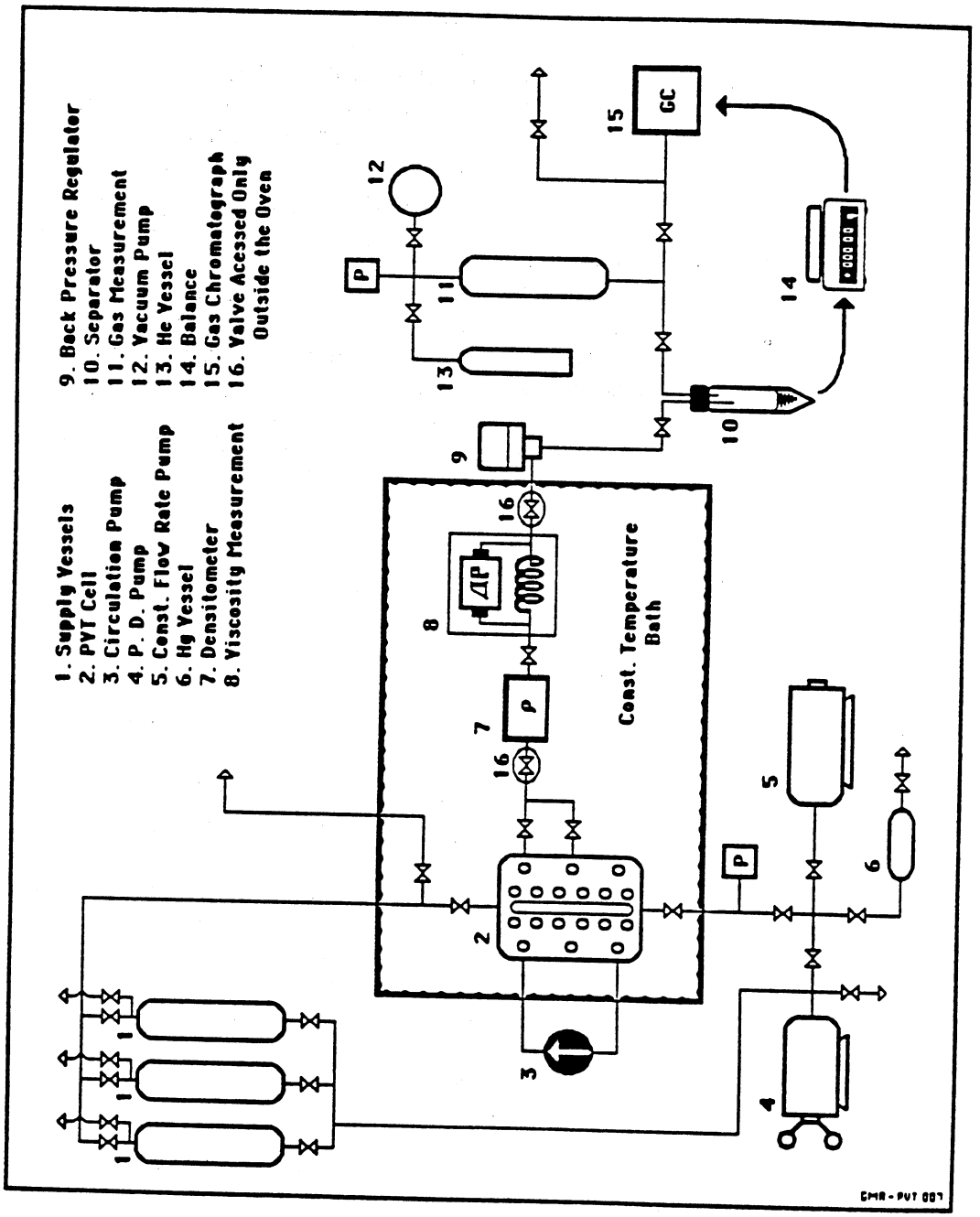

Fig. 2.1-1. Schematic of the PVT apparatus.

the cell is charged, and the desired pressure and temperature conditions are achieved, the mixture is brought to thermodynamic equilibrium by means of a circulation pump. After the equilibrium is reached, the phases present are allowed to separate and the volumes of the phases are measured by a digital height gauge.

The phases are then displaced, one at a time, at known flow rate through the sampling path to the backpressure regulator. The path includes a densitometer for density measurement and a calibrated capillary tube for viscosity measurement. The densitometer has a tube that oscillates at different periods depending on the density of the fluid flowing through it. With proper calibration, the densitometer can measure densities to the accuracy of 0.001 g/cc. The viscosity is determined from the value of the flow rate set by the pump and the pressure difference across the capillary tube measured with a pressure differential transducer.

Once the sample exits the back pressure regulator, it is allowed to separate into a vapor phase and a liquid phase at low pressure. The amount of liquid phase is determined by its weight. If pure component mixtures are under study, the liquid is analyzed directly on the gas chromatograph (GC). Oils are characterized by simulated distillation. The low pressure vapor flows to an evacuated container of known volume at room temperature. Measurement of the pressure in the container allows calculation of the total number of moles of the gas using the ideal gas law. From the amounts and compositions of the liquid and vapor, the phase compositions can be calculated. Thus the apparatus allows measurement of equilibrium phase compositions for all the phases present in the PVT cell as well as their fluid properties. Furthermore, physical samples are obtained, so that more sophisticated compositional analysis can be performed if desired (see sections on supercritical fluid chromatography and gas chromatography-mass spectrometry).

2.1.2 Real-time Data Acquisition, Processing and Control

A DOS based real-time data acquisition, processing and control system was developed on an IBM-AT for the apparatus described above. All the devices in the experimental system are monitored or controlled using appropriate communication protocols. The pump microprocessor is controlled using an IEEE 488 format. An A/D board allows access to a number of temperature and pressure sensors. Normally, an IBM-AT permits communications with only two serial devices. A special multiple port board was installed and configured, so that up to ten serial devices could be accessed. In addition, a special byte register was designed and installed to read the binary parallel data from the digital height gauge.

The software is menu-driven and consists of modules corresponding to specific phases of experimental operation. The software affords complete control over the pump and all chromatographic operations. It allows pressurizing and depressurizing of various vessels, keeps track of the volumes in each of the vessels and records and integrates the data from various stages of operation. The program invokes a commercial package (LABTECH NOTEBOOK) during certain stages of operation mainly for data display. The chromatographic module automates the GC analysis by transferring appropriate analysis files from the GC to the computer and sorting, analyzing, storing and presenting the results. It is capable of handling multiple simulated distillation analyses.

The resulting system allows reliable and accurate acquisition of experimental data and insures that records of an experiment include all the data required for analysis of the results.

2.1.3 Calibration Runs

The accuracy of the results obtained with the apparatus described above depends on the accuracy with which volumes and flow rates are measured. Volumes and flow rates are estimated by the amounts of mercury displaced from the pumps to the system and also by the measurement of the position of fluid interfaces seen through the windows of the cell. The flow

rates must be known for the measurement of viscosity, and they are also related to the amount of mercury displaced from the pumps with time.

As different conditions of pressure and temperature may occur in the pumps and in the cell and the capillary tube, the volumes of mercury that are read directly from the pumps are not necessarily equal to the volume injected or withdrawn from the cell or the capillary tube. Instead, they must be corrected for the compressibility of the mercury, pump seals, and so on. Thus, the response of the internal volumes of the pumps and the cell when subjected to different pressures and temperatures, as well as the relationship between the volume in the cell and the position of the fluid interface seen through the windows of the cell, were evaluated in the calibration runs.

For both the pumps, the relationship between the volume read on the pumps and the volume actually delivered is evaluated as a function of temperature and pressure. The volume actually delivered was determined by gravimetric methods. The compressibilty of the pumps was estimated by compressing mercury in the pumps and reading the volume required to raise the pressure to the value desired.

The digital height gauge was calibrated by using the volume displaced by the pump as the standard. This calibration was performed at different temperatures and pressures and thus the volumetric behavior of the internal chamber of the cell and the volume factor for the height meter were assessed as functions of temperature and pressure.

The densitometers and the capillary tubes were calibrated by charging a fluid of known density and viscosity behavior at different conditions (decane and methane) and displacing the fluid through the sampling branch. A series of measurements was made at different temperatures and pressures. The primary variables measured were the period read by the densitometer and the pressure drop across the capillary tube. The data were used in a two-dimensional spline interpolation scheme to obtain densities and viscosities at desired temperature and pressure, given the period of the densitometer and differential pressure across the capillary tube.

2.1.4 Pure Component Experiments

Several binary CO_2-hydrocarbon experiments were performed to streamline the charging, equilibration and sampling procedures. To study the comparative extractive capacity of different EOR solvents three ternary systems were studied. A C_4-C_{10} mixture was used to simulate oil. The behavior of this mixture when mixed with CO_2, C_1 or N_2 was examined at 160°F and 1250, 1675 and 1890 psia respectively. The molar densities of these three solvents are the same under those conditions.

Results of the phase composition measurements for these three ternary systems are shown in Figs. 2.1-2 to 2.1-4. Detailed phase composition and fluid property data for those measurements are compared in Tables 2.1-1, 2.1-2 and 2.1-3 with predictions of the Peng-Robinson equation of state (1976) and the Lohrenz-Bray-Clark (1964) correlation for fluid viscosities.

Fig. 2.1-2 shows that the measured phase compositions for the CO_2-C_4-C_{10} system at 1250 psia and 160°F agree well with the calculated values. The measurement values are also in reasonable agreement with the data reported by Monroe et al. (1987) and Metcalfe and Yarborough (1979). As Table 2.1-1 indicates, vapor phase densities agreed with the calculated values to within 1-4%. Vapor viscosities also agreed well, with absolute deviations of about 0.002 cp and relative deviations of about 5-10% for the low viscosity values near 0.02 cp. Liquid phase densities did not agree as well with calculated values, as is commonly observed, with calculated values showing deviations of about 0.05 g/cc (7%) below measured values. Calculated liquid phase viscosities were also systematically lower than measured values. One mixture showed a deviation of about 45%, while the others were in the 20-25% range. Thus, the use of Lohrenz-Bray-Clark correlation for this system can result in substantial errors in calculated viscosity for the liquid phase.

Table 2.1-1. Comparison of Measured Phase Compositions and Properties with Values Calculated with Peng-Robinson Equation of State (PREOS) and Lohrenz-Bray-Clark (L-B-C) Correlation for CO_2-C_4-C_{10} Mixtures at 1250 psia and 160°F.

	Expt. mol %	P-R EOS mol %	ρ(g/cc) Expt.	ρ(g/cc) P-R EOS	μ(cp) Expt.	μ(cp) L-B-C
Vapor						
CO_2	100.	99.48	0.1985	0.2028	0.0249	0.0220
n - C_4	0.	0.				
n - C_{10}	0.					
Liquid						
CO_2	56.62	58.20	0.7170	0.6721	0.3123	0.1700
n - C_4	0.	0.				
n - C_{10}	0.	0.				
Vapor						
CO_2	92.00	93.52	0.2156	0.2205	0.0223	0.0228
n - C_4	8.00	5.95				
n - C_{10}	0.	0.53				
Liquid						
CO_2	60.31	58.34	0.6787	0.6410	0.1561	0.1232
n - C_4	15.55	16.50				
n - C_{10}	24.13	25.16				
Vapor						
CO_2	94.48	94.98	0.2052	0.2153	0.0204	0.0225
n - C_4	5.52	4.49				
n - C_{10}	0.	0.53				
Liquid						
CO_2	58.36	58.10	0.7005	0.6520	0.2122	0.1340
n - C_4	15.55	16.50				
n - C_{10}	24.13	25.16				

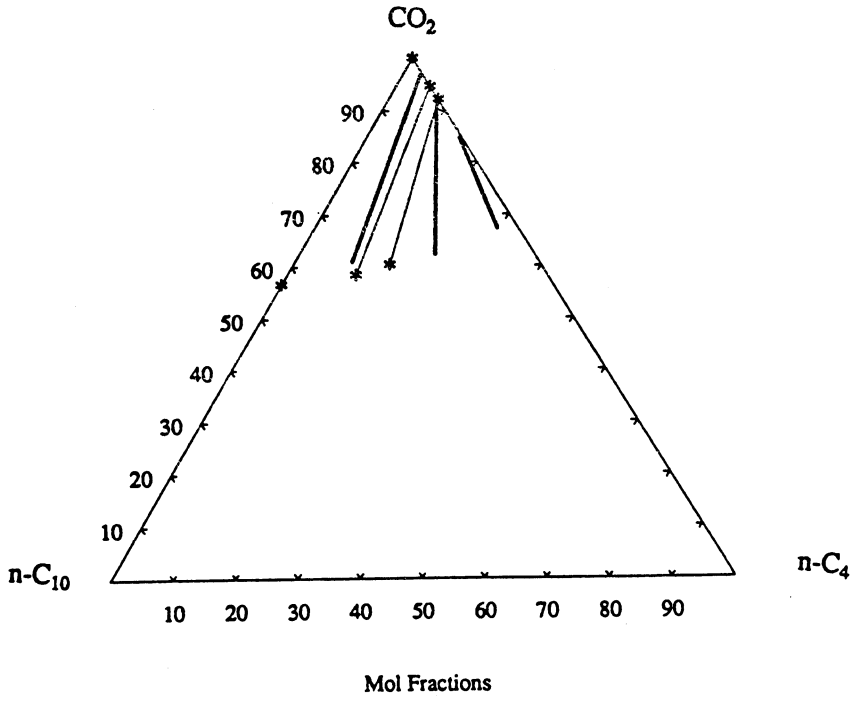

Fig. 2.1-2. Comparison of the measured (*) and calculated (heavy line) tie lines for CO_2-C_4-C_{10} mixtures at 160°F and 1250 psia.

Table 2.1-2. Comparison of Measured Phase Compositions and Properties with Values Calculated with Peng-Robinson Equation of State (PREOS) and Lohrenz-Bray-Clark (L-B-C) Correlation for C_1-C_4-C_{10} Mixtures at 1675 psia and 160°F.

	Expt. mol %	P-R EOS mol %	ρ(g/cc) Expt.	ρ(g/cc) P-R EOS	μ(cp) Expt.	μ(cp) L-B-C
Vapor						
CH_4	100.	99.64	0.0703	0.0746	0.0176	0.0149
n - C_4	0.	0.				
n - C_{10}	0.	0.36				
Liquid						
CH_4	36.63	36.94	0.6446	0.6033	0.3522	0.1923
n - C_4	0.	0.				
n - C_{10}	63.37	63.06				
Vapor						
CH_4	89.77	88.56	0.0974	0.1054	0.0162	0.0158
n - C_4	10.16	11.08				
n - C_{10}	0.07	0.36				
Liquid						
CH_4	35.50	38.36	0.5583	0.5337	0.2244	0.1131
n - C_4	38.62	36.71				
n - C_{10}	25.88	24.93				
Vapor						
CH_4	95.43	94.84	0.0813	0.0868	0.0162	0.0152
n - C_4	4.36	4.79				
n - C_{10}	0.21	0.37				
Liquid						
CH_4	36.17	37.10	0.6083	0.5781	0.2548	0.1581
n - C_4	19.13	18.28				
n - C_{10}	44.70	44.62				

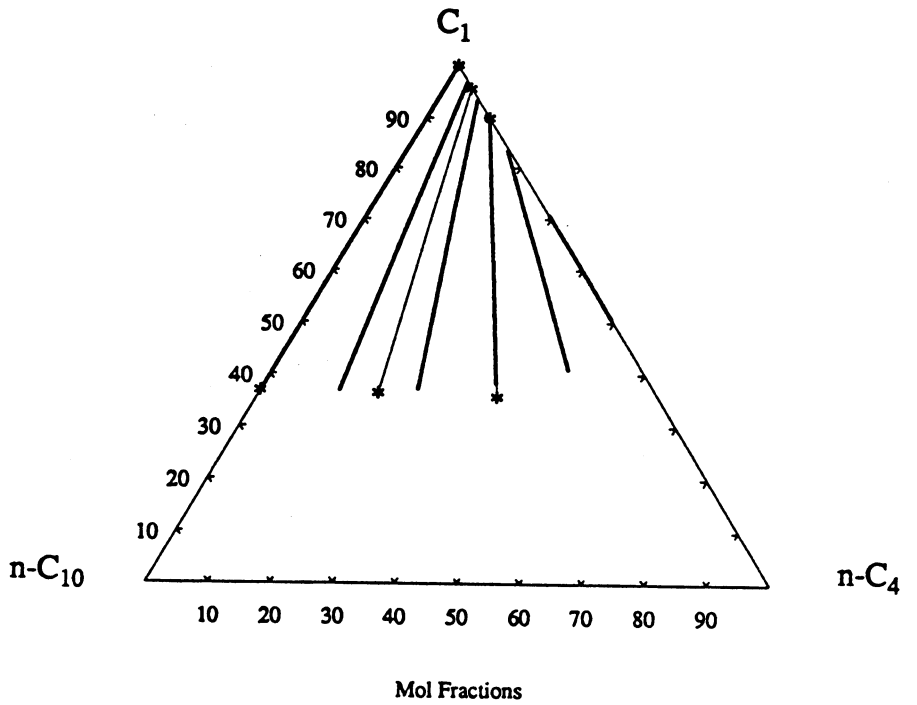

Fig. 2.1-3. Comparison of the measured (*) and calculated (heavy line) tie lines for C_1-C_4-C_{10} mixtures at 160°F and 1675 psia.

Table 2.1-3. Comparison of Measured Phase Compositions and Properties with Values Calculated with Peng-Robinson Equation of State (PREOS) and Lohrenz-Bray-Clark (L-B-C) Correlation for N_2-C_4-C_{10} Mixtures at 1890 psia and 160°F.

	Expt. mol %	P-R EOS mol %	ρ(g/cc) Expt.	ρ(g/cc) P-R EOS	μ(cp) Expt.	μ(cp) L-B-C
Vapor						
N_2	100.	99.87	0.1221	0.1125	0.0216	0.0214
n - C_4	0.	0.				
n - C_{10}	0.	0.13				
Liquid						
N_2	20.51	17.31	0.6955	0.6519	0.4893	0.2319
n - C_4	0.	0.				
n - C_{10}	79.49	82.69				
Vapor						
N_2	92.88	91.29	0.1399	0.1416	0.0243	0.0213
n - C_4	7.12	8.60				
n - C_{10}	0.0	0.10				
Liquid						
N_2	20.23	18.19	0.6247	0.6076	0.2818	0.1613
n - C_4	48.88	49.67				
n - C_{10}	30.89	32.14				
Vapor						
N_2	97.09	95.45	0.1311	0.1333	0.0222	0.0215
n - C_4	2.78	4.42				
n - C_{10}	0.13	0.12				
Liquid						
N_2	14.79	17.55	0.6638	0.6326	0.3477	0.2014
n - C_4	30.70	28.29				
n - C_{10}	54.51	54.16				

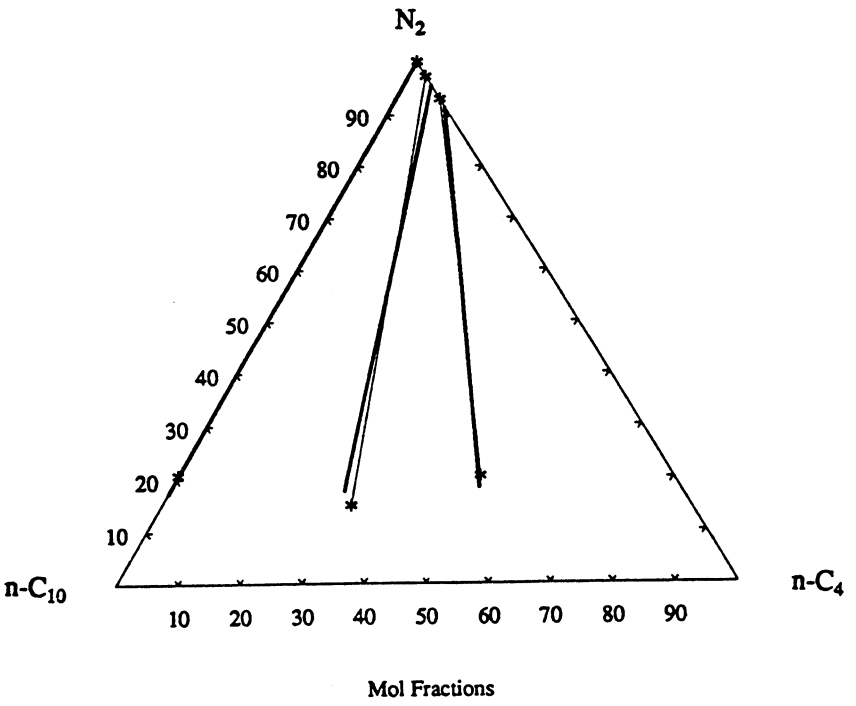

Fig. 2.1-4. Comparison of the measured (*) and calculated (heavy line) tie lines for N_2-C_4-C_{10} mixtures at 160°F and 1890 psia.

Figs. 2.1-2 and 2.1-3 and Tables 2.1-2 and 2.1-3 show similar comparisons for the N_2-C_4-C_{10} and C_1-C_4-C_{10} systems. Again the Peng-Robinson equation of state showed good agreement, as would be expected for these simple well characterized systems. Calculated phase densities agreed well with measured values for the vapor phases and were systematically lower for the liquid phases. Calculated phase viscosities agreed well for the vapor phases, but showed substantial deviations for the liquid phases.

Comparison of Figs. 2.1-2, 2.1-3 and 2.1-4 shows clearly that the solubility of CO_2 in the hydrocarbon (liquid) is greater than that of C_1, which in turn is substantially higher than that of N_2. Thus even at comparable molar densities, the phase behavior characteristics of the three systems differ considerably.

2.1.5 Crude Oil Experiments

Maljamar crude oil, a Permian basin oil from Lea County, New Mexico was used in all experiments. Three sets of experiments were performed at a temperature of 120°F. The CO_2-crude oil experiment was conducted at 1520 psia, the C_1-crude oil experiment at 3790 psia and the N_2-crude oil experiment at 4950 psia. Under these conditions, the molar densities of CO_2, C_1 and N_2 are identical. Thus the experiment tested whether extraction is dominated by molar density, the number of molecules per unit volume, or by interactions between the solvent molecules and the extracted hydrocarbons.

The Maljamar crude was characterized by simulated distillation (SIMDIS). SIMDIS is a standard procedure (ASTM 1976) used to determine the carbon number distribution or the boiling temperature ranges of petroleum fractions. In a typical analysis, the sample is introduced into a gas chromatograph (GC) column, which separates the hydrocarbons, approximately at least, in boiling point order. The oven temperature is programmed, and component elution is monitored with a flame ionization detector. The initial temperature of the column was 30°C. It was increased at a rate of 15°C/min to a final temperature of 350°C. The column was held at this final temperature for 10 minutes. The injector and the detector temperatures were maintained at 350°C.

Elution times for alkanes of various carbon numbers were assigned to the time axis from a calibration curve, obtained under the same chromatographic conditions by running a mixture of hydrocarbons through C_{40}. The amount of sample heavier than C_{40} is estimated by means of an internal standard added to the the sample. Thus the procedure involves making a series of runs under identical chromatographic conditions: a calibration standard, crude sample with an internal standard added to it and the crude sample by itself. The SIMDIS program, which was a part of the overall data acquisition and processing package, was capable of storing a blank run and accounting for the column bleed in the subsequent runs. A typical crude analysis is shown in Table 2.1-4.

In the CO_2, C_1 and N_2 phase behavior experiments, a known amount of crude was charged into the PVT cell, and the EOR agent was added to the cell at appropriate conditions. The overall molar concentration of the agent was high (more than 70%) in all the experiments. The resulting phases were equilibrated and the volumetric behavior of the mixture was studied by changing the pressure in the cell. The resulting upper and lower phases were then sampled in turn. Each of the phases was separated into a liquid and a vapor phase at atmospheric pressure. The liquid phase was weighed and characterized by SIMDIS. The vapor phase was sent directly to the GC and was analyzed on a POROPAK Q column. For this analysis, the initial temperature, 60°C, was maintained for a period of 2 minutes. The temperature was increased at 30°C/min. to a final value of 250°C, where it was held for 10 minutes. The injector and the detector temperatures were held at 250°C. Retention times and response factors for the pure components were determined separately to identify and quantify the peaks obtained in the gas analysis. The amounts and compositions of the liquid and the vapor were used to calculate the

Table 2.1-4. Carbon Number (CN) Distribution for the Maljamar crude Oil by Simulated Distillation (SIMDIS).

Carbon Number	Molecular Weight	Mass Fraction	Mole Fraction
5	72.151	0.0153	0.0436
6	86.178	0.0163	0.0388
7	100.204	0.0512	0.1048
8	114.231	0.0712	0.1279
9	128.258	0.0552	0.0883
10	142.285	0.0498	0.0718
11	156.312	0.0387	0.0508
12	170.339	0.0457	0.0551
13	184.366	0.0321	0.0357
14	198.393	0.0405	0.0418
15	212.420	0.0338	0.0326
16	226.447	0.0318	0.0288
17	240.474	0.0329	0.0280
18	254.501	0.0220	0.0177
19	268.528	0.0343	0.0262
20	282.555	0.0221	0.0161
21	296.582	0.0218	0.0151
22	310.609	0.0221	0.0146
23	324.636	0.0215	0.0136
24	338.663	0.0205	0.0124
25	352.690	0.0120	0.0070
26	366.717	0.0200	0.0112
27	380.743	0.0120	0.0065
28	394.770	0.0193	0.0100
29	408.797	0.0120	0.0060
30	422.824	0.0118	0.0057
31	436.851	0.0113	0.0053
32	450.878	0.0157	0.0072
33	464.905	0.0086	0.0038
34	478.932	0.0104	0.0045
35	492.959	0.0054	0.0023
36	506.986	0.0068	0.0028
37+	563.094	0.1757	0.0640

composition of the phase displaced from the cell as described in Section 2.1.1. As the phase was being sampled, density and viscosity of the phase were also measured.

The compositions, densities and viscosities of the upper and the lower phases formed by the contact of CO_2 with the Maljamar crude are reported in Tables 2.1-5 and 2.1-6. The solubility of CO_2 in the hydrocarbon-liquid phase is very close to the solubility of CO_2 in the hydrocarbon-liquid phase in the CO_2-C_4-C_{10} system studied earlier. The data for C_1 and N_2 systems with the crude are shown in Tables 2.1-7 to 2.1-10. The solubilty of the solvent in the hydrocarbon-liquid phase is lower for C_1 than CO_2 and lower still for N_2. The trend observed is the same as the pattern observed for the pure component systems. This can be observed in the ternary diagram shown in Fig. 2.1-5. In this ternary representation of the phase behavior of the crude with the EOR agents, components C_2-C_{12} have been grouped under one pseudocomponent and the C_{13+} fraction has been lumped into the other pseudocomponent.

2.1.6 Discussion

The phase composition data reported here give some indication of the difference between displacements by CO_2 and displacement by C_1 or N_2. Fig. 2.1-6 illustrates the impact of changes in extraction and solubility on the size of the two-phase region and the slopes of the tie- lines. Fig. 2.1-6a shows favorable behavior. Light components are extracted so efficiently that the region of tie-line extensions is small and the oil lies outside it. For that system, miscible displacement would result in one-dimensional flow (with no dispersion). See Sections 3.1 and 3.3 for extensive discussions of the reasoning behind that statement. The phase compositions of the CO_2/crude oil mixture suggest that a displacement of Maljamar crude oil by CO_2 at 1520 psia would be efficient because the oil is apparently close to the boundary of the region of tie-line extensions. The estimate of the minimum miscibility pressure (MMP) is the extrapolated vapor pressure of CO_2 (Orr and Jensen 1984, Silva and Orr 1987), which at 120°F is 1575 psia.

Fig. 2.1-6 shows the effect of a decrease in solubility with the tie-line slopes held constant. In both cases, the displacement would pass through the two-phase region, entering it along the tie line that extends through the oil composition, but the displacement for the smaller two-phase region would be more efficient for two reasons. First, the displacement composition route would pass closer to the plait point and therefore closer to the vapor portion of the binodal curve (See Sections 3.1 and 3.3). Hence the amount of oil left after passage of the leading edge of the transition zone would be smaller. In addition, the residual oil left in that zone would contain more dissolved solvent. Hence, the phase composition data for C_1 in Fig. 2.1-5 are less favorable than those for CO_2, despite the fact that Fig. 2.1-6c shows the effect of less efficient extraction with the size of the two-phase region fixed to be the same as that in Fig. 2.1-6a. Clearly, the size of the region of tie-line extensions is larger when extraction of hydrocarbons into the upper phase is less efficient. The phase composition data for N_2 in Fig. 2.1-5 show that the vapor phase contained much less extracted hydrocarbons. In addition, the liquid phase contained much less dissolved N_2. Hence, displacement by N_2 would be less efficient still than displacement by C_1.

Additional confirmation of the differences in extraction behavior is shown in Fig. 2.1-7, which reports the carbon number distribution of the extracted hydrocarbons, plotted on a solvent-free basis. Both C_1 and N_2 extracted only light hydrocarbons, while CO_2 extracted much heavier hydrocarbons. Thus, both the quantity and type of hydrocarbons extracted by each solvent indicate that CO_2 interacts much more strongly than either N_2 or C_1 with the hydrocarbons present in the Maljamar crude oil. Those data suggest that volatility of hydrocarbons present in the oil is much more important for C_1 and N_2 than for CO_2. Miscible displacement by N_2 or C_1 evidently would require that substantial quantities of C_2 - C_8 hydrocarbons be present in the oil, while efficient displacement by CO_2 can occur even when those hydrocarbons are not present.

Table 2.1-5. Phase Compositions and Properties for CO_2 Plus Maljamar Crude Oil at 1520 psia and 120°F: Lower Phase Analysis.

	MW	GAS		LIQUID		TOTAL	
		Mass Fraction	Mole Fraction	Mass Fraction	Mole Fraction	Mass Fraction	Mole Fraction
CO_2	44.010	0.9287	0.9568	0.	0.	0.3033	0.6791
C_1	16.043	0.	0.	0.	0.	0.	0.
C_2	30.070	0.	0.	0.	0.	0.	0.
C_3	44.097	0.0078	0.0080	0.	0.	0.0025	0.0057
C_4	58.120	0.0077	0.0060	0.	0.	0.0025	0.0043
C_5	72.151	0.0131	0.0082	0.0019	0.0060	0.0056	0.0076
C_6	86.178	0.0215	0.0113	0.0098	0.0259	0.0136	0.0155
C_7	100.204	0.0213	0.0096	0.0375	0.0855	0.0322	0.0317
C_8	114.231	0.	0.	0.0420	0.0840	0.0283	0.0244
C_9	128.258	0.	0.	0.0509	0.0908	0.0343	0.0264
C_{10}	142.285	0.	0.	0.0489	0.0786	0.0329	0.0228
C_{11}	156.312	0.	0.	0.0440	0.0643	0.0296	0.0187
C_{12}	170.339	0.	0.	0.0374	0.0502	0.0252	0.0146
C_{13}	184.366	0.	0.	0.0405	0.0502	0.0272	0.0146
C_{14}	198.393	0.	0.	0.0279	0.0321	0.0188	0.0093
C_{15}	212.420	0.	0.	0.0430	0.0463	0.0289	0.0134
C_{16}	226.447	0.	0.	0.0425	0.0430	0.0287	0.0125
C_{17}	240.474	0.	0.	0.0276	0.0263	0.0186	0.0076
C_{18}	254.501	0.	0.	0.0354	0.0318	0.0239	0.0092
C_{19}	268.528	0.	0.	0.0256	0.0218	0.0173	0.0063
C_{20}	282.555	0.	0.	0.0252	0.0204	0.0170	0.0059
C_{21}	296.582	0.	0.	0.0248	0.0191	0.0167	0.0055
C_{22}	310.609	0.	0.	0.0254	0.0187	0.0171	0.0054
C_{23}	324.636	0.	0.	0.0240	0.0169	0.0162	0.0049
C_{24}	338.663	0.	0.	0.0229	0.0155	0.0154	0.0045
C_{25}	352.690	0.	0.	0.0223	0.0145	0.0150	0.0042
C_{26}	366.717	0.	0.	0.0150	0.0094	0.0101	0.0027
C_{27}	380.743	0.	0.	0.0218	0.0131	0.0147	0.0038
C_{28}	394.770	0.	0.	0.0145	0.0084	0.0098	0.0024
C_{29}	408.797	0.	0.	0.0145	0.0081	0.0098	0.0024
C_{30}	422.824	0.	0.	0.0200	0.0108	0.0135	0.0031
C_{31}	436.851	0.	0.	0.0125	0.0065	0.0084	0.0019
C_{32}	450.878	0.	0.	0.0113	0.0057	0.0076	0.0017
C_{33}	464.905	0.	0.	0.0097	0.0048	0.0065	0.0014
C_{34}	478.932	0.	0.	0.0112	0.0054	0.0076	0.0016
C_{35}	492.959	0.	0.	0.0060	0.0028	0.0041	0.0008
C_{36}	506.986	0.	0.	0.0070	0.0031	0.0047	0.0009
C_{36+}	563.094	0.	0.	0.1970	0.0800	0.1327	0.0232
Density						0.8550 g/cm^3	
Viscosity						0.6563 cp	

Table 2.1-6. Phase Compositions and Properties for CO_2 Plus Maljamar Crude Oil at 1520 psia and 120°F: Upper Phase Analysis.

	MW	GAS		LIQUID		TOTAL	
		Mass Fraction	Mole Fraction	Mass Fraction	Mole Fraction	Mass Fraction	Mole Fraction
CO_2	44.010	0.9660	0.9830	0.	0.	0.8892	0.9585
C_1	16.043	0.	0.	0.	0.	0.	0.
C_2	30.070	0.	0.	0.	0.	0.	0.
C_3	44.097	0.	0.	0.	0.	0.	0.
C_4	58.120	0.0012	0.0009	0.	0.	0.0011	0.0009
C_5	72.151	0.0051	0.0032	0.0019	0.0046	0.0049	0.0032
C_6	86.178	0.0128	0.0067	0.0102	0.0208	0.0127	0.0070
C_7	100.204	0.0141	0.0063	0.0536	0.0936	0.0179	0.0085
C_8	114.231	0.	0.	0.1131	0.1733	0.0104	0.0043
C_9	128.258	0.	0.	0.1389	0.1895	0.0127	0.0047
C_{10}	142.285	0.	0.	0.1073	0.1320	0.0098	0.0033
C_{11}	156.312	0.	0.	0.0769	0.0861	0.0071	0.0021
C_{12}	170.339	0.	0.	0.0693	0.0713	0.0064	0.0018
C_{13}	184.366	0.	0.	0.0368	0.0350	0.0034	0.0009
C_{14}	198.393	0.	0.	0.0591	0.0522	0.0054	0.0013
C_{15}	212.420	0.	0.	0.0433	0.0357	0.0040	0.0009
C_{16}	226.447	0.	0.	0.0279	0.0215	0.0026	0.0005
C_{17}	240.474	0.	0.	0.0287	0.0209	0.0026	0.0005
C_{18}	254.501	0.	0.	0.0179	0.0123	0.0016	0.0003
C_{19}	268.528	0.	0.	0.0153	0.0100	0.0014	0.0002
C_{20}	282.555	0.	0.	0.0133	0.0082	0.0012	0.0002
C_{21}	296.582	0.	0.	0.0190	0.0112	0.0017	0.0003
C_{22}	310.609	0.	0.	0.0100	0.0056	0.0009	0.0001
C_{23}	324.636	0.	0.	0.0085	0.0046	0.0008	0.0001
C_{24}	338.663	0.	0.	0.0073	0.0038	0.0007	0.0001
C_{25}	352.690	0.	0.	0.0044	0.0022	0.0004	0.0001
C_{26}	366.717	0.	0.	0.0056	0.0027	0.0005	0.0001
C_{27}	380.743	0.	0.	0.0034	0.0016	0.0003	0.0000
C_{28}	394.770	0.	0.	0.0029	0.0013	0.0003	0.0000
C_{29}	408.797	0.	0.	0.	0.	0.	0.
C_{30}	422.824	0.	0.	0.	0.	0.	0.
C_{31}	436.851	0.	0.	0.	0.	0.	0.
C_{32}	450.878	0.	0.	0.	0.	0.	0.
C_{33}	464.905	0.	0.	0.	0.	0.	0.
C_{34}	478.932	0.	0.	0.	0.	0.	0.
C_{35}	492.959	0.	0.	0.	0.	0.	0.
C_{36}	506.986	0.	0.	0.	0.	0.	0.
C_{36+}	563.094	0.	0.	0.	0.	0.	0.
Density						0.6602 gm/cm^3	
Viscosity						0.0848 cp	

Table 2.1-7. Phase Compositions and Properties for C_1 Plus Maljamar Crude Oil at 3790 psia and 120°F: Lower Phase Analysis.

	MW	GAS		LIQUID		TOTAL	
		Mass Fraction	Mole Fraction	Mass Fraction	Mole Fraction	Mass Fraction	Mole Fraction
C_1	16.043	0.7791	0.9506	0.	0.	0.0510	0.4166
C_2	30.070	0.	0.	0.	0.	0.	0.
C_3	44.097	0.	0.	0.	0.	0.	0.
C_4	58.120	0.	0.	0.	0.	0.	0.
C_5	72.151	0.0460	0.0125	0.0030	0.0091	0.0058	0.0106
C_6	86.178	0.0853	0.0194	0.0118	0.0299	0.0166	0.0253
C_7	100.204	0.0897	0.0175	0.0443	0.0964	0.0473	0.0618
C_8	114.231	0.	0.	0.0494	0.0942	0.0462	0.0529
C_9	128.258	0.	0.	0.0564	0.0959	0.0527	0.0539
C_{10}	142.285	0.	0.	0.0529	0.0811	0.0495	0.0456
C_{11}	156.312	0.	0.	0.0474	0.0661	0.0443	0.0371
C_{12}	170.339	0.	0.	0.0398	0.0509	0.0372	0.0286
C_{13}	184.366	0.	0.	0.0422	0.0499	0.0394	0.0280
C_{14}	198.393	0.	0.	0.0285	0.0314	0.0267	0.0176
C_{15}	212.420	0.	0.	0.0437	0.0448	0.0408	0.0252
C_{16}	226.447	0.	0.	0.0423	0.0407	0.0395	0.0229
C_{17}	240.474	0.	0.	0.0274	0.0249	0.0257	0.0140
C_{18}	254.501	0.	0.	0.0347	0.0298	0.0325	0.0167
C_{19}	268.528	0.	0.	0.0249	0.0202	0.0232	0.0113
C_{20}	282.555	0.	0.	0.0243	0.0188	0.0227	0.0105
C_{21}	296.582	0.	0.	0.0238	0.0175	0.0222	0.0098
C_{22}	310.609	0.	0.	0.0243	0.0170	0.0227	0.0096
C_{23}	324.636	0.	0.	0.0228	0.0153	0.0213	0.0086
C_{24}	338.663	0.	0.	0.0218	0.0140	0.0203	0.0079
C_{25}	352.690	0.	0.	0.0212	0.0131	0.0198	0.0073
C_{26}	366.717	0.	0.	0.0142	0.0085	0.0133	0.0047
C_{27}	380.743	0.	0.	0.0206	0.0118	0.0192	0.0066
C_{28}	394.770	0.	0.	0.0137	0.0076	0.0128	0.0042
C_{29}	408.797	0.	0.	0.0137	0.0073	0.0128	0.0041
C_{30}	422.824	0.	0.	0.0191	0.0098	0.0178	0.0055
C_{31}	436.851	0.	0.	0.0121	0.0060	0.0113	0.0034
C_{32}	450.878	0.	0.	0.0110	0.0053	0.0103	0.0030
C_{33}	464.905	0.	0.	0.0096	0.0045	0.0090	0.0025
C_{34}	478.932	0.	0.	0.0114	0.0052	0.0106	0.0029
C_{35}	492.959	0.	0.	0.0062	0.0027	0.0058	0.0015
C_{36}	506.986	0.	0.	0.0074	0.0032	0.0069	0.0018
C_{36+}	563.094	0.	0.	0.1742	0.0674	0.1628	0.0379
Density						0.7494 gm/cm^3	
Viscosity						1.0537 cp	

Table 2.1-8. Phase Compositions and Properties for C_1 Plus Maljamar Crude Oil at 3790 psia and 120°F: Upper Phase Analysis.

	MW	GAS		LIQUID		TOTAL	
		Mass Fraction	Mole Fraction	Mass Fraction	Mole Fraction	Mass Fraction	Mole Fraction
C_1	16.043	0.7496	0.9398	0.	0.	0.7497	0.9398
C_2	30.070	0.	0.	0.	0.	0.	0.
C_3	44.09	0.	0.	0.	0.	0.	0.
C_4	58.120	0.0164	0.0057	0.	0.	0.0164	0.0057
C_5	72.151	0.0585	0.0163	0.	0.	0.0585	0.0163
C_6	86.178	0.0935	0.0218	0.	0.	0.0935	0.0218
C_7	100.204	0.0819	0.0164	0.	0.	0.0819	0.0164
C_8	114.231	0.	0.	0.	0.	0.	0.
C_9	128.258	0.	0.	0.	0.	0.	0.
C_{10}	142.285	0.	0.	0.	0.	0.	0.
C_{11}	156.312	0.	0.	0.	0.	0.	0.
C_{12}	170.339	0.	0.	0.	0.	0.	0.
C_{13}	184.366	0.	0.	0.	0.	0.	0.
C_{14}	198.393	0.	0.	0.	0.	0.	0.
C_{15}	212.420	0.	0.	0.	0.	0.	0.
C_{16}	226.447	0.	0.	0.	0.	0.	0.
C_{17}	240.474	0.	0.	0.	0.	0.	0.
C_{18}	254.501	0.	0.	0.	0.	0.	0.
C_{19}	268.528	0.	0.	0.	0.	0.	0.
C_{20}	282.555	0.	0.	0.	0.	0.	0.
C_{21}	296.582	0.	0.	0.	0.	0.	0.
C_{22}	310.609	0.	0.	0.	0.	0.	0.
C_{23}	324.636	0.	0.	0.	0.	0.	0.
C_{24}	338.663	0.	0.	0.	0.	0.	0.
C_{25}	352.690	0.	0.	0.	0.	0.	0.
C_{26}	366.717	0.	0.	0.	0.	0.	0.
C_{27}	380.743	0.	0.	0.	0.	0.	0.
C_{28}	394.770	0.	0.	0.	0.	0.	0.
C_{29}	408.797	0.	0.	0.	0.	0.	0.
C_{30}	422.824	0.	0.	0.	0.	0.	0.
C_{31}	436.851	0.	0.	0.	0.	0.	0.
C_{32}	450.878	0.	0.	0.	0.	0.	0.
C_{33}	464.905	0.	0.	0.	0.	0.	0.
C_{34}	478.932	0.	0.	0.	0.	0.	0.
C_{35}	492.959	0.	0.	0.	0.	0.	0.
C_{36}	506.986	0.	0.	0.	0.	0.	0.
C_{36+}	563.094	0.	0.	0.	0.	0.	0.
Density						0.1852 gm/cm^3	
Viscosity						0.0341 cp	

Table 2.1-9. Phase Compositions and Properties for N_2 Plus Maljamar Crude Oil at 4950 psia and 120°F: Lower Phase Analysis.

	MW	GAS		LIQUID		TOTAL	
		Mass Fraction	Mole Fraction	Mass Fraction	Mole Fraction	Mass Fraction	Mole Fraction
N_2	28.000	0.7961	0.9224	0.	0.	0.0332	0.2072
C_1	16.043	0.	0.	0.	0.	0.	0.
C_2	30.070	0.	0.	0.	0.	0.	0.
C_3	44.097	0.	0.	0.	0.	0.	0.
C_4	58.120	0.	0.	0.	0.	0.	0.
C_5	72.151	0.0667	0.0300	0.0053	0.0159	0.0078	0.0190
C_6	86.178	0.0596	0.0224	0.0150	0.0375	0.0168	0.0341
C_7	100.204	0.0776	0.0251	0.0500	0.1078	0.0511	0.0892
C_8	114.231	0.	0.	0.0530	0.1003	0.0508	0.0777
C_9	128.258	0.	0.	0.0575	0.0969	0.0551	0.0751
C_{10}	142.285	0.	0.	0.0522	0.0794	0.0501	0.0615
C_{11}	156.312	0.	0.	0.0397	0.0550	0.0381	0.0426
C_{12}	170.339	0.	0.	0.0440	0.0558	0.0422	0.0433
C_{13}	184.366	0.	0.	0.0395	0.0464	0.0379	0.0359
C_{14}	198.393	0.	0.	0.0265	0.0289	0.0254	0.0224
C_{15}	212.420	0.	0.	0.0405	0.0412	0.0388	0.0320
C_{16}	226.447	0.	0.	0.0391	0.0373	0.0375	0.0289
C_{17}	240.474	0.	0.	0.0254	0.0228	0.0243	0.0177
C_{18}	254.501	0.	0.	0.0321	0.0272	0.0307	0.0211
C_{19}	268.528	0.	0.	0.0229	0.0184	0.0219	0.0143
C_{20}	282.555	0.	0.	0.0224	0.0171	0.0215	0.0133
C_{21}	296.582	0.	0.	0.0218	0.0159	0.0209	0.0123
C_{22}	310.609	0.	0.	0.0222	0.0154	0.0213	0.0120
C_{23}	324.636	0.	0.	0.0208	0.0139	0.0199	0.0107
C_{24}	338.663	0.	0.	0.0197	0.0126	0.0189	0.0098
C_{25}	352.690	0.	0.	0.0190	0.0116	0.0182	0.0090
C_{26}	366.717	0.	0.	0.0127	0.0075	0.0122	0.0058
C_{27}	380.743	0.	0.	0.0182	0.0103	0.0174	0.0080
C_{28}	394.770	0.	0.	0.0120	0.0066	0.0115	0.0051
C_{29}	408.797	0.	0.	0.0120	0.0063	0.0115	0.0049
C_{30}	422.824	0.	0.	0.0164	0.0084	0.0157	0.0065
C_{31}	436.851	0.	0.	0.0103	0.0051	0.0098	0.0039
C_{32}	450.878	0.	0.	0.0092	0.0044	0.0088	0.0034
C_{33}	464.905	0.	0.	0.0112	0.0052	0.0107	0.0040
C_{34}	478.932	0.	0.	0.0055	0.0025	0.0053	0.0019
C_{35}	492.959	0.	0.	0.0067	0.0029	0.0064	0.0023
C_{36}	506.986	0.	0.	0.0033	0.0014	0.0032	0.0011
C_{36+}	563.094	0.	0.	0.2140	0.0822	0.2051	0.0637
Density						0.8422 gm/cm^3	
Viscosity						2.9794 cp	

Table 2.1-10. Phase Compositions and Properties for N_2 Plus Maljamar Crude Oil at 4950 psia and 120°F: Upper Phase Analysis.

	MW	GAS		LIQUID		TOTAL	
		Mass Fraction	Mole Fraction	Mass Fraction	Mole Fraction	Mass Fraction	Mole Fraction
N_2	28.000	0.9866	0.9955	0.	0.	0.9866	0.9955
C_1	16.043	0.	0.	0.	0.	0.	0.
C_2	30.070	0.	0.	0.	0.	0.	0.
C_3	44.097	0.	0.	0.	0.	0.	0.
C_4	58.120	0.	0.	0.	0.	0.	0.
C_5	72.151	0.0048	0.0019	0.	0.	0.0048	0.0019
C_6	86.178	0.0038	0.0012	0.	0.	0.0038	0.0012
C_7	100.204	0.0048	0.0014	0.	0.	0.0048	0.0014
C_8	114.231	0.	0.	0.	0.	0.	0.
C_9	128.258	0.	0.	0.	0.	0.	0.
C_{10}	142.285	0.	0.	0.	0.	0.	0.
C_{11}	156.312	0.	0.	0.	0.	0.	0.
C_{12}	170.339	0.	0.	0.	0.	0.	0.
C_{13}	184.366	0.	0.	0.	0.	0.	0.
C_{14}	198.393	0.	0.	0.	0.	0.	0.
C_{15}	212.420	0.	0.	0.	0.	0.	0.
C_{16}	226.447	0.	0.	0.	0.	0.	0.
C_{17}	240.474	.0.	0.	0.	0.	0.	0.
C_{18}	254.501	0.	0.	0.	0.	0.	0.
C_{19}	268.528	0.	0.	0.	0.	0.	0.
C_{20}	282.555	0.	0.	0.	0.	0.	0.
C_{21}	296.582	0.	0.	0.	0.	0.	0.
C_{22}	310.609	0.	0.	0.	0.	0.	0.
C_{23}	324.636	0.	0.	0.	0.	0.	0.
C_{24}	338.663	0.	0.	0.	0.	0.	0.
C_{25}	352.690	0.	0.	0.	0.	0.	0.
C_{26}	366.717	0.	0.	0.	0.	0.	0.
C_{27}	380.743	0.	0.	0.	0.	0.	0.
C_{28}	394.770	0.	0.	0.	0.	0.	0.
C_{29}	408.797	0.	0.	0.	0.	0.	0.
C_{30}	422.824	0.	0.	0.	0.	0.	0.
C_{31}	436.851	0.	0.	0.	0.	0.	0.
C_{32}	450.878	0.	0.	0.	0.	0.	0.
C_{33}	464.905	0.	0.	0.	0.	0.	0.
C_{34}	478.932	0.	0.	0.	0.	0.	0.
C_{35}	492.959	0.	0.	0.	0.	0.	0.
C_{36}	506.986	0.	0.	0.	0.	0.	0.
C_{36+}	563.094	0.	0.	0.	0.	0.	0.
Density						0.2973 gm/cm^3	
Viscosity						0.0321 cp	

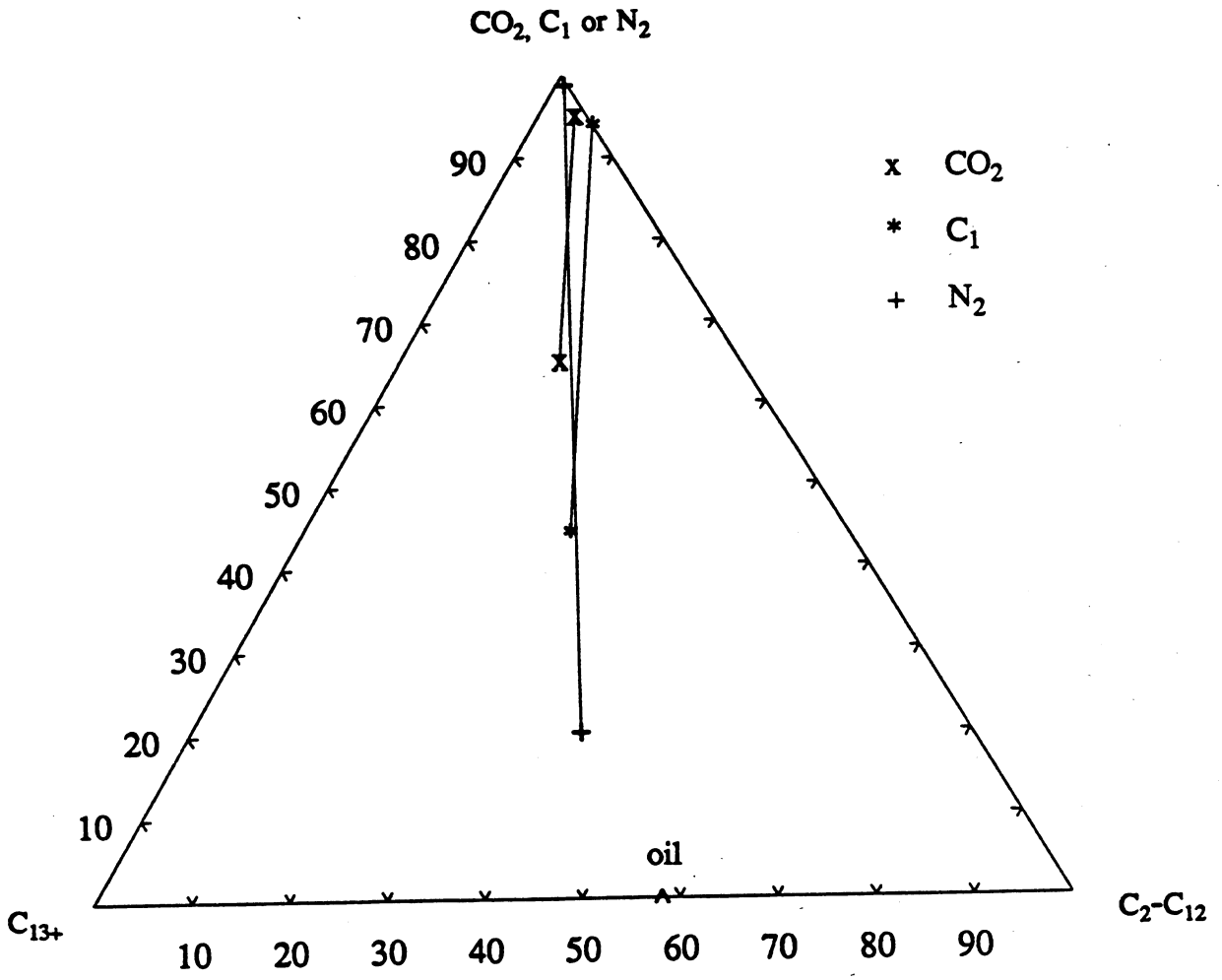

Fig. 2.1-5. Compositions of the upper and the lower phases for the Maljamar crude oil-CO_2 (X), Maljamar crude oil-C_1 (*) and Maljamar crude oil-N_2 (+) systems at 120°F and 1520, 3790 and 4950 psia, respectively.

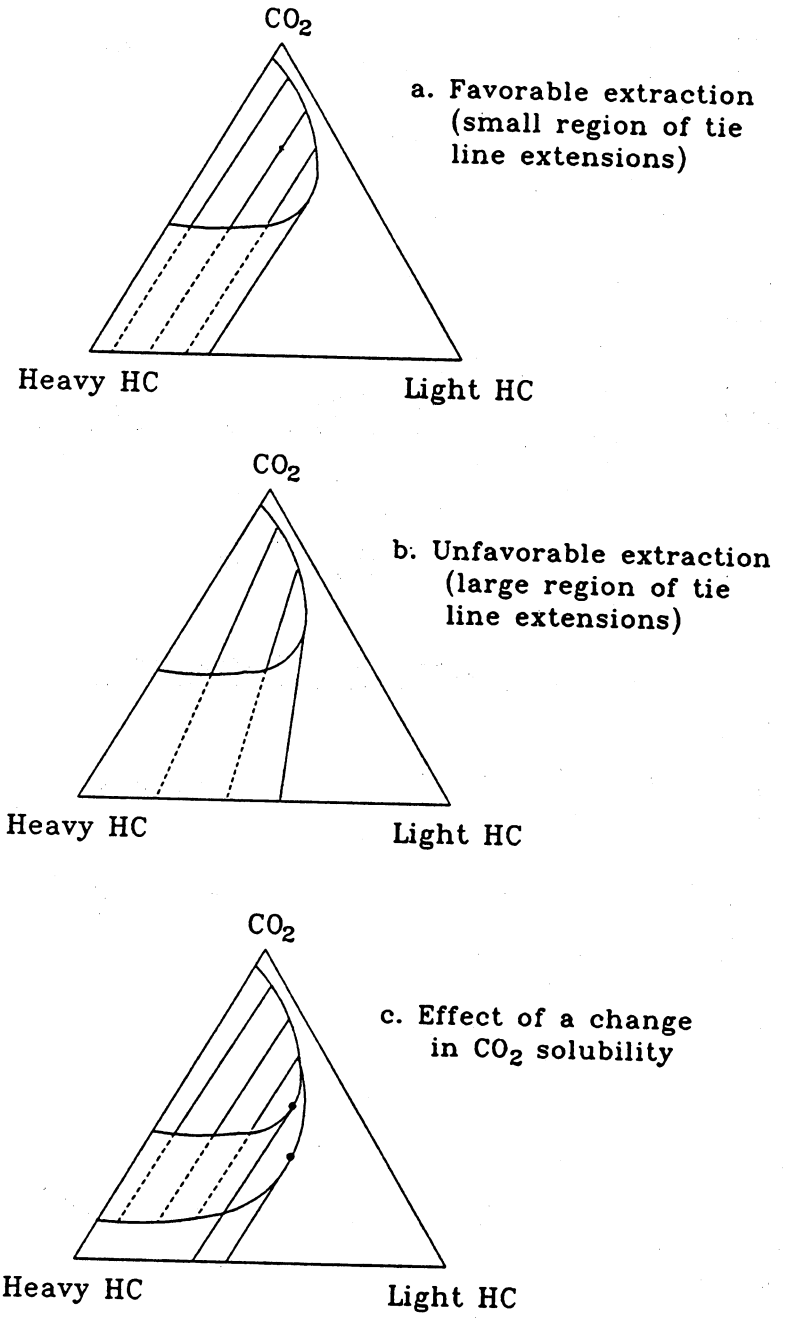

Fig. 2.1-6. Effect of the variations in the slope of the tie lines and of the change in CO_2 solubility.

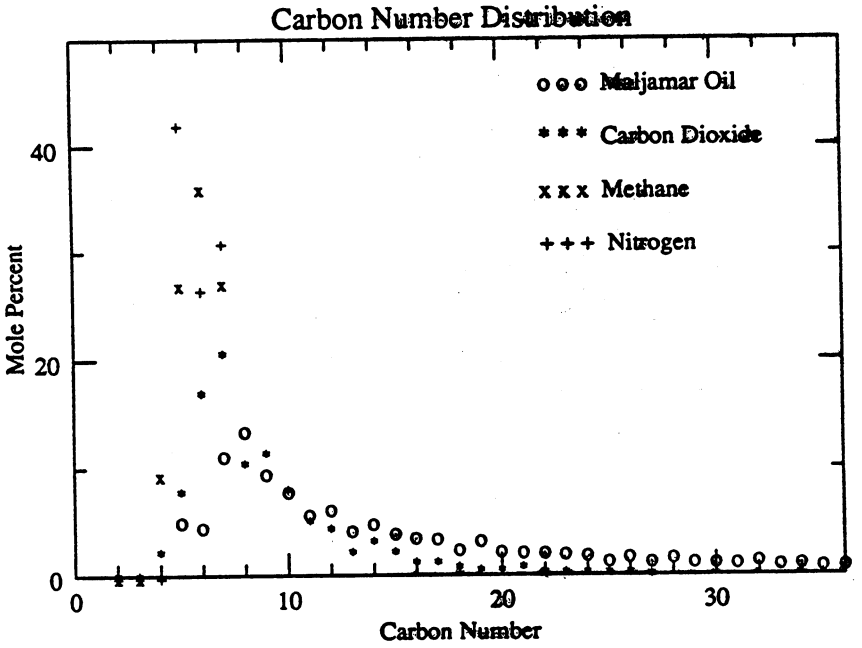

(a) Upper phases

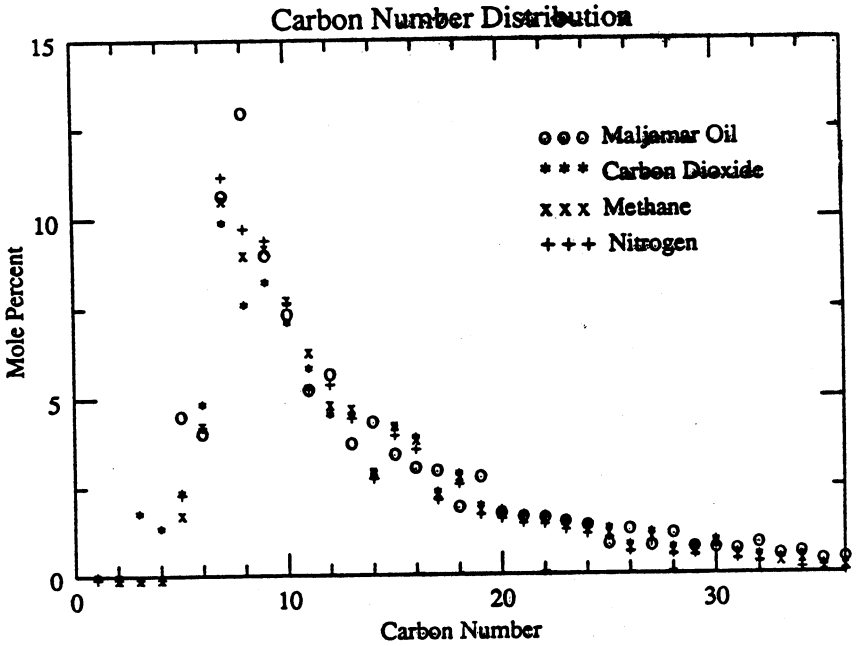

(b) Lower phases

Fig. 2.1-7. Carbon number distributions for the phases formed by the contact of Maljamar crude oil with CO_2, C_1 and N_2 at 120°F and 1520, 3790 and 4950 psia, respectively.

Additional evidence of the effects of extraction and solubility is shown in Fig. 2.1-8, a comparison of fluid properties of the equilibrium phases. The viscosity of the CO_2-rich phase is nearly three times that of pure CO_2 at the same conditions (0.036 cp, Klins 1984). C_1 and N_2, however, show values much closer to the corresponding pure component values (N_2: 0.028 cp; C_1: 0.0214 cp; Vargaftik 1975). Thus the presence of the larger, heavier hydrocarbon molecules in the CO_2-rich phase increases its viscosity substantially more than the light hydrocarbons extracted by methane.

Lower phase viscosities were also affected by the amount of dissolved solvent as Fig. 2.1-8 also indicates. The viscosity of the oil saturated with N_2 was close to that of the original oil (3.1 cp at atmospheric pressure). The larger quantities of dissolved C_1 and CO_2 caused significantly lower oil-rich phase viscosities. For CO_2, at least, the reduction in oil phase viscosity and the increase in vapor phase viscosity causes the viscosity ratio to be only 7.7 compared to approximately 85 for the pure oil and pure CO_2.

Fig. 2.1-9 shows a comparison of phase densities. Again, the CO_2-oil phase densities differ much less than those of the other systems.

The qualitative arguments presented in this section can be made much more quantitative. In Chapter 3, we return to the question of composition path and examine in some detail the effects of the changes in oil composition on displacement composition routes.

2.2 Supercritical Fluid Chromatography for Crude Oil Characterization

Maurice P. Stadler and Milind D. Deo

In supercritical fluid chromatography (SFC), separation of components in a mixture is performed using a relatively dense supercritical fluid as a carrier. In this section we describe chromatography experiments using supercritical CO_2. Since it is supercritical extraction by CO_2 that is the basis for CO_2 miscible flooding, SFC should provide direct information of use in the characterization of crude oils for CO_2 flooding. SFC offers rapid analysis of crude oil mixtures because hydrocarbons partition more efficiently into dense CO_2 than into helium or nitrogen, typical carriers in gas chromatography (GC). The new equipment is being used to characterize oils for miscible flooding, to examine how hydrocarbons partition into dense CO_2 as a function of molecular size and type, and to study how elution behavior is related to minimum miscibility pressure. The recently acquired SFC equipment and the current experimental results are discussed in this section.

2.2.1 SFC Apparatus

The apparatus, supplied by Applied Biosystems, is basically a GC which has been modified to accept supercritical CO_2 as the carrier fluid. This is done by placing a pump between the CO_2 supply vessel and the injection port. A schematic diagram of the entire apparatus is shown in Fig. 2.2-1.

The gas chromatograph used is a Hewlett-Packard Model 5890. A flame ionization detector is used to analyze the material eluted from the column. This type of detector is ideal for analyzing hydrocarbons with a CO_2 carrier fluid because hydrocarbons burn easily whereas CO_2 does not.

An SFC MicroGradient System pump (Applied Biosystems) delivers the CO_2 at high pressures. This pump is designed to deliver fluids accurately at low flow rates. The pump consists of two 10 ml syringe pump cylinders. An important feature of the pump is that it can be pressure programmed, which is equivalent to temperature programming in GC. The pump

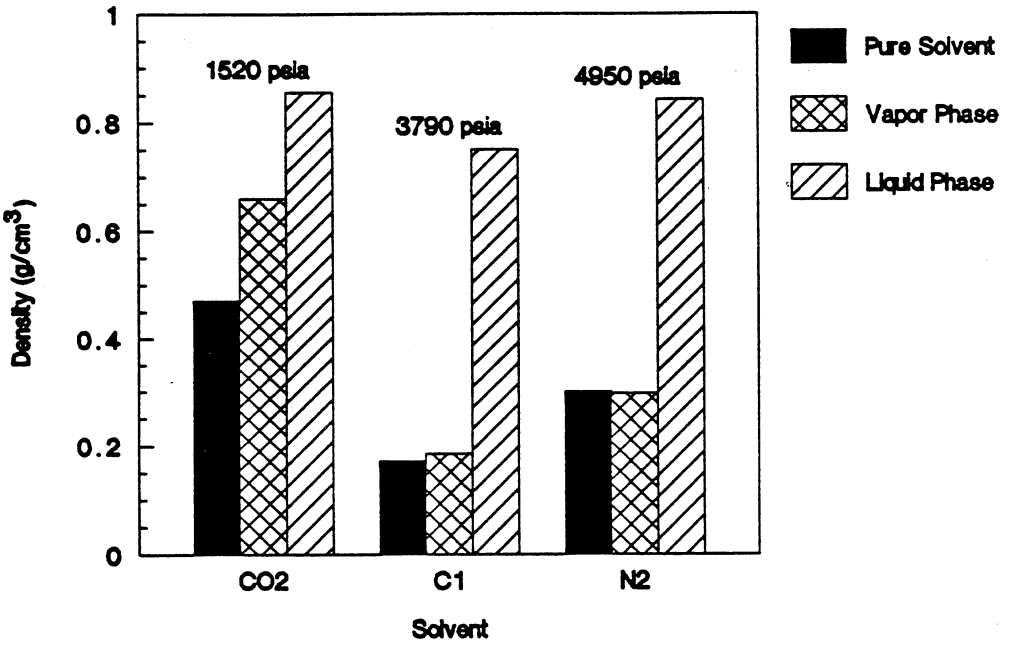

Fig. 2.1-8. Comparison of the densities of the vapor and liquid phases formed by the contact of Maljamar crude oil with CO_2, C_1 and N_2 at 120°F and 1520, 3790 and 4950 psia respectively with the pure solvent densities.

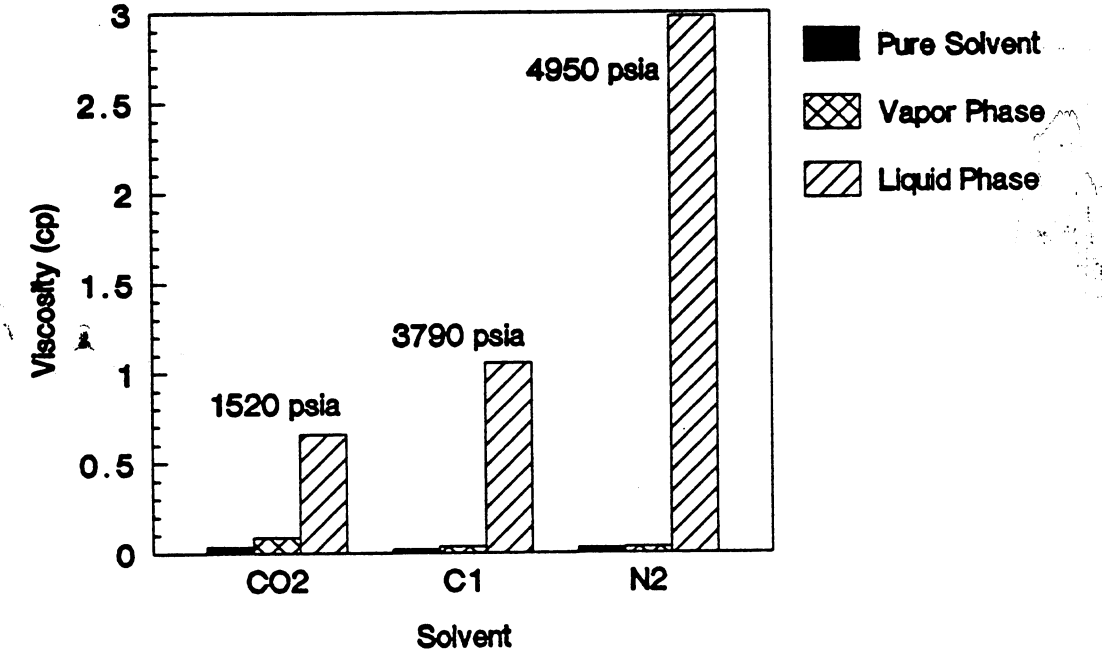

Fig. 2.1-9. Comparison of the viscosities of the vapor and liquid phases formed by the contact of Maljamar crude oil with CO_2, C_1 and N_2 at 120°F and 1520, 3790 and 4950 psia respectively with the pure solvent viscosities.

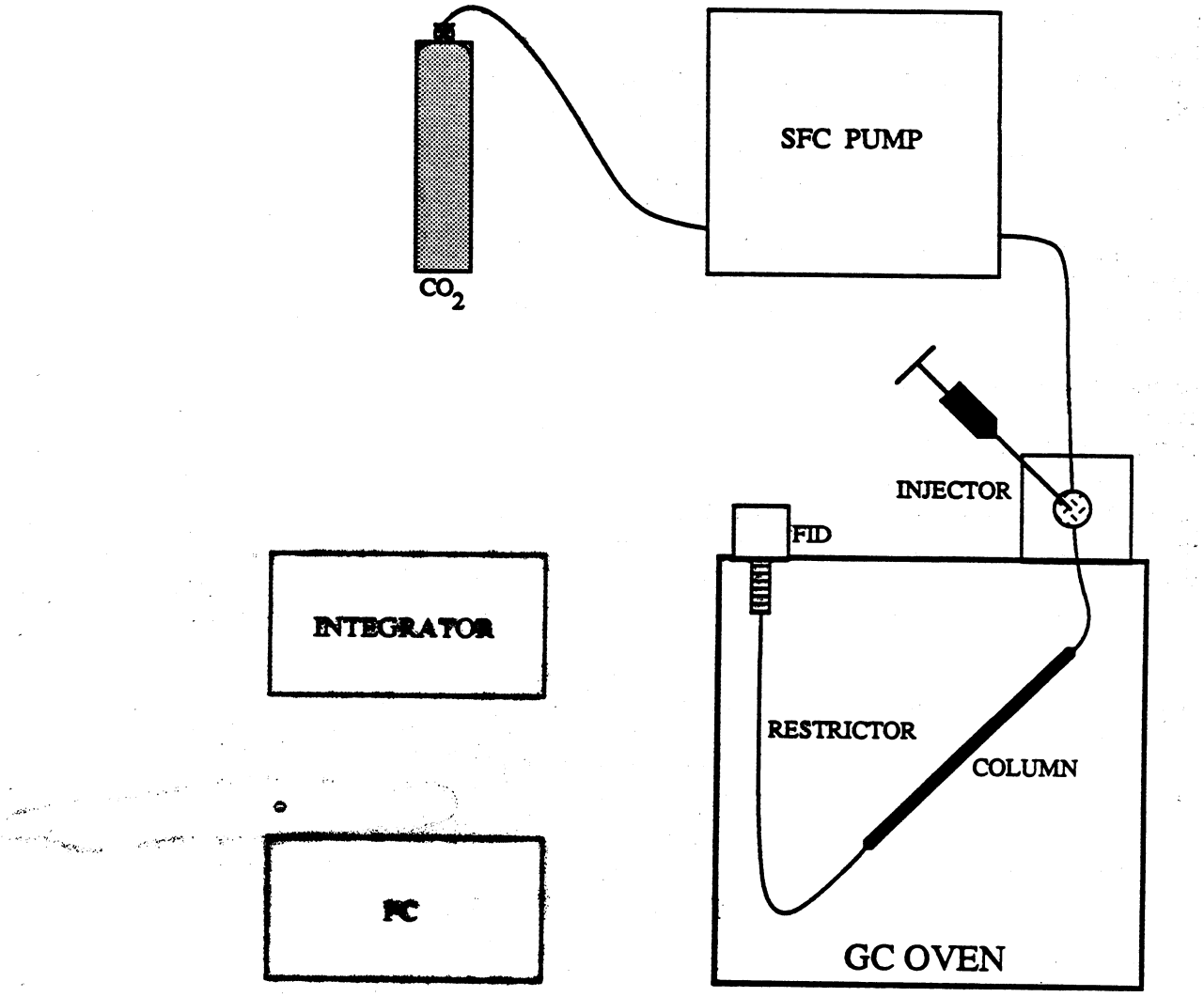

Fig. 2.2-1 SFC Apparatus (Plumbing).

is programmed in steps. At each step, a time and pressure are specified. The pump calculates a linear gradient between each of the steps and delivers the fluid at the calculated pressure. The maximum allowable pressure is 5500 psia.

The injector is a Valco Model C14W manual injection valve. The column (Polysiloxane PM, 20 cm x 1.0 mm) was also supplied by Applied Biosystems. This type of column was chosen because it is relatively inert with respect to hydrocarbons. The column is connected to the detector through a restrictor, which is a 40 cm x .050 mm ID fused silica capillary. For this study, a Hewlett-Packard 3396A Integrator was used.

In order to facilitate the lab work, the experiments and data acquisition were partially automated by linking the components electronically. A schematic of this networking is shown in Fig. 2.2-2. The various parts of this network are described below.

The HP 3396A Integrator and the HP 5890 GC are linked via the Instrument Network (INET). INET digitally transfers the raw detector data to the integrator. Also, the integrator can control all of the setpoints (oven temperature, detector temperature, etc.) of the GC.

The pump also has features for networking. The rear panel of the pump has relays for activating four external devices. Two of these events are used in this study, one for activating the injector and one for remote starting the integrator. These two events are included in the pump pressure program and start at exactly the same time.

Finally, the integrator is linked to an IBM Personal Computer AT through an RS232C port. This is done in order to store the chromatographic runs on the hard drive of the PC since the memory of the integrator is limited. In other words, the PC is simply used as an external disc drive. A file server program was acquired from HP so that files can be transferred from the integrator to the PC and vice versa.

2.2.2 Partitioning of Hydrocarbons into Dense CO_2

The first SFC experiments performed examine the partitioning of hydrocarbons into CO_2. (Some of these experiments were performed at the Applied Biosystems lab in Santa Clara, California, before the purchase of the equipment just described. However, the lab setup there was very similar.)

At a given flow velocity of the carrier, elution time for a component is directly related to how efficiently it is extracted into the carrier. In typical gas chromatography, elution of heavy components is accomplished by increasing the temperature, which increases the volatility of the hydrocarbons. In SFC, the pressure is increased rather than the temperature. The corresponding increase in CO_2 density causes heavy hydrocarbons to be extracted more efficiently. Fig. 2.2-3 shows the chromatogram obtained for a standard mixture of alkanes (C_5 through C_{40}). The pressure program used in this run is shown in Fig. 2.2-4. As Fig. 2.2-3 shows, hydrocarbons up to carbon number 40 elute in only 19 minutes, about twice as fast as in standard simulated distillation with temperature programming at 30°C/min on an OV-101 column. Fig. 2.2-5 shows the chromatogram for Maljamar crude run under the same conditions used to generate Fig. 2.2-3.

Fig. 2.2-6 illustrates the effect of CO_2 density on elution time. In the three experiments described in Fig. 2.2-6, the pressure was initially held constant. When additional elution of hydrocarbons was observed to be small, the pressure was increased to 5000 psia to remove remaining hydrocarbons from the column. The large peaks at the tail of the runs shown for 1600 and 1800 psia were the result of that pressure increase. As Fig. 2.2-6 shows, the amount of hydrocarbons that eluted at the end of the run decreased dramatically as the density of CO_2 increased from 0.51 g/cm^3 to 0.67 g/cm^3. At the highest density, essentially all the hydrocarbons eluted in one large peak at the beginning of the chromatogram. At the lower densities, individual peaks can be recognized. Thus, elution time of a given hydrocarbon is clearly related to the density of the CO_2 carrier.

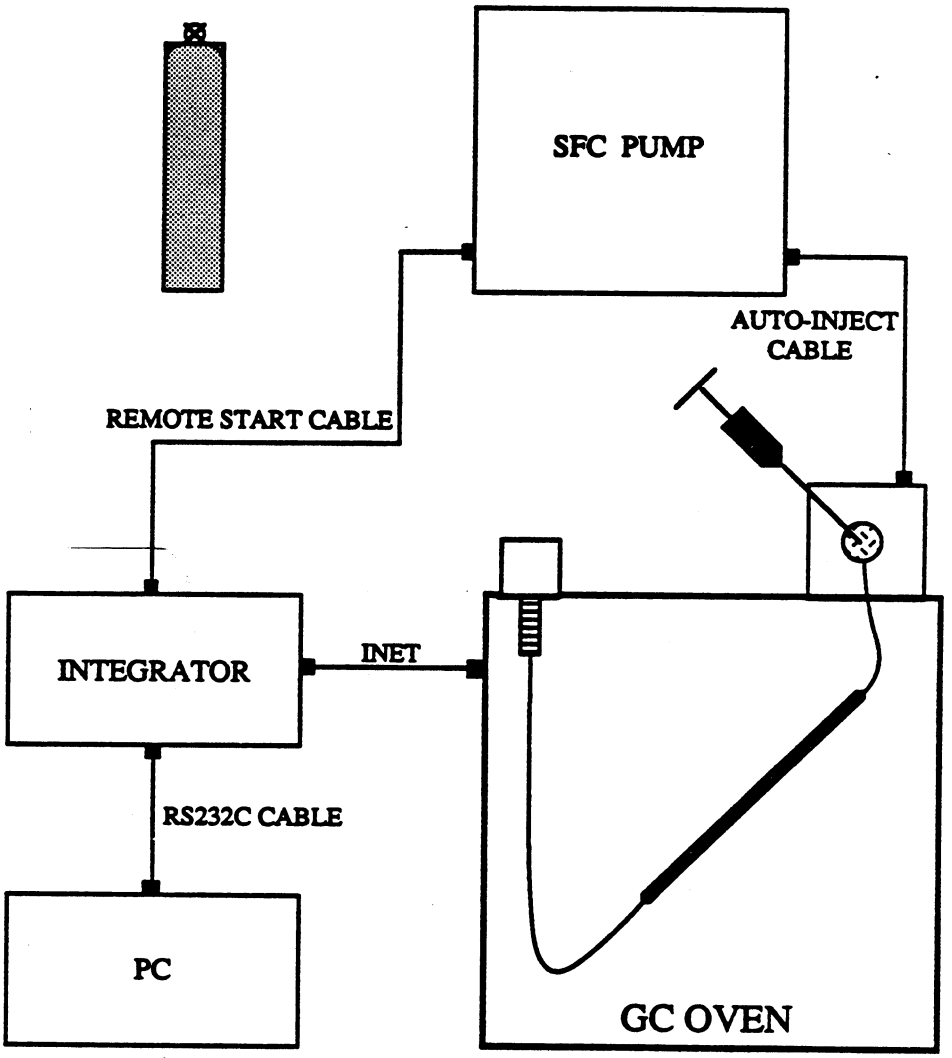

Fig. 2.2-2 SFC Apparatus (Networking).

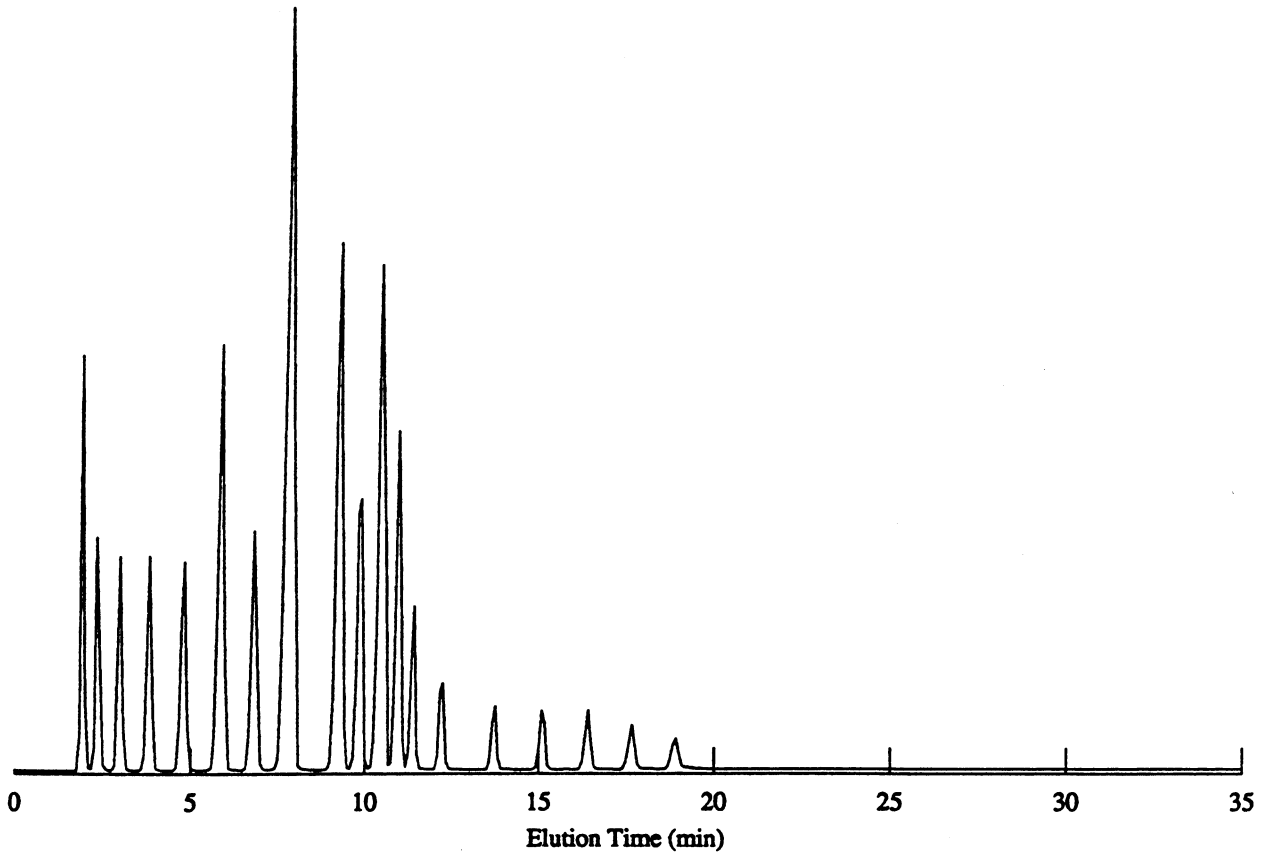

Fig. 2.2-3 SFC chromatogram for a normal alkane mixture.

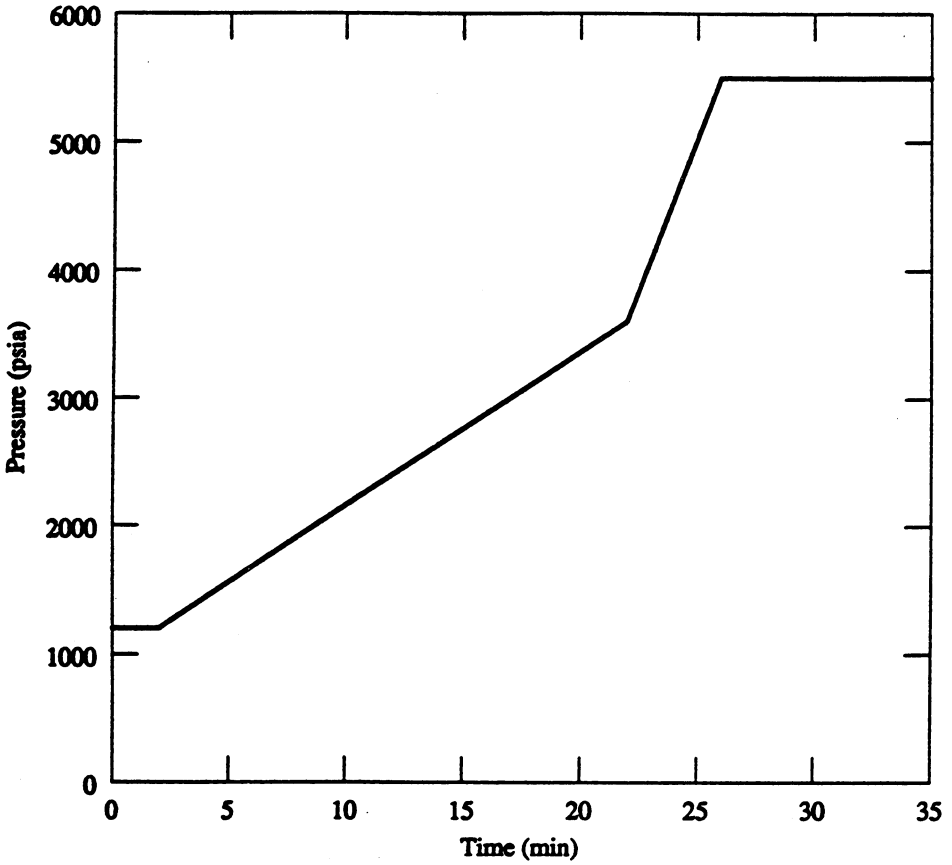

Fig. 2.2-4 Pressure history for Figs. 2.2-3, 2.2-5, and 2.2-7.

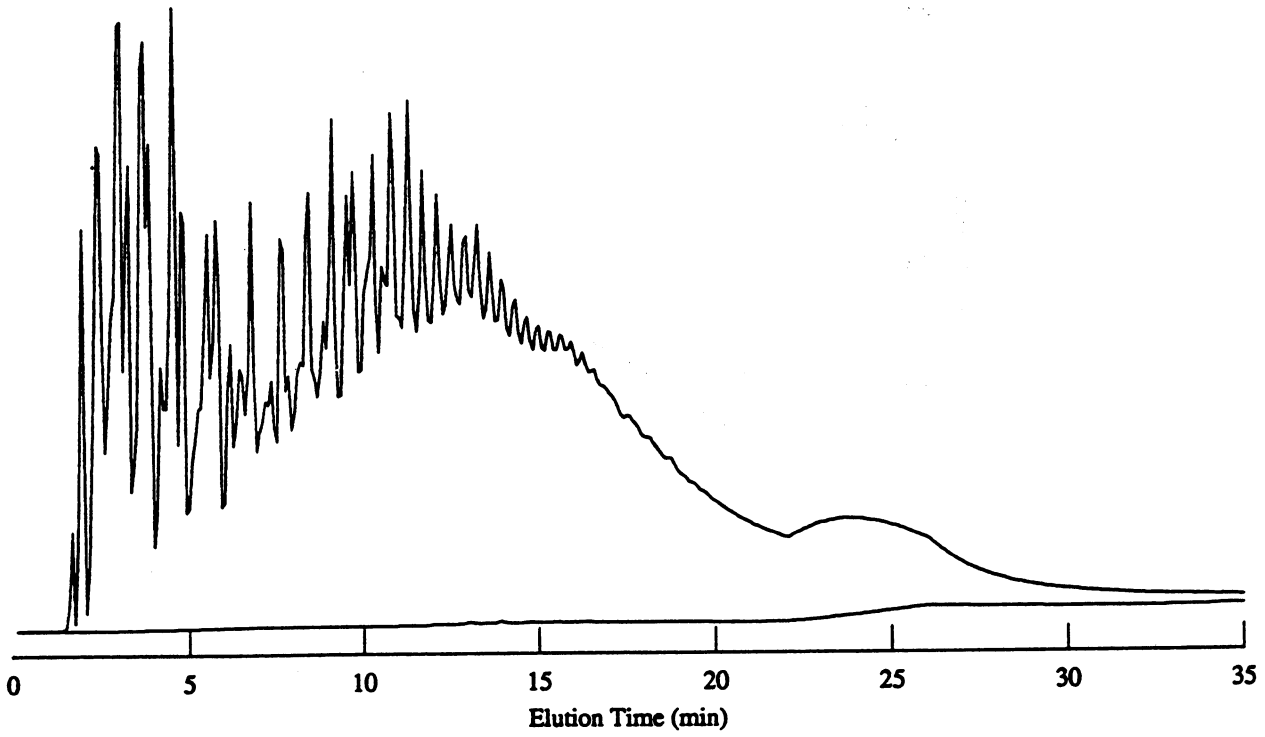

Fig. 2.2-5 SFC chromatogram for Maljamar crude oil.

Maljamar Crude Oil

p = 1600 psig	p = 1800 psig	p = 2000 psig
T = 50 °C	T = 50 °C	T = 50 °C
ρ_{CO_2} = .51 g/ml	ρ_{CO_2} = .61 g/ml	ρ_{CO_2} = .67 g/ml

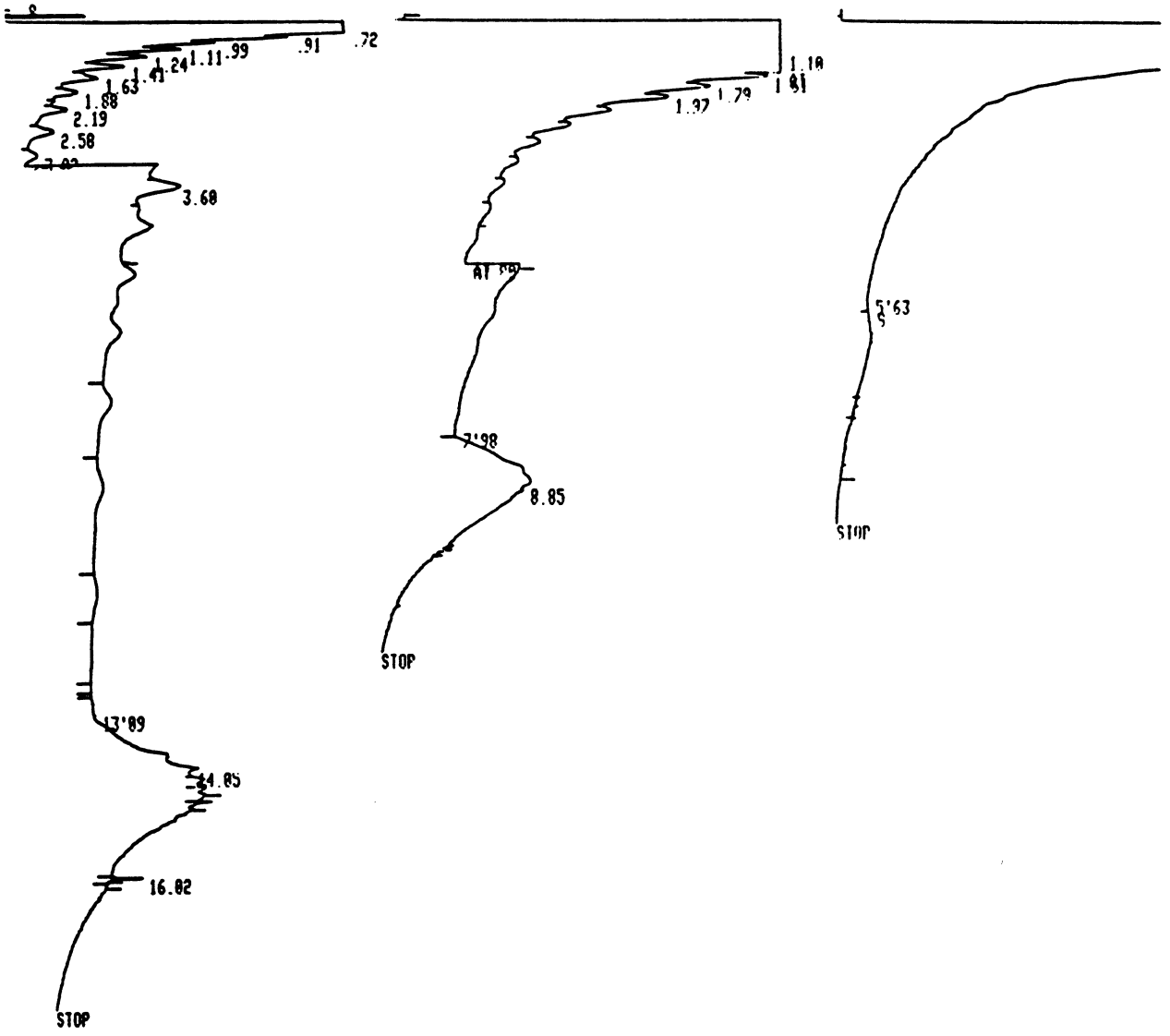

Fig. 2.2-6 Effect of CO_2 density on elution of hydrocarbons.

2.2.3 Compositional Analysis

The next experiments performed were analyses of the carbon number distribution of crude oils. Carbon number distributions were estimated using a technique that is a simplification of simulated distillation (SIMDIS), a method currently used to analyze crude oils.

SIMDIS is a procedure which determines the boiling-point distribution of a crude oil and is described in detail in ASTM D2887 (1986). SIMDIS is an alternative to classical distillation and uses GC with a temperature ramp to analyze a crude oil. Three chromatographic runs are necessary. First, a known hydrocarbon sample is run and a calibration curve (boiling point versus retention time) is made. Next, the crude oil sample is run. Finally, a known amount of a known hydrocarbon mixture (internal standard) is added to the crude oil, and this sample is analyzed. This last run is necessary in order to allow calculation of the total amount of crude oil eluted had all of it passed through the column. It is not possible to elute all of the crude oil because hydrocarbons crack at about 540°C, which is too low of a temperature to boil the heavy fractions. The boiling-point range of the crude oil is determined by comparing the crude oil chromatogram to the calibration curve.

SIMDIS by SFC is a good alternative to GC-SIMDIS because high temperatures are not needed to elute the heavy hydrocarbons. In SFC, a pressure ramp replaces the temperature ramp. Schwartz (1988) has shown that SFC-SIMDIS is feasible using packed columns (as opposed to capillary columns) similar to those used in this study. Some of the advantages of packed column analysis are that it is fast, can analyze components up to C_{100} with good reproducibility and quantitation, and does not require flow splitting or dilution. Results compare favorably with other methods of analyzing crudes (capillary SFC and thermogravimetric analysis).

However, an even simpler method of analyzing crudes should be possible. As described in the previous section, the amount of hydrocarbons eluted is proportional to the density (or pressure) of the CO_2. Thus, if the pressure is high enough, almost all of the crude oil can be eluted. If all or almost all of the crude oil is eluted, then the third run of the SIMDIS procedure (crude oil plus internal standard) is not necessary because the total amount of crude oil eluted is measured directly. In this case, the analysis of the crude oil reduces to comparison of the crude oil chromatogram to the hydrocarbon standard chromatogram. This procedure is much simpler and reduces the number of sources of experimental error.

Experiments performed on Maljamar crude oil verify this idea. A series of chromatograms necessary for the SIMDIS analysis were produced. First, a hydrocarbon standard was run and is shown in Fig. 2.2-3. This standard contains hydrocarbons ranging from C_5 to C_{40}. As before, the pressure program for this and all of the chromatograms to follow is shown in Fig. 2.2-4. The pressure is increased more sharply after 22 minutes because at this point, the last hydrocarbon in the standard (C_{40}) has been eluted and no more resolution of the chromatogram is necessary. All of the oil eluted past the elution time of C_{40} is just lumped into a C_{41}+ fraction. The pressure is held constant at 5500 psia because this is the maximum safe pressure of the SFC equipment.

Also, three crude oils and three crude oils with the internal standard (C_{14}, C_{15}, C_{16}, and C_{17}) were run through the SFC. A typical example from each group is shown in Figs. 2.2-5 and 2.2-7. The baseline is also shown in these figures. It seems evident that almost all of the oil is eluted since the chromatograms almost reach the baseline. To verify this, each of the crude runs was analyzed with each of the crude plus internal standard runs for a total of nine different analyses. For each combination, the total amount of crude oil calculated using the SIMDIS procedure was compared to the actual amount of crude eluted. The average absolute difference between the two amounts was 1.6%, and the maximum difference was 3.9%. Thus, comparison of the crude oil chromatogram to the hydrocarbon standard chromatogram is essentially equivalent to the full SIMDIS analysis since the total amount of crude oil used in the calculations is the same to within an experimental error typical of SIMDIS analyses.

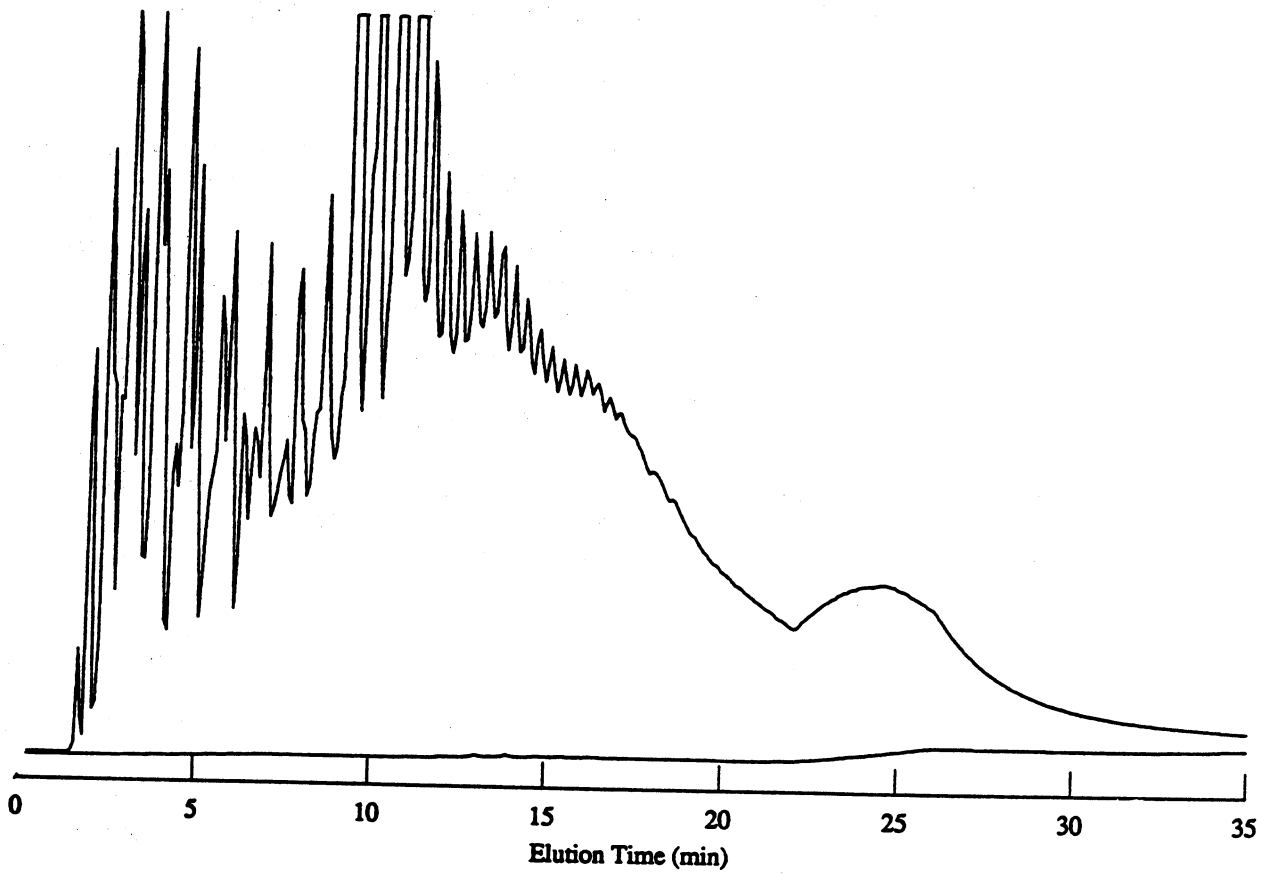

Fig. 2.2-7 SFC chromatogram for Maljamar crude oil plus internal standard.

Fig. 2.2-8 shows the hydrocarbon distribution of Maljamar crude oil obtained by both the GC and SFC analyses. The results from each type of chromatography agree reasonably well. The two curves scatter about each other, but otherwise appear to be consistent.

Additional experiments to verify that the SFC analytical procedure can be used with confidence will be performed with other crude oils. In addition, the question of whether MMP information can be obtained by SFC measurements of extraction efficiency is under investigation, as is the idea that it may be possible to obtain binary interaction parameters from elution time data.

2.3 Mass Spectrometry for the Analysis of Crude Oils

Milind D. Deo, Mustafa Yilmaz and Karen D. Hagedorn

The composition data reported in Section 2.1 for the hydrocarbons extracted by dense CO_2 were obtained by simulated distillation (SIMDIS). That technique gives an indication of the range of molecular sizes present in a mixture, but it does not allow direct identification of specific compounds. Thus, it cannot be used to answer questions about which types of hydrocarbon molecules, alkanes, naphthenes or aromatics, are extracted more efficiently. In this section, we describe the preliminary measurements that can be used to study those questions.

The resolution of capillary gas chromatography (GC) and the identification capability of mass spectrometry (MS) can yield composition information of extraordinary detail. The GC-MS technique is a well established procedure for the quantification of the crude oil compositions (Flory et al. 1978, Zadro et al. 1985), trace compound analysis in environmental and pharmaceutical applications and in the study of biomarkers (Moldowan et al. 1985). The objective of the current set of GC-MS experiments is to determine detailed compositions of crude oils and to measure which of those compounds appear in substantial quantities in phases obtained by contacting the crude with CO_2, C_1 and N_2.

The information will be useful as an independent check on other chromatography techniques, such as the SIMDIS measurements of Section 2.1 or the SFC results of Section 2.2., used for the characterization of the crude. The data obtained will also be useful in the study of lumping techniques for equation of state computations and continuous thermodynamic representation of phase equilibrium.

Analysis of the samples obtained in the experiments described in Section 2.1 will help us understand the effect of chemical type and the distribution of hydrocarbons on the extraction process.

2.3.1 Experimental Equipment and Procedures

The experiments were performed on a Finnigan GC-MS system, model MAT TSQ 70, acquired with funds from the 1987 DOE University Instrumentation Program. The Finnigan MAT TSQ 70 is a high-sensitivity analytical instrument composed of one or more inlet systems, a triple quadrupole mass spectrometer, and a data system (Fig. 2.3-1). A VARIAN 3400 gas chromatograph with a 25 m capillary column is the inlet system. For the experiments described below, the stationary phase in the capillary column was DB-5. Various injection modes including the split/splitless injection are available on the GC.

The mass spectrometer consists of an ion source, an analyzer assembly, and an electron multiplier housed in a vacuum manifold. The other important components of the instrument are the two turbomolecular pumps, two rotary-vane pumps and the electronics cage that operates the instrument.

Mass analysis of a sample occurs in the analyzer assembly, which is located in an evacuated manifold. After traversing through the GC, the sample is introduced into the ion source

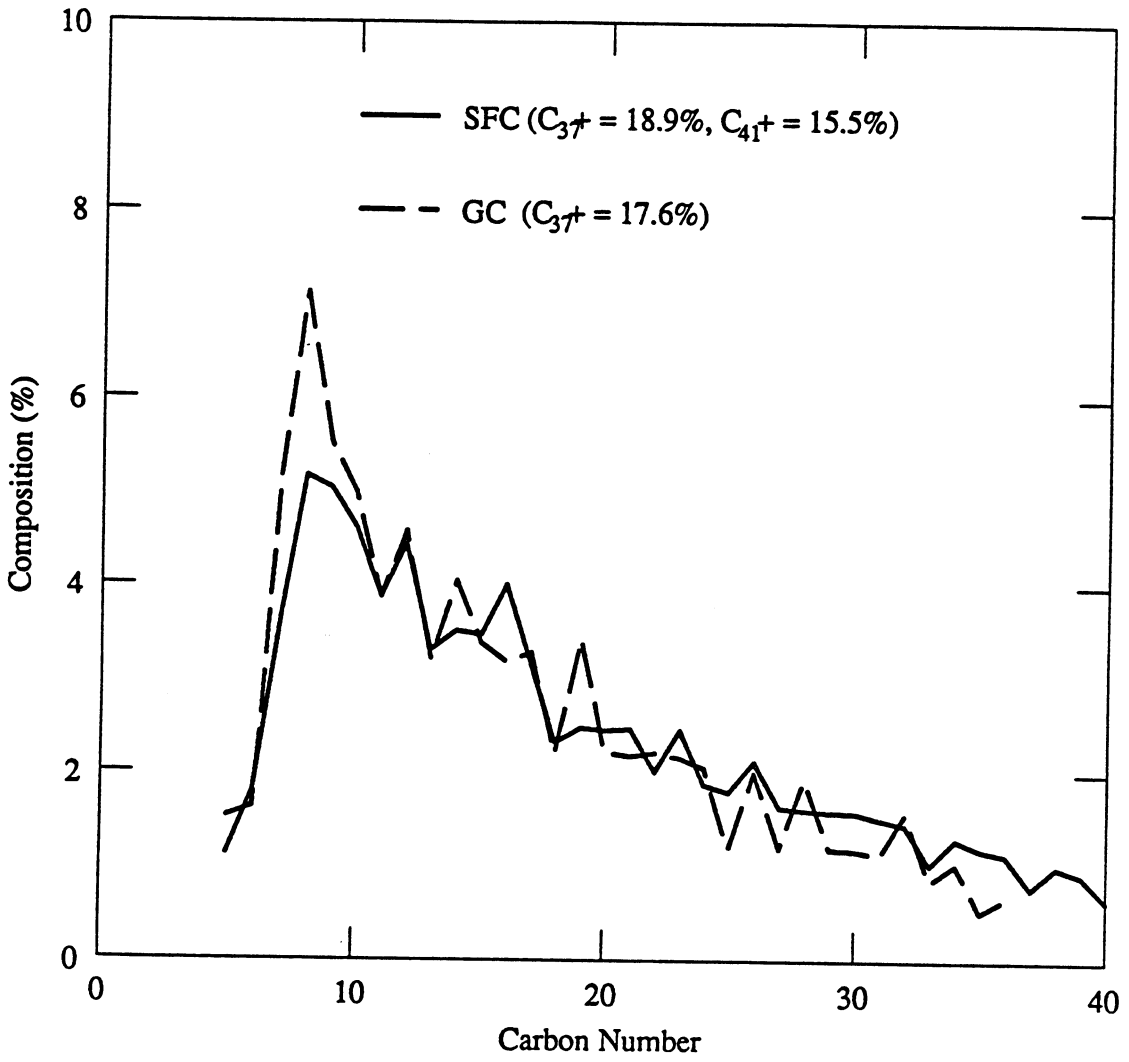

Fig. 2.2-8 Comparison of SIMDIS results for GC and SFC.

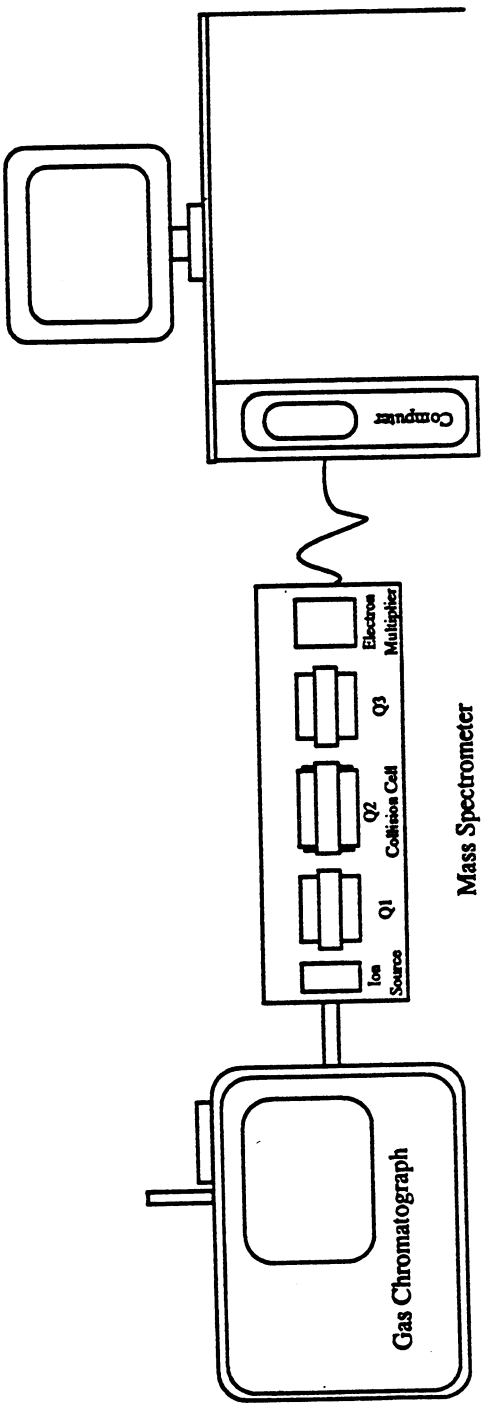

Fig. 2.3-1 Schematic diagram for the GC-MS system.

where it is ionized. The ion source generates a beam of electrons, provides a site for these electrons to interact with sample molecules to form ions, and then focuses the ions into the analyzer assembly. Here, the ions are separated by their mass-to-charge ratio and are then converted into an electrical signal that is detected by the electron multiplier. The signal is amplified and is then passed on for further processing and display.

In the experiments, EI (Electron Impact) ionization mode was employed. With EI, sample molecules interact directly with energetic electrons to produce ions. Positive ion mass spectra, with EI used to generate the positive ions, are the most commonly obtained mass spectra. The conditions for obtaining positive ion EI spectra are well standardized, and these spectra tend to contain a rich array of fragment ions. Therefore, a positive ion EI mass spectra can be used as a "fingerprint" for a compound. The other modes of ionization are CI (Chemical Ionization) and FAB (Fast Atom Bombardment).

The analyzer assembly is composed of three quadrupole rod assemblies, Q1, Q2 and Q3. In our experiments, the TSQ 70 is operated in the mass spectrometer scan mode (Q1MS), that is, only one stage of mass analysis is performed to obtain a mass spectrum. The other two quadrupole rod assemblies (Q2 and Q3) act as ion transmission devices.

All instrument control functions for the TSQ 70 are controlled from a display terminal, which is connected directly to the mass spectrometer. Acquired data are stored in and analyzed by the data system, which is also accessible from the terminal.

Operation

A calibration process, also known as tuning, is performed by using a gas which gives known peaks. These peaks are observed to check how well the instrument is tuned. If the tuning is not satisfactory, then using either an automatic procedure or a manual technique, certain parameters of the instrument are adjusted. Crude oil samples were prepared by mixing 4 microliters of the oil and 1 ml of the solvent (hexane). 0.8 micro liters of this mixture is injected through the split/splitless injection system into the column.

The mass spectrometer was operated in the Q1MS mode where the first quadrupole was scanned for m/z of 50 to 500 at intervals of 1 sec. A temperature program for the GC oven was entered at the terminal and was loaded into the GC. In that program, the initial temperature was 30°C and the oven temperature was increased to 300°C at 3°C/min. The oven was held at the final temperature for 20 minutes. The temperatures of the injector and the transfer line (leading to the MS) were set to 300°C.

2.3.2 Analysis

At each of the scans, the mass spectrometer gives the intensity of all the ions in the m/z range of the scan. Each of the resulting data files occupies as much as 25 megabytes of storage space. The software available with the data processing computer can be used to represent this data in a variety of forms. One of the most commonly used representations is the RIC (reconstituted ion chromatogram), which is a plot of total intensity vs. retention time. The RIC is the equivalent of the trace obtained in ordinary GC analyses. A typical RIC for the Maljamar crude in hexane is shown in Fig. 2.3-2. Mass fragmentograms are the responses to ions of specified m/z's. The individual spectrum at a specific scan, the intensities of all the ions that the detector sees at a particular time, can also be pulled up for analysis. The spectra are normalized with respect to the largest peak, designated the base peak.

The compounds present in a sample are usually identified by using the RIC, the mass fragmentograms and the spectra for individual compounds. The spectra for the prominent peaks are usually unique and are easily identifiable. For the less prominent peaks, this information is pieced together using the evidence from the spectra, the mass fragmentograms and libraries of spectra (EPA-NIH 1978).

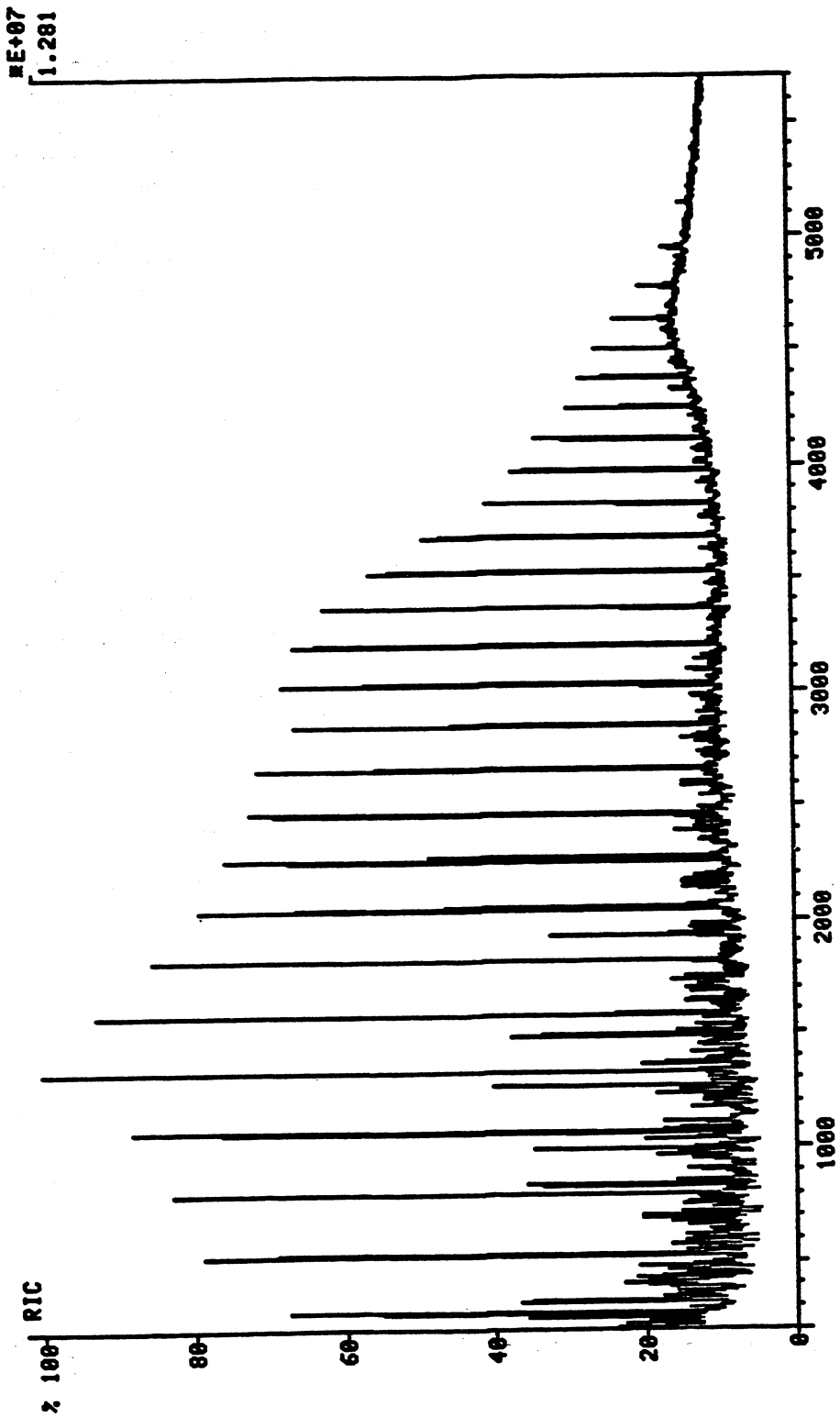

Fig. 2.3-2 Reconstituted ion chromatogram (RIC) for the Maljamar Crude Oil.

As an example, identification of the n-alkane homologous series is illustrated in Figs. 2.3-3 and 2.3-4. The spectra for the n-alkanes C_{12} - C_{nr}%+215 are shown in Fig. 2.3-3. These compounds are fragmented into smaller molecules, and the resulting spectra show a characteristic exponential decrease in intensity as m/z increases. Finally, there is a significant response to the molecular ion. In Fig 2.3.4, the responses to the molecular ions of these alkanes (mass fragmentograms) are superimposed on the RIC, establishing the identity of the series. It can be seen that the traces of these alkanes in the RIC match the respective responses of their molecular ions exactly. This technique can be used for the identification of other homologous series such as the cycloalkanes and the aromatics.

The stages in the analysis of the data obtained are listed below:

(1) Using a definite set of parameters (baseline, width of peaks, etc.), all the peaks in the RIC are quantified in terms of their percentage areas.

(2) All peaks smaller than a certain predetermined value are neglected for the purposes of analysis.

(3) The peaks that survive the screening procedure are identified by the techniques previously explained.

(4) The identified compounds are classified into various categories based on their chemical type, carbon number, molecular weight, etc.

2.3.3 Results

Maljamar crude oil was analyzed using the techniques described above. As many as 271 distinct peaks were separated, and more than 480 major paraffinic, naphthenic and aromatic hydrocarbons present in the crude were identified. Since the crude was dissolved in hexane, smaller hydrocarbons present in the crude eluted with the solvent, and it was not possible to obtain the portion of the crude eluting prior to decane. In fact, compounds up to about undecane ($C_{11}H_{24}$) arrive on the solvent tail making it difficult to quantify them accurately. The maximum temperature during the run was 300°C. The analysis was therefore limited to the number of components that eluted under these conditions. Components that would have eluted at temperatures higher than the maximum temperature used, were not accounted for. The classification of the identified compounds based on chemical type is shown in Table 2.3-1 and Fig. 2.3-5. The classification indicates that the oil is predominantly paraffinic.

In the analysis, individual compounds were identified, and, therefore, it was possible to assign carbon numbers and molecular weights to most of them. Using this information, the carbon number distribution for the crude oil can be computed directly. The carbon number distribution determined in this fashion is shown in Fig. 2.3-6. This can be compared with the distribution obtained by simulated distillation (SIMDIS) on a packed column (see Section 2.1.1). In SIMDIS, the carbon number of a given cut is assigned assuming that the normal alkane of the given carbon number is the last of the isomers to elute. The results presented by Silva and Orr (1987) indicate that this may not necessarily be true and branched alkanes may elute much earlier. The elution behavior of naphthenic and aromatic hydrocarbons of comparable carbon numbers is also not well understood. A typical SIMDIS analysis on a C_{11-}-free basis is shown in Fig 2.3-7. The SIMDIS analysis shows larger percentages of heavier hydrocarbons (C_{25} and above). This may be because higher temperatures (a maximum of 350°C) were used for the the SIMDIS method, making it possible for more of the heavier hydrocarbons to elute. Use of on-column injection in SIMDIS may also have had some effect. More data will be needed to make a quantitative comparison of carbon number distributions obtained by SIMDIS with distributions obtained directly from GC-MS data.

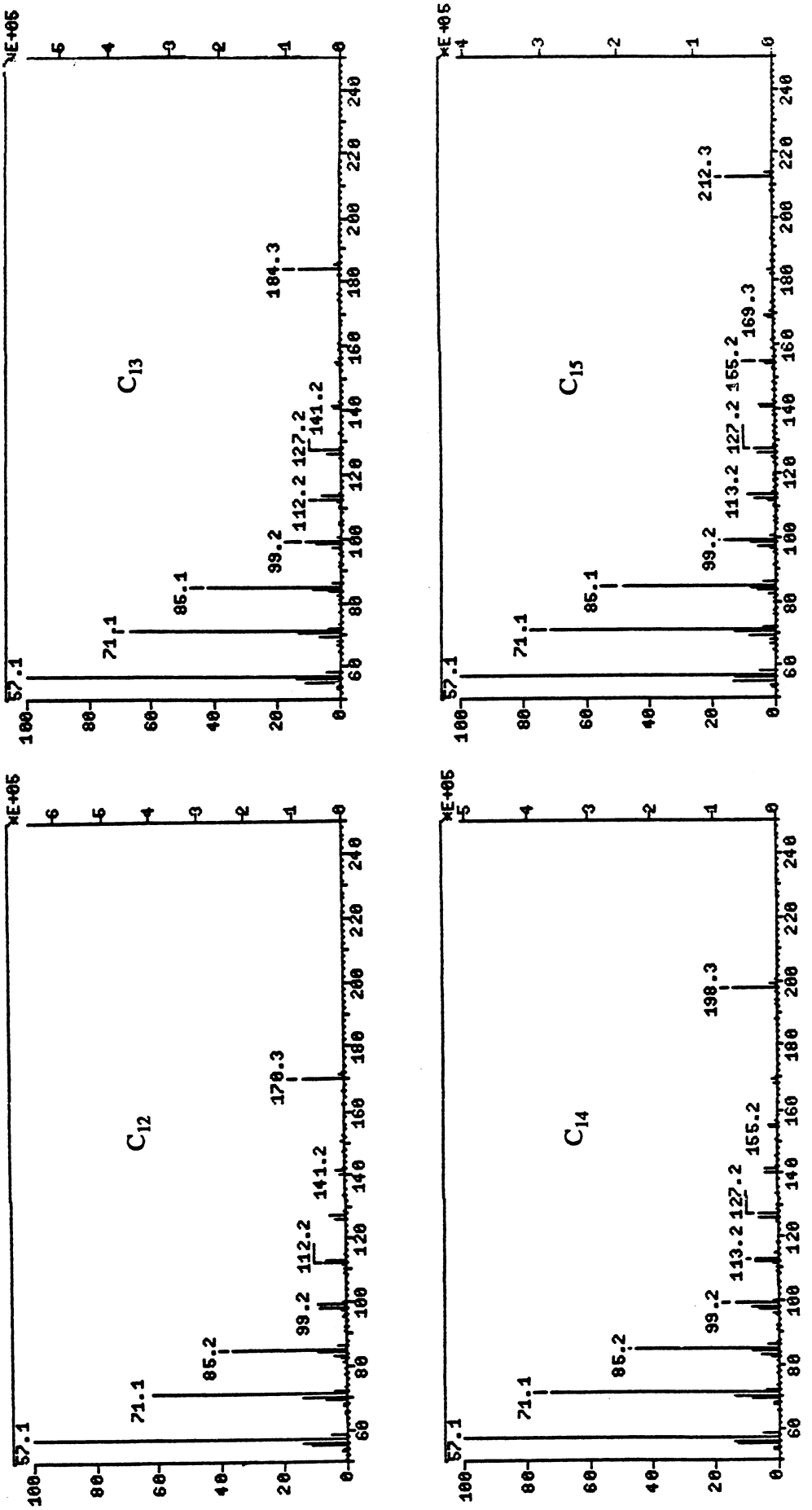

Fig. 2.3-3 Mass spectra of n-C_{12}, n-C_{13}, n-C_{14} and n-C_{15}.

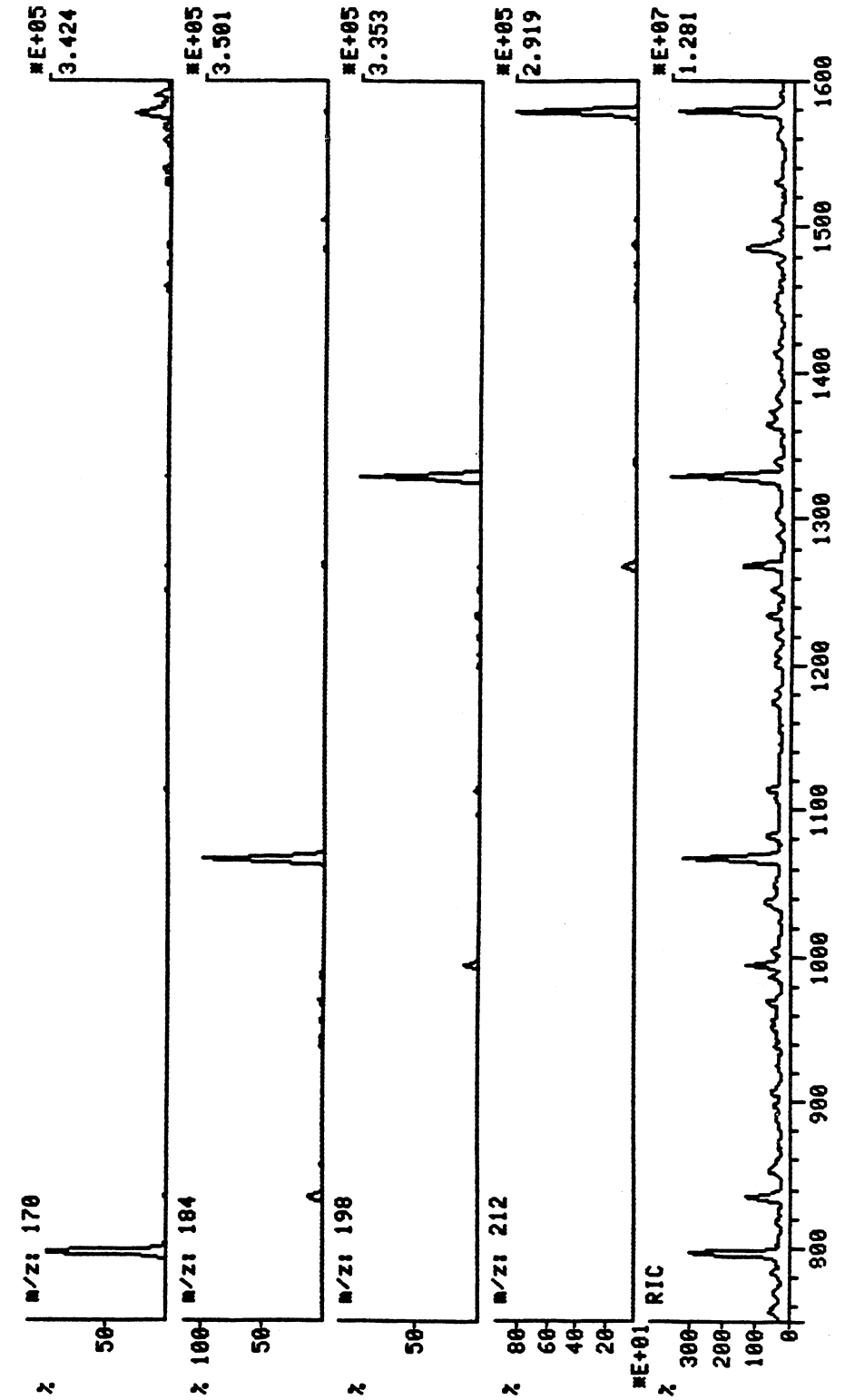

Fig. 2.3-4 Identification of the normal alkane peaks in the reconstituted ion chromatogram.

Chemical Type		Abundance (Area %)
Alkanes		66.50
	n-alkanes	42.23
	Branched alkanes	24.27
Cyclic alkanes		12.28
	Monocyclic alkanes	09.29
	Bicyclic alkanes	01.80
	Tricyclic alkanes	00.16
	Steranes	00.36
	Hopanes	00.67
Aromatics		18.97
	1-ringed aromatics	10.71
	2-ringed aromatics	05.04
	3-ringed aromatics	00.24
	Tetralins	02.29
	Biphenyls	00.69
Unknowns		02.20

Table 2.3-1 Classification of the Maljamar Crude Oil Based on Chemical Type.

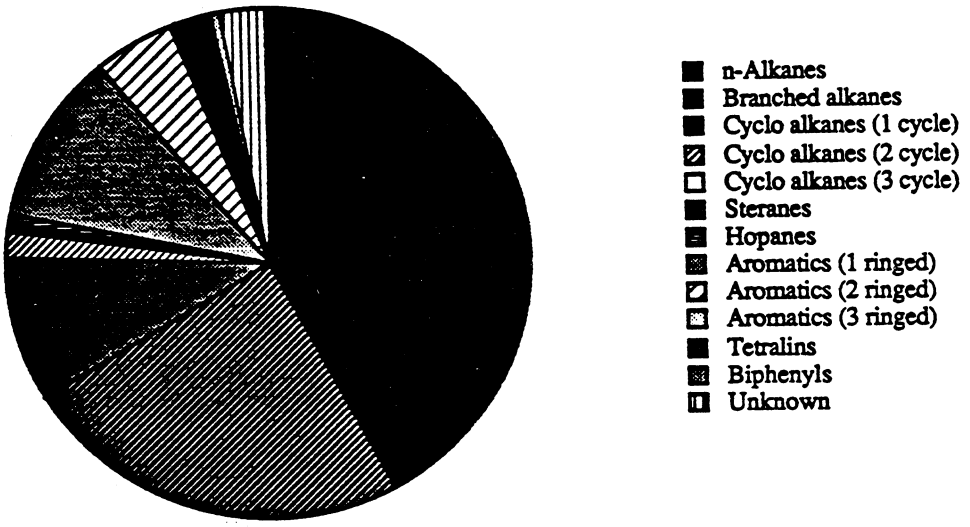

Fig. 2.3-5 Classification of the Maljamar crude oil into different chemical types.

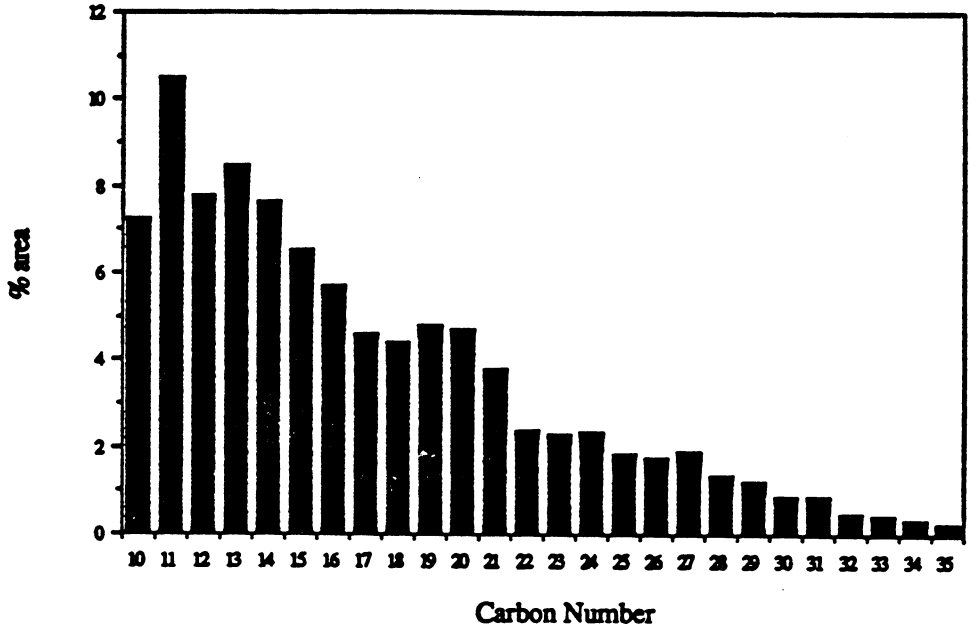

Fig. 2.3-6 Carbon number distribution of the Maljamar crude oil obtained by GC-MS analysis.

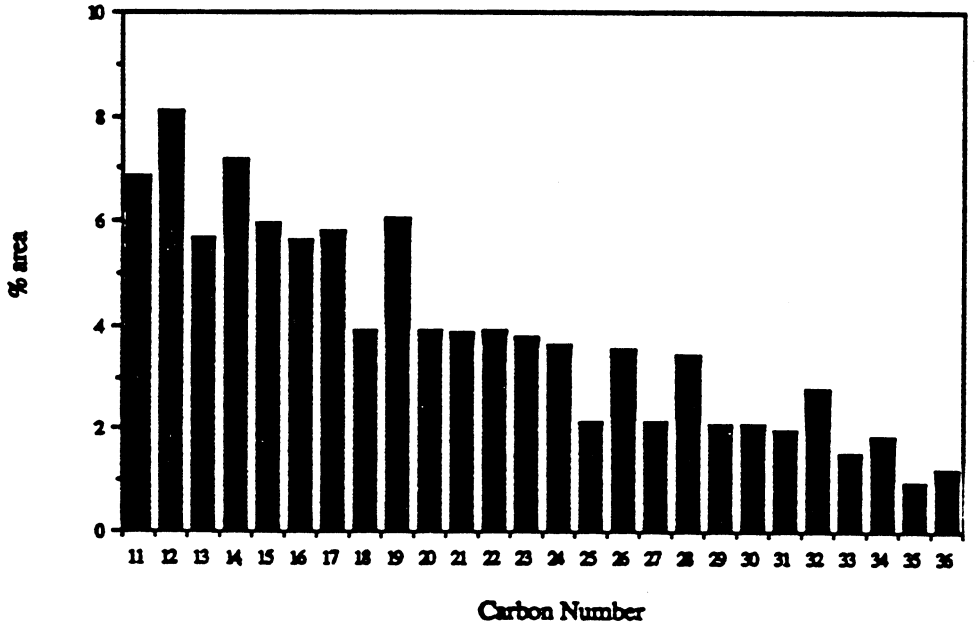

Fig. 2.3-7 Carbon number distribution of the Maljamar crude oil obtained by SIMDIS.

The GC-MS carbon number distribution for the alkanes is shown in Fig 2.3-8. In comparison to the overall carbon number distribution (Fig. 2.3-6), Fig. 2.3-8 shows a shift toward higher carbon number, indicating that cyclic and aromatic compounds are relatively more abundant in the lower ($< C_{15}$) than in the higher carbon numbers. Figs. 2.3-9 and 2.3-10 show the carbon number distributions for the normal and branched alkanes, respectively. Fig. 2.3-9 resembles the RIC because the RIC is dominated by the normal alkanes. In future experiments, similar distributions in the phases extracted by CO_2 will be obtained to determine the effect of branching and size on the extraction of alkanes by CO_2.

Figs. 2.3-11 to 2.3-14 give the size distributions for the aromatics and 1-ringed, 2-ringed and 3-ringed aromatics, respectively. From Fig. 2.3-12, it is clear that compounds with small side chains on the benzene ring are much more abundant than compounds with large side chains. Dimethylnaphthalenes are the most abundant 2-ringed aromatics, though there are considerable quantities of naphthalenes with larger side chains (Fig 2.3-13). Of the 3-ringed aromatics, we were able to identify the ones with, at most, 3-carbon side chains (Fig. 2.3-14). As with the alkane distributions, analysis of hydrocarbon mixtures extracted by dense CO_2 will be used to determine how efficiently aromatics of different size are extracted and whether presence of methyl or longer side chains facilitates the extraction process. Figs. 2.3-15 and 2.3-16 show the carbon number distributions for two different series of aromatic compounds, the tetralins (naphthenoaromatic compounds) and biphenyls, respectively. This type of information will be also useful in identifying the effect of chemical type on the extraction process.

Figs. 2.3-17 to 2.3-20 show the size distributions for the cyclic alkanes and the corresponding distributions for 1, 2 and 3-cycle alkanes, respectively. In the single-cycle naphthenics, compounds with smaller side chains are more abundant than the ones with larger side chains, but the larger compounds are present in considerable quantity (Fig. 2.3-18). Fig. 2.3-19 indicates that most of the 2-cycled naphthenics have smaller side chains. Large 3-cycled compounds were also identified (Fig. 2.3-20). Along with the data for extracted phases, this information can be used to determine the effect of size and presence of side chains on the extraction of naphthenic compounds. It will be interesting to see how efficiently large cyclic compounds like the steranes and hopanes are extracted. Their carbon number distribution is shown in Fig. 2.3-21.

2.3.4 Summary

The preliminary analysis of Maljamar crude oil presented indicates that detailed identification of compounds present in crude oils typical of those subjected to miscible flood processes is feasible. While some additional refinement of operating conditions, injection schemes, solvent choices, and so on is needed, and consistency and repeatability must be demonstrated, the results obtained to date show that detailed composition data can be obtained. These data will be useful in several applications. First, the effect of variations in crude oil composition on the amount and type of hydrocarbons extracted by a miscible flood solvent can be quantified directly. The hydrocarbon samples obtained by extraction with CO_2 from Maljamar crude oil (see Section 2.1) for example, will be used in the first set of experiments to examine that question. In addition, the quantitative performance of analyses such as that obtained by SIMDIS can also be explored. The goal will be to determine whether elution behavior and the resulting carbon number distributions obtained for normal and branched alkanes, naphthenes (single and multiring compounds) in SIMDIS is adequate to characterize oils for miscible flood applications.

The availability of detailed composition data for both the crude oils and hydrocarbons present in equilibrium phases would also make possible a systematic study of the adequacy of the techniques used to define pseudocomponents for equation-of-state (EOS) computations of phase equilibrium. More detailed composition data might allow estimation of pseudocomponent properties from pseudocomponent composition. Such a procedure would be an improvement over techniques in which pseudocomponent properties are obtained by curve-

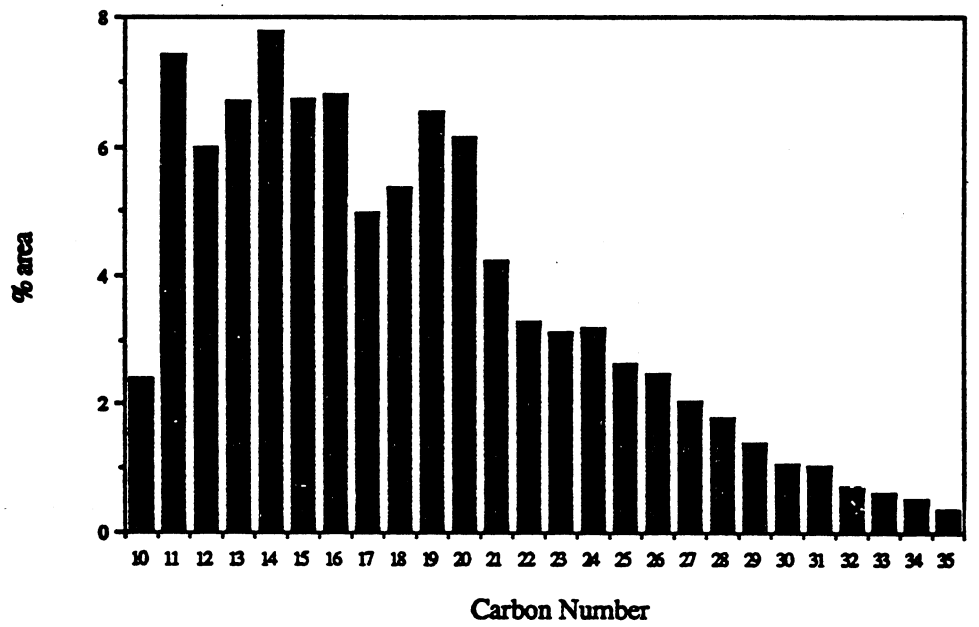

Fig. 2.3-8 Carbon number distribution of alkanes in Maljamar crude oil.

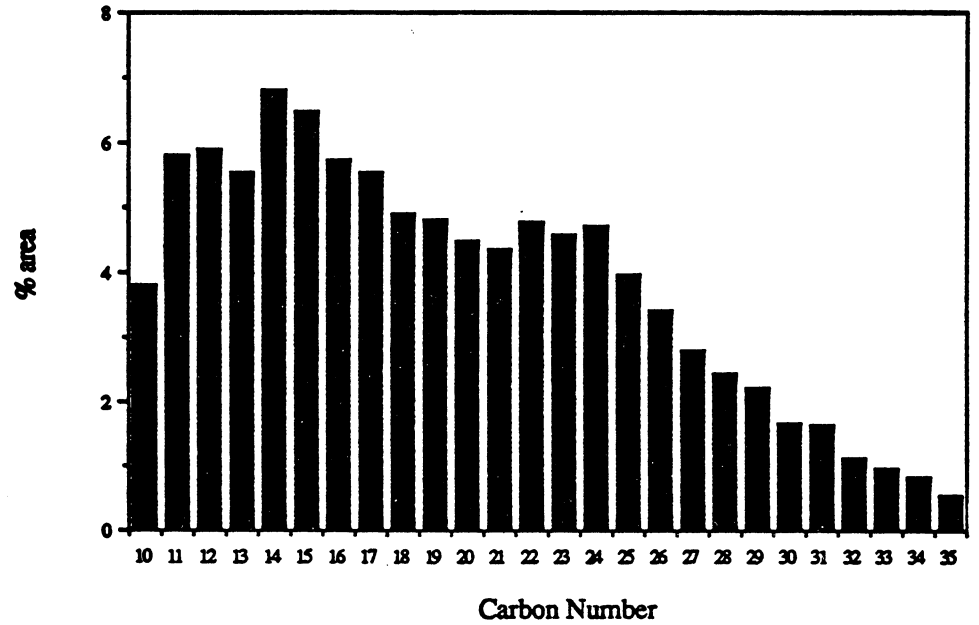

Fig 2.3-9 Carbon number distribution of n-alkanes in Maljamar crude oil.

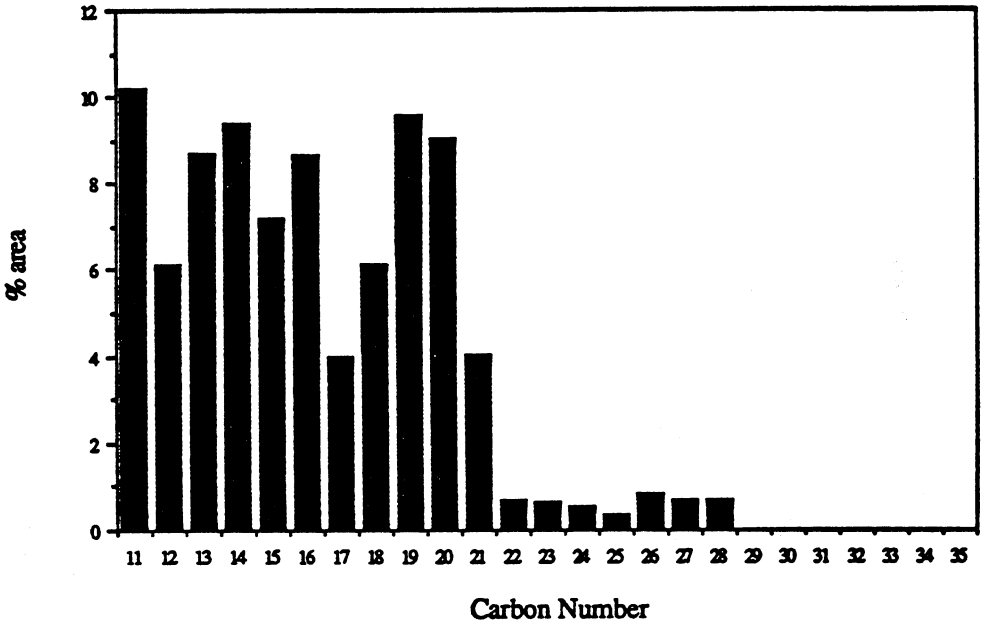

Fig. 2.3-10 Carbon number distribution of branched alkanes in Maljamar crude oil.

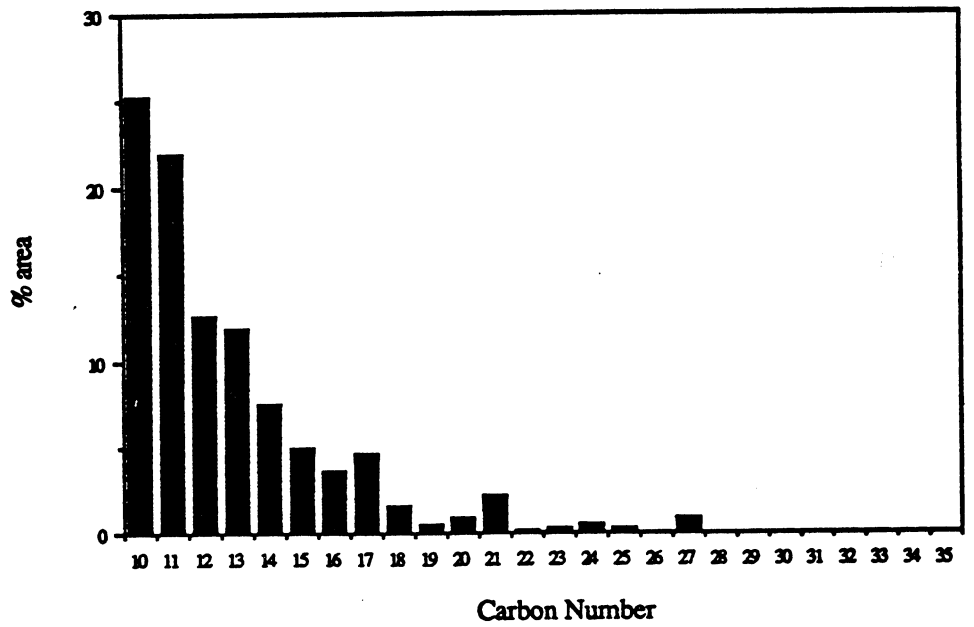

Fig. 2.3-11 Carbon number distribution of aromatics in Maljamar crude oil.

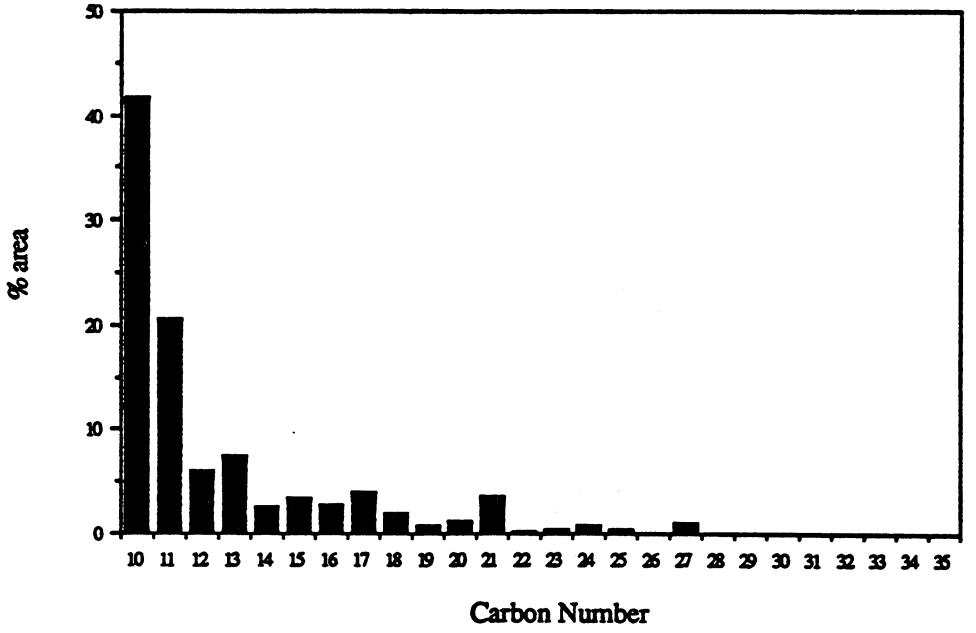

Fig. 2.3-12 Carbon number distribution of 1-ringed aromatics in Maljamar crude oil.

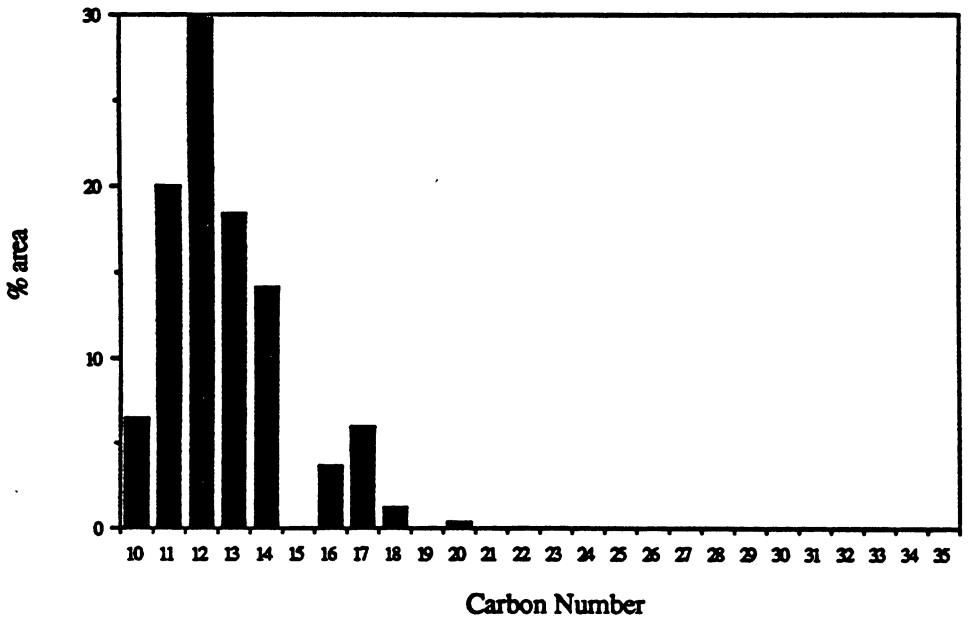

Fig. 2.3-13 Carbon number distribution of 2-ringed aromatics in Maljamar crude oil.

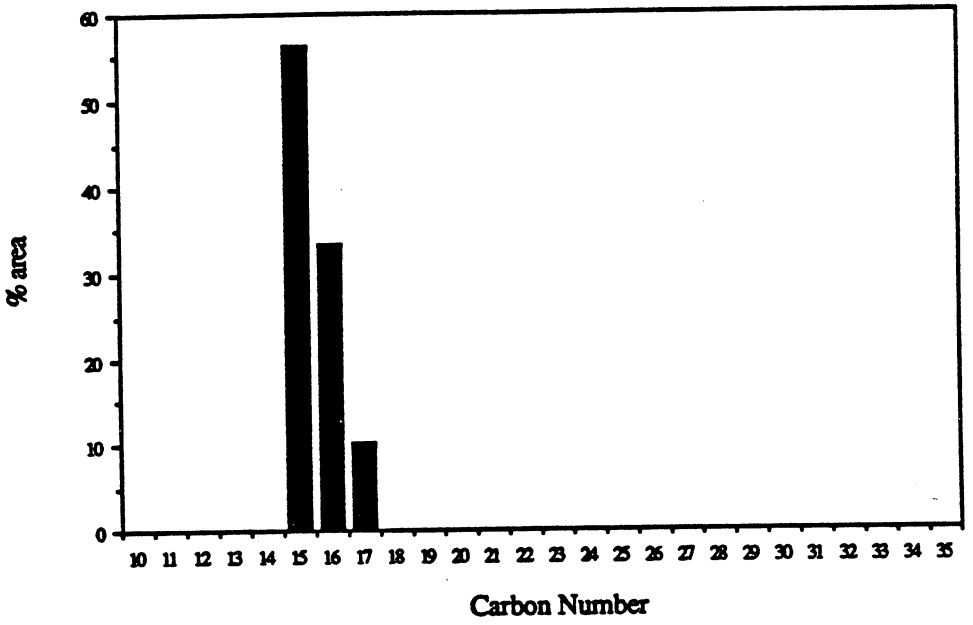

Fig. 2.3-14 Carbon number distribution of 3-ringed aromatics in Maljamar crude oil.

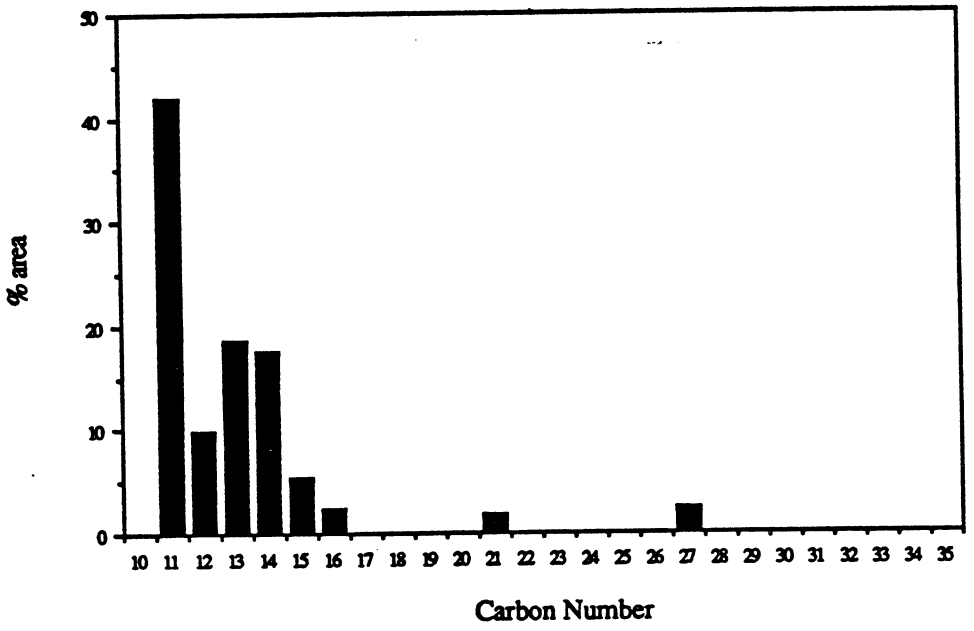

Fig. 2.3-15 Carbon number distribution of tetralins in Maljamar crude oil.

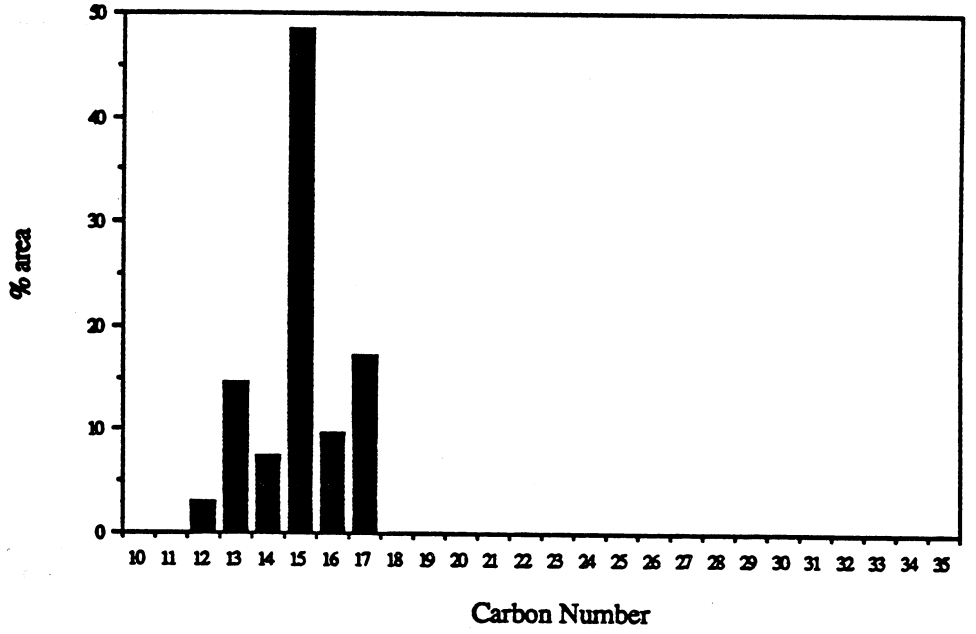

Fig. 2.3-16 Carbon number distribution of biphenyls in Maljamar crude oil.

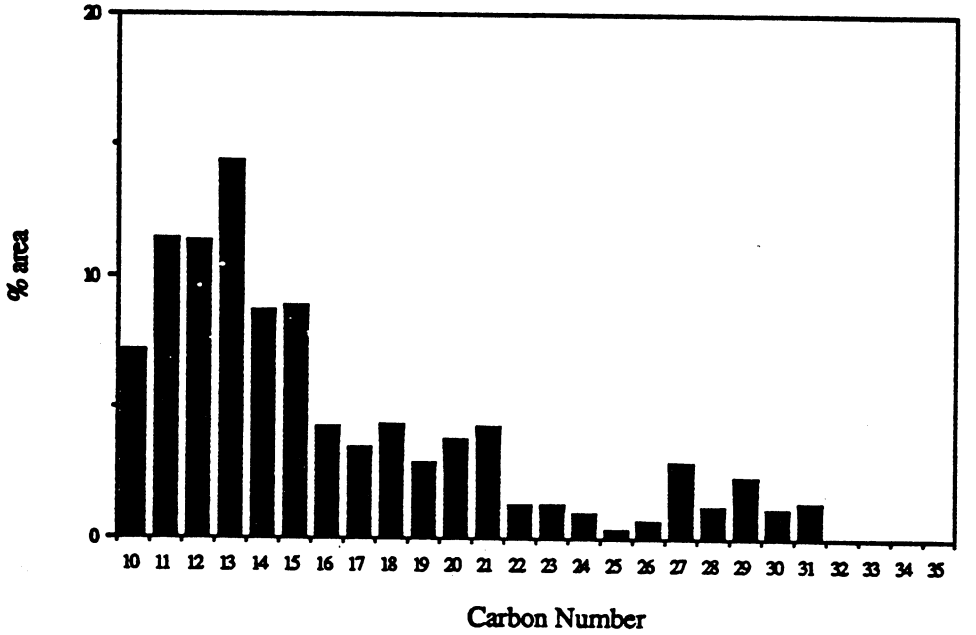

Fig. 2.3-17 Carbon number distribution of naphthenes in Maljamar crude oil.

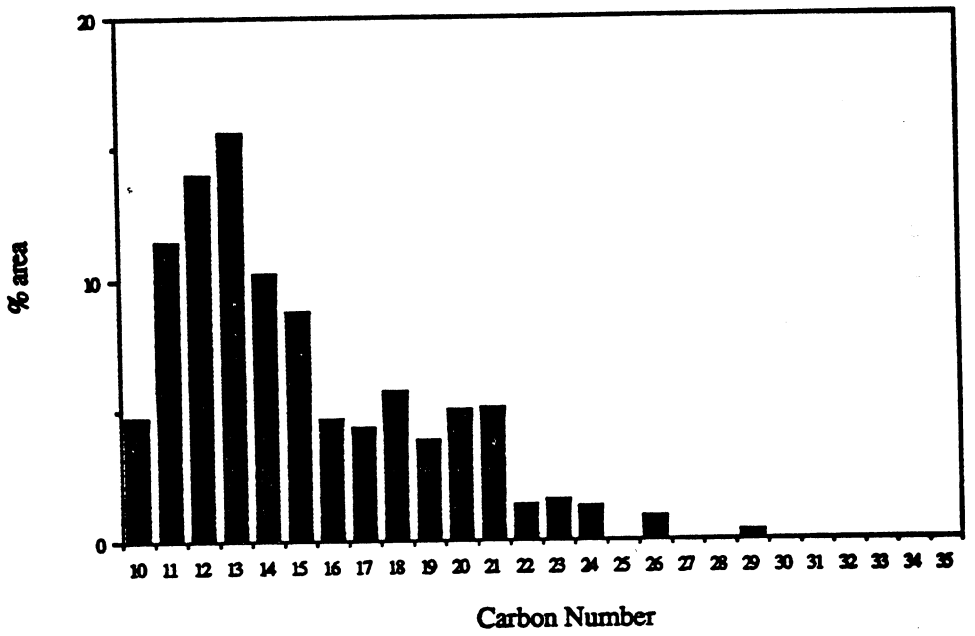

Fig. 2.3-18 Carbon number distribution of 1-cycle naphthenes in Maljamar crude oil.

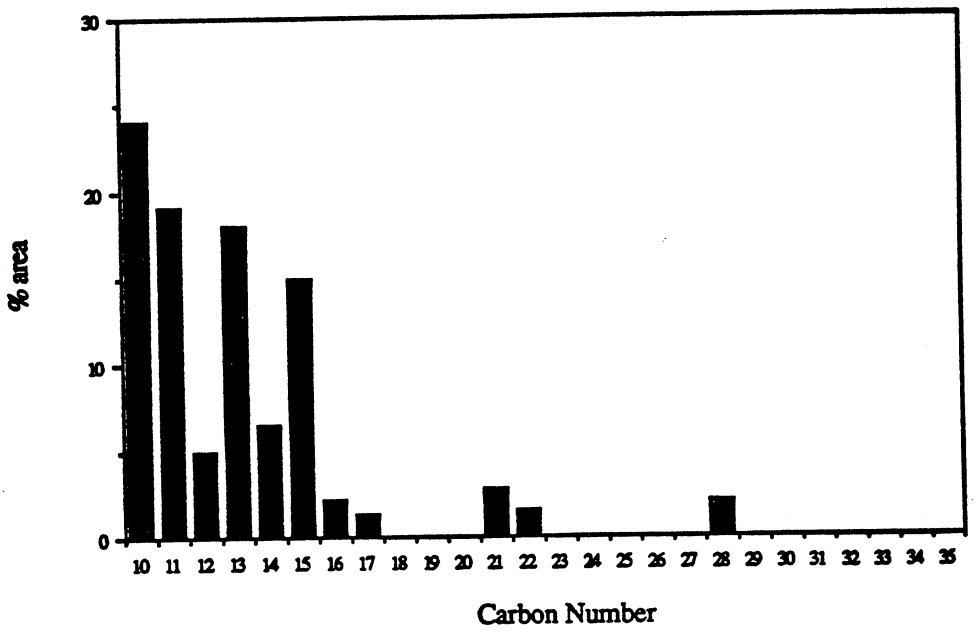

Fig. 2.3-19 Carbon number distribution of 2-cycle naphthenes in Maljamar crude oil.

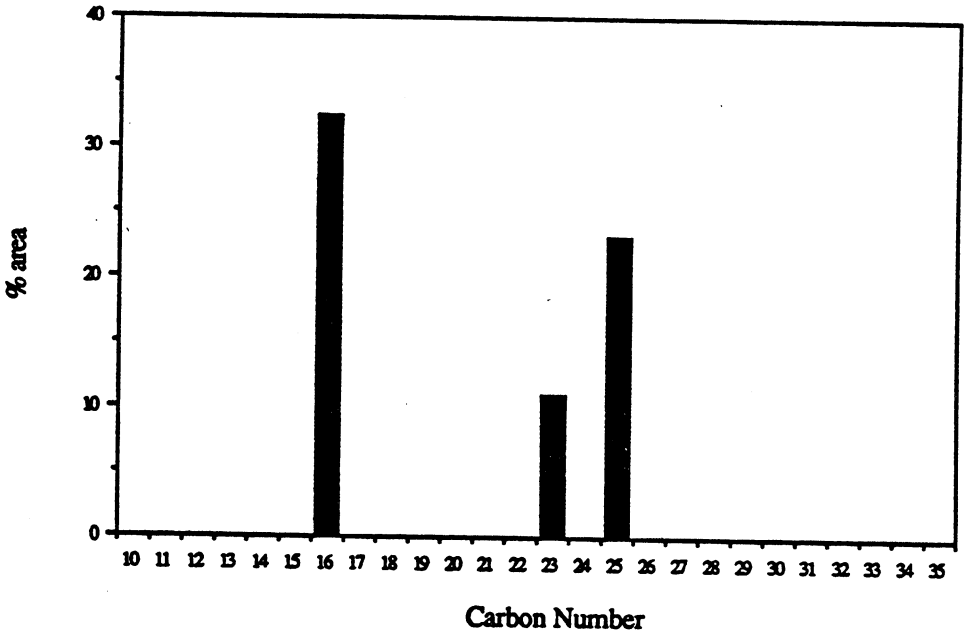

Fig. 2.3-20 Carbon number distribution of 3-cycle naphthenes in Maljamar crude oil.

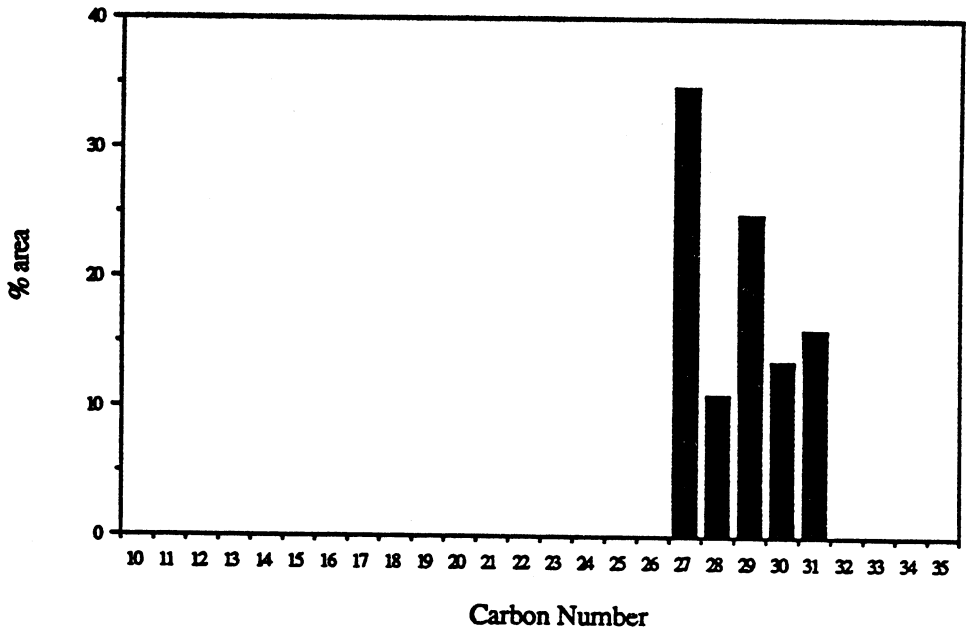

Fig. 2.3-21 Carbon number distribution of steranes and hopanes in Maljamar crude oil.

fitting EOS calculations of the results of PVT experiments. Thus, the improved analytical capability demonstrated in this section should lead to improved understanding of fundamental aspects of extraction behavior and to improved characterization of oils for miscible flood applications.

2.4 Summary

In this chapter, an experimental program to investigate the phase behavior and fluid properties was described. Results of phase composition measurements reported in Section 2.1 indicate that if equilibrium phases are formed for mixtures of a crude oil (Maljamar) with CO_2, N_2, or C_1 at fixed temperature (120°F), and if the pressure is chosen for each solvent to produce equivalent molar density of the pure solvent, the amounts and types of hydrocarbons extracted differ substantially. CO_2 at 1520 psia extracted greater amounts and significantly heavier hydrocarbons than did C_1 at 3790 psia or N_2 at 4950 psia. Correspondingly, the increase in the viscosity of the CO_2-rich phase over the pure component viscosity was much greater than that observed for C_1 or N_2. The results obtained suggest that volatility of hydrocarbons in the C_2 to C_7 range is much more important for miscible displacement with C_1 or N_2 than it is for CO_2 flooding.

In Sections 2.2 and 2.3 application of new analytical techniques to miscible flood systems was considered. Supercritical fluid chromatography (SFC) with CO_2 as a carrier was shown to be useful as an efficient method for simulated distillation analyses of crude oils. Because it relies on increases in CO_2 density for elution of hydrocarbons with increasing molecular size, the technique may allow determination of information about minimum miscibility pressures or information about hydrocarbon solubility in CO_2. Both ideas are under investigation.

The use of mass spectrometry to identify compounds present in a crude oil was also demonstrated. That technique is much more sensitive than simulated distillation or SFC, though at the cost of much more time (computer and human) spent on data acquisition and analysis. It will be used to examine how crude oil composition affects the extraction of hydrocarbons by miscible flood solvents. The data obtained will also permit systematic evaluation of pseudocomponent lumping procedures for equation of state calculations. Thus, the analytical procedures demonstrated should lead to improved understanding of what factors control supercritical extraction by miscible flood solvents and to improved characterizations of the crude oils for which miscible flooding is being considered or applied.

3. Interaction of Phase Behavior and Flow

Understanding of the effects of phase behavior in miscible floods is based on analysis of one-dimensional flow of three-component mixtures. That one-dimensional theory is thus a key underpinning of understanding of flow of more complex mixtures in more than one space dimension, for which numerical simulations are commonly performed. In this chapter we describe significant extensions of that theory to systems containing four components (Section 3.1), to steam/oil/water systems with temperature variation (Section 3.2), and to binary and ternary systems flowing in two layers with different permeability (Section 3.3). In the four-component analysis of Section 3.1, the effect of methane (C_1) dissolved in an oil on development of miscibility is examined, and a long-standing controversy concerning the effect of dissolved gas on minimum miscibility pressure (MMP) is resolved. In Section 3.2, the same mathematical approach, the method of characteristics, is applied to the flow of steam/oil/water systems with temperature variation.

In actual CO_2 floods, the effect of phase behavior on composition path is modified by the nonuniform flow that inevitably results from reservoir heterogeneity and viscous instability. In Section 3.3 we describe an analysis by the method of characteristics of flow of two-phase, ternary mixtures in a two-layer system with crossflow. Because it includes effects of crossflow and nonuniform flow that problem is a simplified model for the effects of phase behavior and heterogeneity or viscous instability. In Section 3.4 we return to the effects of dispersion on composition path and show that the magnitude of the interaction of dispersion and phase behavior depends on the size and shape of the two-phase region. Those results indicate that performance of some miscible floods will be much more sensitive to dispersive mixing than others.

3.1 Composition Paths in Four-Component Systems

Wesley W. Monroe

Understanding of the role of phase behavior in the development of miscibility in CO_2 floods, vaporizing gas drives and condensing gas drives is usually derived from analysis of composition paths represented on ternary or pseudoternary phase diagrams (Slobod and Koch 1953, Hutchinson and Braun 1961, Deffrenne et al. 1961). Consideration of four-component systems has been limited to the qualitative discussions of Deffrenne et al. (1961), Rathmell et al. (1971) and Stalkup (1983). Mathematical analysis of such flows has also been based on ternary representations of the phase behavior of mixtures of the injected and in-place fluids. For example, Welge et al. (1961) calculated composition paths for enriched gas drives and included the effects of volume change as components transferred between phases. Helfferich (1981) generalized the analysis of Welge et al. to systems containing an arbitrary number of components, but restricted consideration to those in which effects of volume change on mixing are negligible. Examples presented by Helfferich dealt with ternary systems only, however. Applications of similar theory to ternary systems of interest in surfactant floods have been presented by Larson (1979) and Hirasaki (1981). Dumoré et al. (1984) extended the analysis of Welge et al. and Helfferich to describe condensing and vaporizing gas drives for ternary systems in which volume change on mixing is important.

All of those mathematical descriptions are for the limiting case of one-dimensional flow in which the effects of dispersion are negligible. In such cases, it can be shown (Welge et al. 1961, Helfferich 1981, Larsen 1979, Hirasaki 1981, Dumoré et al. 1984) that compositions of fluids that form during a displacement of oil by CO_2 do not pass through the two-phase region unless the oil composition lies within the region of tie-line extensions on a ternary diagram. Thus, the critical tie line, the tie line that is tangent to the binodal curve at the plait point, marks the boundary between oil compositions that develop miscibility and those that do not. According to the one-dimensional theory, the minimum miscibility pressure (MMP) is the

pressure at which the oil composition lies on the critical tie line, so that additional pressure increases shrink the two-phase region enough to move the oil composition outside of the region of tie-line extensions. That theory applies equally well to systems containing an arbitrary number of components. In such systems, it is a surface in n_c-1 dimensions that divides original oil compositions that develop miscibility from those that do not (Defrenne et al. 1961).

Experimental determination of the MMP is rarely based on analysis of phase diagrams, however. Instead it is usually obtained from measurements of the fraction of oil recovered in a slim tube displacement at a given pressure (Orr et al. 1982). Several criteria have been proposed by which the MMP can be determined from displacement data. Most require that the recovery be nearly 100 percent (typically greater than 90 percent) and that recovery increase only slightly in displacements at pressures greater than the MMP (Orr et al. 1982, Yellig and Metcalfe 1980, Holm and Josendal 1982). Numerous correlations have also been offered that account for the effects of variations in temperature and oil composition on MMP. Several of the correlations currently available (Yellig and Metcalfe 1980, Holm and Josendal 1982, Orr and Silva 1985) do not account for the effect of the amount of light hydrocarbons, such as methane (C_1), present in the oil. Yellig and Metcalfe (1980) found, for example, that addition of C_1 to an oil did not change MMP's appreciably. Neglect of the presence of light hydrocarbons is based on the assumption that such components volatilize and are transported ahead of the displacement front and hence, do not affect the development of miscibility (Holm and Josendal 1982). Thus, the correlations include the provision that when there is enough of the light components present to raise the bubble point pressure (BPP) of the oil above the MMP predicted for the dead oil, then the BPP is taken to be the MMP.

That provision is inconsistent with the analytical description of the development of miscibility. The composition of an oil at its BPP must be at the end of a tie line. Hence, such a composition must lie within the region of tie-line extensions if the oil composition is plotted on a pseudoternary diagram. Thus, the definition of the MMP based on analysis of one-dimensional flow of a ternary systems is in conflict with a portion of the experimental evidence on the behavior of the MMP as the amount of gas dissolved in the oil increases.

To resolve the inconsistency we investigate the flow of a model four component CO_2-hydrocarbon system, CO_2, C_1, butane $(C)_4$, and decane (C_{10}), for which the Peng-Robinson equation of state (PREOS, Peng and Robinson 1976) reproduces observed behavior with reasonable accuracy (Larsen 1984, Monroe et al. 1987). We describe the extension of the calculations of Dumoré et al. (1984) to four component systems, and then we use the PREOS representation of the phase behavior to construct composition paths for the CO_2-C_1-C_4-C_{10} system. The solutions obtained show that it is indeed possible to have high displacement efficiency even when the original oil composition does not lie outside the region of tie-line extensions.

3.1.1 Mathematical Model

Given the PREOS representation of the phase behavior, composition paths can be calculated. The formulation of the flow equations follows that of Dumoré et al. (1984). Purely convective flow of a multicomponent, multiphase system through a one-dimensional, homogeneous porous medium is governed by the following mass balance equation

$$\frac{\partial}{\partial t}\sum_{j=1}^{n_p} x_{ij}\,\rho_j\,S_j + \frac{\partial}{\partial x}\,\frac{v}{\phi}\sum_{j=1}^{n_p} x_{ij}\,\rho_j\,f_j = 0 \qquad i = 1, n_c \tag{3.1-1}$$

where v is the total velocity, and f_j is the fractional flow of phase j, given by

$$f_j = \frac{k_j/\mu_j}{\sum_{j=1}^{n_p} k_j/\mu_j} \tag{3.1-2}$$

In the derivation of Eqs. (3.1-1) and (3.1-2), effects of dispersion and capillary pressure have been neglected. Substitution of the definitions

$$G_i = \sum_{j=1}^{n_p} x_{ij}\,\rho_j\,S_j \qquad F_i = \frac{v}{\phi}\sum_{j=1}^{n_p} x_{ij}\,\rho_j\,f_j\,. \tag{3.1-3}$$

into Eq. (3.1-1) gives

$$\frac{\partial G_i}{\partial t} + \frac{\partial F_i}{\partial x} = 0 \qquad i = 1,\, n_c. \tag{3.1-4}$$

Here G_i and F_i represent the overall component concentration and the overall flux of component i. Because phases present at any point are assumed to be in chemical equilibrium, the phase compositions and properties can be obtained by performing a flash calculation given the overall composition, C_i. Thus, G_i and F_i are functions of the overall compositions and F_i also depends on the total velocity, v. If the dependent variables C_i and v are represented as functions of a dummy variable $\eta = \eta(x,t)$, Eq. (3.1-4) can be written

$$\frac{dG_i}{d\eta}\frac{\partial \eta}{\partial t} + \frac{dF_i}{d\eta}\frac{\partial \eta}{\partial x} = 0 \qquad i = 1,\, n_c, \tag{3.1-5}$$

where

$$\frac{dG_i}{d\eta} = \sum_{k=1}^{n_c-1}\frac{\partial G_i}{\partial C_k}\frac{dC_k}{d\eta} \qquad i = 1,\, n_c \tag{3.1-6}$$

and

$$\frac{dF_i}{d\eta} = \frac{\partial F_i}{\partial v}\frac{dv}{d\eta} + \sum_{k=1}^{n_c-1}\frac{\partial F_i}{\partial C_k}\frac{dC_k}{d\eta} \qquad i = 1,\, n_c \tag{3.1-7}$$

Because η is a function of x and t

$$d\eta = \frac{\partial \eta}{\partial x}\,dx + \frac{\partial \eta}{\partial t}\,dt \tag{3.1-8}$$

We now seek solutions along characteristic curves, for which $d\eta = 0$. Rearrangement of Eq. (3.1-8) with substitution of any one of Eqs. (3.1-5) gives

$$\frac{dx}{dt} = -\frac{\dfrac{\partial \eta}{\partial t}}{\dfrac{\partial \eta}{\partial x}} = \frac{\dfrac{dF_i}{d\eta}}{\dfrac{dG_i}{d\eta}} \qquad i = 1,\, n_c \tag{3.1-9}$$

There is one equation of the form of Eq. (3.1-9) for each of the n_c components. The solution sought is one for which the velocities, $\frac{dx}{dt} = \lambda$, are the same for all components. If so, Eq. (3.1-9) can be rewritten in matrix form using Eqs. (3.1-6) and (3.1-7) as

$$\left[\bar{\bar{F}} - \lambda\,\bar{\bar{G}}\right]\bar{C} = 0 \tag{3.1-10}$$

where the entries in the i th row of $\bar{\bar{F}}$ are $\frac{\partial F_i}{\partial C_k}$ for k=1, n_c–1 and $\frac{\partial F_i}{\partial v}$, the entries in $\bar{\bar{G}}$, $\frac{\partial G_i}{\partial C_k}$

for k=1, n_c-1 and 0 (because G_i is independent of v), and the vector $\bar{C}$ contains $\frac{dC_i}{d\eta}$ for i=1,n_c-1 and $\frac{dv}{d\eta}$.

Eq. (3.1-10) is an eigenvalue problem for which solutions exist for eigenvalues given by

$$\det\left[\bar{\bar{F}} - \lambda\bar{\bar{G}}\right] = 0 \tag{3.1-11}$$

For a system containing n_c components, there are n_c-1 eigenvalues that represent velocity of an overall composition along a composition (path) direction given by the associated eigenvector, $\bar{C}$. The eigenvectors represent composition variations that satisfy the restriction that individual concentrations, C_i, all move at the same velocity, referred to by Helfferich as coherence (Helfferich 1981). Integration along the eigenvector directions yields a set of composition "paths" that satisfy the coherence condition. Thus, there are three paths through any composition point in a four-component system. The last eigenvalue is infinite. It reflects the fact that changes in overall velocity propagate instantaneously.

Solutions to problems of the form of Eq. (3.1-4) may or may not vary continuously. If the solution varies continuously, Eq. (3.1-4) is the appropriate form of the material balance equation. At jump discontinuities, however, an overall mass balance across the shock yields an expression for its velocity (Welge et al. 1961, Helfferich 1981, Larsen 1979, Hirasaki 1981, Dumoré et al. 1984).

$$\Lambda_i = \frac{F_i^{II} - F_i^{I}}{G_i^{II} - G_i^{I}} \tag{3.1-12}$$

where the superscripts I and II refer to opposite sides of the shock. It can be shown that a two-phase region can be entered only via a shock from a composition in the single phase region to a composition in the two-phase region. Such a shock occurs along the extension of a tie line (Welge et al. 1961, Helfferich 1981, Larsen 1979, Hirasaki 1981, Dumoré et al. 1984). Two types of jump discontinuities are observed in solutions for specific initial and injection compositions. The first occurs when the compositions on one side of the shock are the limit of a continuous variation along a tie line, which can occur because tie lines are themselves paths (Helfferich 1981, Hirasaki 1981, Dumoré et al. 1984). In such cases, the shock velocity is given by (Dumoré et al. 1984)

$$\Lambda_i = \frac{F_i^{II} - F_i^{I}}{G_i^{II} - G_i^{I}} = \frac{v}{\phi}\frac{df}{dS} \tag{3.1-13}$$

because the shock velocity is equal to the velocity of the composition on the two-phase side of the shock, the eigenvalue associated with the eigenvector that points along the tie line. As several investigators have shown, that velocity is $\lambda = \frac{v}{\phi}\frac{df}{dS}$ (Welge et al. 1961, Helfferich 1981, Hirasaki 1981, Dumoré et al. 1984). We refer to such shocks as "tangent" shocks because their velocities can be found from a graphical construction analogous to the familiar Welge tangent construction for Buckley-Leverett solutions. The second type of shock is found when the jump discontinuity occurs between two compositions with no continuous variation on either side of the shock. In that case, the velocity is given directly by Eq. (3.1-12). Such shocks will be called "nontangent" shocks in the discussion that follows.

3.1.2 Quaternary Grid Topology

Construction of a solution for a particular set of initial and injection conditions is completed by integrating along "paths," the directions given by the eigenvectors through a particular composition point (Helfferich 1981). For example, paths through an arbitrarily chosen point can be found by solving Eq. (3.1-10) for the three composition eigenvectors. Then a small step is taken along one of the eigenvector directions and the procedure repeated. Similar integration for each of the three eigenvectors through each composition point in the quaternary diagram yields a mesh of composition paths that fills the diagram. Because paths represent composition variations that satisfy the coherence condition, the solution for specific initial and injection conditions follows a set of paths that connect the initial composition to the injection composition. Of the many potential paths available, only one will also satisfy the constraint that the composition velocity must increase monotonically from the inlet to the outlet, a statement that fast-moving compositions must lie downstream of slow-moving ones.

Fig. 3.1-1 shows selected composition paths for the CO_2-C_1-C_4-C_{10} system. Those paths were calculated using the following expressions for oil and gas phase relative permeabilities

$$k_{ro} = k_{rom}\left[\frac{1 - S_g - S_{or}}{1 - S_{or}}\right]^{n_o} \tag{3.1-14}$$

$$k_{rg} = k_{rgm}\, S_g^{\,n_g} \tag{3.1-15}$$

with $k_{rgm} = k_{rom} = 0.8$, $n_g = n_o = 3$ and $S_{or} = 0.05$. Phase viscosities were calculated using the Lohrenz-Bray-Clark (1964) correlation, and phase compositions and densities were obtained from a flash calculation using the PREOS. The three distinct paths through each point in the quaternary phase diagram are illustrated for a tie line in the CO_2-C_4-C_{10} face. Fig. 3.1-2 is a plot of the variation in eigenvalues with changes in gas saturation along three key tie lines. As in the ternary cases described by Dumoré et al. (1984) and Monroe (1986), tie lines are paths, and the eigenvalue associated with the tie line is proportional to $\frac{df}{dS}$. As Fig. 3.1-2 indicates, composition variations along tie-line paths are slower (have smaller eigenvalues) than other paths at the ends of the tie line, are fastest in the middle of the tie line, and have intermediate velocities in between. Thus, a particular path may be a fast, slow or intermediate path at different positions along it.

Fig. 3.1-1 shows that, in addition to the tie-line path, there are also two nontie-line paths associated with a given composition. As Fig. 3.1-1 illustrates, we use the designation "horizontal" to refer to the nontie-line paths in the C_1-C_4-C_{10} and the CO_2-C_4-C_{10} faces, and "vertical" to refer to those paths that extend from the C_1-C_4-C_{10} face to the CO_2-C_4-C_{10} face. Fig. 3.1-2 shows that there are four points along each tie line where two of the three eigenvalues are equal. At each of those points, labeled **f**, **g**, **h** and **i** in Fig. 3.1-2, one nontie-line path is tangent to the tie-line path. Two of the singular points are at the intersection of the tie line and the horizontal nontie-line paths, and the other two singular points are at the intersection of the tie line and the vertical nontie-line path. Two of the singular points, one horizontal and one vertical path intersection point, are on either side of the equivelocity surface, the locus of points at which the liquid and vapor phase velocities are equal. The equivelocity and saturated phase surfaces are also paths that can be traversed either vertically or horizontally. As in ternary problems (Larsen 1979, Helfferich 1981, Hirasaki 1981 and Dumoré et al. 1984) only singular points on one side of the equivelocity surface are used in the solutions constructed here. Hence Fig. 3.1-1 shows only the two singular points that lie across the equivelocity surface from the initial composition. In the example that follows, we use the description of path geometry shown in Fig. 3.1-1 and plots like Fig. 3.1-2 of velocity (eigenvalue) variations along tie lines to select solution composition paths for given constant initial and injection compositions.

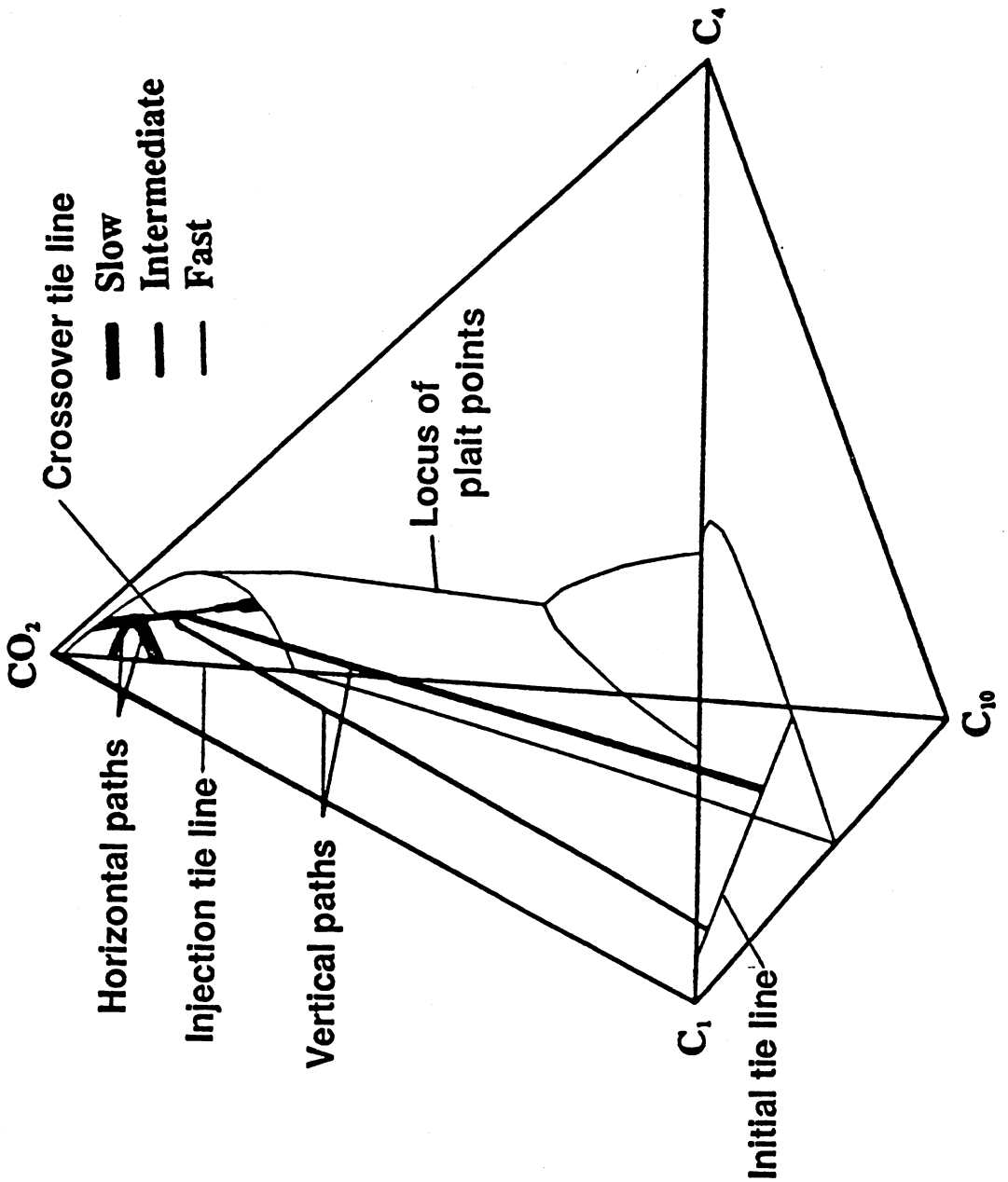

Fig. 3.1-1 Typical composition paths for a CO_2-C_1-C_4-C_{10} system.

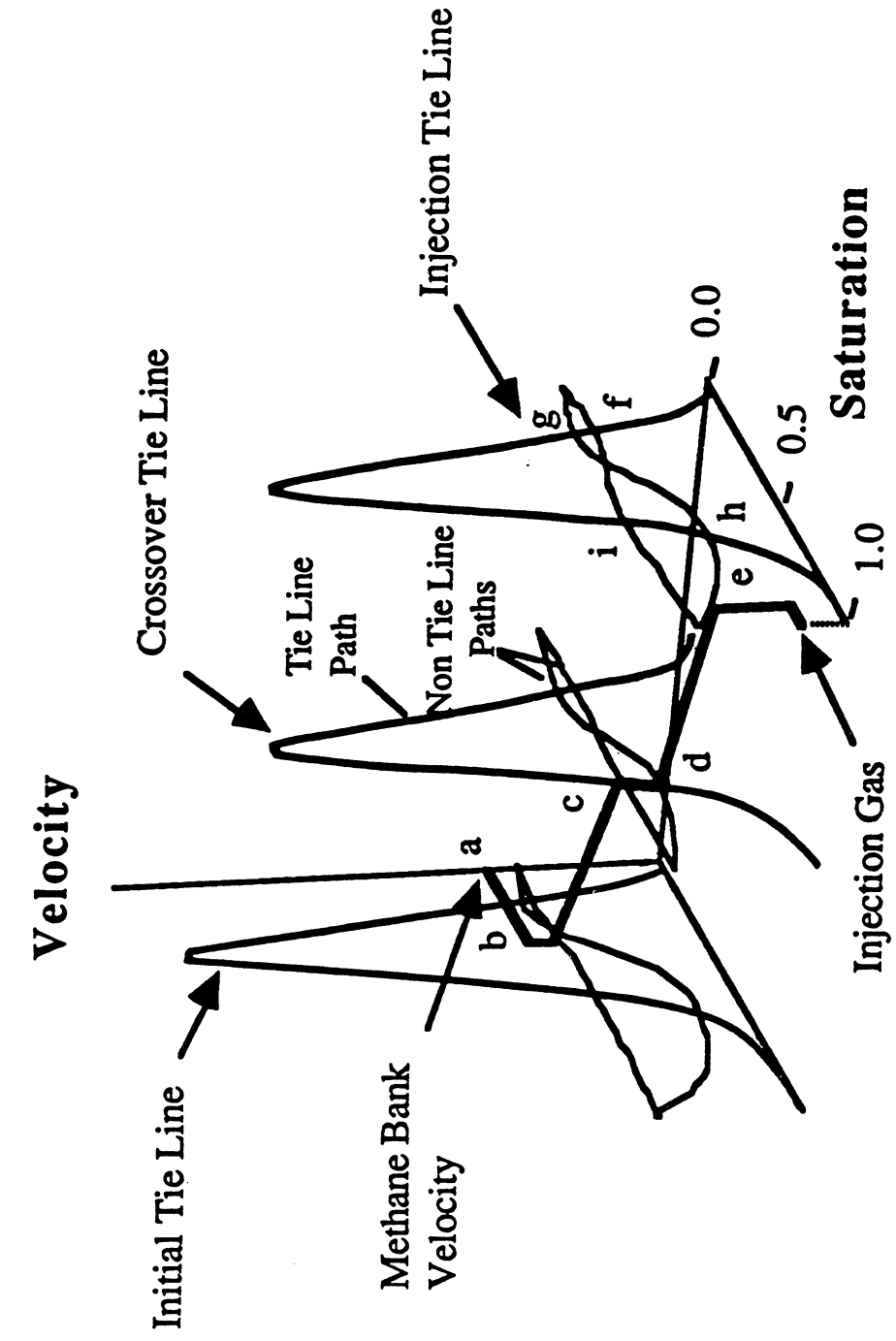

Fig. 3.1-2 Variation of composition velocities (eigenvalues) along key tie lines.

3.1.3 Sample Solution Path

Data for the first example solution are given in Table 3.1-1. At time zero, pure CO_2 is injected into a porous medium containing a single-phase oil of constant composition. The injection velocity is 1.0 m/d. The solution path is plotted on a quaternary diagram in Fig. 3.1-3, and the composition, saturation and velocity data are given in Table 3.1-2.

In the following discussion, the calculated composition path is traced from the initial oil composition to the injection gas composition. The composition variation that is the solution must lie exclusively on paths, and velocities must decrease from the initial oil composition to the injection gas composition. While the solution path may switch from one path to another, the only allowable switch is from a faster path to a slower one (Helfferich 1981, Dumoré et al. 1984). Finally, if there is a leading or fast shock, the composition jump must cross the equivelocity surface, because composition jumps that do not cross that surface have velocities, given by Eq. (3.1-12), that are less than the average interstitial velocity and hence cannot be leading shocks.

The path enters the two phase region via a shock to a fast path along a tie line from the initial oil composition, point **a**, to point **b**. Across the shock there is a step in C_1 concentration with no CO_2 present. At point **b** the path switches immediately from a fast path to an intermediate path. The step change from the initial composition to the two-phase region is not a limit of a continuous variation. Therefore, it is a nontangent shock, and the velocity of the shock can be calculated from the material balance Eq. (3.1-12), once the composition of the point **b** is found. The velocity of the shock from **b** to **c** is given by Eq. (3.1-13) because upstream of that shock the composition varies continuously along the crossover tie line. The procedure used to solve simultaneously for the shocks from **a** to **b** and from **b** to **c** is essentially the same as that for the shocks from **d** to **e** and **e** to **f** described below. Because there are two velocities associated with the same overall composition at point **b**, a bank of fluid flowing at constant composition (zone of constant state) is formed. The leading edge moves with the fast shock velocity and the trailing edge moves with the slower velocity of the shock from **b** to **c**. Fig. 3.1-2 illustrates the velocity change at point **b**. The constant phase saturations and compositions within the bank are illustrated in the profiles shown in Figs. 3.1-4 and 3.1-5.

The shock from **b** to **c** is a self-sharpening wave. It forms because along the vertical, intermediate velocity path that connects the initial tie line with the crossover tie line (see Fig. 3.1-9), the intermediate eigenvalue increases slightly. Hence, a continuous variation along that path is not possible, and a shock forms. Across that shock, the concentration of CO_2 increases discontinuously, while the concentration of the other three components drops. Point **c** is close to the singular point where the vertical path is tangent to a tie line in the CO_2–C_4–C_{10} face and where two of the eigenvalues are equal (see Fig. 3.1-10).

From points **c** to **d** there is a continuous variation along a tie line. There, phase saturations vary, while the phase compositions and the total velocity remain constant. At point **d**, the composition jumps to point **e**, which is on the tie line that extends through the injection composition. That jump is also a self-sharpening wave. As in the case of the shock from **b** to **c**, it occurs because the wave velocity (intermediate eigenvalue) increases slightly along the horizontal nontie-line path that traverses the CO_2–C_4–C_{10} face from the equal eigenvalue point on the crossover tie line. The point at which the jump occurs is not exactly equal to the singular point shown in Fig. 3.1-2, but it is so close to the equal eigenvalue point that the difference cannot be seen on the scale of Figs. 3.1-1 to 3.1-3. Similarly, the landing point **e** is also very close to the intersection of the horizontal nontie-line path with the injection tie line. The procedure for calculation of the compositions on either side of the self-sharpening wave is as follows. The self-sharpening wave is described by shock balances such as Eq. (3.1-13). In this case, the shock velocity (Eq. 3.1-12) equals the intermediate eigenvalue on the crossover tie line, because the shock is the limit of a continuous variation along that tie line. There are three such equations, one each for CO_2, C_4, and C_{10} (recall that no C_1 is present on the ternary

Table 3.1-1 Initial and Injection Composition for Displacements of Live and Dead Oils at 160 °F (71 °C) and 1600 psia (11.0 MPa)

	Composition (mole fraction)				Molar
	CO_2	Methane	Butane	Decane	Density (g-mol/cc)
Injection Gas (mole fraction)	1.00	0.00	0.00	0.00	6.62×10^{-3}
Live Oil (mole fraction)	0.00	0.20	0.34.	0.46	6.86×10^{-3}
Dead Oil (mole fraction)	0.00	0.00	0.42	0.58	5.99×10^{-3}

Table 3.1-2 Composition Path, Saturation and Velocity Results for a Quaternary Displacement at 160 °F (71 °C) and 1600 psia (11.0 MPa)

Comment	Composition (mole fraction)				Total Velocity	Gas Saturation	Wave Velocity
	CO_2	C_1	C_4	C_{10}	u (m/d)	S	λ(m/d)
Injection Composition	1.0	0.0	0.0	0.0	1.0	1.0	
Slow Shock	0.9558	0.0000	0.0000	0.0442	0.9527	0.9080	0.264
Zone of Constant State	0.9558	0.0000	0.0000	0.0442	0.9527	0.9080	0.742
Self Sharpening Wave	0.8490	0.0000	0.0968	0.0542	0.9483	0.6458	0.742
Continuous Variation	0.8490	0.0000	0.0968	0.0542	0.9483	0.6458	0.742
	0.8461	0.0000	0.0978	0.0560	0.9483	0.6245	0.931
Leading Discontinuity	0.0000	0.4934	0.2294	0.2772	0.9132	0.2820	0.984
Zone of Constant State	0.0000	0.4934	0.2294	0.2772	0.9132	0.2820	0.984
Fast Shock	0.0000	0.4934	0.2294	0.2772	0.8718	0.0000	0.984
Initial Oil Composition	0.0000	0.2000	0.3352	0.4648	0.8718	0.0000	

Table 3.1-3 Variations of Saturations and Shock Velocities for Oil Containing Increasing Amounts of C_4 at 160 °F (71°C) and 1600 psia (11.0 MPa)

	Oil Composition (mole fraction)			Slow Shock		Methane Bank		
				Velocity	Saturation	Trailing Vel.	Leading Vel.	Saturation
	C_1	C_4	C_{10}	ν (m/d)	S	ν_t (m/d)	ν_l (m/d)	S
System 1	0.10	0.21	0.69	0.147	0.797	0.935	1.018	0.287
System 2	0.10	0.38	0.52	0.179	0.847	0.933	0.958	0.285
System 3	0.10	0.45	0.45	0.264	0.908	0.931	0.956	0.285
System 4	0.10	0.50	0.40	0.828	0.983	0.930	0.953	0.283

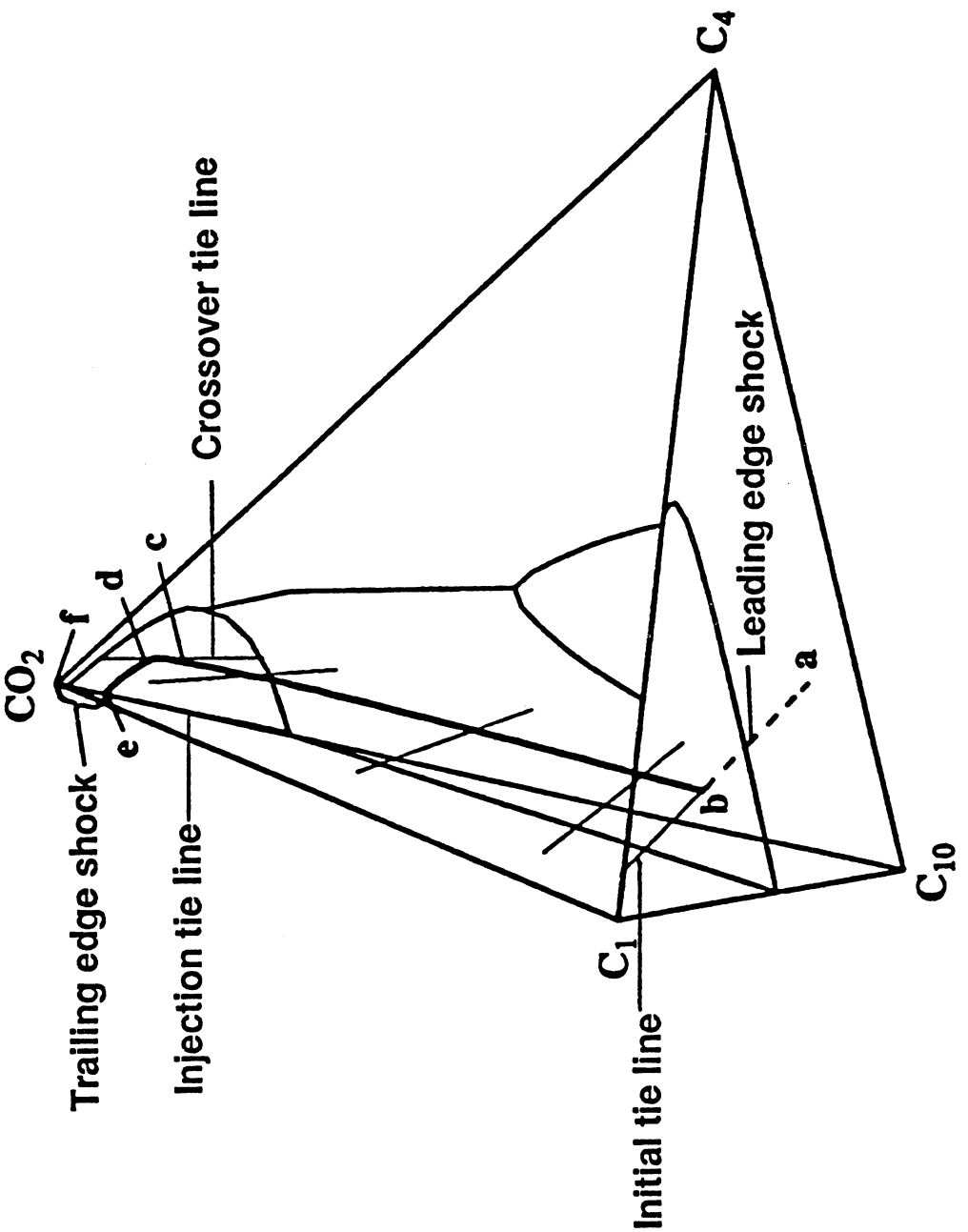

Fig. 3.1-3 Composition path for displacement of a CO_2-C_1-C_4 mixture by CO_2 at 160°F (71°C) and 1600 psia (11.0 MPa).

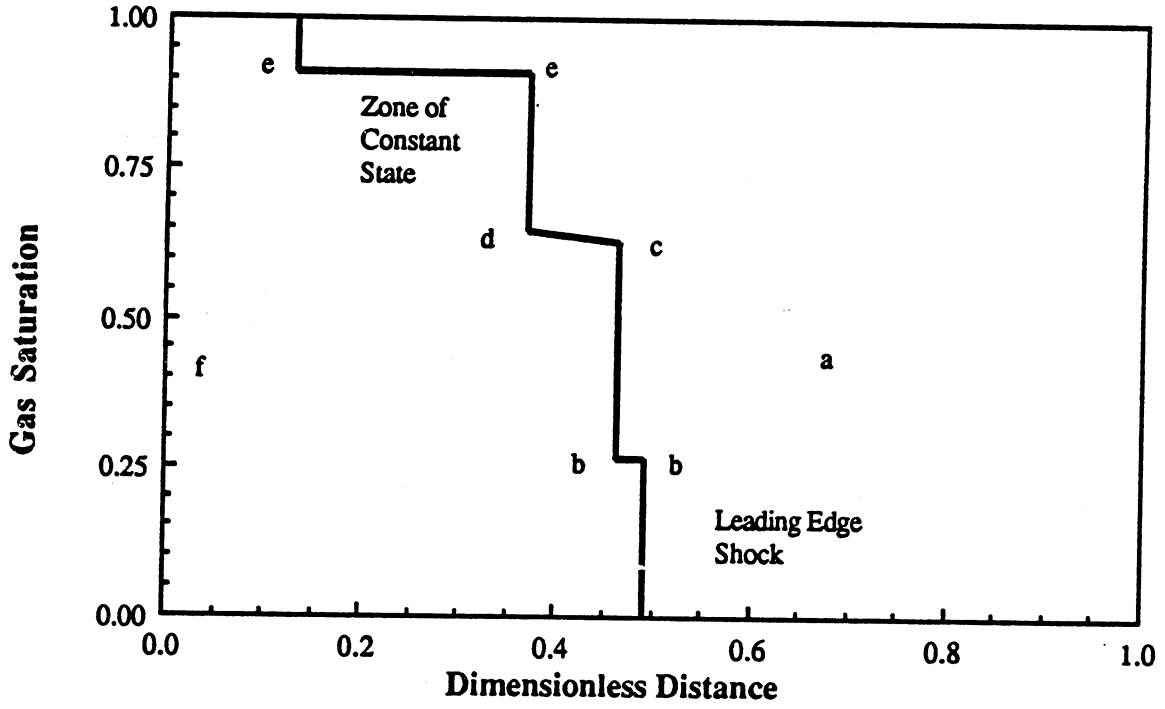

Fig. 3.1-4 Saturation profile at 0.5 pore volumes injected for displacement of a CO_2–C_1–C_4 mixture by CO_2 at 160°F (71°C) and 1600 psia (11.0 MPa).

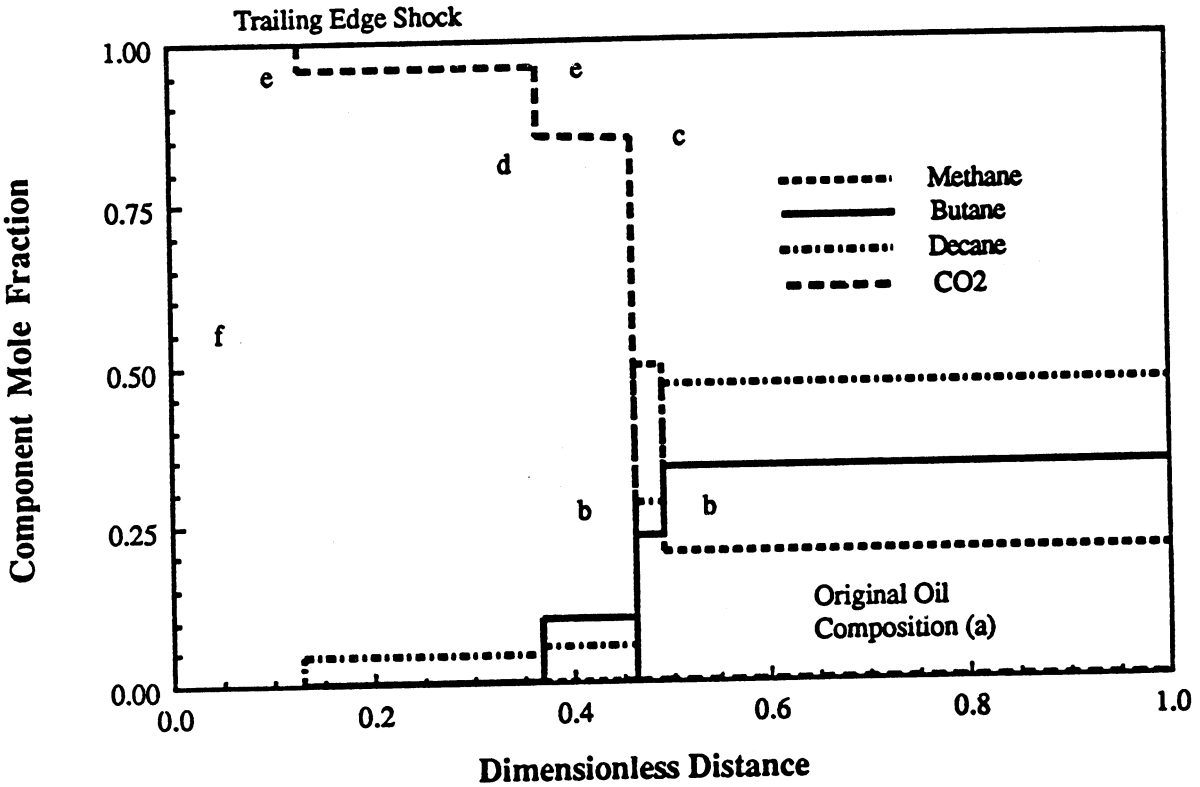

Fig. 3.1-5 Composition profile at 0.5 pore volumes injected for displacement of a CO_2–C_1–C_4 mixture by CO_2 at 160°F (71°C) and 1600 psia (11.0 MPa).

CO_2–C_4–C_{10} face). However, there are four unknowns that must be determined to specify the self-sharpening wave, the gas saturation, S_g, and total velocities, v, on either side of the shock. (Note that gas saturation is sufficient to specify the composition of a point on a tie line once the tie line itself is known.) The fourth equation comes from the fact that the trailing shock is an immediate jump from point e to the injection composition. Its velocity is given by Eq. (3.1-12). Because the shock velocity must be the same for each component, the final equation is

$$\frac{F_1^e - F_1^f}{G_1^e - G_1^f} = \frac{F_3^e - F_3^f}{G_3^e - G_3^f}$$

For initial oil compositions that contain small amounts of C_4, the trailing shock may be a tangent shock, and there will be a continuous variation along the injection tie line. In such cases, the total velocity and gas saturation on the two-phase side of the trailing shock are determined from Eqs. (3.1-13) for components CO_2 and C_{10}. The total velocity at the upstream side of the self-sharpening wave is then known, because total velocity does not vary along a tie line. The remaining unknowns for the self-sharpening wave can then be determined from Eqs. (3.1-13) for components CO_2, C_4 and C_{10}.

The path just described satisfies all of the rules for path construction. A demonstration that the path selected is the only one that satisfies the velocity constraint is given by Monroe (1986). While the qualitative features of the solution can be seen from Figs. 3.1-2-3.1-5, the solution for a particular set of injection and initial compositions must be obtained by an iterative procedure. The key to finding the solution path for the quaternary system is the determination of the "crossover" tie line, the tie line that contains points c and d in Fig. 3.1-3. This tie line is unique for specified injection and initial conditions. It is the only one that is tangent to both the vertical and horizontal nontie-line paths that also intersect the initial and injection tie lines. The tie line shown in the CO_2-C_4-C_{10} face of Fig. 3.1-1 is one such tie line. Each tie line in the CO_2-C_4-C_{10} face, for example, is a crossover tie line for an associated tie line in the C_1-C_4-C_{10} face. In fact, any tie line within the quaternary diagram is a crossover tie line for some set of initial and injection tie lines. Those tie lines intersect the horizontal and vertical paths that are tangent to the crossover tie line.

To construct a solution for given initial and injection compositions for a path that contains two fluid banks, a trial and error solution was required. To identify the crossover tie line, an initial guess was made of the landing composition (point e in Figs. 3.1-2-3.1-5) within the two phase region on the injection tie line. Then the intermediate path was followed to the crossover tie line and down the vertical path to the C_1-C_4-C_{10} face. If the resulting tie line in the C_1-C_4-C_{10} face passed through the original oil composition, the correct crossover tie line was identified. If not, the injection landing point composition was adjusted until the path passed through the appropriate tie line through the initial composition.

3.1.4 Analysis

To determine the effect of dissolved C_1 on composition path, displacements were examined for live and dead oils with compositions shown in Table 3.1-1. Pure CO_2 was injected in both displacements, and the dead oil differed from the live oil only in that the C_1 was removed. Fig. 3.1-6 shows composition paths for the two displacements. The live oil path shows a shock in the C_1-C_4-C_{10} base, followed by a vertical path to the CO_2-C_4-C_{10} face. In the dead oil displacement, the leading shock lies in the CO_2-C_4-C_{10} face. While the two displacements traverse slightly different tie lines in the CO_2-C_4-C_{10} face, those tie lines lie so close together that they are difficult to distinguish in Fig. 3.1-6. Thus the portions of the composition paths for the two displacements that lie in the CO_2-C_4-C_{10} face differ only slightly, as Fig. 3.1-6 indicates. Therefore, if the displacement of the dead oil traverses a tie line that is

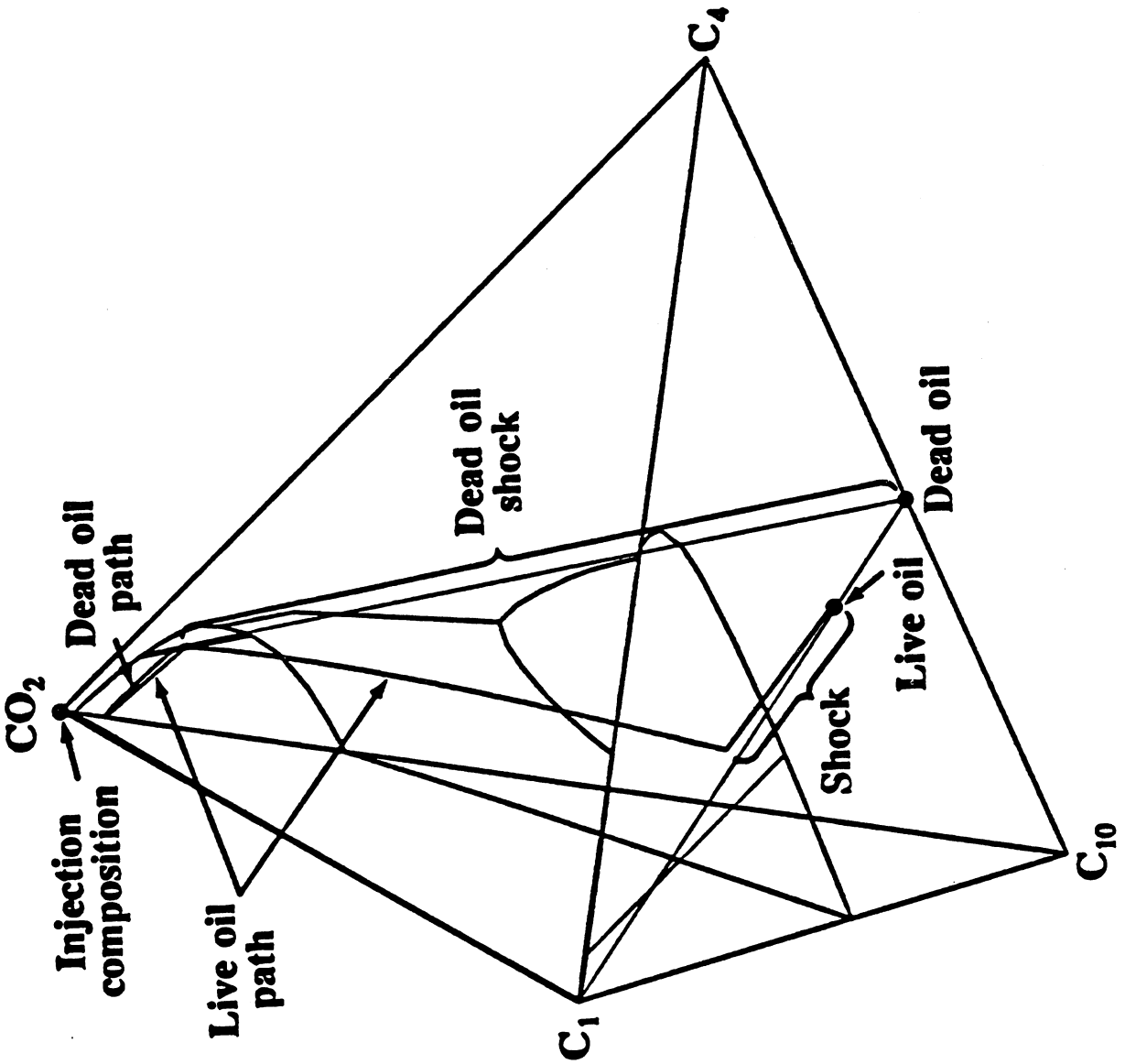

Fig. 3.1-6 Comparison of composition paths for live and dead oil displacements.

close to the plait point in the CO_2-C_4-C_{10} face, the crossover tie line for a corresponding live oil will also be close to the plait point.

Fig. 3.1-7 shows saturation profiles for the same displacements. The primary differences between the saturation profiles shown in Fig. 3.1-7 are the positions of the leading edge shocks and the volumes of the gas saturated zones behind the displacement fronts. Fig. 3.1-5 shows that C_1 is the primary constituent of the leading bank in the live oil displacement, and Fig. 3.1-7 shows that the bulk of the volume difference is also in that region. Behind the leading bank the C_1 composition quickly drops to zero. Thus, all of the C_1 moves in a bank ahead of the CO_2 front. The increased volume of the leading bank in the live oil displacement is the result of smaller volume change on mixing that results when CO_2 dissolves in the live oil, and C_1 vaporizes, replacing some of the lost CO_2 volume in the vapor phase. In the dead oil displacement, CO_2 also dissolves in the oil phase, losing volume as it does so, but smaller amounts of the oil components volatilize and replace the shrinkage of the vapor volume. Thus the leading edge advances more slowly in the dead oil displacement.

Behind the C_1 bank the saturation profiles are nearly identical. Where the composition path varies along the tie line between points **c** and **d** in Fig. 3.1-7, the C_4 travels in a bank. The C_4 partitions more strongly into the vapor phase than does C_{10}, and hence it travels at the front of the transition zone, as expected. C_{10} is the last component to be extracted completely at the trailing solubilization shock.

Fig. 3.1-8 reports C_1, C_4 and C_{10} recovery for the live and dead oil displacements. Before breakthrough of the leading shock, fractional recovery of each component is the same. After that point, the recovery curves show changes in slope that correspond to the arrival at the outlet of the trailing edge of the C_1 bank in the live oil case, the self-sharpening wave, and the trailing edge shock. Nearly all of the C_1 is recovered at CO_2 breakthrough, and all of the C_4 is recovered after the self-sharpening wave breaks through. Comparison of the results of the two displacements confirms that breakthrough of the leading edge shock occurs earlier in the four-component case, but that recovery is nearly the same at later times. That behavior results because there is very little difference in the saturation and composition profiles behind the self-sharpening wave.

Reasons for the observed behavior are made clearer by considering how composition paths change as miscibility develops. Table 3.1-3 shows calculated displacement data and results for four one-dimensional displacements of oils with increasing C_4 concentration. Addition of C_4 moves the overall composition of the oil toward the CO_2-C_1-C_4 face, and thus simulates the development of miscibility by moving the oil composition toward the boundary of the region of tie-line extension. Composition paths for the four oils are shown in Fig. 3.1-9. As the oil is enriched with C_4 from system 1 to 4 the velocity of the leading shock decreases, and the velocity of the trailing shock increases (see Table 3.1-3). In addition, the portion of the path that lies in the CO_2-C_4-C_{10} face approaches the dew point locus on that face. Thus, in system 4, most of the hydrocarbons have been solubilized into the transition zone, and the system is nearly miscible. Because there is no plait point in the C_1-C_4-C_{10} face at 1600 psia, no oil composition at that pressure can develop miscibility completely if the dilution line from pure oil to pure CO_2 intersects the two-phase region.† At some higher pressure (above the C_1-C_4 critical pressure), complete development of miscibility is possible for oils rich enough in C_4. When enough C_4 has been added that the original oil lies on the surface of critical tie lines, the composition path begins with a jump from the initial composition to the plait point in the C_1-C_4-C_{10} face, follows the locus of the plait points to the CO_2-C_4-C_{10} face and then follows the dew point locus.

† V. J. Kremesec and L. E. Baker point out that it is possible to have oil compositions (rich in C_4) for which the dilution line to pure CO_2 does not intersect the two-phase region. Such oil compositions would be first-contact miscible. The region of those oil compositions in the quaternary is a small one near the C_4 apex of the quaternary diagram.

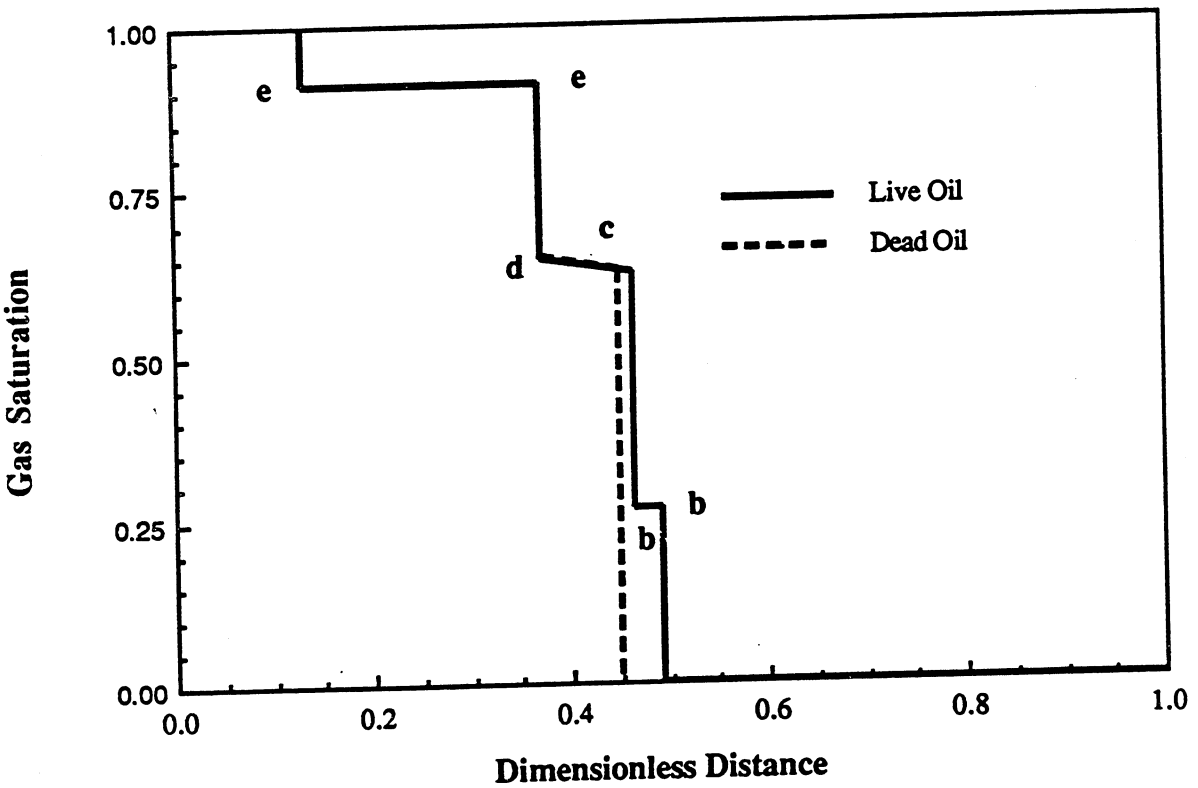

Fig. 3.1-7 Comparison of saturation profiles for live and dead oil displacements.

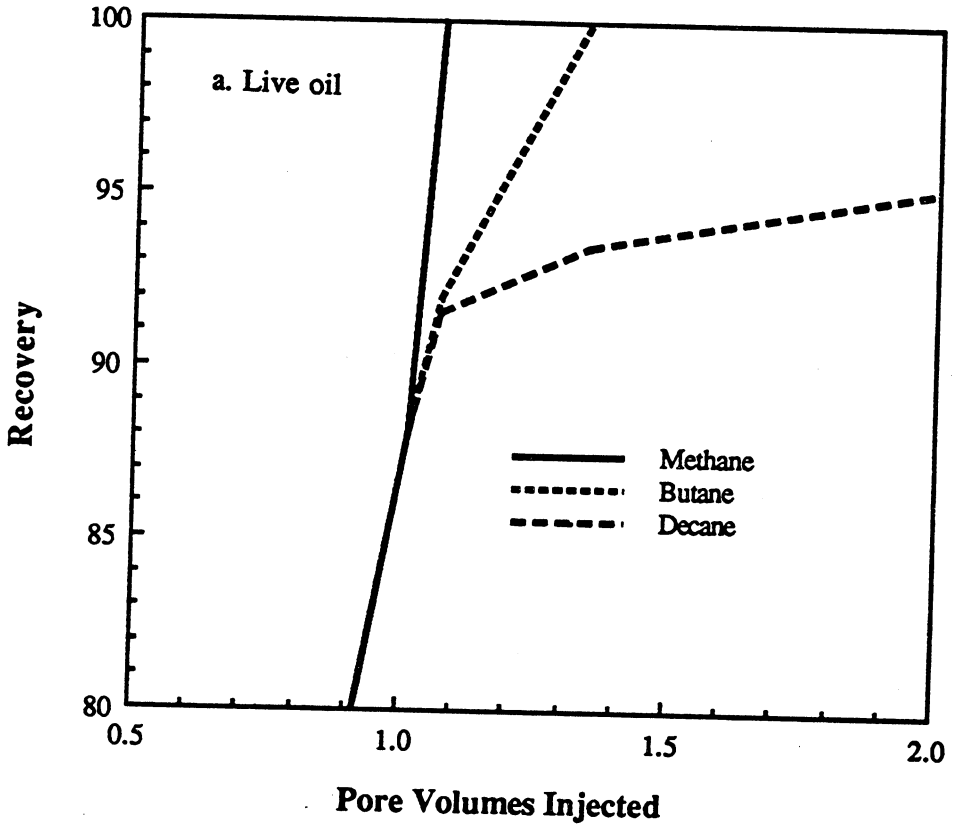

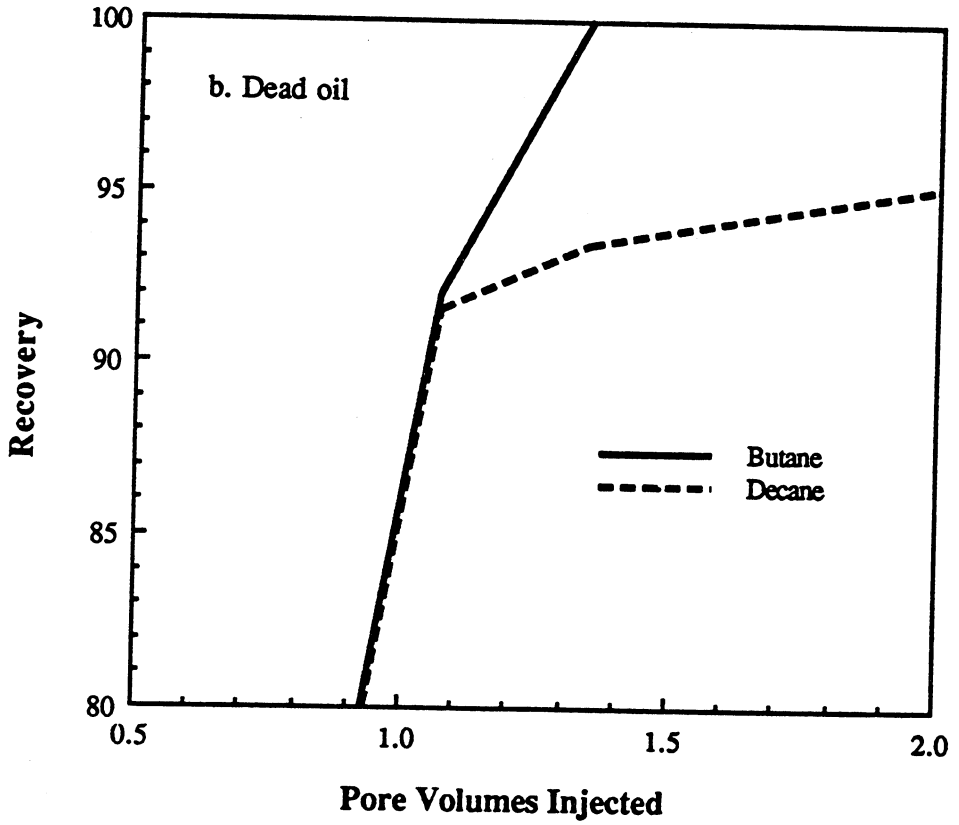

Fig. 3.1-8 Component recovery in live and dead oil displacements at 160°F (71°C) and 1600 psia (11.0 MPa).

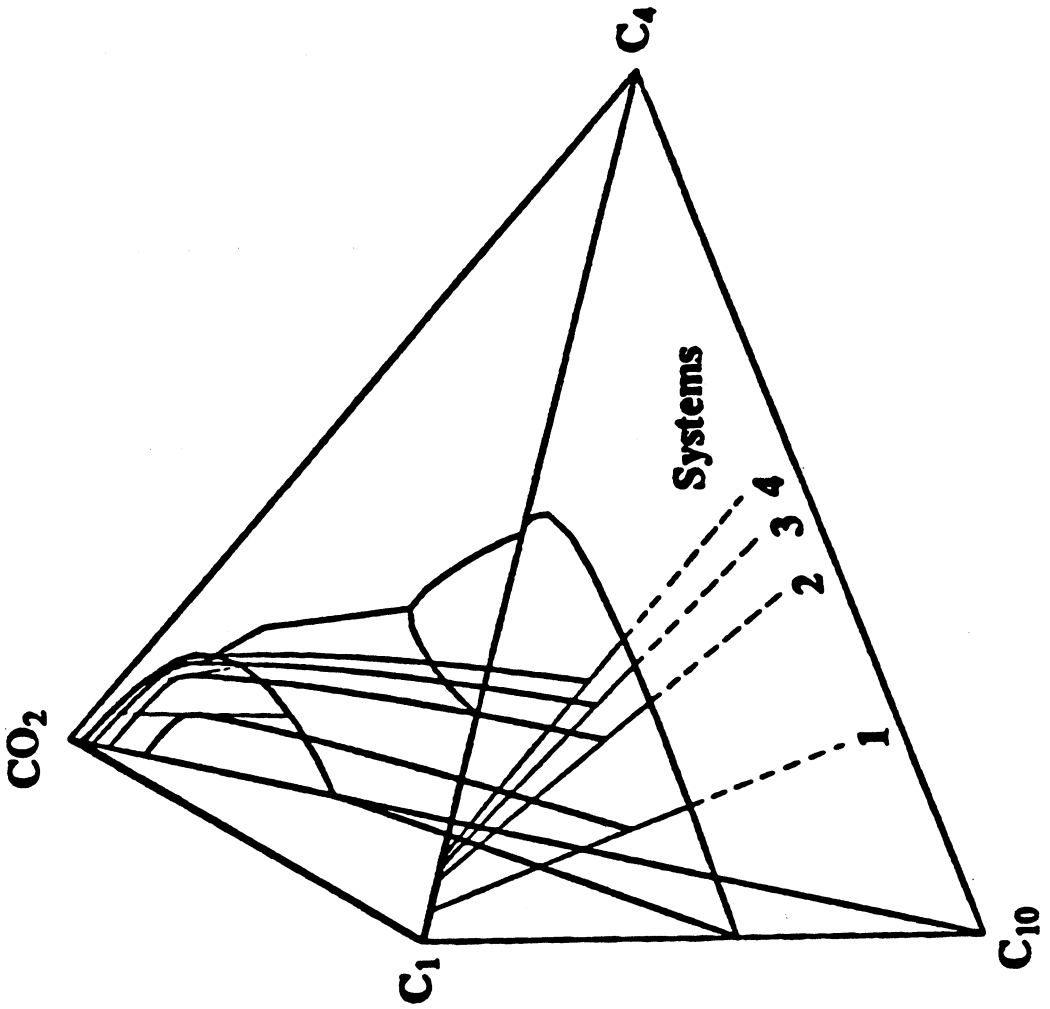

Fig. 3.1-9 Composition paths for displacement of live oils containing varying amounts of C_4 at 160°F (71°C) and 1600 psia (11.0 MPa).

Table 3.1-3 shows what happens to the C_1 bank as the system approaches miscibility. The velocity difference between the leading and trailing edges of the C_1 bank decreases with increasing C_4 concentration in the initial oil. Thus, though the size of the C_1 bank decreases, it does not disappear. In fact, because the two-phase region spans the ternary diagram from the C_1-C_{10} to the C_1-C_{10} binary edge, the analytical solution predicts that it is not possible for displacement of an oil containing C_1 to develop miscibility at that pressure (except for first-contact miscible compositions near the C_4 apex). Recovery efficiency improves as the amount of C_4 is increased, however. Recovery at breakthrough ranged from 81.2% for system 1 to 93.0% and 94.7% for systems 3 and 4. The displacement of systems 3 and 4 would clearly be judged to be miscible by the criteria of Holm and Josendal (1982) or Yellig and Metcalfe (1980).

The explanation for the improvement in recovery is based on the observation that the crossover tie lines for the four oils approach the plait point in the CO_2-C_4-C_{10} face as the amount of C_4 is increased from system 1 to 4. For the oils of systems 3 and 4, the crossover tie lines are very near the plait point on the CO_2-C_4-C_{10} face, even though the composition paths fall well into the two-phase region in the C_1-C_4-C_{10} face. The final portion of the composition path passes so close to the plait point and the dew point portion of the binodal curve that recovery is very high, despite the fact that the displacement passes through the two-phase region.

The effect of the amount of C_1 present originally in the oil can be understood by observing the solution path for a series of oils with increasing C_1 concentration that lie along the same tie-line extension in the C_1-C_4-C_{10} face (Monroe 1986). In such cases, only the velocity of the leading edge shock changes, because the values of F_i^I and G_i^I in Eq. (3.1-12) change. All of the C_1 still moves at the leading edge of the transition zone, and the addition of C_1 has no effect on the remaining composition path. In fact, even if the initial oil composition were inside the two phase region, it would be possible for the oil to be displaced efficiently. As long as the trailing portion of the displacement path passes close to the plait point and the binodal curve, high recovery will be observed. Hence, use of the BPP as the MMP for systems that have BPP's that are above the predicted MMP may be overly conservative. Instead, it is apparently possible, for one-dimensional displacements, at least, to have a nearly miscible displacement for an oil that is below its bubble point pressure.

Finally the effect of addition of CO_2 to the original oil can also be seen from the composition path shown in Fig. 3.1-10. The vertical path intersects a sequence of tie lines in the interior of the quaternary diagram. Thus, the crossover tie line in the CO_2-C_4-C_{10} face is associated with a ruled surface made up of tie lines that all intersect the vertical path that is tangent to the crossover tie line. Any initial oil composition that lies on an extension of a tie line in that surface follows exactly the same composition path in the CO_2-C_4-C_{10} face. Hence, the only effect of changing oil composition within that surface of tie line extensions is to change the velocity and composition at the leading shock. As in the case of "oils" with no CO_2 present initially, it is location of the crossover tie line that has the largest effect on recovery efficiency.

3.1.5 Comparison with Experimental Displacements

Metcalfe and Yarborough (1979) reported results of displacement experiments for CO_2-C_4-C_{10} and CO_2-C_1-C_4-C_{10} mixtures. The displacements were performed in an 8 ft. x 2 in. (2.4 m x 5. cm) Berea sandstone core. Compositions of the mixtures displaced are shown in Fig. 3.1-11. Displacements were performed at 1500, 1700 and 1900 psia (10.3, 11.7 and 13.1 MPa). As Fig. 3.1-11 and similar plots at higher pressures given by Larsen (1984) indicate, the live oil displaced was within the region of tie-line extensions on the C_1-C_4-C_{10} face at all three pressures. The displacement at 1500 psia recovered 80% of the hydrocarbons and was

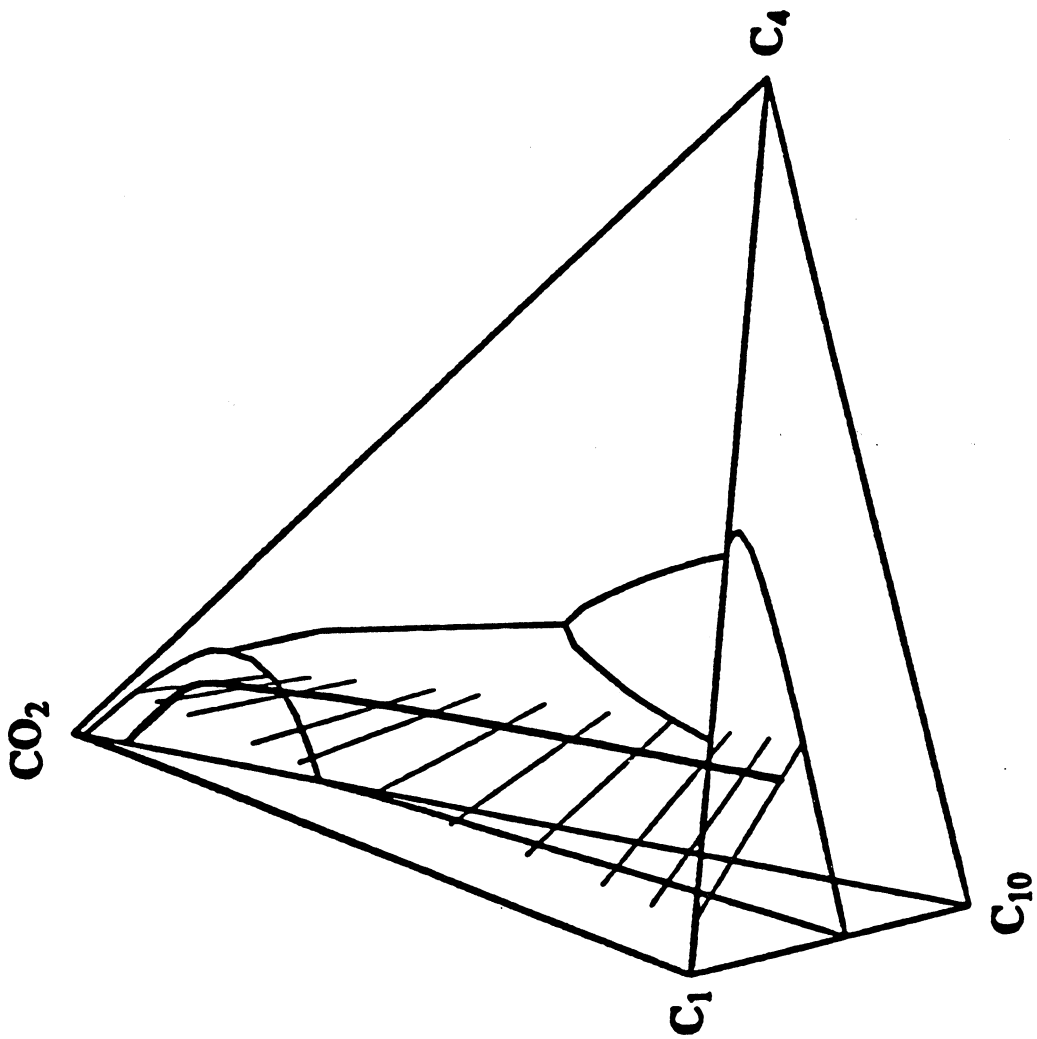

Fig. 3.1-10 Surface of tie lines associated with a vertical path.

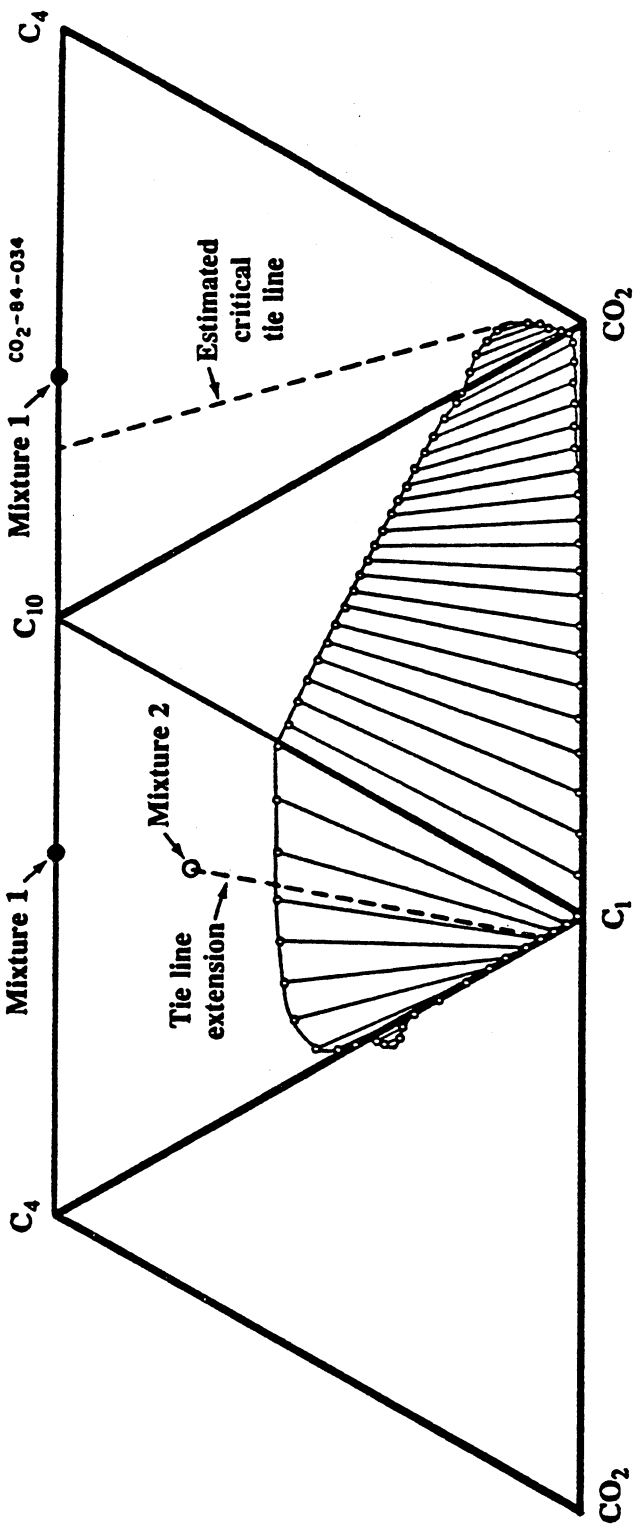

Fig. 3.1-11 Calculated ternary faces of a quaternary phase diagram for CO_2-C_1-C_4-C_{10} mixtures at 160°F (71°C) and 1750 psia (12070 kPa).

judged to be immiscible. The displacement of the corresponding dead oil at 1500 psia recovered 81% and was also taken to be immiscible. Thus, the experimental observation is consistent with the calculated composition paths shown in Figs. 3.1-6 and 3.1-7, which show that after passage of the C_1 bank, displacement performance is nearly the same for both the live and dead oils.

The displacements at 1700 and 1900 psia recovered 90 and 97% of the hydrocarbons and were interpreted to be multiple-contact and first-contact miscible, respectively. Displacements of the dead oil at the same pressures recovered 90 and 99% of the hydrocarbons. Analysis of composition paths suggests, however, that at 1500 and 1700 psia, the displacements passed through the two-phase region, but the crossover tie line at 1700 psia was close enough to the plait point that recovery was high anyway. At 1900 psia, a pressure above the critical pressure of the CO_2-C_{10} binary, the displacement developed miscibility because the injection fluid was outside the region of tie-line extensions. Methane banks were detected experimentally at 1500 and 1700 psia, but no C_1 bank was observed at 1900 psia. That result is also consistent with the composition path calculations, which indicate that the length of the of the C_1 bank should decrease as the pressure increases. Because the displacement at 1500 psia was immiscible, enough liquid phase was left behind the displacement front that the C_1 bank was relatively large, as is required by a simple material balance on C_1. At 1700 psia, the amount of liquid left behind the CO_2 front was much smaller because the dead oil was multiple-contact miscible. Hence, the C_1 bank was much smaller.

At 1900 psia, the displacement was multiple-contact miscible because the displacement pressure was above the critical pressure of the CO_2–C_{10} binary pair (Reamer and Sage 1963). Thus, in this case, it was the fact that the injection composition was outside the region of tie-line extensions that produced the observed multiple-contact miscibility.

Fig. 3.1-12 compares calculated normalized effluent C_1 concentrations with measure values at 1500 psia. Also shown in Fig. 3.1-12 is an effluent C_1 concentration calculated with a one-dimensional finite difference simulator. While the dispersion coefficient was set to zero in that calculation, numerical dispersion from the two-point upstream weighting scheme used caused the C_1 bank to be dispersed slightly. Both calculated C_1 banks arrived later than the measured peak. It is probable that part of the disagreement is due to the presence of viscous instability or gravity segregation (or both) in the corefloods, which would cause early breakthrough of injected CO_2 and faster movement of leading banks. If so, the experimental displacements were not strictly one-dimensional, and thus some disagreement with the analytical solution is to be expected. In any case, the calculated solutions reproduce the qualitative features of the measured effluent compositions. Successive banks rich in C_1 and C_4 were observed, the C_1 bank arrived later, and the length of the bank decreased as displacement pressure increased. The displacement performed at 1700 psia showed clearly that high recovery is possible in a displacement that exhibits a leading C_1 bank. The calculations reported here indicate that at that pressure, the displacement must have passed through the two-phase region, as the observation of a C_1 bank confirms. Thus, experiments and theory indicate that high recovery can be obtained even though the composition path passes through the two-phase region and hence does not meet the strict definition of multiple-contact miscibility.

3.1.6 Discussion

The composition paths described here explain qualitatively why dissolved gas has minimal effect on displacement efficiency, though crude oils are much more complex mixtures than the simple hydrocarbon systems considered here. Because many experimentalists routinely use displacement efficiency as a criterion for "miscibility," the calculated composition paths also explain why the MMP is insensitive to the addition of dissolved gas to an oil. The calculated paths confirm the qualitative argument of Holm and Josendal (1982) that C_1 partitions strongly into the more mobile vapor phase and hence CO_2 following behind can displace efficiently the remaining dead oil.

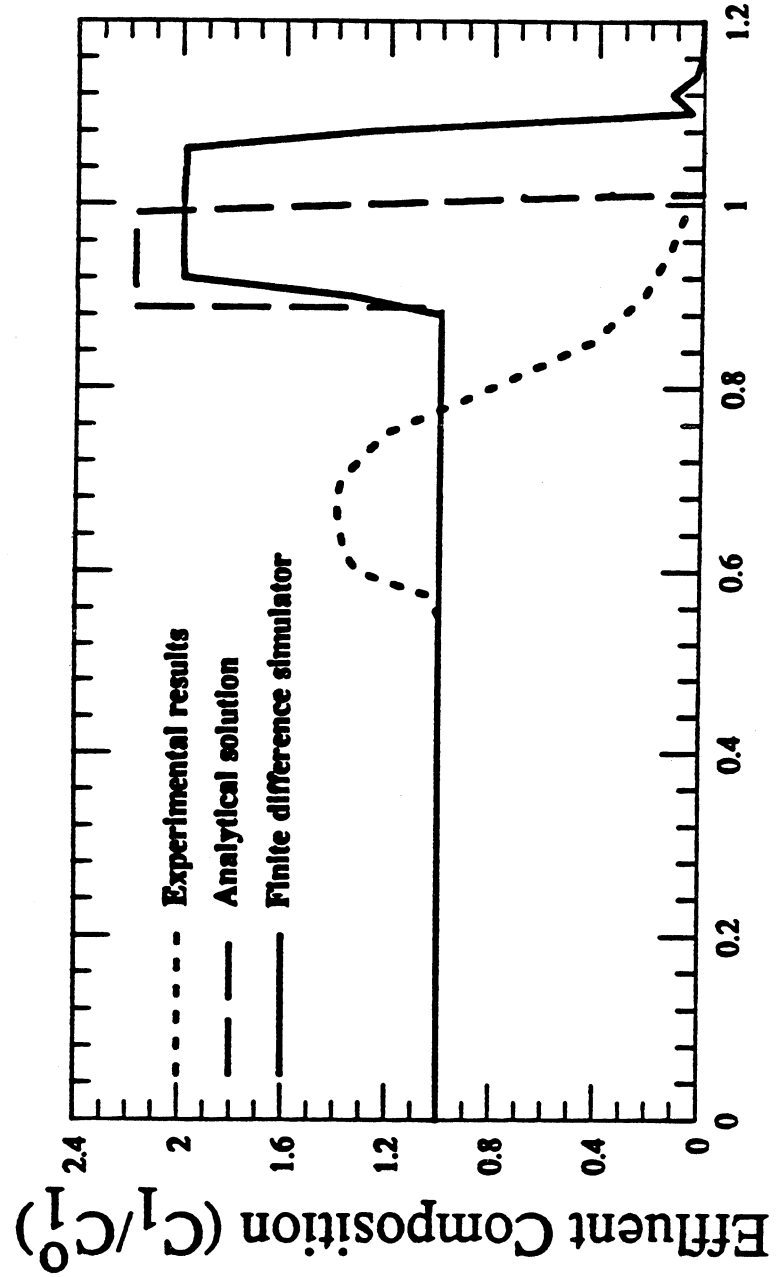

Fig. 3.1-12 Comparison of calculated and measured normalized effluent C_1 concentrations in displacement of a live oil by CO_2 at 160°F (71°C) and 1500 psia (10.3 MPa).

The results presented show that the distinction between miscible and immiscible displacements is not sharp. High local displacement efficiency, which is most important, can occur even when the displacement takes place entirely within the two-phase region. Use of the term "miscible" to describe such displacements is unfortunate because it places the emphasis on the number of phases present rather than on displacement efficiency. Instead, evaluation of appropriate displacement pressures should focus on oil recovery rather than on indications of two-phase flow. According to the composition path calculations, the existence of a C_1 bank is evidence for two-phase flow, but the same calculations, as well as Metcalfe and Yarborough's experiments, indicate that if the definition of the MMP is based on recovery, a criterion for the MMP based on the absence of a C_1 bank is probably too restrictive.

Additional experimental work is needed to confirm the prediction that high efficiency displacement can occur at a pressure below the BPP. Verification of the theory will require that the experimental displacement be nearly one-dimensional. Separate questions of considerable importance for field-scale CO_2 floods are:

(1) What is the optimum displacement pressure when the flow is not one-dimensional, and

(2) Is that pressure substantially different from the one-dimensional MMP?

Answers to those questions will depend not only on the phase behavior of the CO_2-crude oil mixtures, but also on the length scales of the zones of fast and slow flow, whether due to viscous instability or reservoir heterogeneity, and on rates of mixing between those zones caused by dispersion, viscous and capillary crossflow and gravity segregation. Thus, the one-dimensional analysis given here is only a first step toward more complete understanding of the role of phase behavior in field-scale flows.

3.1.7 Conclusions

Analysis of composition paths for dispersion-free, one-dimensional displacement of C_1-C_4-C_{10} mixtures by CO_2 leads to the following conclusions:

(1) Addition of dissolved C_1 to a dead oil causes formation of a leading C_1 bank unless the live oil lies outside the region of tie-line extensions in the quaternary diagram. If the pressure is high enough that the dead oil develops miscibility, however, the C_1 bank will appear at the outlet for a short time only.

(2) Oil recovery is controlled by the location of the crossover tie line. If that tie line lies close to the plait point on the CO_2-C_4-C_{10} ternary diagram, oil recovery will be high, even though the composition path passes through the two-phase region. If the oil that remains after all C_1 is removed develops miscibility, the crossover tie line will be very close to the plait point.

(3) Oils that share the same crossover tie line show the same recovery performance after CO_2 breakthrough. Breakthrough times of leading C_1 banks depend on amounts of C_1 and CO_2 present in the original oil, however.

(4) The presence of a C_1 bank should not be used as a single criterion for evaluating potential displacement pressures. Oil recovery is a more reliable indicator of performance for one-dimensional flows.

(5) Displacement of live oil at a pressure below its BPP will be efficient as long as the flow is one-dimensional, and the dead oil develops miscibility when the C_1 is removed.

3.2 Analytical Model of Steam/Oil/Water Displacements

Jeffrey S. Wingard

In thermal recovery processes, steam is injected to heat the oil, reduce its viscosity and improve recovery. If CO_2 is injected along with the steam, or if CO_2 is created in situ by combustion with injected oxygen, then the transfer of CO_2, water and oil between phases will alter the flow behavior as dissolved CO_2 reduces the viscosity of the oil. If the temperature is constant, solutions for a CO_2/steam/oil displacement can be obtained by the method described in Section 3.1. Examples of such solutions are given by Wingard (Orr and Grader 1987). If the temperature varies, however, the problem is significantly more complex, and analytical solutions have not yet been obtained. However, solutions to a sequence of simpler but still challenging problems have been found and are described in this section.

3.2.1 Mathematical Model

Model Description

The model uses the method of characteristics to solve a simplified flow of an arbitrary number of components that partition into an arbitrary number of phases. The model is similar to that developed by Helfferich (1981) and Dumoré et al. (1984) and described here in Section 3.2, with the addition that the system has a temperature variation along the direction of flow. The assumptions made in the derivation of the material balance equations are

- Flow is one-dimensional
- Pressure is constant over the length of the displacement. This assumption is made with respect to the thermodynamic equilibrium. While there must be a pressure gradient in order for flow to occur, the solutions are independent of the pressure gradient once the injection velocity is set.

  The assumption of constant pressure also allows the use of the enthalpy of the phase in the accumulation term. While it is not correct to say that enthalpy can be accumulated, because the system is at constant pressure and constant total volume, there is no PV work term to consider. Under these conditions, it is correct to consider the total energy and enthalpy balances as identical.
- Porosity is constant.
- Mass and heat transfer are instantaneous.
- Mass transfer by dispersion and diffusion is neglected.
- Heat transfer by conduction and radiation is neglected.
- Heat capacity of the porous medium is constant over the temperature range of interest.

If dispersion can be neglected, a material balance on the i^{th} component gives,

$$\frac{\partial}{\partial t} \sum_{j=1}^{n_p} \phi \, x_{ij} \, \rho_j \, S_j + \sum_{j=1}^{n_p} \nabla \cdot \rho_j \, x_{ij} \, \vec{v}_j = 0 \qquad i=1, \, n_c. \tag{3.2-1}$$

The energy balance can be written in a similar form if all the transport is by convection

$$\frac{\partial}{\partial t} \sum_{j=1}^{n_p} \phi \, H_j \, \rho_j \, S_j + (1 - \phi) \, \rho_m \, H_m + \sum_{j=1}^{n_p} \nabla \cdot \rho_j \, H_j \, \vec{v}_j = 0 \tag{3.2-2}$$

where

n_p = number of phases
n_c = number of components
x_{ij} = mole fraction of component i in phase j
ρ_j = molar density (kg–mole/m^3) of phase j
ρ_m = mass density of the matrix (kg/m^3)
$\vec{v}_j$ = phase velocity vector (m/day)
S_j = saturation of phase j
ϕ = porosity
H_j = molar enthalpy (J/kg–mole) of phase j
H_m = specific enthalpy of the matrix (kJ/kg · m^3)

Eq. (3.2-2) has the same form as Eq. (3.2-1). Thus, under the assumptions listed above, enthalpy can be viewed as another composition variable.

Following the derivation in Section 3.1, equations 3.2-1 and 3.2-2 can be simplified to

$$\frac{\partial G_i}{\partial t} + \frac{\partial F_i}{\partial x} = 0 \qquad i = 1, n_c \tag{3.2-3}$$

and

$$\frac{\partial \Gamma_i}{\partial \Theta} + \frac{\partial F_i}{\partial x} = 0 \qquad i = 1, n_c \tag{3.2-4}$$

where the following definitions have been applied.

$$G_i \equiv \sum_{j=1}^{n_p} x_{ij}\, \rho_j\, S_j\,, \tag{3.2-5}$$

$$\Gamma \equiv \sum_{j=1}^{n_p} H_j\, \rho_j\, S_j + \left[\frac{1-\phi}{\phi}\right] \rho_m\, C_{pm}\, T \tag{3.2-6}$$

$$F_i \equiv \frac{v}{\phi} \sum_{j=1}^{n_p} x_{ij}\, \rho_j\, f_j\,, \tag{3.2-7}$$

and,

$$\Theta \equiv \frac{v}{\phi} \sum_{j=1}^{n_p} H_i\, \rho_j\, f_j\,. \tag{3.2-8}$$

where $f_j = \vec{v}_j \cdot \dfrac{\phi}{u}$ = fractional flow of phase j

$C_{pm} = H_m/T$ = heat capacity of the matrix (kJ/kg · K)

The term G_i represents the local overall concentration of component i, and is similar to the local concentration term in the familiar Buckley-Leverett (1942) equation. The F_i term represents the flux of component i. The Γ term is the energy analog to the local concentration term in the material balance. It differs from the mass terms in that the matrix is also allowed

to accumulate heat from the fluids and vice versa. The $\rho_m C_{pm} T$ term in the definition of Γ accounts for the heat stored in the matrix. Finally, the Θ term accounts for the heat flux in the system. Since the matrix is immobile and conduction has been neglected, there is no term for flux due to the matrix.

Because Eqs. (3.2-3) and (3.2-4) retain their hyperbolic character, the method of characteristics can be used to solve these coupled equations. If solutions are sought for which a given overall mixture composition (including the mixture temperature) moves at a single velocity, the set of $n_c + 1$ balance equations is reduced to a general eigenvalue problem, where component velocities are given by the eigenvalues and characteristic directions by the associated eigenvectors.

If a procedure similar to that outlined in Eqs. (3.1-5)-(3.1-10) is applied to Eqs. (3.2-3) and (3.2-4), the resulting statement of the eigenvalue problem is (Wingard 1989)

$$\begin{bmatrix} \frac{\partial F_1}{\partial C_1} & \frac{\partial F_1}{\partial C_2} & \cdots & \frac{\partial F_1}{\partial C_{nc-1}} & \frac{\partial F_1}{\partial T} & \frac{\partial F_1}{\partial v} \\ \frac{\partial F_2}{\partial C_1} & \frac{\partial F_2}{\partial C_2} & \cdots & \frac{\partial F_2}{\partial C_{nc-1}} & \frac{\partial F_2}{\partial T} & \frac{\partial F_2}{\partial v} \\ \vdots & \vdots & \cdots & \vdots & \vdots & \vdots \\ \frac{\partial F_{nc}}{\partial C_1} & \frac{\partial F_{nc}}{\partial C_2} & \cdots & \frac{\partial F_{nc}}{\partial C_{nc-1}} & \frac{\partial F_{nc}}{\partial T} & \frac{\partial F_{nc}}{\partial v} \\ \frac{\partial \Theta}{\partial C_1} & \frac{\partial \Theta}{\partial C_2} & \cdots & \frac{\partial \Theta}{\partial C_{nc-1}} & \frac{\partial \Theta}{\partial T} & \frac{\partial \Theta}{\partial v} \end{bmatrix} \begin{bmatrix} \frac{dC_1}{d\eta} \\ \frac{dC_2}{d\eta} \\ \vdots \\ \frac{dT}{d\eta} \\ \frac{dv}{d\eta} \end{bmatrix} =$$

$$\lambda \begin{bmatrix} \frac{\partial G_1}{\partial C_1} & \frac{\partial G_1}{\partial C_2} & \cdots & \frac{\partial G_1}{\partial C_{nc-1}} & \frac{\partial G_1}{\partial T} & 0 \\ \frac{\partial G_2}{\partial C_1} & \frac{\partial G_2}{\partial C_2} & \cdots & \frac{\partial G_2}{\partial C_{nc-1}} & \frac{\partial G_2}{\partial T} & 0 \\ \vdots & \vdots & \cdots & \vdots & \vdots & \vdots \\ \frac{\partial G_{nc}}{\partial C_1} & \frac{\partial G_{nc}}{\partial C_2} & \cdots & \frac{\partial G_{nc}}{\partial C_{nc-1}} & \frac{\partial G_{nc}}{\partial T} & 0 \\ \frac{\partial \Gamma}{\partial C_1} & \frac{\partial \Gamma}{\partial C_2} & \cdots & \frac{\partial \Gamma}{\partial C_{nc-1}} & \frac{\partial \Gamma}{\partial T} & 0 \end{bmatrix} \begin{bmatrix} \frac{dC_1}{d\eta} \\ \frac{dC_2}{d\eta} \\ \vdots \\ \frac{dT}{d\eta} \\ \frac{dv}{dx} \end{bmatrix} \qquad (3.2\text{-}9)$$

where η is the dummy variable of the characteristic solution.

Eq. 3.2-9 is a general eigenvalue problem for which a solution exists if and only if $\det [\mathbf{F} - \lambda \mathbf{G}] = 0$. For a three component system $\mathbf{F}$ and $\mathbf{G}$ are 4 x 4 matrices. The eigenvalues correspond to n_c composition velocities, and the last eigenvalue is infinite. The infinite eigenvalue represents the rate at which changes in flow velocity propagate through the system (Monroe 1986). Thus, the remaining n_c velocities for a given overall composition and temperature are real and finite and are possible choices for the velocity of that overall composition (and temperature).

At certain singular points, two of the n_c eigenvalues can be equal. Systems that exhibit this property are called *nonstrictly* hyperbolic. These equal eigenvalue points are important in

the construction of the solution, for at these points, the solution path is free to switch, with no jump in velocity, from one of the characteristics to the other characteristic with the equal eigenvalue. In essence, these points represent a zone of constant state with a length of zero.

Along with the velocities as represented by the eigenvalues, the associated eigenvectors describe the characteristic curve in hodograph space for each of the eigenvalues. The eigenvectors indicate what set of compositions and temperature can lie directly ahead of and behind the current composition and still satisfy the material and energy balances.

Evaluation of Eigenvalues and Eigenvectors

The derivatives in the eigenvalue matrix (Eq. 3.2-9) relate how the saturation and flux terms for each component vary when the overall composition, temperature and flow velocity at a particular location change. Evaluation of those derivatives requires that the properties of all the existing phases be known for a given overall composition and temperature. The properties needed are molar density, composition saturation, enthalpy, viscosity and relative permeability of each phase. With the exception of the viscosity and the relative permeability, all other properties can be obtained directly from an equation of state. Phase viscosities were calculated with empirical correlations. Details of the representations used are given by Wingard (1989, Appendix B).

Relative permeabilities of the wetting and gaseous phases were calculated using a power law of the form

$$k_{rg} = \sigma_g \left[\frac{S_g}{1 - S_{or} - S_{wc}} \right]^{\alpha_g} \tag{3.2-10}$$

and

$$k_{rw} = \sigma_w \left[\frac{S_w - S_{wc}}{1 - S_{or} - S_{wc}} \right]^{\alpha_w} \tag{3.2-11}$$

where

k_{rg} = gaseous phase relative permeability
k_{rw} = wetting phase relative permeability (usually water)
σ_g = end point (maximum) relative permeability of the gaseous phase
σ_w = end point (maximum) relative permeability of the wetting phase
S_g = gaseous phase saturation
S_{wc} = connate wetting phase saturation
S_{or} = residual intermediate phase saturation
α_g = gaseous phase exponent
α_w = wetting phase exponent

In the absence of free gas, the oil phase relative permeability was taken to be

$$k_{row} = \sigma_{ow} \left[\frac{S_o - S_{wc}}{1 - S_{or} - S_{wc}} \right]^{\alpha_{ow}} \tag{3.2-12}$$

where

k_{row} = oil relative permeability in the oil-water system
σ_{ow} = end point (maximum) relative permeability of the intermediate phase

S_o = intermediate phase saturation, $S_o = 1 - S_w$
α_{ow} = oil-water exponent

Oil phase relative permeabilities in three-phase systems were calculated using Stone's (1970) model, as given by Aziz and Settari (1979).

$$k_{ro} = \frac{(k_{row} + k_{rw})\,(k_{rlg} + k_{rg})}{k_{rocw}} - k_{rw} - k_{rg} \tag{5.2-13}$$

where k_{rocw} is the intermediate phase relative permeability at the irreducible water saturation.

Once all the fluid properties are calculated for each phase, G, F, Γ, and Θ can be calculated using the definitions given in Eqs. (3.2-3) to (3.2-6).

Derivatives in Eq. (3.2-9) were calculated by finite differences (Monroe 1986, Wingard 1989). Eigenvalues and the associated eigenvectors were found using an algorithm presented by Moler and Stewart (1973) as implemented in the IMSL routine **EIGZCF**.

Shocks

As in the shock balances of Section 3.1, the wave velocity of a discontinuity is

$$\Lambda = \frac{1}{\phi}\left[\frac{u^+ F^+ - u^- F^-}{G^+ - G^-}\right] \tag{3.2-14}$$

and a similar energy balance across the shock yields

$$\Lambda = \frac{1}{\phi}\left[\frac{u^+\Theta^+ - u^-\Theta^-}{\Gamma^+ - \Gamma^-}\right] \tag{3.2-15}$$

These balances are known as Rankine-Hugoniot conditions.

For a system of n_c components the material and energy balances are given by equating $n_c + 1$ equations like Eq. 3.2-14 and one given by Eq. 3.2-15,

$$\phi\Lambda = \frac{u^+ F_1^+ - u^- F_1^-}{G_1^+ - G_1^-} = \frac{u^+ F_2^+ - u^- F_2^-}{G_2^+ - G_2^-} = \cdots = \frac{u^+ F_{n_c}^+ - u^- F_{n_c}^-}{G_{n_c}^+ - G_{n_c}^-} = \frac{u^+ \Theta^+ - u^- \Theta^-}{\Gamma^+ - \Gamma^-} \tag{3.2-16}$$

Elimination of Λ from this set of equations leaves n_c independent equations relating the conditions on the upstream side of the shock to the downstream conditions. One of these equalities is used to relate the unknown flow velocity the flow velocity on the opposite side of the shock. Constraints on the mole fraction summations and total saturation provide two additional equations. This leaves $n_c + 3$ variables that remain to be determined.

Setting the conditions on one side of the shock fixes $n_c + 1$ of the remaining variables, leaving a single degree of freedom. Physical considerations usually require that the shock velocity, Λ, to be equal to one of the wave velocities adjacent to the discontinuity.

The equality of the wave velocity and shock velocity results in a shock that is known as an intermediate discontinuity. These intermediate discontinuities are the multidimensional equivalent of the Buckley-Leverett "tangent" shock. The equality of eigenvalue (λ) and shock velocity (Λ) is the remaining condition required to fix the shock conditions.

Solution Construction

As in the four-component problem of Section 3.1, the solution for given injection and initial conditions must be selected from the set of composition paths obtained by integrating the eigenvectors. The solution must be on paths when continuous variations occur, and compositions with high wave velocities must lie downstream of those with lower velocities. When continuous composition variations that satisfy the velocity constraint cannot be found, shocks are required (Wingard 1989, Chapter 3). Thus, the solution for specific inlet and initial conditions is constructed from a combination of continuous variations and shocks. Much of the difficulty of the problems considered in this section and in Section 3.3 comes from the variety of combinations of shocks, continuous variations and zones of constant state. In the remainder of this section we demonstrate solutions for several sets of inlet and initial conditions. Additional example solutions are given by Wingard (1989).

3.2.2 Displacement of Liquid Water by Steam

Injection of steam into liquid water is the simplest of the example solutions presented here. This problem isolates the effects of temperature variations and phase changes but eliminates composition variations. The unknown variables here are vapor saturation, temperature, and local flow velocity. Because the pressure is taken to be fixed for calculation of the phase equilibrium, two phases can only exist at one temperature, as the phase rule indicates.

Figs. 3.2-1, 3.2-2, and 3.2-3 show solutions obtained for base conditions summarized in Table 3.2-1. For all three cases, the saturation temperature, fluid densities and enthalpies were found by curve fitting a fifth order polynomial in temperature to the values given by Reynolds (1979) for water at 2.0 MPa (290.16 psia). Viscosities at the saturation pressure were estimated from equations given by Reid et al. (1977). The injection velocity was set at one pore volume of steam per dimensionless time unit. Details of the formulation of the balance equations and construction of solutions for this special case are given by Wingard (1989, Section 4.1).

Fig. 3.2-1 shows the effect of variations in injection temperatures on the saturation distribution. The five saturation profiles are all shown at injection of one pore volume of steam. The major differences between the five profiles are the positions of the leading and trailing shocks as the injection temperature increases. At the leading shock, the shock height remains constant, while the velocity increases with increasing injection temperature. The conditions ahead of the leading shock are constant for all the profiles, and hence the saturation change across the discontinuity is the same for all the cases. The position of the shock changes because the flow velocity in the two-phase region is lower at higher temperatures. At high temperature, the density of the injected fluid is lower, and the fluid carries less heat per unit volume. Therefore, at one pore volume injected, the mass of steam injected is lower and the change in volume is greater when the steam condenses. That volume change reduces the flow velocity in the two-phase region and downstream of it.

The behavior of the trailing shock is explained by the heat balance across the trailing shock. As the injection temperature increases, the enthalpy difference across the shock increases. To compensate for the increased heat crossing the discontinuity at the higher injection temperature, the shock velocity decreases. The trailing shock is also slowed by volume change on condensation.

The second parameter studied was the initial temperature. It causes much smaller changes in the saturation profiles than changes in the initial temperature. Fig. 3.2-2 illustrates the change in location of the leading shock as the initial temperature changes from 300°K to 450°K. The initial temperature only changes the location and height of the leading shock. The hyperbolic nature of the equations means that the conditions downstream do not affect the

Table 3.2-1. Base Conditions for the Generation of Steam/Water Profiles at 2.0 MPa.

Pressure		2.0 MPa
Injection Velocity		1.0 (m/day)
Saturation Temperature	T_{sat}	485.57 K
Irreducible Water Saturation	S_{wi}	0.0
Steam Phase Exponent	n_g	1.0
Water Phase Exponent	n_w	3.0
Fluid Properties at Saturation Temperature		
Steam Viscosity	μ_g	0.0217 $(mPa{\cdot}sec)$
Water Viscosity	μ_w	0.1303 $(mPa{\cdot}sec)$
Steam Density	ρ_g	9.970241 (kg/m^3)
Water Density	ρ_w	850.4723 (kg/m^3)
Steam Enthalpy	H_g	2808.52 (kJ/kg)
Water Enthalpy	H_w	901.41 (kJ/kg)
Matrix Properties		
Density	ρ_m	2650.0 (kg/m^3)
Heat Capacity	C_{pm}	0.0047 $(kJ/kg-K)$
Porosity	ϕ	0.100

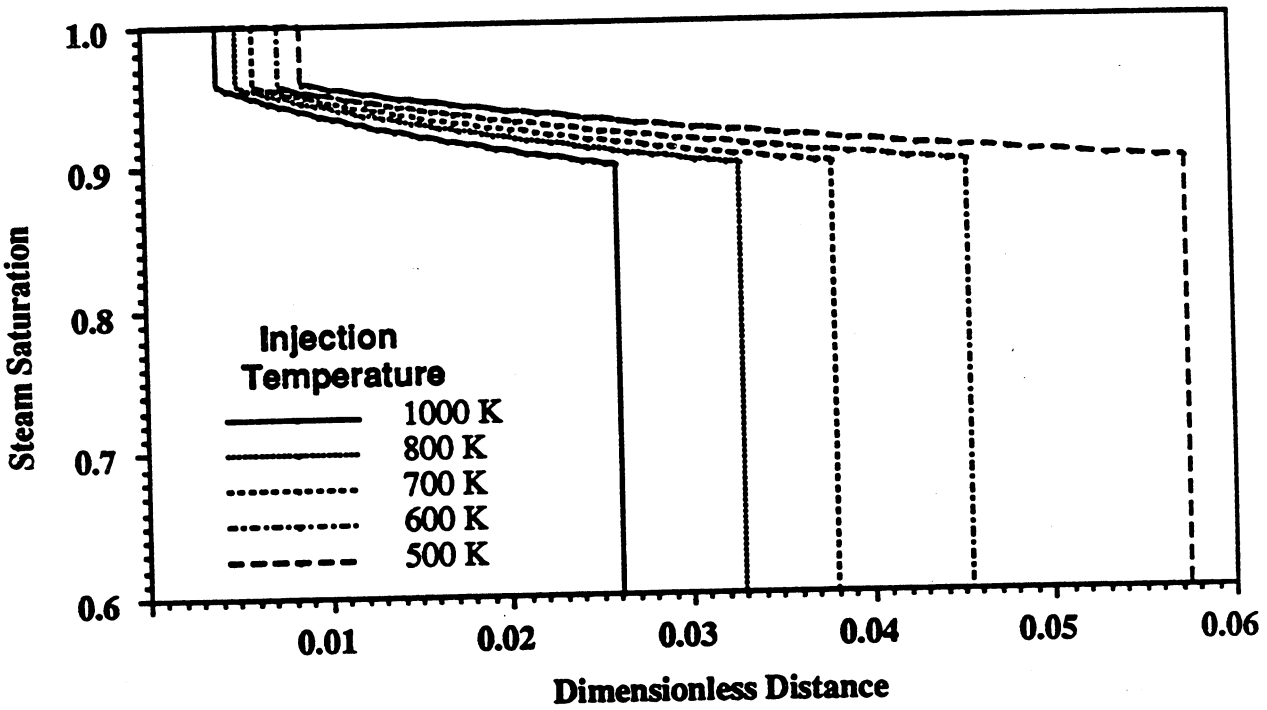

Fig. 3.2-1. Saturation profile after 1.0 pore volumes of steam injection into water at injection temperatures from 500°K-1000°K.

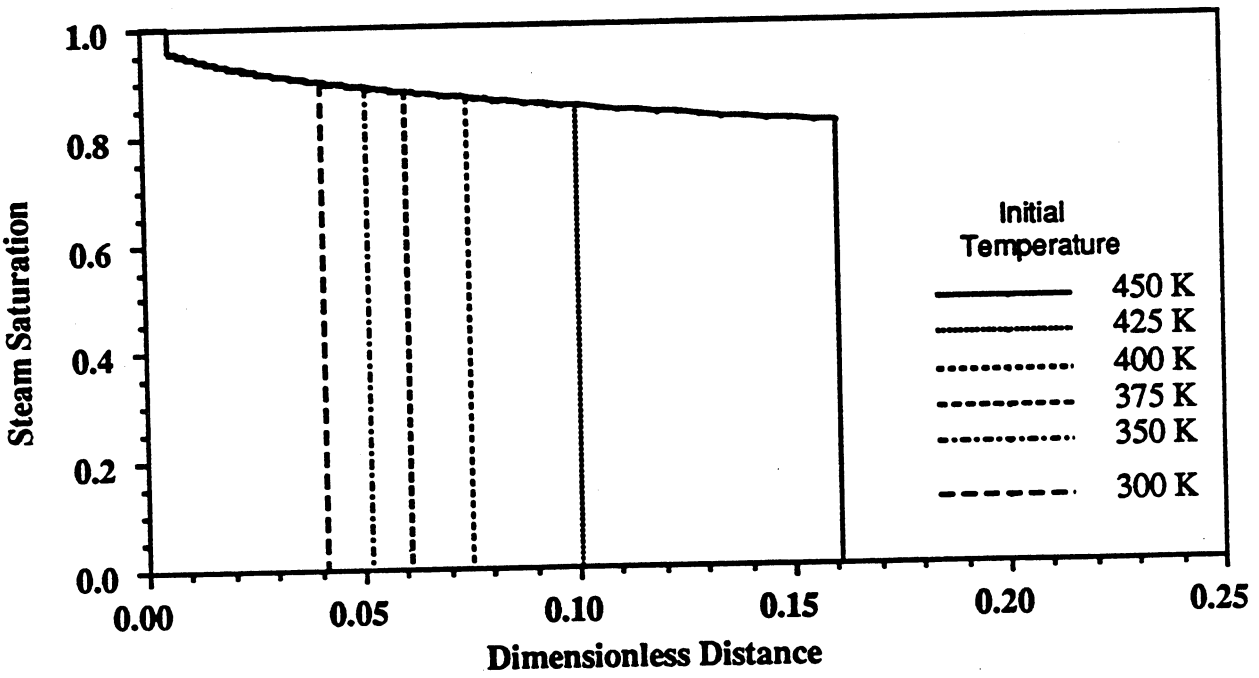

Fig. 3.2-2. Saturation profile after 1.0 pore volumes steam injection into water at initial temperatures from 300°K-450°K.

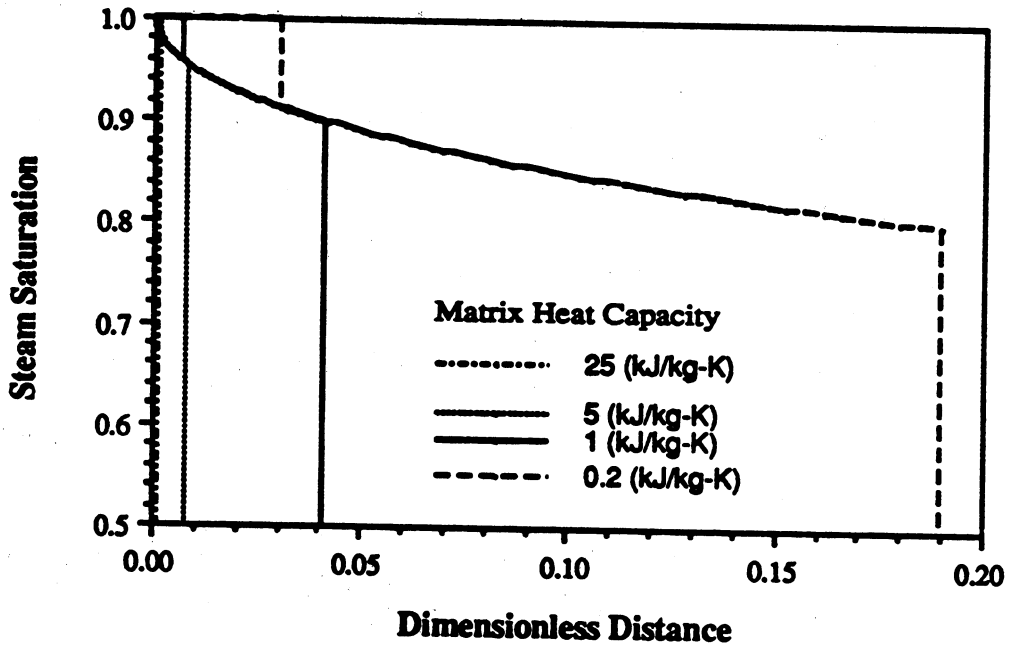

Fig. 3.2-3. Saturation profile after 1.0 pore volumes steam injection into water where the matrix heat capacity varies from 25.0 (kJ/kg–K) to 0.2 (kJ/kg–K).

upstream values. The trailing shock would behave the same regardless of the temperature or saturations downstream of the two-phase region.

Faster shocks at higher initial temperatures occur because fluid from the two-phase region must heat the matrix and surroundings from the initial temperature to the saturation temperature before the leading shock can propagate downstream. If the initial temperature is close to the saturation temperature, little enthalpy is needed and the shock has a high velocity and a low height. When the initial temperature is far below the saturation temperature, much more energy must be added to produce two phases, and the shock travels slowly. The larger transfer of enthalpy via condensation requires a greater shock height.

The third parameter examined was the matrix heat capacity. Fig. 3.2-3 shows how the saturation profile is modified by changes in the matrix heat capacity. As the heat capacity of the matrix is decreased from a value of 25.0 (kJ/kg–K) to zero, the positions of the leading and trailing shocks are affected, while the saturation profile remains unchanged. The explanation for the insensitivity of the two-phase region is clear. Recall that the two-phase region is at constant temperature, therefore no heat transfer can take place from the fluids to the matrix or vice versa. This takes the thermal properties of the matrix out of the equations representing the two-phase region.

The velocities of both the trailing and leading shocks increase as the matrix heat capacity decreases. The explanation is essentially identical to that for the initial temperature variation. Lower heat capacity means that less enthalpy is stored per degree of temperature change. Less enthalpy is therefore required to raise the matrix from the initial temperature to the saturation temperature and subsequently from the saturation temperature to the injection temperature.

3.2.3 Steam Displacement of a Light Oil and Water

If an immiscible oil component is added to the steam/water displacement of Section 3.2.2, the phase behavior of the water is unchanged. However, there is now two-phase (steam/oil) flow at the upstream end, three-phase (steam/water/oil) in the condensation region, and two-phase (water/oil) flow in the downstream region. The three-phase region is still at constant temperature, but the complication of three-phase relative permeabilities is added. As in the previous problem, shocks are required at locations where the number of phases changes. Details of the procedures used to construct the solutions described below are given by Wingard (1989, Section 4.2).

Fig. 3.2-4 shows the viscosities of water, steam and three oils for which solutions were obtained. At the displacement pressure, 2.0 MPa, the saturation temperature of water is 485.57°K. Other properties of water at that temperature are given in Table 3.2-1.

Light Oil Displacement

Fig. 3.2-5 shows the calculated composition path for a displacement of oil (with saturation 88.1%) and water (saturation 11.9%) at an initial temperature of 433.79°K. The diagram shown in Fig. 3.2-5 is a composite of two-phase diagrams (steam/oil and water/oil), in which temperature and saturation vary, and a ternary diagram at the saturation temperature, in which phase saturations can vary but temperature is constant. Table 3.2-2 summarizes saturations, temperatures, and velocities for key points labeled on Fig. 3.2-5. Table 3.2-3 explains the abbreviations used in Table 3.2-2. Figs. 3.2-6, 3.2-7, and 3.2-8 show corresponding saturation temperature, and velocity profiles at one pore volume of steam injection.

The injection condition is point **A**. From point **A** to point **B**, there is a continuous variation in steam and oil saturation (Fig. 3.2-6) at constant temperature (Figs. 3.2-5 and 3.2-7). The three-phase region appears with a shock from point **B** to point **C** in the three-phase

Table 3.2-2. Type 4 Composition Path for Injection of 100% Steam at 650°K into 88.1% Oil and 11.9% Water at 433.79°K.

Label	Composition Point					Wave Velocity	Type of Flow Region
	Saturations			T (K)	Flow Velocity		
	Steam	Oil	Water				
A	1.00000	0.00000	0.00000	650.00	1.0000	0.000000	INJ→SPW
B	0.92000	0.08000	0.00000	650.00	1.0000	0.010777	SPW→UID
C	0.41924	0.39087	0.18989	485.57	0.7058	0.010777	UID→ZCS
D	0.41924	0.39087	0.18989	485.57	0.7058	0.034233	ZCS→SPW
E	0.37839	0.38132	0.24029	485.57	0.7058	0.059471	SPW→ZCS
F	0.37839	0.38132	0.24029	485.57	0.7058	0.076318	ZCS→SPW
G	0.34243	0.39977	0.25780	485.57	0.7058	0.098756	SPW→UID
H	0.00000	0.88119	0.11881	433.79	0.0539	0.098756	UID→INI
I	0.00000	0.88119	0.11881	433.79	0.0539		INI

Table 3.2-3. Abbreviations Used to Describe the Different Flow Regions.

Abbreviation	Flow Region
INJ	Injection Conditions
INI	Initial Conditions
EEP	Equal Eigenvalue Point
ZCS	Zone of Constant State
SPW	Spreading Wave
SSW	Self-Sharpening Wave
UID	Upstream Intermediate Discontinuity
DID	Downstream Intermediate Discontinuity

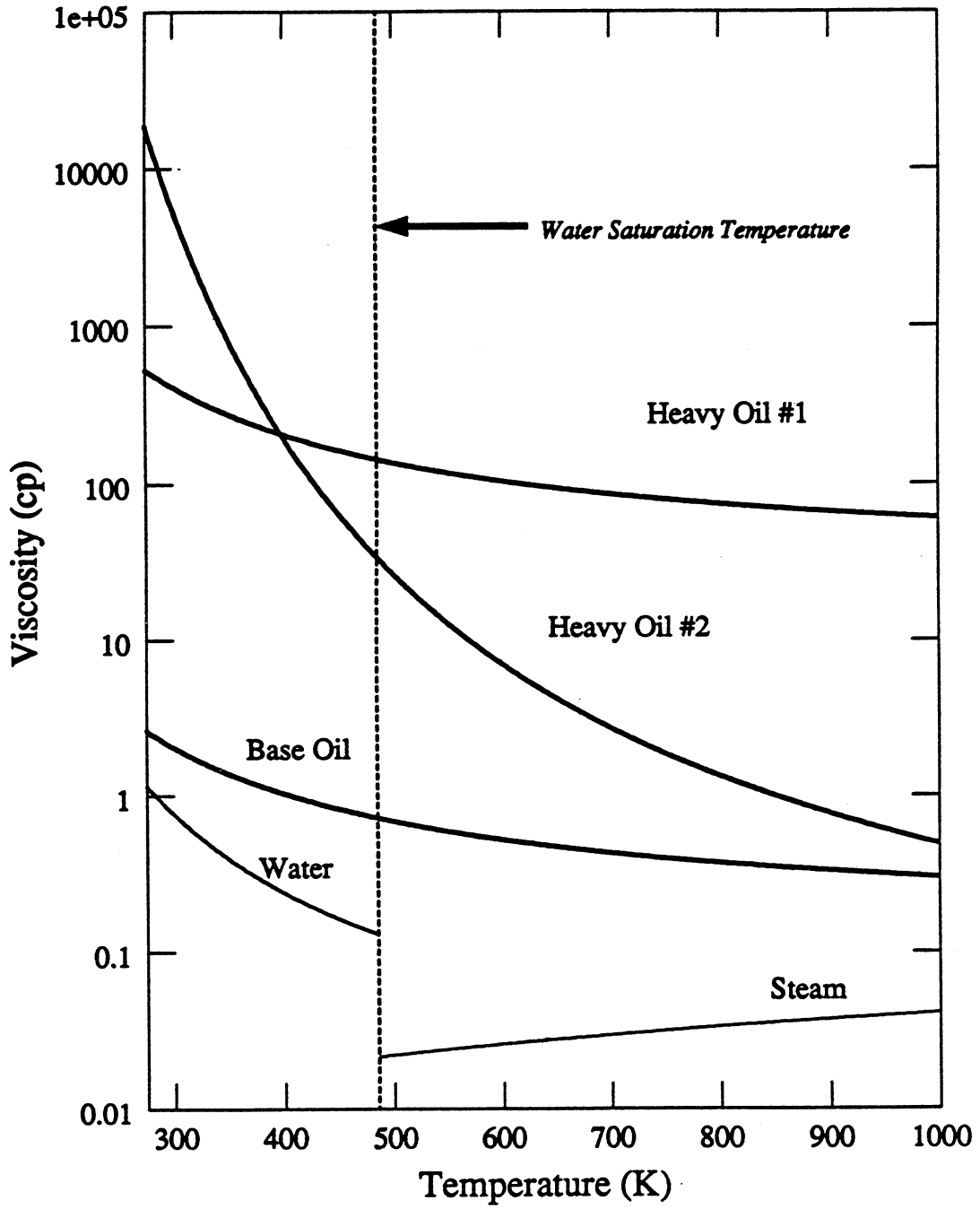

Fig. 3.2-4. Viscosities for water, steam, and three different oils as a function of temperature from 275°K to 1000°K.

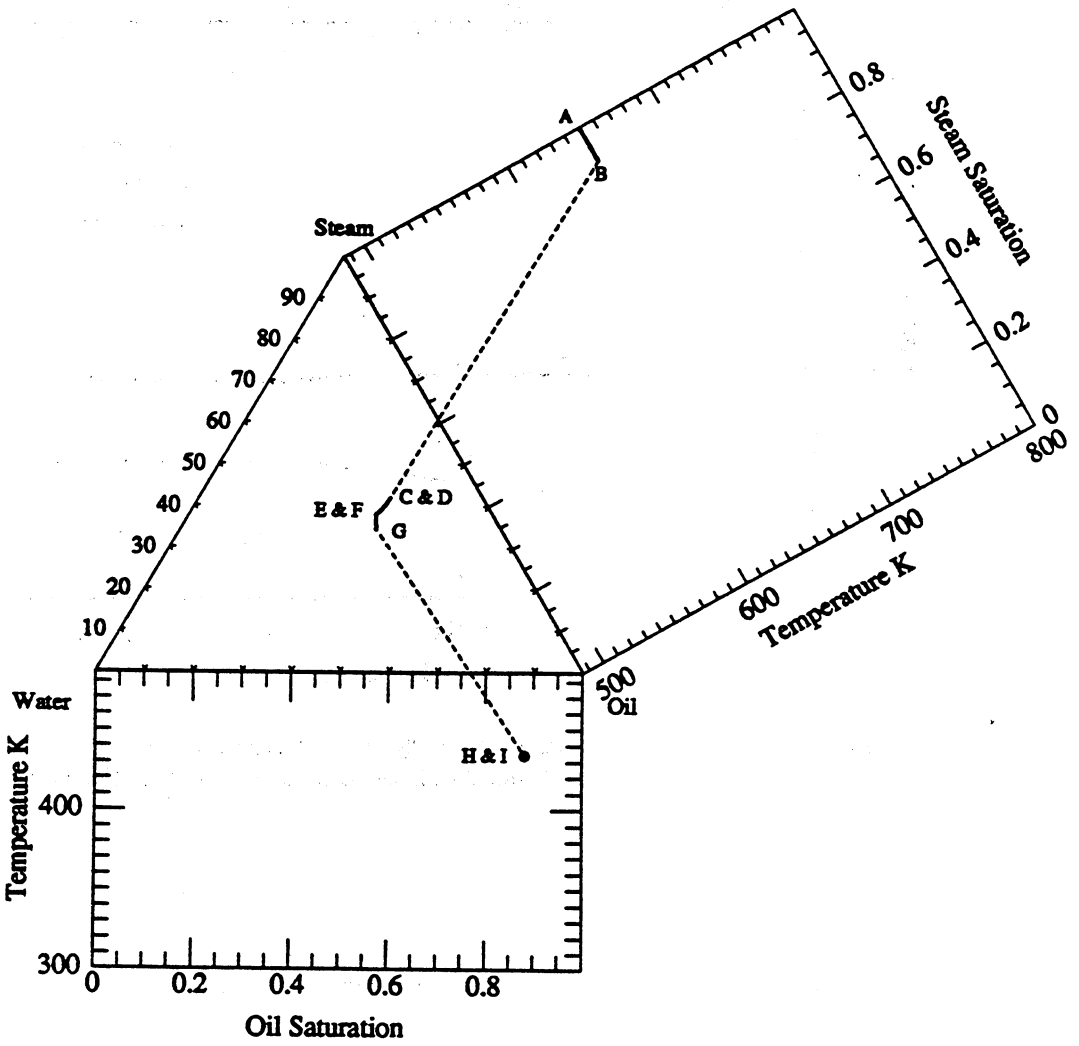

Fig. 3.2-5. Composition path for the injection of 100% steam at 650°K into 88.1% oil and 11.9% water at 433.79°K.

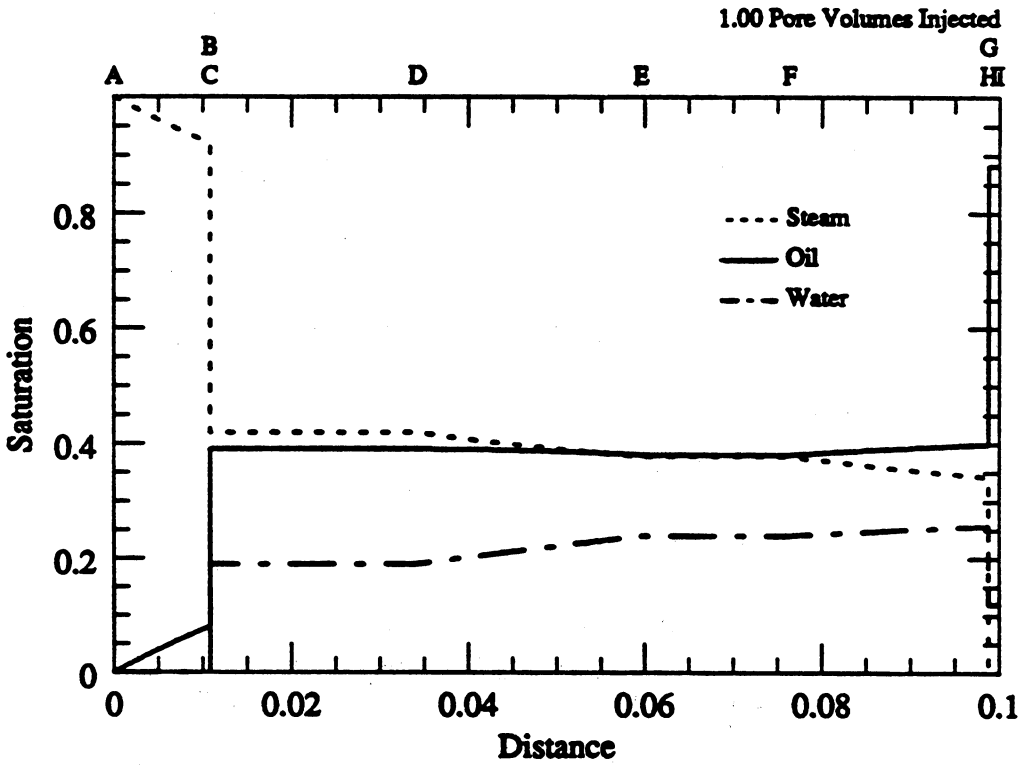

Fig. 3.2-6. Saturation profile for the injection of 1.0 pore volumes of 100% steam at 650°K into 88.1% oil and 11.9% water at 433.79°K.

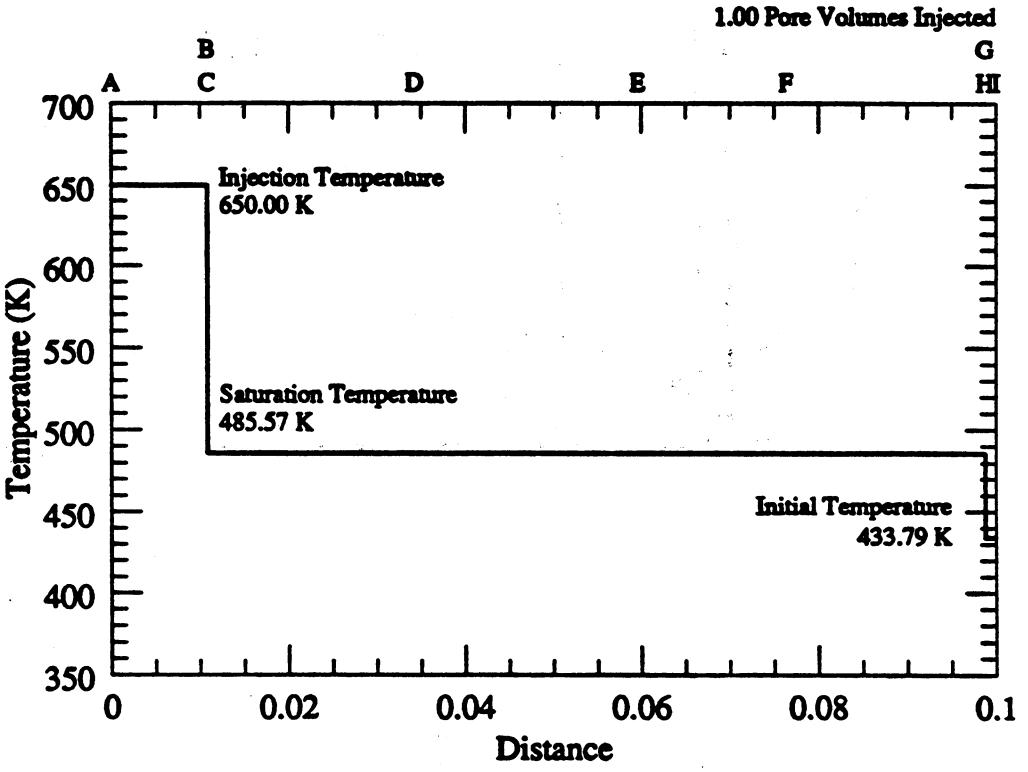

Fig. 3.2-7. Temperature profile for the injection of 1.0 pore volumes of 100% steam at 650°K into 88.1% oil and 11.9% water at 433.79°K.

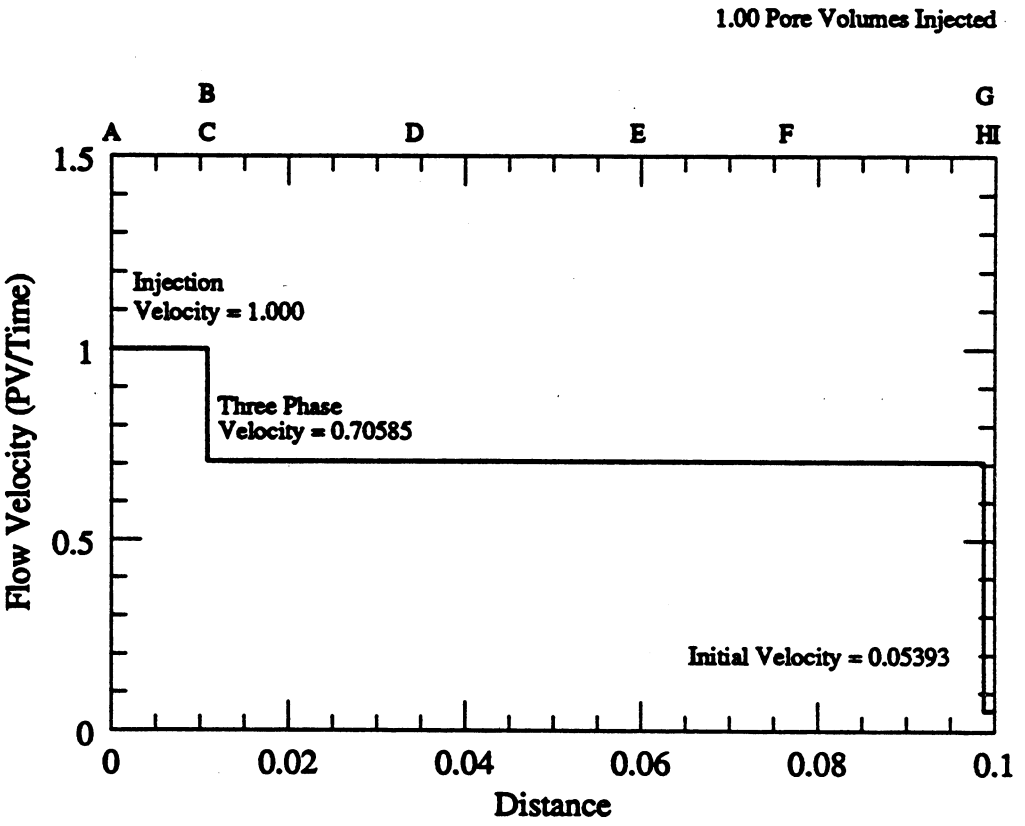

Fig. 3.2-8. Flow velocity profile for the injection of 1.0 pore volumes of 100% steam at 650°K into 88.1% oil and 11.9% water at 433.79°K.

region. Because the wave velocity varies continuously upstream of the three-phase region, the shock from **B** to **C** is an upstream intermediate discontinuity.

Points **C** and **D** coincide in Fig. 3.2-5, but they do not on Fig. 3.2-6. The location of point **C** in Fig. 3.2-6 is given by the shock velocity calculated with Eq. (3.2-16). The velocity of point **D** is the slow eigenvalue on the path in the three-phase region. From points **C** to **D** in Fig. 3.2-6, therefore, is a zone of constant state.

From points **D** to **E**, there is a continuous variation of saturations in the three-phase region (Figs. 3.2-5 and 3.2-6). At point **E**, there is a path switch from the slow path to the fast path with velocity **F**, and hence there is another zone of constant state in Fig. 3.2-6. From points **F** to **G**, there is another spreading wave, or continuous saturation variation, in the three-phase region.

As Fig. 3.2-6 and Table 3.2-2 show, the oil saturation varies only slightly in the three-phase region, though the shapes of the paths are such that the oil saturation decreases slightly (**D**→**E**) and then increases slightly (**F**→**G**) as the solution is traced from the upstream to downstream end of the three-phase region. The water saturation, however, is lower at the upstream end of the three-phase region and increases slowly over its length, while the steam saturation decreases. At point **G** is the shock that is the downstream end of the three-phase region. That shock is an upstream intermediate discontinuity with the initial composition on the downstream side.

Corresponding variations in temperature and flow velocity are shown in Figs. 3.2-7 and 3.2-8. Those variations are much simpler than the saturation variations. Only three temperatures appear in the solution, the injection temperature, the saturation temperature of water and the initial temperature (Table 3.2-2). Because the temperature changes only at shocks, the flow velocity also shows only three values (Fig. 3.2-8). The highest flow velocity occurs at the inlet. The flow velocity in the three-phase region is lower, because low density steam has condensed into higher density water, and the velocity downstream of the leading shock is lower still for the same reason.

3.2.4 Solution Procedure

The complete solution to the steam/oil/water problem can be obtained using the following steps. Additional details and example solutions are given by Wingard (1989).

1. Select the injection conditions. This requires choosing the injection composition, injection temperature and injection velocity.

2. Integrate along the slow path until some point, **B**, is reached. Point **B** can be completely arbitrary with one exception that is noted in the next step.

3. Calculate the composition point in the three-phase region that is reached by crossing an upstream intermediate discontinuity from point **B**, in the steam/oil region, into the three-phase region. This requires that the shock velocity as given by Eq. 3.2-16 be equal to the small eigenvalue at point **B**. The landing point in the three-phase region, **C**, is unique.

   If the velocity of point **B** is too small, there will be no solution for Composition **C** in the allowable hodograph space. This is indicated by having one or more of the saturation values be less than zero or greater than one at the landing point. If this happens, the selected point, **B**, is not a valid jumping point and another composition point further along the injection path (**A**→**B**) must be chosen.

4. Integrate along the slow path from **C** to a new point in the three-phase region, Composition **D**. Composition **D** will be the point of intersection between the slow path and fast path. At this composition, the solution switches paths from the slow to the fast path, creating a zone of constant state at point **D**.

The velocities must increase as the integration moves from C to D. If the velocities decrease, a self-sharpening wave is indicated. A point must be chosen on a spreading portion of the path as the upstream set of conditions. If the eigenvalues immediately decrease in the desired direction, then the landing point must be at the upstream conditions. The self-sharpening wave is calculated by matching the shock velocity to the eigenvalue on either the upstream or downstream side of the shock.

5. Integrate from point D to another composition point, E, on the fast path. This large eigenvalue point cannot be so large that a material balance, or more importantly a heat balance, carries the shock solution out of the allowable hodograph space.

   The limitation on self-sharpening waves also applies as the integration travels from D to E. The self-sharpening wave is resolved by jumping to the water/oil region directly from point D. The self-sharpening wave along the fast path is usually not seen because this takes the solution away from the region where the solution can jump into the water/oil region.

6. Point E is the jumping point into the water/oil region. Calculate the point in the water/oil region that satisfies the material balances and also matches the shock velocity to the large eigenvalue at Composition E. The landing point in the water/oil region, F, is the initial condition.

For the light oil case discussed above, the nature of the eigenvalues in the water/oil region prevents the development of spreading waves in this region. All the eigenvalues in the water/oil region are slower than their three-phase counterparts which necessarily lie upstream of the initial conditions. This situation often occurs in compressible gas dynamics where the leading shock travels faster than all the wave velocities in the region of initial conditions.

The solution procedure outlined here is necessarily iterative for a given set of injection and initial conditions. In fact, the procedure calculates feasible initial conditions for a given solution path. The path must then be adjusted to produce the desired initial conditions.

3.2.5 Viscous Oil Displacements

Fig. 3.2-4 shows the viscosities of two heavier oils. Heavy Oil #1 has a viscosity that is 200 times higher than the base case oil for the entire temperature range. Heavy Oil #2 has a higher viscosity at the initial conditions but a greater dependence on the temperature. This stronger temperature effect lowers the viscosity to near that of the base oil at injection conditions.

Composition points marking the boundaries of the different flow regions are given in Table 3.2-4, and the composition path is shown in Fig. 3.2-9 for Heavy Oil #1. The composition path shown in Fig. 3.2-9 is more complex than the composition paths for the lighter oil. In the steam/oil region, there is a portion of the path that follows along the isothermal portion of the path from point A to point B. At point B there is an equal eigenvalue point where the solution continues along the slow path. After point B, continuing along the slow path to point C lowers the temperature from the injection value of 650°K to 588°K.

Another difference is that the location of the equal eigenvalue point, represented by point B in Fig. 3.2-9 and Table 3.2-4, has a much lower steam saturation than with the light oil. The less favorable fractional flow curve causes the steam to channel through the heavier oil. At a given injection volume of steam, therefore, the steam saturation is substantially lower for Heavy Oil #1 than in the case of the lighter oil, as comparison of Figs. 3.2-6 and 3.2-10, the saturation distribution for Heavy Oil #1 indicates.

In the three-phase region, the heavy oil solution shows a wave pattern similar to that of the light oil, but the composition path is displaced toward the oil apex of the ternary diagram. There is a spreading wave from point E to point F that trails the central zone of constant state.

Table 3.2-4. Composition Path for the Injection of 100% Steam at 650°K into 99.9% Heavy Oil #1 and 0.01% Water at 458.95°K.

Label	Composition Point					Wave Velocity	Type of Flow Region
	Saturations			T (K)	Flow Velocity		
	Steam	Oil	Water				
A	1.00000	0.00000	0.00000	650.00	1.00000	0.000000	INJ→SPW
B	0.22000	0.78000	0.00000	650.00	1.00000	0.00565	EEP
C	0.09651	0.90349	0.00000	588.00	0.88813	0.006054	SPW→UID
D	0.043058	0.915853	0.04109	485.57	0.69682	0.006054	UID→ZCS
E	0.043058	0.915853	0.04109	485.57	0.69682	0.012700	ZCS→SPW
F	0.047199	0.899429	0.053372	485.57	0.69682	0.016852	SPW→ZCS
G	0.047199	0.899429	0.053372	485.57	0.69682	0.053628	ZCS→SPW
H	0.027784	0.914043	0.058173	485.57	0.69682	0.156870	SPW→UID
I	0.00000	0.998536	0.001464	458.95	0.01836	0.156870	UID→INI
J	0.00000	0.998536	0.001464	458.95	0.01836		INI

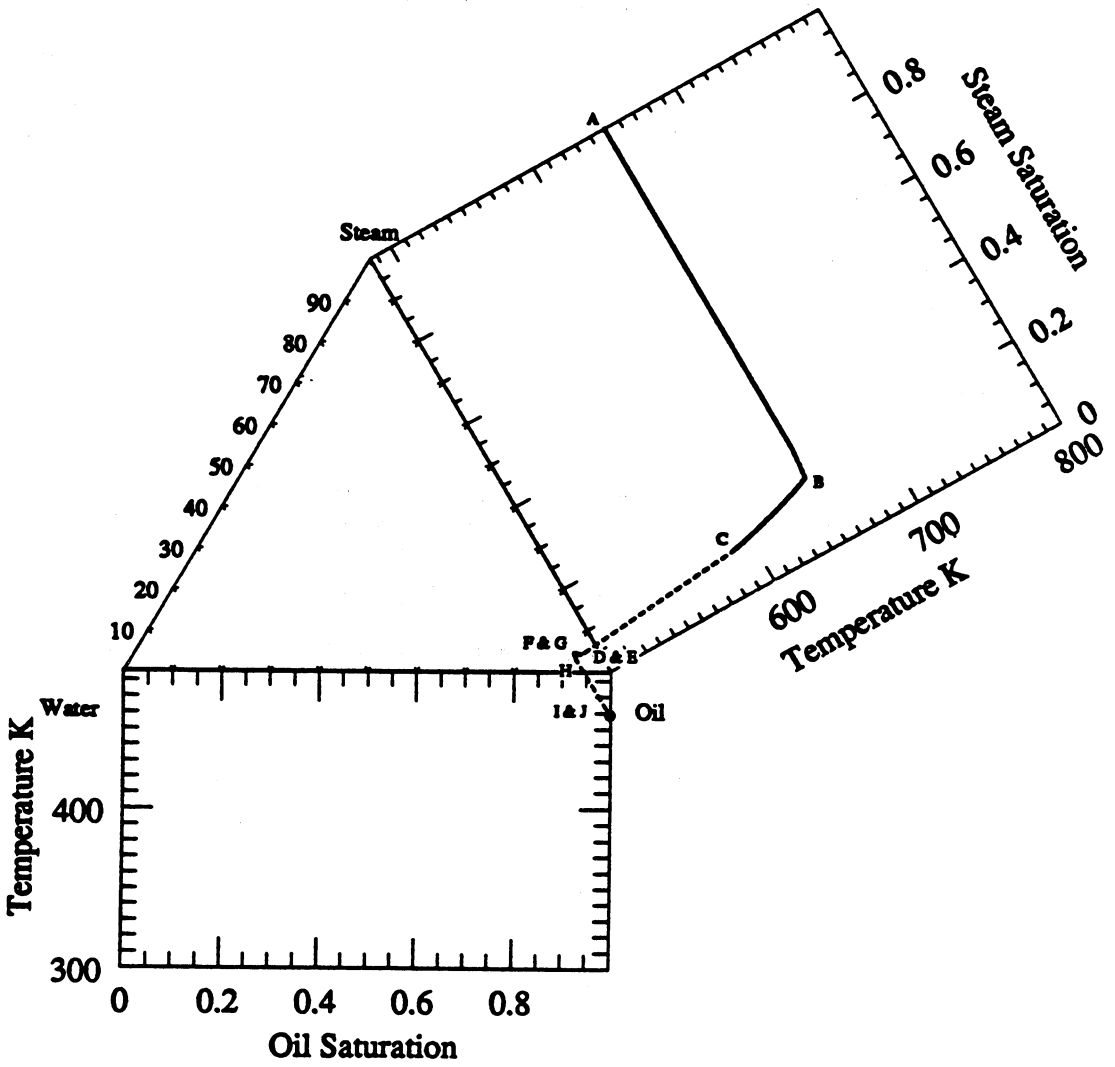

Fig. 3.2-9. Composition path for the injection of 100% steam at 650°K into 99.9% Heavy Oil #1 and 0.1% water at 458.95°K.

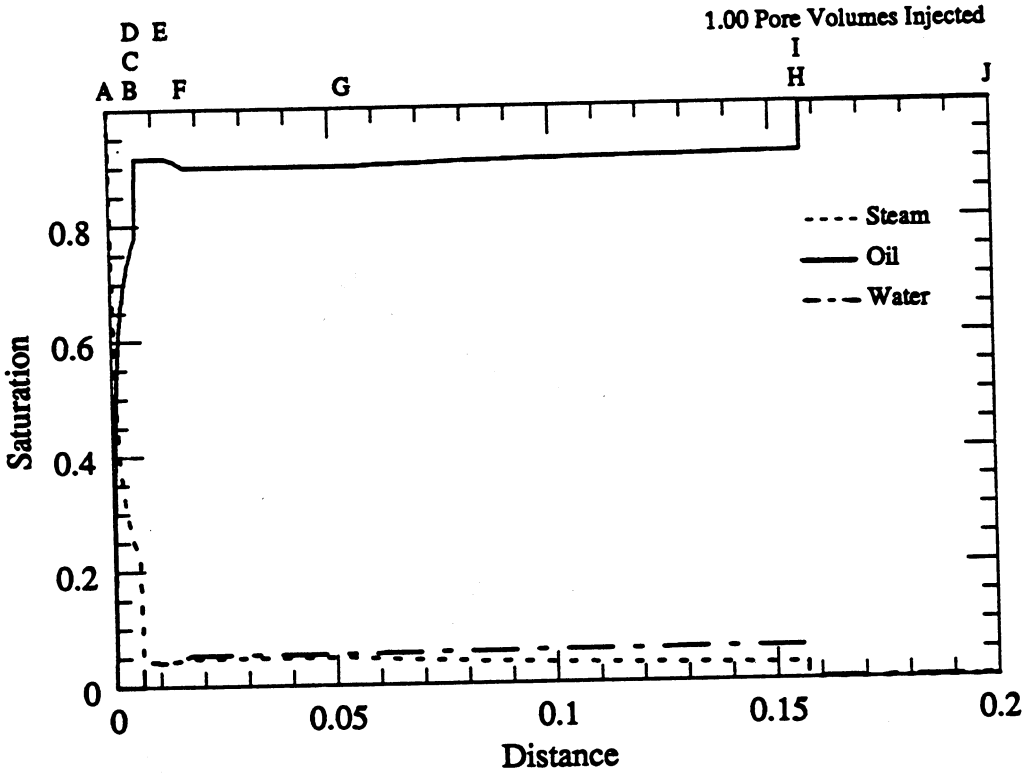

Fig. 3.2-10. Saturation profile for the injection of 100% steam at 650°K into 99.9% Heavy Oil #1 and 0.1% water at 458.95°K.

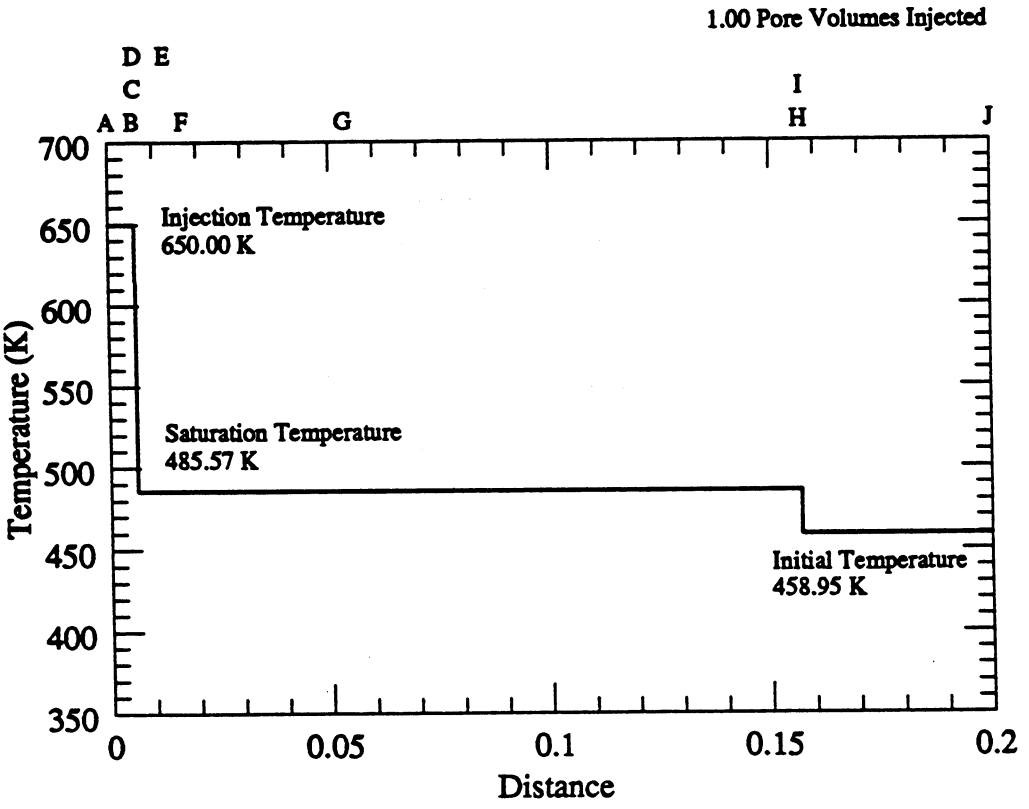

Fig. 3.2-11. Temperature profile for the injection of 100% steam at 650°K into 99.9% Heavy Oil #1 and 0.1% water at 458.95°K.

Another spreading wave precedes the central zone of constant state given by the path from point G to point H. The major difference from the light oil case is that the composition changes along these two waves are very small. The changes in the hodograph variables along the spreading waves are more restricted in the heavy oil solutions. Only a small corner of the three-phase region has flow characteristics that permit passage from the steam/oil region through the three-phase region and into the water/oil region.

Temperature and velocity distributions for displacement of Heavy Oil #1 are shown in Figs. 3.2-11 and 3.2-12. The patterns are similar to those for the light oil with the exception of the continuous variation in temperature and velocity in the steam/oil region.

The nonisothermal portion of the steam/oil region, from point B to Composition C in Fig. 3.2-11 appears to be extension of the actual phase change shock between point C and point D. The portion of the solution path that follows along the nonisothermal section in the steam/oil region is always seen in these solutions. The reason is that the wave velocity at the point where the two eigenvalues are equal is too small to satisfy the material and primarily the heat balance across the shock. The minimum velocity of an intermediate discontinuity is faster than the equal eigenvalue point. In order to satisfy the heat balance, the system must cool towards the saturation temperature before a suitable heat balance across the trailing shock is possible.

The viscosity of Heavy Oil #2 is more dependent on the temperature than the base oil or Heavy Oil #1. The composition path for a displacement of Heavy Oil #2 with the same injection and initial conditions as the light oil, Type 4 displacement shown in Figs. 3.2-5 to 3.2-8 and outlined in Table 3.2-2 is presented in Figs. 3.2-13 to 3.2-16 and Table 3.2-5.

The most direct comparison between the heavy oil and light oil case can be made by comparing the saturation profiles of the light oil case, Fig. 3.2-6, and the heavy oil case, Fig. 3.2-14. Again we trace the solution from the injection conditions downstream. There is an immediate difference in the initial steam/oil region. As Fig. 3.2-14 shows, the solution follows the slow path from the injection conditions at Composition A to the equal eigenvalue point, B. From point B to Composition C, the solution continues along the slow path. This region is characterized by a slightly spreading wave carrying the solution from the injection temperature toward the saturation temperature. This path also changes steam saturation at the same time the temperature is changing. The rapidly changing oil viscosity helps to lengthen the section of the solution that travels along the nonisothermal path, from point B to point C. The increased oil viscosity also raises the oil saturation for a given velocity or temperature along the path from B to C.

The shape of the steam/oil region resembles the steam/oil region of the Heavy Oil #1 displacement, Fig. 3.2-10. The same analysis that applied in the case of Heavy Oil #1 also applies in this case. The high mobility steam rapidly moves downstream of the two-phase region and spreads over the central three-phase region that exists between point D and point I in Fig. 3.2-14.

At point C, an upstream intermediate discontinuity carries the solution into the three-phase region at point D. There are two restrictions that apply to the choice of the jumping point, C. If the eigenvalue at point C is too low, there will be no solution in the three-phase region that satisfies the material and energy balances across the shock. A larger temperature jump across a shock results in a slower shock velocity; for some very slow shock velocities, the temperature jump is so large that the resulting temperature must be less than the saturation temperature. In such cases there is no solution in the three-phase region.

The trailing phase transition shock is much slower in Fig. 3.2-14 than in the profile with the light oil, shown in Fig. 3.2-6. The equal eigenvalue point represents the point where the Buckley-Leverett saturation velocity, $(\partial f_v / \partial S_v)$, is equal to the change in fractional increase in enthalpy transport. This is given by

$$\frac{\partial f_v}{\partial S_v} \approx \frac{\partial}{\partial S_v} \left[\sum_{i=1}^{n_p} H_i f_i \right] \qquad (3.2\text{-}17)$$

Table 3.2-5. Composition Path for the Injection of 100% Steam at 650°K into 88.1% Heavy Oil #2 and 11.9% Water at 433.79°K.

Label	Composition Point					Wave Velocity	Type of Flow Region
	Saturations			T (K)	Flow Velocity		
	Steam	Oil	Water				
A	1.00000	0.00000	0.00000	650.00	1.00000	0.000000	INJ→SPW
B	0.65350	0.34650	0.00000	650.00	1.00000	0.008822	EEP
C	0.11901	0.88099	0.00000	526.00	0.77235	0.009613	SPW→UID
D	0.05251	0.88117	0.06632	485.57	0.69358	0.009613	UID→ZCS
E	0.05251	0.88117	0.06632	485.57	0.69358	0.027298	ZCS→SPW
F	0.05264	0.87995	0.06741	485.57	0.69358	0.028005	SPW→UID
G	0.13794	0.70626	0.15580	485.57	0.69358	0.028005	UID→ZCS
H	0.13794	0.70626	0.15580	485.57	0.69358	0.086357	ZCS→SPW
I	0.13657	0.70645	0.15698	485.57	0.69358	0.088938	SPW→UID
J	0.00000	0.94420	0.05579	433.89	0.02667	0.088938	UID→ZCS
K	0.00000	0.94420	0.05579	433.89	0.02667	0.119812	ZCS→SPW
L	0.00000	0.91321	0.08679	433.89	0.02667	0.197647	SPW→UID
M	0.00000	0.88123	0.11876	433.89	0.02667	0.197647	UID→INI
N	0.00000	0.88123	0.11876	433.89	0.02667		INI

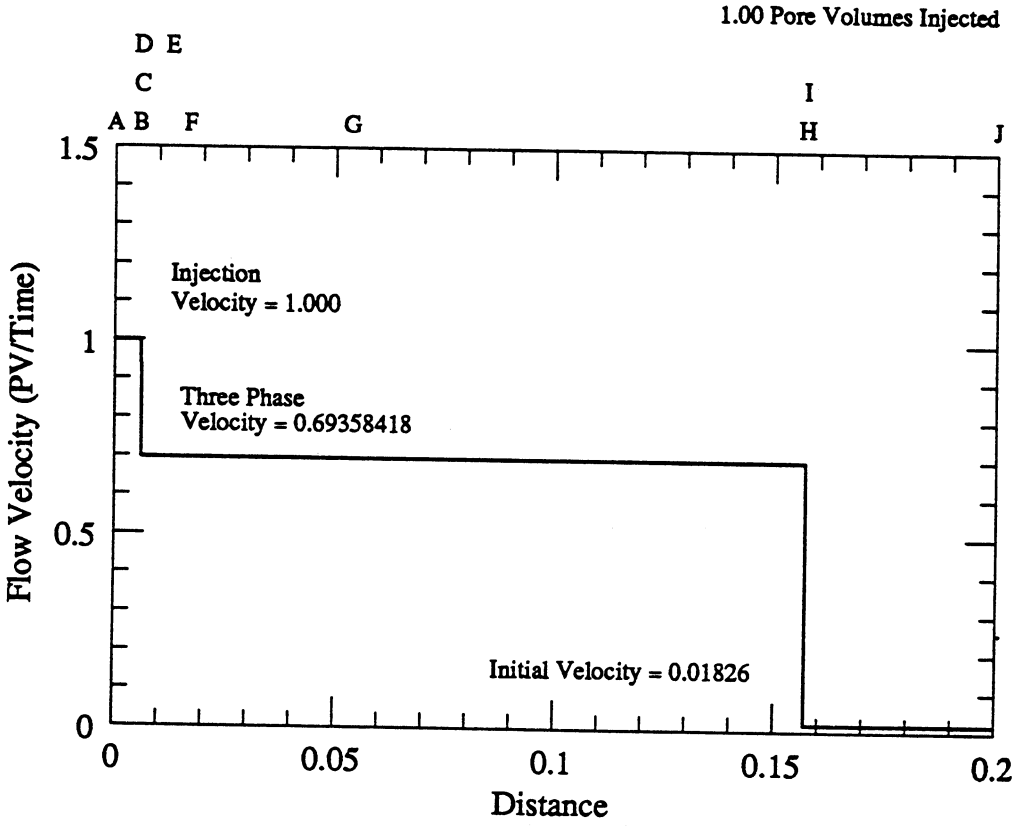

Fig. 3.2-12. Flow velocity profile for the injection of 100% steam at 650°K into 99.9% Heavy Oil #1 and 0.1% water at 458.95°K.

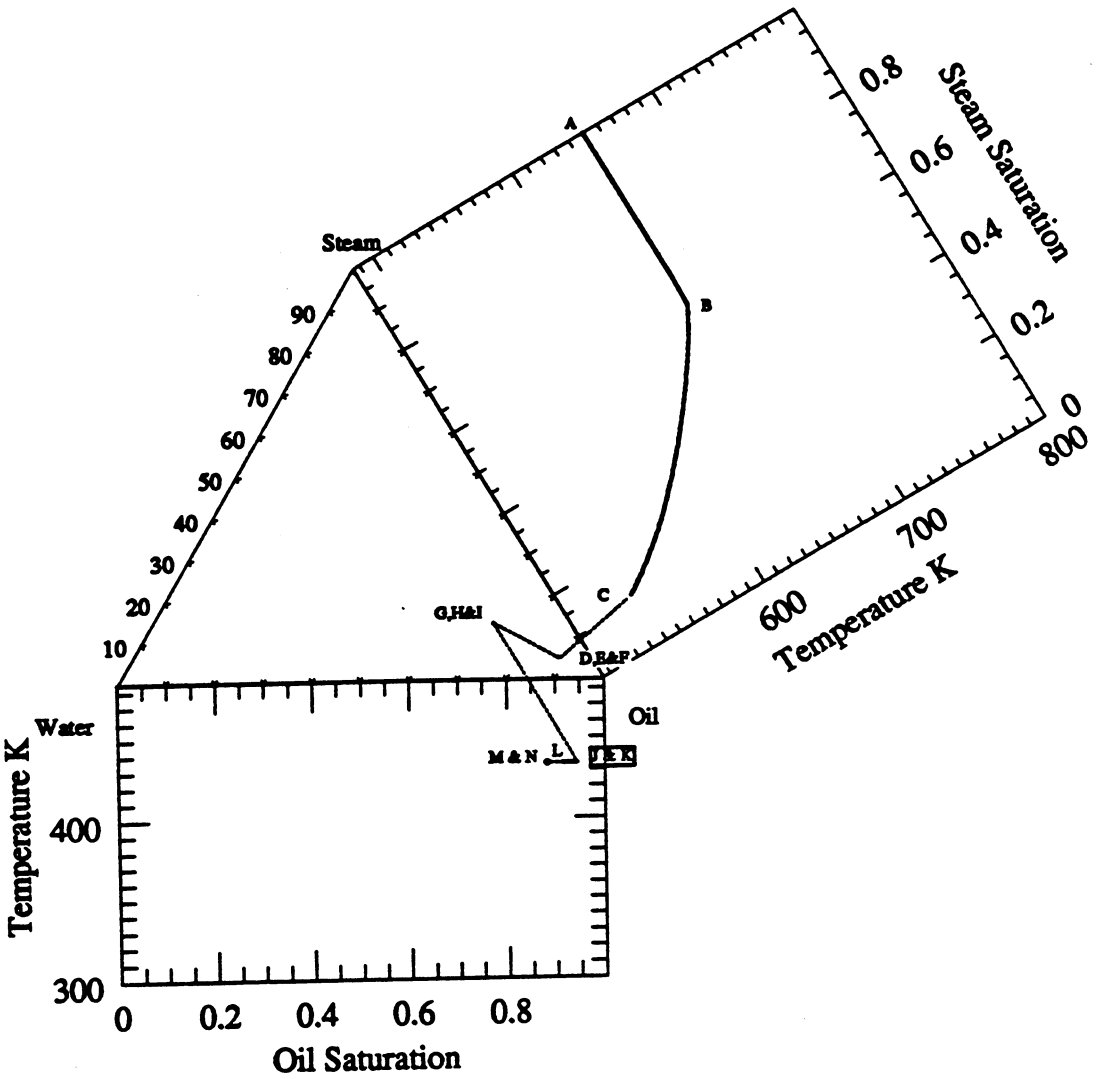

Fig. 3.2-13. Composition path for the injection of 100% steam at 650°K into 88.1% Heavy Oil #2 and 11.9% water at 433.79°K.

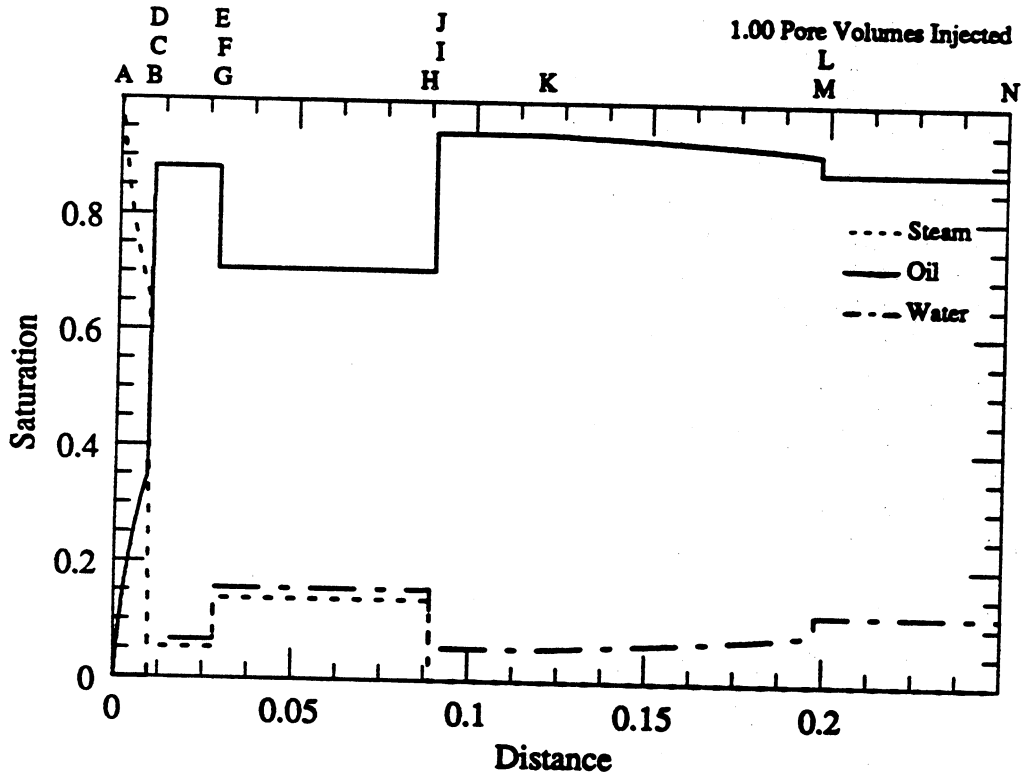

Fig. 3.2-14. Saturation profile for the injection of 100% steam at 650°K into 88.1% Heavy Oil #2 and 11.9% water at 433.79°K.

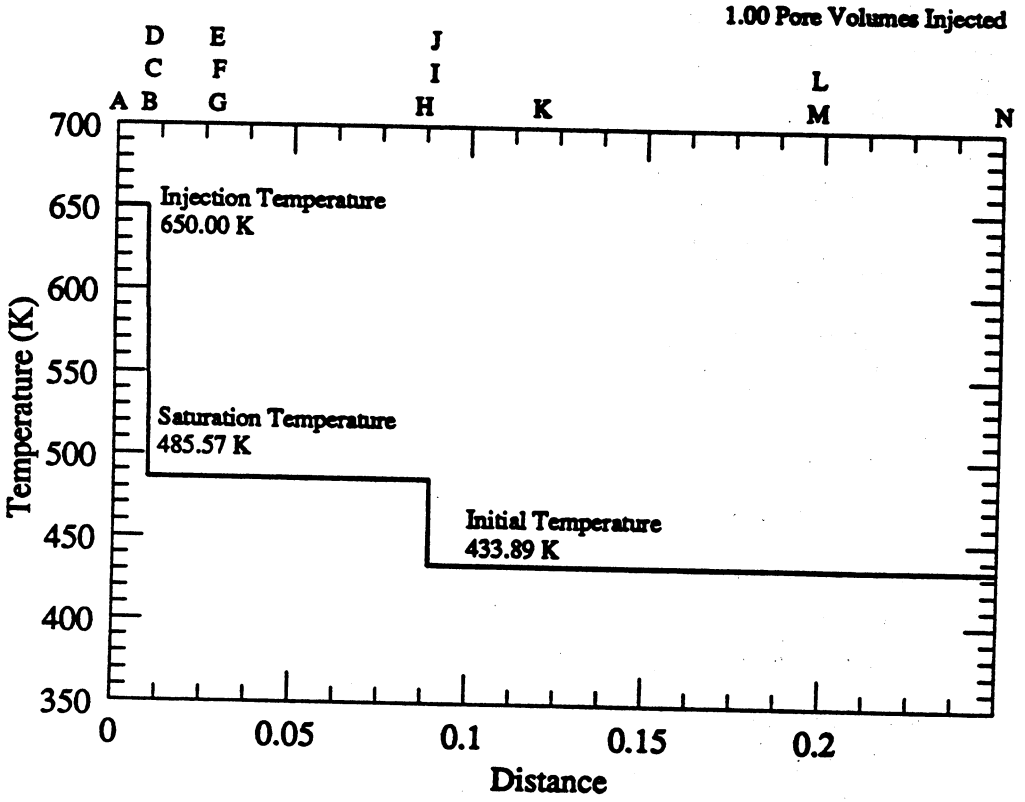

Fig. 3.2-15. Temperature profile for the injection of 100% steam at 650°K into 88.1% Heavy Oil #2 and 11.9% water at 433.79°K.

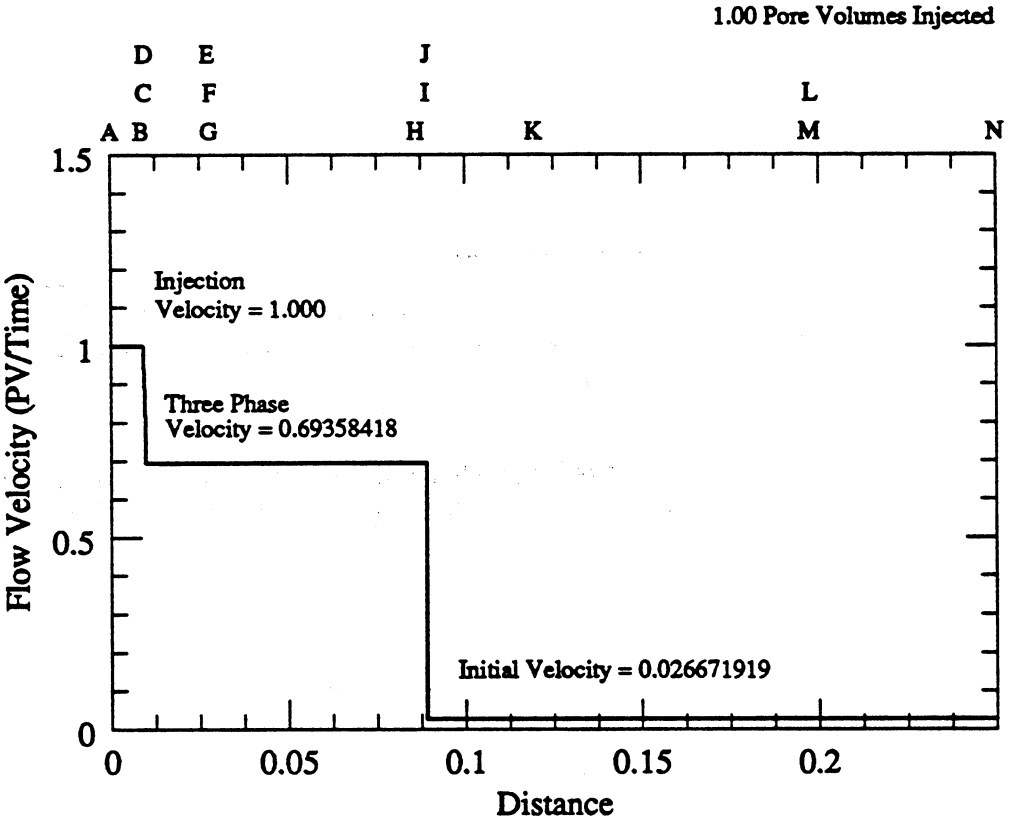

Fig. 3.2-16. Flow velocity profile for the injection of 100% steam at 650°K into 88.1% Heavy Oil #2 and 11.9% water at 433.79°K.

The velocity of the nonisothermal path is nearly independent of the oil viscosity. At a given oil saturation, the velocity of the isothermal path decreases as the oil viscosity increases. Therefore, to reach a given velocity, the oil saturation must be increased dramatically.

In the three-phase region, a zone of constant state, that extends from point **D** to point **E**, couples the shock velocity to the slow eigenvalue at the three-phase landing point **D**. The solution must be able to follow the slow path at the trailing end of the three-phase region. Were the velocity on the slow path, as represented by the smaller eigenvalue, less than the shock velocity, the solution would be restricted to fast paths in the three-phase region. However, if the solution is to move between two arbitrary points in the three-phase region, it must first travel along the slow path.

After the zone of constant state a spreading wave carries the solution from **E** to Composition **F**. The change in composition along this portion of the solution is barely noticeable. Without this small change, however, the solution cannot reach the desired initial temperature. As the length of the spreading wave from **E** to **F** increases, lower and lower initial temperatures result for a fixed initial water saturation.

As the slow path is followed past Composition **F**, the eigenvalues eventually reach a maximum value and begin to decline. The velocity constraint sets a limit on the distance that the integration along the slow path can continue without introducing a discontinuity in the form of a self-sharpening wave. This self-sharpening wave is found by selecting a point on the slow path before the small eigenvalue reaches its maximum value. This selected point is at Composition **F**.

At point **F** an upstream intermediate discontinuity carries the solution to Composition **G**. The shock is necessary to keep the initial conditions in the allowable hodograph space. For the solutions that switch to a fast path before the shock, the velocity of the fast path or the oil saturation on the path is too large. When the oil saturation is too large, the shock solution results in a composition with a negative water saturation. Thus, when the eigenvalue is too fast, the solution results in an initial temperature that is not realizable due to physical consideration, e.g. below the freezing temperature of water.

The shock from **F** to **G** carries the solution to the other side of the maximum point, much like a leading Buckley-Leverett shock that carries the solution past the saturation where $(\partial f_w/\partial S_w)$ is a maximum, to the initial conditions. On this side of the maximum point, the velocity of the fast path and the oil saturation are lower and give solutions that remain in the allowable hodograph space. The distance between the endpoints of the shock depends on how close the jumping point is to the maximum velocity point. The closer the jumping point, the closer the landing point is on the other side, and the closer the shock velocity is to the maximum. Because the self-sharpening wave is an upstream intermediate discontinuity, the shock velocity matches the eigenvalue of the upstream point, Composition **F**.

At point **G**, a second zone of constant state, referred to as the "central" zone of constant state, couples the shock velocity to the wave velocity at **H**. The zone of constant state represents the path switch from the slow path at **G** to the fast path at **H**. There must be a path switch at this point due to the behavior of the compositions that form a self-sharpening wave. Jeffrey (1976) showed that the velocity of the discontinuity formed by a self-sharpening wave must be intermediate between the eigenvalues of the upstream and downstream composition points. Since the wave is self-sharpening, the small eigenvalue at the downstream Composition (point **H**) must be slower than the shock velocity. This requires that the solution on arriving at Composition **H** switch to the fast path.

A spreading wave is attached ahead of the zone of constant state. This spreading wave is also small and does not noticeably change the composition point. Along the path from **H** to **I**, the spreading wave takes the solution to an upstream intermediate discontinuity that carries the solution out of the three-phase region into the water/oil region. The eigenvalues along the fast path change very rapidly and the eigenvalue along this path must remain in a narrow range if the downstream temperature is to remain below the saturation temperature. As the solution

turns out, the length of the integration along this path is short, and the eigenvalues change very little.

The three-phase regions of Figs. 3.2-6 and 3.2-14 show striking differences in the shape of the saturation profiles in this region. The spreading waves in the heavy oil displacements are very small, both in real and hodograph space. The leading spreading wave, from point H to point I in Fig. 3.2-14 has a wave velocity of 0.086357 at the trailing edge of the wave and only 0.088938 at the leading edge of the wave. This means that 387.5 pore volumes of steam would need to be injected before this wave occupied one pore volume of displacement space. In contrast, the leading spreading wave in the base oil case, point F to point G in Fig. 3.2-6, has a wave velocity of 0.076318 at the trailing edge and a velocity of 0.098756 at the leading edge. This requires only 44.6 pore volumes of injected steam for this wave to occupy the same single pore volume.

The physical interpretation for the narrow spreading waves in the heavy oil case is founded in the three-phase relative permeability model. In the region of three-phase space, where all phases can flow, the fractional flow derivatives, $(\partial f_o/\partial S_g)$ and $(\partial f_o/\partial S_w)$, are small and do not change much with saturation. In other words, because the oil is more viscous, it remains relatively immobile over a larger range of saturations than in the lighter oil case.

The upstream intermediate discontinuity at I takes the solution into the water/oil region, point J. At point J there is a path switch to the fast path in the water/oil region. This path switch takes the solution to point K. The solution then travels along the fast path, forming a spreading wave between point K to point L. Finally, a leading upstream intermediate discontinuity carries the solution from the fast path at point L to the initial conditions at point M. This region of the solution resembles a traditional Buckley-Leverett displacement system with an unfavorable mobility ratio. The saturation profile is long and stretched out, and the leading shock is small.

The water/oil region in the heavy oil case can be compared to the same region in the light oil displacement as shown in Fig. 3.2-6 from point H to point I. The wave pattern is much more complex in the heavy oil case than the light oil case. In that case, the eigenvalues in the water/oil region are all slower than those in the three-phase region. This forces the leading phase change shock to jump directly to the initial conditions from the three-phase region. The highly adverse mobility ratio in the heavy oil case shown in Fig. 3.2-14 does not have this restriction.

The eigenvalue on the fast path in the water/oil region is proportional to the derivative of the fractional flow of water with respect to the water-phase saturation. This is the traditional Buckley-Leverett saturation velocity. In the nomenclature used here, λ_3 is proportional to $\partial f_w/\partial S_w$.

When the mobility ratio is close to unity this derivative is small, but when the mobility ratio is high the derivative is also large. For the case of Heavy Oil #2 the derivative is large enough for two-phase flow to occur downstream of the leading phase change shock, between point I and point J.

The wave velocity on the fast path in the water/oil region reaches a maximum value before reaching the initial conditions. This is similar to the situation that created the self-sharpening wave between Compositions F and G in the three-phase region. The final portion of the solution is obtained by calculating an isothermal upstream intermediate discontinuity with downstream conditions that match the desired initial conditions. This shock was found at Composition L. Between K and L, a spreading wave along the fast path moves the solution between the desired points.

The temperature profile shown in Fig. 3.2-7 and the profile for the heavy oil case given in Fig. 3.2-15 show the same basic pattern. The only differences are in the locations of the phase change shocks. There is a portion of the path that remains at the injection conditions until the temperature shocks to the three-phase saturation temperature, 485.57°K and remains at

that temperature throughout the three-phase region. The temperature jumps from the three-phase saturation temperature to the initial conditions at the leading phase change shock.

In the heavy oil case, the steam cannot build up any saturation near the injection conditions because of its high mobility compared to the heavier oil phase. The adverse mobility ratio causes the trailing phase change shock to be slower in the heavy oil solution. The leading phase change shock is only slightly faster in the light oil case. The difference in shock velocity is due primarily to the slower flow velocity on the two-phase side of the shock in the heavy oil case. The heavy oil case actually has less steam condensing across the shock, but the volume lost is a greater portion of the water phase in the heavy oil case. That volume change compensates for the increased energy transfer in the light oil case.

A closer examination of the solution paths in the steam/oil region reveals a subtle difference between the light oil solution and the heavy oil case. In the light oil case, the temperature remains at the injection temperature from the injection conditions to the trailing phase change shock at point **B**. In the heavy oil case, the path follows the isothermal slow path at the injection temperature between point **A** and point **B**. At point **B** a path switch at the equal eigenvalue point takes the solution along the nonisothermal path between point **B** and point **C**. The nonisothermal portion of the path is a "slightly" spreading wave and behaves much like the extension of the trailing phase change shock that is shown between point **C** and point **D**.

The velocity profile for the heavy oil case is shown in Fig. 3.2-16. As in the other solutions, the velocity profile mimics the shape of the temperature profile. The heavy oil solution follows this pattern. Again density changes due to temperature changes are the cause of the flow velocity variations, and in the heavy oil case, this relationship is maintained.

3.2.6 Summary and Conclusions

The example solutions obtained here for two- and three-phase flow with temperature variation demonstrate that the method of characteristics can be used to construct analytical solutions of the hyperbolic material and energy balance equations. Such solutions are useful because they provide understanding of why simulations behave as they do and because they show clearly the sensitivity of process performance to fluid properties and relative permeabilities. The solutions presented demonstrate how richly complex three-phase flow can be and raise many interesting mathematical questions about constraints on path selection, techniques for solution of shock balances, and existence and uniqueness of solutions. Those questions will require additional work. Also of interest is the extension of the analysis to cover cases in which components partition between phases. Such problems are still more complex. While the eigenvalue problem can be solved in a straightforward way, solutions of shock balances are more difficult because the composition on the single-phase side of a shock into a two-phase region is no longer a linear combination of phase compositions on the two-phase side (Wingard 1989), as it is in constant temperature displacements (Dumoré et al. 1984). Thus, construction of solutions for CO_2/steam/water/oil, for example, will be significantly more difficult than for the steam/oil/water systems described here.

Analysis of the example solutions (under the assumptions of Section 3.2.1) presented in this section indicates that

(1) Temperature does not vary in single-phase regions during injection of steam into liquid water. Hence, only three temperatures (injection, saturation and initial) occur in such displacements. Because flow velocities change only when temperature or the number of phases change, only three flow velocities occur.

(2) Solutions for injection of steam into cooler oil and water show three regions, an oil/water region and a steam/oil zone separated by a three-phase steam/oil/water region.

(3) A shock occurs whenever the number of phases changes. For the solutions presented, those shocks are intermediate discontinuities, and they have simultaneous jumps in temperature, saturation and flow velocity.

(4) An increase in oil viscosity causes a reduction in the steam saturation in the steam/oil and steam/oil/water region.

(5) Formation of a water bank ahead of the steam/oil/water zone is possible if the oil viscosity is high enough.

3.3 Interaction of Phase Behavior with Reservoir Heterogeneity

Kiran K. Pande

In any real miscible flood, the flow will be anything but one-dimensional as reservoir heterogeneity and viscous instability produce faster flow in some zones than in others. When mixing between those zones occurs, the composition paths observed in one-dimensional flow must change, and hence the development of miscibility must be altered to some extent at least, in heterogeneous flow systems where crossflow occurs. Better understanding of the scaling of those interactions is an important part of improved accuracy of performance predictions for reservoir-scale flows. In this section we describe an extension of the one-dimensional theory of Helfferich (1981) to flow in the simplest of heterogeneous systems, two layers with different permeability. As a first step toward construction of a detailed picture of the effect of mixing between layers, we consider only the effects of viscous crossflow, though it is clear that capillary crossflow and gravity segregation will also contribute in actual miscible floods.

Immiscible displacement in a layered system with viscous crossflow was modeled by Zapata and Lake (1981). In this section, we extend their work by considering the effects of phase behavior as well. In the subsections that follow we describe the mathematical model and outline the procedures used to construct solutions for binary and ternary phase behavior. In addition we report results of composition path calculations for varying levels of permeability contrast.

3.3.1 Mathematical Model

To examine the interaction between phase behavior and nonuniform flow, we consider a model problem of flow in a two layer reservoir. The nonuniformity of the flow results from the difference in layer permeabilities, and exchange of fluids between the layers is by viscous crossflow only.

To illustrate the driving forces for viscous crossflow, we consider first a displacement in a two layer, linear system with no communication between the layers. The pressure profiles obtained during piston-like displacement of a high viscosity fluid by a low viscosity fluid are shown in Fig. 3.3-1 (Zapata 1981, Zapata and Lake 1981, Dykstra and Parsons 1950). Replacement of high viscosity fluid by low viscosity fluid results in a different pressure profile in each layer. If the barrier between the layers were removed and the layers allowed to communicate, then the difference in pressure between the layers at any point along the displacement length would cause viscous crossflow. The direction of crossflow would be from the low velocity layer to the high velocity layer near the injector (Region A), and from the high velocity layer to the low velocity layer near the producer (Region B), as fluid crossflows down the pressure gradient. There would be no crossflow at the point in the displacement where the pressure in the high velocity layer is equal to the pressure in the low velocity layer.

When the layers are allowed to communicate, the pressure difference between layers is reduced as fluid crossflows from one layer to the other. If there is enough crossflow, the

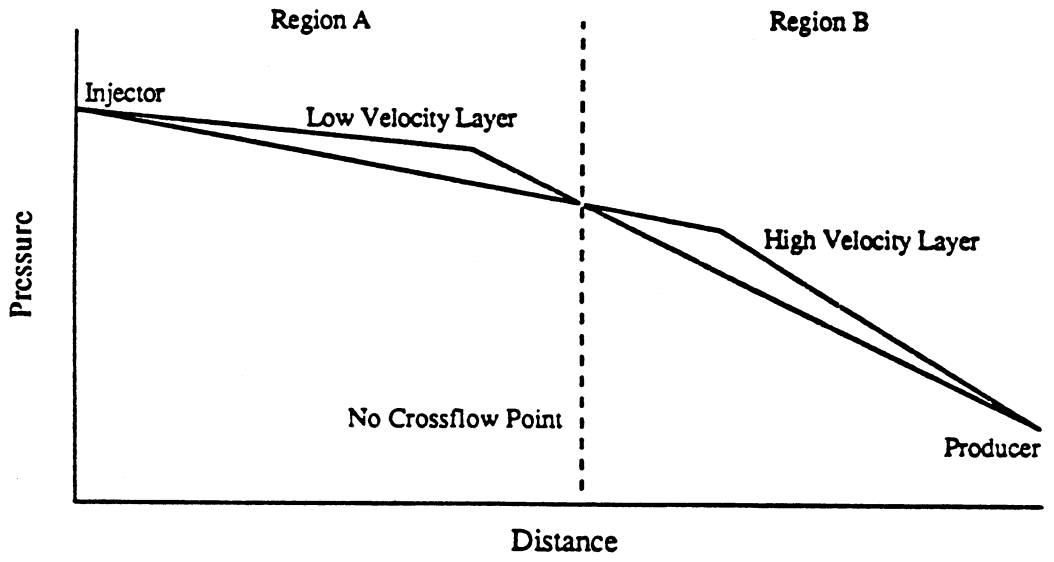

Fig. 3.3-1 Pressure distribution in a noncommunicating, two layer reservoir during piston-like displacement of a less viscous fluid by a more viscous fluid.

pressure difference may be reduced to zero. In the analysis that follows, we assume that the pressure in both layers is equal at any point along the displacement length for all time. In effect, we require that a maximum amount of crossflow occur instantaneously. This assumption is often referred to as the vertical equilibrium assumption (Coats et al. 1967, 1971 and Martin 1968).

The vertical equilibrium assumption reduces the dimensionality of the problem, a significant reduction in complexity, and hence, it is important to understand under what conditions the assumption is appropriate. If the time for flow in the vertical direction is small compared to the time for flow in the horizontal direction, then vertical equilibrium is a good assumption. Zapata and Lake (1981) developed a correlation that describes the degree of vertical equilibrium attained by a reservoir as a function of reservoir properties. They suggest that vertical equilibrium due to viscous crossflow is a reasonable assumption for reservoirs with an R_L value greater than ten, where

$$R_L = \frac{L}{H}\sqrt{\frac{k_v}{k_h}} \tag{3.3-1}$$

and k_v is the thickness-weighted harmonic average vertical permeability, k_h is the thickness-weighted arithmetic average horizontal permeability, L is the total system length, and H is the total system thickness.

Material Balance Equations

Material balance equations for flow in a linear, two-layer system are based on the following assumptions.

- All fluids are incompressible.
- The displacement process is isothermal.
- Each layer has uniform properties.
- Effects of dispersion and capillary pressure are ignored.
- Gravity segregation is ignored, as is viscous fingering.
- Phases are in local equilibrium everywhere.
- Partial molar volumes of components are constant, i.e., there is no change in total volume upon transfer of components between phases.
- The effect of pressure drop across the flow system on phase behavior is negligible.

The qualitative discussion of Fig. 3.3-1 indicated that the direction of crossflow may change during the course of a displacement. Here we define the direction of crossflow in Region A as being from the high velocity layer to the low velocity layer. The direction of crossflow in Region B is reversed. Because the direction of crossflow may change several times during the course of a displacement, there may be more than one region in a displacement that is referred to as Region A or Region B. Also, the high velocity layer is referred to as Layer 1, and the low velocity layer is referred to as Layer 2.

The material balance equations for Region A ($1 \rightarrow 2$) are

Layer 1:

$$\phi_1 h_1 W \frac{\partial}{\partial t}\sum_{j=1}^{n_p} x_{ij}^1 \rho_j^1 S_j^1 + \frac{\partial}{\partial x}\left(\sum_{j=1}^{n_p} x_{ij}^1 \rho_j^1 f_j^1\right) q_1 - \left(\sum_{j=1}^{n_p} x_{ij}^1 \rho_j^1 f_j^1\right)\frac{\partial q_1}{\partial x} = 0\,, \quad i = 1, n_c \tag{3.3-2}$$

Layer 2:

$$\phi_2 h_2 W \frac{\partial}{\partial t} \sum_{j=1}^{n_p} x_{ij}^2 \rho_j^2 S_j^2 + \frac{\partial}{\partial x} \left(\sum_{j=1}^{n_p} x_{ij}^2 \rho_j^2 f_j^2 \right) q_2 + \left(\sum_{j=1}^{n_p} x_{ij}^1 \rho_j^1 f_j^1 \right) \frac{\partial q_1}{\partial x} = 0 \, , \quad i = 1, n_c \qquad (3.3\text{-}3)$$

where:

n_c = number of components

n_p = number of phases

ρ_j = molar density of phase j

x_{ij} = mole fraction of component i in phase j

f_j = fractional flow of phase j = $\frac{q_j}{q}$

S_j = saturation of phase j

q = volumetric flowrate

ϕ = porosity

h = thickness

W = width

and the superscripts in Eqs. (3.3-2) and (3.3-3) represent the layer number. Because we assume incompressible fluids, any change in flow rate in Layer 1 must be accompanied by an equal change in flow rate in Layer 2. Therefore,

$$\frac{\partial q_1}{\partial x} = - \frac{\partial q_2}{\partial x} \qquad (3.3\text{-}4)$$

We also assume that partial molar volumes of components are constant, and rewrite Eqs. (3.3-2) and (3.3-3) as

Layer 1:

$$\phi_1 h_1 W \frac{\partial C_i^1}{\partial t} + \frac{\partial (F_i^1 q_1)}{\partial x} - F_i^1 \frac{\partial q_1}{\partial x} = 0 \, , \quad i = 1, n_c \qquad (3.3\text{-}5)$$

Layer 2:

$$\phi_2 h_2 W \frac{\partial C_i^2}{\partial t} + \frac{\partial (F_i^2 q_2)}{\partial x} + F_i^1 \frac{\partial q_1}{\partial x} = 0 \, , \quad i = 1, n_c \qquad (3.3\text{-}6)$$

where

$$C_i = \sum_{j=1}^{n_p} c_{ij} S_j \, , \quad i = 1, n_c \qquad (3.3\text{-}7)$$

$$F_i = \sum_{j=1}^{n_p} c_{ij} f_j \, , \quad i = 1, n_c \qquad (3.3\text{-}8)$$

and

$$c_{ij} = \frac{x_{ij}\,\rho_j}{\rho_{c_i}}, \qquad i = 1, n_c, \qquad j = 1, n_p \tag{3.3-9}$$

where, c_{ij} is the volume fraction of component i in phase j, and ρ_{c_i} is the molar density of component i. Here C_i is the overall volume fraction of component i, and F_i is the overall fractional flow of component i.

The derivatives in Eqs. (3.3-5) and (3.3-6) may be expanded, and Eq. (3.3-4) used to simplify the material balance equations to the following form,

Layer 1:

$$\phi_1 h_1 W \frac{\partial C_i^1}{\partial t} + q_1 \frac{\partial F_i^1}{\partial x} = 0, \qquad i = 1, n_c \tag{3.3-10}$$

Layer 2:

$$\phi_2 h_2 W \frac{\partial C_i^2}{\partial t} + q_2 \frac{\partial F_i^2}{\partial x} - (F_i^1 - F_i^2)\frac{\partial q_2}{\partial x} = 0, \qquad i = 1, n_c \tag{3.3-11}$$

Eqs. (3.3-10) and (3.3-11) may be made with the definitions

$$t_D = \frac{q_t\, t}{\overline{\phi}\, H\, W\, L} \tag{3.3-12}$$

$$R_{\phi h_k} = \frac{\phi_k\, h_k}{\overline{\phi}\, H} \tag{3.3-13}$$

$$q_{kD} = \frac{q_k}{q_t} \tag{3.3-14}$$

$$\overline{\phi} = \frac{\sum_{k=1}^{n_l} \phi_k\, h_k}{\sum_{k=1}^{n_l} h_k} \tag{3.3-15}$$

$$H = \sum_{k=1}^{n_l} h_k \tag{3.3-16}$$

$$q_k = W\, k_k\, h_k\, \lambda_{rt}^k \left.\frac{dp}{dx_D}\right|_k \tag{3.3-17}$$

$$\lambda_{rt}^k = \text{total mobility in layer } k \tag{3.3-18}$$

$$\lambda_{rt}^k = \sum_{j=1}^{n_p} \lambda_{rj}^k = \sum_{j=1}^{n_p} \frac{k_{rj}^k}{\mu_j^k} \tag{3.3-19}$$

$$q_t = \sum_{k=1}^{n_l} q_k \tag{3.3-20}$$

The resulting dimensionless form of the material balance equations is

Region A ($1 \rightarrow 2$)

Layer 1:

$$R_{\phi h_1} \frac{\partial C_i^1}{\partial t_D} + q_{1D} \frac{\partial F_i^1}{\partial x_D} = 0, \quad i = 1, n_c \tag{3.3-21}$$

Layer 2:

$$R_{\phi h_2} \frac{\partial C_i^2}{\partial t_D} + q_{2D} \frac{\partial F_i^2}{\partial x_D} - (F_i^1 - F_i^2) \frac{\partial q_{2D}}{\partial x_D} = 0, \quad i = 1, n_c \tag{3.3-22}$$

The material balance equations for Region B ($2 \rightarrow 1$) are derived in a similar manner.

Region B ($2 \rightarrow 1$)

Layer 1:

$$R_{\phi h_1} \frac{\partial C_i^1}{\partial t_D} + q_{1D} \frac{\partial F_i^1}{\partial x_D} - (F_i^2 - F_i^1) \frac{\partial q_{1D}}{\partial x_D} = 0, \quad i = 1, n_c \tag{3.3-23}$$

Layer 2:

$$R_{\phi h_2} \frac{\partial C_i^2}{\partial t_D} + q_{2D} \frac{\partial F_i^2}{\partial x_D} = 0, \quad i = 1, n_c \tag{3.3-24}$$

The vertical equilibrium assumption allows evaluation of the dimensionless flow rate. For example, the dimensionless flow rate in Layer 1 is given by

$$q_{1D} = \frac{W k_1 h_1 \lambda_{rt}^1 \frac{dp}{dx_D}|_1}{W k_1 h_1 \lambda_{rt}^1 \frac{dp}{dx_D}|_1 + W k_2 h_2 \lambda_{rt}^2 \frac{dp}{dx_D}|_2} \tag{3.3-25}$$

Vertical equilibrium requires that the vertical pressure gradient be zero everywhere. Therefore, at any point in the reservoir the pressure in Layer 1 is equal to the pressure in Layer 2 ($p^1 = p^2$). Because the total pressure drop across the flow system is the same in each layer, the horizontal pressure gradient in Layer 1 is equal to the horizontal pressure gradient in Layer 2 throughout the displacement, and the vertical equilibrium condition may be stated as

$$\frac{dp}{dx_D}|_1 = \frac{dp}{dx_D}|_2 \tag{3.3-26}$$

As a result, q_{1D} may be calculated without knowledge of the pressure distribution in the reservoir,

$$q_{1D} = \frac{k_1 h_1 \lambda_{rt}^1}{k_1 h_1 \lambda_{rt}^1 + k_2 h_2 \lambda_{rt}^2} \tag{3.3-27}$$

When the total fluid mobility in Layer 1 is equal to the total fluid mobility in Layer 2, q_{1D} is only a function of the permeability thickness product in each layer. This flow rate is referred to as the baseline flow rate, q_{1D}^*.

Method of Characteristics Solution

The velocity of a constant composition may be determined by the method of Section 3.1. In Region A ($1 \rightarrow 2$), the component velocities are

Layer 1:

$$v_{c_i}^1 = \frac{\dfrac{q_{1D}}{R_{\phi h_1}} \dfrac{\partial F_i^1}{\partial x_D}}{\dfrac{\partial C_i^1}{\partial x_D}}, \qquad i = 1, n_c \tag{3.3-28}$$

Layer 2:

$$v_{c_i}^2 = \frac{\dfrac{q_{2D}}{R_{\phi h_2}} \dfrac{\partial F_i^2}{\partial x_D} + \dfrac{(F_i^1 - F_i^2)}{R_{\phi h_2}} \dfrac{\partial q_{1D}}{\partial x_D}}{\dfrac{\partial C_i^2}{\partial x_D}}, \qquad i = 1, n_c \tag{3.3-29}$$

Application of the coherence condition, which states that all components move at the same velocity, requires that

$$\lambda = v_{c_i}^1 = v_{c_i}^2, \qquad i = 1, n_c \tag{3.3-30}$$

For Region A ($1 \rightarrow 2$),

Layer 1:

$$\lambda \frac{\partial C_i^1}{\partial x_D} = \frac{q_{1D}}{R_{\phi h_1}} \frac{\partial F_i^1}{\partial x_D}, \qquad i = 1, n_c \tag{3.3-31}$$

Layer 2:

$$\lambda \frac{\partial C_i^2}{\partial x_D} = \frac{q_{2D}}{R_{\phi h_2}} \frac{\partial F_i^2}{\partial x_D} + \frac{(F_i^1 - F_i^2)}{R_{\phi h_2}} \frac{\partial q_{1D}}{\partial x_D}, \qquad i = 1, n_c \tag{3.3-32}$$

Because F_i^1, F_i^2, and q_{1D} are only functions of the overall compositions, the derivatives, $\partial F_i^1/\partial x_D$, $\partial F_i^2/\partial x_D$, and $\partial q_{1D}/\partial x_D$ may be expanded as

$$\frac{\partial F_i^k}{\partial x_D} = \sum_{m=1}^{n_c-1} \frac{\partial F_i^k}{\partial C_m^k} \frac{\partial C_m^k}{\partial x_D}, \qquad i = 1, n_c, \qquad k = 1, 2 \tag{3.3-33}$$

$$\frac{\partial q_{1D}}{\partial x_D} = \sum_{m=1}^{n_c-1} \left[\frac{\partial q_{1D}}{\partial C_m^1} \frac{\partial C_m^1}{\partial x_D} + \frac{\partial q_{1D}}{\partial C_m^2} \frac{\partial C_m^2}{\partial x_D} \right], \qquad i = 1, n_c \tag{3.3-34}$$

Substitution for the derivatives, $\partial F_i^1/\partial x_D$, $\partial F_i^2/\partial x_D$, and $\partial q_{1D}/\partial x_D$ in the coherence equations for Region A (Eqs. 3.3-31 and 3.3-32) yields

Region A ($1 \rightarrow 2$)

Layer 1:

$$\lambda \frac{\partial C_i^1}{\partial x_D} = \frac{q_{1D}}{R_{\phi h_1}} \sum_{m=1}^{n_c-1} \frac{\partial F_i^1}{\partial C_m^1} \frac{\partial C_m^1}{\partial x_D}, \qquad i = 1, n_c \tag{3.3-35}$$

Layer 2:

$$\lambda \frac{\partial C_i^2}{\partial x_D} = \frac{q_{2D}}{R_{\phi h_2}} \sum_{m=1}^{n_c-1} \frac{\partial F_i^2}{\partial C_m^2} \frac{\partial C_m^2}{\partial x_D} +$$

$$\frac{(F_i^1 - F_i^2)}{R_{\phi h_2}} \sum_{m=1}^{n_c-1} \left[\frac{\partial q_{1D}}{\partial C_m^1} \frac{\partial C_m^1}{\partial x_D} + \frac{\partial q_{1D}}{\partial C_m^2} \frac{\partial C_m^2}{\partial x_D} \right], \qquad i = 1, n_c \tag{3.3-36}$$

The coherence equations for Region B ($2 \rightarrow 1$) may be derived in a similar manner.

Region B ($2 \rightarrow 1$)

Layer 1:

$$\lambda \frac{\partial C_i^1}{\partial x_D} = \frac{q_{1D}}{R_{\phi h_1}} \sum_{m=1}^{n_c-1} \frac{\partial F_i^1}{\partial C_m^1} \frac{\partial C_m^1}{\partial x_D} +$$

$$\frac{(F_i^1 - F_i^2)}{R_{\phi h_1}} \sum_{m=1}^{n_c-1} \left[\frac{\partial q_{1D}}{\partial C_m^1} \frac{\partial C_m^1}{\partial x_D} + \frac{\partial q_{1D}}{\partial C_m^2} \frac{\partial C_m^2}{\partial x_D} \right], \qquad i = 1, n_c \tag{3.3-37}$$

Layer 2:

$$\lambda \frac{\partial C_i^2}{\partial x_D} = \frac{q_{2D}}{R_{\phi h_2}} \sum_{m=1}^{n_c-1} \frac{\partial F_i^2}{\partial C_m^2} \frac{\partial C_m^2}{\partial x_D}, \qquad i = 1, n_c \tag{3.3-38}$$

Shock Balances

In the two-layer flow problem, as in the problems considered in Sections 3.1 and 3.2, shocks are required in most solutions. An expression for the shock velocity may be obtained from an overall material balance around the shock. The shock velocity of component i is given by

Layer 1:

$$\Lambda_i^1 = \frac{(F_i^1 q_{1D})^{II} - (F_i^1 q_{1D})^{I} - F_{xf_i}^k (q_{kD}^{II} - q_{kD}^{I})}{R_{\phi h_1} (C_i^{1\,II} - C_i^{1\,I})}, \quad i = 1, n_c \qquad (3.3\text{-}39)$$

Layer 2:

$$\Lambda_i^2 = \frac{(F_i^2 q_{2D})^{II} - (F_i^2 q_{2D})^{I} + F_{xf_i}^k (q_{kD}^{II} - q_{kD}^{I})}{R_{\phi h_2} (C_i^{2\,II} - C_i^{2\,I})}, \quad i = 1, n_c \qquad (3.3\text{-}40)$$

where for crossflow from Layer 1 to Layer 2

$$F_{xf_i}^k = F_{xf_i}^1 \qquad (3.3\text{-}41)$$

$$q_{kD} = q_{1D} \qquad (3.3\text{-}42)$$

and for crossflow from Layer 2 to Layer 1

$$F_{xf_i}^k = -F_{xf_i}^2 \qquad (3.3\text{-}43)$$

$$q_{kD} = q_{2D} \qquad (3.3\text{-}44)$$

Superscript II refers to the upstream side of the shock, and superscript I refers to the downstream side.

The overall fractional flow of component i in the crossflowing fluid may be evaluated using the vertical equilibrium condition (Zapata 1981). Fractional flow terms are usually only a function of one composition. However, because fluid crossflows from both sides of a shock, the fractional flow expression for the fluid crossflowing at the shock is a function of the compositions on the upstream and downstream sides. The overall fractional flow of component i in the crossflowing fluid is assumed to be given by

$$F_{xf_i}^k = \frac{F_i^{k\,I} q_{xf}^{k\,I} + F_i^{k\,II} q_{xf}^{k\,II}}{q_{xf}^{k\,I} + q_{xf}^{k\,II}}, \quad i = 1, n_c \qquad (3.3\text{-}45)$$

The flow velocities $q_{xf}^{k\,I}$ and $q_{xf}^{k\,II}$ can be evaluated with Darcy's law

$$F_{xf_i}^k = \frac{k_{v_k}^I L^I W F_i^{k\,I} \lambda_{rt}^{k\,I} \frac{\partial p}{\partial y}|^{k\,I} + k_{v_k}^{II} L^{II} W F_i^{k\,II} \lambda_{rt}^{k\,II} \frac{\partial p}{\partial y}|^{k\,II}}{k_{v_k}^I L^I W \lambda_{rt}^{k\,I} \frac{\partial p}{\partial y}|^{k\,I} + k_{v_k}^{II} L^{II} W \lambda_{rt}^{k\,II} \frac{\partial p}{\partial y}|^{k\,II}}, \quad i = 1, n_c \qquad (3.3\text{-}46)$$

where, k_{v_k} is the vertical permeability in layer k, L is the horizontal distance from the shock front, and $\frac{\partial p}{\partial y}|^k$ is the pressure gradient in the vertical direction in layer k.

If we assume that

$$k_{v_k}^I = k_{v_k}^{II}$$

$$L^I = L^{II} \tag{3.3-47}$$

$$\frac{\partial p}{\partial y}|^{k\,I} = \frac{\partial p}{\partial y}|^{k\,II}$$

then Eq. (3.3-46) reduces to

$$F_{xf_i}^k = \frac{F_i^{k\,I}\,\lambda_{rt}^{k\,I} + F_i^{k\,II}\,\lambda_{rt}^{k\,II}}{\lambda_{rt}^{k\,I} + \lambda_{rt}^{k\,II}}\,, \quad i = 1, n_c \tag{3.3-48}$$

The coherence condition requires equality of the shock velocity for all components,

$$\Lambda_i^1 = \Lambda_i^2\,, \quad i = 1, n_c \tag{3.3-49}$$

Phase Behavior and Fluid Properties

The Peng-Robinson equation of state (Peng and Robinson 1976) was used to calculate phase compositions. Phase viscosities were calculated using the Lohrenz et al. (1964) version of the Jossi et al. (1962) correlations. All phase composition and viscosity calculations were performed using the phase behavior package developed by Nutakki et al. (1985). Phase densities were calculated as

$$\rho_j^k = \frac{\sum_{i=1}^{n_c} x_{ij}^k}{\sum_{i=1}^{n_c} \frac{x_{ij}^k}{\rho_{c_i}}}\,, \quad j = 1, n_p \tag{3.3-50}$$

where ρ_{c_i} is the molar density of component i at the reservoir temperature and pressure as obtained from the Peng-Robinson equation of state, and x_{ij}^k is the mole fraction of component i in phase j in layer k. Phase densities were calculated using Eq. (3.3-50) rather than using the phase densities predicted by the Peng-Robinson equation of state because of the assumption of no volume change on mixing. Experience with path calculations with and without volume change on mixing indicates that paths are not strongly affected by the assumption, although local fluid velocity (not wave velocity) is affected.

Relative permeabilities of the fluid phases were calculated using the following expressions

$$k_{rg} = k_{rg}^o \left[\frac{S_g}{1 - S_{wr} - S_{or}}\right]^{n_g} \tag{3.3-51}$$

$$k_{rl} = k_{rl}^o \left[\frac{1 - S_g - S_{or} - S_{wr}}{1 - S_{wr} - S_{or}}\right]^{n_l} \tag{3.3-52}$$

where,

k_{rg} = gas phase relative permeability

k_{rl} = liquid phase relative permeability

k_{rg}^{o} = end point gas phase relative permeability

k_{rl}^{o} = end point liquid phase relative permeability

n_g = relative permeability exponent for gas

n_l = relative permeability exponent for liquid

S_g = gas phase saturation

S_{or} = residual oil saturation

S_{wr} = residual water saturation

The fractional flow expression is derived from Darcy's law based on the assumption of no capillary pressure or gravity effects

$$f_j^k = \frac{\frac{k_{rj}^k}{\mu_j^k}}{\sum_{j=1}^{n_p} \frac{k_{rj}^k}{\mu_j^k}}, \qquad j = 1, n_p \tag{3.3-53}$$

Construction of Solutions

As in the previous two sections of this chapter, solutions are assembled from continuous variations and shocks, which are present when continuous variations are prohibited by the requirement that compositions with high wave velocities (eigenvalues) lie downstream of those with lower velocity. Continuous variations must lie along paths obtained by integration of Eqs. (3.3-35) and (3.3-36) or (3.3-37) and (3.3-38). Shocks must satisfy (3.3-49) and be genuine shocks or intermediate discontinuities. If they are intermediate discontinuities, then the shock velocities of Eq. (3.3-49) are also equal to the eigenvalue of the associated continuous variations. Additional details of the solution of the eigenvalue problems and shock balances are given by Pande (1989).

3.3.2 Binary Mixtures: Displacement of Decane by CO_2

Single-Layer Flow

The solution for binary displacement in a single layer of components with limited solubility was obtained by Helfferich (1982). For the CO_2-decane (C_{10}) displacement of this section, the single-layer solution is described in detail by Pande (1989). At the displacement pressure of 1600 psia at 160°F, the volume fraction of CO_2 in CO_2-saturated C_{10} is C_{11}=0.6402. The saturated vapor phase composition is C_{12}=0.9822. Pure component molar densities and phase relative permeability parameters are given in Tables 3.3-1 and 3.3-2.

Typical solutions for the single-layer compositions and saturations are shown in Figs. 3.3-2 and 3.3-3. As those figures show, single-phase flow of pure C_{10} occurs ahead of a leading shock, an upstream intermediate discontinuity (UID) or tangent shock, behind which there

Table 3.3-1 Molar Densities of Pure Components at 160°F and 1600 psia.

Component	Molar Density (lb–moles/ft^3)
CO_2	0.4129
C_4	0.6126
C_{10}	0.2899

Table 3.3-2 Parameters for Example Problems

Parameter	Value
k_{rl}^o	1.0
k_{rg}^o	1.0
S_{or}	0.1
S_{wr}	0.0
n_g	2.0
n_l	2.0

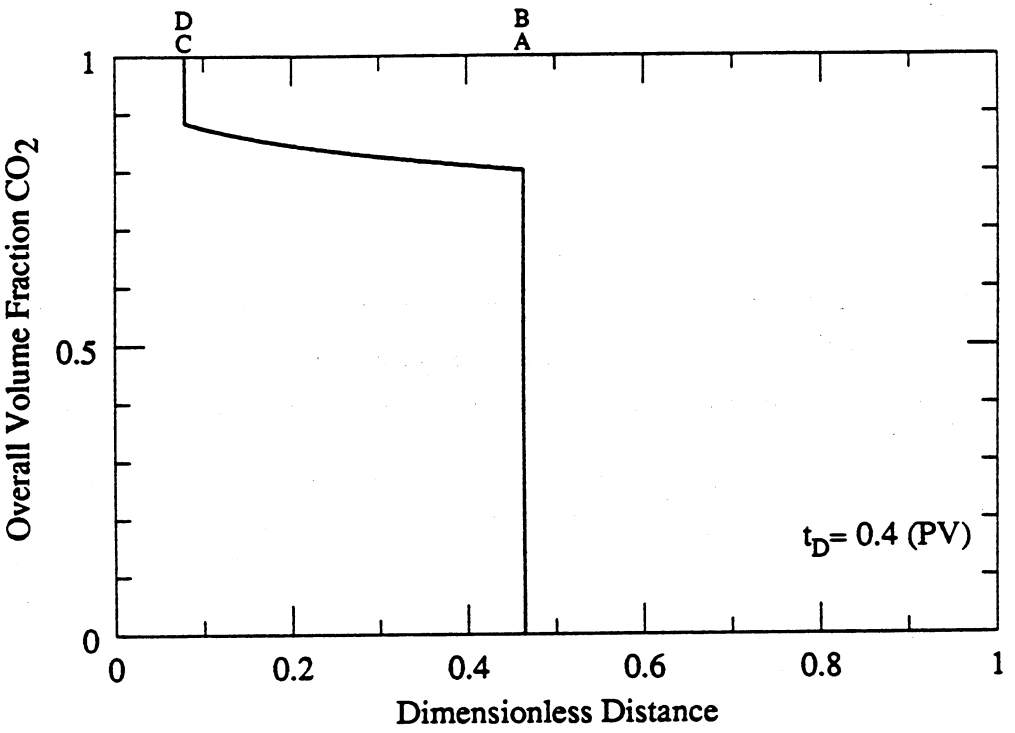

Fig. 3.3-2 MOC composition profile for CO_2-C_{10} displacement in a uniform flow system.

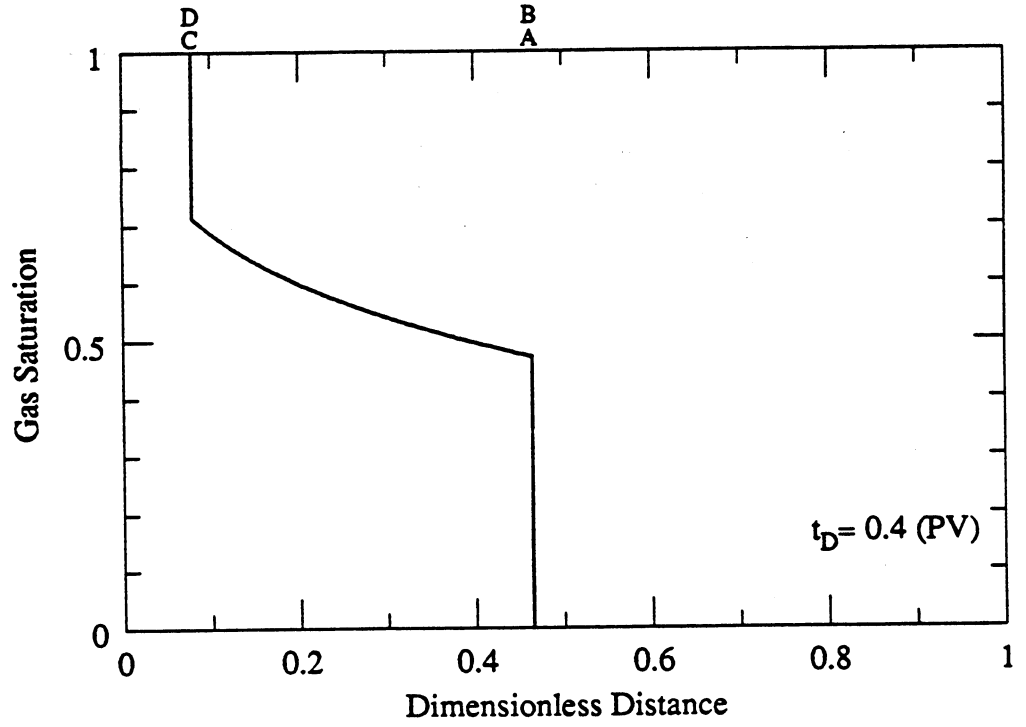

Fig. 3.3-3 MOC saturation profile for CO_2-C_{10} displacement in a uniform flow system.

is a zone of two-phase flow. At the rear of the two-phase zone is a downstream intermediate discontinuity (DID), behind which is a single-phase flow of the injected fluid, pure CO_2.

Low Permeability Contrast

Solutions for two-layer flows are significantly more complex, even for binary systems, because several combinations of shocks can exist. Fig. 3.3-4, constructed from solutions without crossflow, illustrates the possibilities. At low permeability contrast, the regions of two-phase flow overlap, four separate shocks and the directions of crossflow, estimated from the pressure distribution argument of Fig. 3.3-1 and indicated by the arrows, change several times. At high permeability contrast, four shocks also occur, but the flow in the low permeability layer is so slow that the regions of two-phase flow do not overlap. For some intermediate permeability contrast, the trailing shock in the fast layer will be at about the location of the leading shock in the slow layer. When there is crossflow present, a shock in one layer must be accompanied by a shock in the other. As we show below, for intermediate permeability contrasts, the two intermediate shocks coalesce and only three shocks are observed.

In the construction of solutions for the various two-layer cases, approximate finite difference solutions were obtained so that the type of discontinuity and values of compositions near shocks could be estimated. Details of those solutions are also reported by Pande (1989).

Solutions were calculated for three ratios of layer permeabilities, 1.5, 3.0 and 10.0. Fig. 3.3-5 shows composition routes for those solutions and for the uniform case $k_1/k_2=1.0$. The solid straight lines at constant values of C_1^1 or C_1^2 mark the boundaries of the two-phase region in each layer. Solid curves in Fig. 3.3-5 indicate continuous variations, and dashed lines connect compositions on either side of a shock. As Fig. 3.3-4 suggests and Fig. 3.3-5 indicates, only at low permeability contrast does two-phase flow occur in both layers simultaneously.

The details of the solution for a given value of the permeability ratio can be seen more clearly on plots of the composition and saturation profiles. Table 3.3-3 and Figs. 3.3-6, 3.3-7, and 3.3-8 show the composition, saturation and flow velocity profiles at 0.4 pore volumes (PV) injected. Figs. 3.3-9 and 3.3-10 show the corresponding composition and saturation distributions for a displacement with the same permeability ratio but without crossflow.

As Fig. 3.3-4 suggests, four shocks are shown in Figs. 3.3-6 and 3.3-7. Comparison of Figs. 3.3-6 and 3.3-9 indicates that the leading shock velocity in the fast layer is about the same whether or not there is crossflow. Compositions in the slow layer are quite different, however. Without crossflow (Fig. 3.3-9) no CO_2 is present in layer 2 until the leading shock in that layer reaches a given position. When crossflow is present, a significant CO_2 concentration appears in the slow layer as soon as the leading shock passes that position in the first layer. The reason for the jump in CO_2 concentration in the slow layer can be seen in Fig. 3.3-8, which shows the flow rate in layer 1, q_{1D}. At the leading shock, the flow rate drops discontinuously as the shock is crossed from upstream to downstream. Because there is no volume change on mixing in this model, any change in q_{1D} must be due to crossflow. Thus when q_{1D} decreases, as at the leading shock, crossflow from layer 1 to layer 2 is taking place. As Figs. 3.3-6 and 3.3-8 indicate, significant crossflow from the high permeability layer to the low permeability layer occurs at the leading shock.

Behind the leading shock, there is a small continuous variation (point **B** to point **C** in Table 3.3-3 and Figs. 3.3-6 to 3.3-8). Thus, the leading shock is an upstream intermediate discontinuity (UID). The continuous variation is followed by a zone of constant state that precedes the leading intermediate shock (point **C** to point **D**). That shock corresponds to the leading shock in layer 2 (compare Figs. 3.3-6 and 3.3-9), but it moves more slowly when crossflow is present. The reason for the difference again is crossflow. Fig 3.3-8 shows that upstream of the leading intermediate shock, q_{1D} is increasing. Hence the flow rate in layer 2 is decreasing as fluid flows from layer 2 to layer 1. That loss of fluid and flow rate slows the leading intermediate shock.

Table 3.3-3 MOC Solution for CO_2-C_{10} Displacement with Crossflow for k_1/k_2 = 1.5.

Parameter	Label	CO_2 Concentration (volume fraction)		Gas Saturation (volume fraction)		Wave Velocity (1/PV)
		Layer 1	Layer 2	Layer 1	Layer 2	
Injection Gas	H	1.0000	1.0000	1.0000	1.0000	0.1266
Trailing Shock	H	1.0000	1.0000	1.0000	1.0000	0.1266
	G	0.9984	0.8785	1.0000	0.6967	0.1266
Trailing ZCV*	G	0.9984	0.8785	1.0000	0.6967	0.1266
	F	0.9976	0.8637	1.0000	0.6535	0.1670
Trailing ZCS**	F	0.9976	0.8637	1.0000	0.6535	0.1670
	F	0.9976	0.8637	1.0000	0.6535	0.2877
Trailing Int. Shock	F	0.9976	0.8637	1.0000	0.6535	0.2877
	E	0.9137	0.8440	0.7995	0.5957	0.2877
Int. ZCV*	E	0.9137	0.8440	0.7995	0.5957	0.2877
	D	0.9320	0.8036	0.8532	0.4776	0.4417
Leading Int. Shock	D	0.9320	0.8036	0.8532	0.4776	0.4417
	C	0.8160	0.2899	0.5139	0.0000	0.4417
Leading ZCS**	C	0.8160	0.2899	0.5139	0.0000	0.4417
	C	0.8160	0.2899	0.5139	0.0000	1.4873
Leading ZCV*	C	0.8160	0.2899	0.5139	0.0000	1.4873
	B	0.8152	0.2890	0.5118	0.0000	1.5066
Leading Shock	B	0.8152	0.2890	0.5118	0.0000	1.5066
	A	0.0000	0.0000	0.0000	0.0000	1.5066
Initial Oil	A	0.0000	0.0000	0.0000	0.0000	1.5066

* ZCV = Zone of Continuous Variation

** ZCS = Zone of Constant State

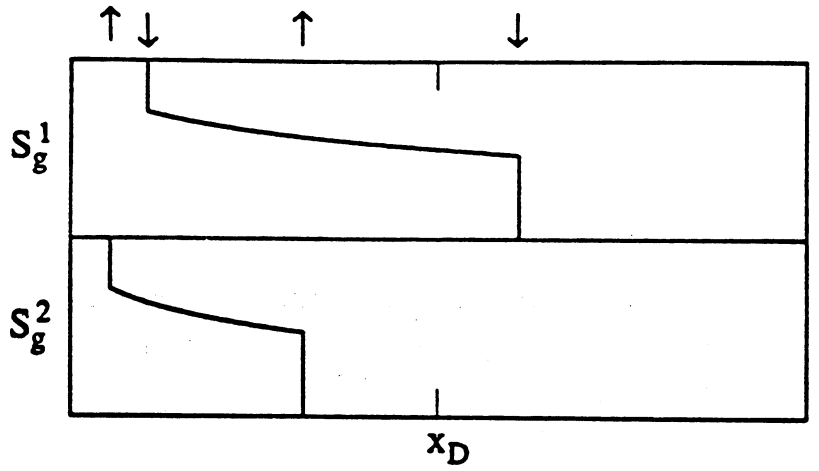

Low Permeability Contrast

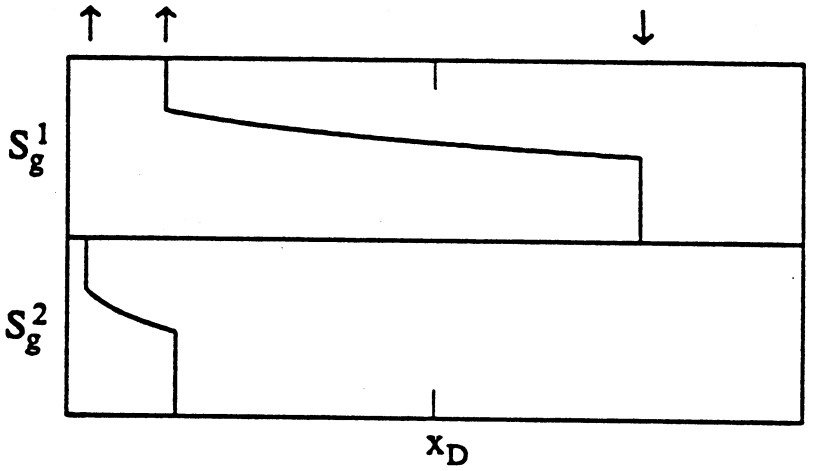

Medium Permeability Contrast

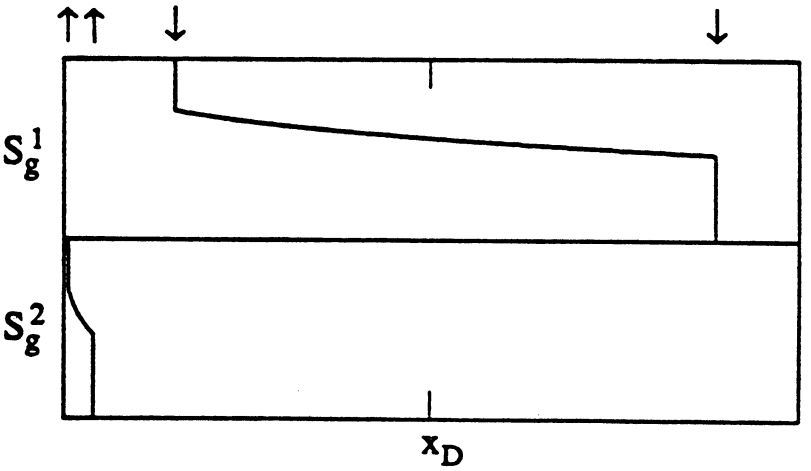

High Permeability Contrast

Fig. 3.3-4 Illustration of three types of binary nonuniform displacements.

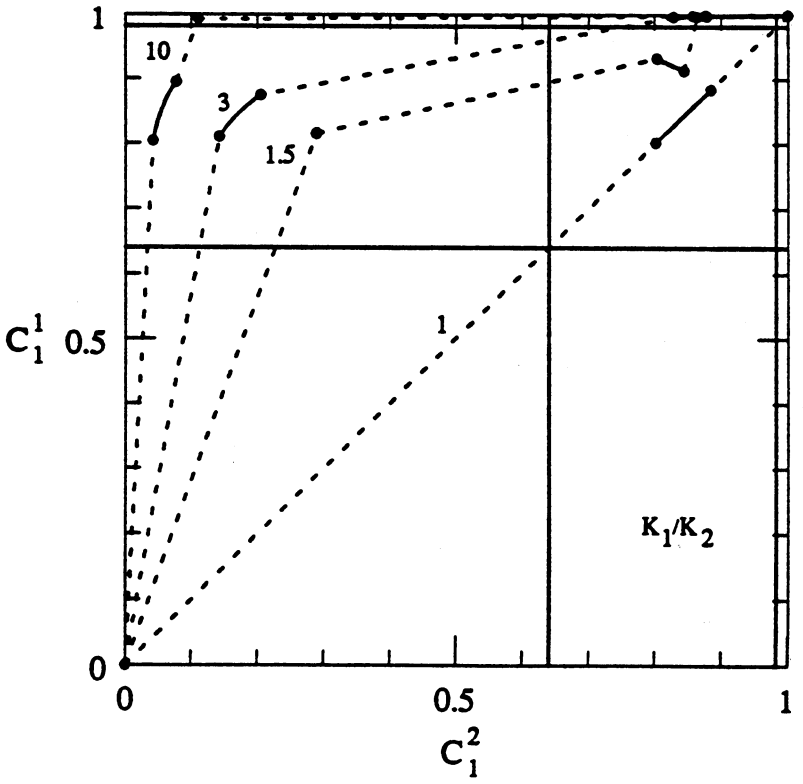

Fig. 3.3-5 MOC solution routes for CO_2-C_{10} displacements with crossflow for k_1/k_2 = 1.0, 1.5, 3.0, 10.0.

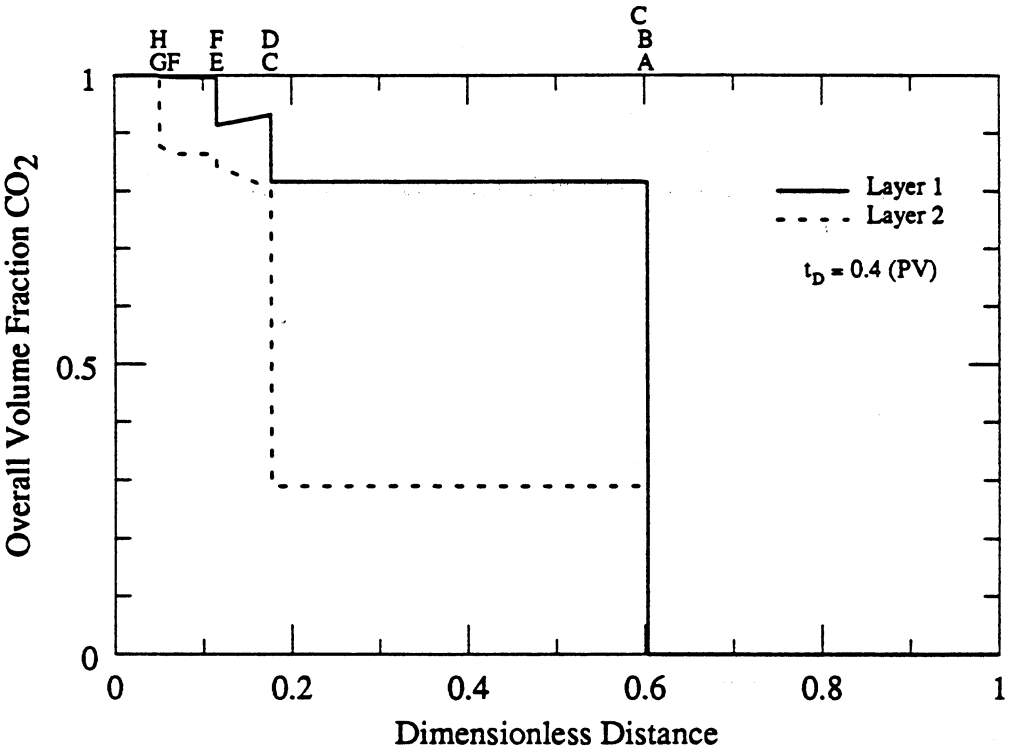

Fig. 3.3-6 MOC composition profiles for CO_2-C_{10} displacement with crossflow for k_1/k_2 = 1.5.

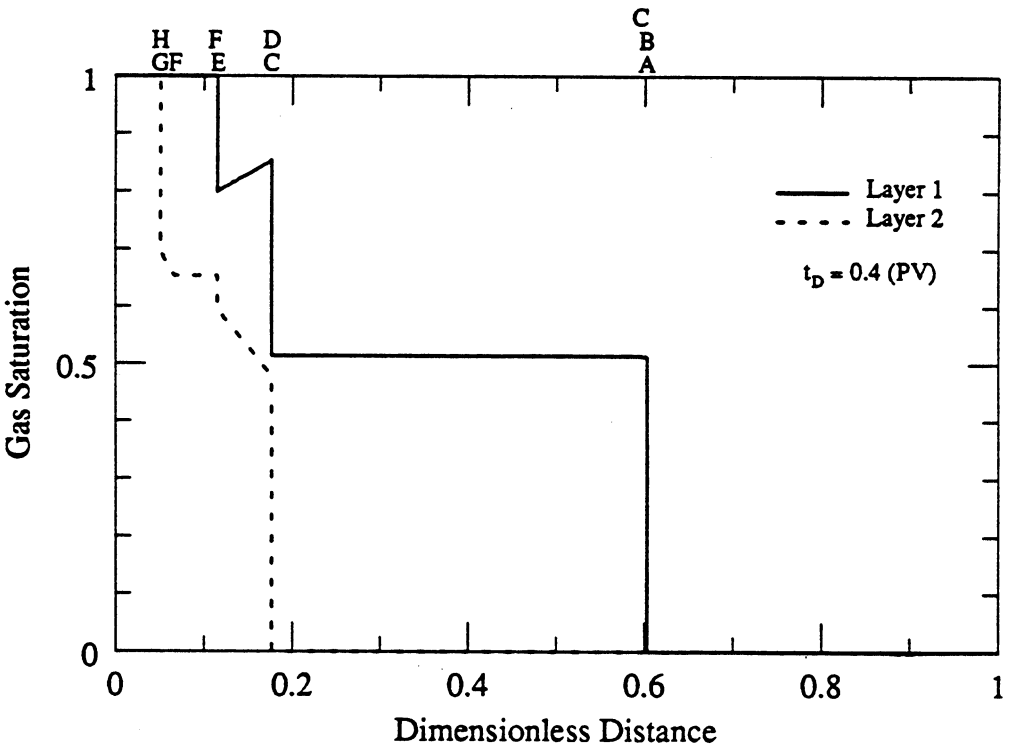

Fig. 3.3-7 MOC saturation profiles for CO_2-C_{10} displacement with crossflow for k_1/k_2 = 1.5.

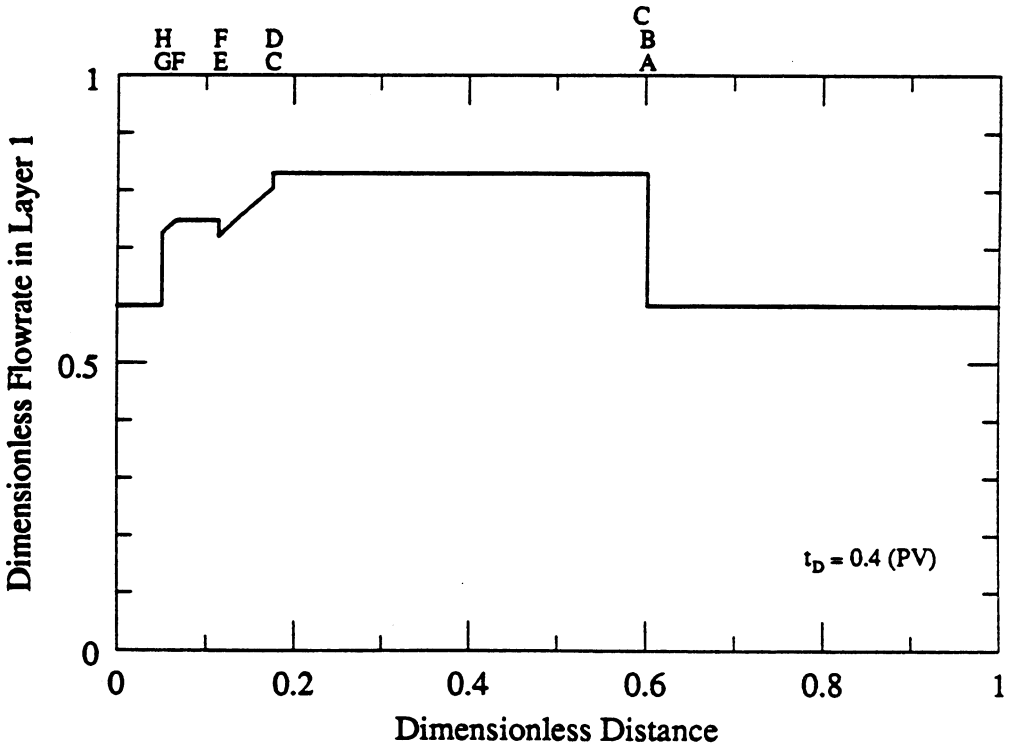

Fig. 3.3-8 MOC flow rate profile for CO_2-C_{10} displacement with crossflow for k_1/k_2 = 1.5.

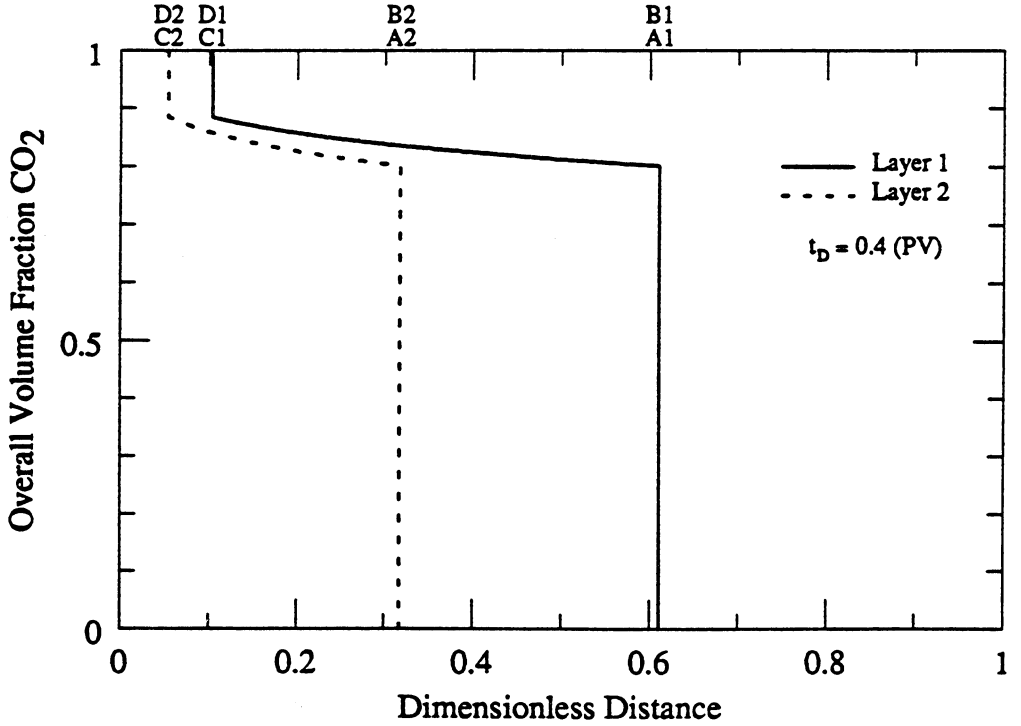

Fig. 3.3-9 MOC composition profiles for CO_2-C_{10} displacement without crossflow for k_1/k_2 = 1.5.

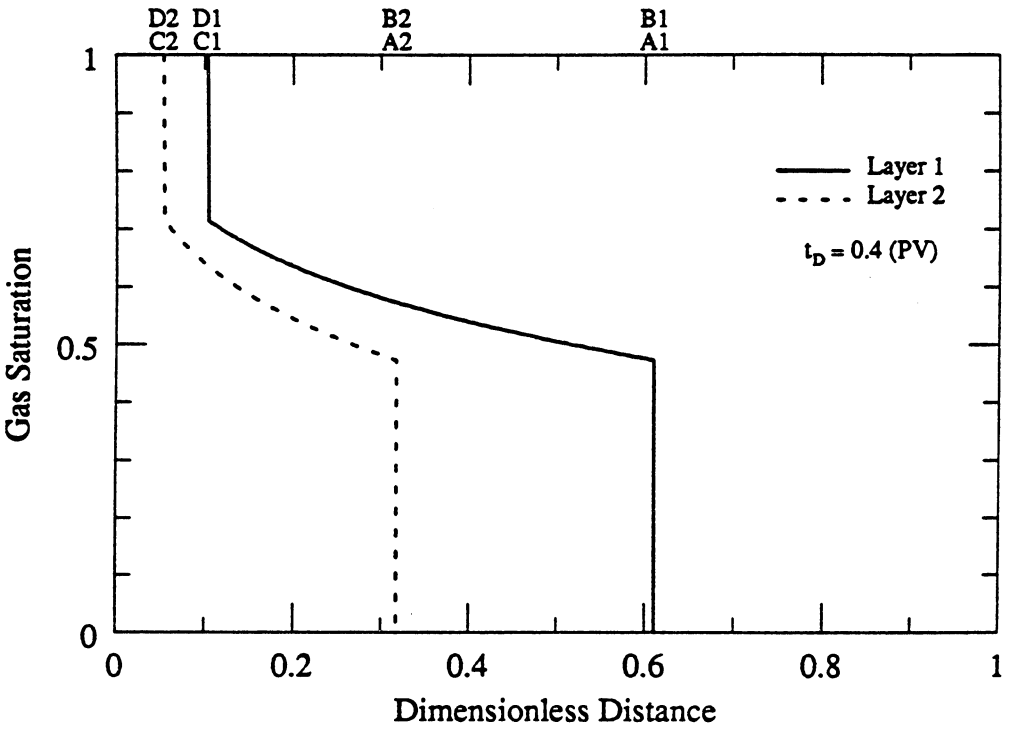

Fig. 3.3-10 MOC saturation profiles for CO_2-C_{10} displacement without crossflow for k_1/k_2 = 1.5.

From point **D** to **E**, the composition varies continuously (Table 3.3-3). The shock from point **E** to point **F** is a downstream intermediate discontinuity (DID) that corresponds to the trailing shock in the fast layer when crossflow is absent. That shock is followed by a zone of constant state, another continuous variation (point **F** to point **G**), and finally the trailing shock (point **G** to point **H**). As the increase in q_{1D} in Fig. 3.3-8 shows, upstream of point **D**, crossflow from layer 2 to layer 1 dominates. The only exception is a small amount of crossflow from layer 1 to layer 2 at the trailing intermediate shock (point **E** to point **F**). Because the C_{10} concentration in layer 2 is relatively high, the crossflow causes the CO_2 concentration and vapor saturation in layer 1 to decline slightly between points **D** and **E**. Without crossflow, the CO_2 concentration increases monotonically, as Fig. 3.3-9 shows. Thus that decline illustrates nicely how crossflow can modify composition paths observed in uniform flow.

Medium Permeability Contrast

The composition path for the medium permeability ratio k_1/k_2=3.0, is shown in Fig. 3.3-5, and the MOC solution is summarized in Table 3.3-4. The corresponding composition, saturation, and velocity profiles are in Figs. 3.3-11, 3.3-12, and 3.3-13. The solution for the no-crossflow case is shown in Figs. 3.3-15 and 3.3-16.

Only three shocks appear when crossflow is present, and there is no place in the displacement where two-phase flow occurs in both layers simultaneously. When crossflow is absent, however, there is a small region of simultaneous two-phase flow (Fig. 3.3-16). Apparently, the leading shock in layer 2 and the trailing shock in layer 1 coalesce into a single shock when crossflow is present. The leading shock in the fast layer is followed by a large zone of continuous variation. In that zone, crossflow from layer 1 to layer 2 occurs, though the amount is small compared to the amount of crossflow at the leading shock (see Fig. 3.3-13). Upstream of point **D**, the intermediate shock, all the crossflow is from the slow layer to the fast one.

High Permeability Contrast

When the permeability ratio is k_1/k_2=10.0, the composition path is displaced still further toward high CO_2 concentrations in layer 1, as Fig. 3.3-5 shows. Comparison of the crossflow solutions in Table 3.3-5 and Figs. 3.3-16 and 3.3-17 to the no-crossflow solution in Figs. 3.3-19 and 3.3-20 indicates that flow in layer 2 is very slow in either case, but is slower when crossflow is present. When the permeability ratio is high enough, four shocks appear again, though the trailing intermediate and trailing shocks are so close together (see Table 3.3-5) that they are difficult to discern in Figs. 3.3-17 and 3.3-18. As comparison of Figs. 3.3-6, 3.3-11 and 3.3-16 shows, the CO_2 concentration in layer 2, due to crossflow at the leading shock, declines as the permeability ratio increases.

Recovery Performance

Fig. 3.3-21 is a comparison of recovery performance for all the permeability contrasts considered. As the permeability ratio increases, complete recovery, which occurs when the trailing shock reaches the outlet, takes longer whether or not crossflow occurs. When crossflow is present, the length of the transition zone increases at any permeability ratio. At a given permeability ratio, crossflow improves recovery just after breakthrough, as C_{10} transferred to the high permeability layer is produced. If the permeability ratio is low, the period of improved recovery is short, however, and the negative effect of the lengthened transition zone soon sets in. For higher permeability ratios, that period is longer. Fig. 3.3-21 shows, therefore, that the interaction of crossflow, phase behavior, and fractional flow leads to partly compensating effects on recovery.

Table 3.3-4 MOC Solution for CO_2-C_{10} Displacement with Crossflow for k_1/k_2 = 3.0.

Parameter	Label	CO_2 Concentration (volume fraction)		Gas Saturation (volume fraction)		Wave Velocity (1/PV)
		Layer 1	Layer 2	Layer 1	Layer 2	
Injection Gas	F	1.0000	1.0000	1.0000	1.0000	0.0755
Trailing Shock	F	1.0000	1.0000	1.0000	1.0000	0.0755
	E	0.9990	0.8768	1.0000	0.6918	0.0755
Trailing ZCV*	E	0.9990	0.8768	1.0000	0.6918	0.0755
	D	0.9972	0.8272	1.0000	0.5468	0.1607
Int. Shock	D	0.9972	0.8272	1.0000	0.5468	0.1607
	C	0.8748	0.2051	0.6860	0.0000	0.1607
ZCS**	C	0.8748	0.2051	0.6860	0.0000	0.1607
	C	0.8748	0.2051	0.6860	0.0000	0.4784
Leading ZCV*	C	0.8748	0.2051	0.6860	0.0000	0.4784
	B	0.8100	0.1422	0.4965	0.0000	1.8243
Leading Shock	B	0.8100	0.1422	0.4965	0.0000	1.8243
	A	0.0000	0.0000	0.0000	0.0000	1.8243
Initial Oil	A	0.0000	0.0000	0.0000	0.0000	1.8243

* ZCV = Zone of Continuous Variation

** ZCS = Zone of Constant State

Table 3.3-5 MOC Solution for CO_2-C_{10} Displacement with Crossflow for k_1/k_2 = 10.0.

Parameter	Label	CO_2 Concentration (volume fraction)		Gas Saturation (volume fraction)		Wave Velocity (1/PV)
		Layer 1	Layer 2	Layer 1	Layer 2	
Injection Gas	G	1.0000	1.0000	1.0000	1.0000	0.0262
Trailing Shock	G	1.0000	1.0000	1.0000	1.0000	0.0262
	F	0.9996	0.8750	1.0000	0.6865	0.0262
Trailing ZCV*	F	0.9996	0.8750	1.0000	0.6865	0.0262
	E	0.9994	0.8568	1.0000	0.6334	0.0352
Trailing Int. Shock	E	0.9994	0.8568	1.0000	0.6334	0.0352
	D	0.9932	0.1102	1.0000	0.0000	0.0352
ZCS**	D	0.9932	0.1102	1.0000	0.0000	0.0352
	D	0.9932	0.1102	1.0000	0.0000	0.2847
Leading Int. Shock	D	0.9932	0.1102	1.0000	0.0000	0.2847
	C	0.8955	0.0773	0.7465	0.0000	0.2847
Leading ZCV*	C	0.8955	0.0773	0.7465	0.0000	0.2847
	B	0.8045	0.0420	0.4805	0.0000	2.1420
Leading Shock	B	0.8045	0.0420	0.4805	0.0000	2.1420
	A	0.0000	0.0000	0.0000	0.0000	2.1420
Initial Oil	A	0.0000	0.0000	0.0000	0.0000	2.1420

* ZCV = Zone of Continuous Variation

** ZCS = Zone of Constant State

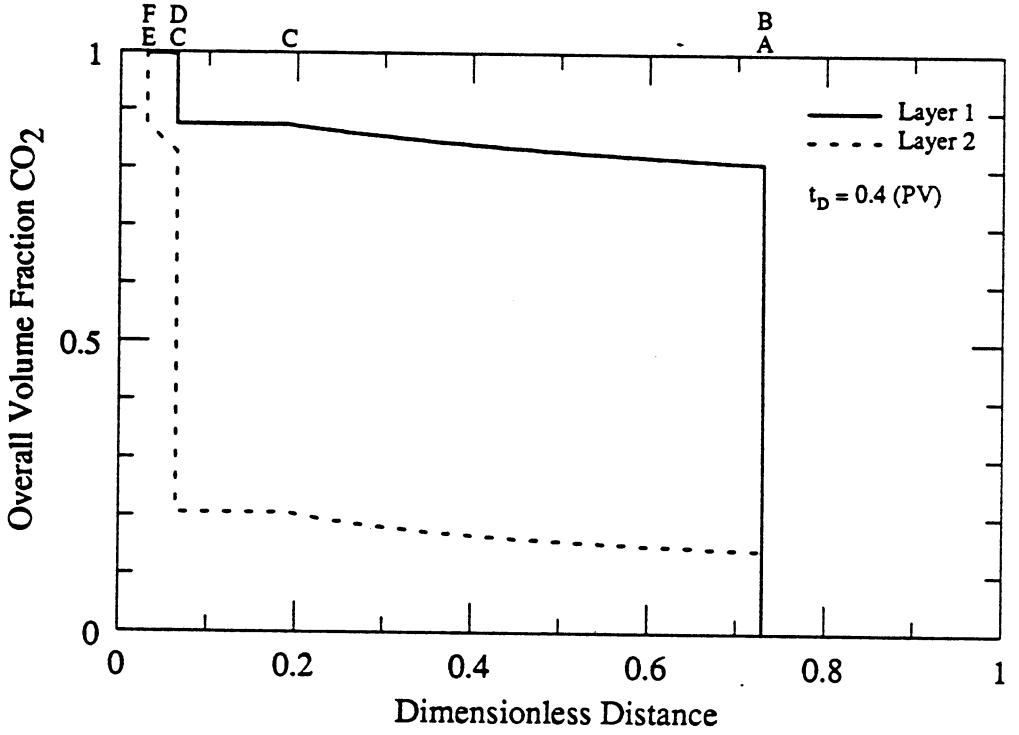

Fig. 3.3-11 MOC composition profiles for CO_2-C_{10} displacement with crossflow for k_1/k_2 = 3.0.

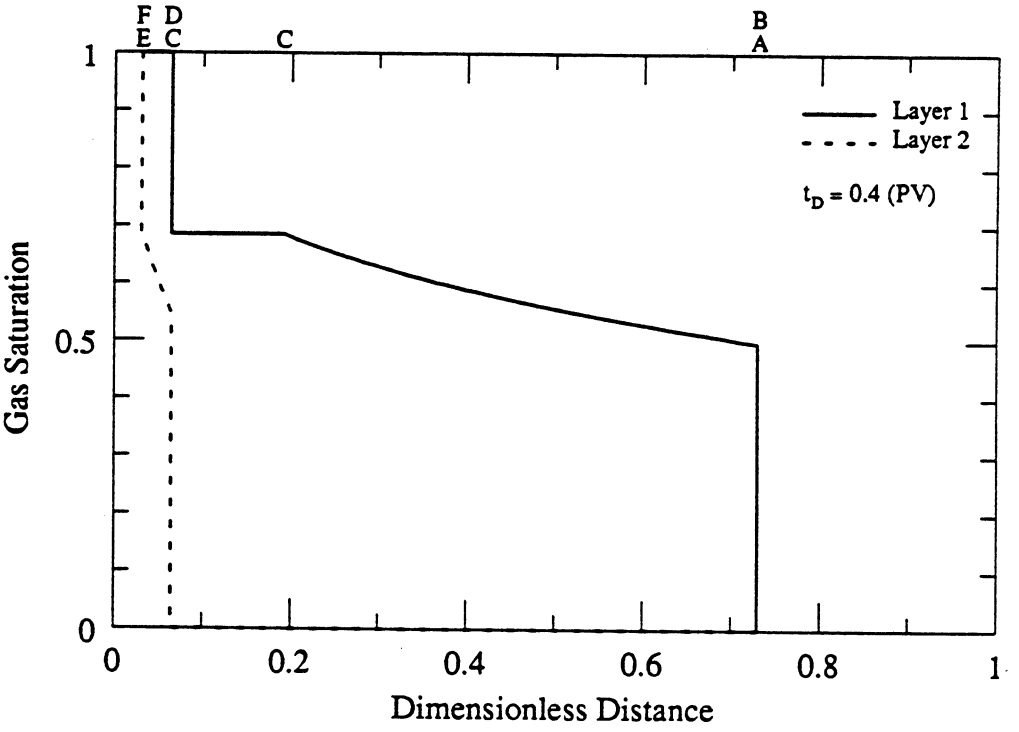

Fig. 3.3-12 MOC saturation profiles for CO_2-C_{10} displacement with crossflow for k_1/k_2 = 3.0.

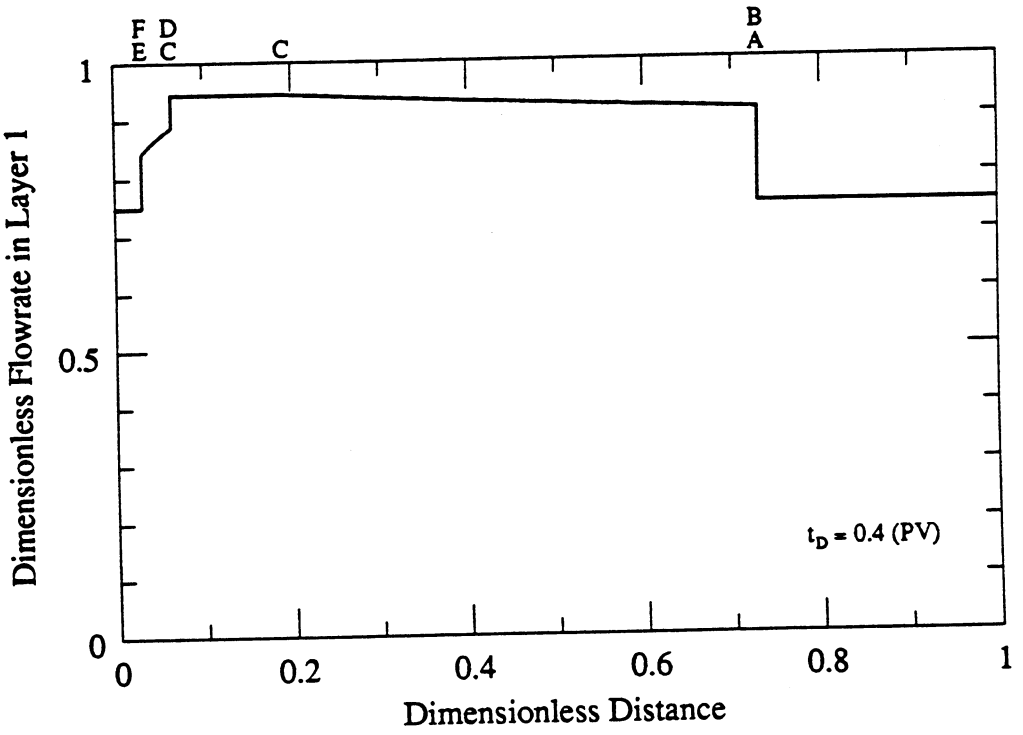

Fig. 3.3-13 MOC flow rate profile for CO_2-C_{10} displacement with crossflow for k_1/k_2 = 3.0.

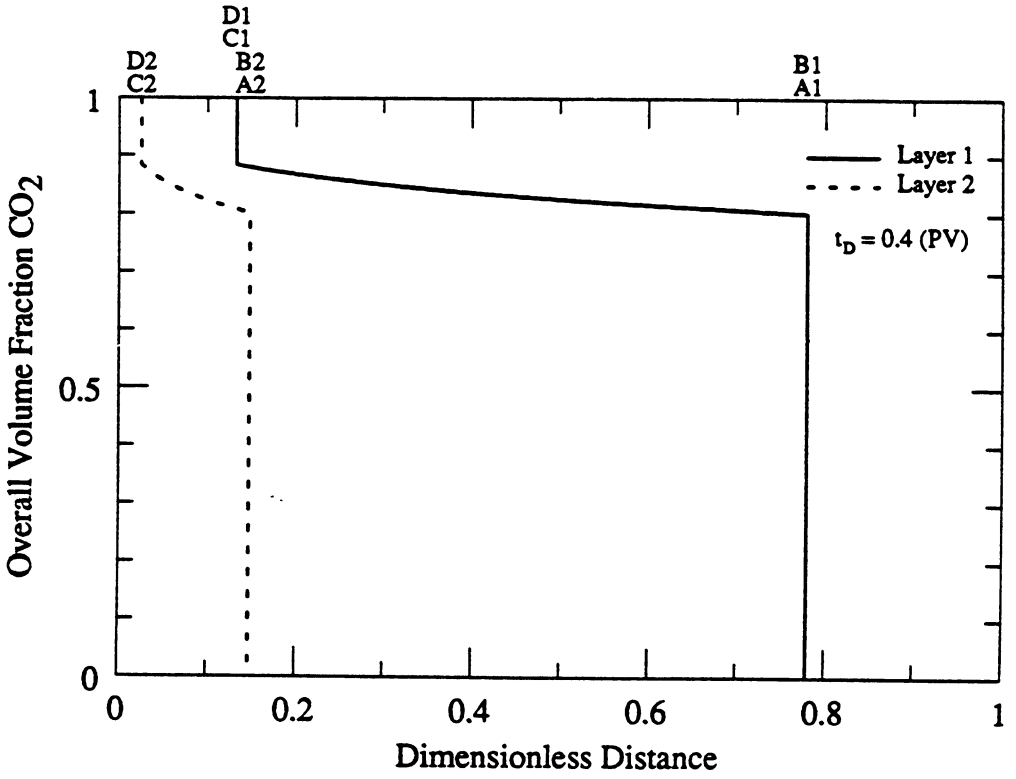

Fig. 3.3-14 MOC composition profiles for CO_2-C_{10} displacement without crossflow for k_1/k_2 = 3.0.

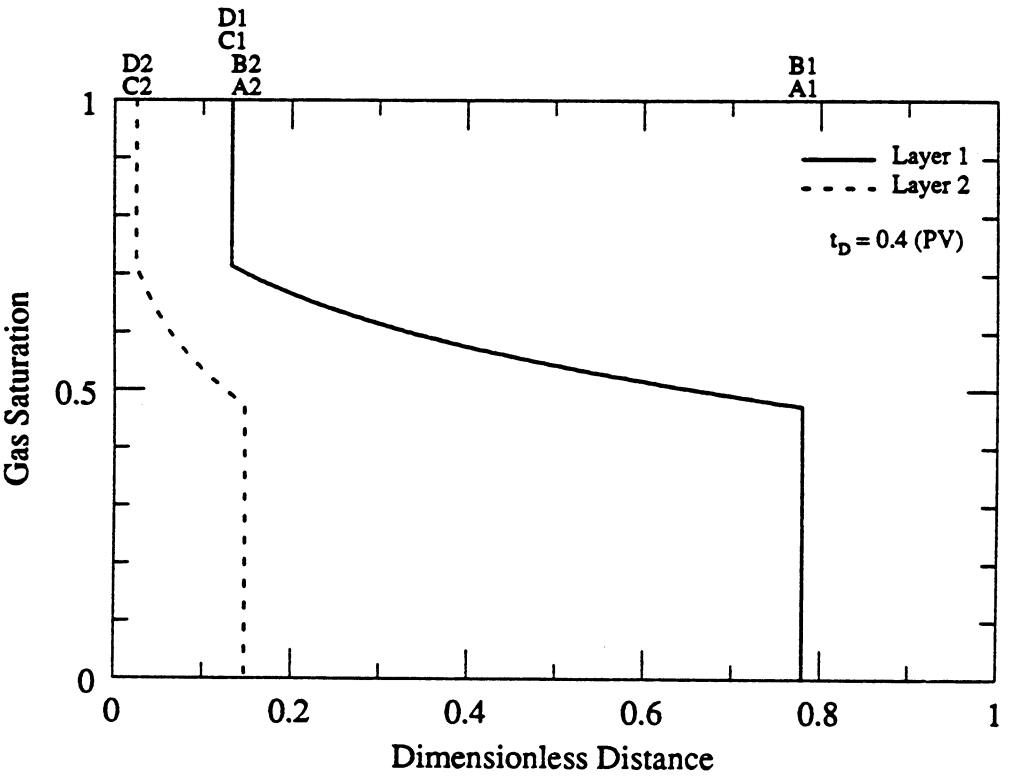

Fig. 3.3-15 MOC saturation profiles for CO_2-C_{10} displacement without crossflow for k_1/k_2 = 3.0.

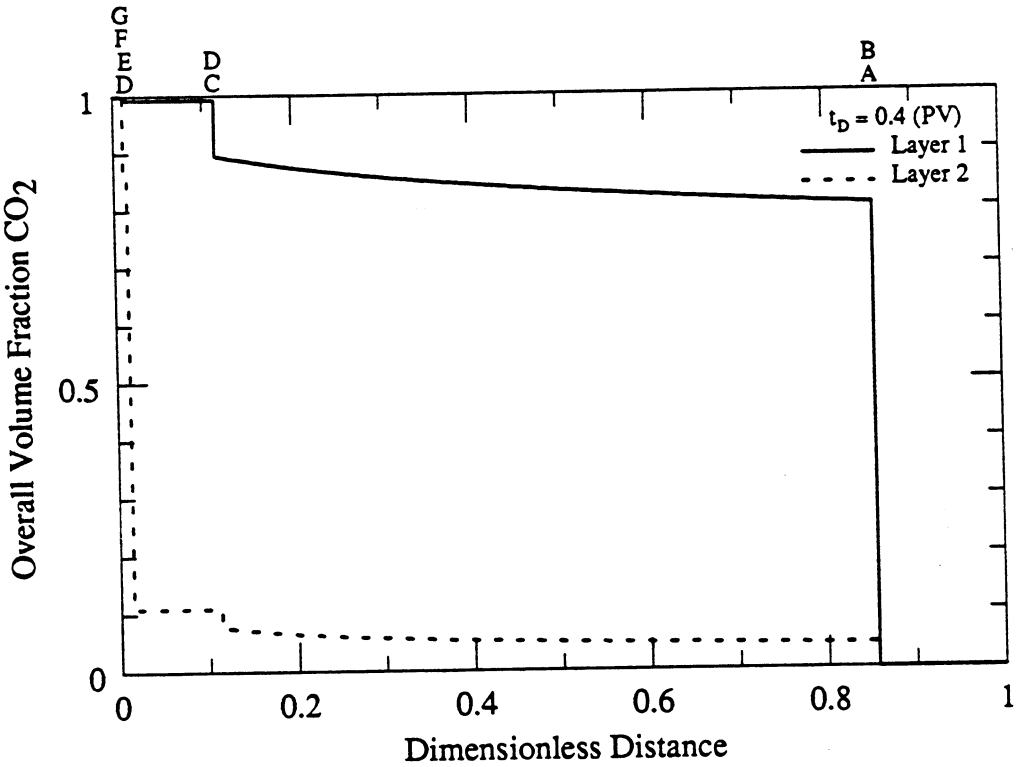

Fig. 3.3-16 MOC composition profiles for CO_2-C_{10} displacement with crossflow for k_1/k_2 = 10.0.

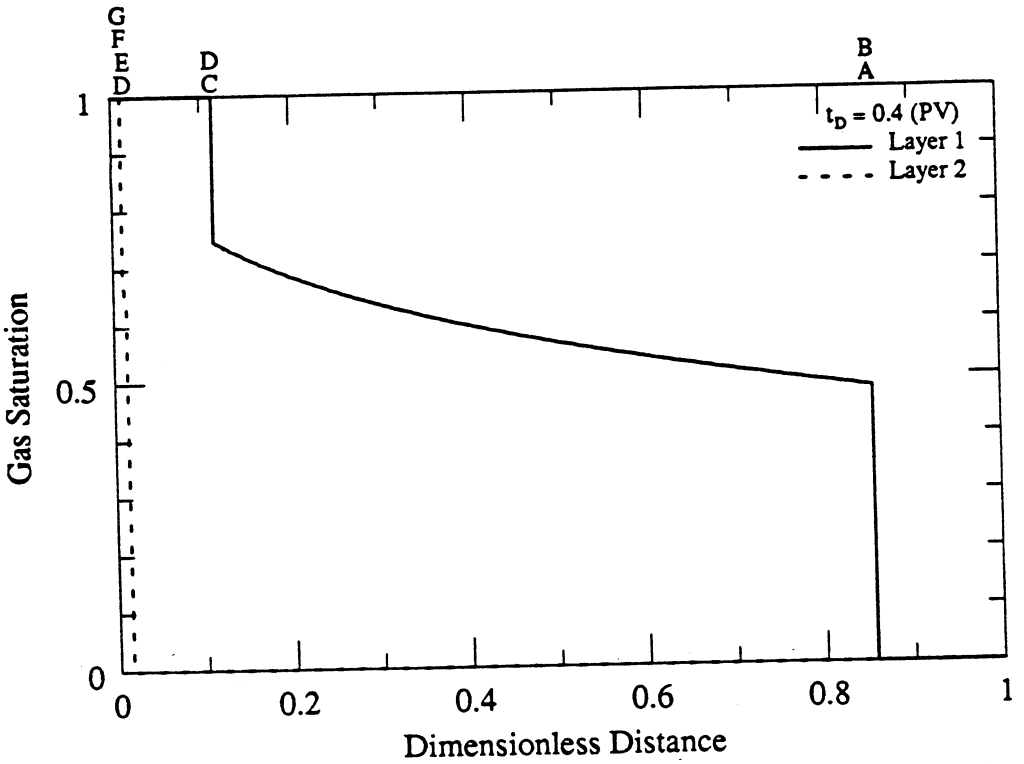

Fig. 3.3-17 MOC saturation profiles for CO_2-C_{10} displacement with crossflow for k_1/k_2 = 10.0.

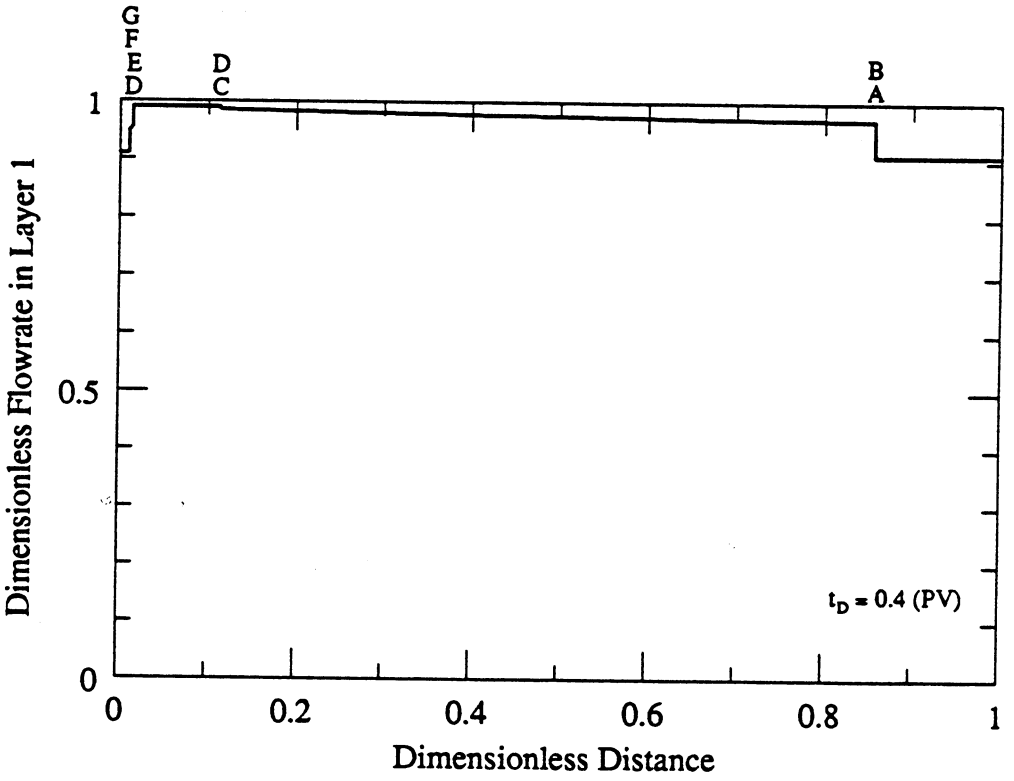

Fig. 3.3-18 MOC flow rate profile for CO_2-C_{10} displacement with crossflow for k_1/k_2 = 10.0.

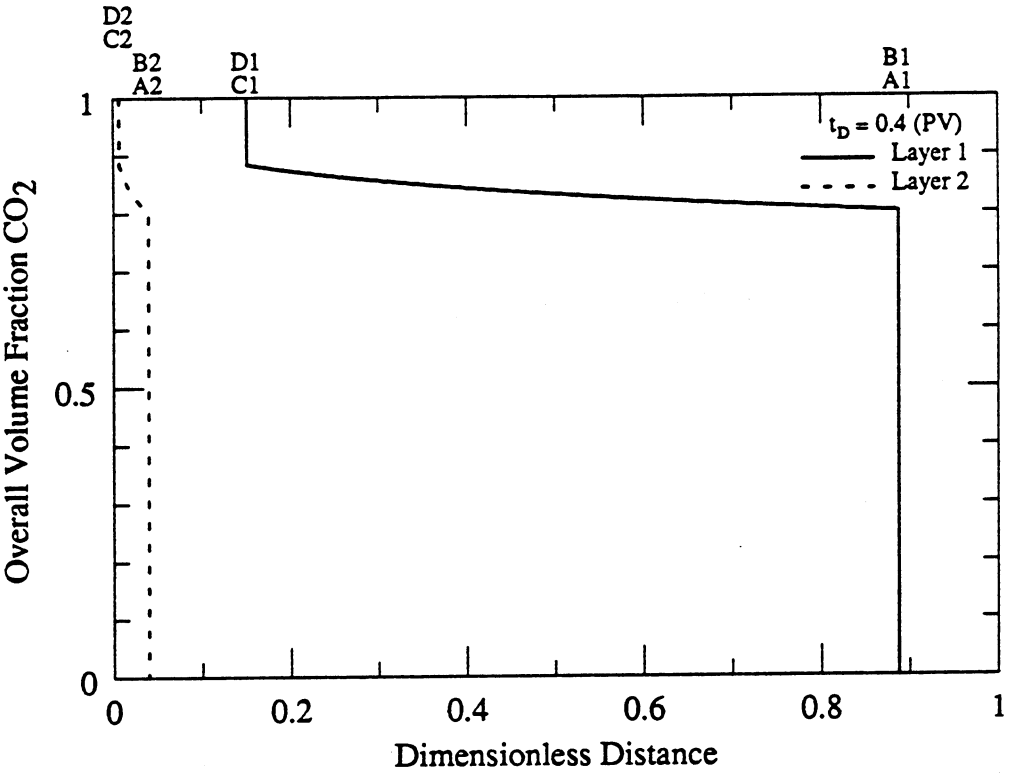

Fig. 3.3-19 MOC composition profiles for CO_2-C_{10} displacement without crossflow for k_1/k_2 = 10.0.

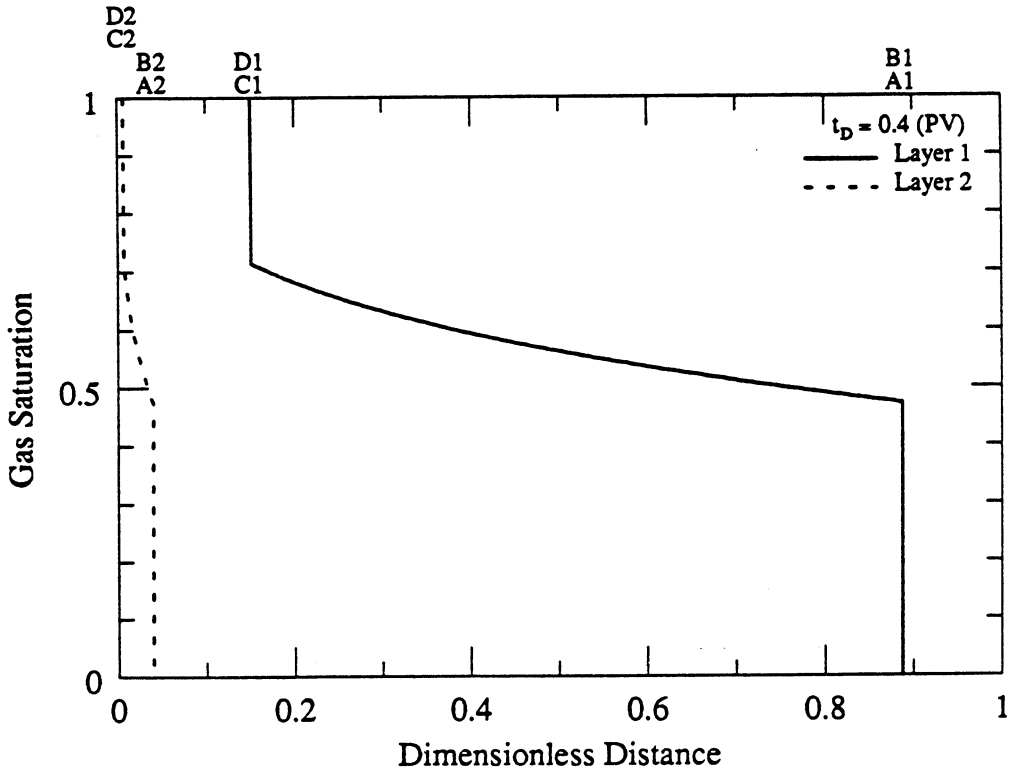

Fig. 3.3-20 MOC saturation profiles for CO_2-C_{10} displacement without crossflow for k_1/k_2 = 10.0.

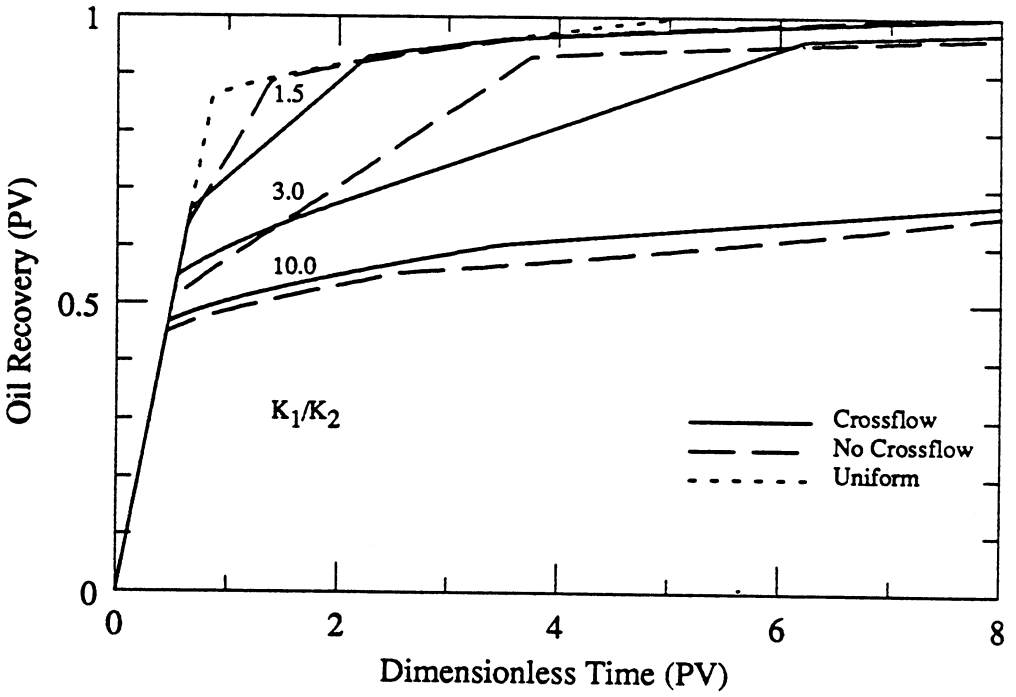

Fig. 3.3-21 MOC oil recovery curves for CO_2-C_{10} displacements with and without crossflow for k_1/k_2 = 1.0, 1.5, 3.0, 10.0.

3.3.3 Ternary Mixtures: Displacement of Two-Component Oils by CO_2

MOC solutions for the complete ternary problem have not been obtained, though important pieces of the solution have been. For instance Pande (1989, Appendix C) has shown that even when crossflow is present, leading and trailing shocks that enter the two-phase region must occur along tie-line extensions, a useful generalization of the similar proof for uniform flow. To examine the behavior of the three-component case, therefore, finite-difference computations were performed. The material balance equations (Eqs. 3.3-21 to 3.3-24) were solved with an explicit finite difference form; details are given by Pande (1989, Appendix B).

The finite difference (FD) solutions reported below were influenced by numerical dispersion, though grid block and time step sizes were small enough (x_D=0.001, t_D=0.0001) that the levels of dispersion were relatively low (see Section 3.4 for a discussion of the interaction of dispersion, numerical and physical, with phase behavior). An indication of the effect of numerical dispersion on the computed solutions is given by Figs. 3.3-22 to 3.3-25 for uniform flow (k_1/k_2=1.0). Figs. 3.3-22 and 3.3-23 show the analytical solutions (Pande 1989) for injection of pure CO_2 at 1600 psia and 160°F into an oil containing 80% C_{10} and 20% C_4, a composition that lies within the region of tie-line extensions. Fig. 3.3-22 reports the MOC composition distribution and Fig. 3.3-23 shows the saturation distribution. Figs. 3.3-24 and 3.3-25 are the same profiles obtained by finite differences. The FD solution clearly reproduces the MOC solution, though some smearing of the shocks is evident.

The amount of smearing of a shock is related to the behavior of eigenvalues of the composition range in the neighborhood of the shock. Of the three shocks, the leading and trailing shocks are much less smeared than the intermediate self-sharpening wave. The leading shock is relatively sharp because wave velocities (eigenvalues) in the neighborhood of the shock vary strongly with saturation. Thus if numerical dispersion creates low gas saturations, they are quickly overrun by larger, faster saturations. The trailing shock is sharp because the C_{10} remaining at the trailing edge can move only by extraction into the moving vapor phase. The intermediate shock is smeared most because eigenvalues on the nontie-line path followed hardly vary with composition. Thus when dispersion smears the compositions (and saturations), they continue to travel at essentially the same velocity.

Immiscible Displacements

We illustrate the effect of crossflow in ternary displacements first with an immiscible displacement: injection of pure CO_2 into an oil with 80% C_{10} and 20% C_4, again at 1600 psia and 160°F. The displacement is "immiscible" in the sense that the oil lies in the region of tie-line extensions on a ternary diagram. Fig. 3.3-26 shows FD composition distributions, and Fig. 3.3-27 shows corresponding saturation profiles for k_1/k_2=3.0. Similar plots for k_1/k_2=1.5 and k_1/k_2=10.0 are given by Pande (1989). Fig. 3.3-28 shows the flow rate in layer 1, q_{1D}, which indicates the level of crossflow at various locations. The composition and saturation profiles show a complex set of shocks and self-sharpening waves discussed in detail by Pande (1989, Chapter 5). As in the binary displacement, fluid flows out of the high permeability layer at the leading shock, but flows into that layer upstream. Thus, crossflow delivers CO_2 to the low permeability layer at the leading edge of the transition zone, and moves oil out of the low permeability layer well behind the front. Hence crossflow causes some CO_2 to reach the low permeability before it would do so without crossflow, and some oil is moved into the faster flow of layer 1. Crossflow is strong enough in this case to cause a reduction in the CO_2 concentration and gas saturation in layer 1 as oil relatively rich in C_{10} but lean in C_4 is transferred into a layer with high CO_2 concentration.

Composition path behavior for the two layers is shown in Fig. 3.3-29, which are plotted in volume fractions. Corresponding points in Figs. 3.3-26 to 3.3-29 are marked as points A-I. In the fast layer (Fig. 3.3-29a), the composition route followed is very close to that of the uniform FD solution from A to D. From D to E, the effects of crossflow from layer 2 to layer 1

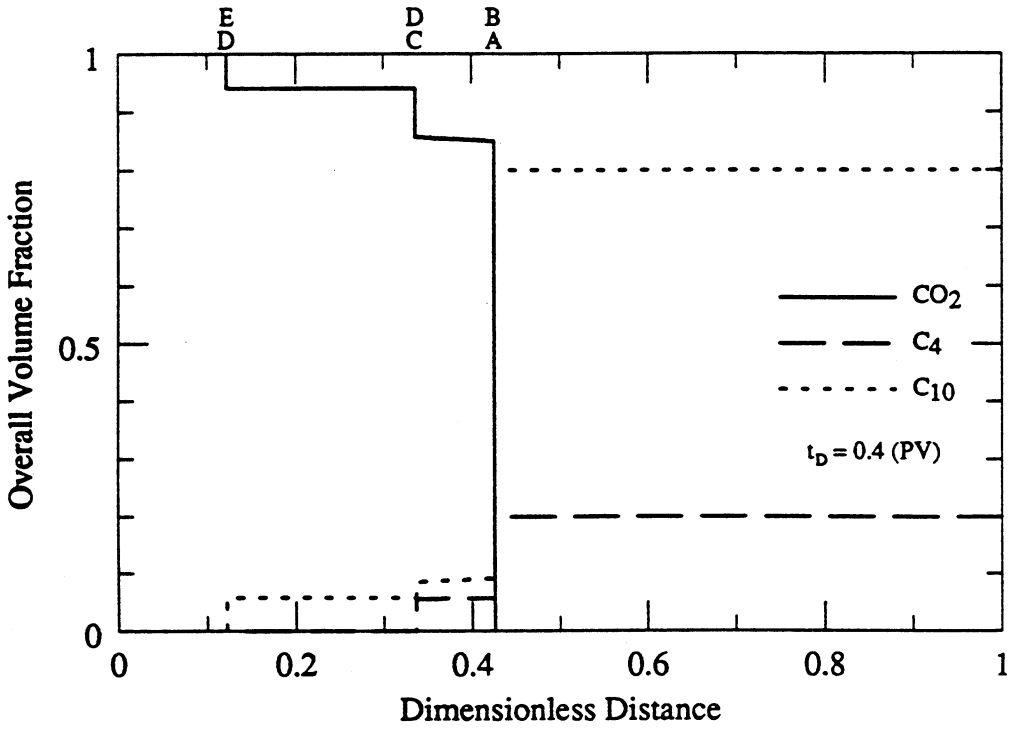

Fig. 3.3-22 MOC composition profiles for CO_2-C_4-C_{10} displacement in uniform flow system, with oil composition 80% C_{10} and 20% C_4.

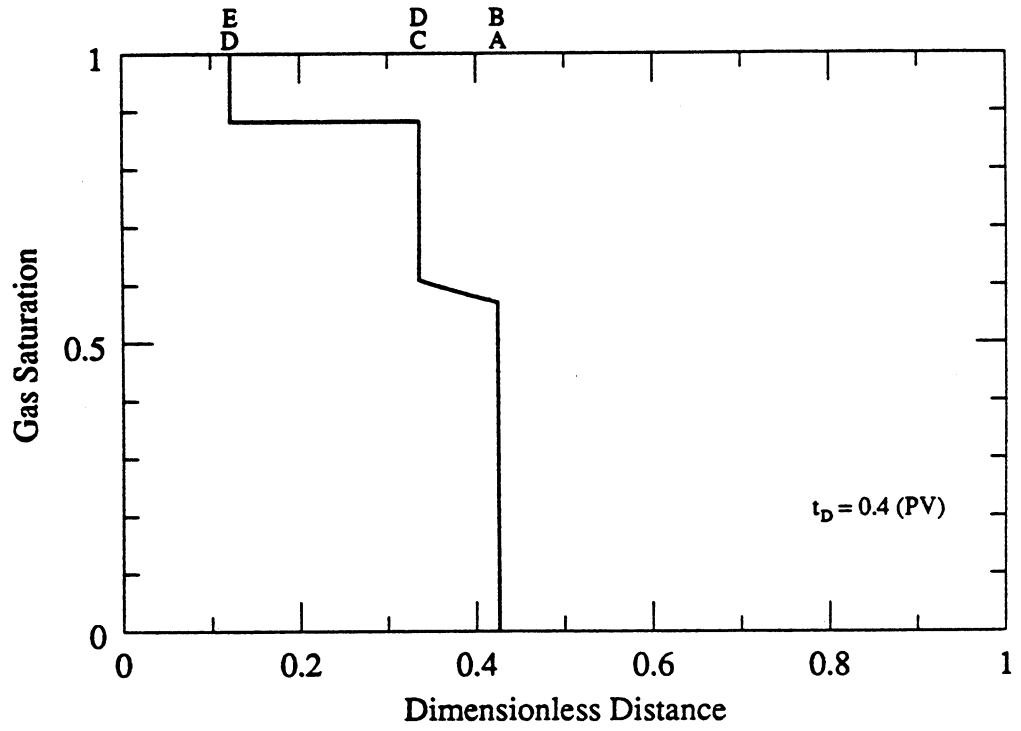

Fig. 3.3-23 MOC saturation profile for CO_2-C_4-C_{10} displacement in uniform flow system, with oil composition 80% C_{10} and 20% C_4.

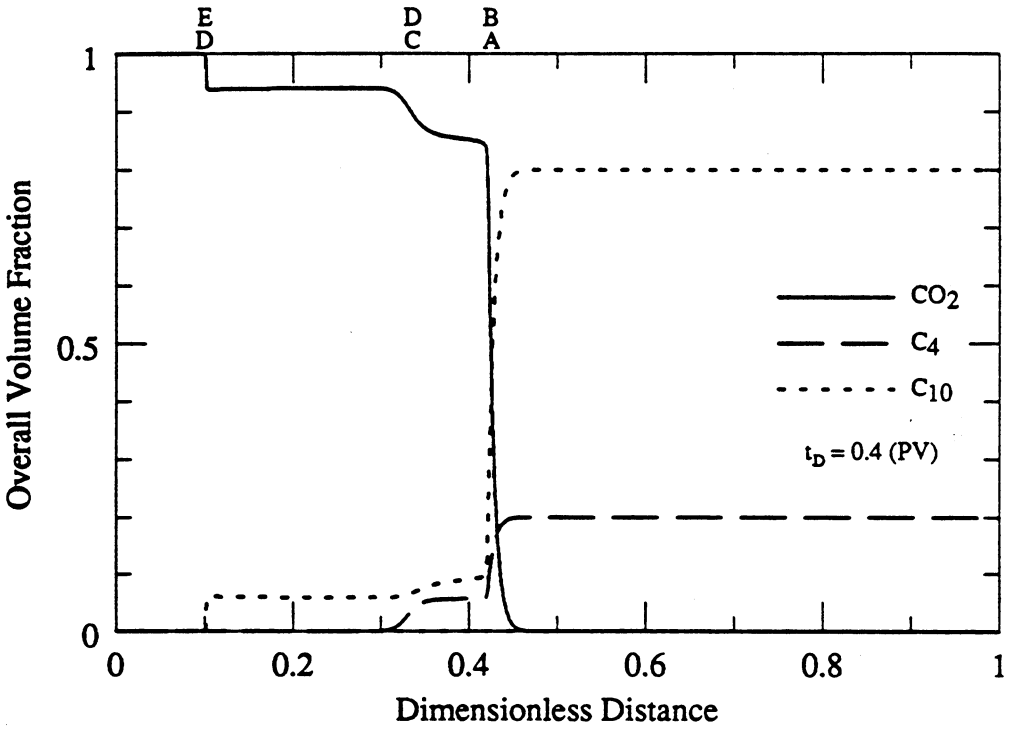

Fig. 3.3-24 FD composition profiles for CO_2-C_4-C_{10} displacement in uniform flow system, with oil composition 80% C_{10} and 20% C_4.

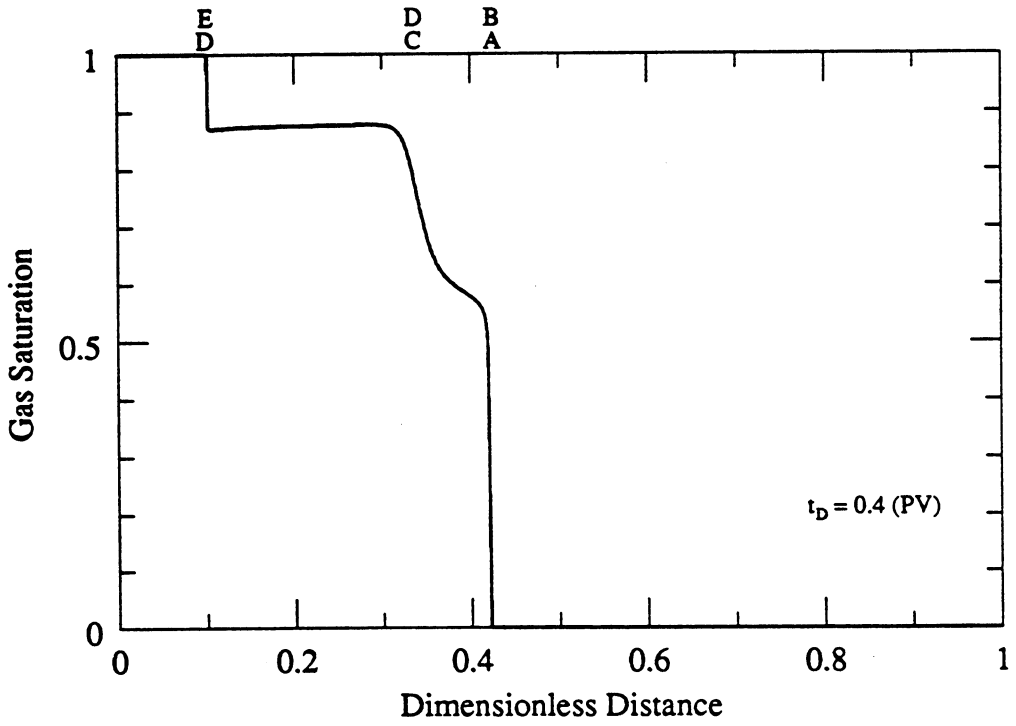

Fig. 3.3-25 FD saturation profile for CO_2-C_4-C_{10} displacement in uniform flow system, with oil composition 80% C_{10} and 20% C_4.

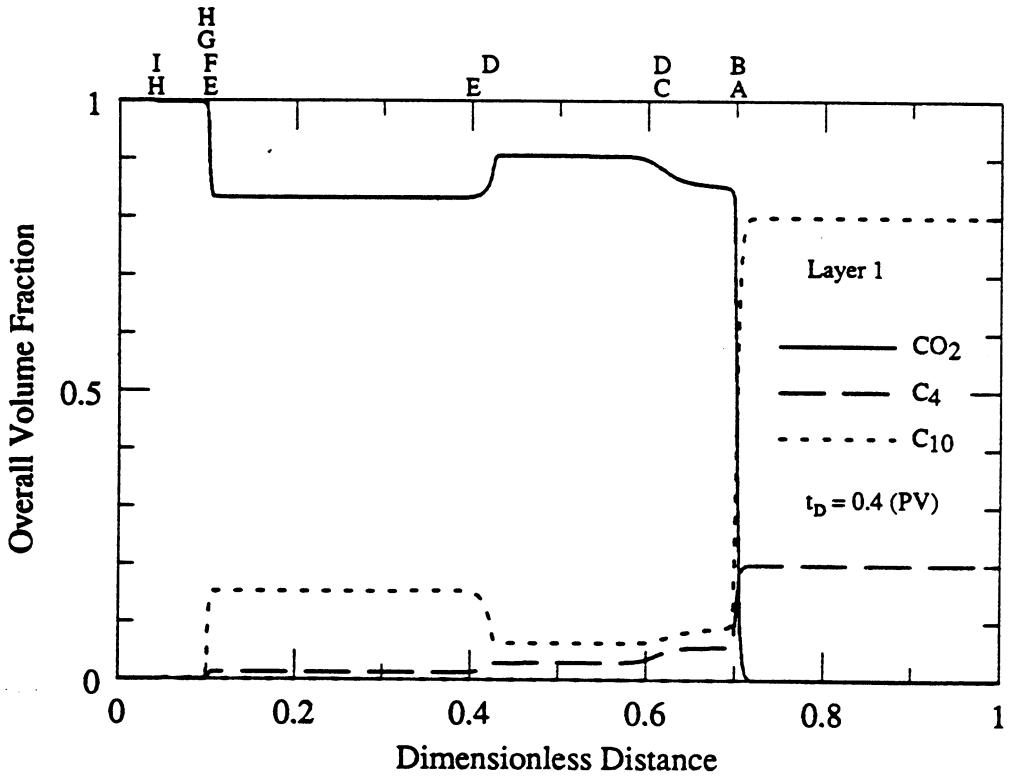

(A) Layer 1

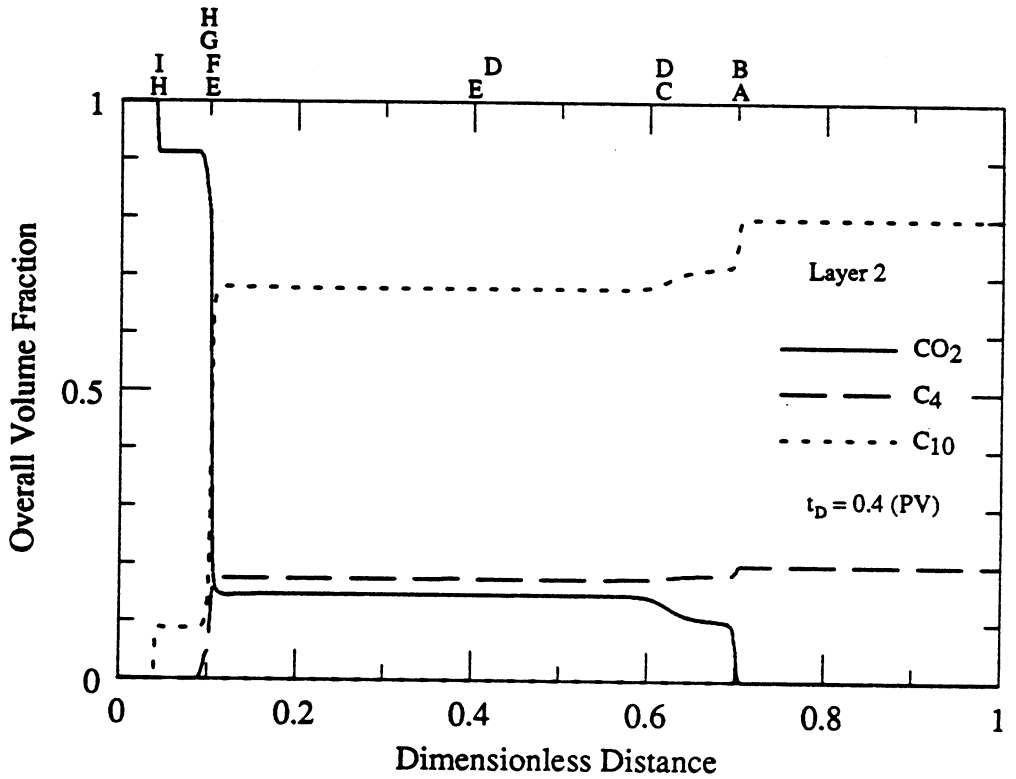

(B) Layer 2

Fig. 3.3-26 FD composition profiles for CO_2-C_4-C_{10} displacement with crossflow for k_1/k_2 = 3.0, with oil composition 80% C_{10} and 20% C_4: (A) Layer 1, (B) Layer 2.

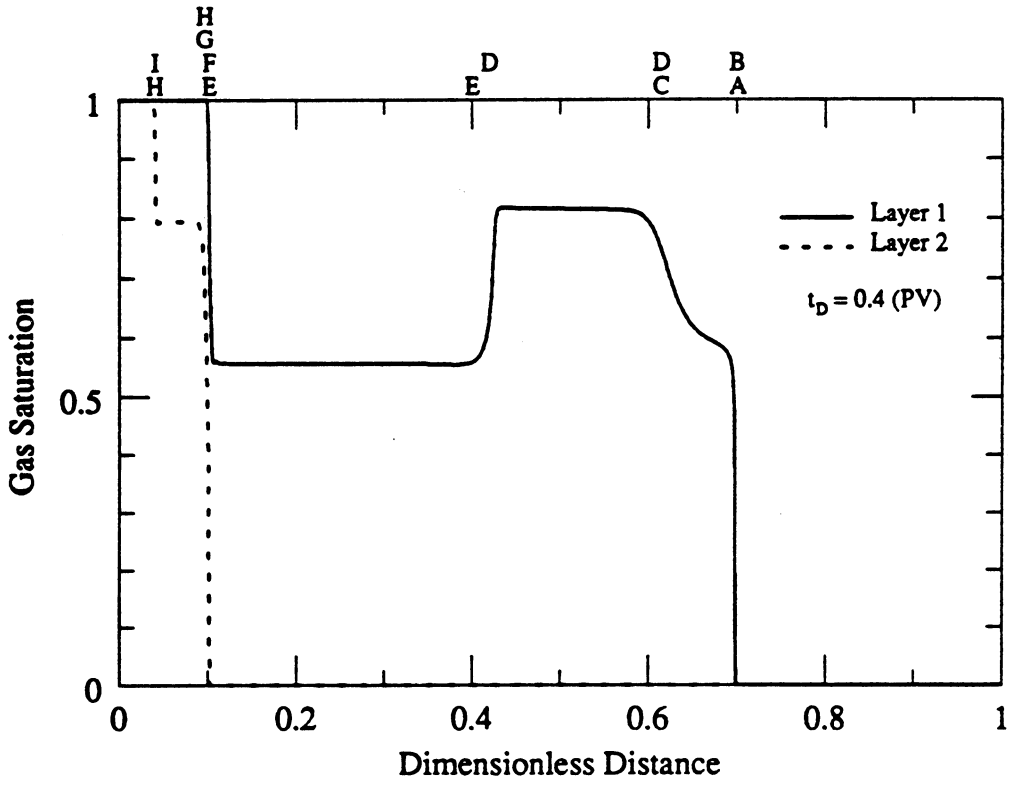

Fig. 3.3-27 FD saturation profiles for CO_2-C_4-C_{10} displacement with crossflow for k_1/k_2 = 3.0, with oil composition 80% C_{10} and 20% C_4.

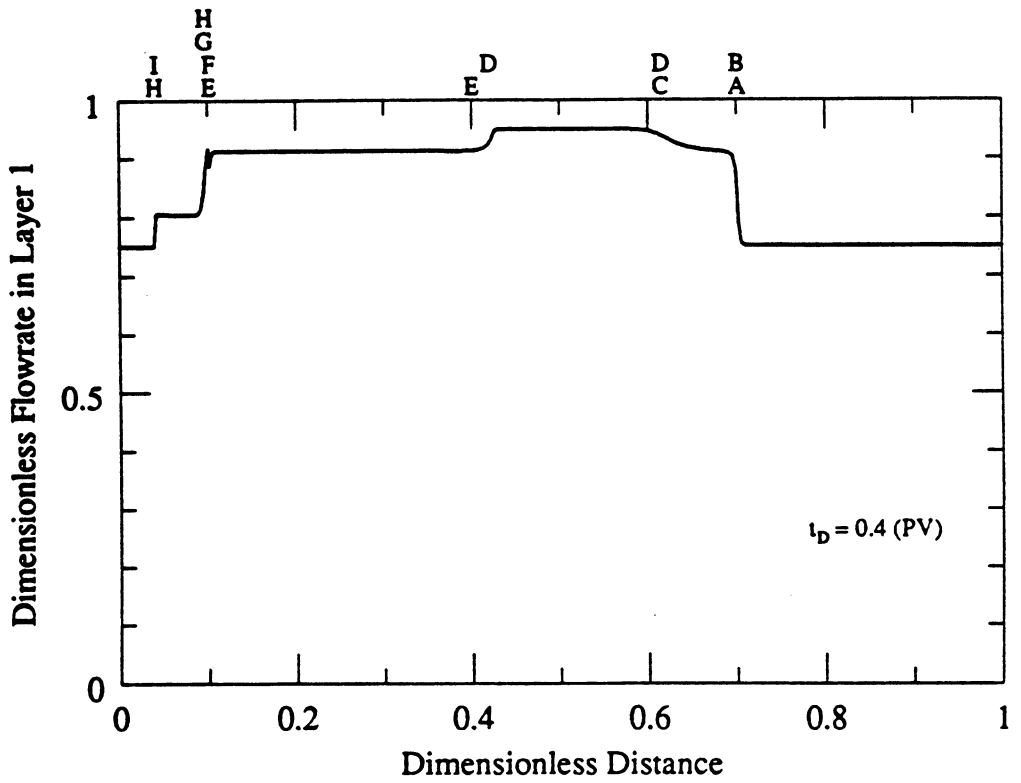

Fig. 3.3-28 FD flow rate profile for CO_2-C_4-C_{10} displacement with crossflow for k_1/k_2 = 3.0, with oil composition 80% C_{10} and 20% C_4.

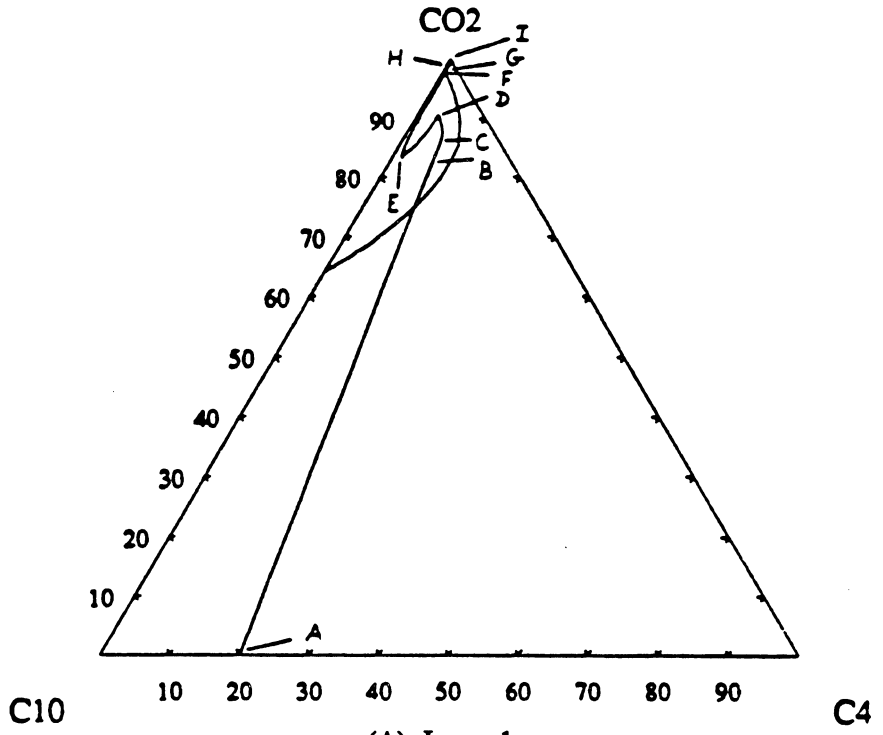

(A) Layer 1

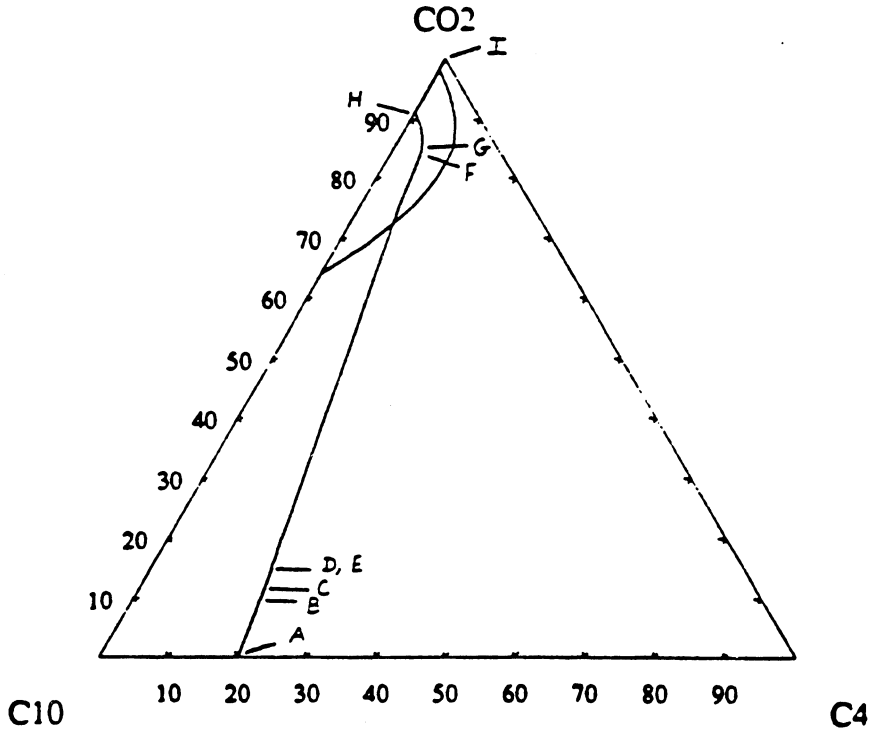

(B) Layer 2

Fig. 3.3-29 FD solution route for CO_2-C_4-C_{10} displacement with crossflow for $k_1/k_2 = 3.0$, with oil composition 80% C_{10} and 20% C_4: (A) Layer 1, (B) Layer 2.

are evident. In the low permeability layer (Fig. 3.3-29b), the composition rate followed lies deeper in the two-phase region than the uniform FD solution path throughout the displacement.

The effect of changes in the permeability ratio can be seen in Fig. 3.3-30, which shows the resulting variation in composition routes. As k_1/k_2 increases, the portion of the route from D to E in Fig. 3.3-29a is pushed toward $CO_2 - C_{10}$ axis. Evidently, the fluid that flows from layer 2 to layer 1 contains less C_4 when k_1/k_2 is large.

The effect of crossflow on oil recovery is shown in Fig. 3.3-31. Heterogeneity, as indicated by high permeability ratio, definitely reduces recovery at a given injection time. For the "immiscible" oil, however, crossflow damages recovery only for low permeability ratio and even then only very late in the life of the flood. In other words, the benefit of moving oil into the high velocity layer more than outweighs the negative effects of the resulting two-phase flow.

"Miscible" Displacements

If the C_4 concentration in the original oil is increased to 50%, the oil lies outside the region of tie-line extensions on a ternary diagram. Such an oil would be "miscible" in the multicontact sense, though numerical dispersion does cause formation of a very small amount of a second phase as the transition zone passes (Pande 1989). Again we illustrate the effects of crossflow for k_1/k_2=3.0. Fig. 3.3-32 shows FD composition profiles for the two layers, and Fig. 3.3-33 gives the corresponding saturation distribution, all for k_1/k_2=3.0. Fig. 3.3-34 shows flow rate behavior. Composition routes for the two layers are shown in Fig. 3.3-35.

As Fig. 3.3-33 indicates, the combination of heterogeneity and crossflow causes formation of a large saturation of second phase in the fast layer. Fig. 3.3-35 shows that compositions in both layers move well into the two-phase region, though the path for a uniform displacement would follow the dewpoint portion of the binodal curve. Thus, a displacement that would be "miscible" in uniform one-dimensional flow, no longer avoids the two-phase region when heterogeneity and crossflow are present.

The effect of variations in permeability ratio on composition routes for the "miscible" case is shown in Fig. 3.3-36. In this case, there is some permeability ratio that causes maximum penetration of the two-phase region in layer 1. When k_1/k_2=1.0, the route in layer 1 follows the binodal curve, as it does when k_1/k_2=10. When k_1/k_2=1.5 or 3.0, however, the route moves well inside the binodal curve. That result is reasonable because in the limit as k_1/k_2 increases to large values, the displacement in the fast layer will be finished before crossflow can affect the composition route appreciably.

Fig. 3.3-37 shows the effect of heterogeneity and crossflow for the "miscible" case. At low permeability ratio (k_1/k_2=1.5) crossflow reduces recovery slightly after 1 PV injected. For higher ratios, however, crossflow is beneficial, despite the fact that it causes two-phase flow.

Effect of Pressure on Displacement Performance

For a given oil composition, say 80% C_{10} and 20% C_4, an increase in displacement pressure improves recovery as the size of the region of tie-line extensions is reduced. Hence as the pressure increases the composition route passes closer and closer to the binodal curve until the pressure is high enough that the oil lies outside the region of tie-line extensions. Fig. 3.3-38 shows the effect of pressure increases on oil recovery at 1.0 PV injected for the 80% C_{10} - 20% C_4 oil. For all three permeability ratios examined, recovery increases with displacement pressure.

For uniform flow (k_1/k_2=1.0), the recovery at 1 PV exceeds 90% at 1600 psia. The effect of an increase in permeability contrast at a given pressure is to cause earlier breakthrough, reduced recovery at fixed injection, and slower recovery after breakthrough. Fig. 3.3-38 shows that it is possible to alleviate part of the negative effects of layering by an increase in

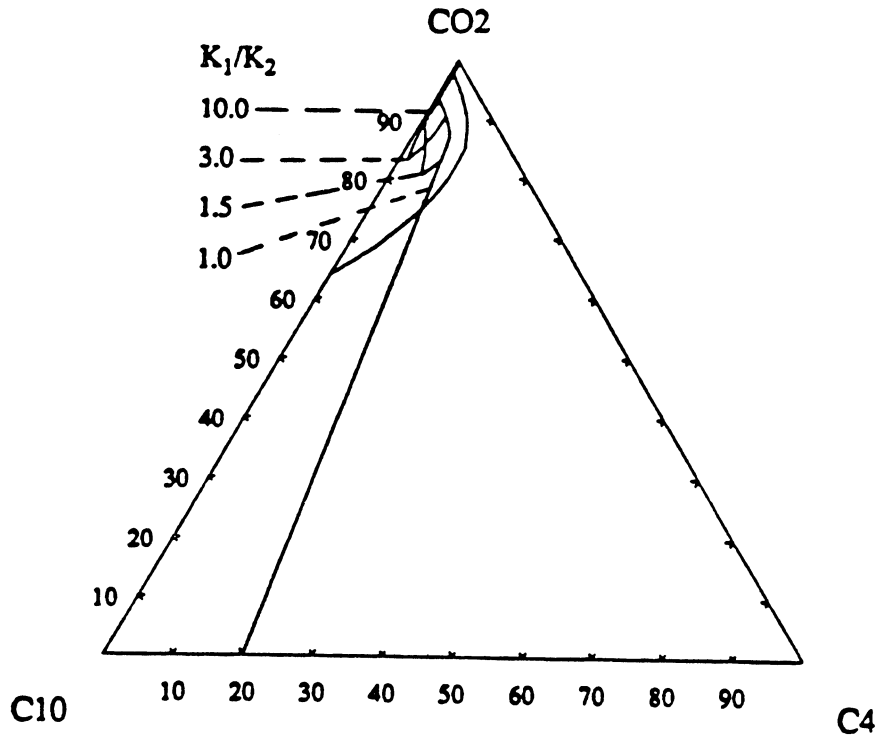

(A) Layer 1

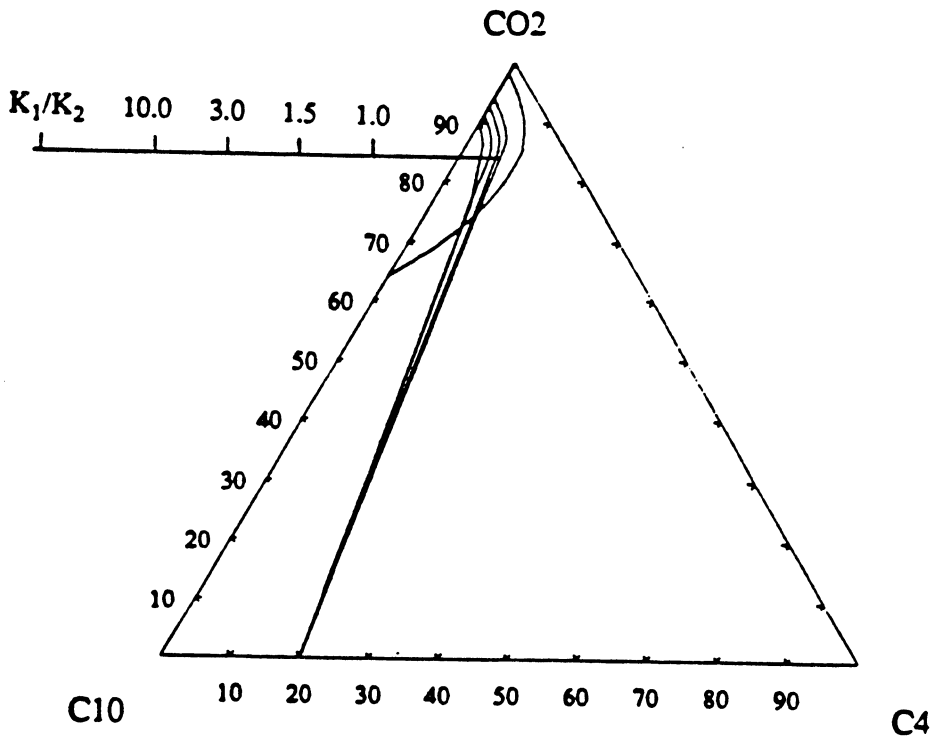

(B) Layer 2

Fig. 3.3-30 FD solution routes for CO_2-C_4-C_{10} displacement with crossflow for k_1/k_2 = 1.0, 1.5, 3.0, 10.0, with oil composition 80% C_{10} and 20% C_4: (A) Layer 1, (B) Layer 2.

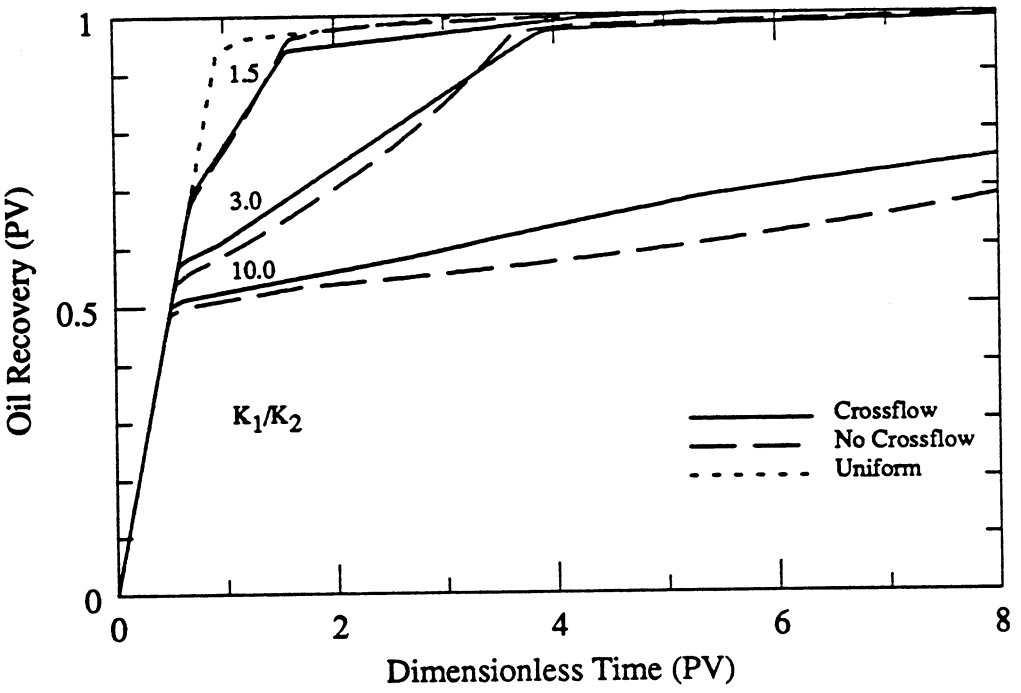

Fig. 3.3-31 Total oil recovery curves for CO_2-C_4-C_{10} displacement with and without crossflow for k_1/k_2 = 1.0, 1.5, 3.0, 10.0, with oil composition 80% C_{10} and 20% C_4.

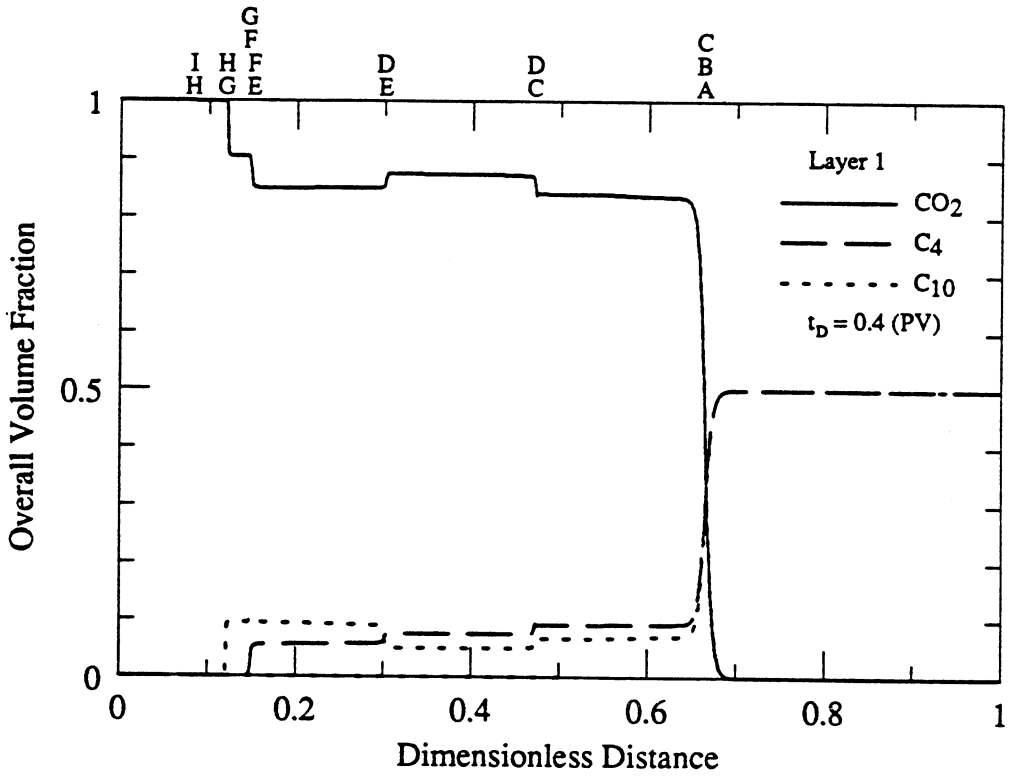

(A) Layer 1

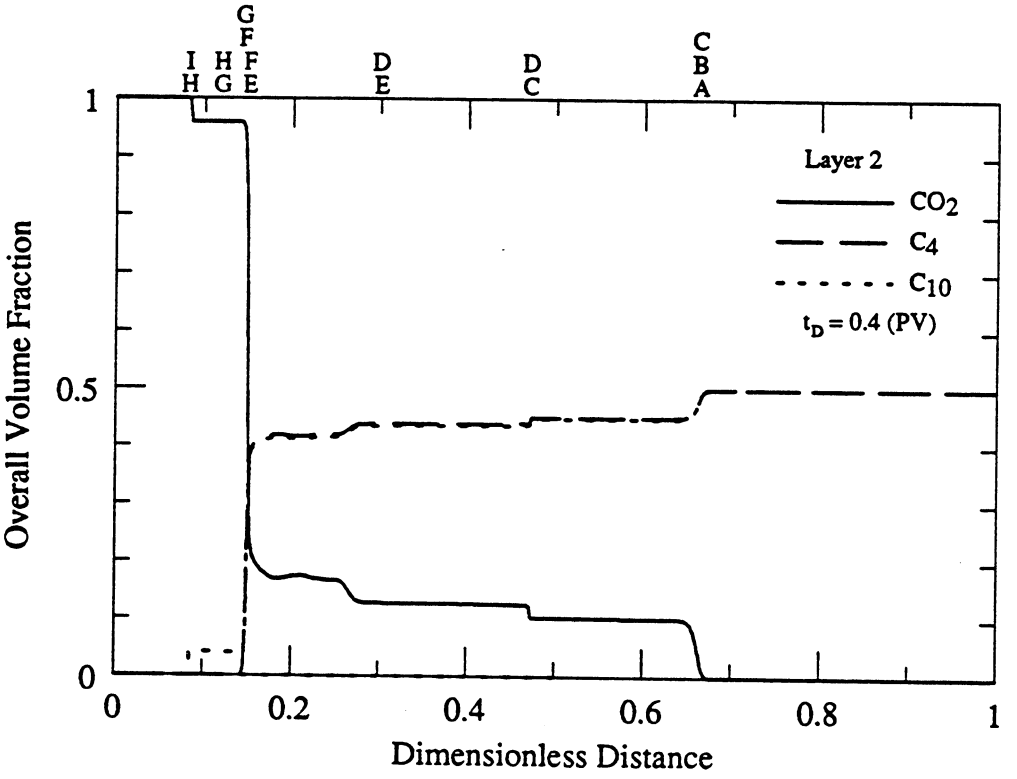

(B) Layer 2

Fig. 3.3-32 FD composition profiles for CO_2-C_4-C_{10} displacement with crossflow for k_1/k_2 = 3.0, with oil composition 50% C_{10} and 50% C_4: (A) Layer 1, (B) Layer 2.

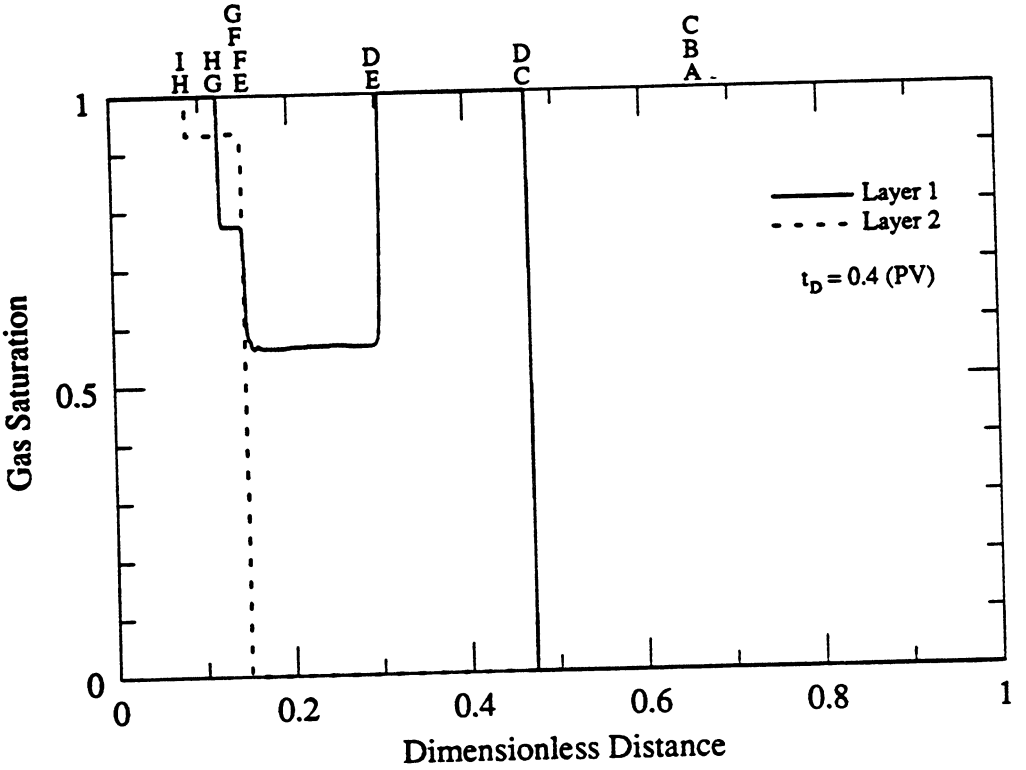

Fig. 3.3-33 FD saturation profiles for CO_2-C_4-C_{10} displacement with crossflow for k_1/k_2 = 3.0, with oil composition 50% C_{10} and 50% C_4.

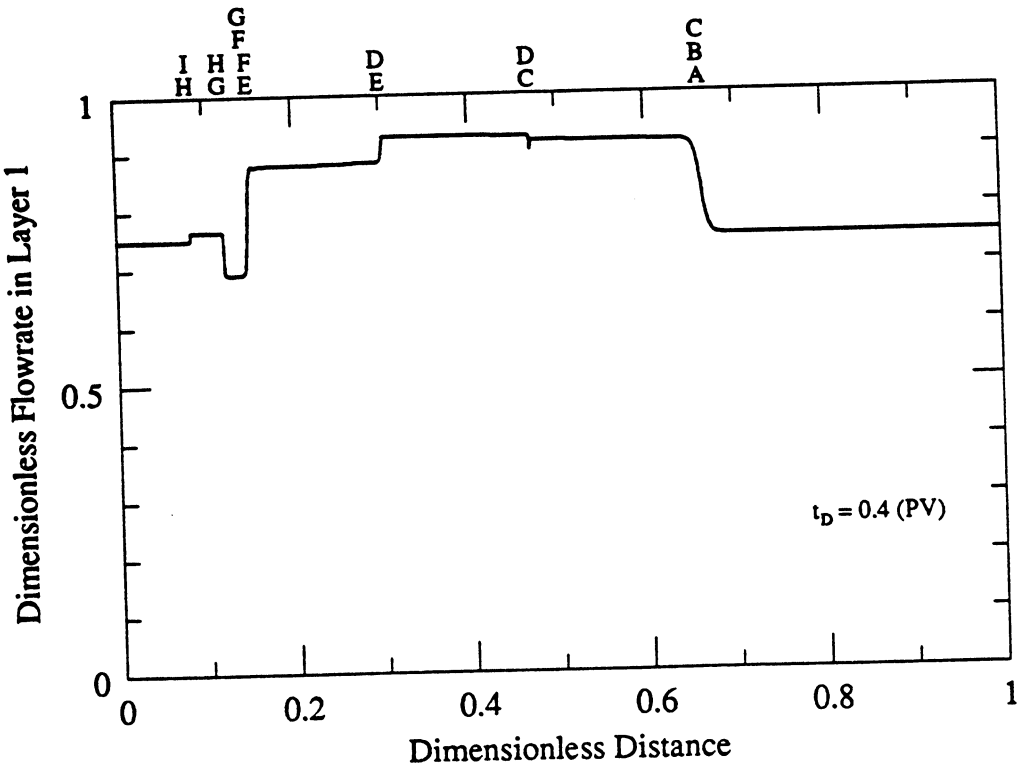

Fig. 3.3-34 FD flow rate profile for CO_2-C_4-C_{10} displacement with crossflow for k_1/k_2 = 3.0, with oil composition 50% C_{10} and 50% C_4.

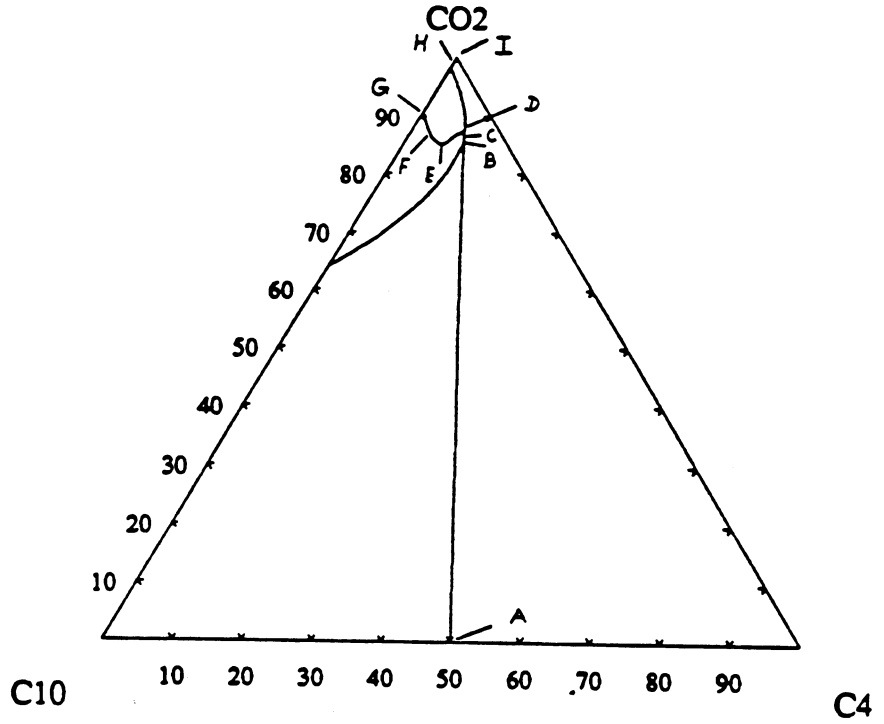

(A) Layer 1

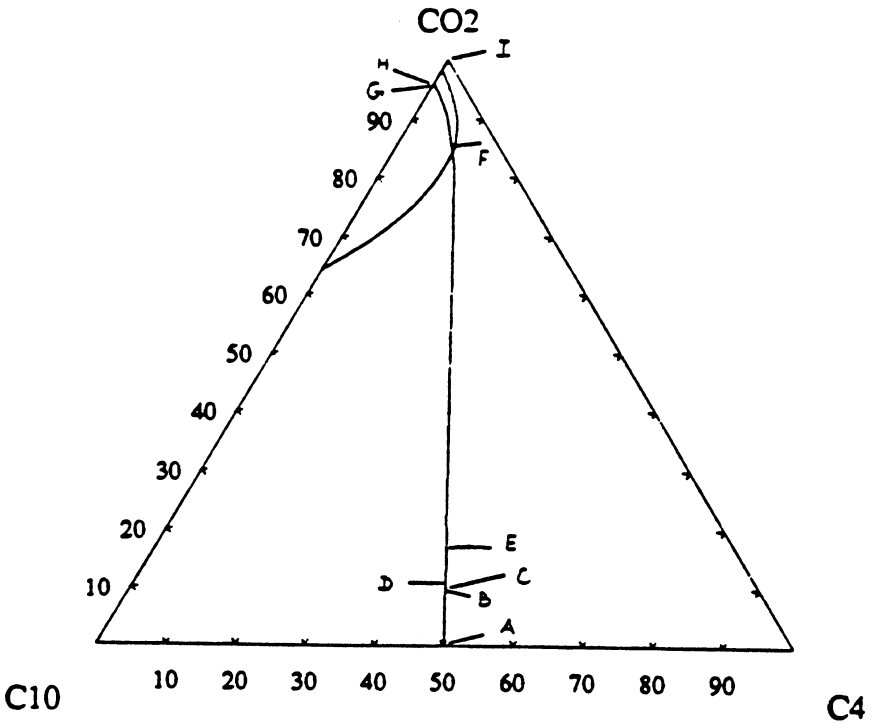

(B) Layer 2

Fig. 3.3-35 FD solution route for CO_2-C_4-C_{10} displacement with crossflow for k_1/k_2 = 3.0, with oil composition 50% C_{10} and 50% C_4: (A) Layer 1, (B) Layer 2.

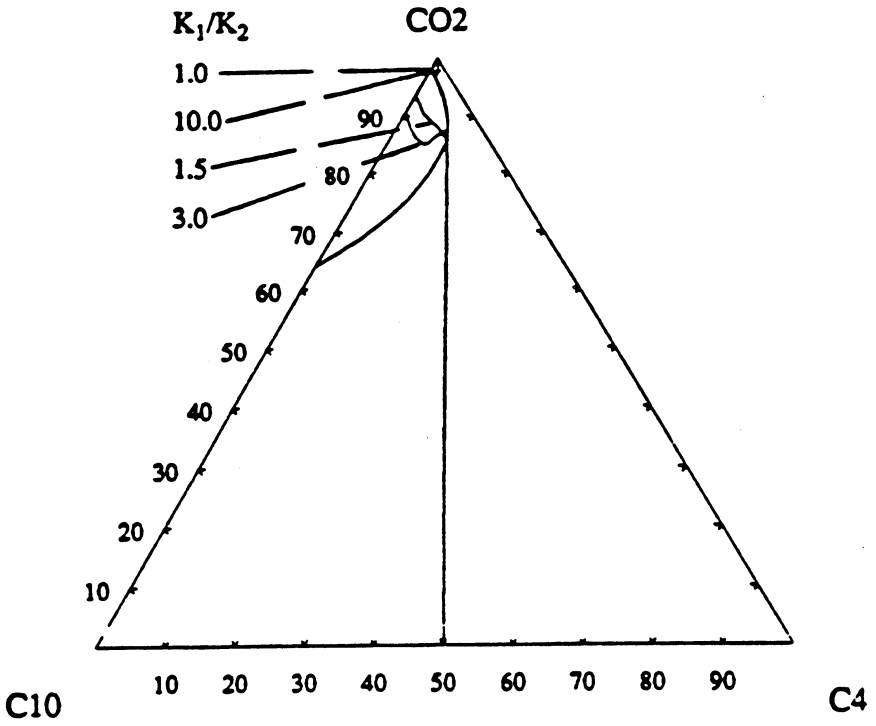

(A) Layer 1

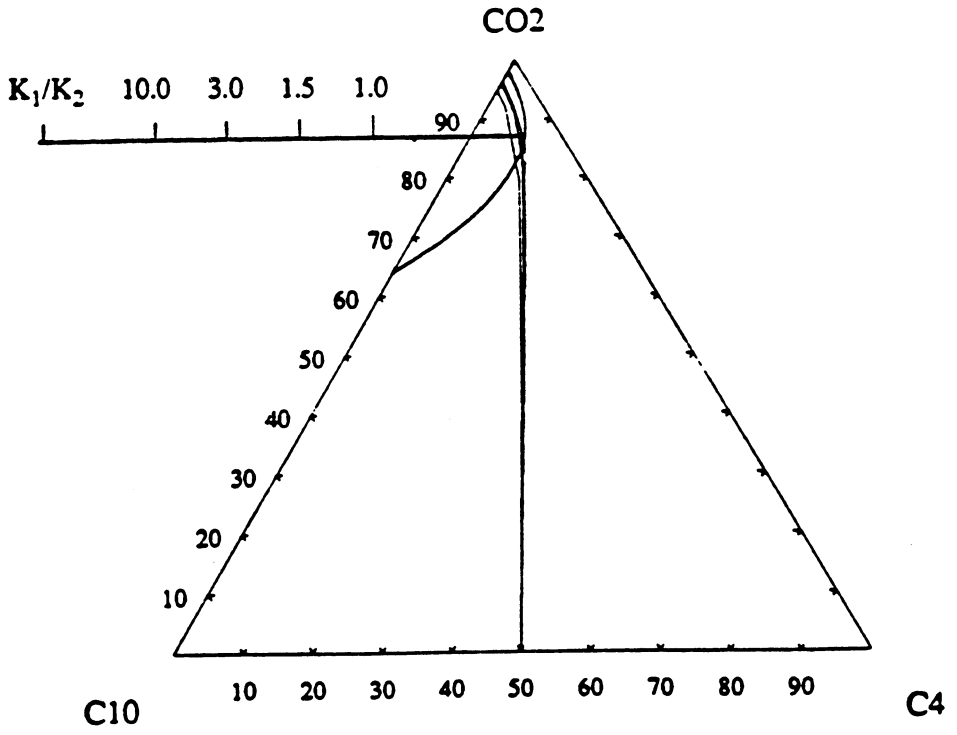

(B) Layer 2

Fig. 3.3-36 FD solution routes for CO_2-C_4-C_{10} displacement with crossflow for k_1/k_2 = 1.0, 1.5, 3.0, 10.0, with oil composition 50% C_{10} and 50% C_4: (A) Layer 1, (B) Layer 2.

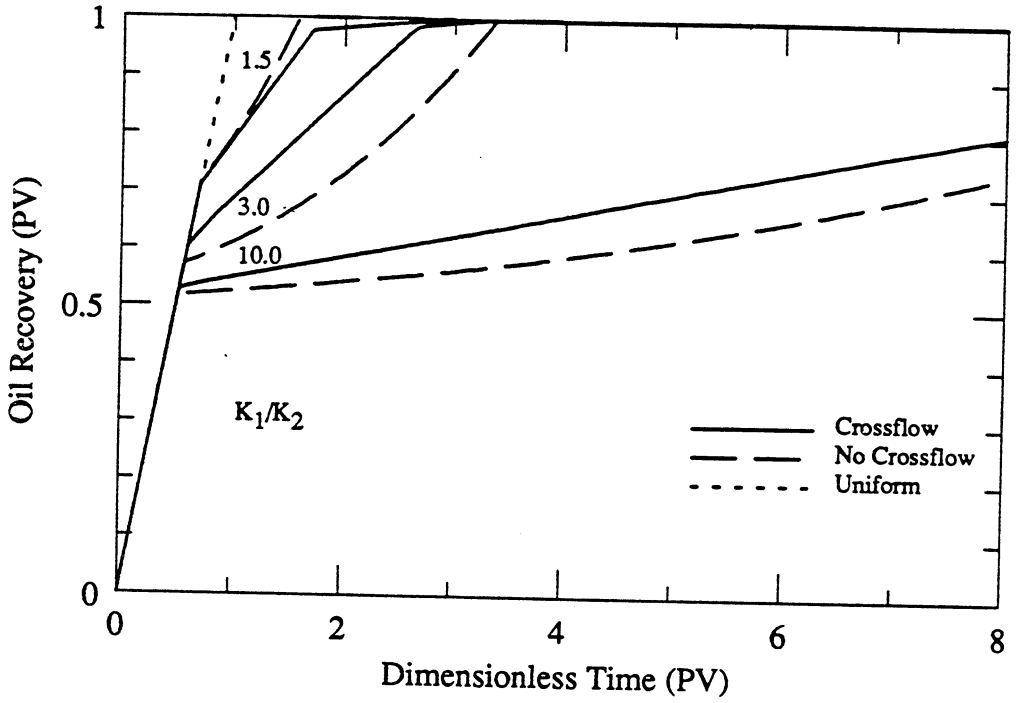

Fig. 3.3-37 Total oil recovery curves for CO_2-C_4-C_{10} displacement with and without crossflow for k_1/k_2 = 1.0, 1.5, 3.0, 10.0, with oil composition 50% C_{10} and 50% C_4.

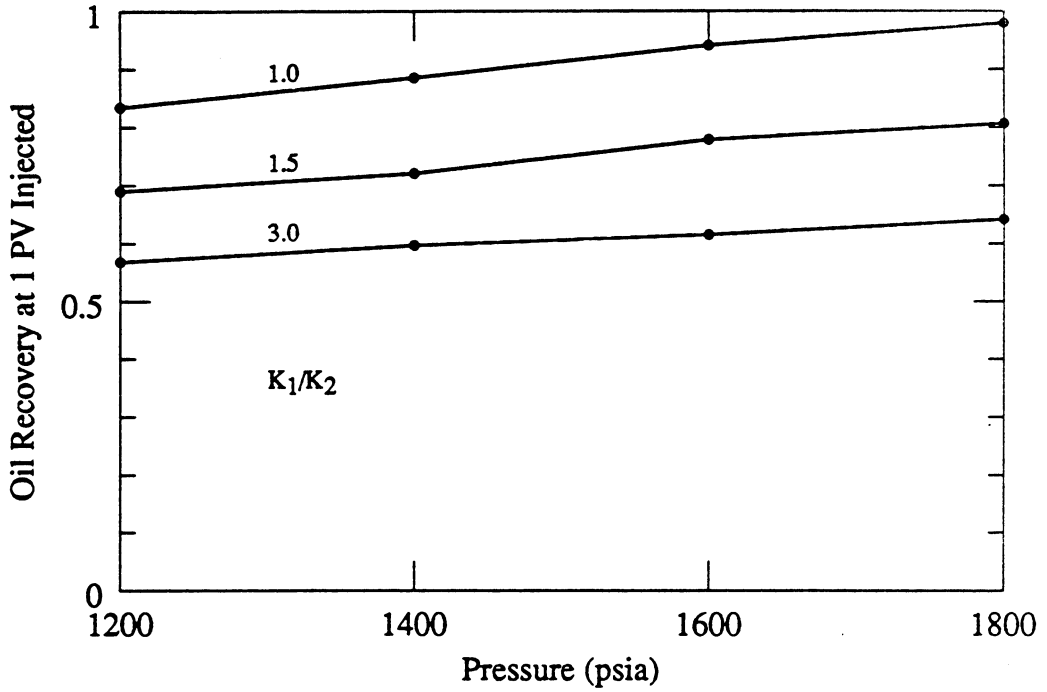

Fig. 3.3-38 Oil recovery at 1 PV injected as a function of pressure for CO_2-C_4-C_{10} displacements with crossflow for k_1/k_2 = 1.0, 1.5, 3.0, with oil composition 80% C_{10} and 20% C_4.

displacement pressure. Recovery increases slowly, however, so large pressure increases would be required to cause substantial improvement. In addition, there must be some limit to the amount of improvement. When the displacement is first-contact miscible, for example, further improvement will be limited to the beneficial effect of the slow increase in the viscosity of CO_2.

3.3.4 Summary and Conclusions

The MOC solutions and FD calculations presented in this section show that the interaction of phase behavior and multiphase flow is significantly more complex in heterogeneous systems than in one-dimensional flow, at least when viscous crossflow is present. In many reservoirs, viscous crossflow is likely to play a significant role, because flow lengths will be long compared to layer thicknesses, and hence values of R_L (Eq. 3.3-1) will be large. In addition, capillary crossflow will be present in many flows, as will gravity-induced vertical flow. Thus, interactions of variations in local flow velocity, crossflow, and phase behavior will affect displacement behavior. Furthermore, viscous fingering will induce variations in local flow velocity even if reservoir heterogeneity does not. Thus, understanding of the scaling of crossflow and its interactions is a key part of accurate performance predictions. The analysis of this section is a step toward that understanding.

The analytical and FD solutions presented lead to the following conclusions.

(1) Construction of MOC solutions for binary and ternary displacements in two-layer systems is made significantly more complex by the presence of more shocks than are present in uniform flow.

(2) A shock in one layer must be accompanied by a corresponding shock in the other layer.

(3) As the permeability ratio increases, injected fluid breakthrough occurs earlier, recovery rate decreases after breakthrough, and recovery at given injection decreases, whether or not crossflow is present.

(4) When the permeability ratio is low (~1.5), interactions of phase behavior and crossflow reduce recovery below that calculated for flow in noncommunicating layers. When permeability ratio is high (>3), however, crossflow improves recovery by moving oil from the slow moving layer to the high velocity flow.

(5) An increase in displacement pressure can partly compensate for the negative effects of heterogeneity, but the rate of improvement with increases in pressure is low.

3.4 Prediction of Miscible Flood Performance: The Effect of Dispersion on Composition Paths in Ternary Systems.

Barry W. Walsh

Finite difference compositional simulations of the performance of miscible flood processes inevitably include some contribution due to dispersion. Even if dispersion is represented explicitly and accurately in the finite difference form of the material balance equations, some numerical dispersion will also be present. The numerical dispersion results from truncation error in the finite difference form of the convection terms (Lantz, 1971). The level of dispersion present in a simulation can be important for processes like miscible floods, which rely on the interaction of phase behavior and multiphase flow to generate fluid compositions that avoid (or nearly avoid) the two-phase region. For example, several investigators have shown that for multicontact miscible floods, composition path, and hence displacement performance, is altered by dispersion (Gardner et al., 1981; Orr et al., 1981; Gardner and Ypma, 1984; Ypma, 1985).

As the use of compositional simulations for field-scale flows increases (Bette and Heinemann, 1986; Young, 1988), so grows the need for better quantitative assessment of the impact of dispersion, numerical or otherwise, on predicted process performance. In this paper, we report results of an investigation of the interaction of dispersion with phase behavior for multicontact miscible ternary systems, and we show that the effect of dispersion on process performance depends strongly on the size and shape of the two-phase region. For some systems, therefore, process performance will be much more sensitive to the level of dispersion than for others.

3.4.1 Model Formulation

Differential Equation, Boundary and Initial Conditions

In the following discussion, we consider an explicit finite difference representation of a material balance on the i^{th} component.

$$\frac{\partial}{\partial \tau} \sum_{j=1}^{n_p} x_{ij}\, \rho_j\, S_j + \frac{\partial}{\partial \xi} \sum_{j=1}^{n_p} x_{ij}\, \rho_j\, f_j = 0 \qquad i = 1, n_c \tag{3.4-1}$$

where x_{ij} is the mole fraction of component i in phase j, n_c and n_p are the numbers of components and phases, and ρ_j, S_j, and f_j are the molar density, saturation and fractional flow of the j^{th} phase. The fractional flow is given by:

$$f_j = \frac{k_{rj} / \mu_j}{\sum_{j=1}^{n_p} (k_{rj} / \mu_j)} \tag{3.4-2}$$

where k_{ij} and μ_j are the relative permeability and viscosity of phase j.

The dimensionless time scale is given in pore volumes by

$$\tau = \int_0^t \frac{q\, dt}{\phi\, AL}$$

and the dimensionless length is scaled by the system length

$$\xi = z / L$$

where q is the injection volumetric flow rate, ϕ the porosity, A the flow area, L the flow length, z the length coordinate along the flow direction, and t is time. Eq. (3.4-1) is derived based on the assumptions that (a) the flow is one dimensional, (b) effects of capillary pressure can be neglected, (c) component transport occurs only by convection in flow phases, and (d) phases present at any location are in chemical equilibrium.

For all the calculations described here, pure component 1 (CO_2) was injected continuously,

$$x_{11} = S_1 = f = 1.0 \qquad \xi = 0,\ \tau > 0 \tag{3.4-3}$$

and the flow system contains a uniform distribution of mixture of components 2 and 3.

$$S_2 = 1.0$$

$$x_{22} = x_2^0 \qquad \tau = 0, \ 0 \le \xi \le 1.0 \tag{3.4-4}$$

$$x_{23} = 1 - x_2^0$$

For most of the calculations described below, the initial oil composition was 20 mol % C_2-C_6 ($x_{22} = 0.2$).

If the partial molar volume of each component is always the same in each phase (no volume change on mixing), then volume is also conserved, and hence Eq. (3.4-1) can be written (Orr, 1980)

$$\frac{\partial}{\partial \tau} \sum_{j=1}^{n_p} c_{ij} S_j + \frac{\partial}{\partial \xi} \sum_{j=1}^{n_p} c_{ij} f_j = 0 \qquad i = 1, n_c \tag{3.4-5}$$

where c_{ij} is the volume fraction of component i in phase j.

$$c_{ij} = \frac{x_{ij}\rho_j}{\rho_i}$$

where ρ_i is the (constant) molar density of component i. For the analysis of composition paths, it is convenient to define an overall volume fraction, C_i, and an overall fractional flow, F_i, for each component

$$C_i = \sum_{j=1}^{n_p} c_{ij} S_j \tag{3.4-6}$$

$$F_i = \sum_{j=1}^{n_p} c_{ij} f_j$$

Substitution of those definitions into Eq. (3.4-5) yields

$$\frac{\partial C_i}{\partial \tau} + \frac{\partial F_i}{\partial \xi} = 0 \qquad i = 1, n_c \tag{3.4-7}$$

Eq. (3.4-6) can be solved easily by a forward time, backward space finite difference representation of the derivatives (Pope and Nelson, 1978; Orr, 1980).

$$C_{i,k}^{n+1} = C_{i,k}^{n} + \alpha \left[F_{i,k-1}^{n} - F_{i,k}^{n} \right] \qquad i = 1, n_c \tag{3.4-8}$$

where $\alpha = \Delta\tau/\Delta\xi$.

In effect, this finite difference form represents the flow system as a sequence of mixing cells, with the flow rates of phases in and out of each cell determined by phase fractional flows. As Aris and Amundson (1957) showed, the transition zone that develops in a sequence of mixing cells approaches that obtained as a solution to the convection-dispersion equation as the number of cells increases. Thus, it is not surprising that this finite difference formulation exhibits numerical dispersion. It does so because injected fluid that flows into a mixing cell is available to flow out of the cell in the next time step, because fluid within the cell is treated as well mixed. Thus, some fraction of the injected fluid can leave the cell earlier than it would if it traversed the cell length at the prevailing fluid flow velocity.

An alternate analysis of numerical dispersion was given by Lantz (1971). He showed that truncation error in the finite difference representation of the convective term of the single-phase version of Eq. (3.4-7) produces a second-order error term that mimics the contribution of physical dispersion in the convection-dispersion equation. For single-phase flow, the level of numerical dispersion is given by

$$\left[N_{Pe}^{num}\right]^{-1} = \frac{\Delta\xi}{2}\left[1 - \alpha\right] \tag{3.4-9}$$

where N_{Pe}^{num} is the numerical Peclet number (ul/D^{num}), u is the flow velocity ($q/\phi A$), and D^{num} is the numerical dispersion coefficient. When two-phase flow occurs, the level of numerical dispersion is no longer constant. Instead, it is given by

$$\left[N_{Pe}^{num}\right]^{-1} = \frac{\Delta\xi}{2}\,\frac{df}{ds}\left[1 - \alpha\,\frac{df}{ds}\right] \tag{3.4-10}$$

Thus, in two-phase flow, the nonlinearity of the fractional flow relationship also influences the level of dispersion. For the displacements considered below, however, two-phase flow occurs in only a relatively small fraction of the flow length. Hence, in the discussion that follows, we use Eq. (3.4-9) to provide a reasonable, though not exact, indication of the level of numerical dispersion (Orr, 1980).

Representation of Phase Behavior

In typical compositional simulations, an equation of state would be used to calculate phase behavior. For this investigation, however, we choose to use ternary diagrams defined directly, so that the diagram themselves can be varied easily. In the examples presented below, we consider only systems of three components or pseudocomponents: solvent (CO_2, C_1, or N_2), light hydrocarbons (say C_2-C_6), and heavy hydrocarbons (say C_{7+}). The use of ternary systems permits straightforward graphical presentation of calculated composition paths, and also allows comparison with analytical solutions to the dispersion-free flow equations obtained by the method of characteristics (MOC) (Helfferich, 1981). The analyses developed here could be applied to systems containing more components, but the graphical representation of calculated paths would be more difficult to interpret, and the analytical solutions would be more difficult to obtain (Monroe et al., 1987).

Fig. 3.4.1 is a pseudoternary diagram typical of conditions appropriate to a CO_2-enhanced oil recovery process. In Fig. 3.4.1, about one-third of the composition space is in the two-phase region (i.e., from about 40% to 99.5% CO_2 and 0 to 35% C_2-C_6). Within the two-phase envelope (or binodal curve), the fluid splits into two phases whose compositions are determined by tie lines. At the plait point or critical point of the system, the compositions of the two phases become identical, and the "critical tie line" is the tangent to the binodal curve at that point.

In this section we consider the interaction between phase behavior, as represented by the shape of the binodal curve and the slopes of tie lines, and dispersion in a one-dimensional vaporizing gas-drive process. In the development of the argument, we compare composition paths calculated for various cases. In order to keep some uniformity in these comparisons, the ternary-phase diagrams for all cases were constructed using the following rules:

(1) The size and shape of the two-phase regions are determined by the phase compositions of the solvent-C_{7+} "binary" pair, and the plait-point composition. Normally we have used a solubility of 0.5% C_{7+} in solvent as the upper binary composition (99.5% CO_2).

(2) The system does not exhibit a three-phase region.

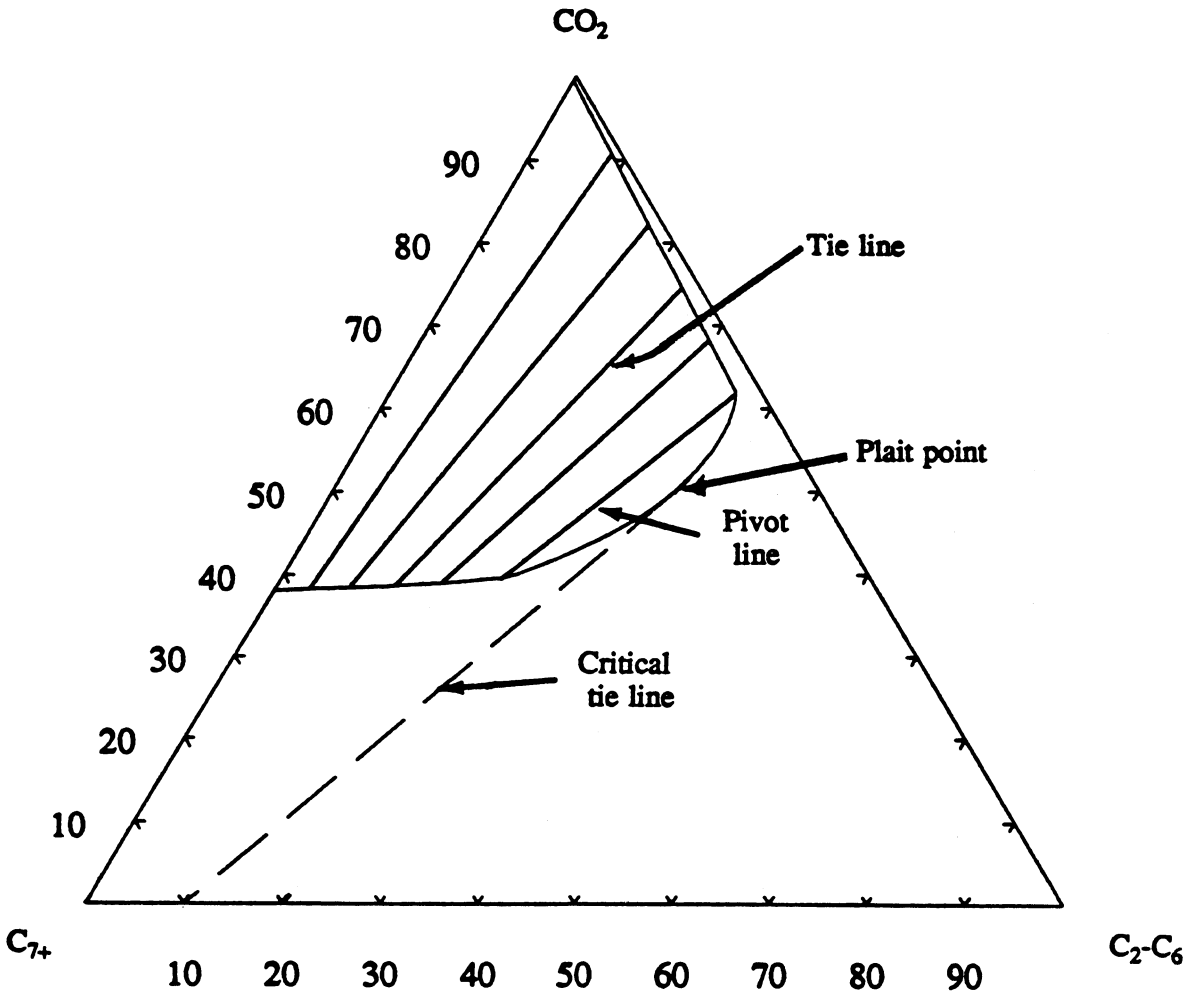

Fig. 3.4-1 Typical phase diagram used in composition path calculations.

(3) Tie lines in most of the two-phase region are fan-like from a common apex on the zero-C_2-C_6 axis. In the phase diagram of Fig. 3.4-2 and in all the diagrams that follow it, only one tie line is shown, which we will call the pivot line. The remaining tie lines are constructed in the following manner: tie lines to the left of the pivot line have a common point at the intersection of the zero-C_2-C_6 axis and the pivot line; tie lines to the right of the pivot line have a common point at the intersection of the pivot line and the tangent to the binodal curve at the plait point.

(4) The tangent at the plait point passes through 0.1 C_2-C_6 on the zero-solvent axis.

Construction of Composition Paths

If an oil is displaced by CO_2 in a slim tube in which there is no dispersion and in which local phase equilibrium always exists, the composition path can be calculated using the method of characteristics (Helfferich, 1981). In such a (nearly) one-dimensional displacement process the dependent variables can be represented as either a profile or a history. In Helfferich's definition of those terms, a graph showing a dependent variable as a function of distance at fixed time is called a profile, and a graph showing a dependent variable as a function of time at fixed location is called a history. In this paper we discuss the composition history at the exit of a slim tube. In Helfferich's terms, this can be represented as a "composition route" (though we will refer to it as a "path") on a pseudoternary diagram. In the examples that follow, we trace the path from the initial oil composition to the (final) solvent composition.

If the system can be adequately represented on a pseudoternary phase diagram, then Helfferich's analysis indicates that there are two classes of paths, examples of which are illustrated in Fig. 3.4-2.

(1) When the oil composition lies in the region of tie-line extensions, the path enters the two-phase region via a leading shock along a tie-line extension. It then follows a path within the two-phase region until that path intersects the tie line whose extension contains the injected fluid composition. The path there switches to the "injection" tie line and leaves the two-phase region by a trailing shock.

(2) When the oil composition lies outside the region of tie-line extensions (in our case, to the right of the critical tie line), the path stays in the single-phase region, curving around the dewpoint arm of the binodal curve. This single-phase displacement is an example of developed miscibility.

Fig. 3.4-2 shows examples of both of these paths. In addition, Fig. 3.4-2 shows the path calculated for the developed miscibility case when the finite difference simulator is used for the calculation.

3.4.2 Simulation of One-Dimensional Displacements

For the simulations described here, phase equilibrium information was stored as binodal curve coordinates with tie-line slopes specified by the appropriate tie-line intersection points. Effects of volume change on mixing were ignored. Comparisons of solutions with and without volume change (Helfferich, 1981; Monroe et al., 1987; Pande 1989) indicates that volume change affects composition paths only slightly, though local flow velocity is more strongly influenced. Because composition path is the focus of this discussion, therefore, the complications of volume change on mixing were not included in the simulations.

In most of the cases reported, the simulator solved Eq. (3.4-7) using the finite difference form given in Eq. (3.4-8). Thus, in those simulations, only numerical dispersion was present. In some cases described in the next section, however, a direct representation of a physical dispersion was included (see Appendix 3.4-A) in the finite difference formulation. In all the cases considered, the initial fluid composition was outside the region of tie-line extensions, and hence developed miscibility would be observed in the absence of dispersion.

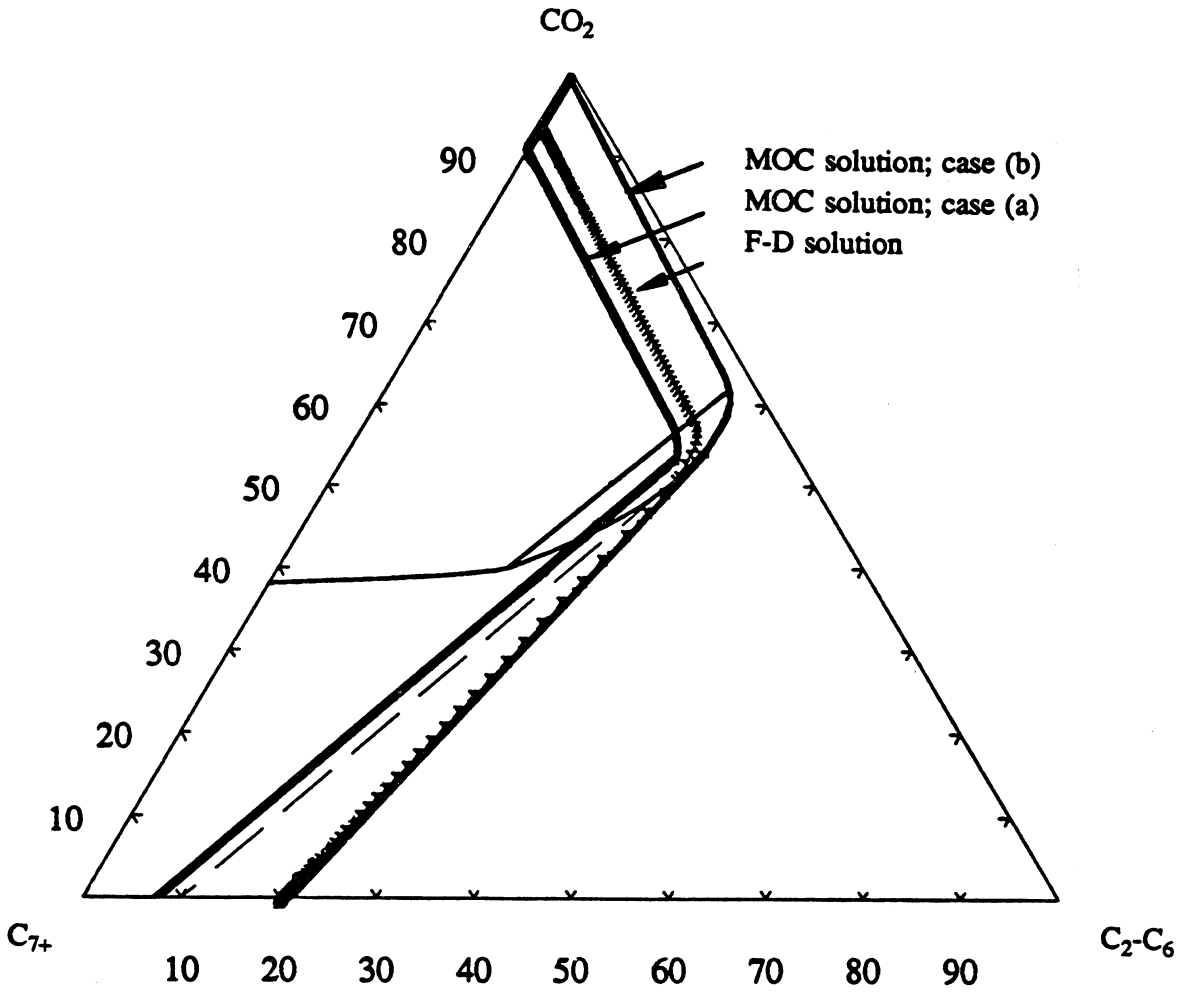

Fig. 3.4-2 Composition paths calculated by method of characteristics and by finite-difference methods.

Typical input data for the simulations are summarized in Table 3.4-1. A simple linear relationship was used for liquid phase relative permeability

$$k_{rL} = 0.65S \tag{3.4-11}$$

$$S = \frac{S_L - S_{Lr}}{1 - S_{Lr} - S_{Gr}}$$

For the gas phase, the relative permeability was taken to be

$$k_{rG} = (1-S)^{1.2} \tag{3.4-12}$$

Mixture viscosities were calculated from phase compositions by a quarter-power blending rule (Orr, 1980), and mixture densities were calculated based on the assumption of no volume change on mixing. For all of the calculations described below, α, the ratio of dimensionless time-step size to dimensionless grid-block size, was held fixed at 0.25.

Fig. 3.4-3 shows composition paths calculated for the exit fluid when the flow is modeled with 20, 100 or 200 grid blocks. The initial oil contained 20 mol % C_2-C_6 and 80 mol % C_{7+}, and the injected fluid was pure CO_2. If there was no numerical dispersion present, the composition path would follow the dewpoint portion of the binodal curve. Clearly, the finite difference simulation does not exactly reproduce the dispersionless path calculated by the method of characteristics, but increasing the number of grid blocks causes the simulated path to approach the analytical solution.

Representation of Physical Dispersion by Numerical Dispersion

The change in composition path with the change in the number of grid blocks can be viewed two ways. Because there is no length scale implied in the dimensionless form of the material balance equations, Fig. 3.4-3 can be taken to represent:

(1) composition paths at locations corresponding to 10%, 50% and 100% of the tube length, or

(2) the composition path at the end of the tube, where the full tube length has been represented by 20, 100 or 200 grid blocks.

on the vaporizing gas-drive enrichment process (though since there is no length scale in the equations, the length corresponding to a single grid block could be of the order of mm, cm, or m). It is important to recognize that the length dependence is the direct result of numerical dispersion. If dispersion were absent, there would be no length dependence at all, and each grid block would show exactly the same composition path. The relationship between implied length and number of grid blocks can be seen from a rearrangement of Eq. (3.4-9),

$$L = \frac{D^{num}}{bu\Delta\xi} = \frac{a}{b\Delta\xi} = \frac{a}{b} N \tag{3.4-13}$$

where a is the numerical dispersivity, D^{num}/u, and

$$b = 1/2\left[1 - \alpha\right] \tag{3.4-14}$$

According to Eq. (3.4-14) with fixed dispersivity, a, the flow length grows in proportion to the number of grid blocks, N. Thus, it is the dispersivity that sets the length scale for the problem.

Table 3.4-1

Data Used in Simulations

Residual Saturations:	$S_{Lr} = 0.2$	$S_{Gr} = S_{Gc} = 0.1$	
Relative Permeabilities:	$S = (S_L - S_{Lr}) / (1 - S_{Lr} - S_{Gr})$		
	$k_{rL} = 0.65S$	$k_{rG} = (1-S)^{1.2}$	
Fluid Properties:	CO_2	$C_2 - C_6$	$C_7 +$
Viscosity (cp)	0.021	0.89	19.0
Density (g/cm^3)	0.23	0.70	0.98
Mole Weight	44	119	322
Mixtures:	Viscosities by quarter power mixing rule. Densities assuming zero volume change.		
Time Step:	$\alpha = \Delta\tau / \Delta\xi = 0.25$		

Table 3.4-2

Comparison of F-D and MOC Solutions
for Parallel Binodal Curve

Viscosity Ratio	S_L at Switch* (MOC Solution)	S_L for Parallel Path Section (F-D Solution)
1.0	0.738	0.72 - 0.73
10.0	0.424	0.42 - 0.43

* The composition path switches from a tie-line path to a cross patch at S_L such that the two eigenvalues of Eq. (3.4-17) are equal.

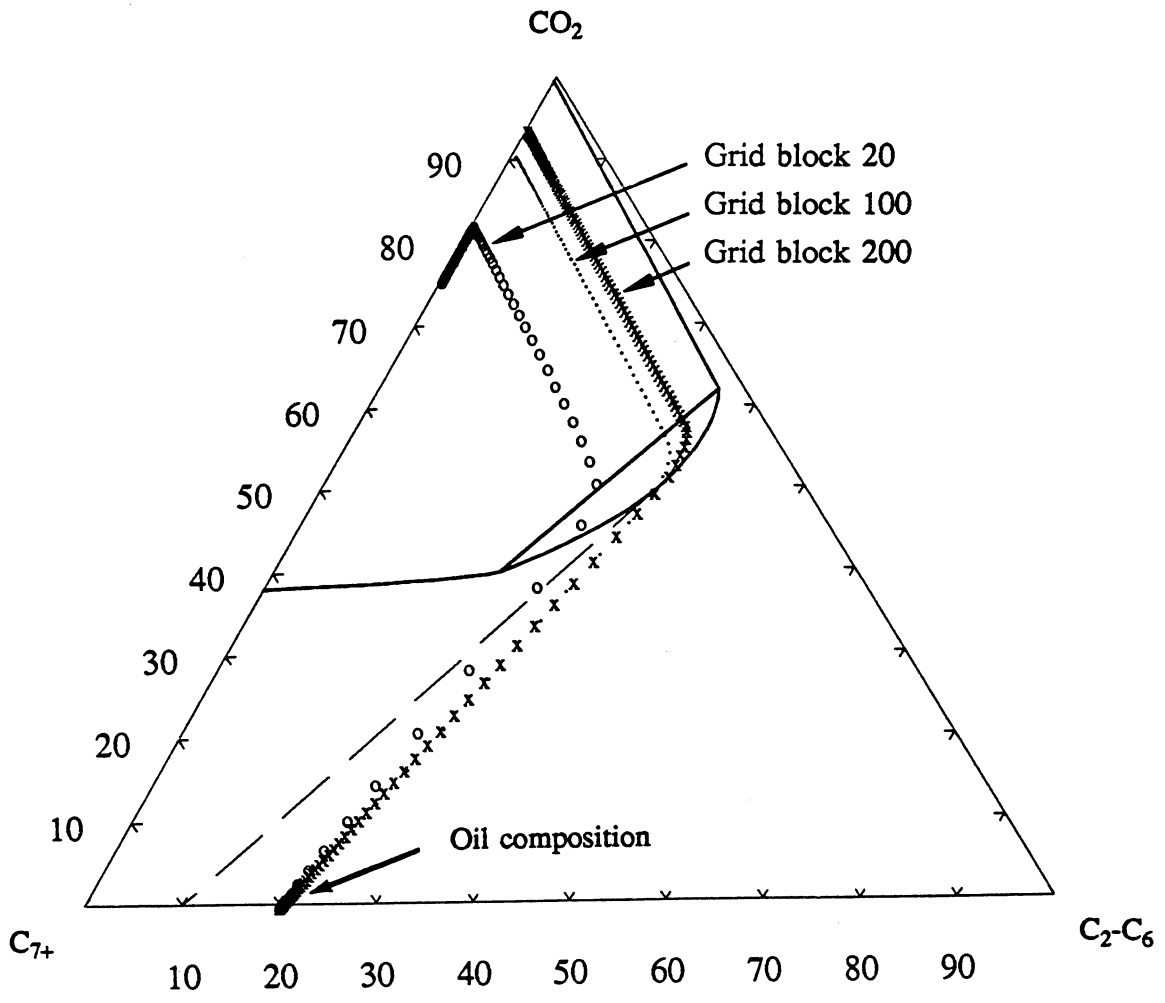

Fig. 3.4-3 Composition paths calculated by an explicit finite-difference simulation using 20, 100, and 200 grid blocks.

When considered in the second way, Fig. 3.4-3 illustrates the improved recovery of heavy hydrocarbons associated with either an increased number of equilibrium mass transfer stages or a lower level of dispersion. In this case, rearrangement of Eq. (3.4-9) with u and L held constant gives

$$D^{num} = buL\Delta\xi = \frac{buL}{N} \tag{3.4-15}$$

Thus, in this view, the dispersion coefficient is inversely proportional to the number of grid blocks.

The composition paths in Fig. 3.4-3 give an indication of recovery efficiency in the one-dimensional displacements. As the composition path approaches the binodal curve, recovery of the original oil approaches 100%. Fig. 3.4-4 confirms that point for displacements identical to those of Fig. 3.4-3, but with N = 50, 200 and 1000. Eq. (3.4-9) indicates that the corresponding numerical Peclet numbers are 135, 533 and 2667.

Given the dependence of the level of numerical dispersion on the nonlinearity of the fractional flow curves (Eq. 3.4-10), it is clear that use of numerical dispersion to mimic the effects of physical dispersion can only be approximate. For example, Ypma (1985) reported on a comparison made for simulations of nitrogen displacement of a light oil, using truncation error to represent dispersion in the first set of runs, and then including a finite difference representation of dispersion in the simulator and repeating the runs with very low levels of numerical dispersion. He observed that when actual physical dispersion was included, the simulator predicted higher recoveries. Fig. 3.4-5 is replotted from Ypma's paper. It indicates differences in calculated recoveries of about 5% at a dispersion number of 0.01. (Ypma uses "dispersion number," $N_D = D/uL = (N_{Pe})^{-1}$ instead of the inverse Peclet number.) That value corresponds to 40 grid blocks and $\alpha = 0.2$, if based on numerical dispersion only.

For the mildly nonlinear relative permeability curves used here, the difference between simulations with and without physical dispersion represented in the finite difference formulation was much smaller. Fig. 3.4-6 recasts results from Fig. 3.4-4, and from other simulations, in the form used by Ypma, and also presents results of simulations in which physical dispersion was included in the model. Minor (of the order of 1%) differences between the two cases were observed, but the differences did not widen as dispersion number increased, as Ypma had observed.

We therefore constructed a phase diagram which was similar in its general features to the one used by Ypma (Fig. 3.4-7) and repeated the comparison at total dispersion numbers of 0.0023 and 0.023. Our recoveries were higher than those reported by Ypma, but once again we obtained differences of only 1-1.5% between the cases at both levels of dispersion. Thus, for the comparisons presented here the inclusion of explicit physical dispersion terms in the finite difference simulator does not add substantially to the accuracy of the solution. This conclusion was confirmed also in simulations reported in the next section (Figs. 3.4-10 and 3.4-11). The use of numerical dispersion is attractive, of course, because the simulations run faster than those in which very small blocks are used so that numerical dispersion is kept at very low levels. In any case, Ypma's results in Fig. 3.4-5 suggest that for Peclet numbers greater than 1000, the difference will be very small.

Effect of Phase Diagrams on Composition Paths

We observed when describing the features of Fig. 3.4-3 that the location of the composition path is an indicator of the degree of dispersion that is being simulated. Figs. 3.4-8 and 3.4-9 show the extent to which composition paths are modified by changing either the composition of the oil being displaced or the size of the two-phase region. For example, comparison of Figs. 3.4-3 and 3.4-8 shows the effect of increasing the initial C_2-C_6 fraction to 40 mol % from 20 mol %. At the higher C_2-C_6 fraction, the composition paths lie closer to

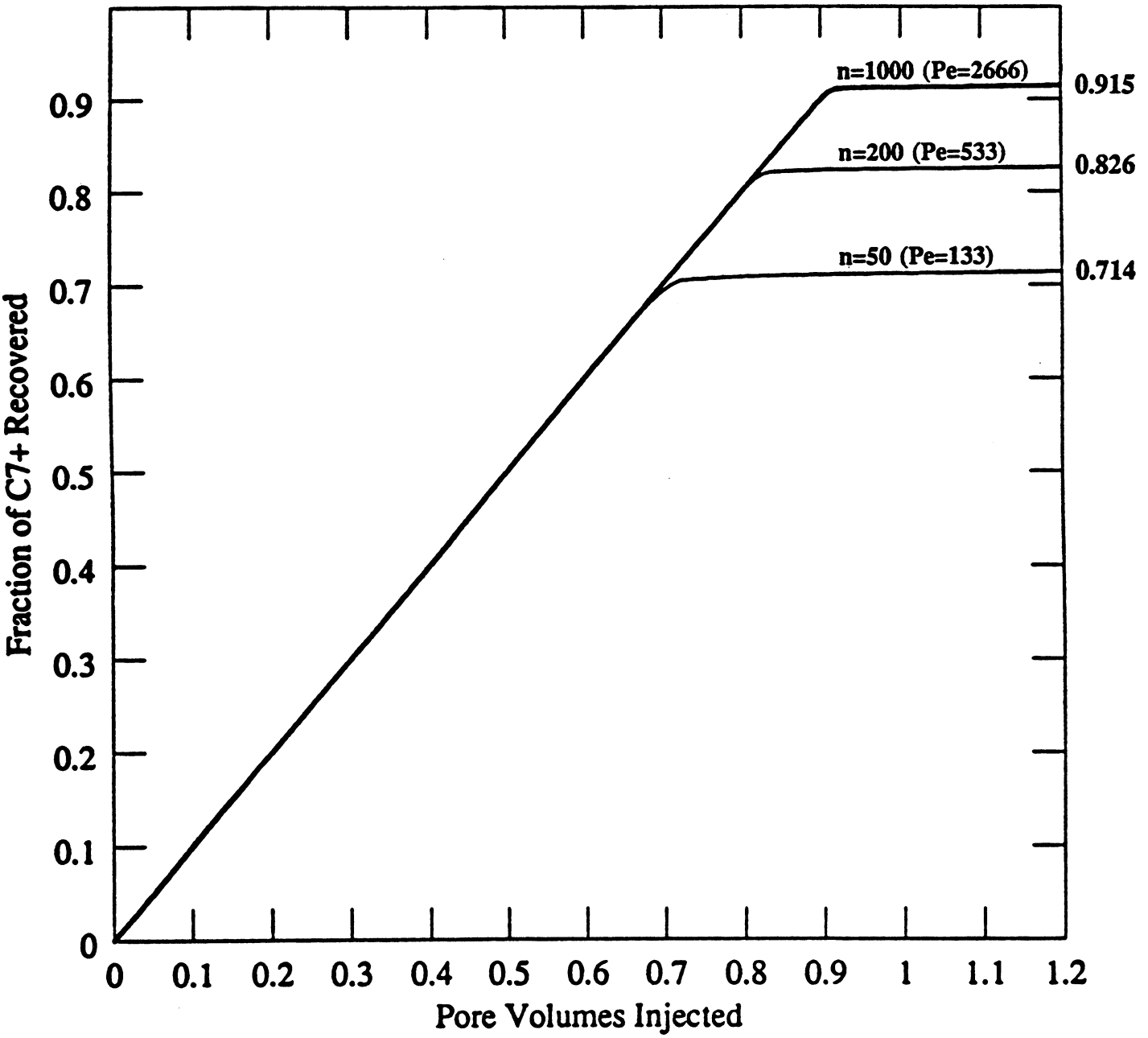

Fig. 3.4-4 Recovery of heavy hydrocarbons in displacements with varying levels of numerical dispersion.

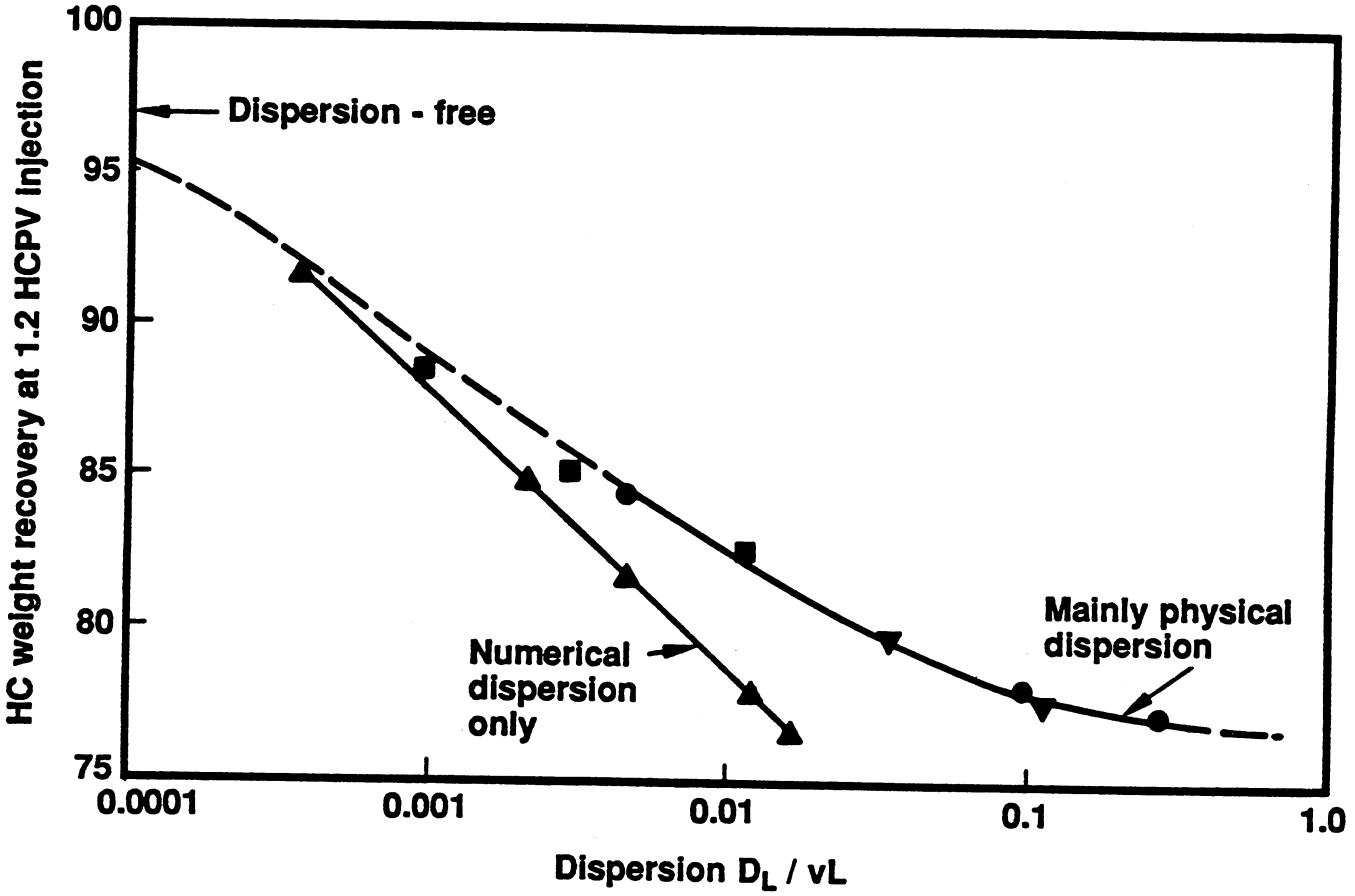

Fig. 3.4-5 Dependence of recovery on longitudinal dispersion level (after Ypma 1985).

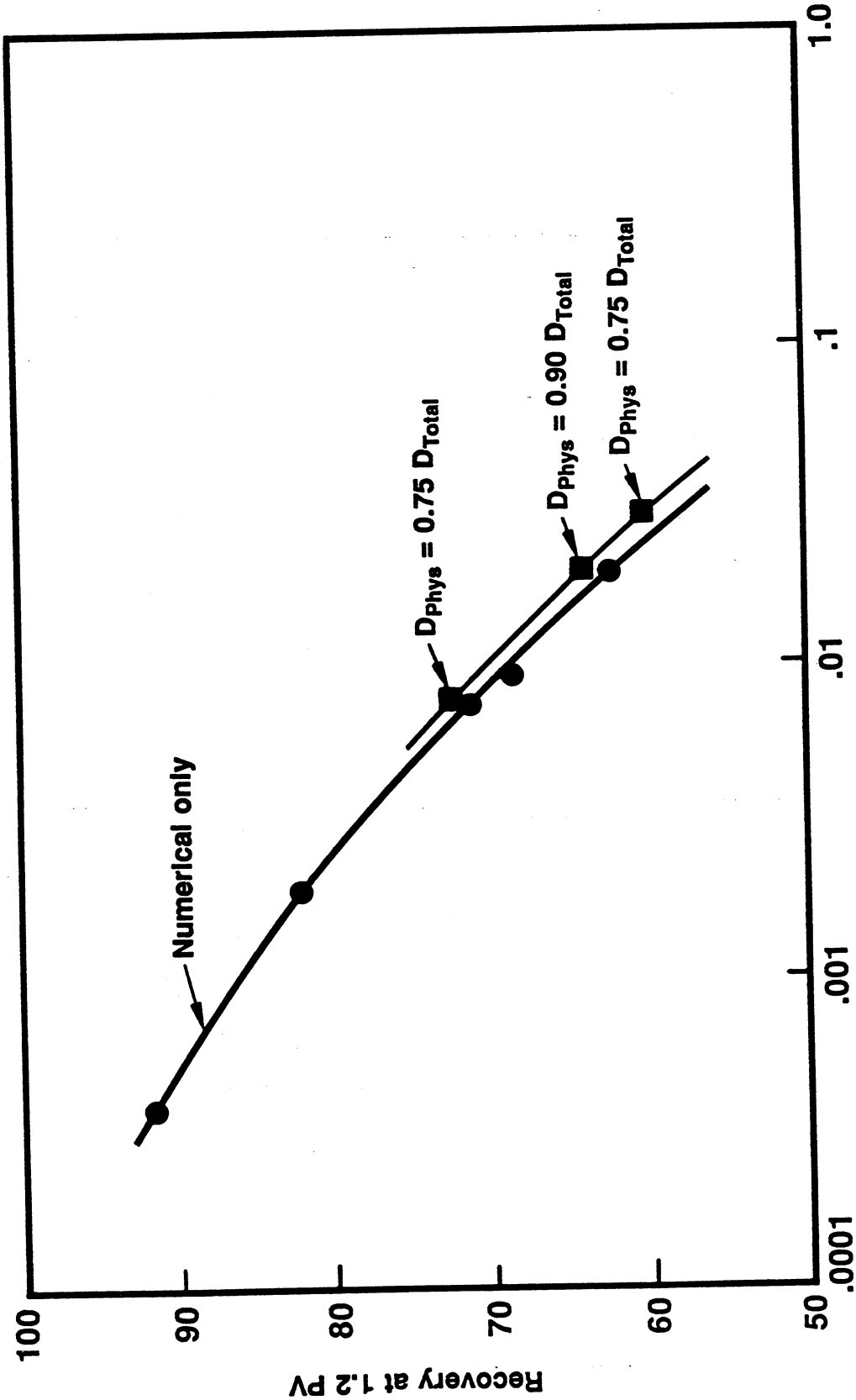

Fig. 3.4-6. Comparison of the effects on recovery of numerical dispersion with that of a finite-difference representation of the dispersion term.

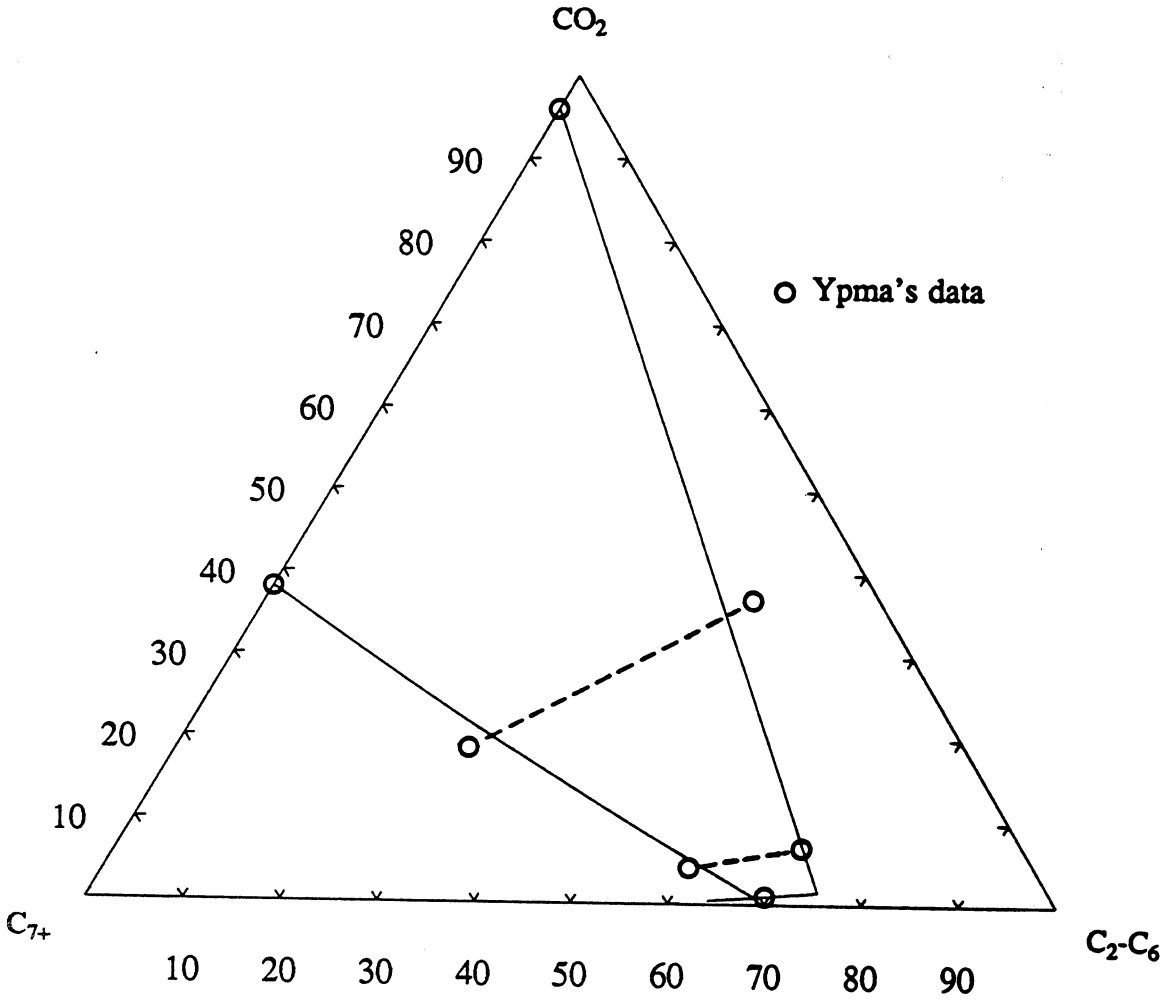

Fig. 3.4-7. Phase diagram based on Ypma's data (1985).

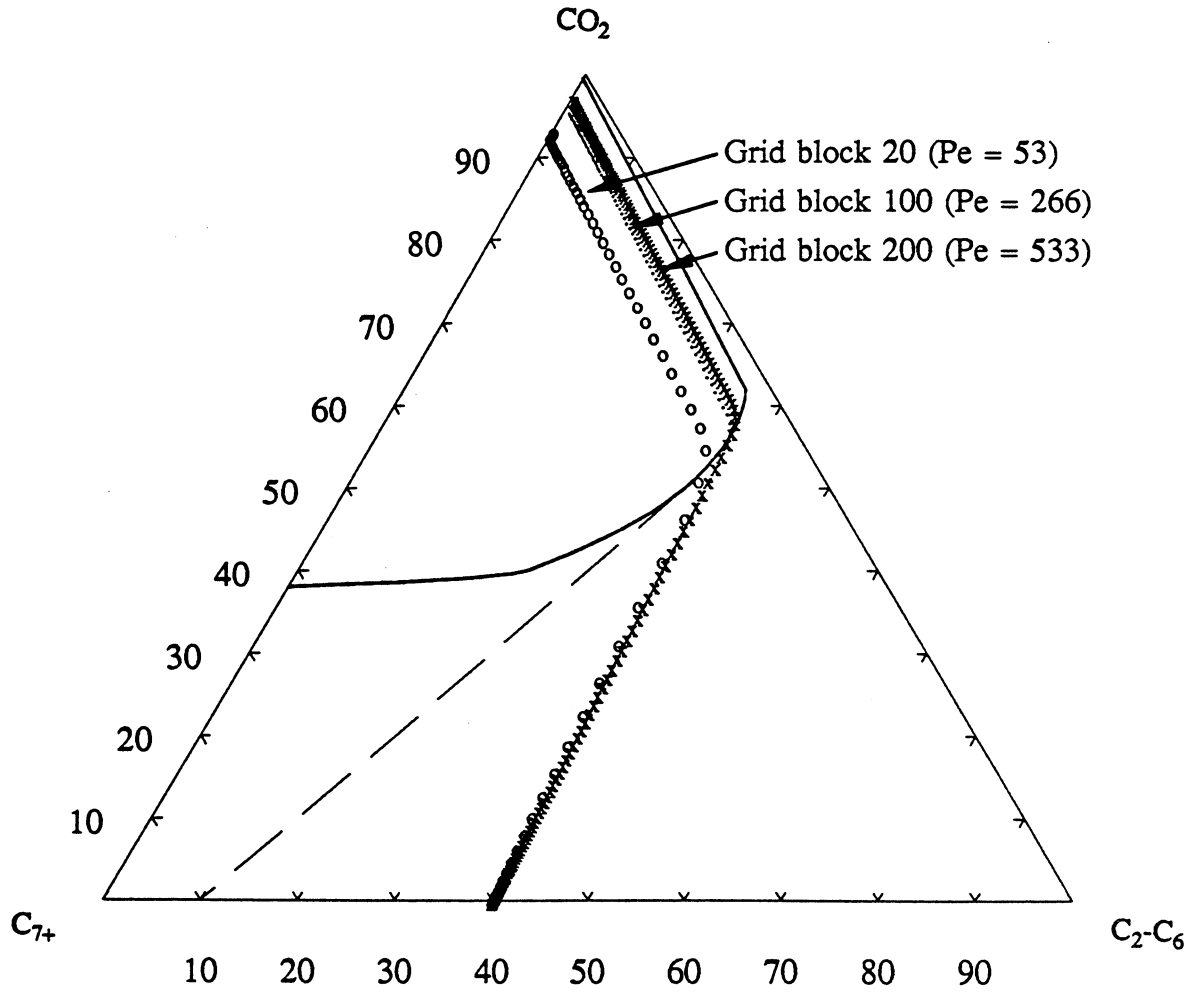

Fig. 3.4-8. Composition paths for a CO_2-hydrocarbon system with a large two-phase region and varying levels of numerical dispersion.

the binodal curve at all levels of dispersion. Displacement efficiency improves, therefore, as the "oil" is enriched in extractable components. Comparison of Figs. 3.4-3 and 3.4-9 shows the effect of a decrease in the size of the two-phase region, with the initial oil composition fixed at 20 mol % C_2-C_6. Decreasing the size of the two-phase region also causes composition paths to pass closer to the dewpoint curve.

Fig. 3.4-10 shows the composition paths observed with an unusually shaped phase diagram. In this case the trend towards the dewpoint curve is still observed with decreasing levels of dispersion (increasing n), but the rate of approach is extremely slow. Note that the composition paths here are for 100 and 1000 grid blocks, instead of the 20, 100, 200 used previously.

The phase diagram shown in Fig. 3.4-10 is similar to that of a light crude oil from an Australian oil field, "Tirrawarra" in South Australia (Jap et al., 1985). Note that the oil composition is to the right of the critical tie line, so the method of characteristics would indicate a composition route that stays in the single-phase region. The unusual composition paths observed prompted us to ask again whether truncation error adequately represents physical dispersion in a case like this. When the runs were repeated with a finite difference representation for physical dispersion and much lower truncation errors, we obtained essentially identical paths for corresponding values of total dispersion number. Fig. 3.4-11 shows in a more familiar way the comparison between effective dispersion levels as reflected in the relative shapes and heights of the C_2-C_6 slug in simulations with 200 grid blocks (N_{Pe} = 500) and 1000 grid blocks (N_{Pe} = 2500). Thus, even though larger numbers of grid blocks cause the composition path to move only slightly closer to the dewpoint curve, they still can be taken as a measure of the level of dispersion.

Geometrical Interpretation

The observations of the preceding sections indicate (Figs. 3.4-3, 3.4-8 and 3.4-9) that the finite-difference solution allows investigation of the interaction of phase behavior with dispersion, and that dispersion (quantified by the Peclet number) determines the extent to which the composition path enters the two-phase region. However, the results shown in Fig. 3.4-11 suggest that the magnitude of the interaction may be strongly influenced by the shape of the binodal curve.

In order to explain these effects, we first recast the phase diagram (normally expressed in mole fractions) into volume fractions. Given the assumption of zero volume change on mixing, straight lines on the mole fraction diagram map to straight lines on a volume fraction diagram.

The explicit finite difference simulator solves the component balance (Eq. 3.4-8), for the updated volume fraction of component i in cell number k. In what follows we drop the subscript i to simplify the notation. Eq. (3.4-8) can then be rewritten as

$$C_k^{(n+1)} + \alpha F_k^{(n)} = C_k^{(n)} + \alpha F_{k-1}^{(n)} \qquad (3.4\text{-}16)$$

where $C_k^{(n)}$ is the volume fraction of component i in the kth grid block at time n. $F_k^{(n)}$ is the volume fraction of component i in the flowing stream leaving the kth grid block at time n.

Eq. (3.4-16) shows how $C_k^{(n+1)}$ is determined by the compositions in the current grid block and in the upstream grid block at the previous time level. The equation can be represented geometrically, as is shown in Fig. 3.4-12. In this formulation, each side of the equation can be taken to represent a volume balance for a mixing process in which a unit volume of fluid of composition C is mixed with α volumes of fluid of composition F. On a ternary diagram the resultant mixture will have a composition M that lies on the straight line joining C and F, and whose location on that line is determined by the "lever rule."

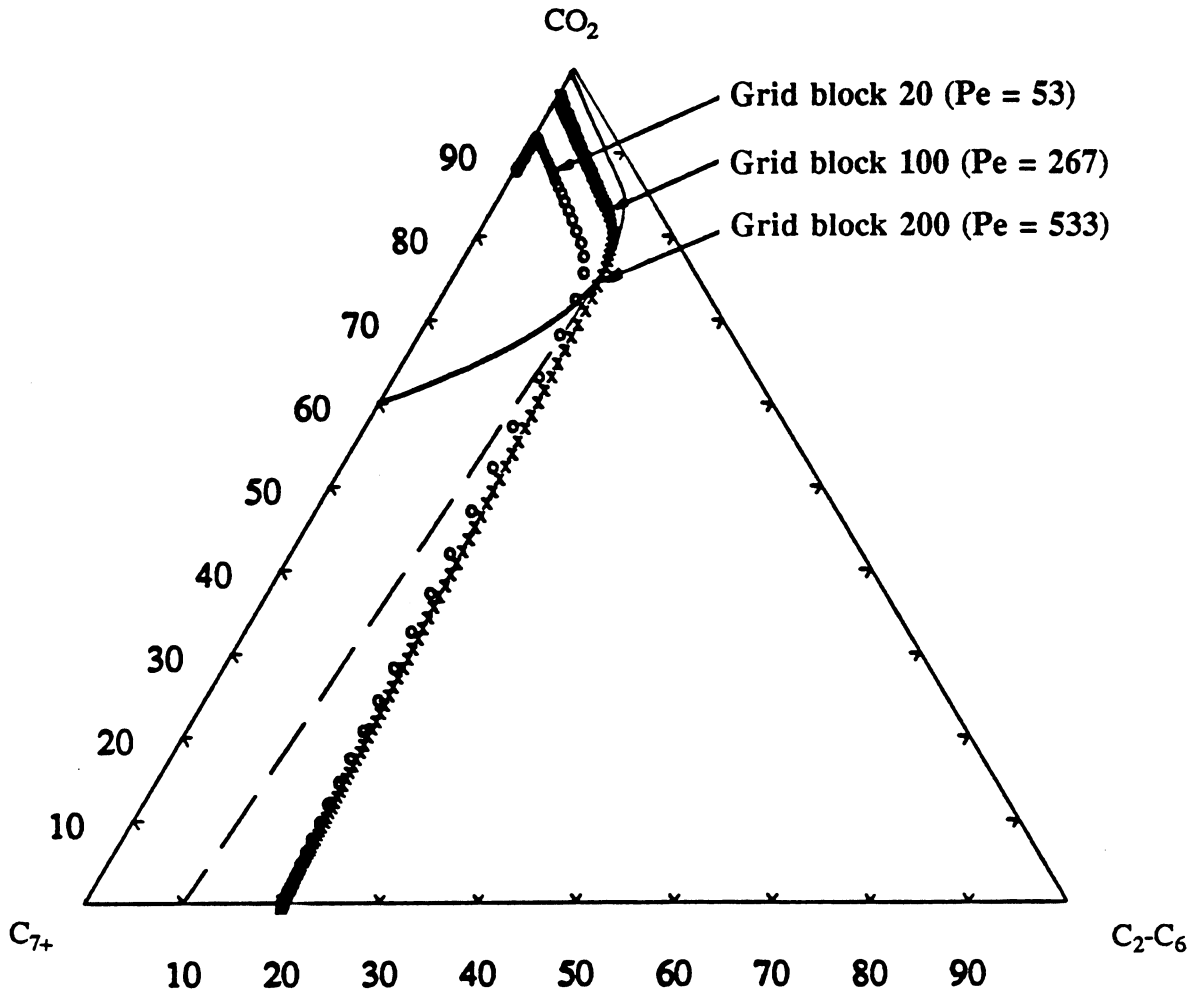

Fig. 3.4-9. Composition paths for a CO_2-hydrocarbon system with a small two-phase region and varying levels of numerical dispersion.

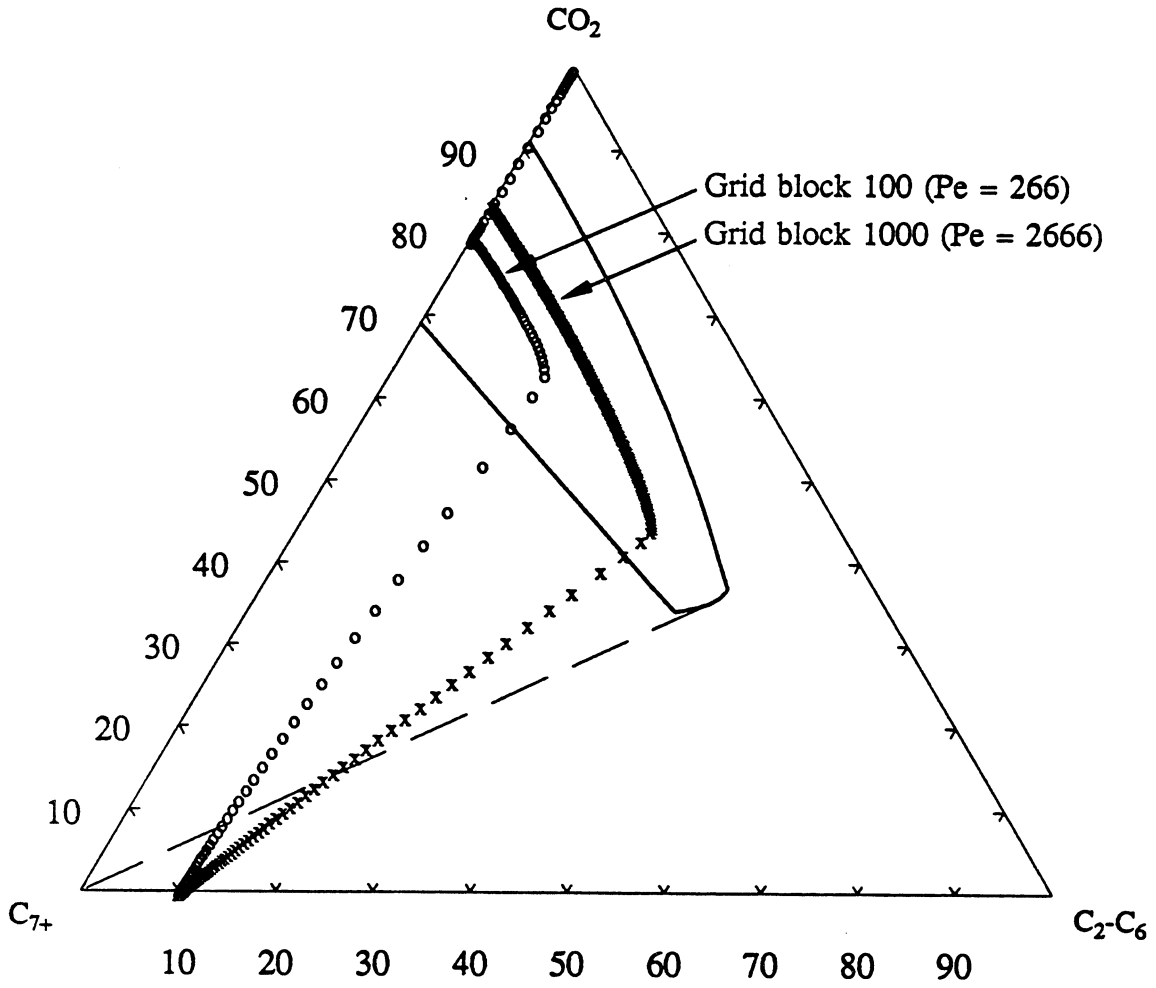

Fig. 3.4-10. Composition paths calculated for varying levels of dispersion for a phase diagram like that of Tirrawarra (Jap 1985).

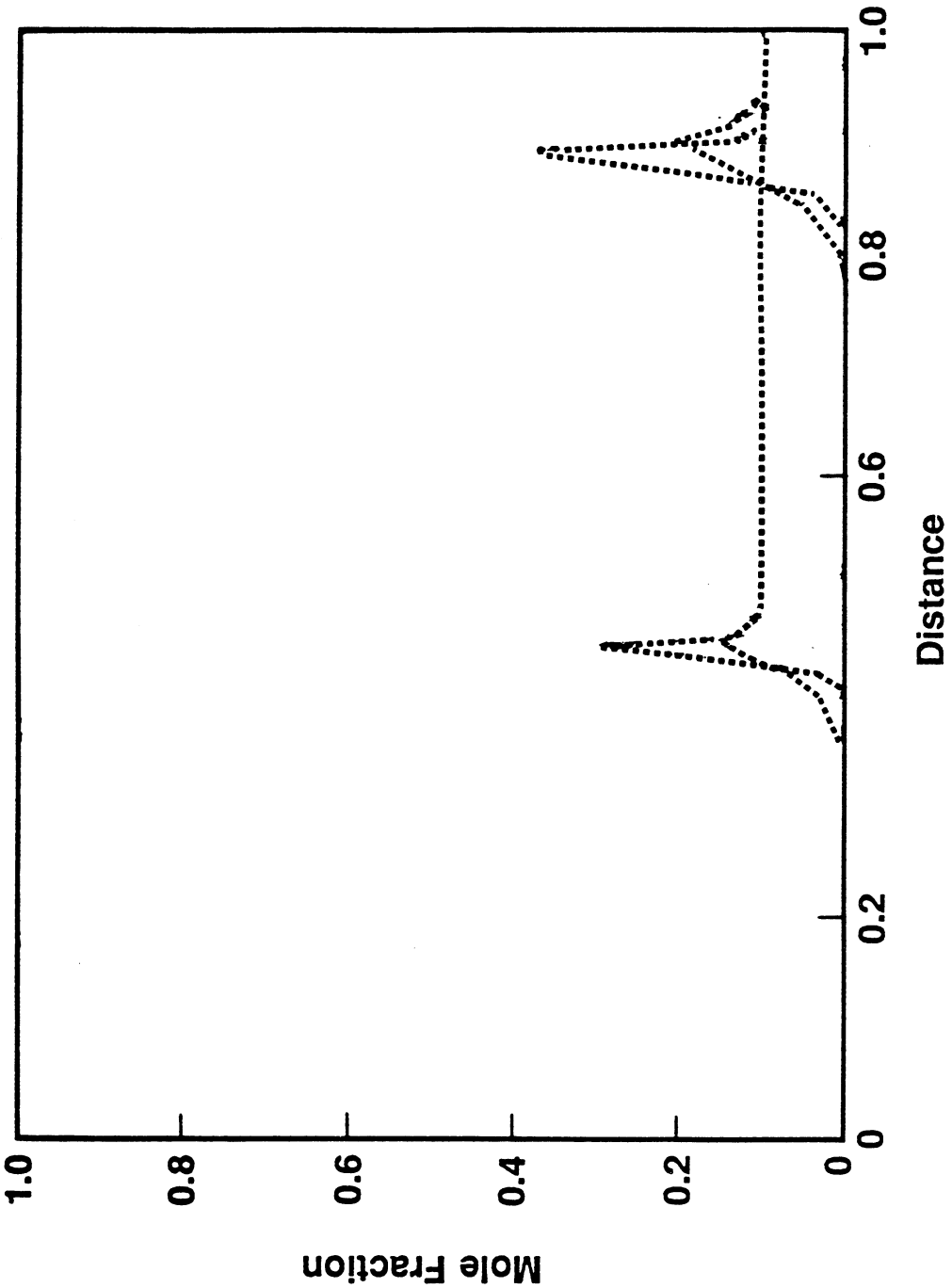

Fig. 3.4-11. Effect of numerical dispersion on composition profiles for the C_2-C_6 fraction for the phase diagram of Fig. 3.4-10.

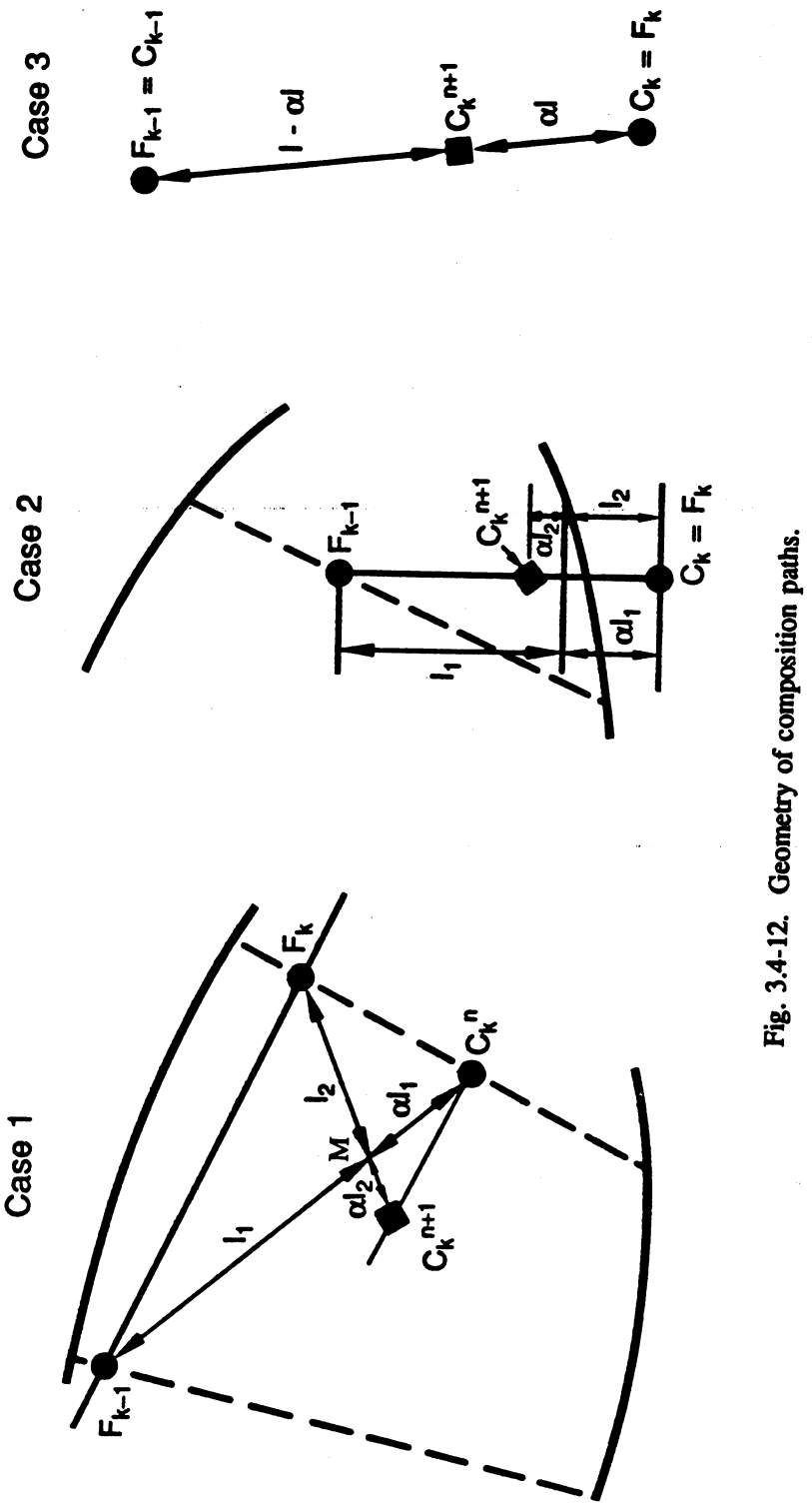

Fig. 3.4-12. Geometry of composition paths.

Fig. 3.4-12 illustrates the geometrical solution of the equation for the three possible cases that would be encountered along a composition path. (Where the superscript is omitted, the nth time step is implied.)

Case 1. The composition C_k is already in the two-phase region. F_k is on the same tie line as C_k since the flowing stream composition is a mixture of the two phases that are in equilibrium with C_k. F_{k-1} is on the tie line that contains C_{k-1}. M is determined by C_k and F_{k-1} by the lever rule. Hence, $C_k^{(n+1)}$ is determined from M and F_k, also by the lever rule. From the geometry, the trajectory $C_k^{(n)}$ to $C_k^{(n+1)}$ is parallel to the line joining F_k and F_{k-1}.

Case 2. C_{k-1} and F_{k-1} are in the two-phase region, but C_k is still single phase. M is on the line joining F_{k-1} and C_k. In the single-phase region, $C_k = F_k$. Since C_k and F_k are coincident, $C_k^{(n+1)}$ must be on the same line. The relative distances between C_k, F_{k-1}, etc., and M are shown on the diagram. A simple calculation demonstrates that $C_k^{(n+1)}$ will be located at a fractional distance α along the line joining $C_k^{(n)}$ to $F_{k-1}^{(n)}$ (see the diagram for Case 3).

Case 3. Both C_{k-1} and C_k are single phase. The same construction applies as in Case 2.

Once the composition path enters the two-phase region, it will follow a path parallel to lines joining the flowing stream compositions leaving the previous and the current grid block. Since in most EOR processes the solvent-rich phase has gas-like viscosities, the flowing stream compositions quickly approach the dewpoint curve. Hence, the composition paths are parallel to the dewpoint curve.

Successive grid blocks must enter the two-phase region to the right of the previous block, so long as the tie line at the point of entry has a lower slope than the entry path. This is illustrated in Fig. 3.4-13. Suppose that the composition of fluid flowing out of the (k–1)th grid block is as shown in Fig. 3.4-13a. The labels are for the n–2, n–1, and nth time step. (Note that in the case of an explicit finite difference simulator, it is possible to solve the composition paths for all times for each grid block in turn, even though it is conventional to solve for all grid blocks at each time, and then to increment the time. It is this property that is the basis for the comment on the duality of interpretation of Fig. 3.4-3 made previously.) $C_k^{(n-2)}$ is still in the single-phase region.

Fig. 3.4-13b illustrates the construction of the C_k path at successive times for $\alpha = 0.25$. The composition does not enter the two-phase region until the nth time step. Here it is almost all liquid, so the fractional flow of vapor is relatively small. Hence, $F_k^{(n)}$ has a value close to the liquid portion of the binodal curve. The trajectory $C_k^{(n)}$ to $C_k^{(n+1)}$ is parallel to the line joining $F_{k-1}^{(n)}$ and $F_k^{(n)}$. Because $F_k^{(n)}$ is the sum of the phase compositions weighted by the fractional flow and because the fractional flow of the low viscosity vapor is relatively high, F_k^n will lie to the right of the C_k composition path for the tie-line slopes shown, so the (k+1)th path will enter the two-phase diagram to the right of the kth path.

As implied in Fig. 3.4-13b, the starting points for the two-phase trajectories will be determined by the fractional flow curve for the system and by the (random) entry saturation for each grid block. We observe, however, that within a few time steps after entry into the two-phase region, the final straight-line composition path is established at about the same initial liquid saturation for all grid blocks; i.e., at the same fractional distance along the local tie line.

Figs. 3.4-14 and 3.4-15 demonstrate the consequences of these geometrical rules for two arbitrary phase diagrams. Fig. 3.4-14 is similar to Fig. 3.4-2 and others we have used. The composition paths move to the right as the number of grid blocks is increased; they are approximately parallel to the dewpoint line; and successive paths are higher than previous ones. That behavior occurs because, though each path is established on entry at a liquid saturation of about 40%, the shape of the binodal curve and the fact that the paths are parallel to the dewpoint line cause relative liquid volumes to decrease with time.

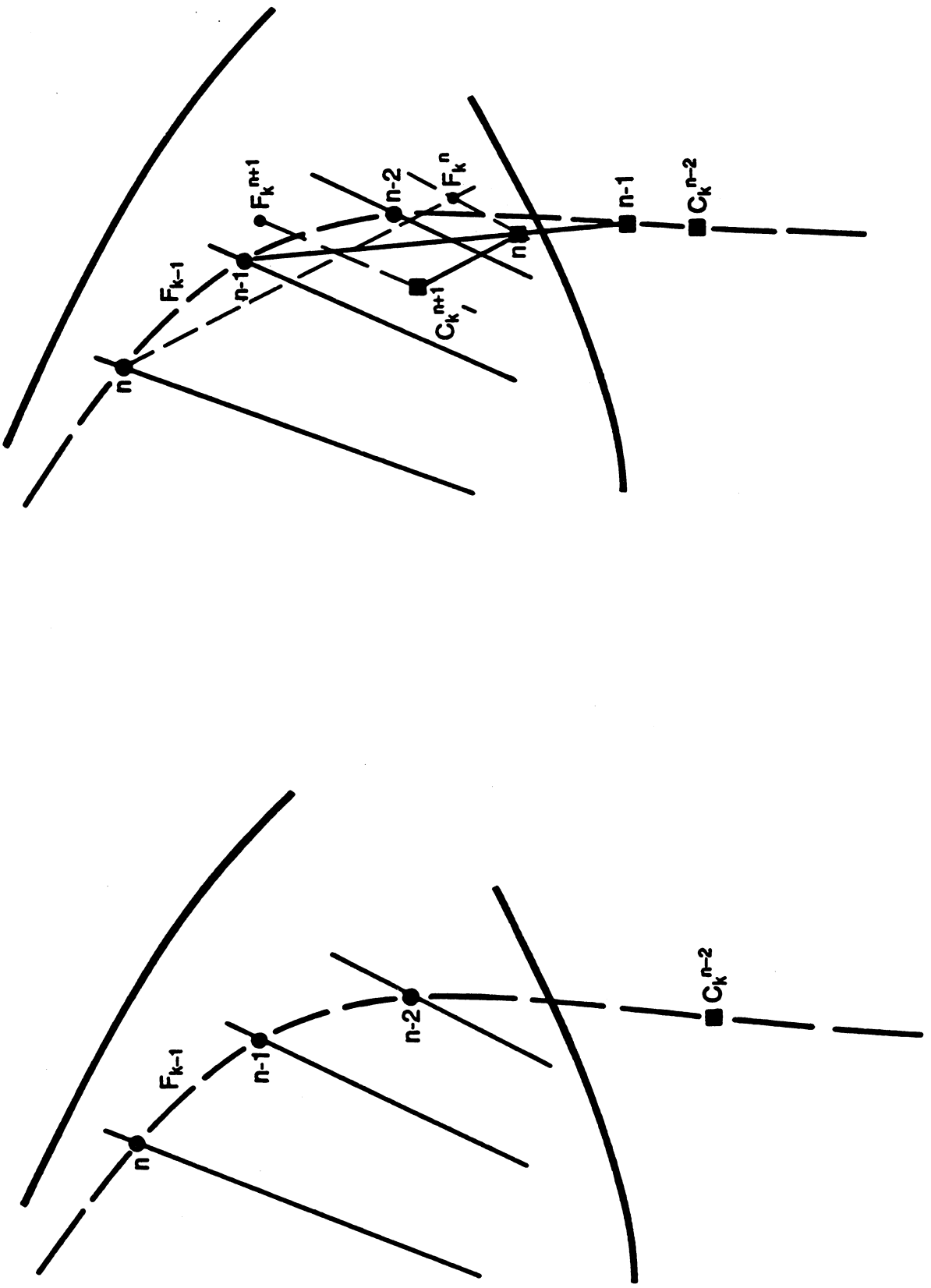

Fig. 3.4-13. Evaluation of composition paths in successive time steps.

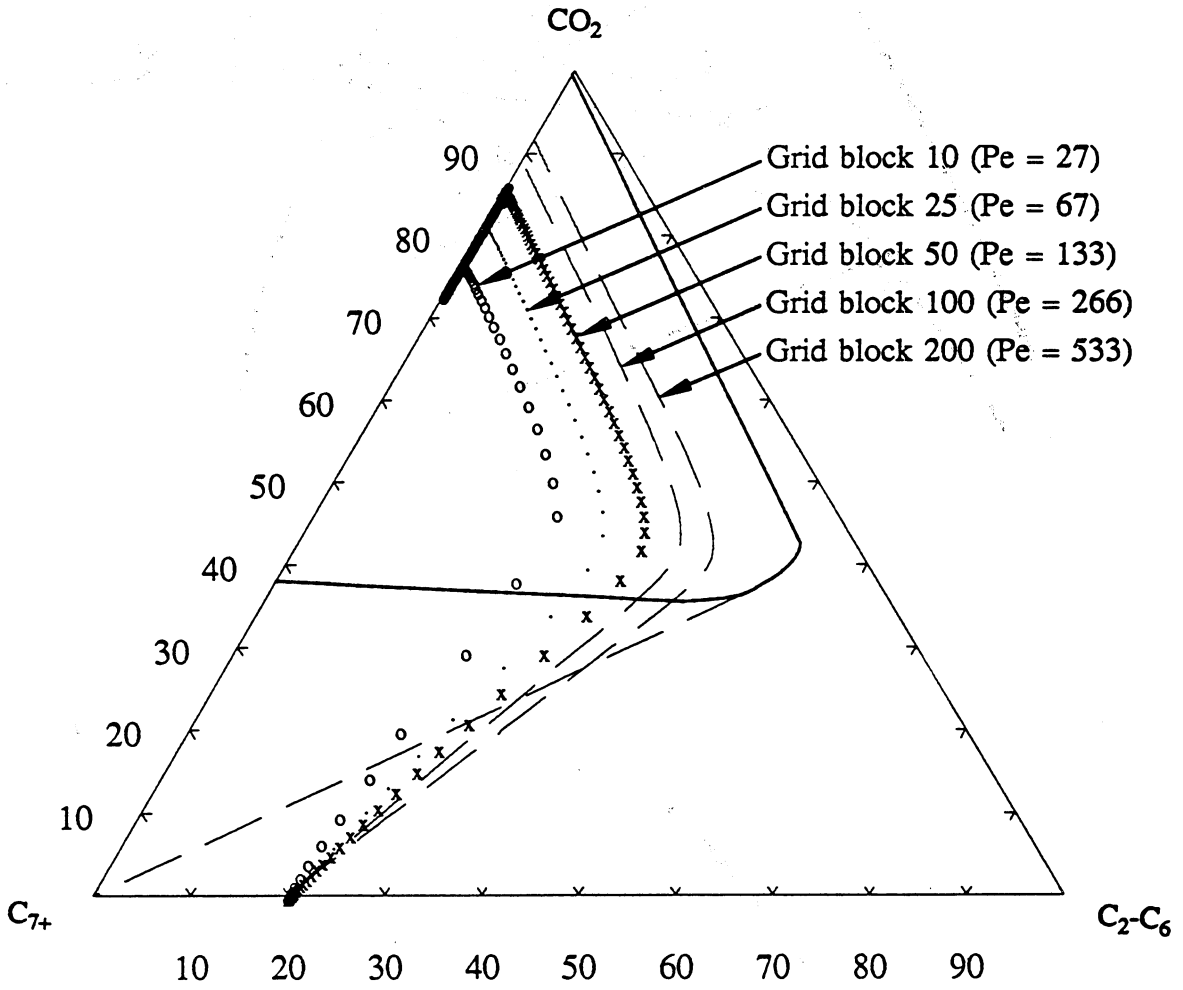

Fig. 3.4-14. Composition paths calculated for varying levels of numerical dispersion.

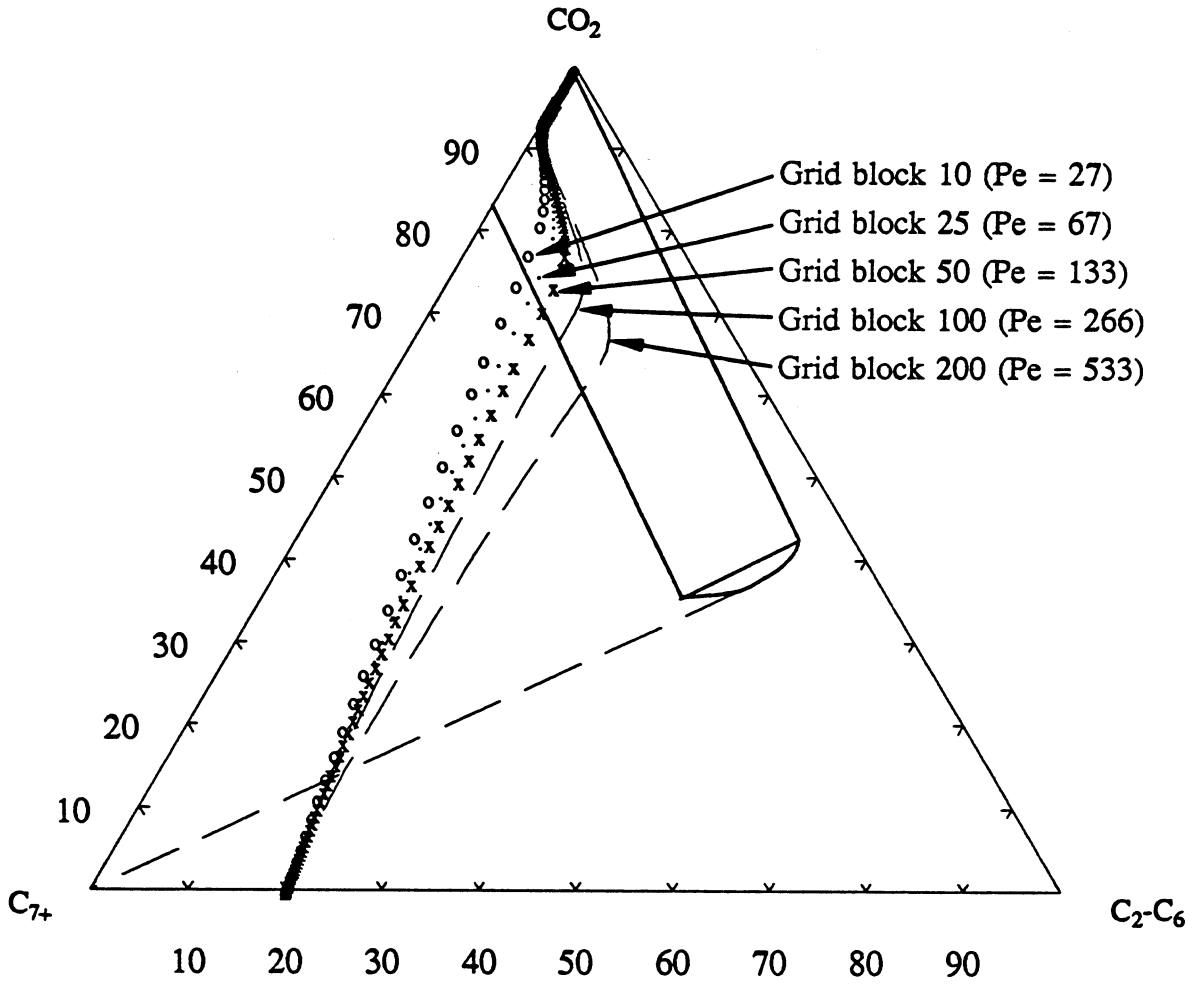

Fig. 3.4-15. Composition paths for varying levels of numerical dispersion for a binodal curve with parallel sides.

The phase diagram of Fig. 3.4-15 is similar to Fig. 3.4-10, but we have made it more extreme by making the dewpoint and bubblepoint curves parallel. Once again the paths in the two-phase region are parallel to the dewpoint line; successive paths enter to the right of the previous paths; all paths establish about the same liquid saturation on entry; in this case, however, the parallelism of the dewpoint and bubblepoint lines causes the paths to be nearly colinear.

In summary,

(1) successive composition paths enter the two-phase region richer in C_2-C_6 by virtue of the difference in slopes between the tie lines and the entry path;

(2) within a few time steps the final straight-line composition path is established at a liquid saturation determined by the fractional flow curves for the system;

(3) the composition paths are then all approximately parallel to the dewpoint curve.

3.4.3 Solution by the Method of Characteristics

The method of characteristics (MOC) solutions for the cases presented here are single-phase composition paths that follow the dewpoint arm of the binodal curve. However, when dispersion is taken into account, finite-difference calculations show that the composition path enters the two-phase region, following the geometrical rules explained in the preceding section. It is instructive in that case to compare that composition path with the path that would be predicted by the MOC for an initial oil composition to the left of the critical tie line.

In order to make this comparison, we simplify further our data set. These simplifications are summarized below:

(1) Dewpoint and bubblepoint curves are straight lines in the area of interest (to the left of the plait point).

(2) Tie lines are fan-like from the lower left-hand apex; a tie line can therefore be specified by its angle of elevation.

(3) Viscosities of the vapor and liquid phases remain constant as their compositions change.

(4) Residual saturations are 0.0; end-point relative permeabilities are 1.0; and relative permeabilities are given by:

$$k_{rL} = S_L^2 \text{ and } k_{rG} = S_G^2$$

The MOC solution for an initial composition lying on the extension of one of the tie lines is as follows:

(1) The composition path enters the two-phase region along the tie line and its extension.

(2) Within the two-phase region the path switches from the tie line to a nontie-line path when the eigenvalues λ of Eq. (3.4-17) are equal

$$\left[\frac{\partial F_1}{\partial C_1} - \lambda\right]\left[\frac{\partial F_2}{\partial C_2} - \lambda\right] - \frac{\partial F_1}{\partial C_2}\,\frac{\partial F_2}{\partial C_1} = 0 \quad . . \qquad (3.4\text{-}17)$$

where the subscripts refer to components 1 and 2 (e.g., CO_2 and C_2-C_6; C and F are as defined previously.

(3) The composition path switches from the nontie-line path to the tie line containing the injected fluid composition. (In the cases considered here, that is the zero C_2-C_6 axis.)

An example of a composition path calculated in this way is shown in Fig. 3.4-2.

We have calculated composition paths for cases similar to those shown in Figs. 3.4-14 and 3.4-15 using first finite-difference simulation as previously described, and then the method of characteristics. In the latter we choose an entry tie line close to the entry point given by the simulation.

Case 1. Parallel binodal curve.

A plot of the eigenvalues λ_1 and λ_2 that satisfy Eq. (3.4-16) versus S_L (i.e., between the dewpoint and bubblepoint lines) indicates that for this case the same functions are obtained for all tie lines. Consequently, $\lambda_1 = \lambda_2$ at the same value of S_L on all tie lines, and the nontie-line path is essentially a path of constant S_L. In this case, therefore, the method of characteristics suggests that the path switch will occur at constant saturation and direct calculation of nontie-line paths indicates that S_L hardly changes from the value at the switch point. This is as observed in Fig. 3.4-15.

We can quantify this for the parallel binodal curve case. The "switch" saturations are compared with the constant saturation along the path predicted by the simulator for two mobility ratios in Table 3.4-2. There is striking agreement between the two sets of values. Thus, once calculated compositions enter the two-phase region, the path followed is a close approximation to the path of the corresponding MOC solution.

Case 2. Converging binodal curve.

A nonparallel binodal curve like the one in Fig. 3.4-14 does not exhibit the same $\lambda(S_L)$ functions for all tie lines. Hence, different "switch" saturations occur on different tie lines. However, the variation is not large: for a binodal curve similar to the one in Fig. 3.4-14 the "switch" saturation is between 0.72 and 0.74 for tie-line angles from 45° to 70° and unit mobility ratios. These are similar to the "switch" saturations in Table 3.4-2, and support the observation made earlier that composition paths in the two-phase region are established at about the same saturation soon after entry, and then proceed essentially parallel to the dewpoint curve. We observe the same agreement at other viscosity ratios. Fig. 3.4-16 shows composition paths calculated by the simulator for a viscosity ratio of 10.0, using 10, 50 and 200 grid blocks, and superimposes MOC paths starting at comparable entry tie lines. It is clear that in this case also the two procedures give comparable results. Thus, the principal effect of dispersion is to cause the composition path to enter the two-phase region. Once it does so, and a two-phase saturation is established, the path followed is essentially that given by a dispersion-free calculation. In Fig. 3.4-16, for example, the path for 200 grid blocks tracks very closely the MOC path.

Discussion

The examples prescribed here confirm that results of compositional simulations to predict displacement performance in multiple contact miscible processes will be affected by numerical dispersion. That dependence has long been recognized (Gardner et al., 1981; Stalkup, 1988), but the fact that the size and shape of the two-phase region affects the sensitivity of displacement performance to the level of dispersion has not been demonstrated previously.

The interaction of phase behavior with dispersion has two important implications. First, displacement processes with phase diagrams like Fig. 3.4-10 will require careful control of numerical dispersion if accurate predictions of local displacement efficiency are to obtained. Thus, if a procedure like that used by Stalkup (1988) is used to extrapolate results for finite grid block size to low levels of numerical, the amount of mesh refinement required to establish the extrapolation will depend on the system phase behavior.

The second implication is that some systems will be much more sensitive than others to physical dispersion (and perhaps to additional mixing induced by viscous fingering or heterogeneity in combination with viscous and capillary crossflow). Thus, an examination of the phase diagram in question should be undertaken as part of the interpretation of flow experiments.

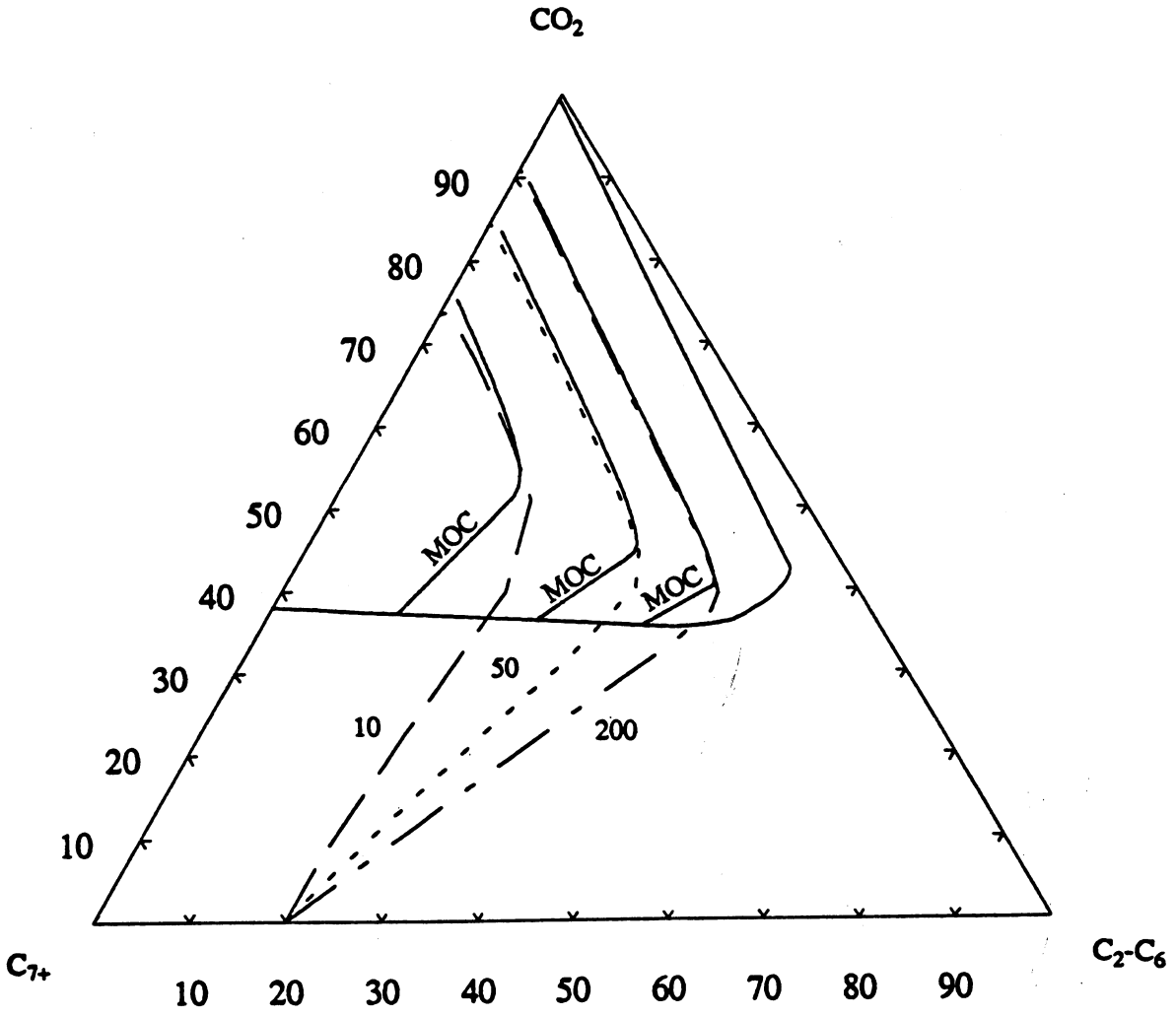

Fig. 3.4-16. Comparison of finite-difference solutions for 10, 50 and 200 grid blocks, with method of characteristics solutions for selected tie lines. Mobility ratio = 10.0.

3.4.4 Conclusions

The comparison of analytical (MOC) and finite difference solutions given in this section leads to the following conclusions.

(1) In simulations of slim tube displacements of oil by CO_2, the composition path passes through the two-phase region even when the method of characteristics predicts single-phase, developed miscibility. The two-phase flow is the result of dispersion, which may be represented in the simulator explicitly by including terms in $\partial^2C/\partial x^2$, or implicitly by numerical dispersion.

(2) As the number of grid blocks is increased, the path predicted by finite-difference simulation approaches the MOC solution, and recovery of C_{7+} increases. That behavior is consistent with the observation that increasing the number of grid blocks is equivalent to reducing the level of dispersion.

(3) However, the effects of simulated dispersion on the composition path, and hence recovery, are modified by the shape and characteristics of the binodal curve. That is, there is interaction between the effects of dispersion and phase behavior.

(4) This effect can be demonstrated by reference to the geometry of the ternary diagram.

   (a) The calculated composition path approaches the dewpoint curve with increases in the number of grid blocks (and hence increased recovery) for a "conventional" phase diagram; i.e., when the bubblepoint and dewpoint curves converge uniformly toward the plait point.

   (b) When the bubblepoint and dewpoint curves are parallel, or nearly parallel, recovery increases very slowly with increased numbers of grid blocks. Displacement performance for systems exhibiting such phase diagrams will be sensitive to even small levels of dispersion.

(5) The composition paths predicted by the finite-difference simulator at given levels of numerical dispersion are essentially the same as those calculated by the method of characteristics for comparable entry points into the two-phase region.

Appendix 3.4.A

Assume a single dispersion coefficient, D, for all components in all phases, and rewrite Fick's law with the overall volume fraction C_i, as the potential variable. The dispersive flux contribution is then

$$R_i = -A\phi\,\rho_i\,D\,\frac{\partial C_i}{\partial z} \qquad (3.4.A\text{-}1)$$

Incorporating Eq. (3.4.A-1) into the mass balance equation and transforming the variables by Eq. (3.4-6) we obtain the following modified version of Eq. (3.4-7)

$$\frac{\partial C_i}{\partial \tau} + \frac{\partial F_i}{\partial \xi} - \left[\frac{1}{P_e}\right]\frac{\partial^2 C_i}{\partial \xi^2} = 0 \qquad (3.4.A\text{-}2)$$

Eq. (3.4.A-2) was solved using the finite difference technique already referred to (Eq. 3.4-8), plus central differencing for the second derivative

$$C_{i,k}^{n+1} = C_{i,k}^{n} + \alpha\left[F_{i,k-1}^{n} - F_{i,k}^{n}\right] + \frac{\alpha}{P_e(\Delta\xi)}\left[C_{i,k+1}^{n} - 2C_{i,k}^{n} + C_{i,k-1}^{n}\right] \qquad (3.4.A\text{-}3)$$

3.5 Summary

In this chapter, the basic theory of miscible flood processes has been extended substantially. The previously existing theory was for one-dimensional flow of up to three components in two phases. In Section 3.1 that theory was extended to include a fourth component. The resulting analysis of calculated composition paths for displacement by CO_2 of oils containing dissolved C_1 resolves a longstanding inconsistency between the three-component theory and experimental observations. The analytical solutions obtained show that dissolved C_1 has small effect on recovery because C_1 partitions so strongly into the more mobile phase that it flows in a bank at the leading edge of the transition zone. Thus, CO_2 following behind displaces oil without methane and does so efficiently if the displacement pressure exceeds the MMP for the dead oil. The new theory also indicates that displacements of an oil below its bubblepoint pressure can also be efficient. That prediction has not been tested experimentally, however.

In Section 3.2, the basic theory was extended to include effects of temperature variation, though effects of longitudinal conduction and transverse heat loss were ignored. Analytical solutions were obtained for steam displacement of liquid water and for steam displacement of oil and water. The more difficult problem of displacement of oil and water by steam and CO_2 remains to be solved, however. The solutions reported extend the theory substantially, however, because they include three-phase flow as well as temperature variation. Those solutions will be useful as tests of thermal simulator accuracy and performance, and will also be used to develop understanding of the behavior of three-phase relative permeability models.

In Section 3, the effect of nonuniform flow on displacement performance was examined. To make the problem tractable, vertical equilibrium crossflow was assumed for displacements in two layers with differing permeability. That assumption makes the flow problem one-dimensional again in the sense that flow equilibrium between the two values of mixture composition in each layer is established instantaneously. The flow problem can then be solved by the method of characteristics. Analytical solutions for displacement of a one-component oil by CO_2 showed up to four shocks and also showed significant effects of crossflow on composition paths.

For three-component systems analytical solutions were not obtained, but finite-difference solutions indicated, as expected, that heterogeneity reduces displacement efficiency at breakthrough and reduces the rate of recovery after breakthrough below that calculated for noncommunicating layers. For low values of the layer permeability ratio, crossflow reduces recovery due to an interaction of crossflow and phase behavior that causes increased two-phase flow, even for multicontact miscible systems. For high permeability ratio, crossflow improves recovery, however, as the benefits of moving oil from the low velocity layer outweigh the negative effects of the resulting two-phase flow.

In Section 3.4, the interaction of dispersion, numerical or physical, with phase behavior was examined. That dispersion affects displacement performance in first-contact and multicontact miscible displacements has long been recognized. What is new here is the fact that the impact of the interaction between phase behavior and dispersion depends strongly on the shape of the two-phase region. The mathematical methods of Sections 3.1-3.3 also play a role here; we use a MOC calculation of composition paths to show that once the flow with dispersion enters the two-phase region, it follows a path that is the same as that calculated by MOC for dispersion-free flow. The calculations indicate that some displacements will be much more sensitive to the effects of dispersion than others.

The flow problems considered in this chapter are all special cases of the more complex flows that occur in real miscible floods. We have deliberately chosen limiting cases that highlight specific interactions so that a rational picture of the quantitative impact of individual mechanisms can be assembled. Thus, while the phase behavior mechanisms examined here are

the basis for high local displacement efficiency, they are not the only ones that influence process performance. For example, the effects of viscous instability have been ignored here, though the two-layer flow calculations offer an indication of how fingering and phase behavior would interact. In subsequent chapters, we return, therefore, to the question of how fingering and heterogeneity act and interact to influence displacement performance.

4. Viscous Instability and Reservoir Heterogeneity

Miscible displacement processes, such as CO_2 flooding, rely on coupled phase behavior and flow to generate compositions that avoid the two-phase region. Because there are no capillary forces, which are responsible for oil entrapment, a miscible displacement can be very efficient. In practice, however, high recovery may not be realized because hydrodynamic instability leads to macroscopic fingering of the displacing fluid, resulting in a nonuniform displacement. This unfavorable behavior is inevitably influenced by the heterogeneity of the porous media. The physical processes involved in this interaction are not fully understood.

Most miscible displacement processes will be influenced to some extent by viscous fingering phenomenon because the ratio of the mobility of the in-place oil to that of the displacing solvent is usually unfavorable. In addition, all oil reservoirs are heterogeneous on some length scale. Therefore if process simulations are to be accurate, some description of unstable flow in heterogeneous porous media must be included in the formulation of a reservoir simulator. Before this can be achieved, a better understanding of the length scales associated with the fingering phenomenon and the porous media heterogeneities will be required. These length scales control the extent of the mass transfer between the unswept oil and the displacing fluid and, hence, control the kind of interactions described in Section 3.3. Mixing is important because it influences the phase behavior of the CO_2-hydrocarbon mixtures, which controls microscopic displacement efficiency. If, for example, fingers that grow in field-scale flows are large and widely spaced, then compositional effects of mixing between oil and CO_2 will be confined to a small portion of the reservoir and hence will have minimal impact on displacement performance. For such cases, simulators need only represent the gross movements of fluids in the reservoir. If, on the other hand, fingers are small and closely spaced, mixing will be important and representations of the phase behavior of CO_2-hydrocarbon mixtures will have to be included in the simulations. Thus, resolution of these questions of scale is needed for design of improved reservoir simulation tools.

In this chapter we consider the question of whether viscous forces or reservoir heterogeneities control the dimensions of fingers. In Section 4.1 we describe a new computational approach to simulation of the growth of fingers. We show first that calculations performed with the new model agree very well with available experimental data. Then we use the model to examine the relationship between finger growth and heterogeneity. In Section 4.2, we report results of flow visualization experiments that test model prediction for heterogeneous flow systems.

4.1 Numerical Simulation of the Growth of Viscous Fingers in Heterogeneous Porous Media

Udo G. Araktingi

Much of the theory of viscous instability has been based on the analysis of the onset of instability (Gardner and Ypma 1984, Heller 1966, Perrine 1963, Peters et al. 1984, Lee et al. 1984, Tan and Homsy 1988, Schowalter 1965) in an attempt to predict growth rates and critical wavelengths (see Homsy 1987 for a recent review). The resulting linear stability theory can be used to determine the conditions for the initiation of unstable flow but cannot be used to predict the long term behavior of the unstable displacement, because the resulting perturbations are no longer small.

An alternate approach, the use of conventional finite difference techniques (Peaceman and Rachford 1962) was attempted early in the study of miscible displacement processes. However, the poor resolution of early attempts masked any potential viscous fingers, and the use of a permeability fluctuation was required to initiate the instabilities. Resulting effluent

curves were found to be dependent on the permeability distribution used. With the advent of faster computers and the development of more accurate numerical techniques, fine grid simulations of the growth of viscous fingers have been performed with better results though some sort of artificial finger initiation is usually required (Christie and Bond 1987, Christie 1987, Giordano et al. 1985). In another approach, empirical models (Koval 1963, Todd and Longstaff 1972, Dougherty 1963, Fayers 1988, Fayers and Newly 1988, Odeh 1987) have been used to provide simple representations of the effects of fingering for use in field-scale simulators. These models suffer from the fact that the principal parameters involved have little or no direct physical significance. These parameters can be fitted to simple one-dimensional laboratory experiments, for example, but translation of the same parameter values to a three-dimensional reservoir is uncertain at best.

Recently a computational approach (Hatziavramidis 1987, Tan and Homsy 1987), based on the method of weighted residuals, has been proposed. Chebyshev polynomials and Fourier expansions have both been used for the transform functions. The advantages of this method are high accuracy and computational speed. The use of fast Fourier transform (FFT) techniques allows the use of fine grids, which gives good finger resolution with relatively low computation times. There are also drawbacks. First, periodic boundary conditions are required in order to avoid any Gibbs overshoot phenomena in the solutions. The method is also awkward for long time simulations because the domain must be extended. Thus, it is inconvenient to compute solutions after breakthrough of injected fluid.

Finally, a probabilistic approach (King and Scher 1986, DeGregoria 1985, King and Scher 1985) based upon random walk simulations of the solution of Laplace's equation has been investigated. In the limit of infinite mobility ratio, the method produces solutions to the problem of diffusion-limited aggregation. This method uses a finite difference solution of the material balance equations. Tracer particles carrying a fixed solvent volume are added to the domain at a rate of one per time step. To determine where this particle should go, a streamline and an injected fluid concentration are chosen randomly. The intersection of those two contours gives the location at which a tracer particle is added. Fingers are generated because low viscosity fluid replaces high viscosity fluid, streamlines become more closely spaced, increasing the probability that a streamline in that neighborhood will be selected in subsequent time steps. However, these models produce lower recoveries than observed in laboratory experiments due to the absence of any transverse dispersion (Orr and Sageev 1986, Araktingi 1988). We show below that even when effects of transverse dispersion are included, the probabilistic model does not reproduce experimental observations accurately.

To investigate further the combined effects of instability and permeability variations, a new model was formulated. This scheme uses a finite difference solution of the material balance equations to determine the pressure field, given the distribution of permeability and the current distribution of fluid viscosities. Tracer particles that carry a finite concentration of injected fluid are then moved with velocities based on the pressure field. Effects of transverse and longitudinal dispersion are included by perturbing the position of the particles after the convection step by amounts selected from a normal distribution with a mean of zero and a variance that sets the relevant dispersion coefficient. In effect, we assume that local velocity variations at scales smaller than a grid block can be represented adequately by dispersion. Once the locations of all the tracer particles are determined, local viscosities can be evaluated and the process repeated for the next time step. This scheme has the advantage that it controls the effects of numerical dispersion, but it requires that many particles be tracked. In the remainder of this section, the computational scheme is described in more detail. Accuracy of the resulting solutions is evaluated using analytical results, and calculated recoveries from displacement runs at different mobility ratios are compared to experimental results. Next, a brief description of a method to generate heterogeneous permeability fields is given. These permeability distributions are used in the random-walk model to study the interaction between the viscous fingers and the porous media.

4.1.1 Formulation of the Random-Walk Model

In the development of the model we assume that:

(1) Injected and in-place fluids are first contact miscible and incompressible.

(2) The viscosity of mixtures of the two fluids can be calculated from a quarter power blending rule.

(3) Darcy's law applies.

(4) Flow is two dimensional.

The random-walk technique is based on the concept that dispersion in porous media is a random process. This idea was explored in some detail by Prickett et al. (1981) for single-phase flows in which the fluid viscosity is everywhere the same. In this section, we summarize the approach they used for unit mobility flows, verify that our code reproduces their results, and then show that the technique can also be applied to flows with variable viscosity.

Prickett et al. argued that at the microscopic level, dispersion occurs because fluid elements that start at adjacent positions follow a distribution of flow paths with slightly different lengths and local flow velocities. To represent that behavior, Prickett et al. modeled the motion of a collection of particles, each of which is taken to represent an increment of volume of the displacing fluid. Each particle is assumed to move in two ways during a time step. First, the particle is moved with the mean flow velocity in the direction of the streamline passing through the particle's current location. Then the particle position is perturbed by random amounts (governed by scaled probability distributions) to reflect the effects of transverse and longitudinal dispersion.

The problem examined here is a first contact miscible flood in which a displacing fluid is injected into a porous medium initially saturated with a resident fluid that is miscible in all proportions with the displacing fluid. The mathematical model for such a displacement, neglecting gravity effects and assuming incompressible fluids, is

$$\nabla \cdot (\vec{D} \cdot \nabla C) - \vec{v} \cdot \nabla C = \frac{\partial C}{\partial t} \pm Q \tag{4.1.1}$$

$$\vec{v} = -\frac{k}{\mu} \nabla p \tag{4.1.2}$$

$$\nabla \cdot \vec{v} = 0 \tag{4.1.3}$$

where $\vec{v}$ is the local velocity, C, the local composition, $\vec{D}$, the dispersion tensor, Q, the injection rate per unit volume, k, the permeability, μ the viscosity and p, the pressure.

In this method, the convection-dispersion equation (Eq. 4.1.1) is not solved. Instead, the continuity equation (Eq. 4.1.3), in conjunction with Darcy's law (Eq. 4.1.2) is solved using a point finite difference scheme. As a result, velocity components are obtained at each grid point. The basis for the displacement calculations is that the distribution of the concentration of displacing fluid in a porous medium can be represented by the distribution of a finite number of discrete particles. Each of these particles is moved by Darcy flow and is assigned a volume that represents a fraction of the total volume of displacing fluid involved. In the limit, as the number of particles gets extremely large and approaches the molecular level, an exact solution to the actual situation is obtained. However, it will be shown that relatively few particles are needed to arrive at a solution accurate enough for the applications considered here.

The connection between the random-walk approach and the statistics of the particles was demonstrated by Prickett et al. They considered the motion of a unit slug of tracer in an infinite one-dimensional medium. In that case, the solution to Eq. 4.1.1 is (Bear, 1972)

$$C(x,t) = \frac{1}{(4\pi D_L t)^{1/2}} \exp\left[- \frac{(x - Vt)^2}{4D_L t} \right] \tag{4.1.4}$$

where D_L is the longitudinal dispersion coefficient, V is the flow velocity, and x and t are space and time.

To see how the flow problem is connected to the statistics of particles, consider a normal probability distribution, which has the density function, n(x),

$$n(x) = \frac{1}{\sqrt{2\pi}\sigma} \exp\left[- \frac{(x-u)^2}{2\sigma^2} \right] , \tag{4.1.5}$$

If we set

$$\sigma = \sqrt{2D_L t} , \tag{4.1.6}$$

and

$$u = Vt , \tag{4.1.7}$$

then Eqs. 4.1.4 and 4.1.5 are equivalent, and

$$n(x) = C(x,t) . \tag{4.1.8}$$

Therefore, the dispersion of particles can be represented as a random process.

Details of how the random-walk representation is implemented in a computational algorithm are given by Prickett et al. Our code follows closely their implementation for the portion of the code that deals with particle convection and dispersion.

An analogous procedure is used to represent the effects of transverse dispersion. An advantage of the random-walk representation of dispersion is that the perturbations of particle locations need not be aligned with the coordinate system. Instead, the perturbations in the longitudinal and transverse directions are determined by the directions of the local velocity field.

Model Algorithm

The steps used to implement these concepts are:

(1) Update the concentrations of each grid block by counting the number of particles in the given block. For the first time step all concentrations are zero. Note that before the start of each simulation, the number of particles required to obtain a unit concentration in a grid block is specified.

(2) Solve the continuity equation by finite differences to determine the pressure field. A backward space difference with a standard matrix inversion was used.

(3) Calculate the velocity field using Darcy's law and the pressure field. The pressures are known at each node point. Velocities are calculated at the midpoint between pressure nodes. Velocities for particles not located at such nodes are obtained by linear interpolation.

(4) Generate new particles representing the amount of displacing fluid injected during the current time step. This is done by calculating the number of particles corresponding to the volume of fluid injected and placing the particles at evenly spaced locations along the inlet.

(5) Determine the current time step. For an explicit solution to be stable, the front cannot travel more than a distance equivalent to a grid block during a time step. In this model, the motion of each particle is the sum of a convection step and a dispersion step. Thus, to avoid having particles travel a distance greater than a grid block, the time step is chosen to allow movement equal to half a grid block length (or width) traveled at the highest existing velocity.

(6) Calculate a new position for each particle. First move it the appropriate distance in the direction of the local velocity. Then draw random perturbations from that position to represent longitudinal and transverse dispersion.

(7) Return to Step (1).

4.1.2 Model Validation

Several tests were performed to validate the random-walk model. First, calculated solutions were compared to available analytical solutions and with solutions reported by Prickett et al. for unit mobility displacements. Second, ideal miscible displacements similar to those used to measure longitudinal and transverse dispersion coefficients were simulated to determine if the input dispersivities were recovered in the calculated Peclet numbers. Finally, calculated displacement performance was compared to experimental results (Blackwell et al., 1959) for displacements in a linear two-dimensional model at various mobility ratios.

Analytical Solutions

Three different cases were simulated, all with unit mobility ratio and for a homogeneous porous medium.

Case 1. Longitudinal dispersion in uniform one-dimensional flow with continuous injection at the inlet.

The solution for this case is approximated well (except for early times close to the inlet) by:

$$C / C_o = \frac{1}{2} \operatorname{erfc} \left[\frac{x - Vt}{2\sqrt{D_L t}} \right] \tag{4.1.9}$$

where $D_L = 4.5$ ft^2/day, $V = 1$ ft/day. The transverse dispersivity was set to zero. This calculation is identical to that described in Fig. 51 of Prickett et al. (the same random number generator and seed were used). Fig. 4.1-1 shows the results plotted for two times. The numerical solution approximates the analytical one, and the results reproduce those of Prickett et al., an indication that the implementation in our code is correct. The match can be improved by increasing the number of particles used (in the case shown it was 100 particles to represent unit solvent concentration in a grid block) and finer grid mesh (3x30 grid was used here). Note that $C/C_o > 1$ at the inlet. That behavior is a statistical phenomenon, which could be eliminated by increasing the number of particles injected and the number of grid blocks. It occurs when the composition of a block is near 1.0 because occasionally random motions cause the number of particles to exceed that required to give a concentration of 1.0. In

subsequent time steps, however, the concentration drops again due to the same random motions.

Case 2. Longitudinal dispersion in uniform one-dimensional flow with a slug of tracer injected at inlet.

The data for this problem are the same as the those used in the previous case, except that a slug is injected. This calculation duplicates that reported by Prickett et al. in their Fig. 53. Fig. 4.1-2 compares the results of this simulation with the analytical solution given by Bear (1972).

$$N = \frac{N_o dx}{\sqrt{4\pi D_L t}} \exp\left[- \frac{(x - Vt)^2}{4D_L t} \right] \tag{4.1.10}$$

where N_o dx is the number of particles times the grid length over which particles are counted. The agreement between the approximate solution and the analytical solution improves as the number of particles taken to represent unit concentration increases.

Case 3. Longitudinal and transverse dispersion in uniform one-dimensional flow with a slug of tracer injected at the inlet.

Again, the data for this problem are the same as previously used except that the transverse dispersivity is no longer zero. These results reproduce those reported by Prickett et al. in their Fig. 58. Now D_T = 1.125 ft ^{2}/day. The theoretical solution for this case is given by Fried (1975)

$$N = \frac{N_o}{4\pi Vt\sqrt{d_L d_T}} \exp\left[- \frac{(x - Vt)^2}{4d_L Vt} - \frac{y^2}{4d_T Vt} \right] \tag{4.1.11}$$

where N_o is the number of particles in the injected pulse and $d_L = D_L/V$, $d_T = D_T/V$. Figs. 4.1-3 and 4.1-4 show that the agreement between the analytical and numerical results is good.

Recovery of Input Dispersion Values

In order to examine how the random-walk model mimics numerically the effects of dispersion, ideal miscible displacement simulations were performed. Approximate longitudinal Peclet numbers were obtained by fitting calculated effluent composition data to a straight line

---

NOTE: This report was revised on July 20, 1995. The text of this portion of the report continues on p. 189.

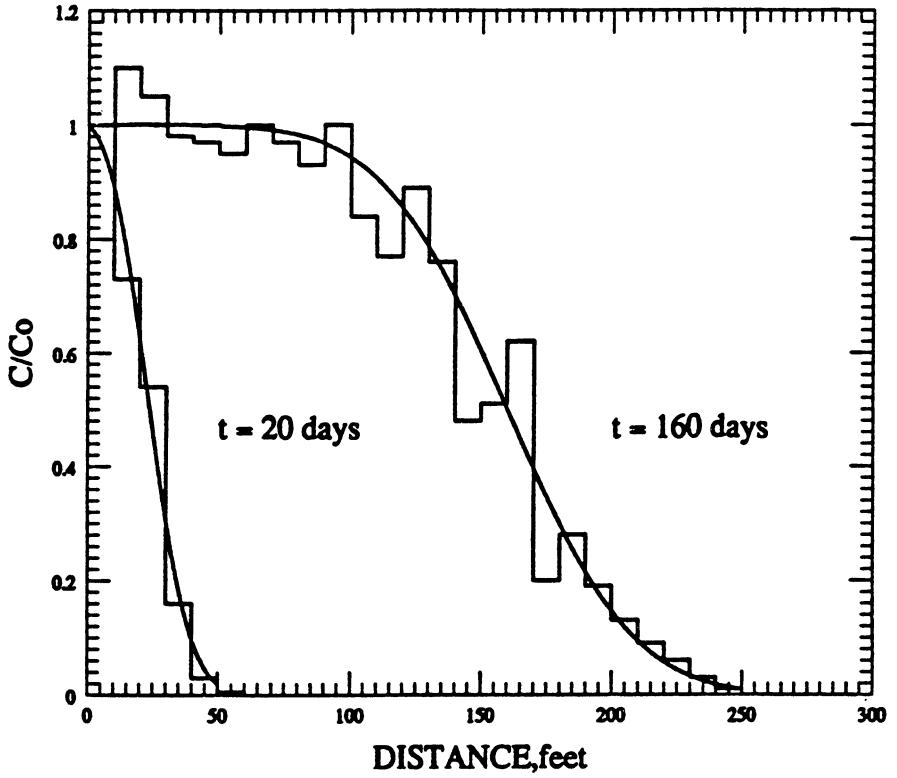

Fig. 4.1-1 Longitudinal dispersion in one-dimensional flow with continuous injection at inlet.

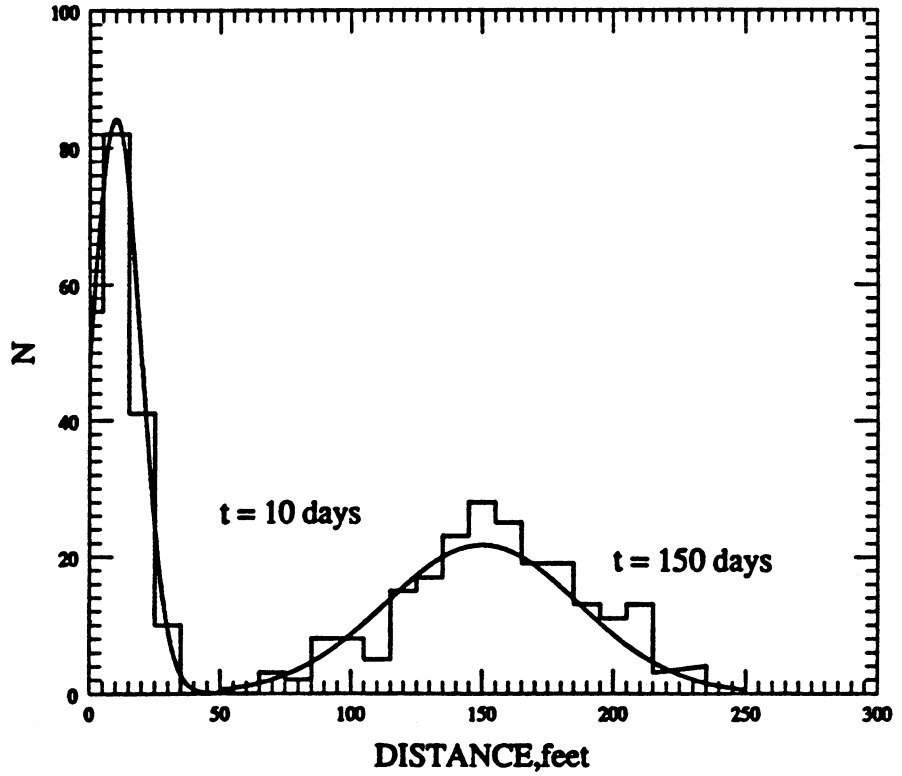

Fig. 4.1-2 Longitudinal dispersion in uniform one-dimensional flow with a slug of tracer injected at inlet (200 particles).

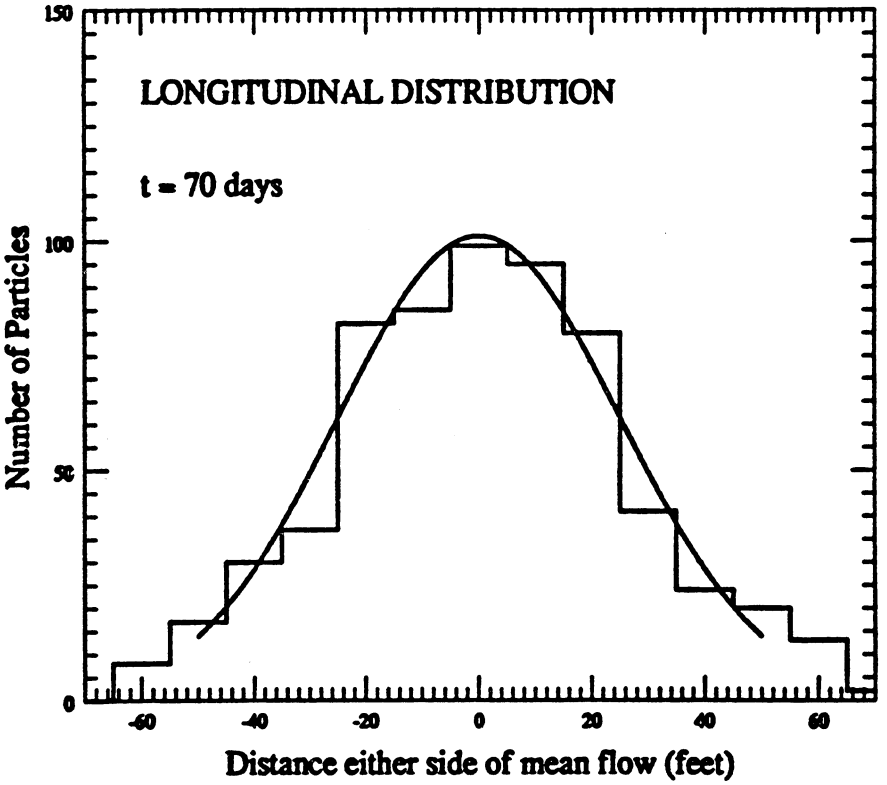

Fig. 4.1-3 Longitudinal distribution on both sides of the mean flow after 70 days.

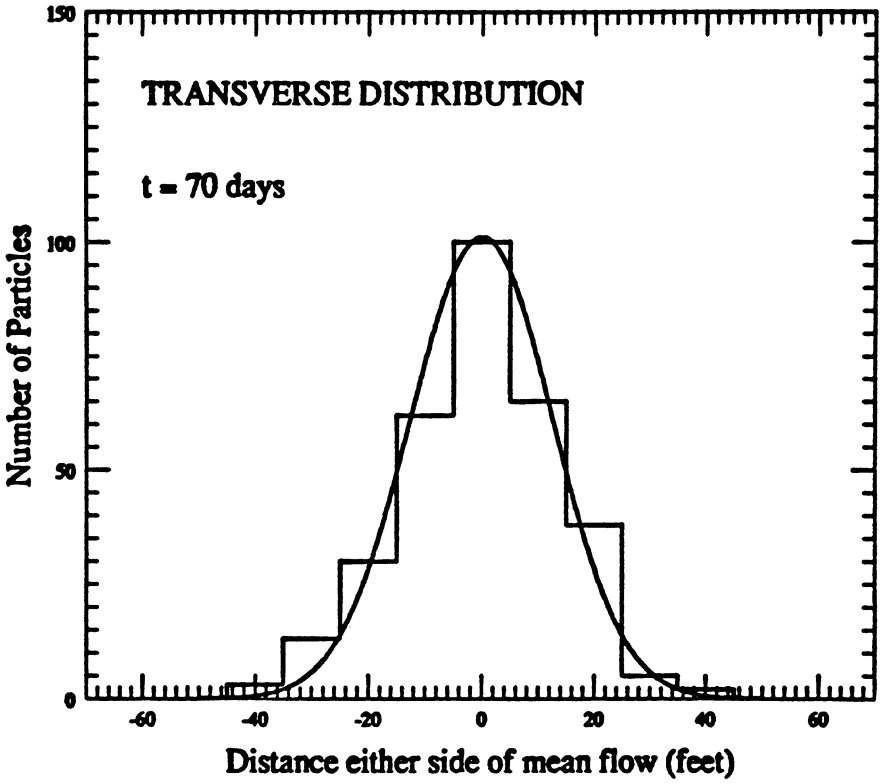

Fig. 4.1-4 Transverse distribution on both sides of the mean flow after 70 days.

in arithmetic probability coordinates. The longitudinal dispersion coefficient was then calculated from the Peclet number as

$$D_L = \frac{vL}{Pe} \tag{4.1-14}$$

where v = 40 ft/day , L_x = 6 ft , L_y = 2 ft and the input D_L = 0.1457 ft^2/day. Fig. 4.1-5 shows the range of the calculated dispersion coefficients and its dependence on grid size and seed number for the random number generator.

Transverse Peclet numbers were measured by developing code that simulated the sandpack column arrangement (Perkins and Johnston 1963) shown in Fig. 4.1-6. The transverse dispersion number was then obtained from the Peclet number in the same manner described above. The data used were also the same with D_T = 0.0055 ft^2/day.

For both cases, the magnitudes of values calculated increased with increasing mesh size and were nearly independent of the seed number used. The ranges varied from about ± 20% for a 30 × 20 grid to about ± 5% for a 90 × 20 grid in the longitudinal dispersion case. Figs. 4.1-5 and 4.1-7 indicate that the computational scheme used reproduces well the input values, provided that the mesh used is fine enough.

Comparison with Experimental Results

Blackwell et al. (1959) carried out experiments to investigate fingering in homogeneous sands. The results used were those obtained from a sandpack model with dimensions 3/8" x 24" x 72" at reported flow rates between 30 – 50 ft/day. There was no difference in density between the fluids used, so gravity effects were not present in the horizontal displacements. The sandpack was tested to assess the homogeneity of the packing using equal density and viscosity fluids containing dyes. The results of the assessment also allowed determination of the effective dispersion coefficient. The values of dispersion coefficients used in these simulations were calculated with the correlations of Pozzi and Blackwell (1963). At a flow rate of 40 ft/day the calculated dispersion coefficients were

$$D_L = 0.1457 \text{ ft}^2/\text{day} \quad \left[1.6\text{x}10^{-3} \text{ cm}^2/\text{S}\right]$$

$$D_T = 0.0045 \text{ ft}^2/\text{day} \quad \left[6.5\text{x}10^{5} \text{ cm}^2/\text{S}\right]$$

Fig. 4.1-8 shows the experimental data for four different mobility ratios ranging from 5 to 375 (Blackwell et al. 1959), and the results obtained from the simulation runs. The agreement between calculated and experimental values of the oil recovery is very good. For the mobility ratios of 5, 86 and 150 a 60×60 grid was used. For the last mobility ratio case (M = 375) a finer grid (80×60) was needed in order to simulate the experimental results satisfactorily. Except for refinement of the grid, no adjustment of input parameters was made to achieve the agreement shown in Fig. 4.1-8. That agreement is convincing evidence that the numerical scheme described represents with reasonable accuracy the physical processes that generate viscous fingers.

For the calculations summarized in Fig. 4.1-8, adequate transverse grid resolution was critical to a good match of the experimental results. However, once adequate refinement was used, further refinement did not change calculated results. For example, runs were made with even finer grid meshes (120×60) but the results were unchanged. The number of grid blocks in the longitudinal direction did not affect the outcome of the simulations as strongly. Additional numerical experiments showed that the choice of seed number for the random number generator also did not alter the results significantly. The positions of individual fingers

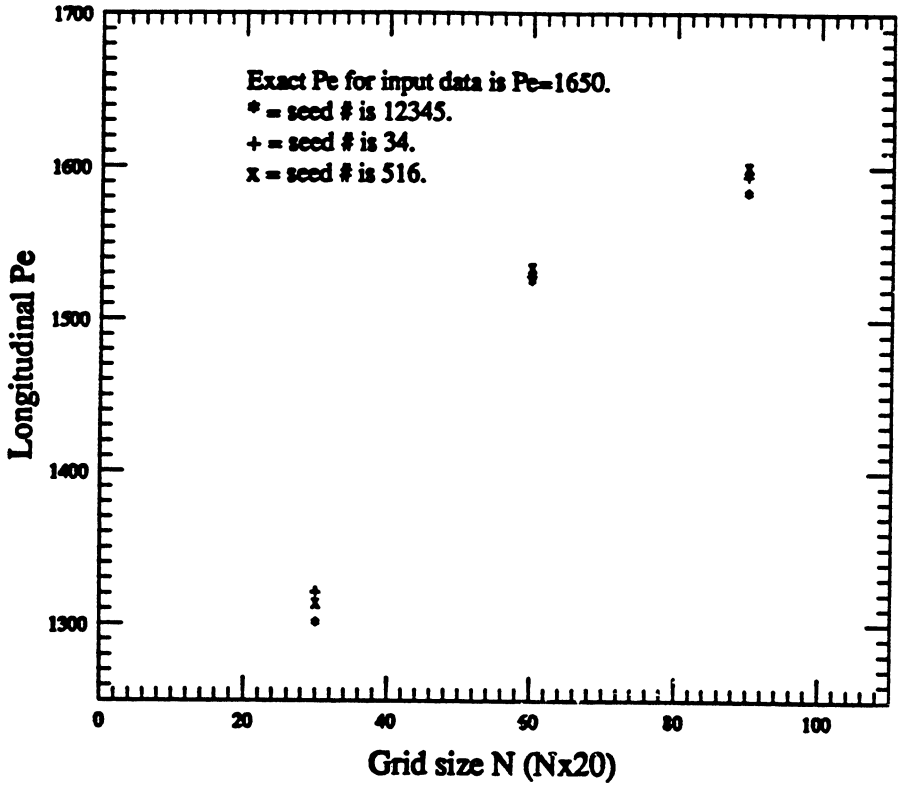

Fig. 4.1-5 Longitudinal Pe number as a function of grid size and seed number.

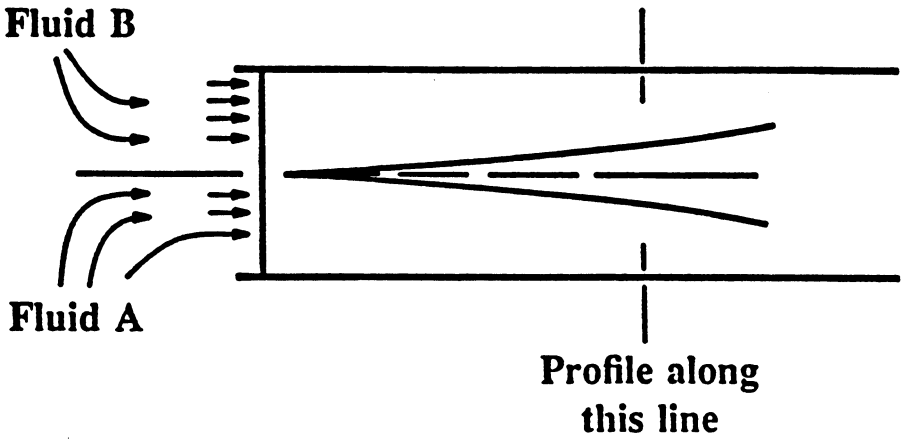

Fig. 4.1-6 Measurement of transverse dispersion coefficients.

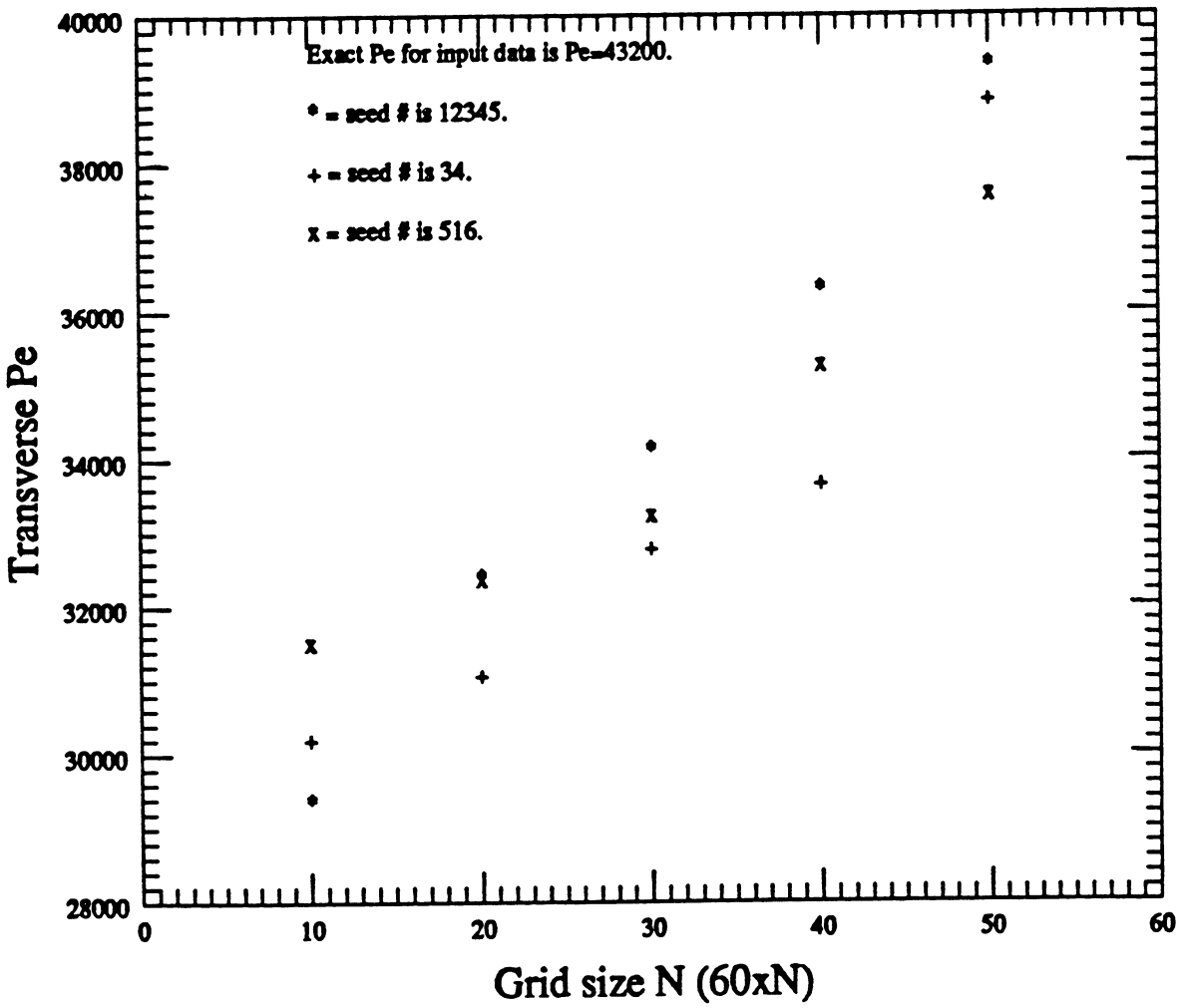

Fig. 4.1-7 Transverse Pe number as a function of grid size and seed number.

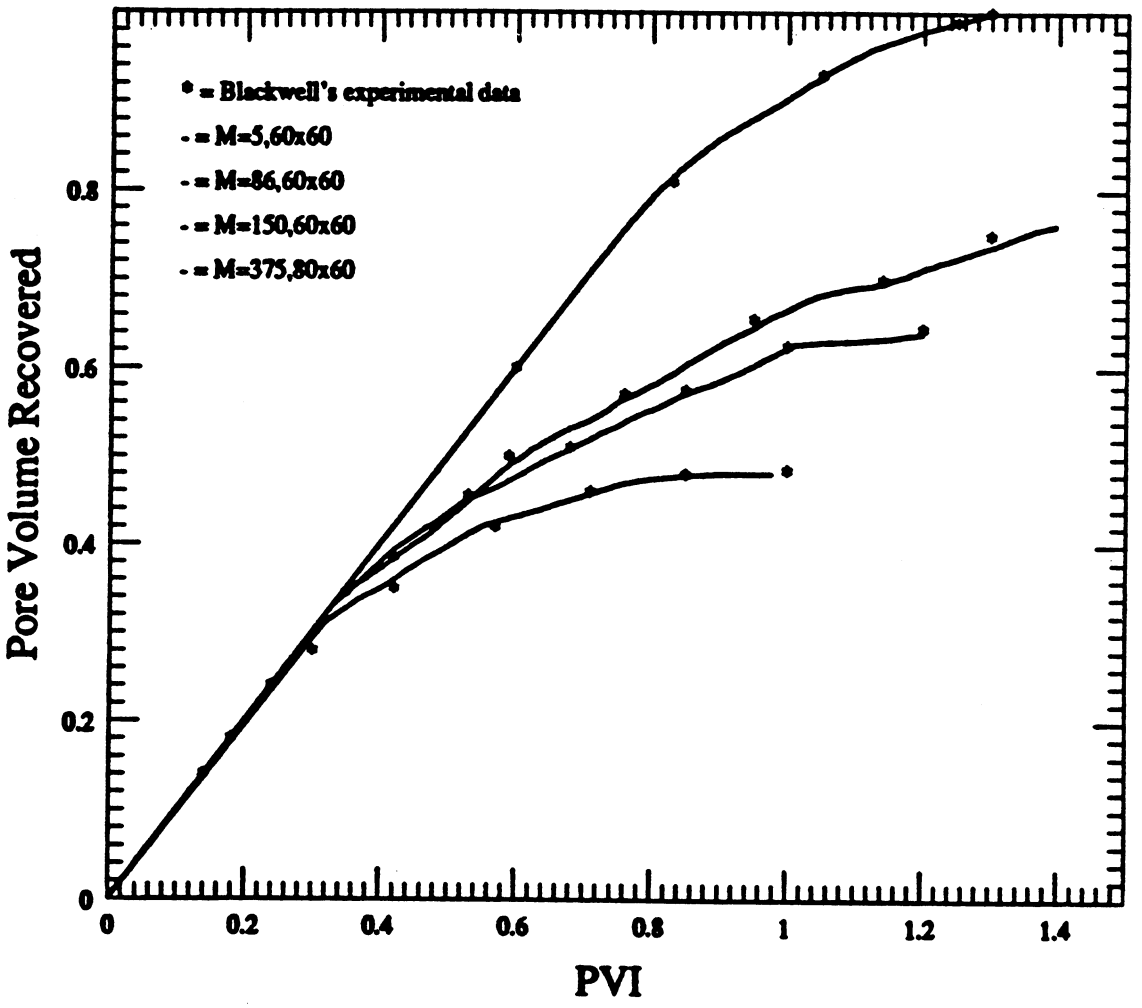

Fig. 4.1-8 Comparison of random-walk model results with Blackwell's experimental results.

changed with the seed numbers, and there were small changes in recovery curves, but there was no change in the level of agreement of recovery curves with experimental data (Araktingi 1988).

The random-walk model was also tested against experimental results published by Pozzi and Blackwell (1963) for displacements in a vertical two-dimensional homogeneous model. Those experiments investigated the combined effects of gravity and viscous fingering in homogeneous sands. The ratio of characteristic viscous pressure drop to gravity head is given by the viscous to gravity ratio

$$N_{gr} = \frac{u\mu_o L}{kg\Delta\rho H} \tag{4.1-15}$$

Various mobility ratios, aspect ratios (L/H), and viscous to gravity ratios (N_{gr}) were examined. The results were summarized by plotting the dimensionless solvent penetration versus pore volume injected (PVI). The solvent penetration was defined as the greatest distance reached by a finger or gravity tongue. The parameters describing these displacements are given in Table 4.1-1. The dispersion coefficients for these displacements were calculated from the correlation of Pozzi and Blackwell (1963). Fig. 4.1-9 shows the experimental data for five different displacement experiments with mobility ratios ranging from 1.85 to 69 and viscous to gravity ratios ranging from 89 to 200,000, along with the results obtained from the random-walk model. Transverse Peclet numbers ranged from 3700 to 51000 and longitudinal Peclet numbers from 580 to 7100. The agreement between the calculated and experimental values of the solvent penetration is very good. As with the linear model, transverse grid resolution was very important in obtaining a good match of the experimental results. Runs were made with finer grids (100x60), but the results remained unchanged.

Some of the concentration contours (C=0.05) obtained from the simulations run to validate the vertical model are shown in Fig. 4.1-10. These contours clearly display the flow regimes described by Stalkup (1983). At low flow velocity (low N_{gr}), gravity forces dominate, and a single, smooth gravity tongue forms (Fig. 4.1-10a). As the viscous to gravity ratio increases, fingers appear on the gravity tongue (Fig. 4.1-10b). With additional increases in N_{gr}, the gravity tongue disappears, and the viscous instability dominates. Figs. 4.1-9 and 4.1-10 indicate, therefore, that the random-walk model also reproduces the quantitative and the qualitative features of unstable displacements caused by viscosity and density differences.

Evaluation of Probabilistic Model

Given the encouraging results obtained with the random-walk model, the probabilistic model of King and Scher (1985) was modified to treat dispersion in a way similar to that described in the previous section. After determining the intersection of the randomly chosen streamline and concentration contour, that location is perturbed by random amounts corresponding to longitudinal and transverse dispersion, as described for the random-walk scheme. The injected fluid concentration at that location is then incremented. This method generates fingers because low viscosity fluid replaces high viscosity fluid, streamlines become more closely spaced, and hence the probability increases that a streamline in the neighborhood will be selected in subsequent time steps.

If some representation of dispersion is not included in the model of King and Scher (1985), there is no mechanism for damping the growth of fingers only a grid block in diameter. Hence, fingers become finer and finer as the mesh is refined, and the simulations do not agree well with recovery data after breakthrough. Unfortunately, as shown in Fig. 4.1-11, recoveries obtained with the modified probabilistic model also do not agree well with experimental results. As the number of grid blocks is increased, breakthrough occurred earlier, an indication that the viscous fingers developed were functions of the grid block size. Also, agreement of calculated and experimental recovery curves was poor for both course and fine meshes. This

Table 4.1-1. Input Data Used to Simulate Pozzi and Blackwell's Experimental Results.

L/H	Mobility Ratio	$\Delta\rho$(g/cm^3)	Inlet Velocity(ft/day)	N_{gr}	D_l (ft^2/day)	D_t (ft^2/day)
14.4	16.3	0.192	0.510	68	0.00272	0.000423
105	16.3	0.335	2.20	12,319	0.0115	0.00222
193	1.85	0.555	16.1	84,461	0.0178	0.00247
105	7.4	0.552	1.60	119,870	0.00252	0.00190
105	69	0.170	1.98	51,452	0.0112	0.00277

Table 4.1-2. Comparison of Linear Stability Theory with Simulation Results.

v(ft/day)	M	λ_C(ft)	λ_{model} (ft)
40.0	10	0.00241	0.00291
40.0	50	0.00201	0.00243
40.0	100	0.00205	0.00265
10.0	10	0.00962	0.00956
10.0	50	0.00821	0.00901
10.0	100	0.00804	0.00948
0.5	10	0.192	0.238
0.5	50	0.164	0.218
0.5	100	0.161	0.204

Table 4.1-3. Permeability Field Parameters.

Field number	V_{dp}	λ_D	HI
1	.1	.1	0.0011
2	.1	.1	0.0011
3	.1	.2	0.0022
4	.3	.3	0.0381
5	.2	.8	0.0398
6	.4	.6	0.2882
7	.4	.6	0.2882
8	.7	.2	0.2890
9	.4	.5	0.1304
10	.6	.7	0.5877
11	.7	.5	0.7247
12	.8	.3	0.7771
13	.7	.7	1.0140
14	.8	.6	1.5540
15	.8	.8	2.0722
16	.8	.8	2.0722
17	.9	.4	2.1208
18	.1	.9	0.0099
19	.8	.1	0.2590
20	.7	.3	0.0890

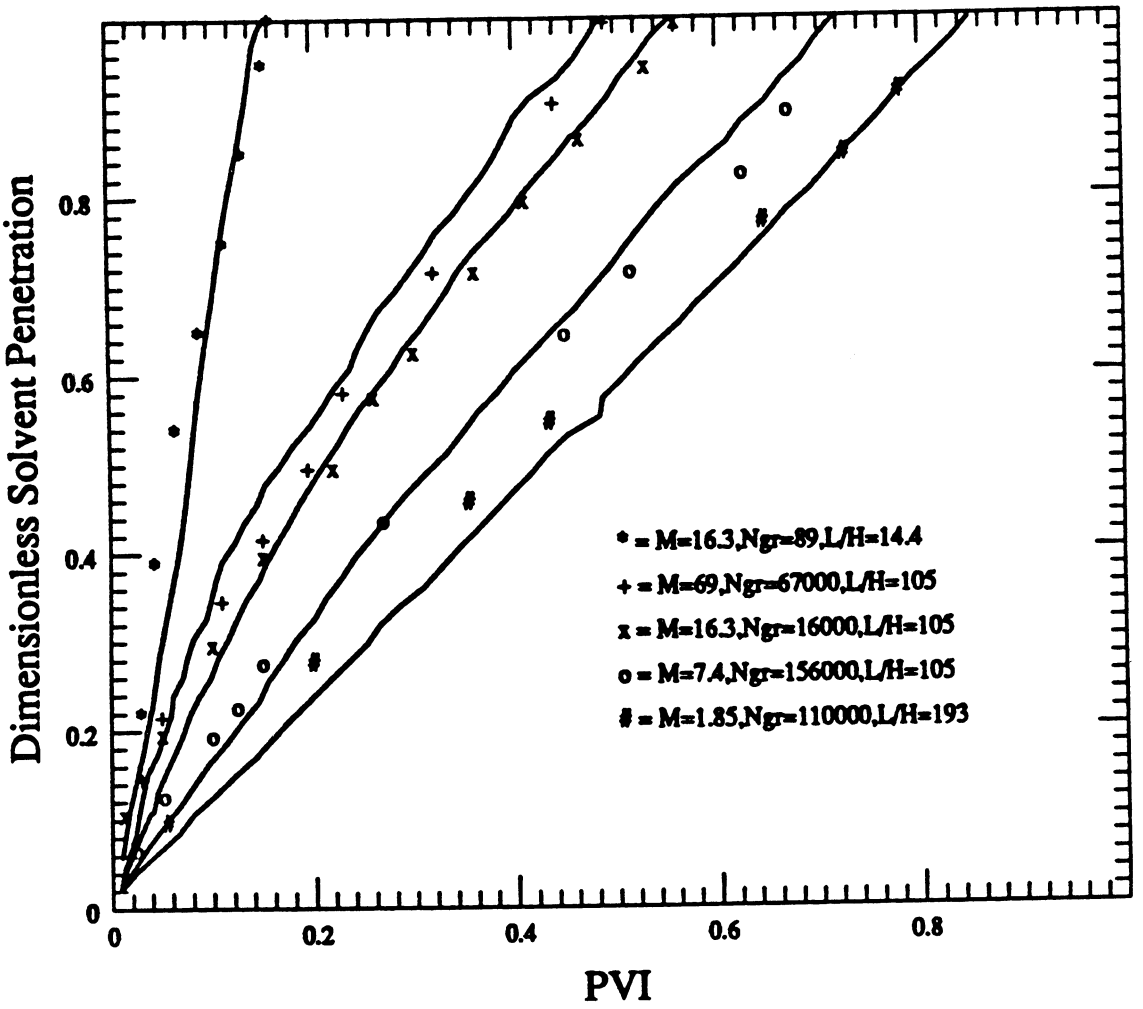

Fig. 4.1-9 Comparison of random-walk model results (with gravity included) with Blackwell's experimental results. Simulation predictions are shown as solid lines.

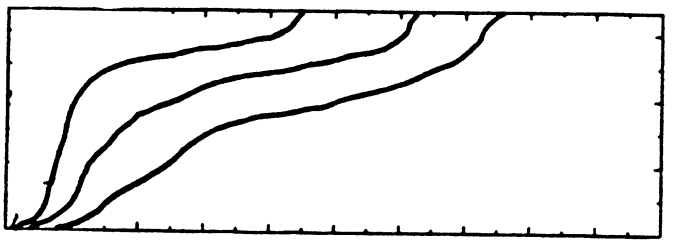

M=1.85, Ngr=89, L/H=3.1

a

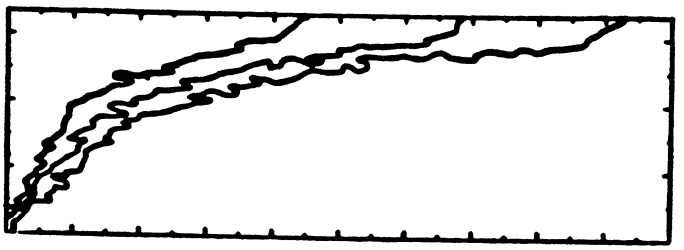

M = 16.3, Ngr = 929, L/H = 11.8

b

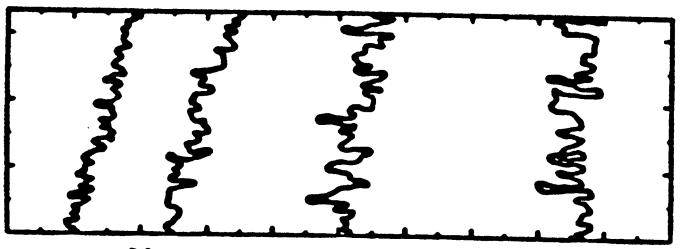

M = 16.3, Ngr = 16,015, L/H = 105.0

c

Fig. 4.1-10 Cross-sectional displacements for the conditions indicated showing .05 concentration contour line at different times.

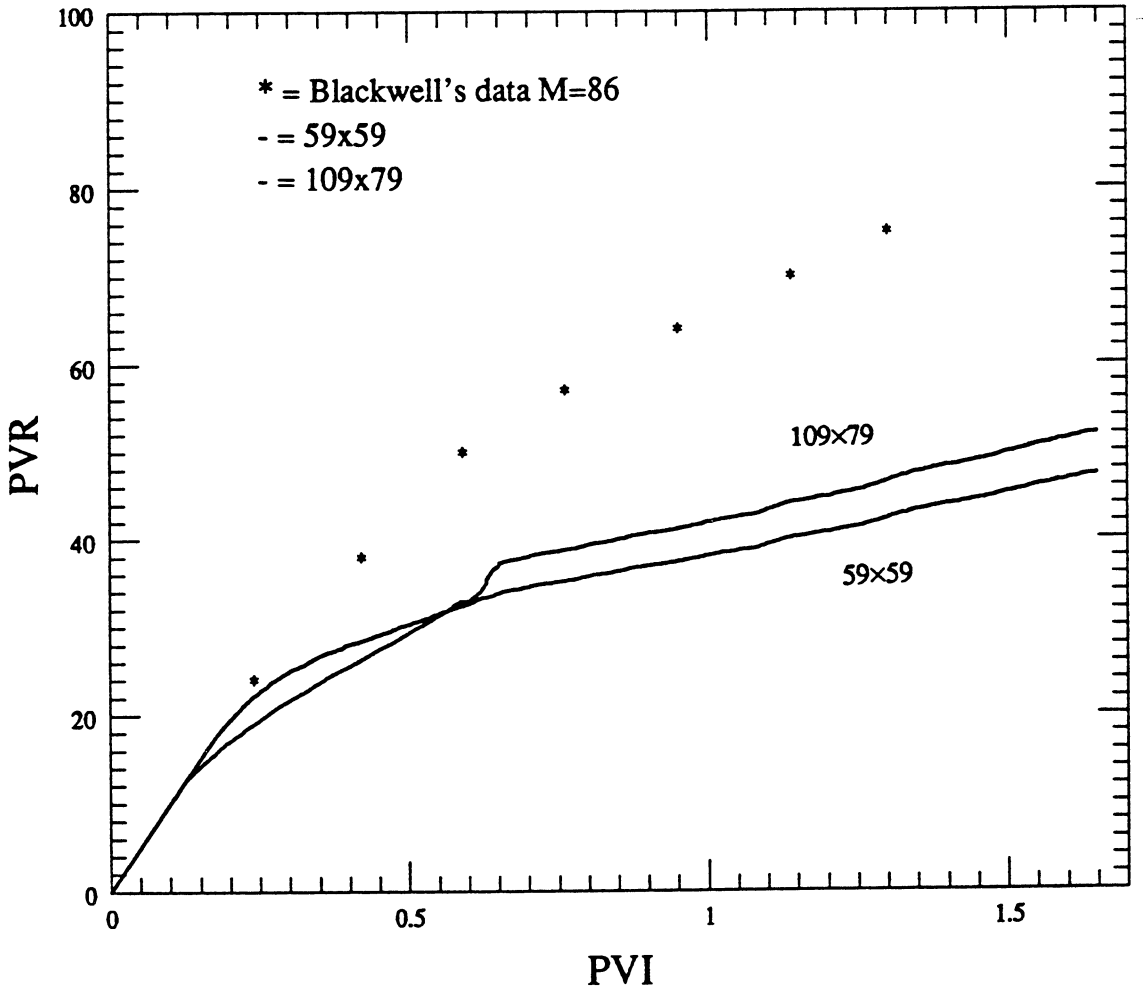

Fig. 4.1-11 Comparison of modified King model results with Blackwell's experimental results.

failure to reproduce experimental results was to be expected since the input dispersivities were also not recovered in unit mobility displacements as described previously. Thus, the inclusion of dispersion as an additional perturbation of the position of the streamline and saturation chosen for evolution by the probabilistic scheme is apparently not consistent with the convection-dispersion equation. For that reason, computations with the probabilistic model were abandoned.

4.1.3 Displacements in Homogeneous Porous Media.

Fig. 4.1-12 shows the appearance of the typical viscous fingers and their evolution with time. Note that due to storage capabilities of the contour plotter used here only the inner 50x50 grid blocks (60x60 grid simulated) are shown. For the case shown in Fig. 4.1-12 the flow velocity was 40 ft/day ($1.4\ 10^{-2}$ cm/s), the viscosity ratio was 10, and the longitudinal and transverse Peclet numbers were 1640 and 51000. At 0.1 PVI, approximately ten small fingers coexist. As injection proceeds, fingers of the more mobile fluid broaden, and the number of fingers is reduced. That behavior occurs because a finger slightly ahead of its neighbors quickly outruns them and shields them from further growth (Homsy 1987). In addition, the high speed flow in the finger generates transverse pressure gradients that cause the tips of fingers to spread, and tails of fingers to become narrower. The resulting complex crossflow patterns can cause fingers of different length to join together, leaving islands of original fluid surrounded by solvent. Thus, at 0.2 PVI, only four fingers remain. At 0.3 PVI, the four previously existing fingers have coalesced to form two large fingers. Simultaneously, the front of the combined fingers has spread and split into two or more new smaller fingers (Tan and Homsy 1988). After the split, one of these fingers outgrows the other and the whole sequence just described is repeated. Thus, the combined effects of spreading, tip-splitting, shielding and coalescence lead to quite complex two-dimensional concentration distributions in unstable displacements in homogeneous porous media.

Similar finger patterns are observed in the displacements with mobility ratios of 50 and 100 run at the same injection rate. As Fig. 4.1-12 shows clearly, fingering patterns well after initiation bear little resemblance to the patterns predicted by linear stability analysis. The wavelengths of fingers generated initially can be compared, however, with Gardner and Ypma's (1984) calculation of the most unstable wavelength at onset of fingering.

$$\lambda_c = 2^{5/2}\,\pi\,\frac{\mu_o + \mu_s}{\mu_o - \mu_s}\,\frac{D_T}{u} \qquad (4.1\text{-}16)$$

A spectral technique, applied in experimental methods (Sigmund et al. 1988), was used to determine the dominant Fourier wavelength of the viscous fingers. Details are given in Araktingi (1988). The finger widths obtained from the random-walk model are compared in Table 4.1-2 with the analytical results from linear stability theory. The numerical results are, on average, about 35% larger than the analytical results. They do, however, exhibit the same trends predicted by Eq. (4.1-16). The critical finger width increases with decreasing average interstitial velocity as expected from Eq. (4.1-16). The difference between the results can be explained as follows. The finger wavelengths measured with the random-walk model were obtained at times that are larger than those assumed in the linear stability analysis. The fingers obtained in the simulation are larger than those predicted by the linear theory because some spreading of finger tips has already taken place at the time that fingers were large enough to be examined in the simulation results. Thus, the simulation results are roughly consistent with the results of the linear analysis, and the differences are in the expected direction given the observed behavior of developing fingers.

A second example of fingering in a homogeneous porous medium is shown in Fig. 4.1-13, this time for M = 20 with other parameters the same. As in the case of the lower mobility

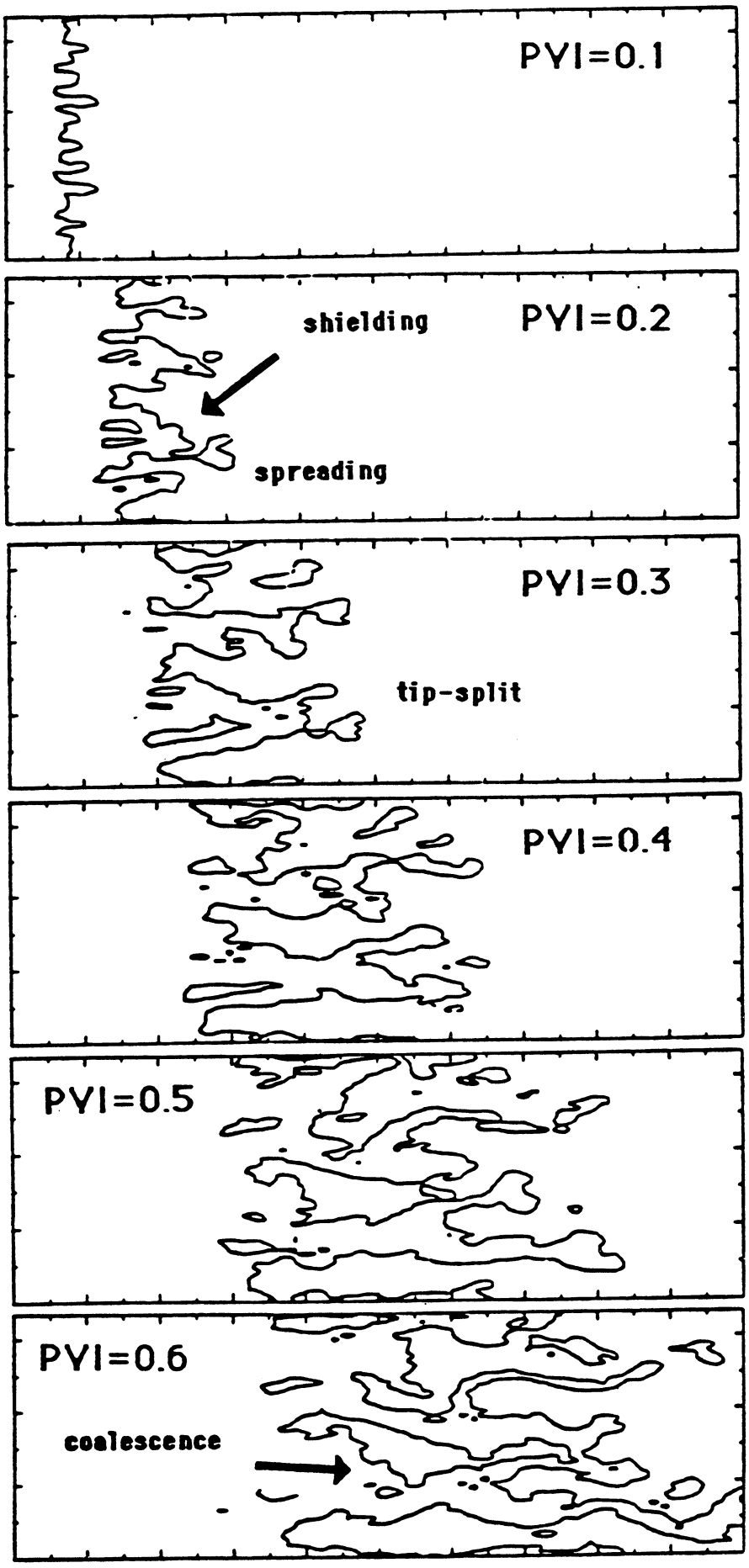

Fig. 4.1-12 Displacement for M = 10 and v = 40 ft/day in a homogeneous permeability field. The 0.2 concentration contour is shown.

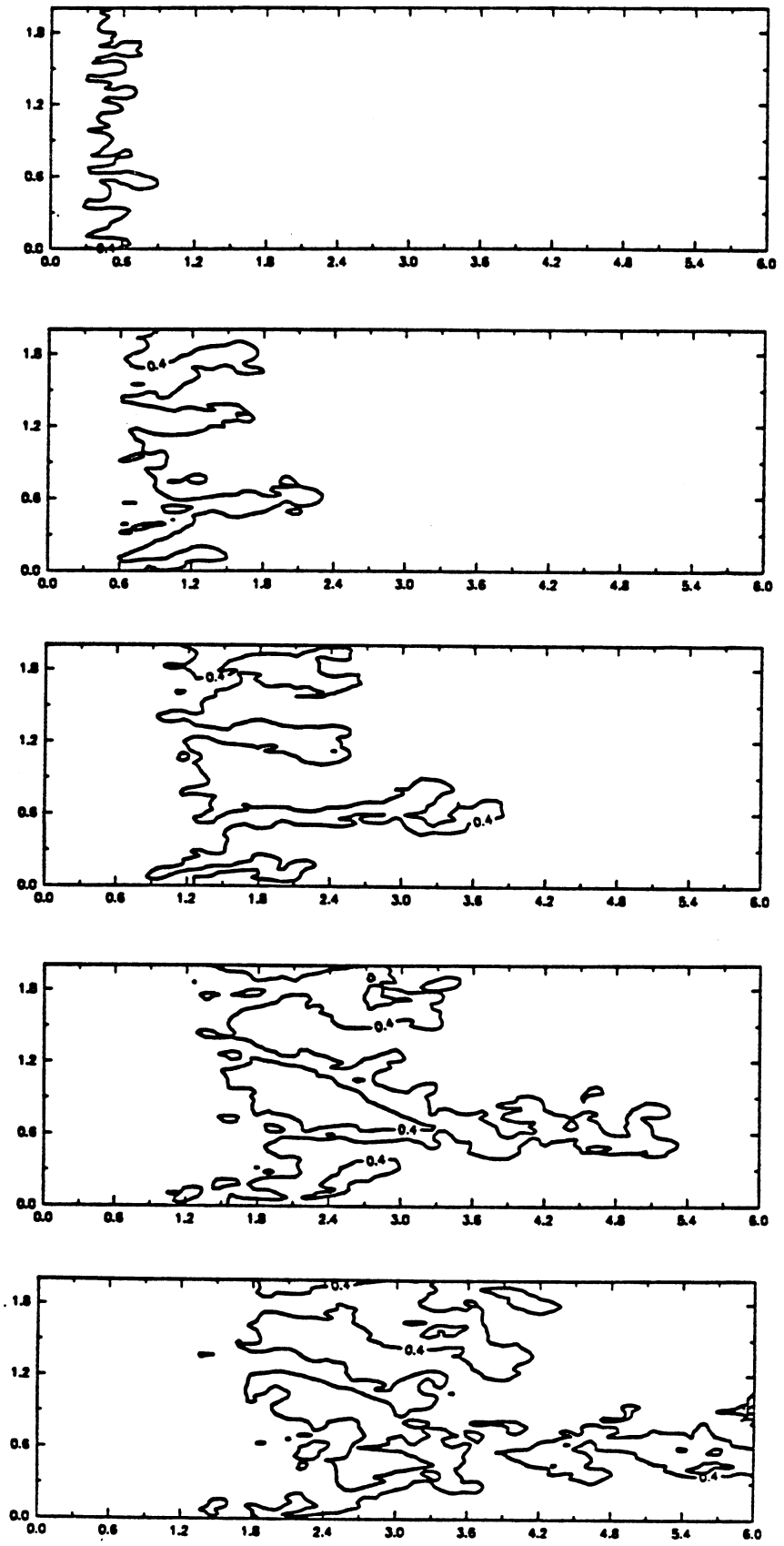

Fig. 4.1-13 Displacement for M = 20 and v = 40 ft/day in a homogeneous permeability field. The 0.4 concentration contour is shown.

ratio, the large number of fingers present at 0.1 PVI has dropped to four at 0.2 PVI. Broadening at finger tips is evident at 0.3 PVI, as is tip-splitting. Coalescence is demonstrated again at 0.4 PVI. Thus, the patterns described for M = 10 also apply at M = 20.

Comparison with Koval's Model

Koval (1963) proposed a very simple one-dimensional representation of the effects of viscous fingering based on the empirical observation that a given average concentration moves through the porous medium at roughly constant characteristic velocity. Koval then selected fractional flow and effective viscosity functions that produced good agreement with the experiments of Blackwell et al. (1959) when used in a Buckley-Leverett calculation. A similar approach has been used by several other investigators to represent the effects of fingering (Fayers 1988, Fayers and Newley 1988, Todd and Longstaff 1972). If Koval's assumption is correct, then a plot of the position of a fixed average concentration against time (or pore volume injected) should yield a straight line with a different slope for each concentration. Fig. 4.1-14 shows such a plot for the calculated displacement shown in Fig. 4.1-12. The concentrations shown in Fig. 4.1-14 were obtained by averaging arithmetically in the direction transverse to the mean flow. For clarity, only three concentrations (0.1, 0.5 and 0.9) are shown. Also shown are the characteristic lines calculated with Koval's model. Because of the chaotic nature of the fingers, an averaged concentration can have several positions at a given time, as Fig. 4.1-14 shows for C=0.5. Clearly the assumption of a single characteristic velocity can only be approximately satisfied. It cannot be strictly satisfied if specific concentrations can exist at more than one location.

Koval's assumption does not reflect accurately the behavior of averaged concentrations within the transition zone because the one-dimensional form of the model cannot represent the effects of spreading, tip-splitting and coalescence that lead to the concentration fluctuations shown in Fig. 4.1-14. It is possible, however, to construct an average straight line for concentrations in the middle of the 0.1 to 0.9 range that agrees roughly with the overall trend. It is this fact that is responsible for the success of Koval's model in it's representation of recovery data. Fig. 4.1-14 also shows that the overall length of the transition zone grows approximately linearly in time, as the rough linearity of the characteristic curves for the 0.1 and 0.9 concentrations indicates. Thus, for this flow system, Koval's assumption is reasonably consistent with the arrival times at the outlet of the leading and trailing edges of the transition zone.

4.1.4 Displacements in Heterogeneous Porous Media.

To study unstable displacements in heterogeneous porous media, permeability fields were generated stochastically. The permeability variations were created based on the assumption that permeability is a regionalized variable with second order stationarity (Journel and Huijbregts 1978). That is, the mean of the distribution is assumed to be independent of location and spatial correlation between any two samples is assumed to depend only on the distance separating them.

If the permeability distribution is log normal, the Dykstra-Parsons coefficient (1950), V_{dp}, can be used to describe the permeability variation

$$V_{dp} = \frac{k_{50} - k_{84.1}}{k_{50}} = 1 - e^{-\sigma_{lnk}} \qquad (4.1\text{-}17)$$

To express spatial correlation, a correlation length scale, λ, was introduced. The degree of correlation between the permeabilities at two points decreases as the distance separating them increases. When the distance becomes greater than the correlation length scale, the

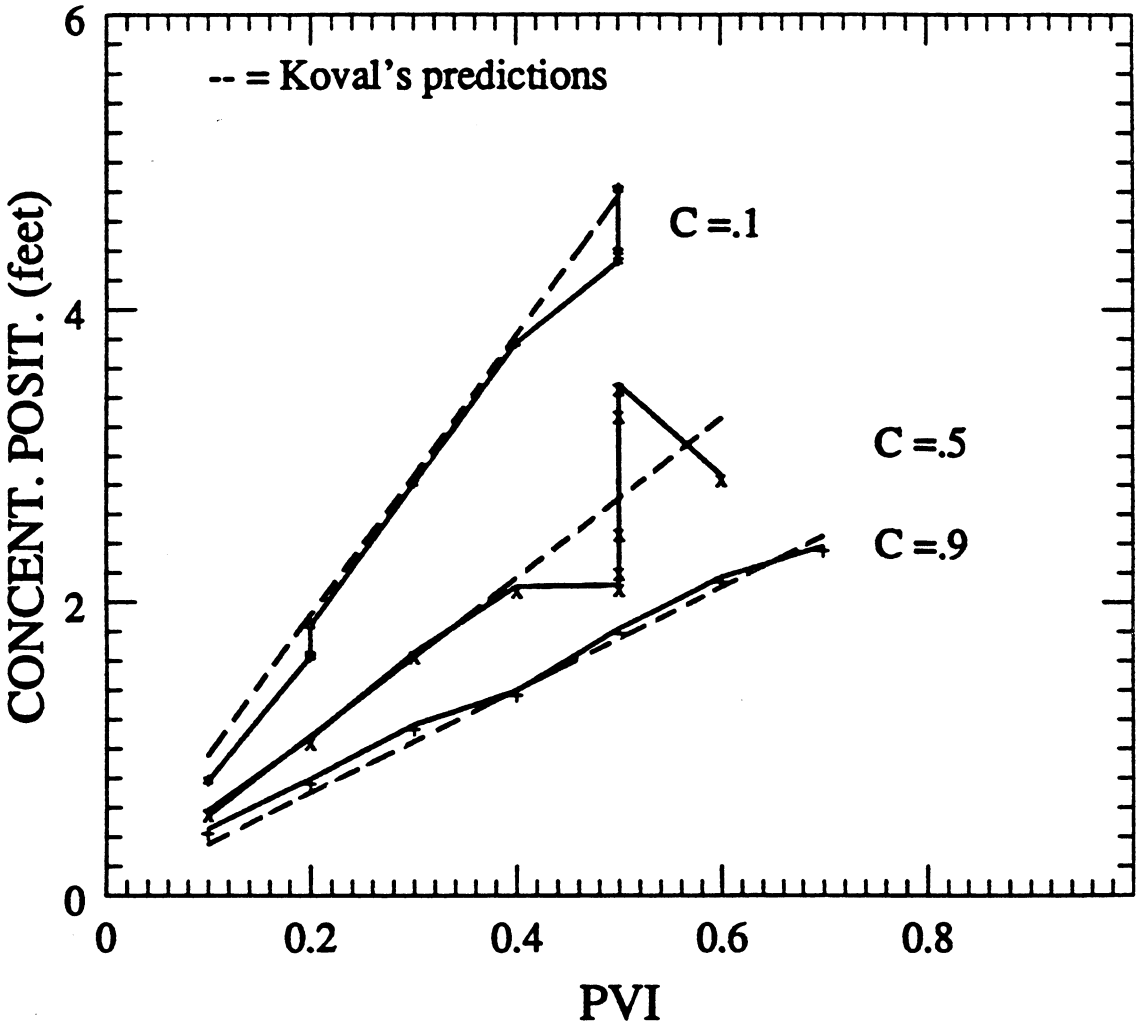

Fig. 4.1-14 Comparison of positions of averaged concentrations with Koval's model.

permeabilities are uncorrelated. The correlation length is made dimensionless by normalizing it as

$$\lambda_D = \frac{\lambda}{L} \tag{4.1-18}$$

where L is the length of the system.

The moving average method (Luster 1984, Mishra 1987) was used to generate a correlated field. A more detailed description of the technique appears in Section 5.1. Using an average permeability of 100 md. with Dykstra-Parsons coefficients ranging between 0.1 and 0.9 and correlation lengths also ranging between 0.1 and 0.9, twenty permeability fields were generated using the same seed number for each field. All the simulations were performed with transverse and longitudinal Peclet numbers of 51000 and 1640, the same values as were used in the simulations of the homogeneous laboratory-scale displacements described above. For the simulations for heterogeneous permeability fields, the mobility ratio was fixed at 20.

Heterogeneity Index

In the discussion that follows, we use a heterogeneity index (HI) (Mishra 1987, Gelhar and Axness 1981) to characterize the permeability fields. The heterogeneity index is defined as

$$HI = \sigma^2_{ln(k)}\, \lambda_D \tag{4.1-19}$$

a convenient measure of the heterogeneity, though there are undoubtedly other measures that also have useful properties. This parameter increases with the variance of the log normal permeability distribution ($\sigma^2_{ln(k)}$) and the correlation length (λ_D). Therefore, it combines the variability and the spatial continuity of the permeability field. The rationale behind the choice of $\sigma^2_{ln(k)}\, \lambda_D$ as the heterogeneity index is outlined in Section 5.2. This parameter ranged from zero to 4.8 in the simulations discussed below. The heterogeneity indices of the permeability fields used in the simulations are shown in Table 4.1-3. It should be noted that fields with different values of $\sigma_{ln(k)}$ and λ_D can still have the same heterogeneity index. Permeability fields with correlation lengths greater than 1.0 were not considered.

Qualitative Validation

Fluid flow visualization experiments have been recently conducted utilizing X-ray computed tomography (CT) methods (Withjack 1987). The images of fluid flow patterns obtained during miscible core floods with the CT scanner serve as a qualitative benchmark for the random-walk model for displacements in heterogeneous porous media. Two displacements were simulated at mobility ratios of one and 69 in the permeability field shown in Fig. 4.1-15. An approximate representation of the permeability field was obtained by observing the preferential flow paths that appeared in a unit mobility displacement and by taking surface permeability measurements. The resulting finger patterns are presented in Figs. 4.1-16 and 4.1-17. As expected, for unit mobility ratio (Fig. 4.1-16), three fingers develop that follow the higher permeability streaks until breakthrough occurs. However, at a mobility ratio of 69, the initial three fingers coalesce into two large fingers at a later stage of the coreflood. Similar behavior was observed in the CT scanner images, as Figs. 11-14 reported by Withjack (1987) show. Hence, the random-walk model also captures the physical mechanisms of flow in heterogeneous porous media, at least qualitatively.

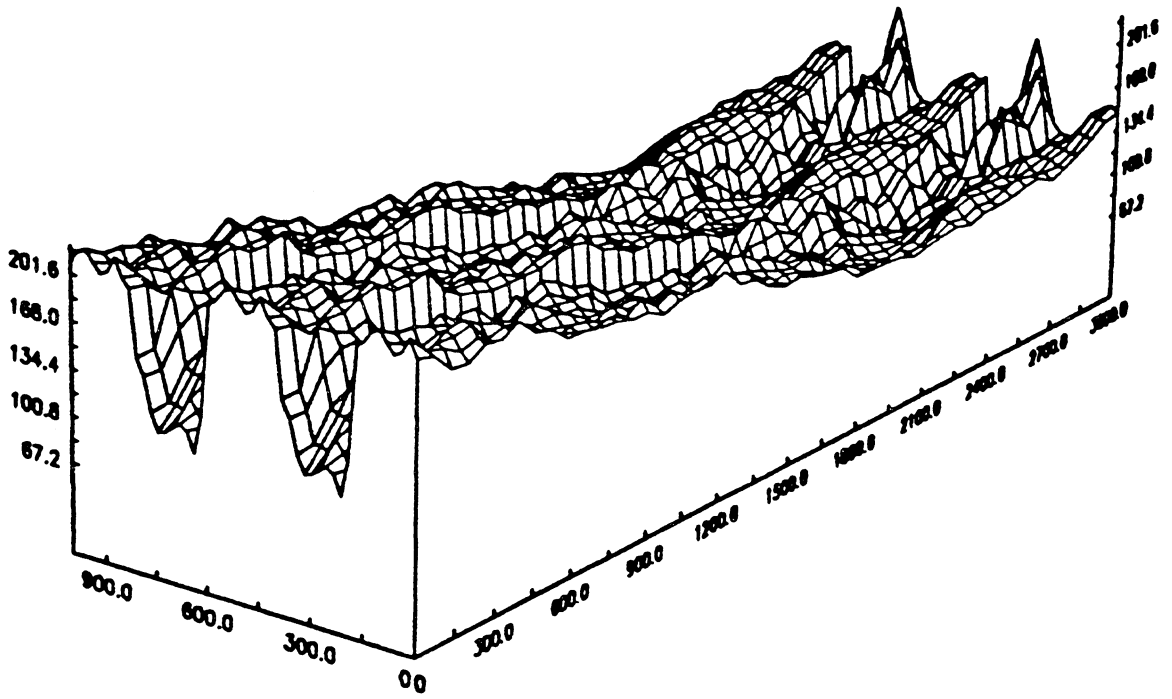

Fig. 4.1-15 Estimated permeability field for flow visualization experiments of Withjack (1987).

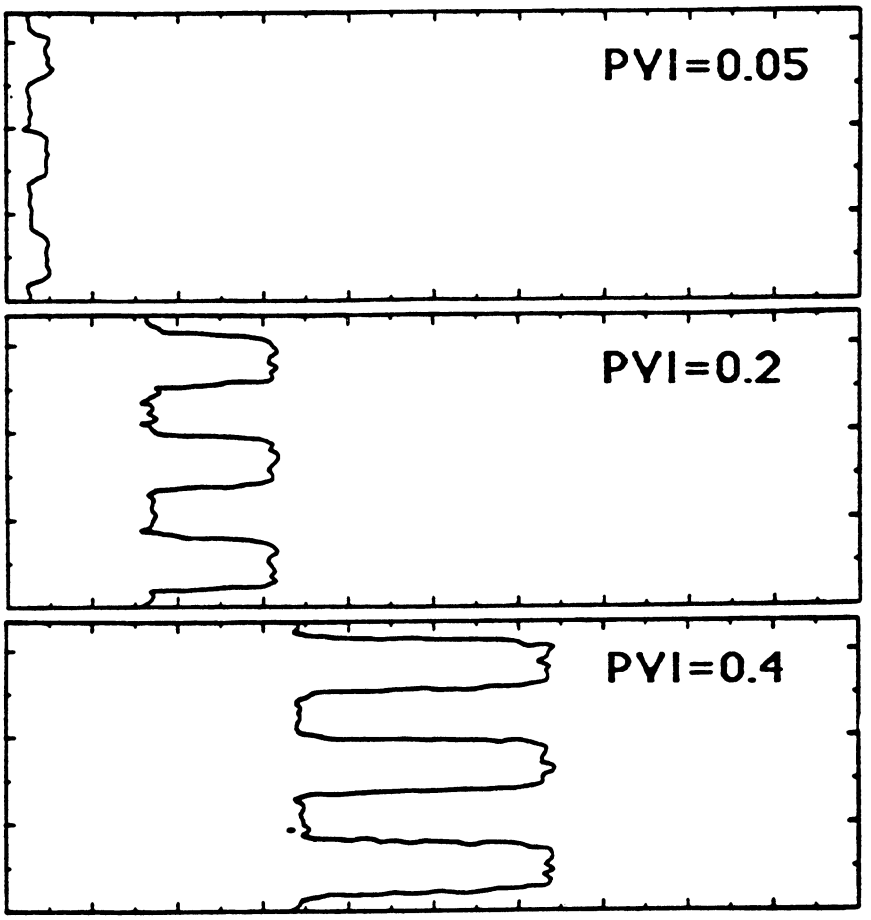

Fig. 4.1-16 Displacement in the permeability field of Fig. 4.1-15 for M = 1.0 and v = 40ft/day. The 0.2 concentration contour is shown.

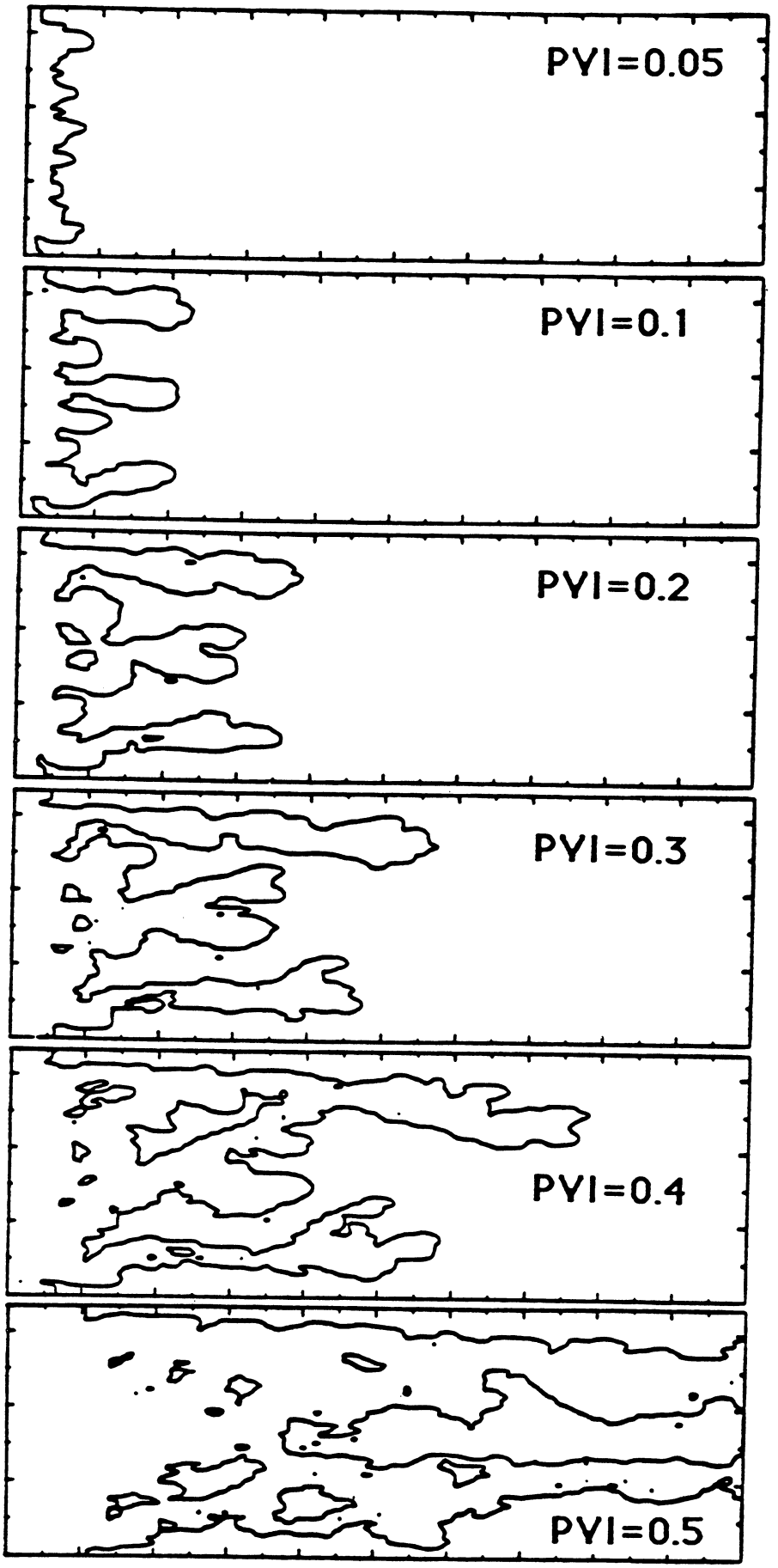

Fig. 4.1-17 Displacement in the permeability field of Fig. 4.1-15 for M = 69 and v = 40ft/day. The 0.2 concentration contour is shown.

Flow Behavior

Two distinct types of behavior were observed for the limits of low HI and high HI at a mobility ratio of 20. For permeability fields with HI less than about 0.3, finger patterns were similar to those observed in homogeneous displacements. Fig. 4.1-18 shows calculated fingering behavior for a permeability field with HI = 0.0011. The permeability field itself is shown in Fig. 4.1-19. Spreading, tip-splitting, shielding and coalescence create complex concentration distributions for flow at adverse mobility ratios. That behavior is observed when either the variance ($\sigma^2_{ln(k)}$), or the correlation length is small (Gelhar and Axness 1981). Plots of finger patterns for all displacements listed in Table 4.1-3 are given by Araktingi (1988).

For examples at the low end of the HI scale (HI < 0.1) several permeability fields were generated with correlation lengths close to 1 and small values of $\sigma^2_{ln(k)}$. Another group of permeability fields was also generated with small correlation length and high variance. In both cases, the resulting fingers exhibited behavior typical of displacements in homogeneous media. That behavior is not really surprising. For systems with high variance but low λ_D, permeability variations near the inlet aid the initiation of fingers, but zones of high permeability do not persist, and viscous effects take over in subsequent finger development. If the variance is low on the other hand, the permeability varies only slightly, and it really does not matter whether it is correlated. Viscous effects still dominate. Numerical experiments indicate that fingering behavior is more sensitive to the level of transverse dispersion in systems with low HI, presumably because it controls the size of fingers that are damped initially.

For displacements in permeability fields with HI greater than about 0.5, the finger pattern was determined by the permeability field. Fig. 4.1-20 shows finger patterns for a displacement in a permeability field with HI = 2.12 shown in Fig. 4.1-21. When both $\sigma^2_{ln(k)}$ and λ_D are relatively large, it is likely that resulting permeability realizations will include correlated high and low permeability zones. The preferential flow paths induce high flow velocities even when at unit mobility ratio. When M > 1, the flow simply follows the same path, though the difference in velocity between fast and slow zones is increased. In Fig. 4.1-20, for example, the single finger that develops follows the high permeability streak near the bottom edge of the flow field. While breakthrough occurred at 0.132 PVI for M = 1, however, it occurred somewhat earlier at 0.116 PVI for M = 20.

Another example of unstable flow in a heterogeneous porous medium is shown in Fig. 4.1-22, with the corresponding spatial permeability distribution shown in Fig. 4.1-23. In this case, there is a high permeability streak near the central longitudinal axis. The injected fluid follows the high permeability streak, and no tip-splitting is observed until the injected fluid reaches the low permeability zone near the outlet. Even then the path followed is set by the highest permeabilities in the region. Thus, when the permeability is sufficiently variable and sufficiently correlated, the fingering pattern appears to be induced by the permeability field.

Additional evidence that the permeability distribution can determine the flow pattern is shown in Fig. 4.1-24. The corresponding spatial permeability distributions are shown in Figs. 4.1-25, 4.1-26 and 4.1-27. Fig. 4.1-24 compares concentration distributions at breakthrough for displacements at M = 1 and M = 20 for several permeability fields. For the displacements at high HI, the flow pattern was essentially the same for both mobility ratios. At low HI, the patterns were completely different, as viscous effects dominated the formation of fingers. The limited number of simulations performed here suggest that the transition from low-HI, homogeneous flow to high-HI, permeability-dominated flow begins at about HI = 0.25-0.30 when the mobility ratio is 20. For example , the flow behavior shown in Fig. 4.1-24a (HI = 0.25) is clearly dominated by viscous effects. The finger pattern is nearly uniform for the unit mobility dispacement, but is badly fingered for M = 20. The corresponding permeability field in Fig. 4.1-25 is highly variable, but the correlation length is low, and hence viscous effects dominate. For the permeability realization shown in Fig. 4.1-26, however, the unit mobility pattern in Fig. 4.1-24b is quite similar to that of M = 20, though some viscous fingering is also apparent. At HI = 0.77 (Figs. 4.1-25c and 4.1-27), however, it is clear that the permeability

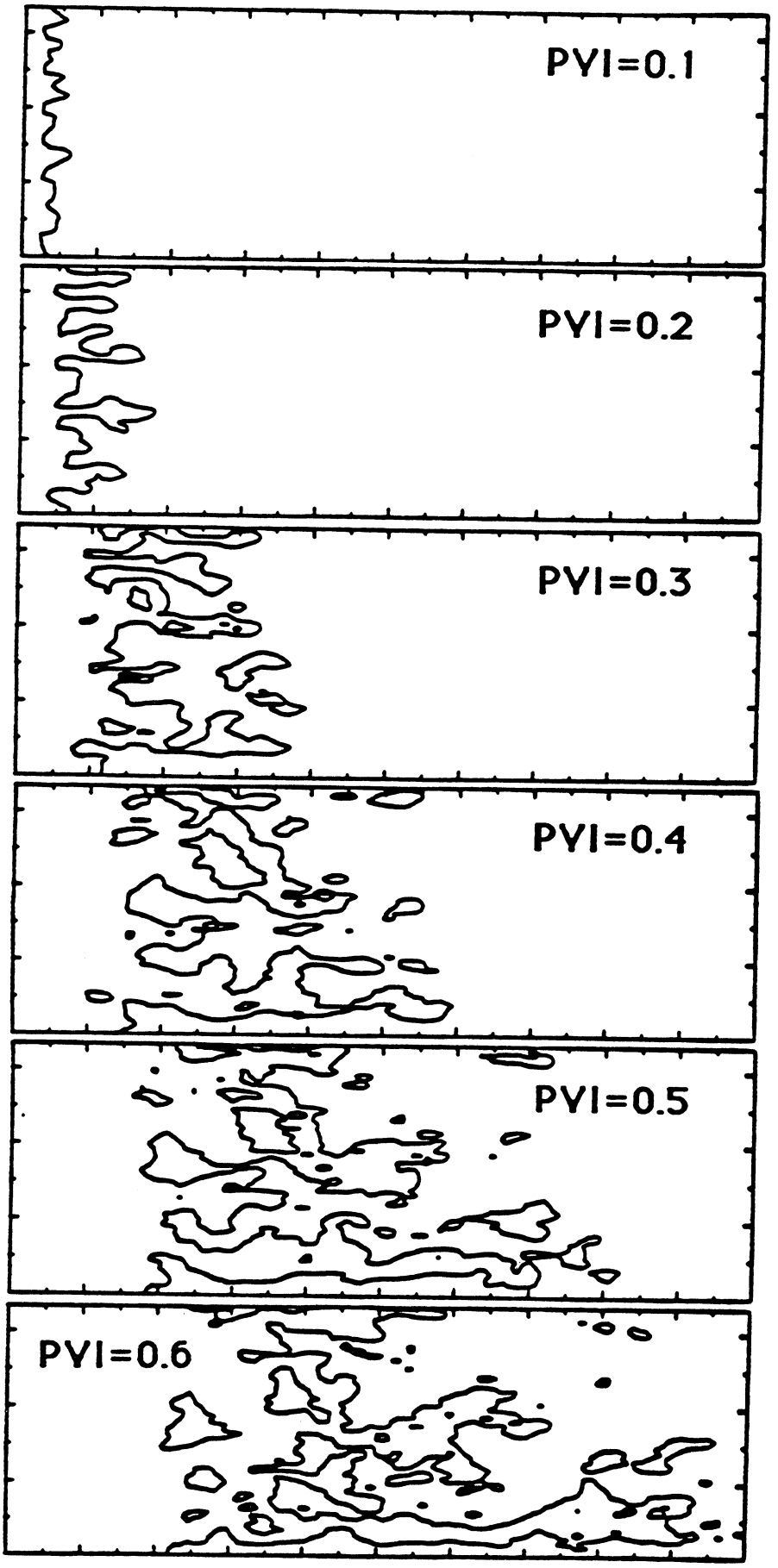

Fig. 4.1-18 Displacement in a heterogeneous permeability field with HI = 0.0011 shown in Fig. 4.1-19 for M = 20 and v = 40ft/day. The 0.2 concentration contour is shown.

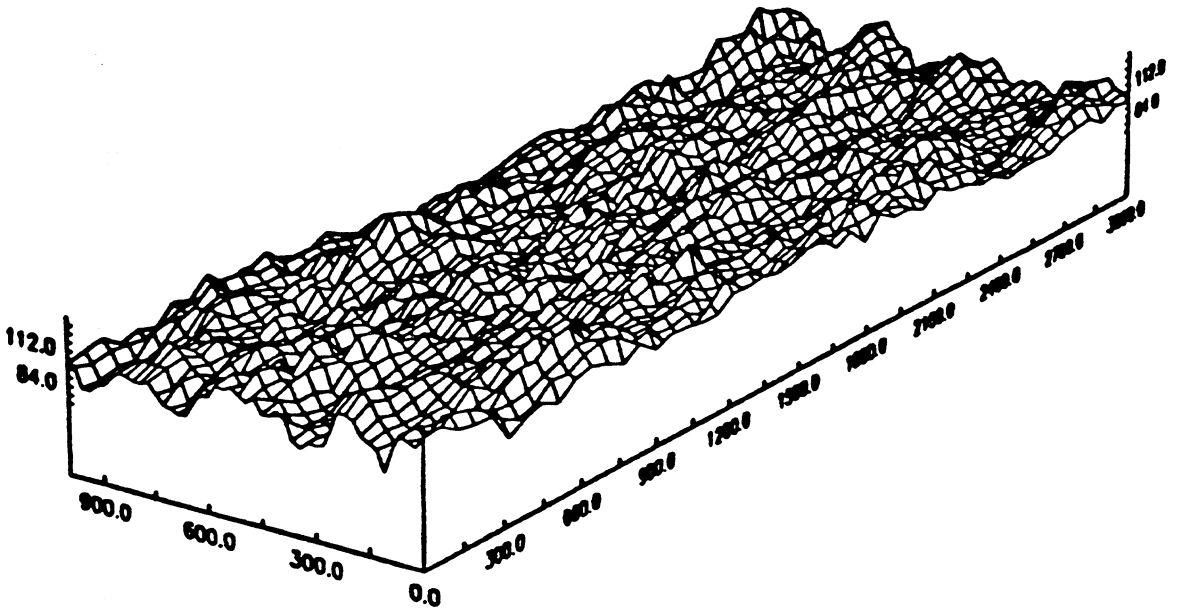

Fig. 4.1-19 Heterogeneous permeability field with HI = 0.0011 ($V_{dp} = 0.1$, $\sigma^2_{ln(k)} = 0.0111$, $\lambda_D = 0.1$).

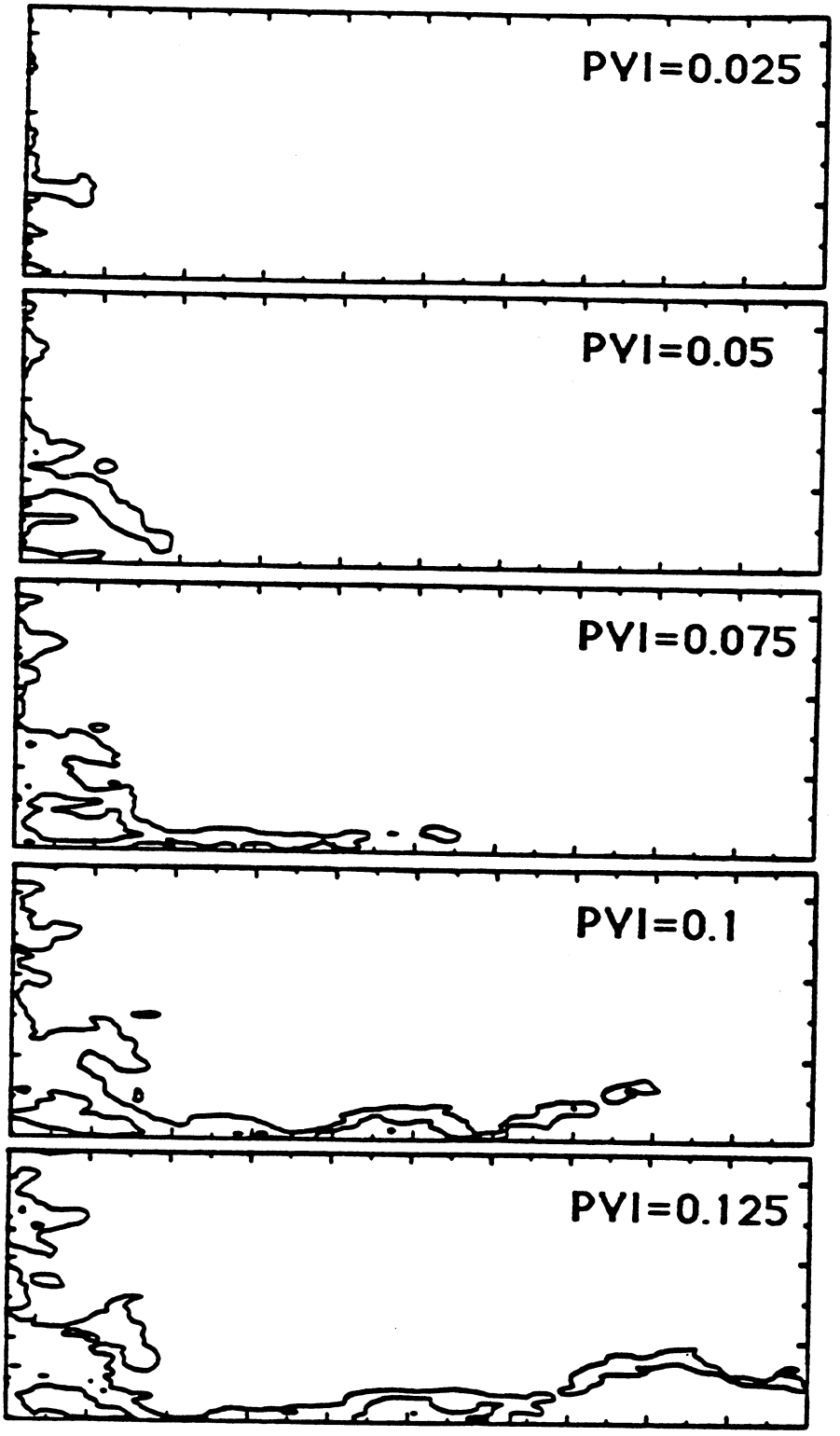

Fig. 4.1-20 Displacement in a heterogeneous permeability field with HI = 2.12 shown in Fig. 4.1-21 for M = 20 and v = 40ft/day. The 0.2 concentration contour is shown.

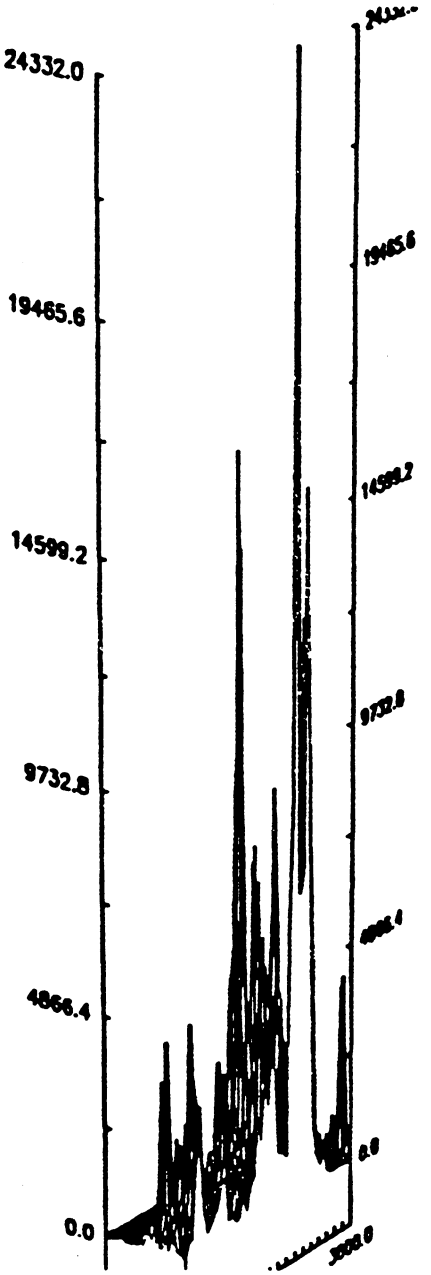

Fig. 4.1-21 Heterogeneous permeability field with HI = 2.12 ($V_{dp} = 0.9, \sigma^2_{ln(k)} = 5.30, \lambda_D = 0.4$).

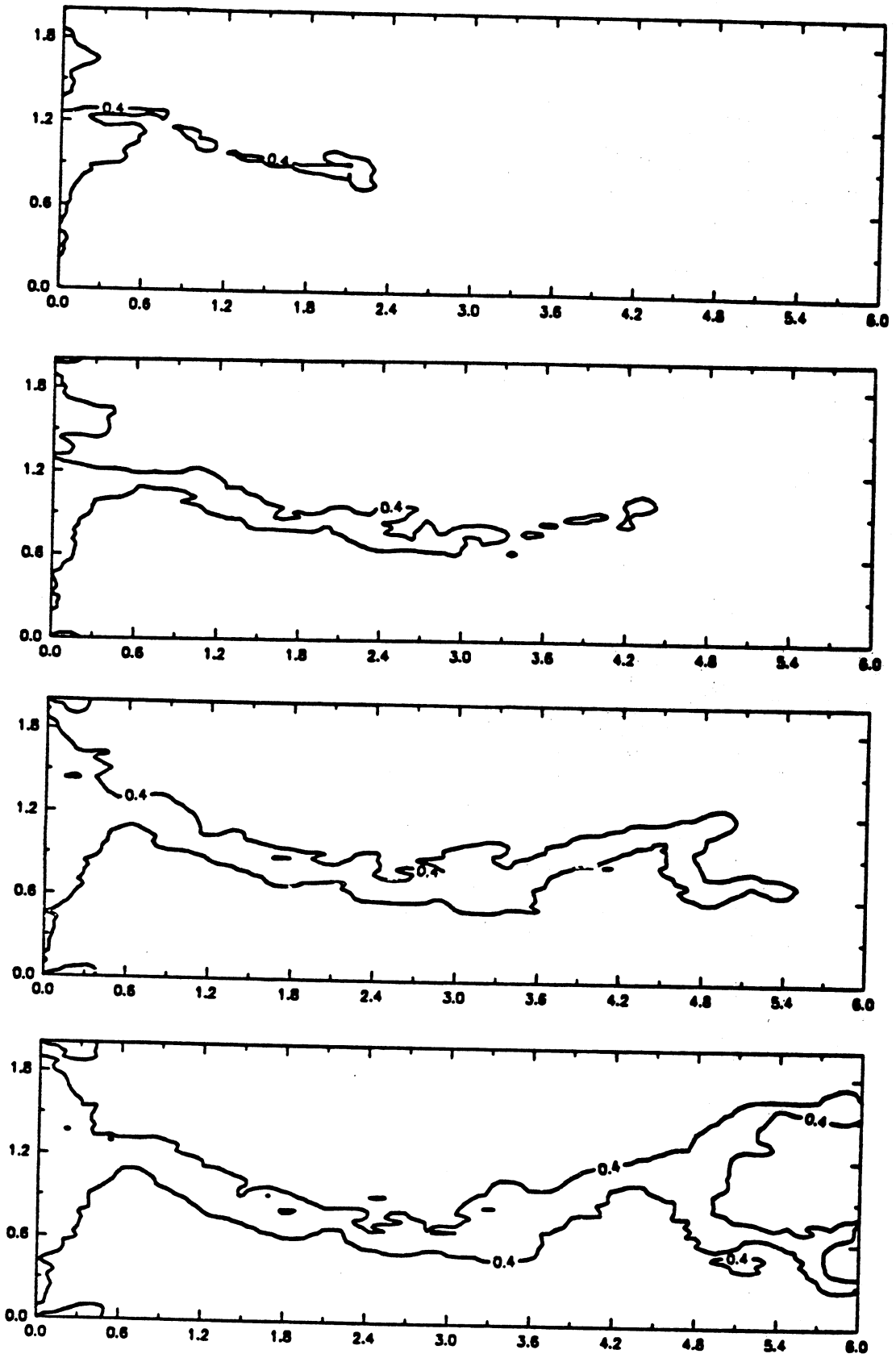

Fig. 4.1-22 Displacement in heterogeneous permeability field with HI = 2.1 for M = 20 and v = 40ft/day. The 0.4 concentration contour is shown.

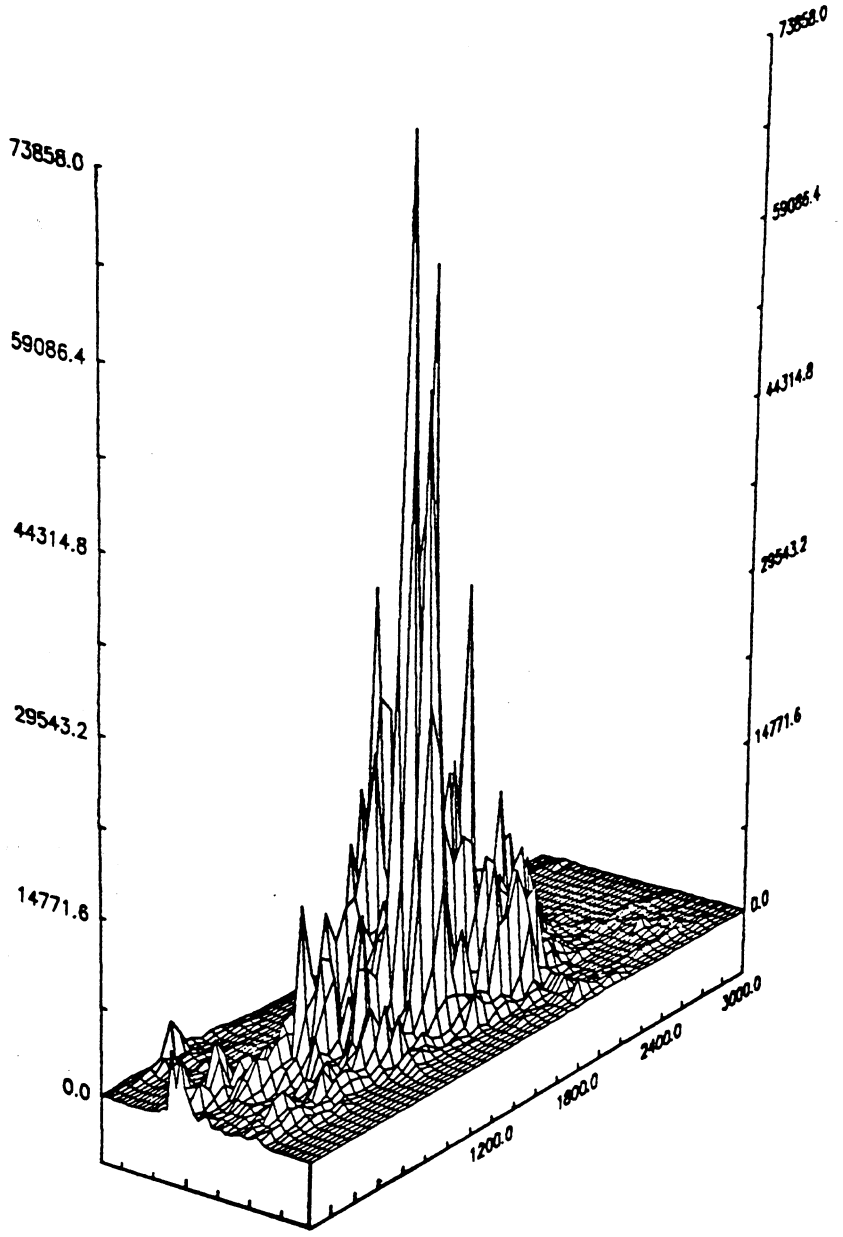

Fig. 4.1-23 Heterogeneous permeability field with HI = 4.77 (V_{dp} = 0.9,$\sigma^2_{ln(k)}$ = 5.30, λ_D = 0.9).

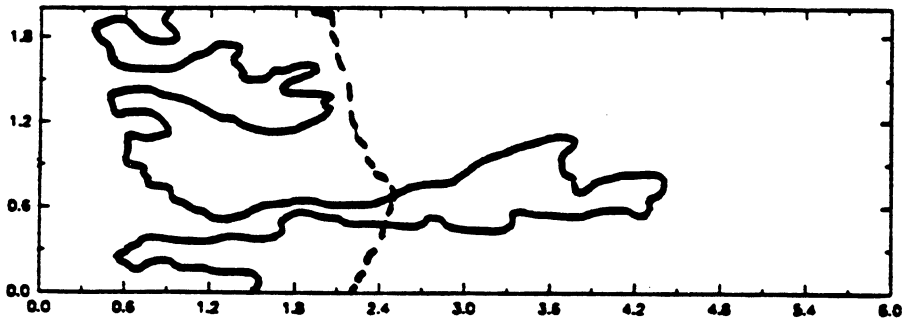

a. Displacement in Permeability Field #19 with HI = 0.259.

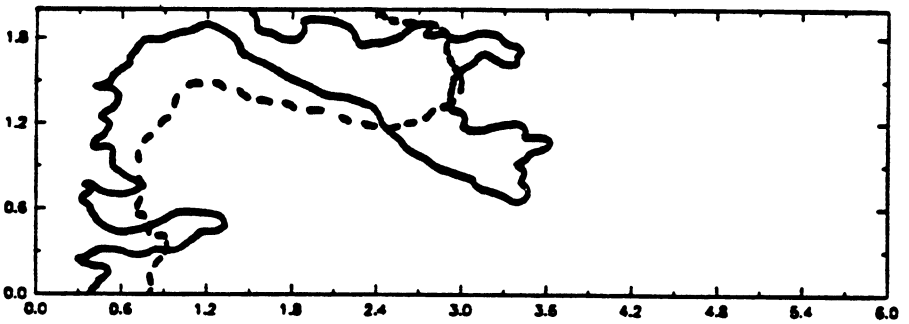

b. Displacement in Permeability Field #7 with HI = 0.288.

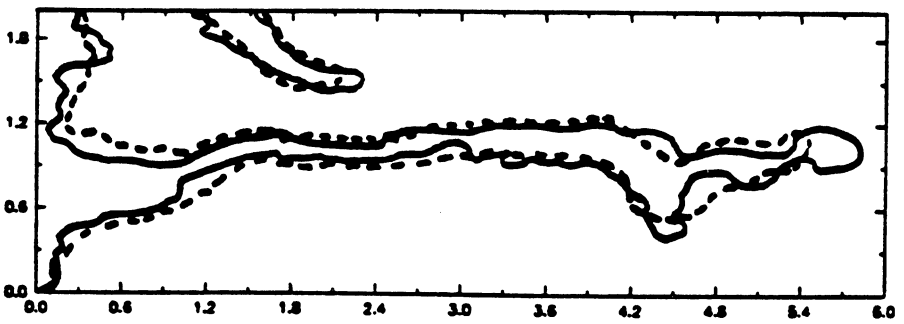

c. Displacement in Permeability Field #11 with HI = 0.725.

Fig. 4.1-24 Comparisons of displacements for M = 1 (dashed line) and M = 20 (solid line) for three permeability fields at 0.2 PVI. The 0.2 concentration contour is shown. Permeability fields are shown in Figs. 4.1-25, 4.1-26 and 4.1-27.

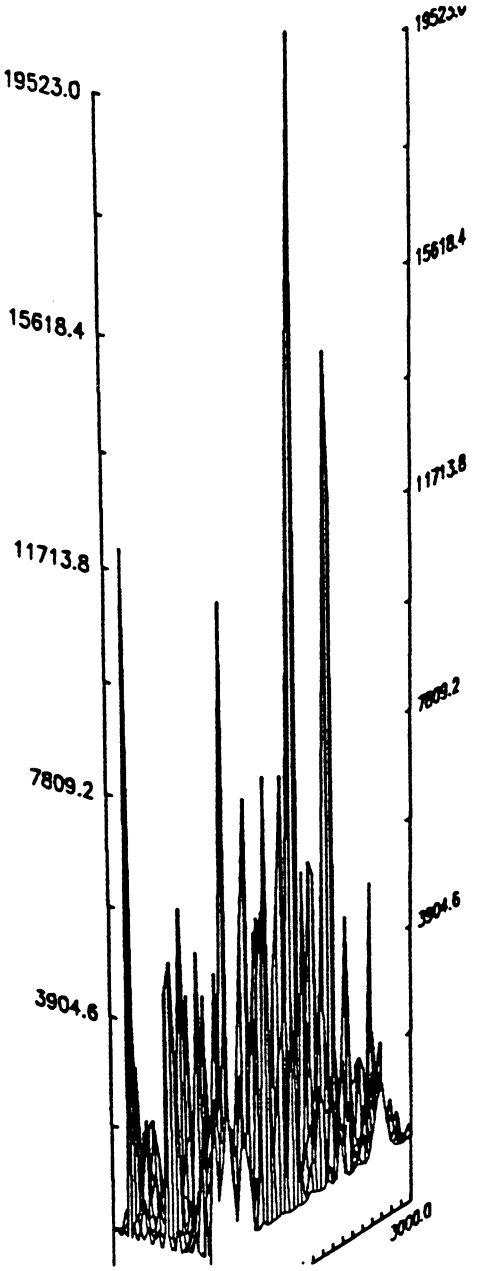

Fig. 4.1-25 Permeability field with HI = 0.25 for the displacements of Fig. 4.1-24a ($V_{dp} = 0.8, \sigma^2_{ln(k)} = 2.590, \lambda_D = 0.1$).

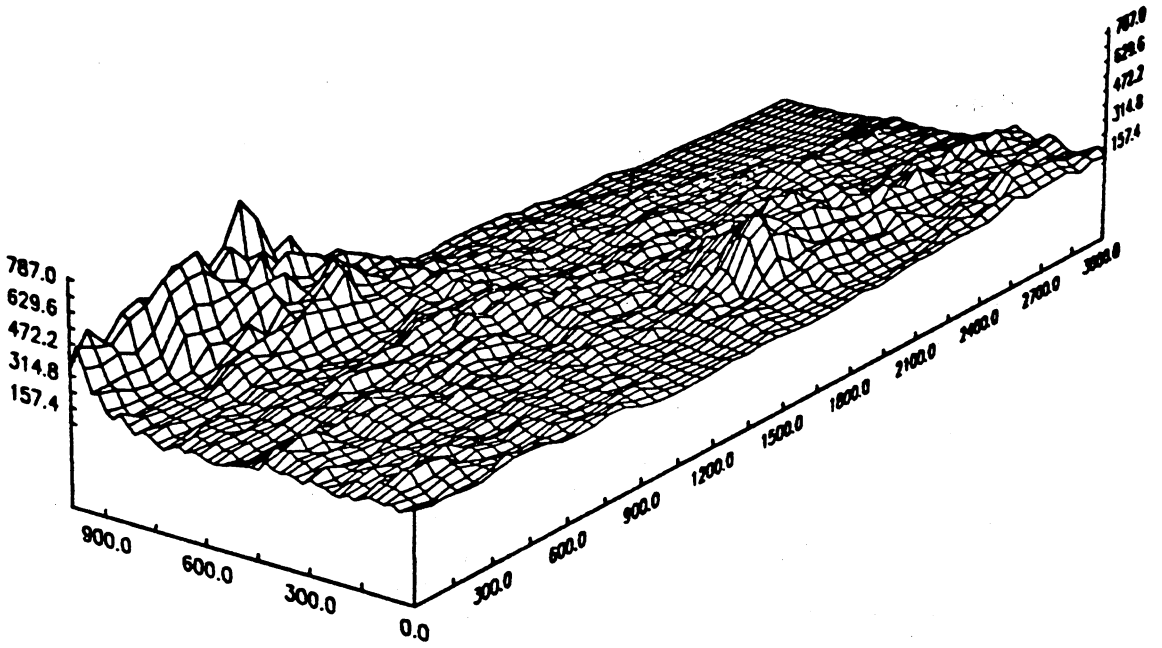

Fig. 4.1-26 Permeability field with HI = 0.288 for the displacements of Fig. 4.1-24b ($V_{dp} = 0.4, \sigma^2_{ln(k)} = 2.61, \lambda_D = 0.6$).

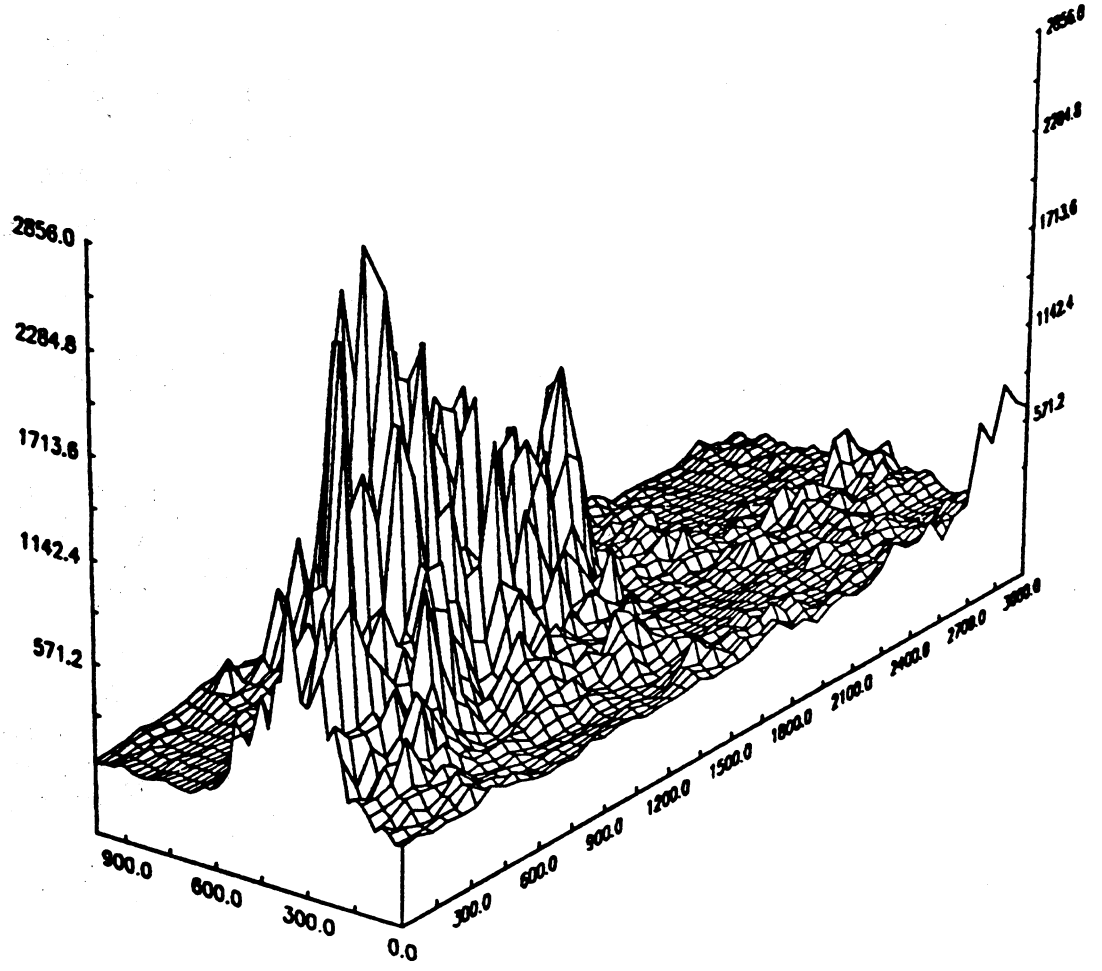

Fig. 4.1-27 Permeability field with HI = 0.725 for the displacements of Fig. 4.1-24c ($V_{dp} = 0.7$, $\sigma^2_{ln(k)} = 1.450$, $\lambda_D = 0.5$).

distribution dominates finger formation. In that case the finger patterns are nearly identical for both mobility ratios.

For HI's above about 0.5 the probability of preferential flow paths is high enough that permeability-dominated fingering is very likely. For the transition region $0.3 < HI < 0.5$, the fingering pattern is likely to be dependent on the particular permeability realization. Thus, the transition from low HI to high HI behavior is certainly not a sharp one. In addition, permeability distributions that are not log-normally distributed or that have different correlation lengths in the longitudinal and transverse directions, for example, undoubtedly show different transition behavior, and some dependence of the transition on mobility ratio is also likely. In any case, the exact value of HI at which the transition begins is less important than the indication that if the permeability is sufficiently variable and sufficiently correlated, it will dominate finger formation.

Simulations for heterogeneous permeability fields were also compared with predictions of Koval's model, which represents the effects of heterogeneity by a factor determined from the time of breakthrough in a unit mobility displacement. When the HI was small, the agreement obtained was good, as Fig. 4.1-28 shows. Even at moderately high values of HI, agreement was still reasonable, as Fig. 4.1-29 indicates for permeability field #11 with HI = 0.725. When the HI was large, however, agreement was poor. Fig. 4.1-30 illustrates the poor agreement for permeability field #16 with HI = 2.072. Thus, Koval's heterogeneity factor does represent well the effect of high correlation length in the permeability field.

Fingering at Field Scale.

The simulations described so far were performed for laboratory-scale displacements, though the flow rates and model dimensions used by Blackwell et al. (1959) were meant to mimic field-scale displacements. In principle, simulations of larger scale displacements could be accomplished simply by increasing the number of grid blocks. In effect, each grid block represents the same physical length in small or large scale simulations. In practice, the size of the flow field that can be simulated is limited by the size memory of the computer used and by the accompanying increase in run time. Another possibility is to use the same number of grid blocks but allow each grid block to represent a larger physical length. This approach is based on the assumption that the effect of variations in permeability at scales smaller than a grid block can be represented by a dispersion coefficient. Such an assumption is undoubtedly questionable for some if not many reservoir settings. It is reasonable only if the correlation length for subgrid variation is a small fraction of the grid block length. Field studies have shown that dispersivity (determined by fitting tracer test data to the one-dimensional convection-dispersion equation) increases with distance from the injection point as the displacing fluid encounters successively larger scales of heterogeneity (Lallemand-Barres and Peaudecerf 1978). Modeling a displacement over a typical interwell distance of 1500 feet with sixty grid blocks results in blocks that are 25 feet in length. In such a case, a longitudinal dispersivity of 3.3 feet was estimated from data reported by Lallemand-Barres and Peaudecerf (1978) to represent velocity variations at length scales less than 25 feet. In order to maintain the same ratio (30) of longitudinal to transverse dispersivity as in the laboratory scale simulations, the transverse dispersivity was set to 0.11 feet. The average interstitial velocity used was one foot per day, an order of magnitude typical of many reservoir floods. The resulting longitudinal and transverse Peclet numbers were 1610 and 49500, values very close to those appropriate at the laboratory scale. Additional simulations with those data confirmed that finger patterns and recovery results were essentially identical to the laboratory-scale simulations for the same permeability fields. Thus under the very restrictive assumptions that (1) small-scale variation in permeability can be represented by a dispersivity and (2) the permeability distribution is appropriate to the larger-scale flow, the results presented here for homogeneous and heterogeneous permeability fields can be taken to represent flow at field-scale.

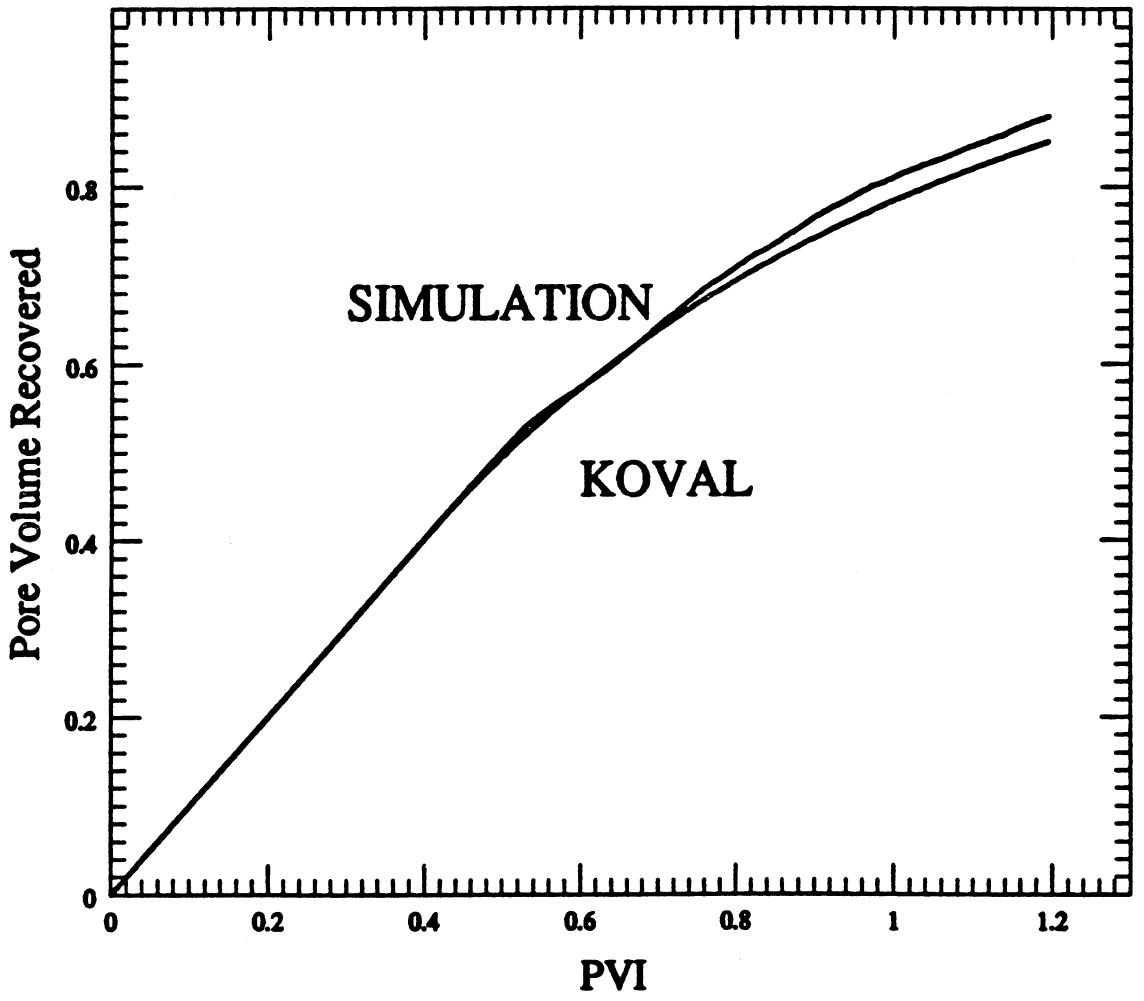

Fig. 4.1-28 Comparison of Koval's prediction with random-walk model's results. Recoveries are for displacements with M = 20, v = 40 ft/day in permeability field #1 (HI = 0.0011).

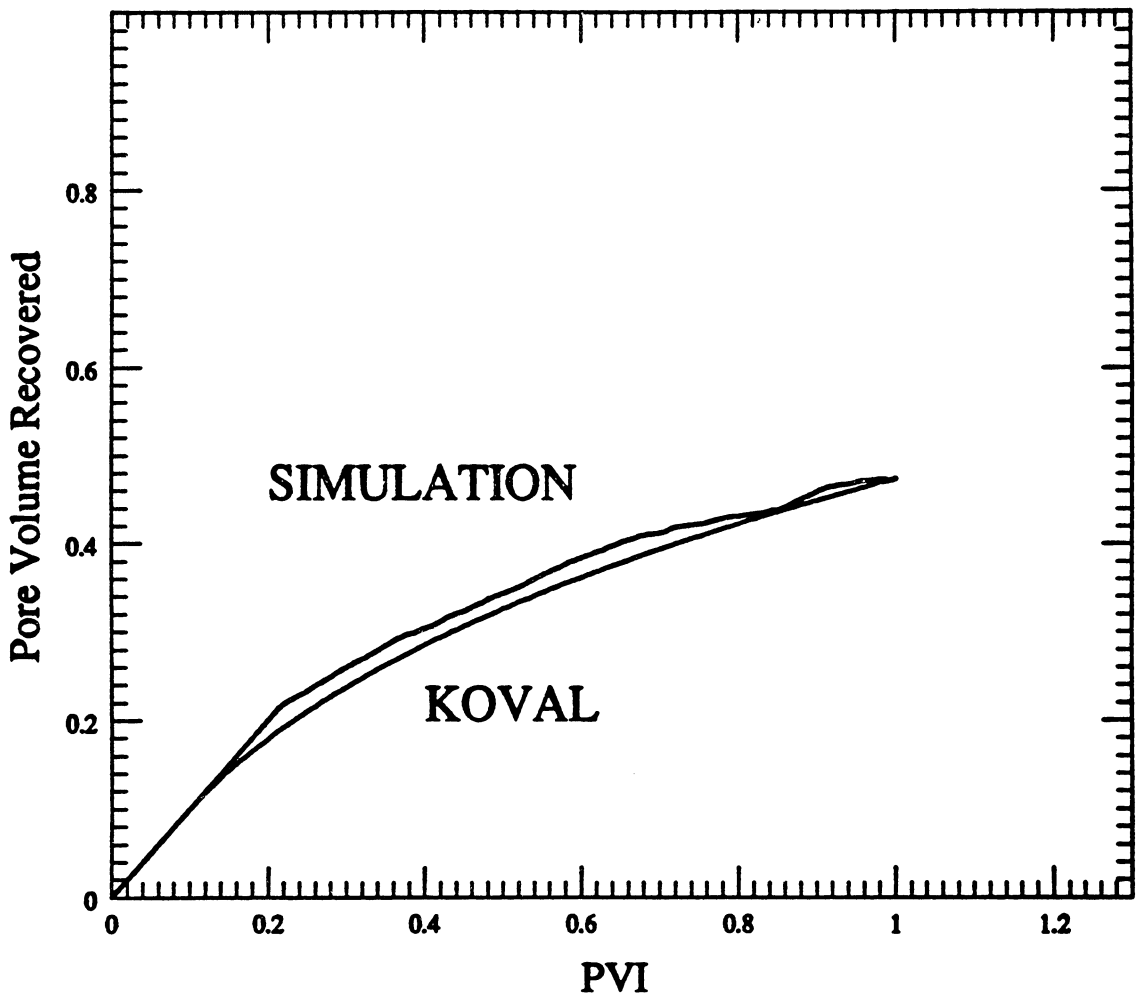

Fig. 4.1-29 Comparison of Koval's prediction with random-walk model's results. Recoveries are for displacements with M = 20, v = 40 ft/day in permeability field #11 (HI = 0.725).

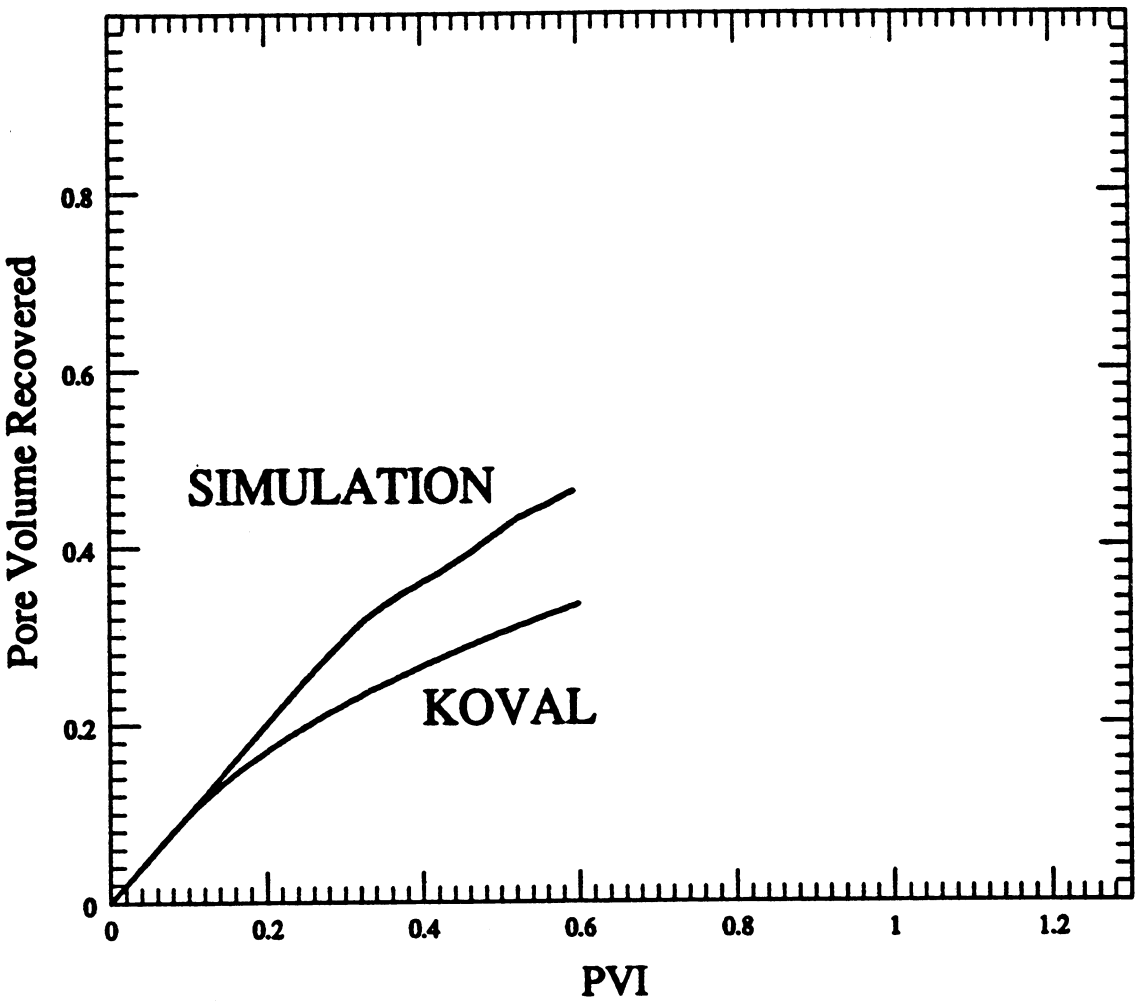

Fig. 4.1-30 Comparison of Koval's prediction with random-walk model's results. Recoveries are for displacements with M = 20, v = 40 ft/day in permeability field #16 (HI = 2.072).

We emphasize, however, that for many permeability fields, those assumptions will not be satisfied. For example, Mishra (1987) found that dispersive behavior was likely only for values of HI less than about 0.04. Arya et al. (1988) obtained similar results, with dispersive behavior observed for HI < 0.03-0.06. It is easy to imagine permeability variations for blocks of rock 25 feet in length that do not have such low values of HI. In any case, the simulations presented here suggest strongly that for many fields, adequate definition of the permeability distribution is the factor that is most important to accurate predictions of unstable miscible displacements. It is clear that adequate resolution of permeability variations at field scale is not currently available. Nevertheless the indication that the details of finger development dominated by viscous forces may not have to be represented offers some hope that more accurate predictions of field-scale flow patterns will be feasible as, for example, cross-borehole seismic methods improve the resolution of reservoir structure data.

4.1.5 Discussion

The random-walk model has several advantages over methods used previously. Artificial perturbation of the initial flow field (Withjack 1987) is not required because the representation of dispersion as random velocity fluctuations provides perturbations naturally at each time step. The representation of transverse and longitudinal dispersion with respect to the local flow direction means that there is no need for any assumption that the directions for longitudinal and transverse dispersion be aligned with the coordinate system (Giordano et al. 1985). Mesh refinement studies with the random-walk model showed that good agreement with experimental data could be obtained with somewhat courser meshes (60x60) than those used by Christie and Bond (1987) (100x150). Run times were accordingly about two to four times lower for the random-walk model. There is also no restriction on the form of boundary conditions, a limitation that applies to spectral methods. Very high Peclet numbers can also be handled easily, though finer meshes are required for high Pe. Effects of numerical dispersion in the random-walk calculation are minimal, a significant advantage over standard finite difference simulations. Computed recovery data were also only mildly sensitive (differences ranged from 2 to 5 percent at most) to variations in the seed numbers used in the random number generator.

As with any computational model, this one also has limitations. Because the numerical technique is explicit, time steps are limited by numerical stability requirements. Simulations that include gravity-driven crossflow may be quite lengthy, therefore, as the combination of high transverse grid resolution and substantial transverse flow velocity reduces allowable time step size. In addition, computer storage required to follow the locations of many tracer particles can be substantial when fine meshes are used. Thus, typical computation times are about two times longer than those reported by Tan (1988), for example, for spectral methods.

The computational results presented here also apply only to two-dimensional first contact miscible displacements. If two phases are present, as they undoubtedly will be in multiple-contact miscible floods, then capillary crossflow will also play some role in determining the scale of fingers that develop. Gravity segregation will also modify finger formation. Thus, many questions remain about finger dimensions and spacing at field scale. The results presented, therefore, are a first step in the investigation of fingering at field scale. They do suggest, however, that when significant correlation exists in the permeability field, viscous fingering and heterogeneity will be closely coupled.

4.1.6 Conclusions

The simulation results presented lead to the following conclusions for unstable, two-dimensional flow of first-contact miscible fluids:

(1) Comparison of random-walk simulations with experimental data indicates that the model represents adequately the essential physical mechanisms that control finger growth in homogeneous porous media.

(2) Finger wavelengths calculated by linear stability theory are accurate for only a limited period at onset of fingering. In subsequent finger growth, spreading and splitting of finger tips and coalescence of fingers due to crossflow lead to very complex finger patterns in homogeneous porous media.

(3) Koval's assumption that average concentrations move at constant velocity is satisfied approximately for linear flow in homogeneous porous media. For sufficiently heterogeneous porous media that show significant permeability correlation, Koval's heterogeneity factor does not represent effects of heterogeneity adequately.

(4) Finger patterns are determined by the permeability distribution when the permeability distribution has a large variance and significant correlation. For log-normal permeability distributions with equal correlation lengths in all directions, permeability-dominated flow occurs for $\sigma^2_{\ln(k)}\,\lambda_D$ greater than 0.25-0.30 for M=20.

(5) If permeability is uncorrelated or the variance of permeability is small, then finger patterns are similar to those observed for homogeneous porous media.

4.2 Scaled Flow Visualization Experiments

David C. Brock

Experimental data with which the theoretical predictions of Section 4.1 can be tested are limited. Indeed, there are only minimal data for systems with permeability variation. In this section, we describe a series of scaled flow visualization experiments in models with known, controlled permeability variations, using miscible fluids. Thus phase behavior effects are not included. Phase behavior of CO_2/oil and other miscible systems are being examined separately in other parts of the project and will be included in subsequent experiments. Because the experiments are scaled, the results will describe reservoir behavior more accurately than unscaled experiments.

Little work has been published on the combined effects of viscous instability and heterogeneity. Blackwell et al. (1959) described experiments using miscible fluids with unstable viscosity ratios in unconsolidated sands. It was determined that permeability heterogeneity decreased overall recovery in their experiments. Habermann (1960) studied the effect of mobility ratio on finger patterns in a quarter five-spot geometry. Although the experiments were solely in uniform packs, the effects of heterogeneity were discussed qualitatively. Slobod and Thomas (1963) reported on finger shapes and effluent compositions as a function of rate. These experiments were done only in uniform sand packs. Giordano et al. (1985) reported experiments in which finger development in a Berea sandstone slab was studied. In that study, finger dimensions were measured by microwave attenuation. The flow experiments were performed in slabs for which extensive surface permeability measurements were obtained. The permeability variations present were mild, however.

Geertsma et al. (1956) gave the following description of scaling for unstable flows. The behavior of an oil reservoir under production is governed by a number of variables. These variables may be combined into dimensionless groups which fall into three categories: independent groups (e.g. dimensionless time and length); dependent groups (e.g. dimensionless recovery and pressure: quantities that are at least in theory measurable during the experiment); and similarity groups, which are dimensionless groups of independent constants (e.g. reservoir length to height ratio, fluid viscosity ratio). If the values of similarity groups are equal for the model and prototype, the model is properly scaled. In such a properly scaled model, when the independent groups are equal for the model and prototype, the dependent groups will also be

equal. Thus, the results of a properly scaled experiment can be directly interpreted in terms of field performance.

The dimensionless groups may be determined using either or both of two methods: dimensional analysis and inspectional analysis. In dimensional analysis, all the variables relevant to the problem are determined, then combined into independent dimensionless groups in an essentially trial-and-error process. The Buckingham theorem states that the number of variables less the number of fundamental dimensions (generally mass, length, and time) is the number of independent dimensionless groups. In inspectional analysis, the pertinent mathematical equations are converted into dimensionless form to yield the dimensionless groups. Since they come directly from the system equations rather than from trial-and-error combination, the physical meaning of the dimensionless variables derived by inspectional analysis is usually more apparent. Thus, inspectional analysis is the preferred method. A basic inspectional analysis of the convection-dispersion equation and Darcy's Law shows that a linear reservoir 500 feet long by 100 feet thick, with permeability varying from 5 to 40 mD can be represented using a model measuring 1 foot by 2.4 inches, with permeabilities ranging from 2.4 to 19.2 D, which correspond to permeabilities that can be obtained using glass bead packs.

The question of scaling a miscible flood was studied by Offeringa and van der Poel (1954). Using inspectional analysis, they determined the similarity groups for a linear miscible flood in a homogeneous porous medium. They then validated their scaling arguments experimentally by core flood experiments. The simplicity of the one-dimensional homogeneous system allowed them to have strictly scaled experiments.

Pozzi and Blackwell (1963) modeled a more complex system. They were concerned with modeling the important mechanism of transverse mixing of solvent and oil in miscible floods. It was found that rigorously scaling this more complex system dictated unreasonable experimental conditions. (A sample given called for a model 167 feet long, with injection of 1 pore volume over 86 days.) Out of necessity, they investigated which scaling criteria could be relaxed and still yield models which accurately simulate the processes of interest.

In the present experiment, heterogeneity is an added complexity. Even a simple heterogeneity such as a higher permeability layer adds the variables of permeability ratio and thickness ratio at least. When regions of differing permeability do not extend the entire length of the model, an additional parameter is required to specify the length scale of the heterogeneity compared to the length scale of the displacement. Just as in the systems described my Pozzi and Blackwell, rigorous scaling requirements for such systems must be relaxed in order to obtain workable models.

4.2.1 Experimental Apparatus and Procedures

The experimental apparatus is shown in Fig. 4.2-1. The pack is fully saturated with an initial fluid (clear), and the displacing fluid (dyed) is injected into the model at constant rate using a liquid chromatography pump. The pump delivers at constant flow rates from 0.1 to 9.9 ml/min. After flowing through the bead pack, the effluent passes through a refractive index detector or a spectrophotometer (so that effluent composition is recorded), and is collected for material balance confirmation. The flow in the model is recorded using a high-resolution video tape system. Video images are digitized to give the spatial distribution of compositions. Thus, composition information is available in time and space.

The bead pack model used in these experiments is shown in Fig. 4.2-2. Glass beads of uniform diameter, in a slurry with water, are loaded into the glass casing. The water is withdrawn under vibration to compact the pack by capillary action. When the pack appears to be uniform, the model is sealed, attached to inlet and outlet lines, evacuated, and loaded with the initial fluid. The uniformity of the pack is tested by conducting a stable displacement and verifying that the front moves in a piston-like manner. Etched glass baffles at inlet and outlet cause uniform injection across those faces, giving the proper boundary conditions for two-

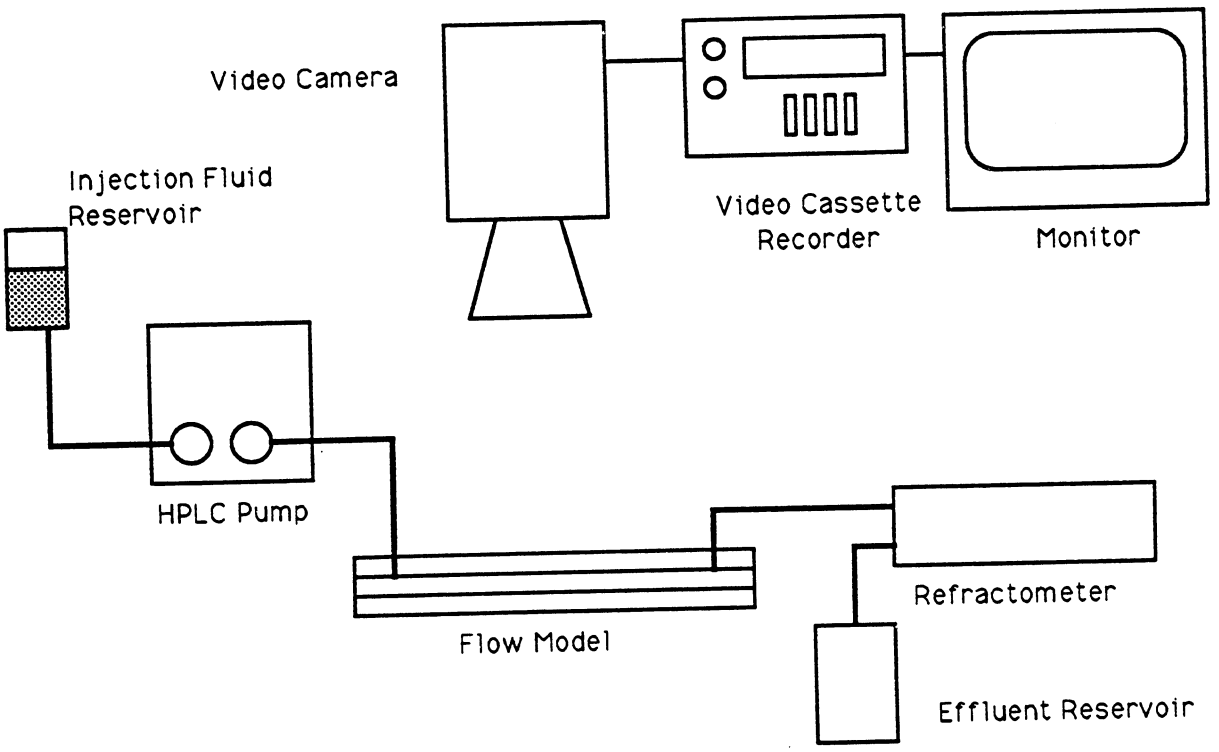

Fig. 4.2-1 The porous bead pack model with schematic of the experimental flow system.

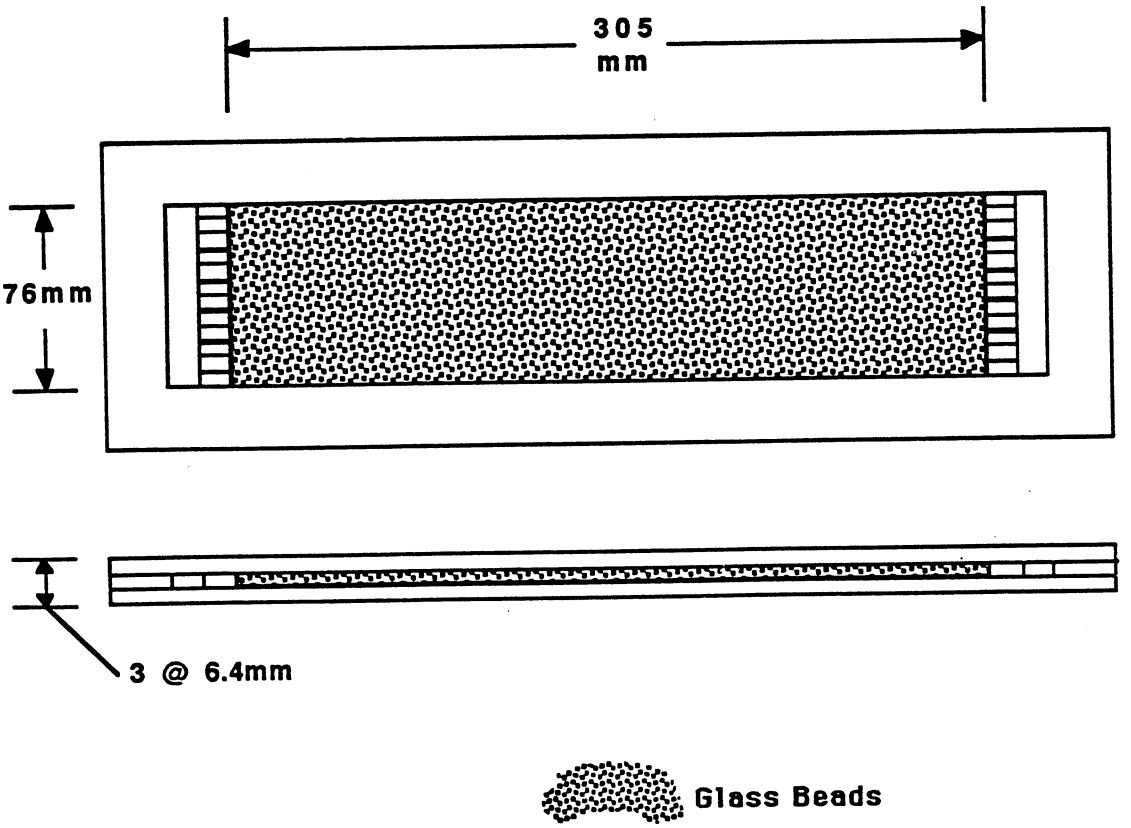

Fig. 4.2-2 Bead pack model dimensions.

dimensional linear flow. The results presented here are for displacements in a uniform and a heterogeneous (2-layer) bead pack. The homogeneous pack had beads with diameter 0.5 mm, and the two-layer pack had layers of 0.5 and 0.25 mm diameter beads. Permeability was estimated from the Blake-Kozeny equation to be 145 and 36 Darcies respectively for the 0.5 and 0.25 mm bead packs. The flow length is 12 inches, with 3 inch width and 1/4 inch thickness.

The base fluids used are refined hydrocarbon oils: light and medium mineral oils, and a series of isoparaffin oils. The mineral oils (Spectrum Chemical Manufacturing Corporation) have viscosities of 20 and 45 cp. The isoparaffin oils are Soltrol 10 through Soltrol 220 (Phillips Petroleum Company), a series of mixtures of C_7 to C_{17} isoparaffins. They range in viscosity from 0.05 to 3.7 cp. The densities of the fluids are matched (using toluene) to eliminate gravity effects. For flow visualization, the fluids are dyed (Automate Red B, Morton Chemical Division). The effluent composition is monitored using either a refractometer or spectrophotometer calibrated for the fluids used in a given flow experiment. The effluent signal along with the pressure drop across the model are collected on a microcomputer-based data acquisition system.

The displacements are recorded on a 3/4" format video tape system. From these video tapes, frames of interest are digitized on a microcomputer into arrays of 512 by 480 grey scale intensity values. The intensities are integers ranging from 0 to 255. Calibrations can be performed to transform the intensities into compositions. Such quantitative information on the spatial distribution of composition is useful for computing cross-sectional averages, front tracking, and display of data. Contour plots presented here come from digitized video images of the laboratory displacements.

4.2.2 Results

Contours of a flow visualization in a homogeneous porous medium are shown in Fig. 4.2-3. The initial fluid in place was a medium-grade mineral oil. The displacing fluid was dyed Soltrol 10, and hence the displacement was unstable with a mobility ratio of 64. This experiment was done in an older prototype model. The model had the all the same dimensions, but was not packed as uniformly, and fluids did not have matched densities. The resulting gravity contrast caused some override along the upper bead-glass interface, which gave fronts that advanced more quickly than would be expected if the flow were uniform in the vertical direction. Because the effects of gravity override were also present, the results shown in Fig. 4.2-3 illustrate finger growth that is the result of conditions that do not match exactly those of the simulations. In particular, fronts in the experiment move faster than those in the simulations, because the flow was not uniform in the vertical direction. Thus, the comparison given below of simulated and experimental results is only qualitative for this case.

In the experiment, many fingers are present at early time (Fig. 4.2-3a). In fact, the geometry of the inlet created about 25 small fingers with a width of about 0.15 cm as the displacing fluid entered the bead pack. As flow continued, however, a few fingers moved ahead of the others, shielding them from further growth (Homsy 1987). As Fig. 4.2-3b shows, only two fingers remained a short time after that shown in Fig 4.2-3a. The fingers were narrow at the tails and broader at the tips. Tan and Homsy (1988) showed that the replacement of high viscosity fluid by low viscosity fluid in the finger induces transverse gradients in the pressure field at the tip of a finger, which causes the spreading. Their numerical simulations using a spectral method showed that the spreading causes a steepened concentration gradient, which in turn causes a tip-splitting instability. The tip-splitting mechanism was seen repeatedly throughout the experiment, and is illustrated in Figs. 4.2-3b and c. As is shown in Fig. 4.2-3c, one finger outdistanced the other, and thereafter dominated the flow. The secondary finger was pulled into the wake of the dominant finger, leaving an island of unswept fluid (Fig. 4.2-3d). Thus, the mechanisms of spreading, shielding and tip-splitting (Homsy 1987), as well as coalescence of fingers created quite complex concentration distributions as the fingers evolved.

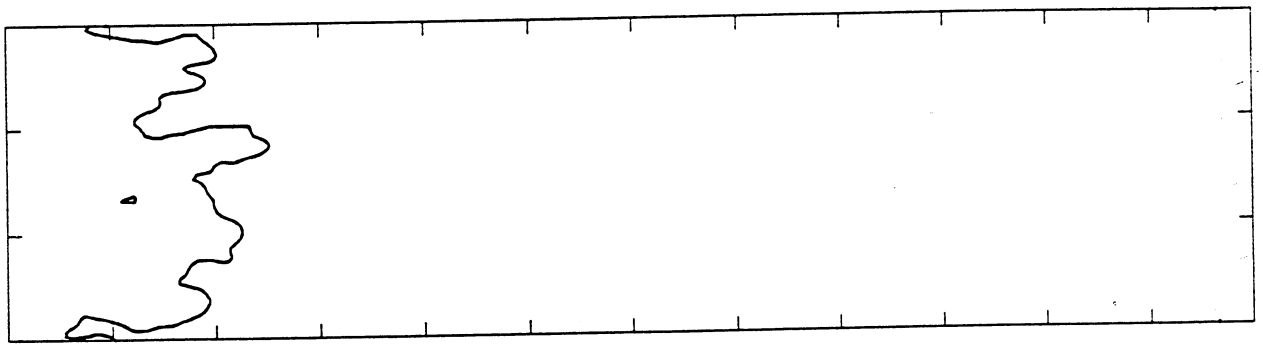

(a)

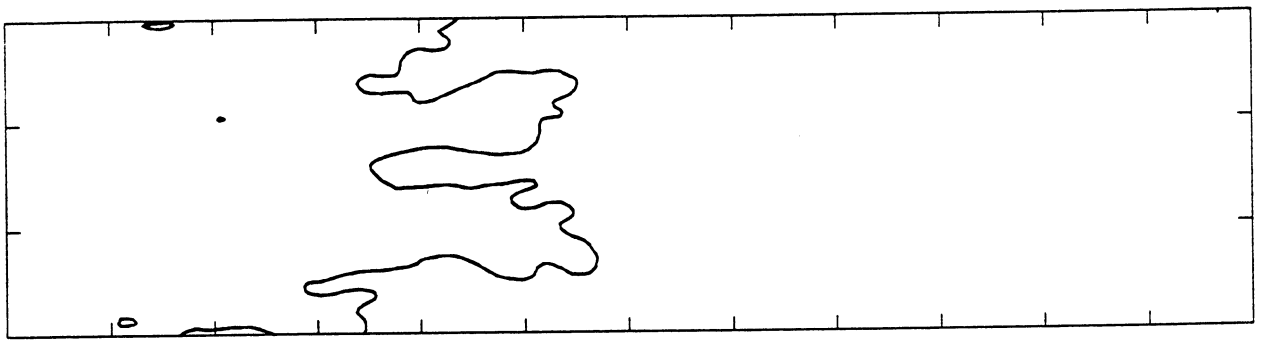

(b)

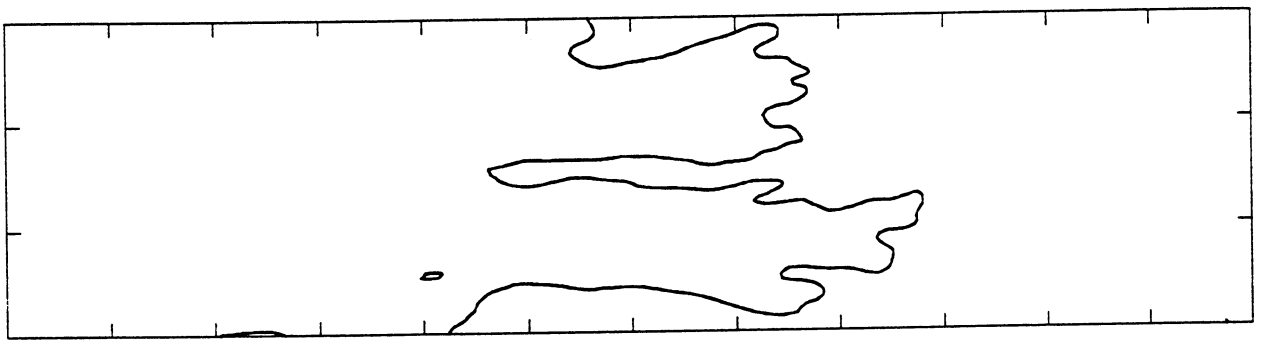

(c)

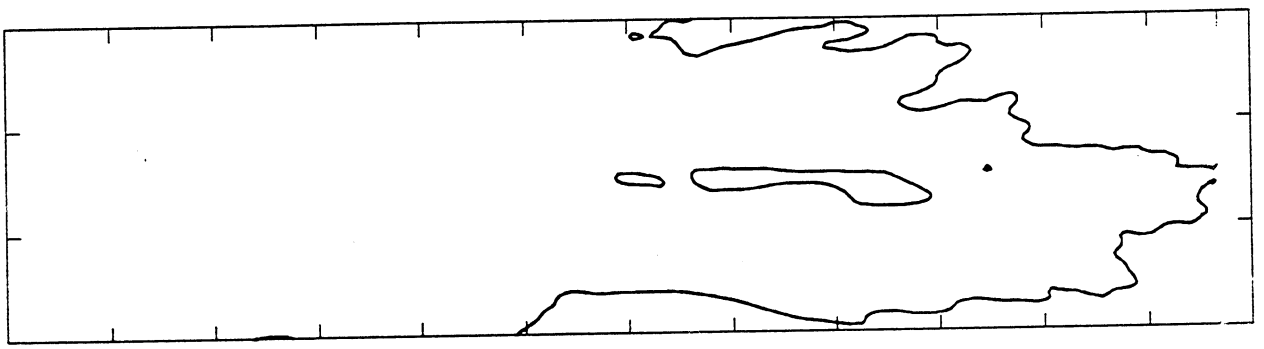

(d)

Fig. 4.2-3 Displacement of mineral oil by Soltrol 10 (M=64) at 0.05 cm/sec.

Fig. 4.2-4 shows the results of a simulation of the homogeneous displacement experiment. In the simulations, the correlation of Pozzi and Blackwell (1963) was used to estimate the dispersion coefficients from the flow velocity and particle size. Values used were 4.2 x 10^{-3} and 4.2 x 10^{-4} cm^2/s for longitudinal and transverse dispersion coefficients respectively. The simulations showed the same mechanisms of finger growth that were seen in the experiment. Many initial fingers (Fig. 4.2-4a) grew into two dominant fingers. Those fingers were broad at the tips and narrow at the tails. Tip-splitting is visible in all of the frames of Fig. 4.2-4. Just as in the experiments, repeated spreading, shielding and tip-splitting occurred. In addition the simulations showed coalescence at later times (Fig 4.2-4d). Thus, the simulation correctly captures the important qualitative features of finger growth in a homogeneous medium.

Flow visualizations were also carried out in a heterogeneous (two-layer) medium. First, a stable displacement was performed to verify that the layers present had reasonably uniform permeability. The permeability contrast between the layers was 4.0. Fig. 4.2-5 shows snapshots of a stable displacement, dyed mineral oil displacing the same mineral oil without dye. The flow rate is the same as in the homogeneous case, 0.1 PV/minute, a linear velocity of about 0.05 cm/s. In a displacement at unit mobility ratio in a perfect layered medium, there should be piston-like displacement (at different rates) in each layer. Fig. 4.2-5 indicates that there was a slight preferential flow channel along the edge of the high-permeability zone, however.

Figs. 4.2-6 and 4.2-7 compare an unstable experimental displacement in the two-layer model with a simulation of the same experiment. In this case, the fluid densities were much more closely matched, and so Figs. 4.2-6 and 4.2-7 may be compared not only for qualitative growth mechanisms, but for quantitative finger penetration distances as well. The fluid initially present was the medium-grade mineral oil. It was displaced by a dyed mixture of Soltrol 10 and toluene. The mixture had the same density as the mineral oil, and the mobility ratio was 60. In the experimental displacement, a single finger grew in the high-permeability layer, along the layer interface. Tip-splitting still occurred throughout the process (Figs. 4.2-6a-c). The finger followed the interface partly because of the slightly higher permeability there, but also due to crossflow. In a two-layer system, crossflow is from the high- to low-permeability layer near the leading tip and is from low- to high-permeability layer at the tail. Hence the tip is pulled toward the interface.

The simulation results were similar. Tip-splitting is visible in Figs. 4.2-7a and b, and small bypassed zones indicate coalescence occurred. In both the simulation and the experiment, fingers that formed as the flow entered the high permeability layer were dominated eventually by the single finger in that layer. The finger grew near the interface, but was not quite as strongly pulled toward it as in the experiment. In the simulation, there was no preferential flow path, so the finger moved toward the interface driven by crossflow only. Finger penetration distances in the simulation agreed well with penetration distances observed in the experiment. Thus, the simulation and experimental results also agreed well when a simple permeability variation was present. That agreement suggests, therefore, that the simulator can be used to study the interaction of viscous instability and permeability heterogeneity. Additional experiments to test the agreement for more complex permeability variations are underway.

4.3 Summary

The results presented in this chapter represent substantial progress toward quantitative prediction of the effects of viscous fingering in porous media with variable permeability. The numerical technique developed shows good agreement with all available experimental evidence, both for homogeneous and mildly heterogeneous systems. The most important result obtained is the demonstration that for permeabilities that are sufficiently variable and that correlate over a significant fraction of the flow length, the permeability field controls finger dimensions. Not nearly enough is known about the correlation structure of field-scale systems, but both the

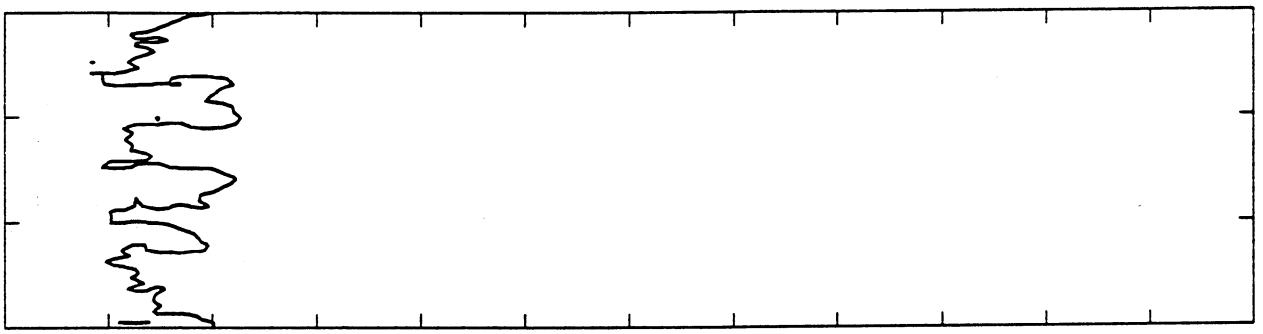

(a)

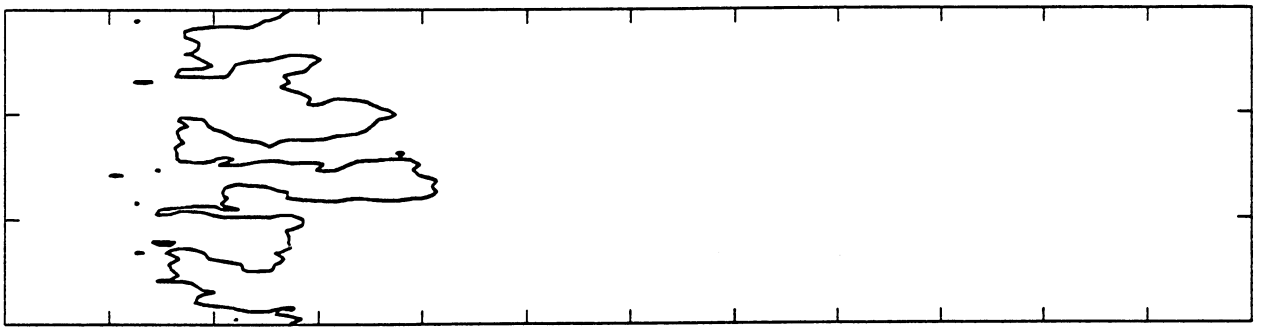

(b)

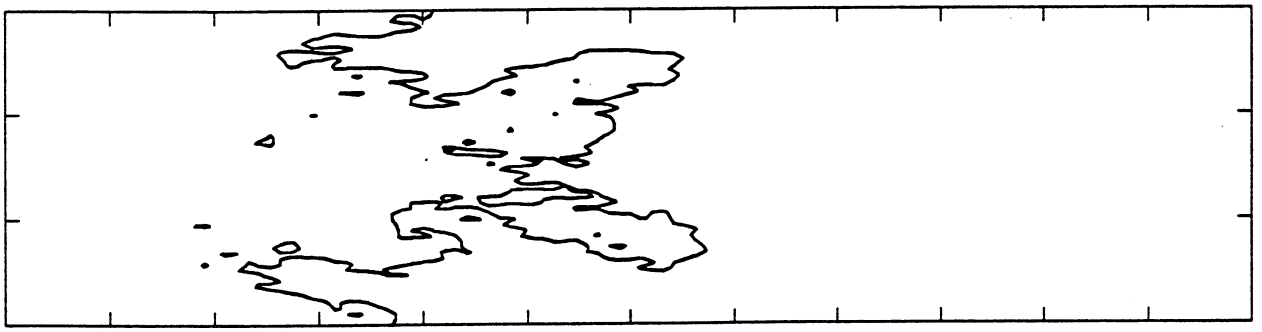

(c)

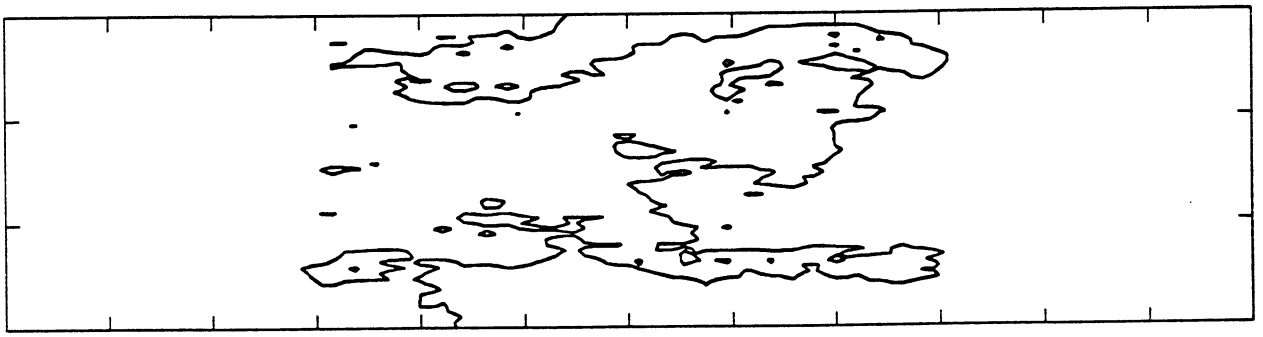

(d)

Fig. 4.2-4 Simulation of displacement in a homogeneous medium, M=64.

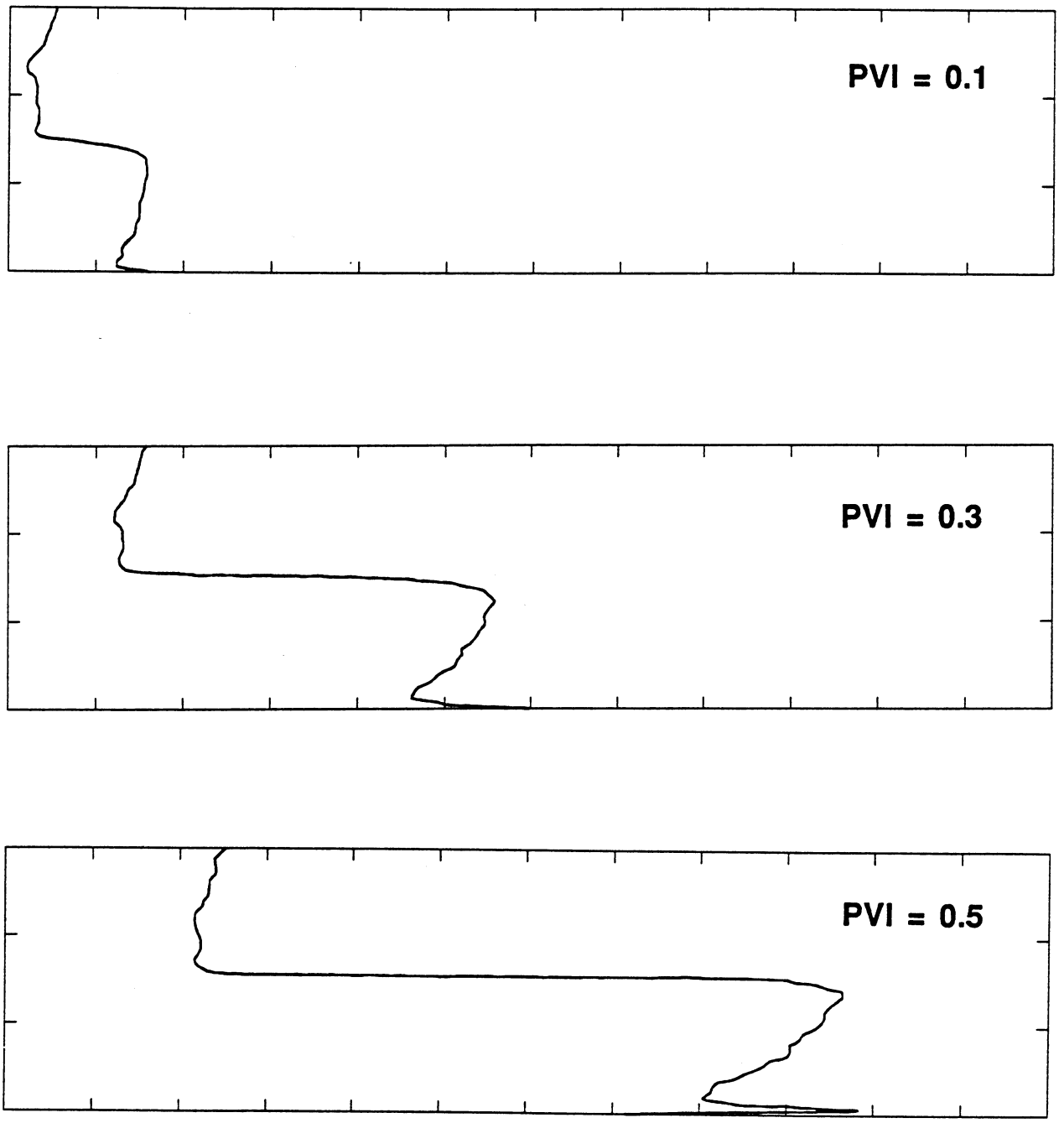

Fig. 4.2-5 Matched mobility experimental displacement in the two-layer system.

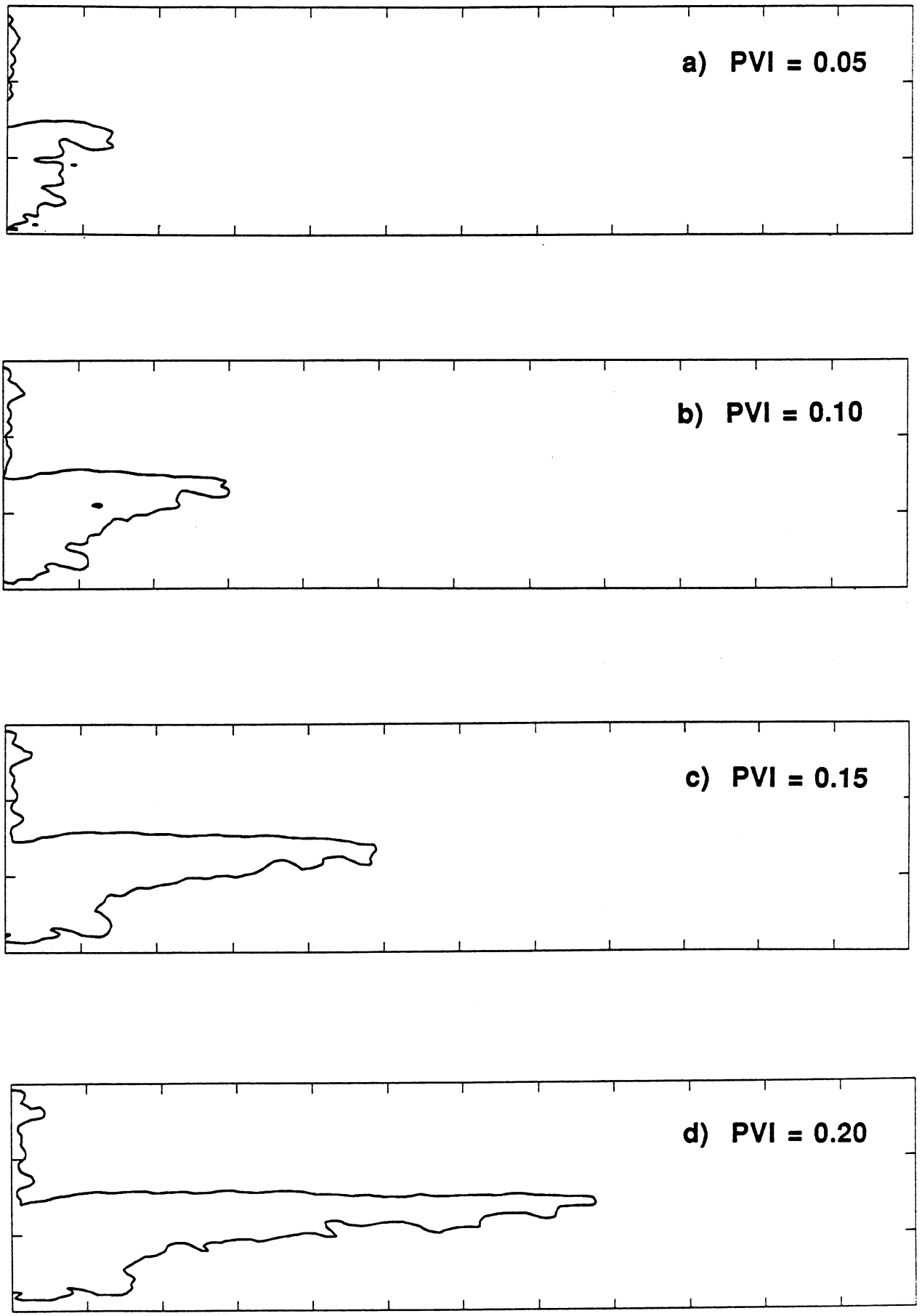

Fig. 4.2-6 Unstable experimental displacement in the two-layer system, with M=60 and permeability contrast 4:1.

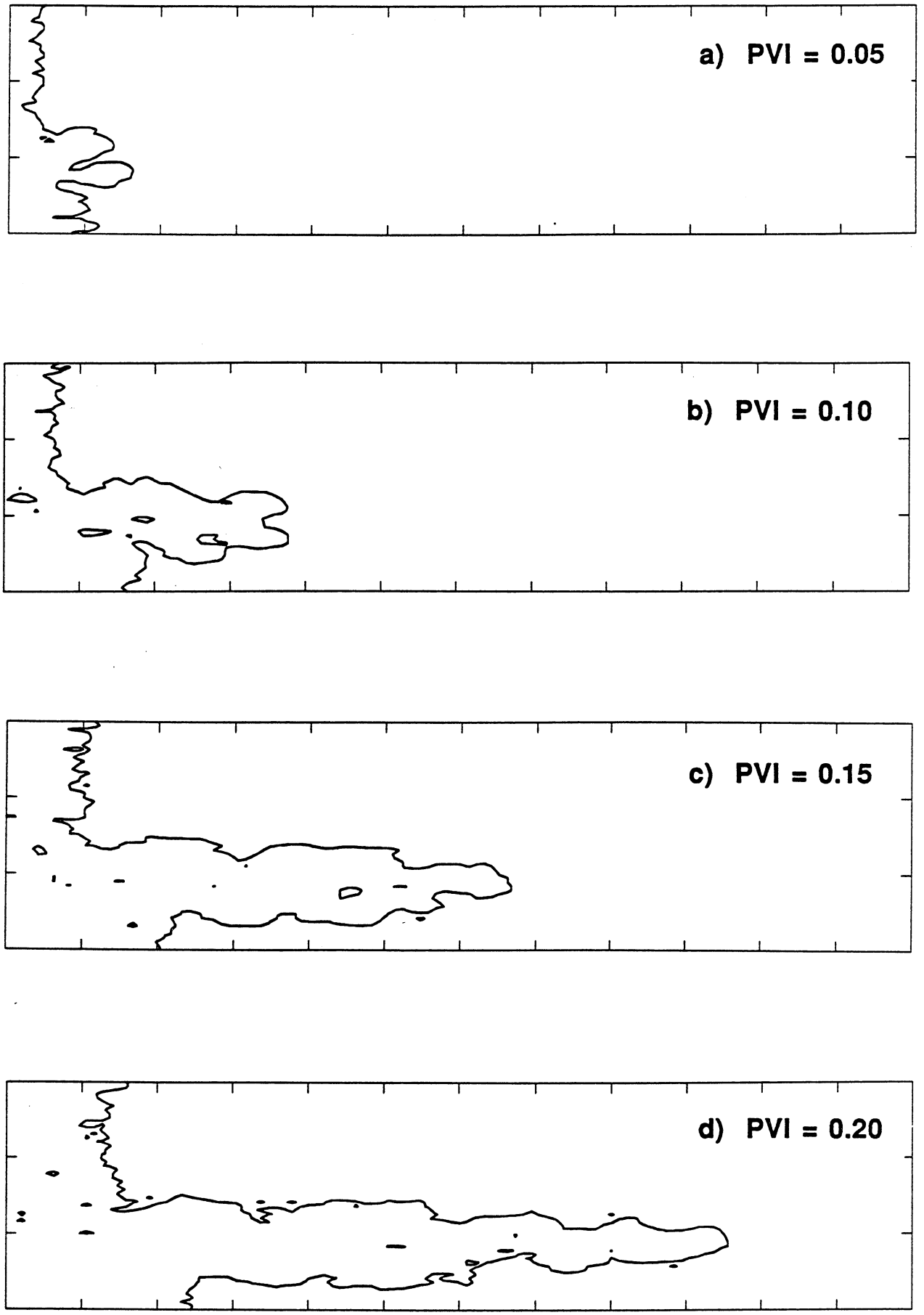

Fig. 4.2-7 Simulation of displacement in the two layer system, with M=60 and permeability contrast 4:1.

experiments and the simulations indicate how the transition to permeability dominated flow might occur for layers with lengths much greater than thicknesses. In a layer of given thickness, for example, many fingers would form near an injection well, but shielding and coalescence would steadily reduce the number of fingers until a single finger filled the entire thickness. For large-scale simulations, therefore, calculations of the details of finger growth would probably not be needed. Instead, some average representation like Koval's model or one of the later variations on that theme would probably be adequate. The value of the simulation technique presented here is that it can be used to test the adequacy of simpler average representations.

The simulation and experimental result presented do not, of course, answer all of the questions of interest. The evidence for crossflow in both simulations and experiments suggests that interactions with phase behavior may be significant. In addition, only two-dimensional fingers have been simulated, and only log-normal permeability variations with simple correlation structures have been examined. Effects of density-driven crossflow should also be investigated. Nevertheless, the results presented here suggest that the combined effects of interacting physical mechanisms can be investigated by the techniques developed here.

5. Detection of Reservoir Heterogeneity

The computations of the growth of viscous fingers in heterogeneous porous media reported in Chapter 4 indicate that description of the permeability within a reservoir will be an important component of improved performance predictions. Information about the permeability distribution can be obtained in a variety of ways. Plugs taken from cores obtained from wells give direct information about the vertical distribution, though it is often true that sampling of core plugs is biased to leave out low permeability zones. When porosity and permeability can be correlated, permeability data can be inferred from log data, though there is inevitable averaging that occurs given the limits of resolution of the logging tools used. Core plugs and logs give detailed information in the vertical direction, but little information about variations in permeability in the areal direction. In this chapter we consider the use of pressure transient and tracer tests to obtain additional information about the presence of heterogeneities. In Section 5.1 we examine how correlation in the permeability field influences the performance of both pressure transient and well-to-well tracer tests. Based on the analysis, a test method that makes use of both tracer and pressure test results is proposed. In Section 5.2, the detection in impermeable regions by pressure testing is considered. That study shows that certain large regions that disturb the flow near a well can be detected. In Section 5.3, the effects of a partially communicating fault dividing regions of different flow properties are considered, and the problem of uniqueness of parameters determined is considered.

5.1 Analysis of Pressure and Tracer Test Data for Characterization of Areally Heterogeneous Reservoirs

Srikanta Mishra

The performance of an enhanced oil recovery process depends primarily on the interaction of the injected fluid with the oil in situ, the heterogeneity of the reservoir rocks and the coupling between these two effects. While fluid mixing and phase behavior can be studied in the laboratory, the nature of variations in the properties of porous media (e.g. permeability, porosity) can only be unraveled through indirect means. Typically, some disturbance is imposed on the physical system, and the resultant response is analyzed to obtain a qualitative and/or quantitative description of the material properties of the system. Thus the detection of reservoir heterogeneities represents a classic inverse problem. Two kinds of well tests are commonly used for this purpose, well-to-well tracer testing and transient pressure testing.

Interwell tracer tests are used to track subsurface fluid movement and infer formation characteristics (Brigham and Abbaszadeh-Dehghani 1987). Such a test involves injecting a tracer slug, driven by a chase fluid, and monitoring the tracer concentration at an adjacent producer. Quantitative interpretation of tracer test data is based on solutions of the convection-dispersion equation

$$\frac{\partial C}{\partial t} = \nabla \cdot \left[D \nabla C - vC \right] \tag{5.1-1}$$

where C is the concentration of tracer and D is the dispersion coefficient.

Pressure transient tests are useful for estimating average formation properties and wellbore conditions, and detecting barriers for fluid flow (Ramey 1982). Such a test is carried out by perturbing the flow rate at one well and monitoring the resultant pressure response at the same or adjacent wells. Analysis of pressure data is based on solutions of the pressure-diffusion equation

$$\nabla \cdot \left[k \nabla p \right] = \phi \mu c_t \frac{\partial p}{\partial t} \tag{5.1-2}$$

where k is the permeability, p the pressure, ϕ the porosity, μ the viscosity and c_t the total compressibility.

Most well test interpretation models compute an *effective* medium property (e.g. permeability, dispersivity) corresponding to a fictitious homogeneous system, whose behavior matches that of the real heterogeneous system. However, if distributed heterogeneities are to be detected qualitatively and/or quantitatively by well tests, some knowledge of the relationship between these effective parameters and system heterogeneities is required. An associated question of importance is the definition of conditions under which such effective medium approximations can be used for describing heterogeneous media. It is also useful to know the relation between tracer and pressure test responses for the same system, so that information from both tests can be integrated.

This study is concerned with the use of well tests for characterizing macroscopic variations in permeability at the interwell scale. The system of interest, shown schematically in Fig. 5.1-1, is one quarter of a single-layer five-spot within a repeated and balanced production-injection pattern in two-dimensional areal geometry. Our objective is to simulate both well-to-well tracer tests and transient pressure tests in order to examine (a) the sensitivity of well test responses to a heterogeneous permeability field, and (b) the quantification of in-situ permeability variation from the analysis of well test data.

We focus on pressure responses at the injection and production wells, as well as on apparent mixing (dispersion) at the interwell scale due to purely convective tracer flow. Previous studies of flow and transport through heterogeneous permeable media have been restricted to analysis of either the pressure test response (Warren and Price 1961), or the tracer test response (Warren and Skiba 1964, Heller 1972, Smith and Brown 1984, Arya et al. 1985). Similar work in the groundwater literature has been summarized recently (Gelhar 1986). In this section, and the companion work of Mishra and Ramey (1985), we assess the impact of heterogeneities on pressure and tracer test responses.

The methodology adopted in this study, which is similar to the Monte Carlo simulation procedure first presented by Warren and Price (1961), can be briefly described as follows. First, permeability values are assigned to each node of the grid shown in Fig. 5.1-1, such that the assumed statistics of permeability variation are honored. Then pressure history at the injection and production wells is simulated till the attainment of steady-state, and pressure-time data is analyzed. Finally, convective tracer flow is simulated (so that observed tracer dispersion is due to permeability variation only) and breakthrough tracer concentration data are analyzed. This procedure is then repeated for several arrangements of the permeability field for each set of statistical parameters.

5.1.1 Representation of Heterogeneous Media

Field evidence indicates that properties of porous media such as permeability and porosity vary from point to point in a random manner, and also exhibit spatial correlation. In the petroleum literature, variation of permeability has been analyzed statistically by many investigators (Law 1944, Jensen et al. 1985). However, measurements of spatial continuity have been undertaken only recently using geostatistical techniques (Da Costa e Silva 1985). An analysis of the spatial variability and structure of material properties from several groundwater aquifers is also available (Hoeksema and Kitanidis 1985).

Our discussion is restricted to heterogeneous media with variations in permeability only, since the effects of porosity variations on subsurface fluid flow and transport have been shown to be small (Journel and Huijbregts 1978). As it is difficult to describe heterogeneities (i.e. permeability variations) in complete deterministic detail, a stochastic approach is adopted. Permeability is assumed to be a random function with known mean, variance and spatial correlation structure. Furthermore statistical homogeneity is also assumed to be valid in the flow domain, which implies that (i) the mean is independent of location, and (ii) spatial

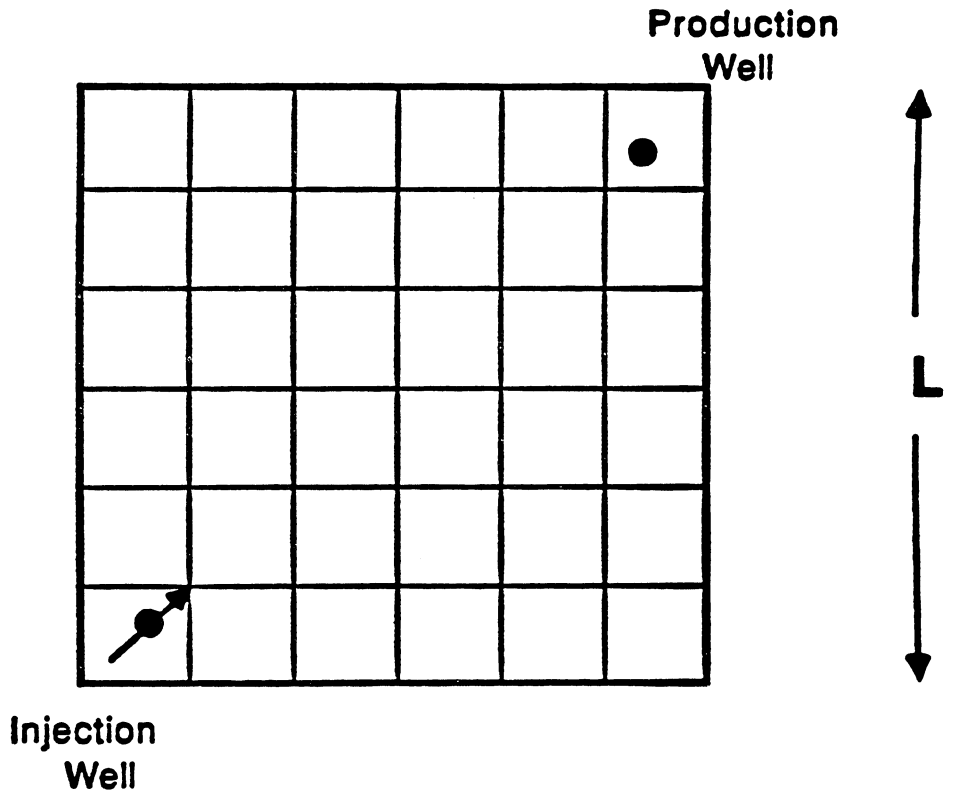

Fig. 5.1-1 System schematic, showing a quadrant from a repeated five-spot.

correlation between two samples depends only on their separation (Journel and Huijbregts 1978).

Permeability is characterized by a log-normal frequency distribution, so that variability can be expressed by the Dykstra-Parsons coefficient, V_{DP} (Dykstra and Parsons 1950)

$$V_{DP} = \frac{k_{50} - k_{84.1}}{k_{50}} = 1 - \exp\left(-\sigma_{\ln(k)}\right) \qquad (5.1\text{-}3)$$

where k_{50} and $k_{84.1}$ are the 50^{th} and the 84.1^{th} percentile values from a log-permeability cumulative distribution function (CDF) and $\sigma^2_{\ln(k)}$ is the variance. Fig. 5.1-2 shows a hypothetical log-permeability CDF.

Spatial continuity implies correlation between permeabilities of grid blocks that fall within a given area in a two-dimensional system, or a given volume in a three-dimensional system. This can be expressed quantitatively through the semivariogram, which measures variability, and hence, inversely reflects spatial correlation. For a discrete grid in one dimension, the semivariogram estimator is given by (Journel and Huijbregts 1978)

$$\gamma(l) = \frac{1}{2(n-l)} \sum_{i=1}^{(n-l)} \left[z(i+l) - z(i) \right]^2 \qquad (5.1\text{-}4)$$

where γ is the semivariance of z and z is the parameter of interest, in this case $z = \ln(k)$, i is the grid-block index, l the lag, the distance between block i and block $i + l$ expressed in grid-block lengths and $(n-l)$ the number of samples at lag l. Fig. 5.1-3 shows a hypothetical semivariogram. Notice that variability increases (and correlation decreases) with increase in lag l. Variability reaches a maximum and equals the variance, $\sigma^2_{\ln(k)}$, at some lag, a, beyond which parameter values will be uncorrelated. If Δx is the lag length (i.e. the grid block dimension), then the product $a\Delta x$ is defined to be the range, λ, of the semivariogram. We shall use the term correlation length scale in preference to range. A dimensionless measure of correlation is then given by the correlation length, λ_D, obtained by normalizing λ with some characteristic flow length, L (see Fig. 5.1-1).

Generation of Autocorrelated Permeability Fields

Several methods are available for generating spatially correlated parameter fields when the mean, variance and correlation length scales are known (Luster 1985). We have used the moving average method, which is conceptually simple and produces an isotropic log-permeability field with a circular semivariogram in two-dimensions. Briefly, this technique can be described as follows.

1. Extend the simulation grid in each dimension by λ, and generate a set of uniform random numbers, r(u), ranging from zero to one, over the entire augmented grid.
2. Attribute to each node, s, in the simulation grid a value, y(s), equal to the sum of all r(u) located inside a circle of diameter, λ, and centered at s .
3. Standardize the resulting realization, y(s), to a mean of zero and a variance of one, and then rescale so that the mean equals $\ln(\bar{k})$, and variance equals $\sigma^2_{\ln(k)}$. This produces the normally distributed log-permeability field, z(s).
4. Exponentiate these values of z(s) to obtain permeability values over the required simulation grid.

Fig. 5.1-4a shows the perspective of a typical permeability data set (shown as the natural log of permeability, ln(k)) generated using this procedure, and Fig. 5.1-4b shows the corresponding semivariogram, which is obtained by weighting equally the x- and y-directional semivariograms calculated with Eq. (5.1-4). As seen from Fig. 5.1-4b, the moving average procedure

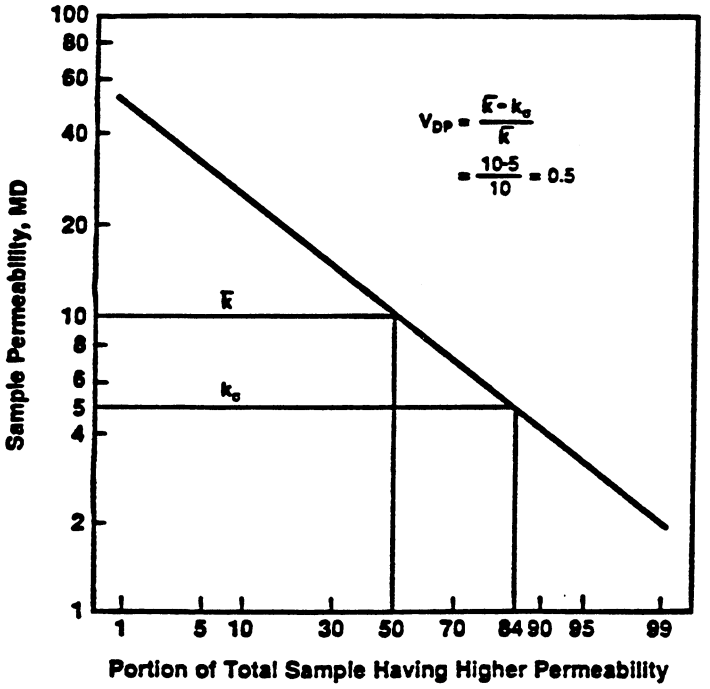

Fig. 5.1-2 Hypothetical log-normal CDF of permeability.

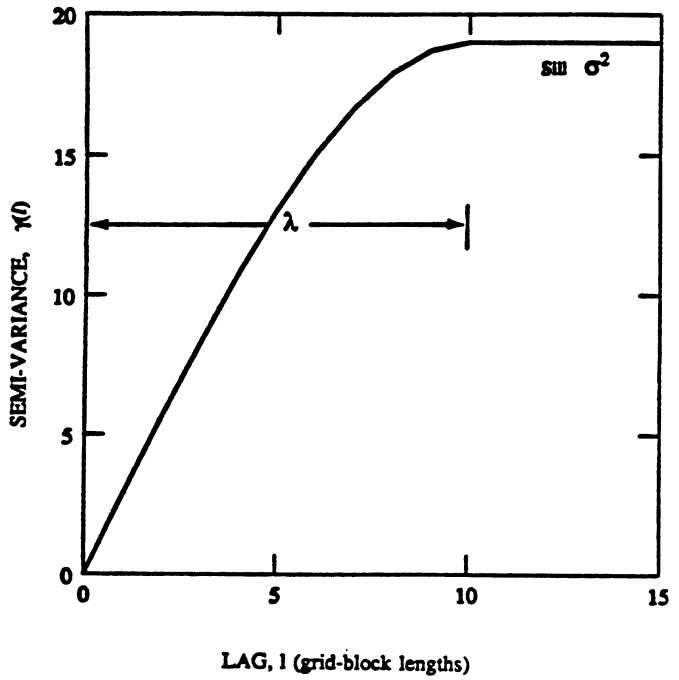

Fig. 5.1-3 Hypothetical semivariogram.

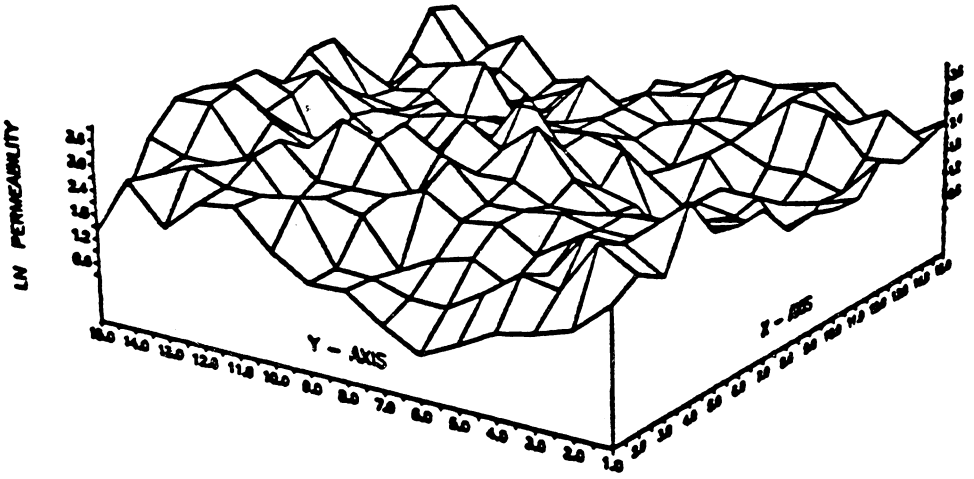

A

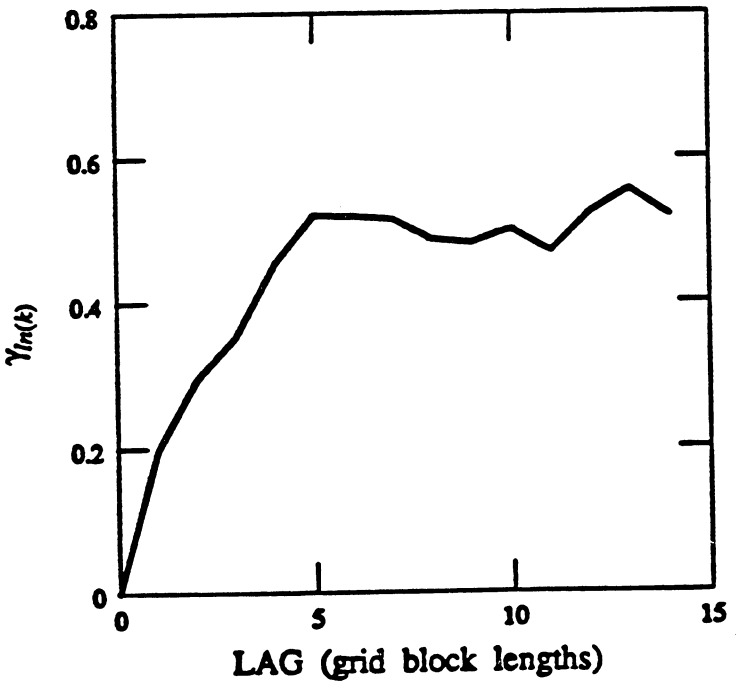

B

Fig. 5.1-4 Simulated permeability field with $V_{DP} = 0.50$ and $\lambda_D = 6/15$; A: perspective plot; B: experimental semivariogram.

reproduces reasonably the input variance ($\sigma^2_{ln(k)} = 0.48$) and correlation length ($\lambda_D = 6/15$). For each set of V_{DP} and λ_D, twenty permeability realizations were generated and used as input to the pressure and tracer test simulation codes. Other input parameters are given in Table 5.1-1.

5.1.2 Pressure Test Response

A common observation from well test analysis to date is that field pressure data can be matched with homogeneous system models, even when *a priori* information suggests that the system is heterogeneous. In effect then, pressure tests act like filters to smooth the effect of heterogeneous elements. However, effective medium properties (e.g. permeability) obtained from a homogeneous system match could still contain some information regarding the distribution of heterogeneities, particularly when the medium is sampled at different spatial locations. In what follows, we examine this identification problem in some detail.

Simulation of Pressure Behavior

Pressure behavior was modeled with a single phase simulator, which solves a finite difference analog of Eq. (5.1-2) in two space dimensions. The discretization procedure results in a system of equations implicit in pressure, which is solved directly using a banded-matrix solver. An automatic time-step selector was used to ensure logarithmic time incrementing suitable for conventional pressure analysis. Details of the simulation procedure are given by Mishra (1987).

Since we are considering a balanced injection-production pattern, the system will reach steadystate some time after the onset of injection and withdrawal. The transient pressure decline at the production well, and the transient pressure rise at the injection well, can be analyzed to estimate effective permeabilities around these wells. Assuming infinite-acting radial flow, we can relate permeability k_j to the slope m_j of the linear portion in a semilog pressure-time graph

$$k_j = \frac{162.6\, q\mu}{m_j\, h} \tag{5.1-5}$$

where q is the flow rate, and h the thickness and the subscript j denotes injection (inj) or production (prd) as the case may be. The effective permeability calculated with Eq. (5.1-5) measures some average property in a finite zone of influence around the well block. We refer to this value as the injection (or production) well permeability. Note that the well permeability is not necessarily the permeability of the block containing the well.

The steady-state pressure drop between the wells, Δp_{ss}, can also be used to calculate a steady-state interwell permeability, k_{ss}. The appropriate interpretive equation, based on the injectivity equation for a repeated 5-spot, is given as

$$k_{ss} = \frac{282.4\, q\mu F}{h\, \Delta p_{ss}} \tag{5.1-6}$$

The geometric factor F is a function of the interwell distance, d, and effective well radius, r_o, which was calculated by calibrating a steady-state simulation of a homogeneous system with known permeability. This value of r_o was checked with that computed using an analytical well model formula derived for the same geometry as Fig. 5.1-1 (Abou-Kassem and Aziz 1985), and was found to agree within 1%.

Table 5.1-1 System Data for Modeling Pressure and Tracer Response

Area, A	20 acres
Grid size (NX * NY)	15 * 15
Thickness, h	10 ft
Porosity, ϕ	0.10
Median k, k_{50}	10 md
Injection rate, q_{inj}	106.3 bbl/day (0.50 pore volumes/year)
Production rate, q_{prd}	106.3 bbl/day (0.50 pore volumes/year)
Tracer Slug size, V_{TR}	0.10 pore volumes
V_{DP} $[\sigma^2_{ln(k)}]$	0.35(0.18), 0.50(0.48), 0.65(1.10)
λ_D	1/15, 6/15, 16/15

Analysis of Pressure Test Data

For each combination of V_{DP} and λ_D, pressure responses were simulated for the twenty different permeability realizations. Only a few sample pressure-time graphs are shown in Figs. 5.1-5-5.1-7. Notice that when permeability variation and spatial correlation are small, injection and production well responses are nearly symmetrical around the initial pressure level of 4000 psi, and the variability from one realization to another is small (i.e. Fig. 5.1-5). As the measures of heterogeneity V_{DP} and λ_D increase, however, there is greater asymmetry in production and injection well behavior, as well as greater variability in the response of different realizations (i.e. Figs. 5.1-6-5.1-7).

Use of Eq. (5.1-5) for computing transient permeabilities requires the development of a semilog straight line on a pressure-time graph. Acceptable straight lines were found in all cases, and internal consistency checks were made to verify that appropriate dimensionless time bounds (as calculated from homogeneous system simulations) were satisfied. The slopes of these semilog straight lines were then used to calculate effective injection and production well permeabilities. Steady-state permeabilities k_{ss} were calculated from Eq. (5.1-6), and with only a few exceptions, these values were found to lie between k_{inj} and k_{prd}. That behavior suggested that some weighted average of k_{inj} and k_{prd} could be used as an estimator of k_{ss}. The geometric mean was tested for this purpose and found to yield good results. Fig. 5.1-8 shows the agreement between k_{ss} values calculated from Eq. (5.1-6), and those predicted by the geometric mean approximation.

Also investigated was the possibility that variation between injection and production well permeabilities could be correlated with some measure of heterogeneity. For this purpose, we define a dimensionless permeability difference as

$$\Delta k_D = \frac{| k_{inj} - k_{prd} |}{k_{ss}} \tag{5.1-7}$$

For each combination of V_{DP} and λ_D, the average value of this parameter was calculated from twenty simulation runs. Fig. 5.1-9 shows the behavior of the averaged value of Δk_D as a function of V_{DP} and λ_D. Notice that as the correlation length λ_D increases, the mean value of Δk_D also increases, and the increase is larger when V_{DP} is also large. This trend suggests that some suitable combination of V_{DP} and λ_D might prove to be a single correlating parameter. One possible grouping is $\sigma^2_{ln(k)}\lambda_D$, since V_{DP} and $\sigma^2_{ln(k)}$ are related through Eq. (5.1-3). This parameter group, termed *heterogeneity index*, is a convenient measure of heterogeneity because it captures both variability and spatial continuity of the stochastic permeability field.

The choice of $\sigma^2_{ln(k)}\lambda_D$ as a correlating parameter was based on two lines of reasoning. Studies of tracer dispersion in stochastic velocity fields have shown that dispersivity due to convective effects is related to this parameter group (Gelhar 1986). Since the objective is to compare pressure and tracer responses, it is useful to establish the way in which permeability variation (as obtained from pressure test analysis) can be linked to this group. The second argument, which is more heuristic in nature, is as follows. The dimensionless parameter Δk_D, which is a measure of the difference in mean effective permeability at the two wells, quantifies the significance of the trend in the permeability distribution over the scale of the problem. When trends are significant, i.e. when λ_D is of the order of unity, the probability of clustering of like-permeability blocks is high. Thus, if the average permeability around the injection well is higher than the median, the average permeability around the injection well would be lower than the median. The difference between these two values would then be proportional to σ_k. Since the steady-state interwell permeability is related to $\bar{k}$, this implies that $\Delta k_D \approx \sigma_k / \bar{k} \approx \sigma_{ln(k)}$. It follows that the group $\sigma^2_{ln(k)}\lambda_D$ is a suitable correlating parameter, at least over some range of Δk_D. Fig. 5.1-10 is a graph of the expected value of Δk_D against $\sigma^2_{ln(k)}\lambda_D$ in log-log coordinates. Also shown are the 95% confidence intervals

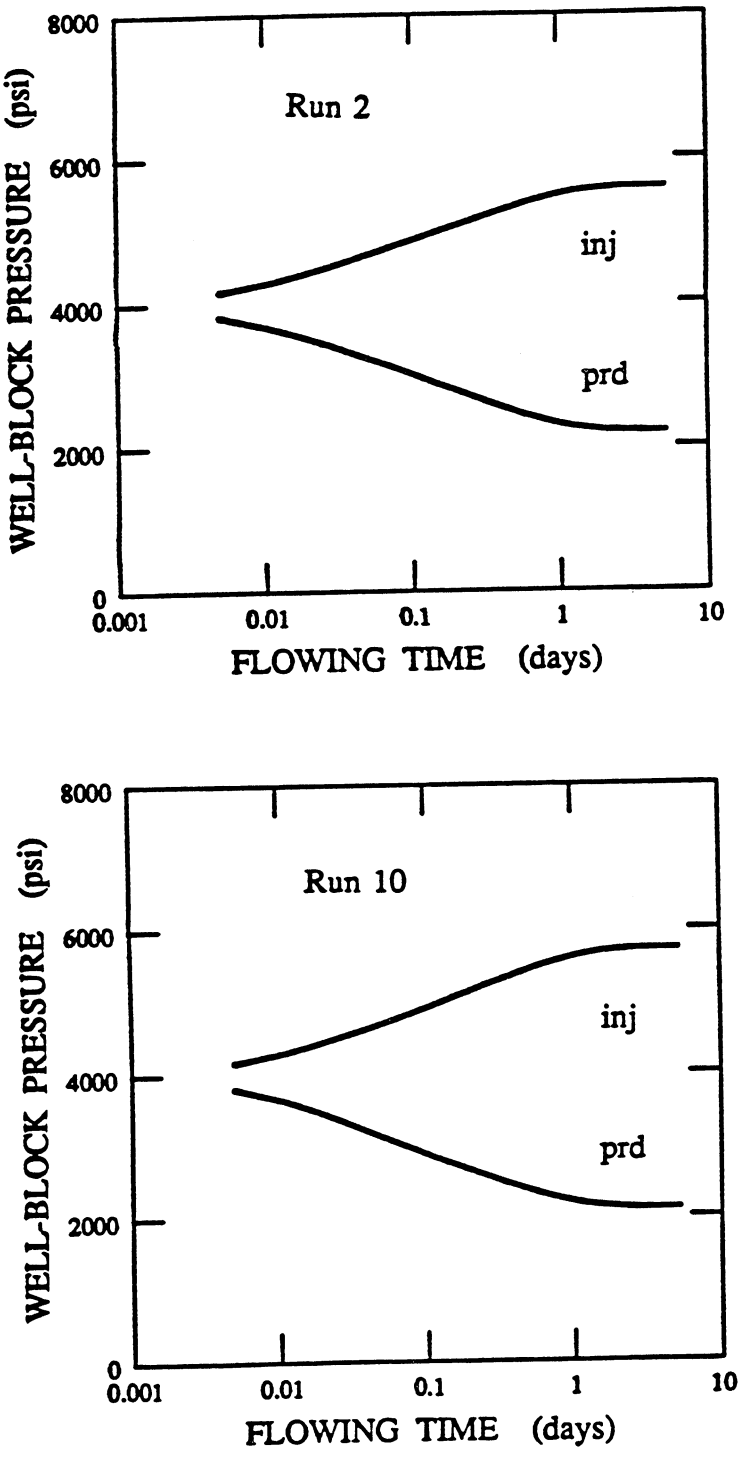

Fig. 5.1-5 Simulated pressure response, $V_{DP} = 0.35$, $\lambda_D = 1/15$.

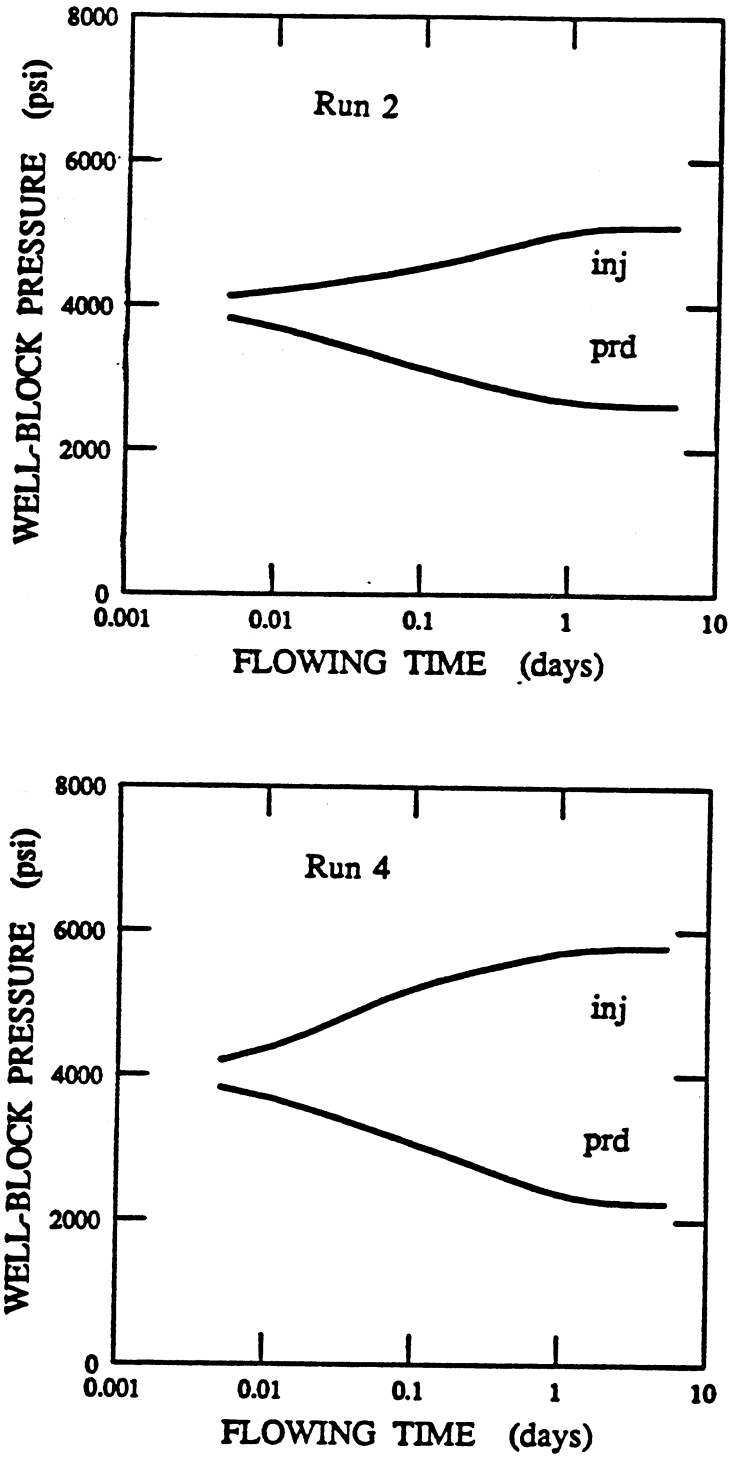

Fig. 5.1-6 Simulated pressure response, $V_{DP} = 0.50$, $\lambda_D = 6/15$.

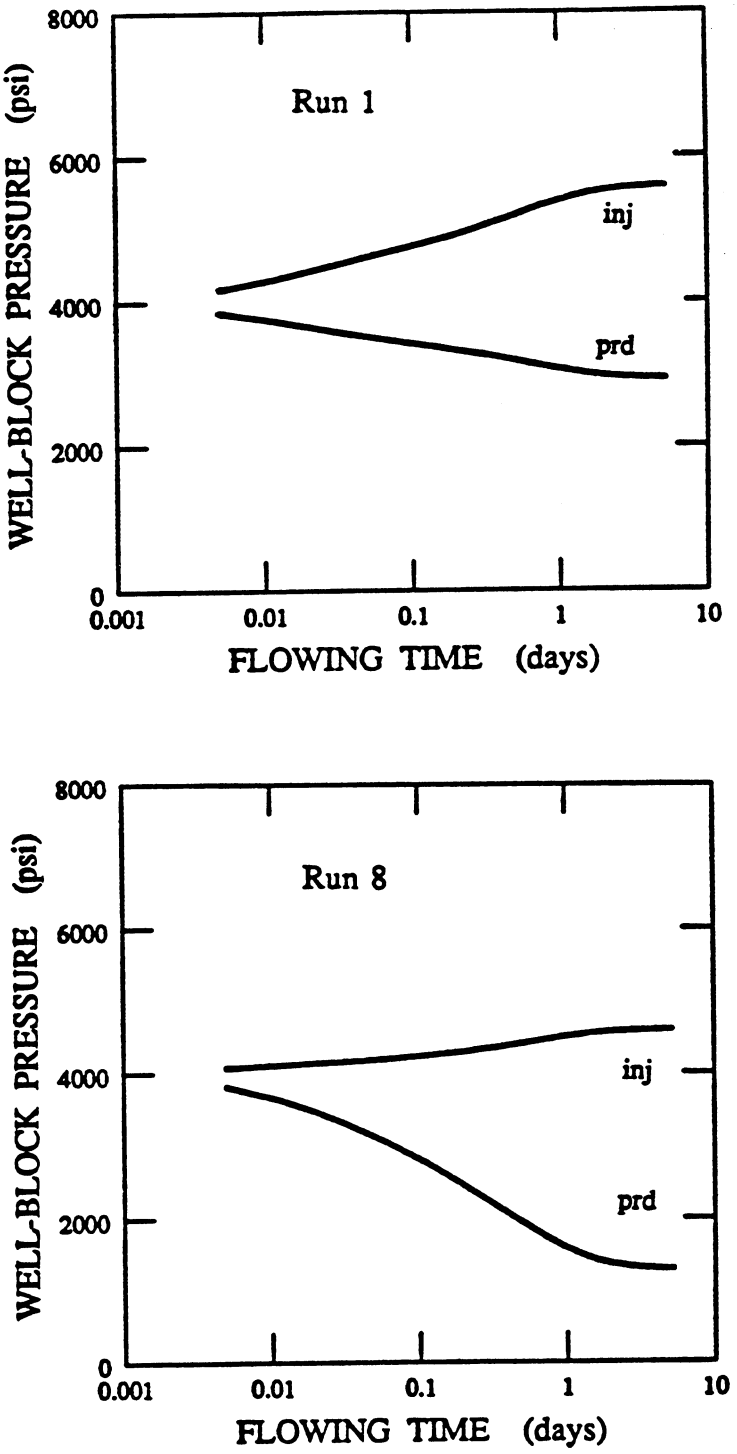

Fig. 5.1-7 Simulated pressure response, $V_{DP} = 0.65$, $\lambda_D = 16/15$.

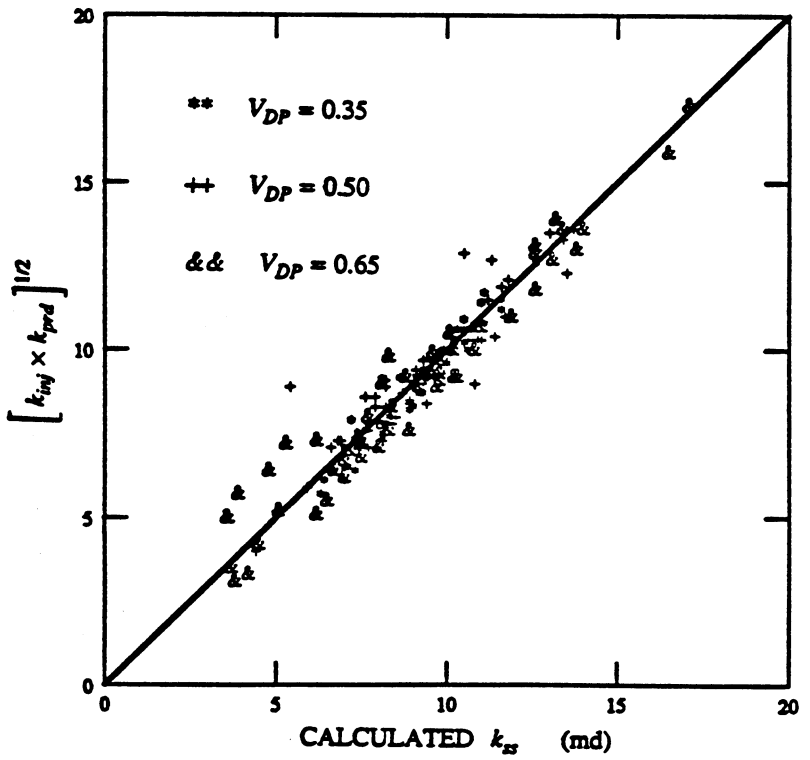

Fig. 5.1-8 Comparison between calculated and predicted k_{ss} values.

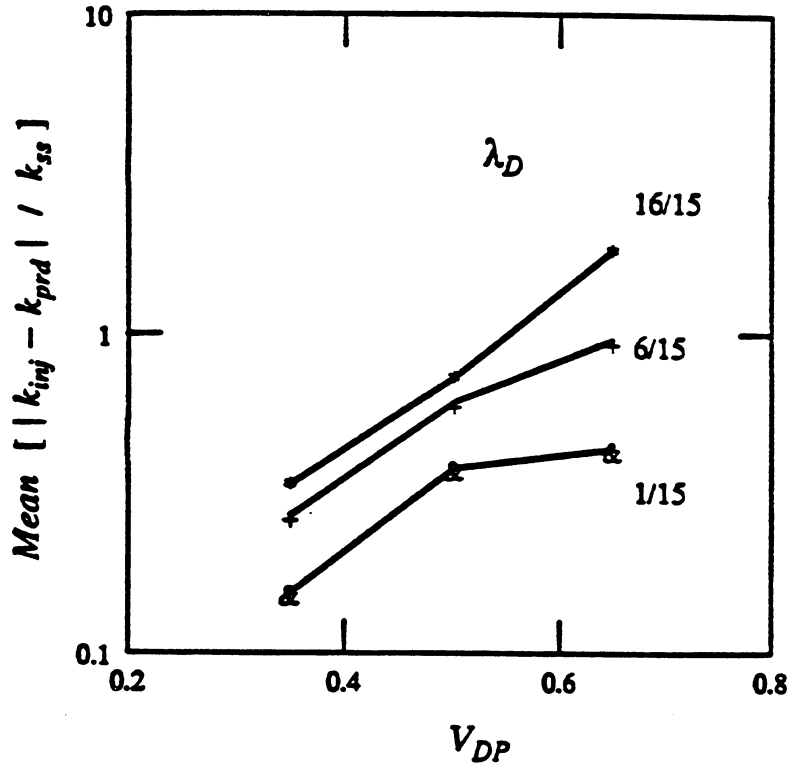

Fig. 5.1-9 Dimensionless permeability difference Δk_D as a function of V_{DP} and λ_D.

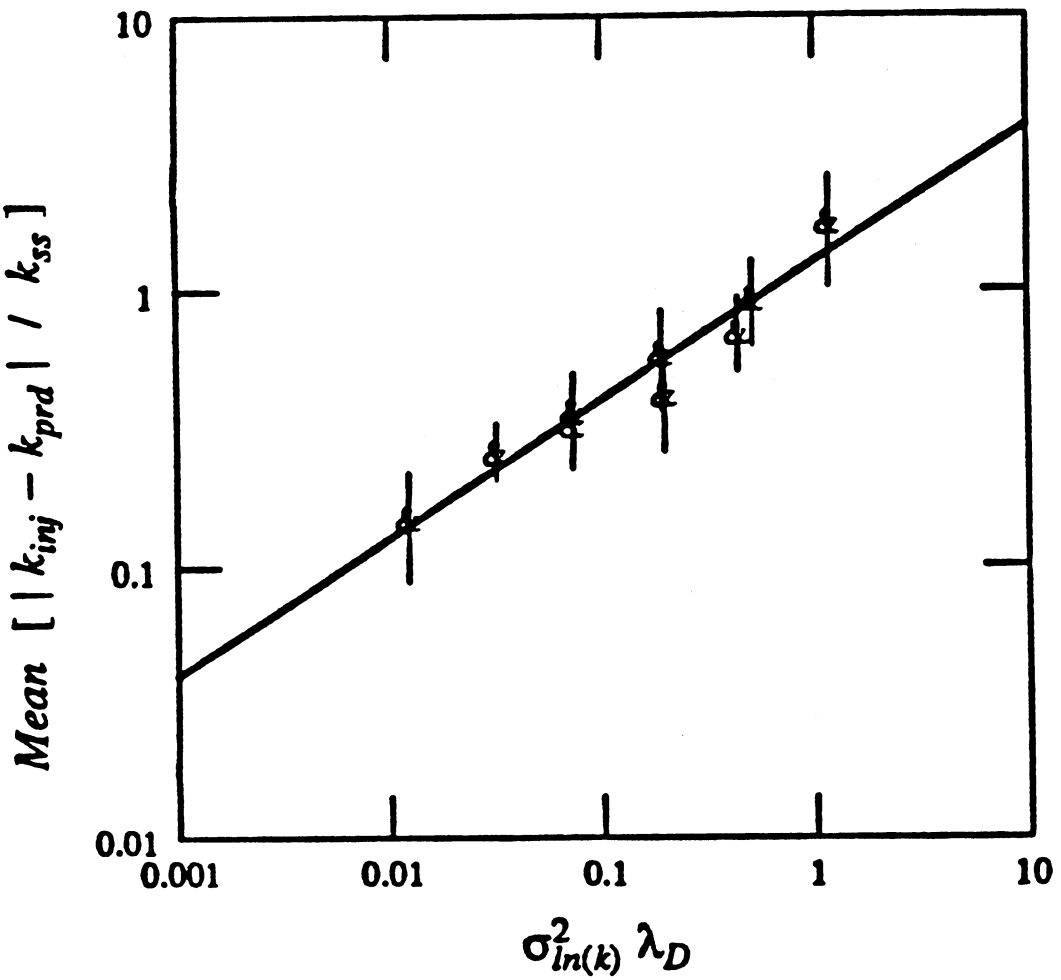

Fig. 5.1-10 Relationship between Δk_D and heterogeneity index $\sigma^2_{ln(k)}\lambda_D$.

around the data points. A least-squares fit of this data set yields the following power law relationship

$$\Delta k_D = 1.3 \left[\sigma^2_{\ln(k)} \lambda_D \right]^{1/2} \qquad (5.1\text{-}8)$$

This simple relation can be used to quantify in situ permeability variation from pressure transient data alone.

5.1.3 Tracer Test Response

The convection-dispersion equation (Eq. 5.1-1), which is commonly used to model tracer flow in porous media, represents tracer transport as the result of two physical processes, convection and dispersion (Bear 1972). Convection refers to bulk fluid flow, and dispersion to spreading of the tracer slug due to a combination of molecular diffusion and local velocity fluctuations. Diffusional effects are important only at the pore scale, and/or at low displacement velocities (Perkins and Johnston 1963). Consequently, it is customary to lump all dispersive factors into one transport parameter, the dispersion coefficient, D. Based on laboratory measurements, D is generally expressed as the product of displacement velocity, v, and a constant, α, known as dispersivity, a characteristic of the medium (Bear 1972). Such a representation is sometimes referred to as the Fickian model, by analogy with molecular diffusion processes.

Application of the Eq. (5.1-1) to field scale problems has yielded inconsistent results, particularly with respect to dispersivity. Field dispersivities have been found to be orders of magnitude higher than those measured in the laboratory, even for similar media. Moreover, dispersivity has also been observed to be dependent on the time and scale of displacement. Such anomalies have been ascribed to large-scale formational heterogeneities which are successively encountered as tracer transport progresses in space. See Gelhar et al. (1985) for a review of pertinent field evidence.

A tracer test is essentially a displacement experiment at the interwell scale, and hence convective effects (caused by local permeability/velocity variations) are likely to be the dominant mechanism of tracer transport. Therefore it is necessary to examine the appropriateness of the convection-dispersion equation for modeling tracer flow at this scale. Of particular interest is whether the solutions of Abbaszadeh-Dehghani and Brigham (1982), derived for homogeneous systems, can be used to analyze tracer breakthrough curves for heterogeneous media and yield effective dispersivities. Associated objectives are to examine the conditions under which Eq. (5.1-1) is valid, and to relate dispersivity to measures of permeability variation.

Simulation of Tracer Flow

The numerical tool used in modeling tracer flow under steady-state unit mobility ratio miscible displacement conditions was the USGS 2-D Solute Transport simulator (Konikow and Bredehoeft 1978), which is based on a method of characteristics scheme first proposed for solving miscible displacement problems (Garder et al. 1964). This simulator solves a finite-difference approximation to the flow equation (Eq. 5.1-2) to calculate the steady-state velocity distribution. A particle tracking procedure is then used to represent convective flow, and a two-step explicit procedure to solve a finite-difference equation that describes the effects of hydrodynamic dispersion and fluid sources and sinks. Details of the model and the computer code is given by Konikow and Bredehoeft (1978).

The computer program was verified by matching simulated tracer breakthrough curves for homogeneous systems with the analytical solutions of Abbaszadeh-Dehghani and Brigham (1982). Comparison of the analytical and numerical model results, shown in Fig. 5.1-11,

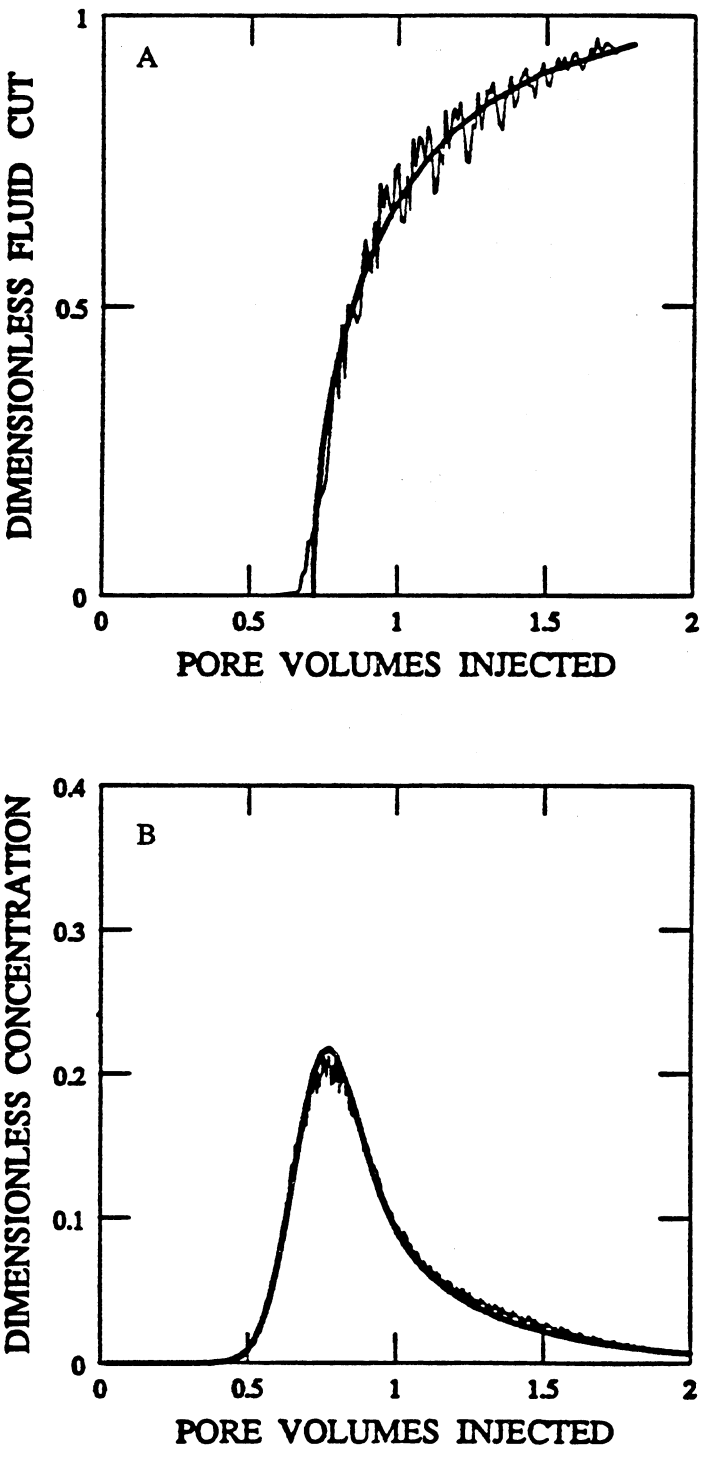

Fig. 5.1-11 Tracer flow simulator validation; A: continuous injection; no dispersion; B: slug injection, α = 10 ft.

indicates that use of the method of characteristics effectively eliminates the problem of numerical dispersion, a drawback of conventional finite-difference or finite-element modeling of the convection-dispersion equation.

The basis for interpreting simulated tracer test data is an analytical solution of the Eq. (5.1-1), derived for unit-mobility ratio flow in a repeated 5-spot (Abbaszadeh-Dehghani and Brigham 1982). The expression for pattern tracer breakthrough curve is developed by first combining the mixing that occurs within each streamline with its time of travel, and then integrating this result over all the streamlines. Details of the derivation are given by Abbaszadeh-Dehghani and Brigham (1982). Here we present only the final solution

$$C = 0.57726\, C_i\, F_r \sqrt{\frac{a}{\alpha}} \int_0^{\frac{\pi}{4}} \frac{\exp\left[\frac{0.645776}{Y(\psi)}\,\frac{a}{\alpha}\left[V_{pDBT}(\psi) - V_{pD}\right]^2\right] d\psi}{Y(\psi)} \qquad (5.1\text{-}9)$$

where C is the concentration of tracer in the produced fluid, C_i the injected concentration, a the distance between wells in a five spot (2L), $V_{pDBT}(\psi)$ is the pore volumes injected at breakthrough of streamline ψ, V_{pD} is the total pore volumes injected and F_r is the injected tracer slug size expressed in pore volumes. The $Y(\psi)$ function is a hyperelliptic integral relating velocity in a streamline and dispersivity to total spreading in the streamline. Note that when the system size and injection parameters are known, observed tracer concentration is a function of only one parameter, dispersivity, α.

Analysis of Tracer Test Data

Tracer responses were generated for several cases, only a few of which are presented here. Figs. 5.1-12-5.1-14 show tracer breakthrough curves for the same physical systems for which pressure responses were graphed in Figs. 5.1-5-5.1-7. As expected, tracer concentration-time data show greater sensitivity to permeability variation than transient pressure data. Similar behavior has been observed for the case noncommunicating layered reservoirs in a repeated 5-spot (Mishra and Ramey 1985).

Breakthrough in all simulated tracer tests occurred much earlier than a time corresponding to an injected volume of approximately 56,000 bbl (0.72 pore volumes), which is the theoretical value for breakthrough in a homogeneous 5-spot. Early breakthrough indicates the presence of preferential flow paths or substantial fluid mixing. Since the simulation model considers no dispersion and numerical dispersion effects have been minimized through the use of the method of characteristics, the breakthrough behavior must have been caused by velocity fluctuations in a spatially varying permeability field.

The overall shapes of the tracer breakthrough curve also indicate the nature of the flow system. In general, two types of flow behavior can be distinguished qualitatively. The first kind (e.g. Fig. 5.1-12), which we term diffusive, or Fickian, produces a tracer response resembling that of a homogeneous system where the slug has been dissipated by mixing. In this case, the tracer response can be matched with the appropriate solution of the convection-dispersion equation (Abbaszadeh-Dehghani and Brigham 1982) to determine an effective dispersivity. Since slug dilution is attributable only to velocity/permeability variations in a heterogeneous flow field, the computed effective dispersivity is essentially a measure of permeability variation.

The second kind of flow behavior (e.g. Figs. 5.1-13 and 5.1-14), termed convective, or non-Fickian, is characterized by multiple peaks in the tracer breakthrough curve, indicating the presence of more than one channel for fluid flow. Such a geometry, consisting of multiple discrete flow channels within a single layer, is effectively equivalent to a layered system with several noncommunicating strata. Because the mobility ratio is unity, tracer response in this system can be modeled by superposition of individual layer solutions, and a nonlinear

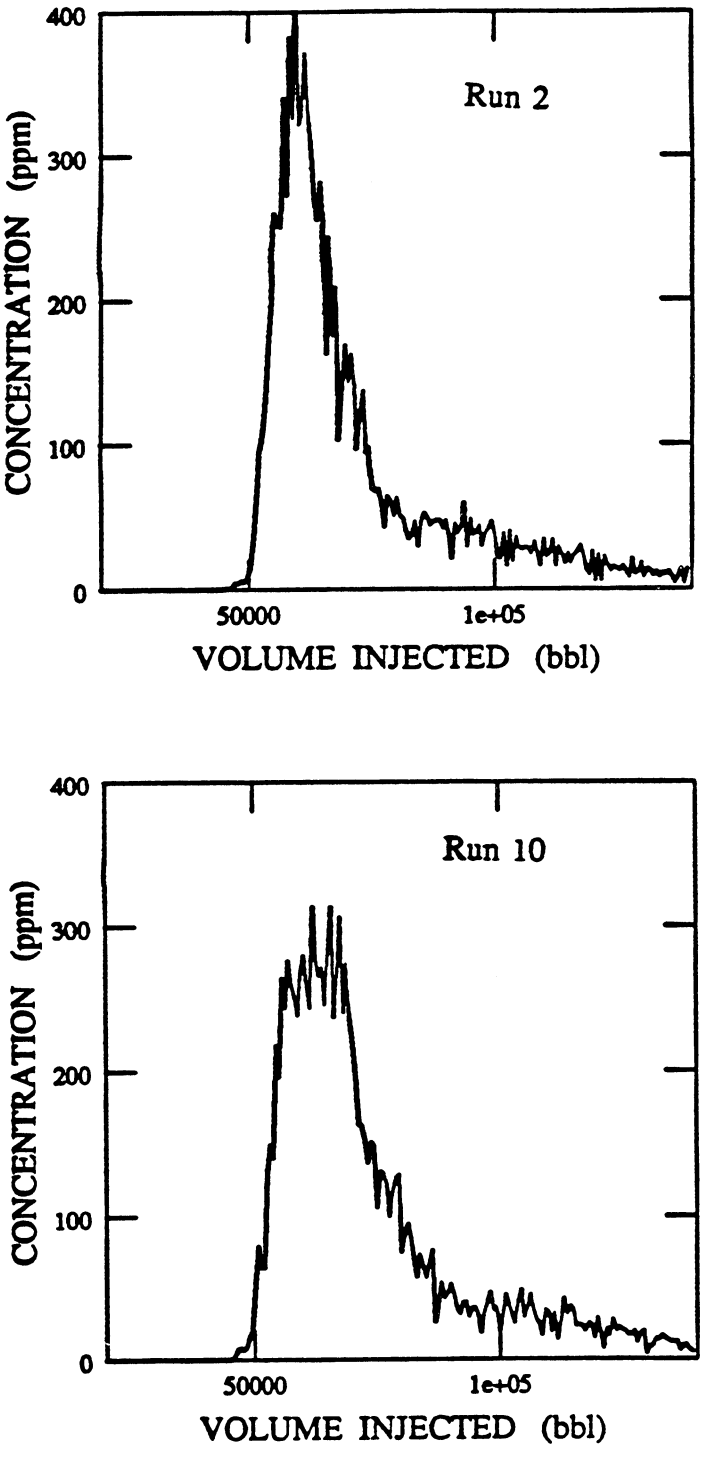

Fig. 5.1-12 Tracer breakthrough curve, $V_{DP} = 0.35$, $\lambda_D = 1/15$.

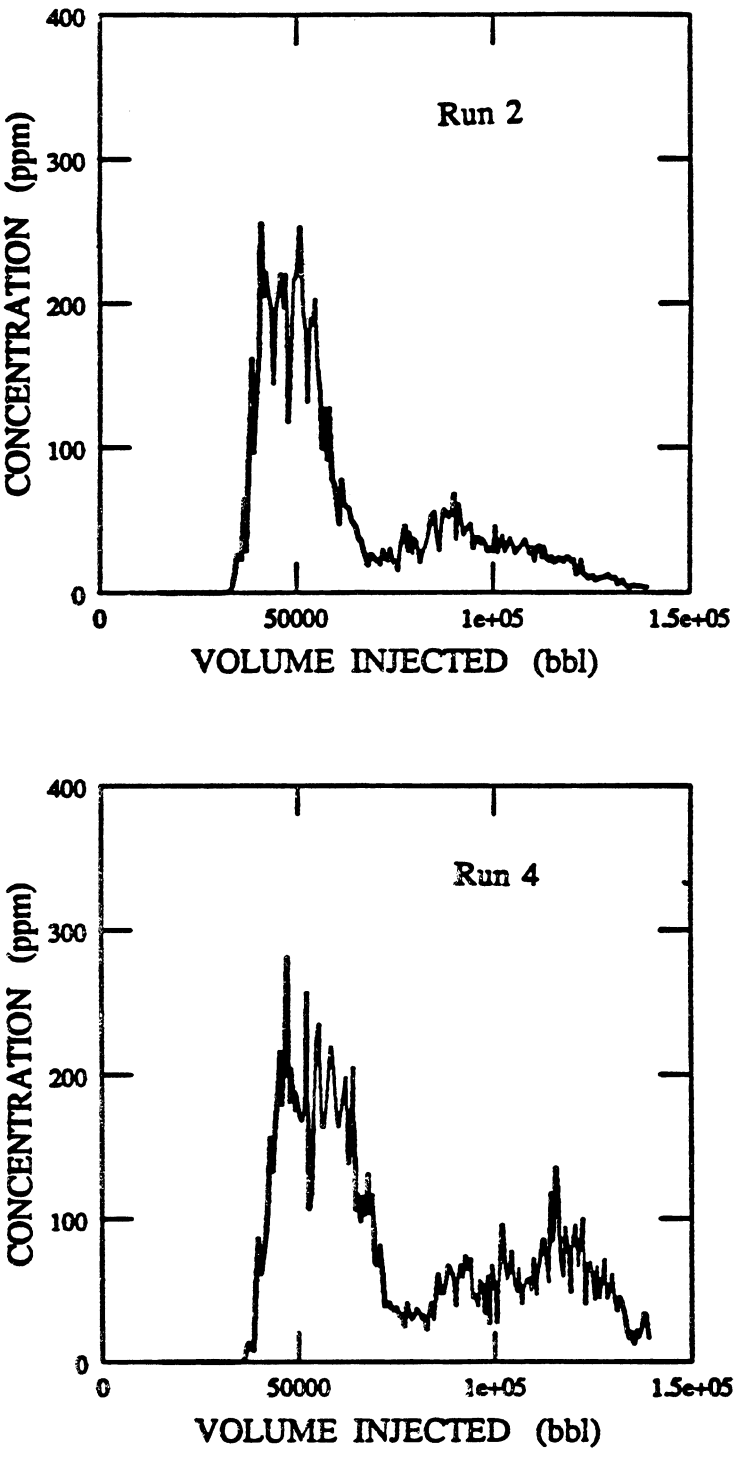

Fig. 5.1-13 Tracer breakthrough curve, $V_{DP} = 0.50$, $\lambda_D = 6/15$.

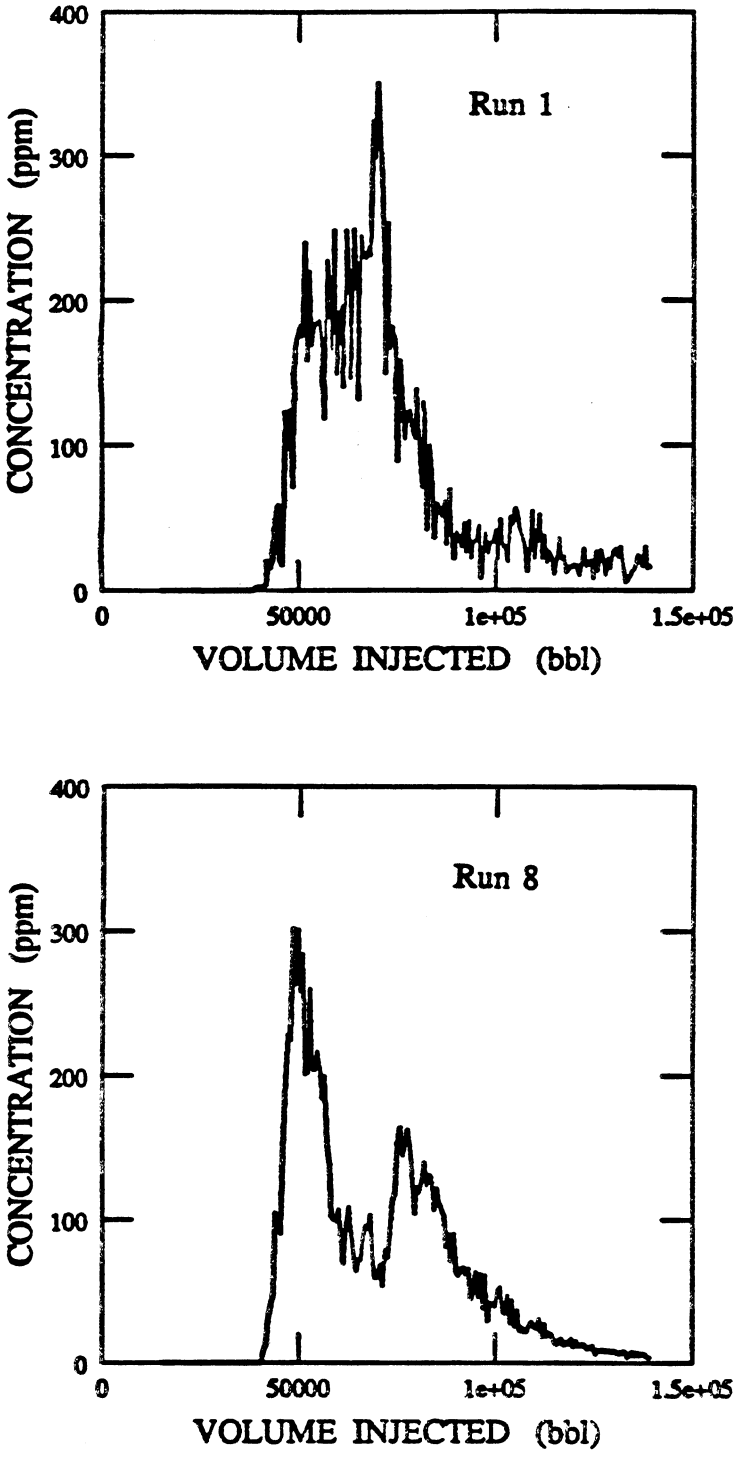

Fig. 5.1-14 Tracer breakthrough curve, $V_{DP} = 0.65$, $\lambda_D = 16/15$.

optimization scheme can be used to deconvolve the integrated tracer breakthrough curve for estimating effective-layer properties (Abbaszadeh-Dehghani and Brigham 1982).

Validity of the Convection-Dispersion Equation

It has been pointed out that the Fickian model of field-scale dispersion is appropriate only for large time and length scales (Gelhar 1986). Thus, when the dimensions of the flow field are fixed, as in this study, Fickian behavior can be expected only if permeability variation and correlation lengths are small enough to permit sufficient averaging of spatial velocities during tracer transport. In the simulations described here, Fickian behavior was observed for small V_{DP} and λ_D. For larger values of V_{DP} and λ_D preferential flow paths were generated and caused a non-Fickian (multimodal) tracer response, and the convection-dispersion equation with a single-value of dispersivity could no longer be used to match effluent tracer concentration data.

These observations can be quantified using the heterogeneity index ($\sigma^2_{ln(k)}\lambda_D$) defined previously. This group contains information on the degree of permeability variation, as well as the spatial scale over which such variations persist. In Fig. 5.1-15, we plot the percentage of Monte Carlo runs showing non-Fickian behavior as a function of $\sigma^2_{ln(k)}\lambda_D$. As expected, the relationship is monotonically increasing, and asymptotically approaches Fickian and non-Fickian limits at the two extremes. Note that the dashed portions represent extrapolation beyond the range of available data. Fig. 5.1-15 establishes the uncertainty associated with Monte Carlo simulation results of convective flow processes, even when the statistics of the medium are known. However, it is possible to deduce approximately conditions under which Fickian or non-Fickian behavior will be dominant. Fig. 5.1-15 suggests that Fickian behavior is restricted to values of $\sigma^2_{ln(k)}\lambda_D$ less than about 4×10^{-2}, and non-Fickian behavior is expected for values of $\sigma^2_{ln(k)}\lambda_D$ greater than about 4×10^{-1}.

Smith and Brown (1984) computed effective dispersivities in a two-dimensional heterogeneous medium by fitting space-averaged concentration-time data to a Fickian model. The maximum value of $\sigma^2_{ln(k)}\lambda_D$ considered was about 8×10^{-2} (see their Fig. 5.1-6a), which is slightly higher than our limiting criterion for diffusive behavior. This also explains the general success of the Fickian model in matching their simulated data.

Arya et al. (1985) followed a similar procedure for matching concentration-time data in two-dimensional randomly heterogeneous media, and found that the Fickian model may not be appropriate when permeability variation and correlation length scale are large. Their results suggest that diffusive behavior is limited to cases when λ_e is less than 0.1–0.2 L, where λ_e is the integral range of an exponential semivariogram of log-permeability values, and is approximately equal to $0.32\,\lambda$. They used a V_{DP} value of 0.6 (Arya, A., personal communication), for which case their criterion becomes equivalent to $\sigma^2_{ln(k)}\lambda_D < 3\text{–}6 \times 10^{-2}$, which is consistent with our results.

Significance of Effective Parameters

At this stage, we ask if the effective parameters calculated from tracer test data (i.e. dispersivities and effective-layer properties) can be correlated with some measure of permeability variation such as the heterogeneity index. Based on the criteria derived from Fig. 5.1-15, we inferred that Fickian behavior was probable for (a) $V_{DP} = 0.35$, $\lambda_D = 1/15$, and (b) $V_{DP} = 0.50$, $\lambda_D = 1/15$. For these two cases, effective dispersivities were computed from all simulation runs exhibiting qualitative Fickian behavior (unimodal tracer breakthrough response). The average value of dispersivity, α, for each of these two data sets, normalized by the characteristic flow length, L, is plotted in Fig. 5.1-16 as a function of $\sigma^2_{ln(k)}\lambda_D$. The straight line shown is the analytical result of Gelhar and Axness (1983) for two-dimensional isotropic media derived from stochastic theory

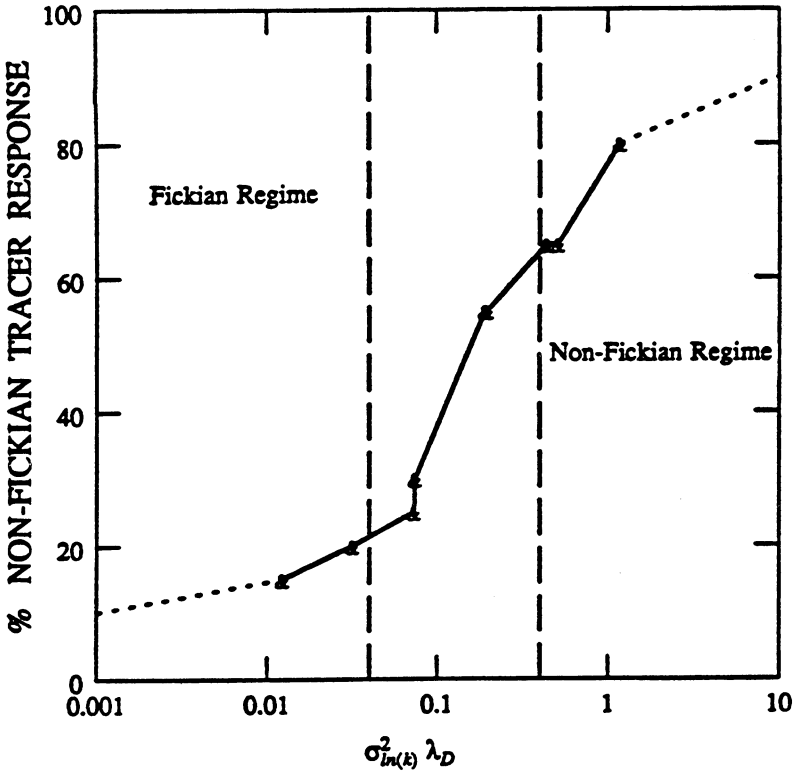

Fig. 5.1-15 Influence of $\sigma^2_{ln(k)}\lambda_D$ on nature of tracer response.

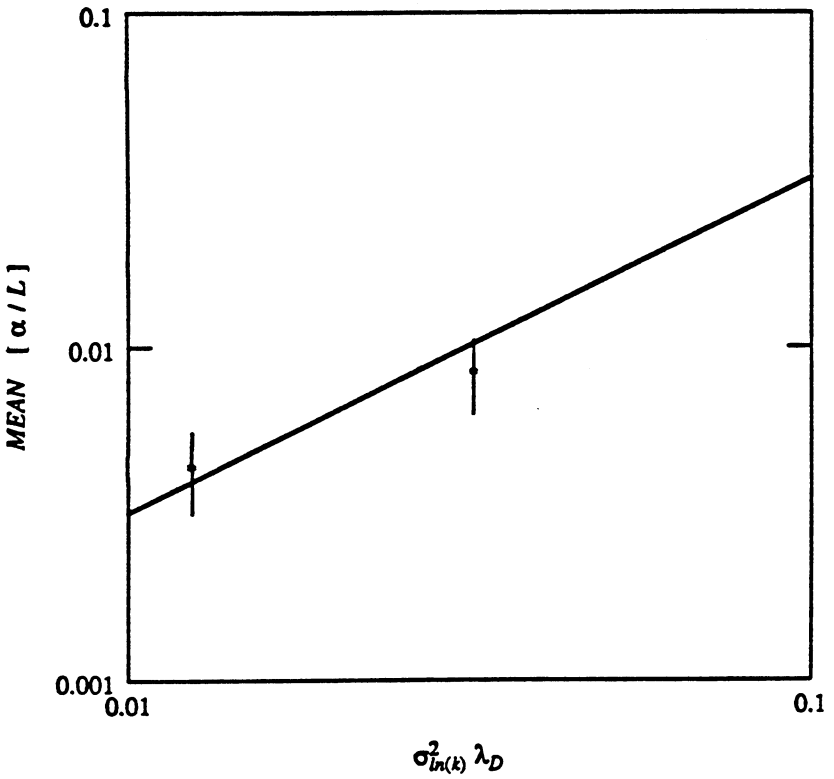

Fig. 5.1-16 Comparison of computed Fickian dispersivities with analytical results.

$$\frac{\alpha}{L} = 0.32\,\sigma^2_{\ln(k)}\lambda_D \qquad (5.1\text{-}10)$$

where α is the dispersivity.

Also shown are 95% confidence intervals around the data points. The agreement between simulation results and predictions of stochastic theory is reasonable in view of the limited number of Monte Carlo runs used for averaging.

For the non-Fickian examples, it was possible to match most tracer breakthrough curves with a 2-layered model. In each case, the dispersivity, α, was fixed at an arbitrary value of 1 ft. so as to make the problem convection dominated. A nonlinear regression program (Abbaszadeh-Dehghani and Brigham 1982) was then used to fit the simulated breakthrough data to the appropriate analytical solution. Each match yielded four parameters, two for each pseudolayer, the fractional ϕh and kh products. No trend was observed in either of these parameters as a function of V_{DP}, λ_D or a combination of the two. Thus, an effectively layered interpretation model can be used to reproduce tracer response, though it is clear that the parameters obtained apply only at that scale. Such parameters can also be used in conjunction with simple models for computing displacement performance (Pande et al 1987). It is obvious that when the scale of heterogeneities is comparable to system dimensions, the tracer flow response is strongly dependent on the exact arrangement of permeability in the flow field. Thus, even when average measures (variance, correlation length scale) of permeability variation are the same, tracer flow behavior (as well as the recovery behavior from an EOR process) might be completely different. An example is Fig. 5.1-14, where two distinctly differing breakthrough curves are shown for the same statistical parameters. Their effective-layer properties are also quite different, as given in Table 5.1-2. An additional statistical parameter, which measures the *connectivity* effect of permeability, would improve correlation of non-Fickian tracer responses, though it is not obvious what that parameter should be.

5.1.4 Discussion

Using a Monte Carlo approach, we have demonstrated how pressure and tracer test data show different degrees of sensitivity to the presence of a heterogeneous permeability field. A parametric connection between the two test responses has been established empirically using the concept of heterogeneity index. This parameter also forms the basis of a proposed reservoir description procedure:

1. From transient pressure data, compute k_{inj} and k_{prd}. Calculate k_{ss} from steady-state data, or use the geometric mean of k_{inj} and k_{prd} as a working approximation.
2. Compute dimensionless permeability difference Δk_D from Eq. (5.1-7), and estimate heterogeneity index $\sigma^2_{\ln(k)}\lambda_D$ from Eq. (5.1-8).
3. Predict the qualitative nature of the tracer test response (Fickian or non-Fickian) using Fig. 5.1-15.
4. If Fickian behavior is expected, calculate effective dispersivity from Eq. (5.1-10).
5. When tracer test data is available, verify the results of step (3), or compute effective-layer properties.

Simulation results reported here are based on a V_{DP} range of 0.35-0.65, and a λ_D range of 1/15-16/15 ($60 < \lambda < 1000$ ft). We believe the V_{DP} values to be representative of actual field conditions, even though these are less than typical core V_{DP} bounds, because a reduction in variance occurs when core measurements are scaled up to grid-block values (Journel and Huijbregts 1978). However, the same degree of confidence cannot be assigned to the λ values used. The uncertainty arises from the lack of information regarding permeability correlation length scales in actual reservoirs. Data from groundwater aquifers suggest that λ may be of the order of tens of kilometers, (Hoeksema and Kitanidis 1985) and may also be scale dependent (Gelhar 1986).

Table 5.1-2 Pseudolayer Parameters from Simulated Tracer Test Data

$V_{DP} = 0.65$, $\lambda_D = 16/15$

Run	Layer 1		Layer 2	
	$kh/\Sigma kh$	$\phi h/\Sigma\phi h$	$kh/\Sigma kh$	$\phi h/\Sigma\phi h$
1	0.43	0.39	0.56	0.60
8	0.56	0.48	0.38	0.45

Da Costa e Silva (1985) presented data on permeability variation and continuity from a North Sea oil reservoir. He fitted a spherical semivariogram model (the three-dimensional analog of the circular model used in this study) to permeability measurements, and estimated $\sigma^2_{\ln(k)} = 0.85$, and $\lambda = 3.4$ miles. We have used these parameters to calculate heterogeneity index as a function of well spacing. The results of this computation, shown in Fig. 5.1-17, suggest that under typical field scale displacement conditions, non-Fickian behavior can be expected to be the norm based on the criterion derived from Fig. 5.1-15.

The computations reported here indicate that routine use of the convection-dispersion equation for modeling tracer (and miscible fluid) displacement in heterogeneous media is open to question. In the groundwater literature, the current philosophy is to obtain some knowledge of the spatial variation and continuity of the permeability field and then use stochastic theory to calculate the components of an apparent dispersion tensor (Gelhar 1986). Such an approach may be useful in the context of contaminant transport, but its applicability in petroleum reservoir engineering seems limited because of the small number of wells available for sampling the permeability distribution. An alternative is to ignore the dispersion formulation, and view spreading of the tracer slug as the result of convective effects in a heterogeneous flow field. This modeling approach also requires a detailed knowledge of the permeability field. However, by using information from cores, logs and pressure tests, permeability values can be obtained at some pilot points (wells). Conditional simulation (Journel and Huijbregts 1978) can then be used to construct the entire permeability field with some interpolation in the interwell region that honors known information at the wells.

The need for well-designed field tests for detection of reservoir heterogeneities is paramount. A single-well pressure test would reveal only an average permeability in its drainage area, but the combination of several such tests has the potential to reveal structures in permeability variation, albeit in some averaged sense. Even though there are limits to detection with well tests, procedures such as those developed in this study can yield simple measures of in situ permeability variation. That, in itself, is an important first step.

5.1.5 Conclusions

The major conclusions from this numerical study of pressure and tracer responses in single-layer areally heterogeneous permeable media are:

(1) For a single five-spot in a repeated pattern, the steady-state interwell permeability is approximated by the geometric mean of injection and production well permeabilities.

(2) A dimensionless permeability difference, defined in terms of these quantities, is related to a measure of permeability variation $\sigma^2_{\ln(k)}\lambda_D$, termed the heterogeneity index.

(3) When the heterogeneity index is small, tracer test data can be matched with solutions of the convection-dispersion equation to calculate dispersivities, which are proportional to the heterogeneity index.

(4) For larger values of heterogeneity index the convection-dispersion equation alone is inappropriate for modeling tracer flow, since preferential flow channels are created and cause tracer breakthrough curves to behave as if resulting from a layered flow system.

(5) A reservoir description scheme, based on the analysis of pressure and tracer test data and the concept of heterogeneity index, is proposed. This procedure can be used to obtain an estimate of the likelihood of significant permeability correlation at interwell distances.

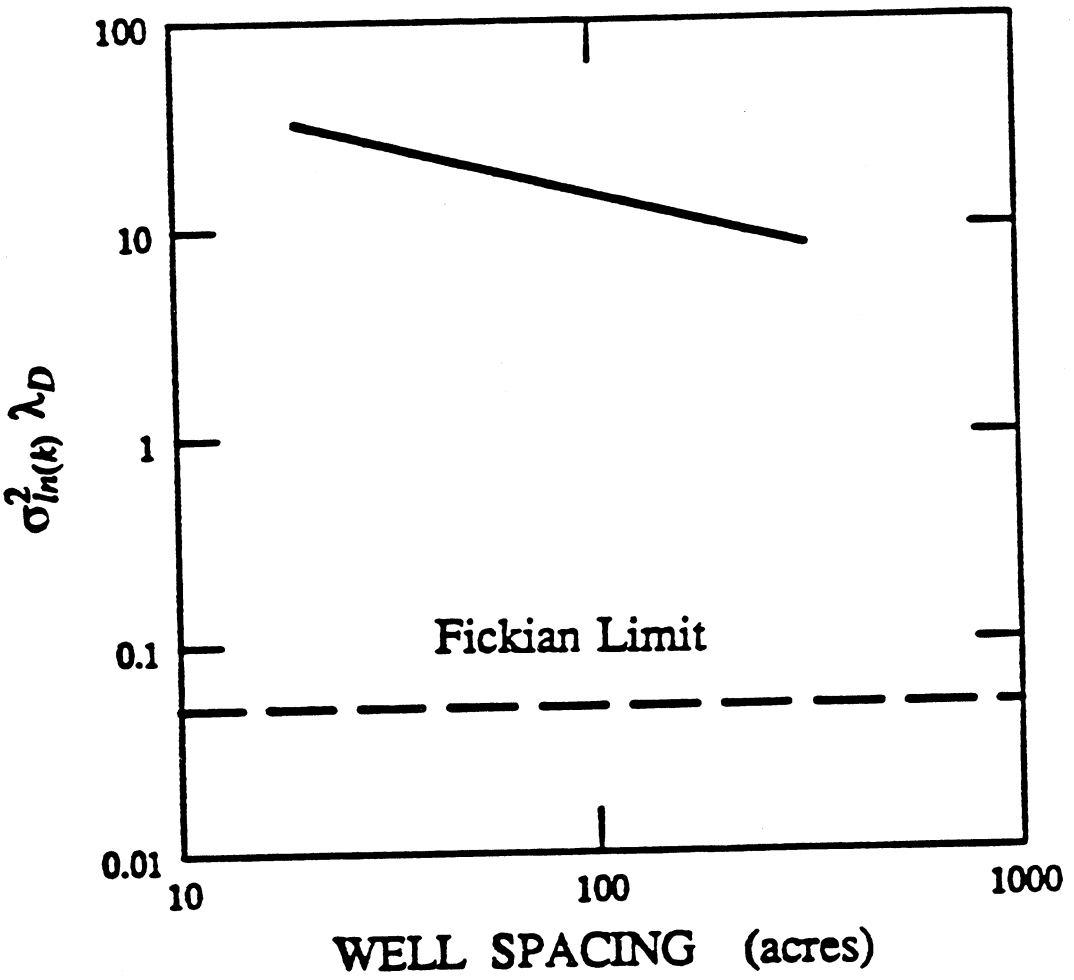

Fig. 5.1-17 Heterogeneity index as a function of well spacing, North Sea reservoir data.

5.2 The Effects of Size, Shape, and Orientation of an Impermeable Region on Transient Pressure Testing

Paulo Britto and Abraham S. Grader

Conventional well test methods are based on the assumption that reservoir properties are uniform, an assumption that is never satisfied rigorously. In this section we consider the extent to which certain heterogeneities can be detected by pressure transient testing. In particular, we consider the effects of the shape, size, and orientation of an impermeable reservoir region on transient pressure testing. The constant rate production well is external to the impermeable region. Impermeable regions may be in the form of sealing fractures of finite length that have little volume associated with them and are only a local restriction to fluid flow. These regions may also be shale lenses or reduced permeability regions that, in addition to being a restriction to flow, occupy a significant reservoir volume. This section considers a single impermeable region with various sizes, shapes, and orientations with respect to the active source well.

The transient pressure response of the constant rate well is generated by replacing the impermeable boundaries by a set of line sources, and then applying the method of superposition. This method can be extended to include pressure responses of interference wells. The method is validated by matching the pressure responses of simple cases like a linear no-flow boundary and an internal circular no-flow boundary.

The key issue here is the detectability of large scale impermeable reservoir regions by transient pressure analysis. The presence of an impermeable region causes the pressure response to deviate from the homogeneous line source response. This pressure deviation is the indication that the reservoir is heterogeneous. Four major parameters affect the pressure response of the active source well in the presence of an impermeable region: (1) the shortest distance between the well and the impermeable region, (2) the size of the region, (3) the shape of the region, and (4) the orientation of the region. This section presents combinations of these four parameters that significantly affect the transient pressure response as well as some criteria for deciding what impermeable regions may be detected uniquely.

Most of the transient pressure problems that are posed in petroleum engineering have their counterpart in the heat transfer field. The differential equations, or system of equations, and the boundary conditions are of the same kind, and, therefore, the techniques used to solve problems in one field are used to solve the corresponding problems in the other. Carslaw and Jaeger (1959) presented the solution for the heat conduction problem corresponding to the constant flow rate line source well in a homogeneous infinite slab porous medium. Van Everdingen and Hurst (1949) extended the solution for a finite wellbore radius. Their results demonstrated that at intermediate times, after the effects of wellbore storage and skin have ended, finite size reservoirs show an "infinite-acting" flow behavior.

By using line source imaging, Stallman (1952) generated the response of a well producing at constant flow rate near an infinite linear boundary. He presented log-log curves for both constant pressure and impermeable linear boundaries. The pressure responses of other semiinfinite reservoirs bounded by linear boundaries have been described in the literature. Tiab and Kumar (1980) studied the transient pressure behavior of a constant rate well arbitrarily located between two parallel sealing faults. Tiab and Crichlow (1979) presented type curves for the case of multiple sealing faults and bounded reservoirs. Prasad (1975) considered the case of a well located near two intersecting boundaries in an otherwise infinite system. He developed an analytical solution that is valid for all angles of intersection and well locations using the concept of fluid flow in a wedge. Yaxley (1985) described the effects of a partially communicating fault on transient pressure behavior. In his approach he treated the well as a constant rate line source, and the partially communicating fault as an infinitely long vertical semipermeable barrier. Van Everdingen and Hurst (1949) studied circular reservoirs with different internal and external boundary conditions. Earlougher and Ramey (1973) described interference testing in closed rectangular reservoirs.

The effects of internal reservoir discontinuities have not been considered extensively in the literature. Carslaw and Jaeger (1959) derived the Green's function for a point source external to a nonconductive circular boundary in an infinite slab medium. However, this solution is not readily integrated in space and time to yield the continuous line source. Cinco et al. (1976) studied the transient flow behavior of a well near an infinite conductivity natural fracture of finite length. Sageev and Horne (1983a) considered single well transient pressure analysis near a circular constant pressure or impermeable subregion. Their method allows the detection of the minimum distance between the active well and the circular boundary. Sageev and Horne (1983b) and Sageev (1985) presented an interpretation method for analyzing single well tests and interference tests in the presence of a steam cap or a local compressible two-phase region. Sageev and Horne (1986) described the detection of impermeable and constant pressure circular regions using interference pressure data.

In this study, we consider composite reservoirs with two different regions, one that is continuous and homogeneous in its properties, and another that acts as an impermeable internal boundary to the first. The effects of size, shape, and orientation of the impermeable reservoir subregion on the pressure response observed in an active well are presented. By analyzing transient pressure data from an active well, it may be possible to infer the presence of an impermeable subregion.

5.2.1 Theory

In the following derivation, we assume that the reservoir is horizontal, with isotropic properties, and infinite in the lateral extent. We consider a line source well, without wellbore storage and skin, producing at a constant rate near a single large scale impermeable subregion. The impermeable subregion may have volume associated with it or may be a linear feature like a fracture. The pressure response of any point in the reservoir is described by the diffusivity equation and by the internal boundary condition associated with the shape and the location of the impermeable subregion.

The transient dimensionless pressure response of a well producing with constant flow rate near an impermeable subregion is calculated by replacing that region by a set of line source wells producing with variable flow rates, and then applying the method of superposition. The dimensionless pressure is calculated at the production (active) well, but can also be calculated at any other observation well external to the impermeable subregion.

Fig. 5.2-1A shows schematically an impermeable line boundary of finite length and arbitrary shape. The impermeable boundary is approximated by a set of image wells located a few wellbore radii away from the location of the boundary, as is illustrated in Fig. 5.2-1B. The image wells are all line source wells that have a variable flow rate. However, during a time step, we assume that the image well flow rates are constant. Fig. 5.2-1B shows points on the actual impermeable boundary where the normal velocity to the boundary is computed and required to be zero. The number of zero velocity points is equal to the number of image wells. The dimensionless pressure and the normal derivative at a point on the boundary are calculated by adding the contributions of the active well and all the image wells for each time step, using the method of superposition. For each time step we have a system of linear equations, and the unknowns are the flow rates at all the image boundary wells for the time step.

The dimensionless pressure and time are defined in the standard manner

$$p_D = \frac{2\pi k h (p_i - p)}{q_0 B \mu} \tag{5.2-1}$$

$$t_D = \frac{k t}{\phi \mu c_t r_w^2} \tag{5.2-2}$$

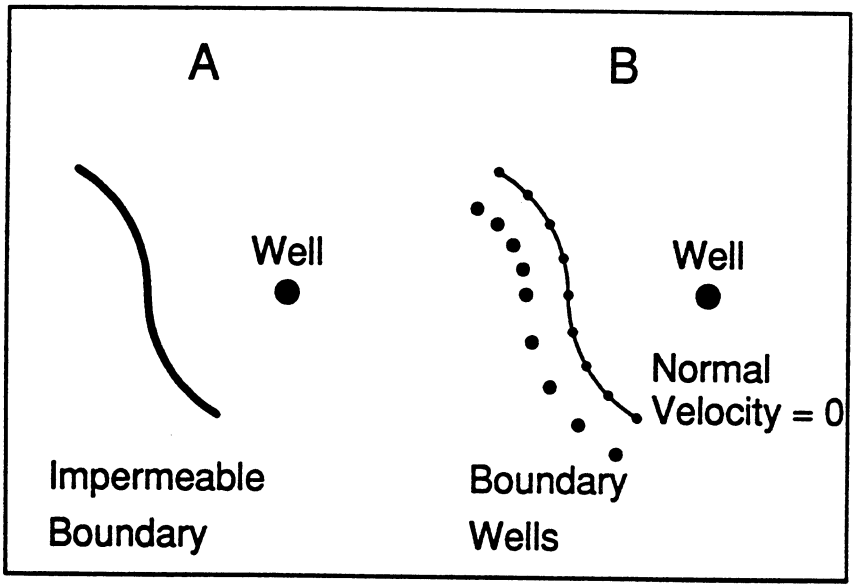

Fig. 5.2-1 Schematic diagram for a well near an impermeable boundary. A-actual, B-model.

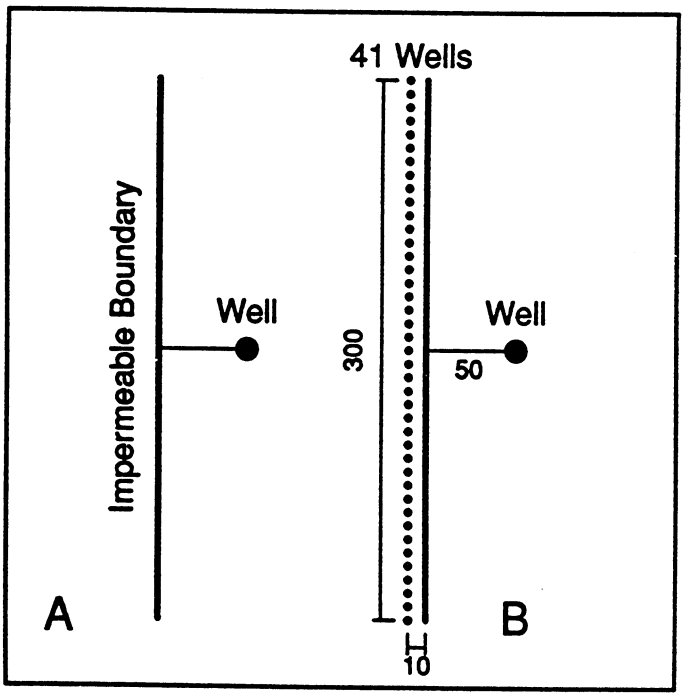

Fig. 5.2-2 Schematic diagram for a well near an infinite impermeable linear boundary. A-actual, B-model.

where:

p_D = dimensionless pressure
k = permeability
h = formation thickness
p = pressure
p_i = initial pressure
q_0 = active well flow rate
B = formation volume factor
μ = viscosity
t = time
t_D = dimensionless time
ϕ = porosity
c_t = total compressibility
r_w = wellbore radius

Let r be the number of line source wells used to replace the boundary, and j any point on the boundary. The dimensionless pressure $p_{Dj}\,(t_{Dn})$ at point j at time t_{Dn} is given by

$$p_{Dj}(t_{Dn}) = p_{Dj,0}(t_{Dn}) + \frac{1}{q_0}\Big\{ \Big[q_{1,1}\, p_{Dj,1}(t_{Dn}) + \cdots + (q_{1,n} - q_{1,n-1})\, p_{Dj,1}(t_{Dn} - t_{Dn-1}) \Big] + \Big[q_{2,1}\, p_{Dj,2}(t_{Dn}) + \cdots + (q_{2,n} - q_{2,n-1})\, p_{Dj,2}(t_{Dn} - t_{Dn-1}) \Big] + \cdots + \cdots + \Big[q_{r,1}\, p_{Dj,r}(t_{Dn}) + \cdots + (q_{r,n} - q_{r,n-1})\, p_{Dj,r}(t_{Dn} - t_{Dn-1}) \Big] \Big\} \qquad (5.2\text{-}3)$$

where:

p_{Dn} = dimensionless pressure at time step n
t_{Dn} = dimensionless time at time step n
$q_{r,n}$ = flow rate of line source well r at time step n

The first term in the right hand side of Eq. (5.2-3) represents the dimensionless pressure caused by the active well. The next group of terms represents the dimensionless pressure caused by the line source well 1 at time steps 1, 2, $\cdots$, n ; the subsequent group represents the dimensionless pressure caused by line source well 2, and so on, up to the line source well r. We define the following term

$$\Delta q_i^k = \frac{q_{i,k} - q_{i,k-1}}{q_0} \qquad (5.2\text{-}4)$$

Substituting Eq. (5.2-4) into Eq. (5.2-3) yields

$$P_{Dj}(t_{Dn}) = p_{Dj,0}(t_{Dn}) + \Big\{ \Big[\Delta q_1^1\, p_{Dj,1}(t_{Dn}) + \cdots + \Delta q_1^n\, p_{Dj,1}(t_{Dn} - t_{Dn-1}) \Big] + \Big[\Delta q_2^1\, p_{Dj,2}(t_{Dn}) + \cdots + \Delta q_2^n\, p_{Dj,2}(t_{Dn} - t_{Dn-1}) \Big] + \cdots + \cdots +$$

$$\left[\Delta q_r^1 \, p_{Dj,r} (t_{Dn}) + \cdots + \Delta q_r^n \, p_{Dj,r} (t_{Dn} - t_{Dn-1}) \right] \Bigg\} \tag{5.2-5}$$

In Eq. (5.2-5) the p_D's are given by

$$p_{Dj,0} (t_{Dn}) = -\frac{1}{2} E_i \left[-\frac{r_{j,0}^2}{4 \, t_{Dn}} \right] \tag{5.2-6}$$

and

$$p_{Dj,m} (t_{Dn} - t_{Dk}) = -\frac{1}{2} E_i \left[-\frac{r_{j,m}^2}{4 (t_{Dn} - t_{Dk-1})} \right] \tag{5.2-7}$$

where E_i is the Exponential Integral, $r_{j,0}$ is the distance between point j and the active well, and $r_{j,m}$ is the distance between point j and line source boundary well m.

Eq. (5.2-5) is valid for any impermeable boundary geometry. However, the next step in the algorithm is to impose the no-flow condition at point j at time step n. In doing so, we need to calculate the normal spatial derivative of $p_{Dj} (t_{Dn})$, that depends on the geometry of the system. Therefore, each different geometry gives rise to a different equation. The mathematical algorithm derived here is for the impermeable linear boundary cases: linear, circular, and elliptical.

Linear Boundary

Fig. 5.2-2A presents a schematic diagram of a well near an impermeable linear boundary. This linear boundary is replaced by a set of line source wells, as shown schematically in Fig. 5.2-2B. The zero velocity points are not presented in Fig. 5.2-2B, but are located on the impermeable boundary opposite the line source image wells. The line of image wells and the impermeable boundary are separated by a dimensionless distance d.

In the case of a finite length linear boundary presented in Fig. 5.2-2, all the image wells are positioned on the side of the boundary not containing the active production well. Also, all the image boundary wells are producers. The local pressure depressions around these wells prevent fluid from flowing through the impermeable boundary toward the production well.

The dimensionless distances $r_{j,0}$ and $r_{j,m}$ are written in terms of an (x–y) coordinate system centered at the active production well. Hence,

$$r_{j,0}^2 = x_j^2 + y_j^2 \tag{5.2-8}$$

and

$$r_{j,m}^2 = (x_j - \overline{x}_m)^2 + (y_j - \overline{y}_m)^2 \tag{5.2-9}$$

where:

x_j = x coordinate of point j
$\overline{x}_m$ = x coordinate of line source well m
y_j = y coordinate of point j
$\overline{y}_m$ = y coordinate of line source well m

Notice that (x,y) refers to a point on the no-flow linear boundary, while $(\overline{x}, \overline{y})$ are the coordinates of a line source boundary well. Also, we note that for the linear boundary case considered here:

$$x_j = \overline{x}_j - d \tag{5.2-10}$$

and

$$y_j = \overline{y}_j \tag{5.2-11}$$

where:

D = dimensionless distance between point j and the corresponding line source boundary well j

Substitution of Eqs. (5.2-6), and (5.2-7) into Eq. (5.2-5) yields

$$\begin{aligned}
p_{Dj}(t_{Dn}) &= -\frac{1}{2} E_i\left[-\frac{r_{j0}^2}{4\,t_{Dn}}\right] \\
&-\frac{1}{2}\left\{\Delta q_1^1 E_i\left[-\frac{r_{j,1}^2}{4\,t_{Dn}}\right] + \cdots + \Delta q_1^n E_i\left[-\frac{r_{j,1}^2}{4\,(t_{Dn}-t_{Dn-1})}\right]\right\} \\
&-\frac{1}{2}\left\{\Delta q_2^1 E_i\left[-\frac{r_{j,2}^2}{4\,t_{Dn}}\right] + \cdots + \Delta q_2^n E_i\left[-\frac{r_{j,2}^2}{4\,(t_{Dn}-t_{Dn-1})}\right]\right\} \\
&- \cdots - \cdots - \\
&-\frac{1}{2}\left\{\Delta q_r^1 E_i\left[-\frac{r_{j,r}^2}{4\,t_{Dn}}\right] + \cdots + \Delta q_r^n E_i\left[-\frac{r_{j,r}^2}{4\,(t_{Dn}-t_{Dn-1})}\right]\right\}
\end{aligned} \tag{5.2-12}$$

We now impose the no-flow condition at point j on the linear boundary. Mathematically,

$$\frac{\partial}{\partial x_j} p_{Dj}(t_{Dn}) = 0 \tag{5.2-13}$$

The derivative of the Exponential Integral is given by

$$\frac{\partial}{\partial w} Ei(-G) = -\frac{Exp(-G)}{G}\frac{\partial G}{\partial w} \tag{5.2-14}$$

where G = generic argument of the Exponential Integral function.

Combining Eqs. (5.2-8), (5.2-9), (5.2-12), (5.2-13), and (5.2-14) and rearranging yields

$$\begin{aligned}
0 &= \frac{x_j}{r_{j,0}^2} Exp\left[-\frac{r_{j,0}^2}{4\,t_{Dn}}\right] \\
&+\frac{(x_j-\overline{x}_1)}{r_{j,1}^2}\left\{\Delta q_1^1 Exp\left[-\frac{r_{j,1}^2}{4\,t_{Dn}}\right]\right. \\
&\left.+ \cdots + \Delta q_1^n Exp\left[-\frac{r_{j,1}^2}{4\,(t_{Dn}-t_{Dn-1})}\right]\right\} \\
&+\frac{(x_j-\overline{x}_2)}{r_{j,2}^2}\left\{\Delta q_2^1 Exp\left[-\frac{r_{j,2}^2}{4\,t_{Dn}}\right]\right. \\
&\left.+ \cdots + \Delta q_2^n Exp\left[-\frac{r_{j,2}^2}{4\,(t_{Dn}-t_{Dn-1})}\right]\right\} \\
&+ \cdots + \cdots + \\
&+\frac{(x_j-\overline{x}_r)}{r_{j,r}^2}\left\{\Delta q_r^1 Exp\left[-\frac{r_{j,r}^2}{4\,t_{Dn}}\right]\right. \\
&\left.+ \cdots + \Delta q_r^n Exp\left[-\frac{r_{j,r}^2}{4\,(t_{Dn}-t_{Dn-1})}\right]\right\}
\end{aligned} \tag{5.2-15}$$

The unknowns in Eq. (5.2-15) are $\Delta q_1^n, \Delta q_2^n, \cdots, \Delta q_r^n$. The other Δq's were already determined in the previous time steps. Eq. (5.2-15) is written in a more concise form as follows:

$$\left\{ \frac{(x_j - \overline{x}_1)}{r_{j,1}^2} \text{Exp}\left[- \frac{r_{j,1}^2}{4\,(t_{Dn} - t_{Dn-1})} \right] \right\} \Delta q_1^n +$$
$$\left\{ \frac{(x_j - \overline{x}_2)}{r_{j,2}^2} \text{Exp}\left[- \frac{r_{j,2}^2}{4\,(t_{Dn} - t_{Dn-1})} \right] \right\} \Delta q_2^n +$$
$$+ \cdots + \left\{ \frac{(x_j - \overline{x}_r)}{r_{j,r}^2} \text{Exp}\left[- \frac{r_{j,r}^2}{4\,(t_{Dn} - t_{Dn-1})} \right] \right\} \Delta q_r^n$$
$$= - \frac{x_j}{r_{j,0}^2} \text{Exp}\left[- \frac{r_{j,0}^2}{4\,t_{Dn}} \right]$$
$$- \sum_{p=1}^{r} \sum_{k=2}^{n} \left\{ \frac{(x_j - \overline{x}_p)}{r_{j,p}^2} \text{Exp}\left[- \frac{r_{j,p}^2}{4\,(t_{Dn} - t_{Dk-2})} \right] \right\} \Delta q_p^{k-1} \qquad (5.2\text{-}16)$$

Eq. (5.2-16) holds for j=1,2,....r, and, therefore, represents a linear system of equations that must be solved at each time step. In this system, AX=B, matrix A is symmetric.

The pressure effects of the boundary line source wells on the active well are computed only after $t_{Dn} / r_{min}^2 \geq 0.1$, where r_{min} is the minimum distance between the active well and the impermeable boundary. Hence, defining z as the number of time steps that boundary well effects are computed, Eq. (5.2-16) becomes

$$\left\{ \frac{(x_j - \overline{x}_1)}{r_{j,1}^2} \text{Exp}\left[- \frac{r_{j,1}^2}{4\,(t_{Dn} - t_{Dn-1})} \right] \right\} \Delta q_1^n +$$
$$\left\{ \frac{(x_j - \overline{x}_2)}{r_{j,2}^2} \text{Exp}\left[- \frac{r_{j,2}^2}{4\,(t_{Dn} - t_{Dn-1})} \right] \right\} \Delta q_2^n +$$
$$+ \cdots + \left\{ \frac{(x_j - \overline{x}_r)}{r_{j,r}^2} \text{Exp}\left[- \frac{r_{j,r}^2}{4\,(t_{Dn} - t_{Dn-1})} \right] \right\} \Delta q_r^n$$
$$= - \frac{x_j}{r_{j,0}^2} \text{Exp}\left[- \frac{r_{j,0}^2}{4\,t_{Dn}} \right]$$
$$- \sum_{p=1}^{r} \sum_{k=2}^{z+1} \left\{ \frac{(x_j - \overline{x}_p)}{r_{j,p}^2} \text{Exp}\left[- \frac{r_{j,p}^2}{4\,(t_{Dn} - t_{Dn-k})} \right] \right\} \Delta q_p^{n-k+1} \qquad (5.2\text{-}17)$$

The linear system of equations is solved using the IMSL subroutine LEQ2S that is suitable for symmetric matrices. Once the flow rates at time step n are determined, the dimensionless pressure at the active well is computed by

$$p_{D0}(t_{Dn}) = - \frac{1}{2} E_i \left[- \frac{1}{4\,t_{Dn}} \right]$$
$$- \frac{1}{2} \sum_{m=1}^{r} \sum_{k=1}^{z} \Delta q_m^{n-k+1} E_i \left[- \frac{\overline{r}_{m,0}^2}{4\,(t_{Dn} - t_{Dn-k})} \right] \qquad (5.2\text{-}18)$$

where $\overline{r}_{m,0}$ is the distance between boundary well m and the active production well

$$\overline{r}_{m,0}^2 = \overline{x}_m^2 + \overline{y}_m^2 \qquad (5.2\text{-}19)$$

The first term in the right hand side of Eq. (5.2-18) is the contribution of the active well, while the double summation terms represent the superposition effects of the line source boundary wells from previous and current time steps.

Circular Boundary

To derive the algorithm for the no-flow circular boundary we start with Eq. (5.2-12) of the theory section. The no-flow condition at point j on the boundary is expressed as

$$\frac{\partial}{\partial s} p_{Dj} (t_{Dn}) = 0 \tag{5.2-20}$$

where s is the direction normal to the boundary at point j. The normal derivative of a general function f is given by

$$\frac{\partial f}{\partial s} = \vec{s} \cdot \nabla f \tag{5.2-21}$$

where $\vec{s}$ is the unitary vector normal to the boundary, and ∇f is the gradient of the function f. The unitary normal vector $\vec{s}$ at point j is given by

$$\vec{s} = \frac{(x_j - x_o) \vec{i} + (y_j - y_o) \vec{j}}{\left[(x_j - x_o)^2 + (y_j - y_o)^2 \right]^{1/2}} \tag{5.2-22}$$

where $\vec{i}$ and $\vec{j}$ are the unitary vectors in the directions x and y respectively, and (x_o,y_o) are the coordinates of the center of the circular boundary. Let the function f be any one of the Exponential Integral terms that appear in Eq. (5.2-12). Thus,

$$f = - Ei \left[- \frac{(x_j - \bar{x}_b)^2 + (y_j - \bar{y}_b)^2}{4 (t_{Dn} - t_{Dp})} \right] \tag{5.2-23}$$

By definition

$$\nabla f = \frac{\partial f}{\partial x_j} \vec{i} + \frac{\partial f}{\partial y_j} \vec{j} \tag{5.2-24}$$

The derivative of the Exponential Integral is

$$\frac{\partial}{\partial w} Ei (-G) = - \frac{Exp (-G)}{G} \frac{\partial G}{\partial w} \tag{5.2-25}$$

Substitution of Eq. (5.2-23) into Eq. (5.2-24), and using Eq. (5.2-25) yields

$$\nabla f = \left\{ - \frac{2(x_j - \bar{x}_b)}{r_{j,b}^2} Exp \left[- \frac{r_{j,b}^2}{4 (t_{Dn} - t_{Dp})} \right] \right\} \vec{i} + \left\{ - \frac{2(y_j - \bar{y}_b)}{r_{j,b}^2} Exp \left[- \frac{r_{j,b}^2}{4 (t_{Dn} - t_{Dp})} \right] \right\} \vec{j} \tag{5.2-26}$$

where

$$r_{j,b}^2 = (x_j - \bar{x}_b)^2 + (y_j - \bar{y}_b)^2 \tag{5.2-27}$$

Substituting Eqs. (5.2-22), (5.2-26), and (5.2-27) into Eq. (5.2-21) we obtain

$$\frac{\partial f}{\partial s} = -\frac{2\,(x_j - x_o)\,(x_j - \bar{x}_b)}{\left[(x_j - x_o)^2 + (y_j - y_o)^2\right]^{1/2} r_{j,b}^2} \mathrm{Exp}\left[-\frac{r_{j,b}^2}{4\,(t_{Dn} - t_{Dp})}\right]$$

$$-\frac{2\,(y_j - y_o)\,(y_j - \bar{y}_b)}{\left[(x_j - x_o)^2 + (y_j - y_o)^2\right]^{1/2} r_{j,b}^2} \mathrm{Exp}\left[-\frac{r_{j,b}^2}{4\,(t_{Dn} - t_{Dp})}\right] \qquad (5.2\text{-}28)$$

For each well in the system there is a term given by Eq. (5.2-28). Therefore, when the no-flow condition is imposed at point j on the boundary, and after the cancellation of common terms, we obtain the following equation:

$$0 = \left[\frac{x_j\,(x_j - x_o) + y_j\,(y_j - y_o)}{r_{j,0}^2}\right] \mathrm{Exp}\left[-\frac{r_{j,0}^2}{4\,t_{Dn}}\right] +$$

$$\left[\frac{(x_j - \bar{x}_1)\,(x_j - x_o) + (y_j - \bar{y}_1)\,(y_j - y_o)}{r_{j,1}^2}\right] \left\{\Delta q_1^1 \mathrm{Exp}\left[-\frac{r_{j,1}^2}{4\,t_{Dn}}\right]\right.$$

$$\left. + \cdots + \Delta q_1^n \mathrm{Exp}\left[-\frac{r_{j,1}^2}{4\,(t_{Dn} - t_{Dn-1})}\right]\right\} +$$

$$\left[\frac{(x_j - \bar{x}_2)\,(x_j - x_o) + (y_j - \bar{y}_2)\,(y_j - y_o)}{r_{j,2}^2}\right] \left\{\Delta q_2^1 \mathrm{Exp}\left[-\frac{r_{j,2}^2}{4\,t_{Dn}}\right]\right.$$

$$\left. + \cdots + \Delta q_2^n \mathrm{Exp}\left[-\frac{r_{j,2}^2}{4\,(t_{Dn} - t_{Dn-1})}\right]\right\}$$

$$+ \cdots + \cdots +$$

$$\left[\frac{(x_j - \bar{x}_r)\,(x_j - x_o) + (y_j - \bar{y}_r)\,(y_j - y_o)}{r_{j,r}^2}\right] \left\{\Delta q_r^1 \mathrm{Exp}\left[-\frac{r_{j,r}^2}{4\,t_{Dn}}\right]\right.$$

$$\left. + \cdots + \Delta q_r^n \mathrm{Exp}\left[-\frac{r_{j,r}^2}{4\,(t_{Dn} - t_{Dn-1})}\right]\right\} \qquad (5.2\text{-}29)$$

The unknowns in Eq. (5.2-29) are Δq_1^n, Δq_2^n, $\cdots$ Δq_r^n, since the remaining Δq's were already computed in the previous time steps. Eq. (5.2-29) is rearranged and written in a concise form that also accounts for interference only after $t_{Dn}/r_{min}^2 \geq 0.1$, in the same way that was done for the linear boundary case. Hence

$$\left\{\frac{(x_j - \bar{x}_1)(x_j - x_o) + (y_j - \bar{y}_1)(y_j - y_o)}{r_{j,1}^2} \mathrm{Exp}\left[-\frac{r_{j,1}^2}{4(t_{Dn} - t_{Dn-1})}\right]\right\} \Delta q_1^n +$$

$$\left\{\frac{(x_j - \bar{x}_2)(x_j - x_o) + (y_j - \bar{y}_2)(y_j - y_o)}{r_{j,2}^2} \mathrm{Exp}\left[-\frac{r_{j,2}^2}{4(t_{Dn} - t_{Dn-1})}\right]\right\} \Delta q_2^n$$

$$+ \cdots + \cdots +$$

$$\left\{ \frac{(x_j-\bar{x}_r)(x_j-x_o) + (y_j-\bar{y}_r)(y_j-y_o)}{r_{j,r}^2} \, \mathrm{Exp}\left[- \frac{r_{j,r}^2}{4(t_{Dn}-t_{Dn-1})} \right] \right\} \Delta q_r^n$$

$$= - \left[\frac{x_j\,(x_j - x_o) + y_j\,(y_j - y_o)}{r_{j,0}^2} \right] \mathrm{Exp}\left[- \frac{r_{j,0}^2}{4\,t_{Dn}} \right] - \sum_{p=1}^{r} \sum_{k=2}^{z+1}$$

$$\left\{ \left[\frac{(x_j-\bar{x}_p)(x_j-x_o) + (y_j-\bar{y}_p)(y_j-y_o)}{r_{j,p}^2} \right] \mathrm{Exp}\left[- \frac{r_{jp}^2}{4(t_{Dn}-t_{Dn-k})} \right] \right\} \Delta q_p^{n-k+1} \qquad (5.2\text{-}30)$$

Finally, the pressure drop at the production well is computed by Eq. (5.2-18).

Elliptical Boundary

The starting point is Eq. (5.2-12) of the theory section. The no-flow condition at point j on the boundary is expressed as

$$\frac{\partial}{\partial s}\, p_{Dj}\,(\,t_{Dn}\,) \;=\; 0 \qquad (5.2\text{-}31)$$

where s is the direction normal to the boundary at point j. The normal derivative of a general function f is given by

$$\frac{\partial f}{\partial s} \;=\; \vec{s}\,.\,\nabla f \qquad (5.2\text{-}32)$$

where $\vec{s}$ is the unitary vector normal to the boundary, and ∇f is the gradient of the function f. For an elliptical boundary centered at (x_o,y_o), whose major axis is parallel to the Y axis, $\vec{s}$ is given by

$$\vec{s} = \frac{(\,x_j - x_o\,)\,\vec{i}}{b^2 \left[\dfrac{(\,x_j - x_o\,)^2}{b^4} + \dfrac{(\,y_j - y_o\,)^2}{a^4} \right]^{1/2}} + \frac{(\,y_j - y_o\,)\,\vec{j}}{a^2 \left[\dfrac{(\,x_j - x_o\,)^2}{b^4} + \dfrac{(\,y_j - y_o\,)^2}{a^4} \right]^{1/2}} \qquad (5.2\text{-}33)$$

Now, let the function f be any one of the exponential integral terms that appear in Eq. (5.2-12). Thus,

$$f \;=\; -\,\mathrm{Ei}\left[-\frac{(\,x_j - \bar{x}_b\,)^2 + (\,y_j - \bar{y}_b\,)^2}{4\,(\,t_{Dn} - t_{Dp}\,)} \right] \qquad (5.2\text{-}34)$$

The gradient of f is given by

$$\nabla f \;=\; \left\{ -\frac{2(\,x_j - \bar{x}_b\,)}{r_{j,b}^2}\, \mathrm{Exp}\left[-\frac{r_{j,b}^2}{4\,(\,t_{Dn} - t_{Dp}\,)} \right] \right\} \vec{i} \;+$$

$$\left\{ - \frac{2(y_j - \overline{y}_b)}{r_{j,b}^2} \, \mathrm{Exp} \left[- \frac{r_{j,b}^2}{4 \, (t_{Dn} - t_{Dp})} \right] \right\} \vec{j} \qquad (5.2\text{-}35)$$

For each well in the system there is a term given by Eq. (5.2-35). Thus, imposing the no-flow condition at point j on the boundary, and cancelling the common terms, we get

$$\begin{aligned}
0 \; = \; & \left[\frac{x_j \, (x_j - x_o)}{b^2 \, r_{j,0}^2} + \frac{y_j \, (y_j - y_o)}{a^2 \, r_{j,0}^2} \right] \mathrm{Exp} \left[- \frac{r_{j,0}^2}{4 \, t_{Dn}} \right] + \\
& \left[\frac{(x_j - \overline{x}_1) \, (x_j - x_o)}{b^2 \, r_{j,1}^2} + \frac{(y_j - \overline{y}_1) \, (y_j - y_o)}{a^2 \, r_{j,1}^2} \right] \left\{ \Delta q_1^1 \, \mathrm{Exp} \left[- \frac{r_{j,1}^2}{4 \, t_{Dn}} \right] \right. \\
& \left. + \cdots + \Delta q_1^n \, \mathrm{Exp} \left[- \frac{r_{j,1}^2}{4 \, (t_{Dn} - t_{Dn-1})} \right] \right\} + \\
& \left[\frac{(x_j - \overline{x}_2) \, (x_j - x_o)}{b^2 \, r_{j,2}^2} + \frac{(y_j - \overline{y}_2) \, (y_j - y_o)}{a^2 \, r_{j,2}^2} \right] \left\{ \Delta q_2^1 \, \mathrm{Exp} \left[- \frac{r_{j,2}^2}{4 \, t_{Dn}} \right] \right. \\
& \left. + \cdots + \Delta q_2^n \, \mathrm{Exp} \left[- \frac{r_{j,2}^2}{4 \, (t_{Dn} - t_{Dn-1})} \right] \right\} \\
& + \cdots + \cdots + \\
& \left[\frac{(x_j - \overline{x}_r) \, (x_j - x_o)}{b^2 \, r_{j,r}^2} + \frac{(y_j - \overline{y}_r) \, (y_j - y_o)}{a^2 \, r_{j,r}^2} \right] \left\{ \Delta q_r^1 \, \mathrm{Exp} \left[- \frac{r_{j,r}^2}{4 \, t_{Dn}} \right] \right. \\
& \left. + \cdots + \Delta q_r^n \, \mathrm{Exp} \left[- \frac{r_{j,r}^2}{4 \, (t_{Dn} - t_{Dn-1})} \right] \right\}
\end{aligned} \qquad (5.2\text{-}36)$$

The unknowns in Eq. (5.2-36) are Δq_1^n, Δq_2^n, $\cdots$ Δq_r^n, since the remaining Δq's were already computed in the previous time steps. Eq. (5.2-36) is rearranged and written in a concise form that also accounts for interference only after $t_{Dn}/r_{min}^2 \geq 0.1$, in the same way that was done for the linear boundary case. Hence

$$\begin{aligned}
& \left\{ \frac{(x_j - \overline{x}_1)(x_j - x_o)}{b^2 \, r_{j,1}^2} + \frac{(y_j - \overline{y}_1)(y_j - y_o)}{a^2 \, r_{j,1}^2} \, \mathrm{Exp} \left[- \frac{r_{j,1}^2}{4(t_{Dn} - t_{Dn-1})} \right] \right\} \Delta q_1^n + \\
& \left\{ \frac{(x_j - \overline{x}_2)(x_j - x_o)}{b^2 \, r_{j,2}^2} + \frac{(y_j - \overline{y}_2)(y_j - y_o)}{a^2 \, r_{j,2}^2} \, \mathrm{Exp} \left[- \frac{r_{j,2}^2}{4(t_{Dn} - t_{Dn-1})} \right] \right\} \Delta q_2^n \\
& + \cdots + \cdots + \\
& \left\{ \frac{(x_j - \overline{x}_r)(x_j - x_o)}{b^2 \, r_{j,r}^2} + \frac{(y_j - \overline{y}_r)(y_j - y_o)}{a^2 \, r_{j,r}^2} \, \mathrm{Exp} \left[- \frac{r_{j,r}^2}{4(t_{Dn} - t_{Dn-1})} \right] \right\} \Delta q_r^n
\end{aligned}$$

$$= -\left\{\frac{x_j(x_j-x_o)}{b^2\, r_{j,0}^2} + \frac{y_j(y_j-y_o)}{a^2\, r_{j,0}^2}\, \mathrm{Exp}\left[-\frac{r_{j,0}^2}{4\, t_{Dn}}\right] - \sum_{p=1}^{r}\sum_{k=2}^{z+1}\right.$$

$$\left.\left\{\frac{(x_j-\bar{x}_p)(x_j-x_o)}{b^2\, r_{j,p}^2} + \frac{(y_j-\bar{y}_p)(y_j-y_o)}{a^2\, r_{j,p}^2}\, \mathrm{Exp}\left[-\frac{r_{j,p}^2}{4(t_{Dn}-t_{Dn-k})}\right]\right\}\Delta q_p^{\,n-k+1}\right. \qquad (5.2\text{-}37)$$

For the case in which the major axis of the elliptical boundary is parallel to the X axis, an equation similar to Eq. (5.2-37) is obtained, with a and b interchanged. Finally, the pressure drop at the production well is computed by Eq. (5.2-18).

5.2.2 Validation

In this section we present two applications of the new model to generation of the effects of impermeable boundaries for cases that have analytical solutions. These two cases are an impermeable linear boundary and an impermeable internal circular subregion near an active constant rate production well. These two reservoir configurations characterize two classes of impermeable boundaries. The impermeable linear boundary is infinitely long, and the internal circular region is of finite size having reservoir volume associated with it.

Figs. 5.2-2A and 5.2-2B present the geometrical configuration of the actual and approximated reservoir configurations respectively for a well near an impermeable linear boundary. The dimensions in Fig. 5.2-2 are all in dimensionless units based on the active well radius. The infinite linear boundary is approximated by 41 line source image boundary wells with about seven well radii between every two wells. The line of boundary wells is ten wellbore radii away from the actual location of the impermeable linear boundary. Also, the infinite linear boundary is approximated by a boundary with a dimensionless length of 300, located at a dimensionless distance of 50 away from the active well.

The comparison of the new model and the analytical solution for a well near an impermeable linear boundary is presented in Fig. 5.2-3. The lower curve in Fig. 5.2-3 is the line source solution, or the Theis (1935) solution for a constant rate well in an infinite homogeneous reservoir. The upper solid curve represents the analytical pressure response of a well near an impermeable linear boundary, generated by the method of superposition presented by Stallman (1952). The dotted data represent the results of the new model developed in this section. The pressure response in the presence of an impermeable linear boundary deviates from the line source solution, doubling the semilog slope. The data from the new model match the analytical model for two log cycles beyond the beginning of boundary effects. As shown by Sageev et al. (1985) this match is sufficient for determining the distance between the well and the linear boundary. The late time data from the new model deviates below the analytical solution since we used a finite number of boundary wells. The pressure response computed with the new model represents a finite length linear boundary, and the late time semilog slope, not shown in Fig. 5.2-3, is identical to the line source semilog slope. The effects of the number of boundary wells and their distance from the actual impermeable boundary on the performance of the new model are considered in Section 5.2.4.

Next, we examine the application of the new model to a finite volumetric impermeable circular subregion. Fig. 5.2-4 shows the geometrical configuration of this case. The distances presented in Fig. 5.2-4 are dimensionless, based upon the active well radius. The image boundary wells are located inside the impermeable subregion, ten wellbore radii away from the actual boundary. During the test, the image boundary wells located along the portion of the boundary facing the active well are producers. The other image boundary wells facing away

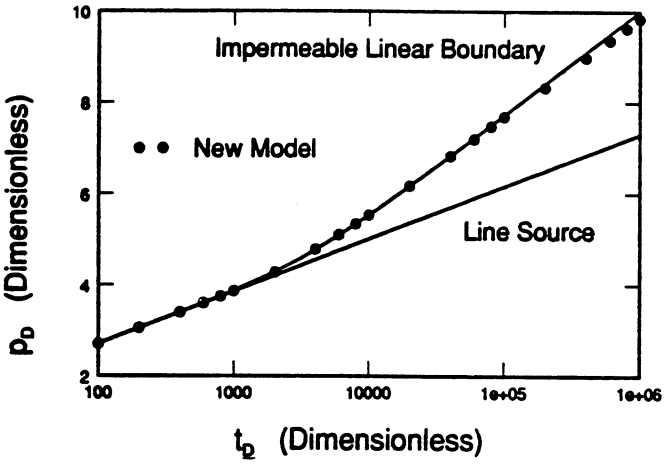

Fig. 5.2-3 Semilog pressure response for a well near an impermeable linear boundary.

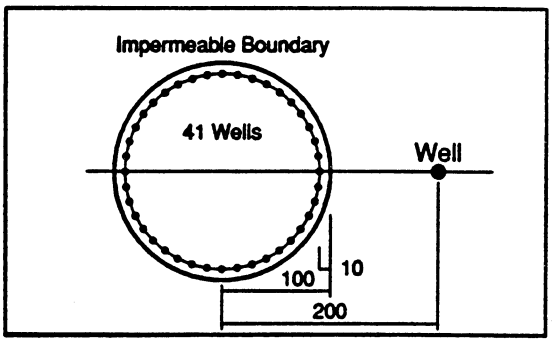

Fig. 5.2-4 Schematic diagram for a well near an impermeable circular boundary.

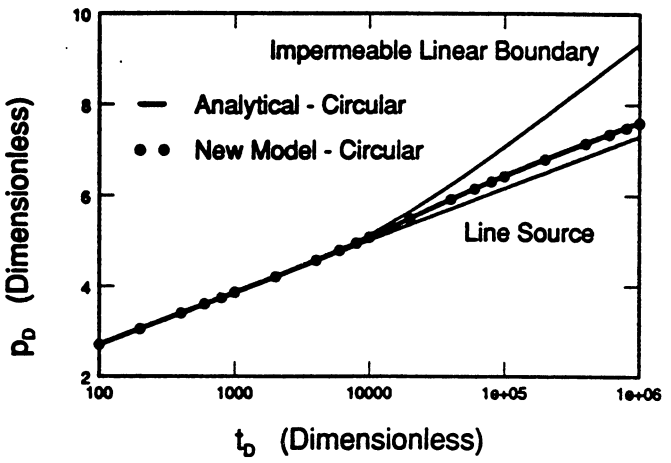

Fig. 5.2-5 Semilog pressure response for a well near an impermeable circular boundary.

from the active well are injectors. This injection-production distribution allows the image wells to prevent fluid from flowing out of the impermeable region toward the active well. Also, this distribution prevents fluid from flowing through the impermeable region, and forces the fluid to flow around the boundary.

Fig. 5.2-5 presents a comparison of the new model to the analytical solution for a constant rate well near a circular impermeable boundary. The analytical solution was presented by Sageev and Horne (1983a) and is the heavy solid curve. The line source solution and the impermeable linear boundary solution are presented in Fig. 5.2-5 as a reference. The dotted data, representing the pressure response generated by the new model, match well the analytical solution. Since the impermeable region is finite in size, the late time pressure response is parallel to the line source solution response. The constant pressure separation between the late time line source curve and the curve for the boundary case is considered as a late time skin, and was discussed by Sageev and Horne (1983a)

5.2-3 Results

Effect of Size

In this section we examine the effect of the size of impermeable regions on the pressure responses of a constant rate well. Two shapes of boundaries are considered: circular and elliptical. One of the important parameters affecting the pressure response is the shortest distance between the active well and the impermeable boundary. For a given set of different sizes of impermeable boundaries with the same shape and orientation, the shortest distance between the well and the boundaries is maintained constant.

Fig. 5.2-6 presents a suite of circular boundaries external to a well in an infinite reservoir. The relative size of the circular boundary is defined as:

$$F = R/T \quad . \tag{5.2-38}$$

where R is the radius of the circular boundary, and T is the distance between the active well and the center of the boundary. Hence, F varies between zero for relatively small boundaries, and unity for relatively large boundaries. The shortest distance between the well and the boundaries is 100 wellbore radii, and the relative size of the boundaries varies between 0.4 and 0.9.

The pressure responses of a well near these impermeable circular boundaries are presented in Fig. 5.2-7. As the relative size of the boundary increases, the magnitude of the pressure deviation from the line source solution increases. The impermeable subregion has to be relatively large in order to be detected by the first deviation from the line source solution. The detection of the finiteness of the impermeable region depends on the resumption of the line source semilog slope. The transition from the linear boundary slope to the line source slope occurs later for relatively large impermeable regions. However, since all the circular boundaries shown in Fig. 5.2-6 have the same shortest distance to the production well, all the corresponding pressure responses shown in Fig. 5.2-7 deviate from the line source response at the same time. Hence, the shortest distance is determined from the first deviation from the line source response, and the size of the impermeable circular region is determined by the deviation of the pressure response from the linear boundary response.

We now consider the effects of the size of impermeable regions with elongated shapes on pressure responses of the active production well. Fig. 5.2-8 presents three elliptical impermeable boundaries. Again, the shortest distance between the well and the boundaries is 100 wellbore radii. The elliptical boundaries have the same shape, with an axis ratio $b/a = 0.25$. Here, a is the length of the long axis of the ellipse, and b is the length of the short axis of the ellipse. The ellipses denoted by A, B, and C have dimensionless a values of 400, 200, and 100 respectively.

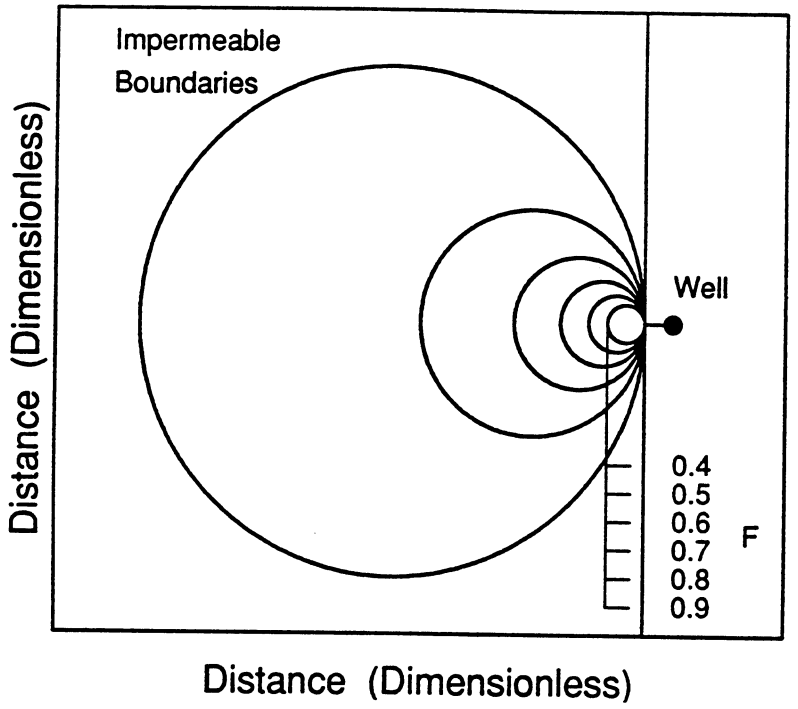

Fig. 5.2-6 Schematic diagram for a well near impermeable circular regions of different sizes.

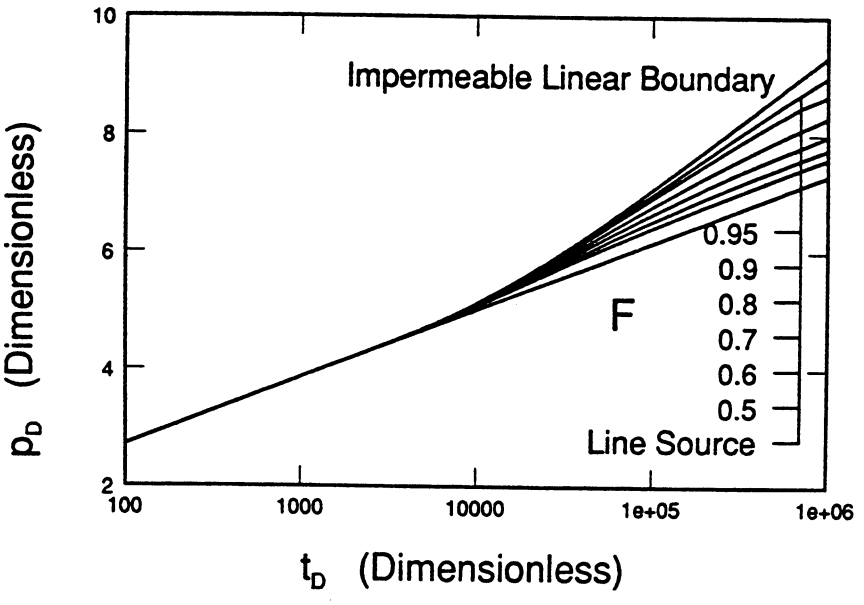

Fig. 5.2-7 Semilog pressure responses for a well near impermeable circular regions of different sizes.

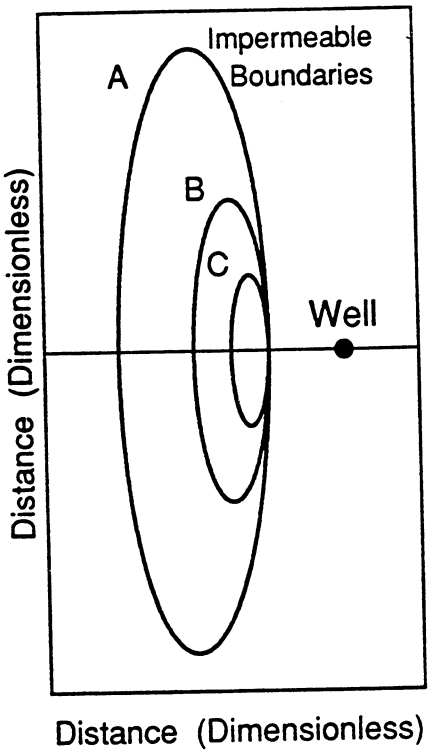

Fig. 5.2-8 Schematic diagram for a well near impermeable elliptical regions of different sizes and the same b/a ratio; r_{min} = 100; A: a = 400, b = 100; B: a = 200, b = 50; C: a = 100, b = 25.

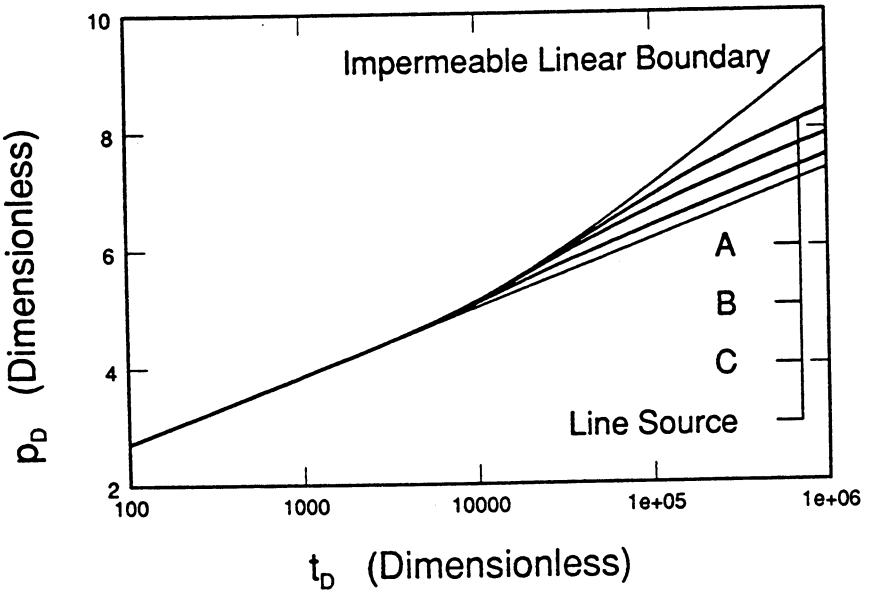

Fig. 5.2-9 Semilog pressure responses for a well near impermeable elliptical regions of different sizes and the same b/a ratio; r_{min} = 100; A: a = 400, b = 100; B: a = 200, b = 50; C: a = 100, b = 25.

Fig. 5.2-9 presents the pressure responses of the three elliptical boundaries of Fig. 5.2-8. The three responses are all between the line source curve and the impermeable linear boundary curve, and exhibit the early and late time line source slope. The magnitude of the deviation from the line source curve depends on the size of the elliptical boundary. The relatively small impermeable ellipse denoted by C can hardly be detected from the pressure response. However, the relatively large impermeable ellipse denoted by A exhibits a significant deviation from the line source pressure response, and the presence of the impermeable boundary can be detected. Also, the pressure response of the relatively large impermeable ellipse follows the linear boundary curve for about one log cycle of time after the first deviation from the line source curve.

From the deviation time, and the early transition flow period, the shortest distance between the well and the boundary can be determined. We also note that, in order to detect the fact that the impermeable region is finite in size, the test must be continued for at least one log cycle of time beyond the first deviation from the line source response. However, the pressure response curves for elliptical shapes are similar to the curves for circular shapes, which prevents independent determination of the shape of the impermeable boundary from a transient pressure test.

Effect of Shape

In this section we examine the effect of the shape of impermeable regions on the pressure responses of a constant rate well. Three shapes of boundaries are considered: linear, circular and elliptical. Fig. 5.2-10 shows circular and elliptical boundaries having the same area, and the same shortest distance between them and the active well of 100 wellbore radii. The circular boundary has a radius of 100 wellbore radii, and the ellipse axis ratio is 0.25, with the long axis equal to 200 wellbore radii. The pressure responses in the presence of the boundaries shown in Fig. 5.2-10 are presented in Fig. 5.2-11.

The effect of the shape of the impermeable boundary is significant. The long axis of the elliptical boundary is parallel to an impermeable linear boundary, and disrupts the homogeneous stream lines more than the circular boundary. Hence, the elliptical boundary causes a larger deviation of the pressure response from the line source homogeneous response than the circular case. A linear boundary can be considered as an elliptical boundary with an infinitely long axis and a zero short axis. Hence, the uppermost curve in Fig. 5.2-11, represents the largest observable pressure deviation caused by an impermeable boundary having the same area as the circle and the ellipse shown in Fig. 5.2-10, and located the same distance from the production well. However, the effects of the shape depends upon the orientation of elongated impermeable boundaries with respect to the production well. These effects are considered in the next section.

Effect of Orientation

In this section we consider the effects of the orientation of elongated impermeable boundaries. Fig. 5.2-12 shows four elliptical boundaries, denoted by A, B, C, and D. The ellipses are identical in size and shape, but have different locations and orientations with respect to the active production well. The ellipses denoted by B, C, and D are simply rotated around a pivot point located at one end of the ellipse.

The pressure responses for the cases described in Fig. 5.2-12 are shown in Fig. 5.2-13. The effects of orientation are linked to the disturbing of the homogeneous radial stream lines. Hence, the ellipse denoted by A causes the largest deviation from the line source solution curve. The ellipse denoted by D, where the long axis of the ellipse is in the direction of the production well, cannot be detected from the pressure response. The curves for ellipses B, C, and D are close to each other in the cases presented here. Yet, if the axis ratio were smaller

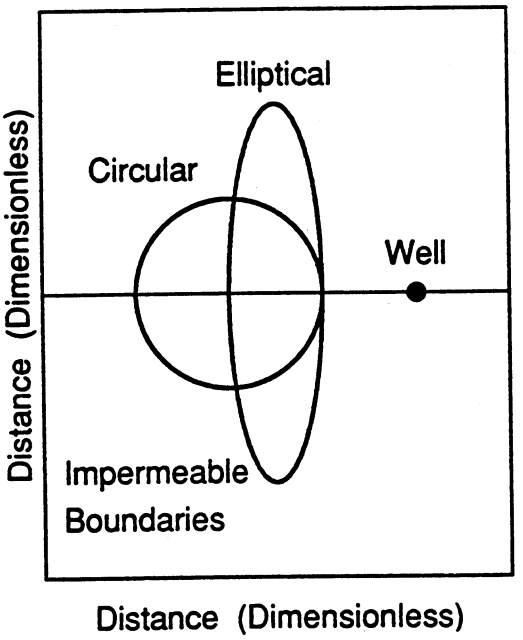

Fig. 5.2-10 Schematic diagram for a well near impermeable regions of different shapes and the same area; r_{min} = 100; Circle: R = 100; Ellipse: a = 200, b = 50.

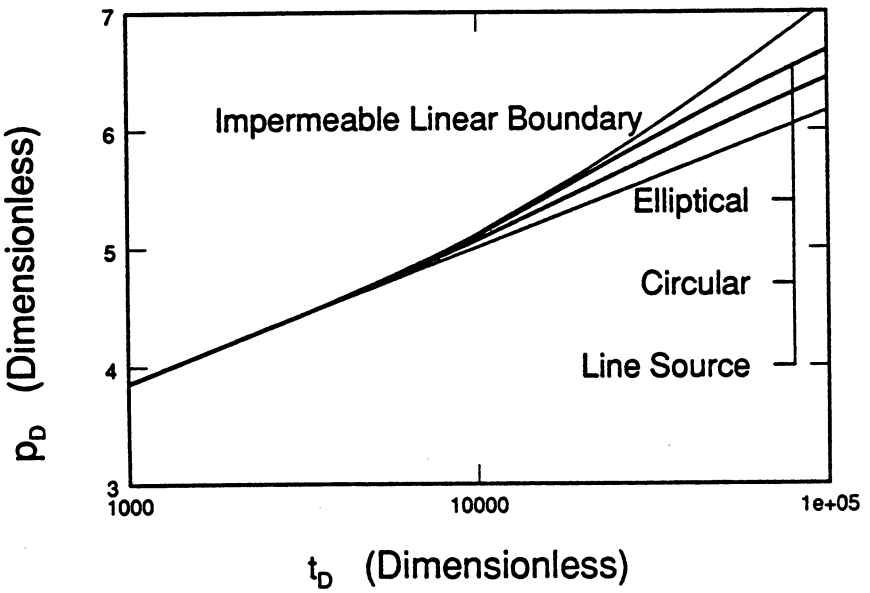

Fig. 5.2-11 Semilog pressure responses for a well near impermeable regions of different shapes and the same area; r_{min} = 100; Circle: R = 100; Ellipse: a = 200, b = 50.

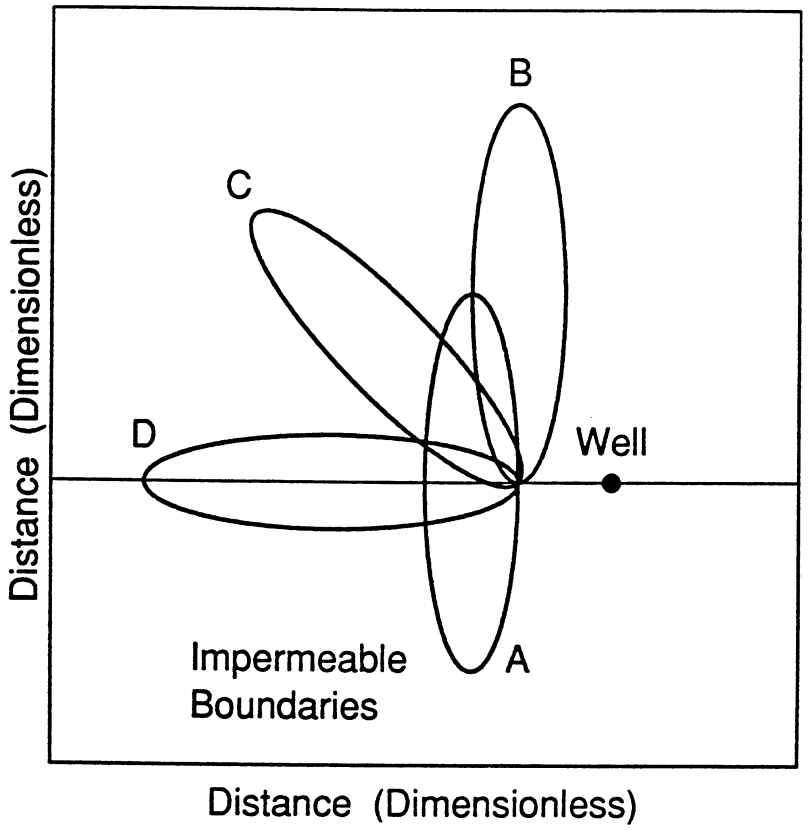

Fig. 5.2-12 Schematic diagram for a well near impermeable regions of different orientations and the same shape and area; Ellipse: a = 200, b = 50.

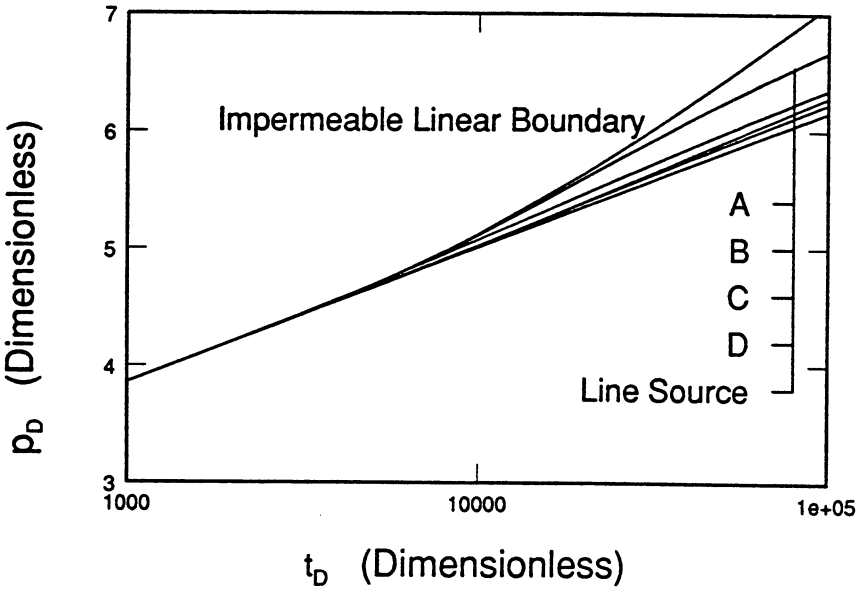

Fig. 5.2-13 Semilog pressure response for a well near impermeable regions of different orientations and the same shape and area.

(the ellipses were relatively longer), and if the production well were closer to the impermeable region, these three pressure responses would be greatly different.

We note that the pressure responses of ellipses C and D are practically identical. This observation is explained by the fact that the orientation of the long axis of these ellipses is almost parallel to the homogeneous radial stream lines, hence, minimizing the deviation from the line source response. The pressure responses shown in Fig. 5.2-13 imply that even relatively large impermeable regions near an active well may not be detected by transient pressure tests if the orientation of these regions is in the direction of the radial stream lines.

Effect of A Fracture

Next we consider the effects of line impermeable boundaries on the pressure responses of a constant rate well. We examine the combination of the effects of shape and orientation of an impermeable boundary that has no reservoir volume associated with it. Fig. 5.2-14 shows three impermeable fracture boundaries, denoted by A, B, and C. The ellipse denoted by A is half of ellipse A shown in Fig. 5.2-12. The semicircle denoted by B, is half of a circular boundary presented in Fig. 5.2-6, with a relative size, F, of 0.5. The second ellipse in Fig. 5.2-14, denoted by C, is half of ellipse D shown in Fig. 5.2-12. The shortest distance between the well and the boundaries is 100 wellbore radii.

Fig. 5.2-15 presents the pressure responses corresponding to the reservoir configurations shown in Fig. 5.2-14. Again, the more the radial stream lines are disturbed, the larger the deviation from the line source response. Also, the early time deviation from the line source curve is determined by the portion of the impermeable boundary facing the production well. Only the late time response could possibly indicate the difference between an impermeable boundary with volume and an impermeable boundary without volume. The pressure responses during the first log cycle of time after the deviation from the line source response for the complete elliptical and circular boundaries are practically identical to the pressure responses of the semielliptical and semicircular boundaries. For example, curve A in Fig. 5.2-15 is practically identical to curve A in Fig. 5.2-13. Hence, in order to detect the volume of an impermeable boundary in addition to the shortest distance to it, long tests, fine pressure resolution and a relatively large impermeable boundary are needed.

5.2.4 Discussion

The main issue considered in this section is the detection of large scale impermeable reservoir regions from transient pressure tests. The approach we have taken is similar to a finite difference or a finite element approach in that the analytical solution to the true problem is not readily attainable. In a finite difference approach, for example, the diffusivity equation and the boundary conditions are kept and discretized in space and in time yielding a set of algebraic equations that must be solved for each time step. In the method presented in this section, we represent the boundary condition by a finite set of boundary wells, and impose the boundary condition at discrete points. In addition, we discretize the time domain, and assuming a constant rate per time step at the boundary wells, we solve the new problem analytically using the method of superposition.

Another way to look at our approach is that the true system, which is infinite in the lateral extent and contains a single well and a single impermeable boundary, is replaced by a system with wells without an impermeable boundary. By controlling the rates of production and injection at the boundary wells, we create the effects of an impermeable boundary. This method is directly applicable for finite volumetric impermeable boundaries. The boundary wells that are distributed inside the impermeable region along its boundary allow us to achieve three objectives: (1) prevent the early time migration of fluid from within the impermeable region toward the production well; (2) prevent the late time flow of reservoir fluid into the impermeable region and movement through it to the production well; and (3) produce the

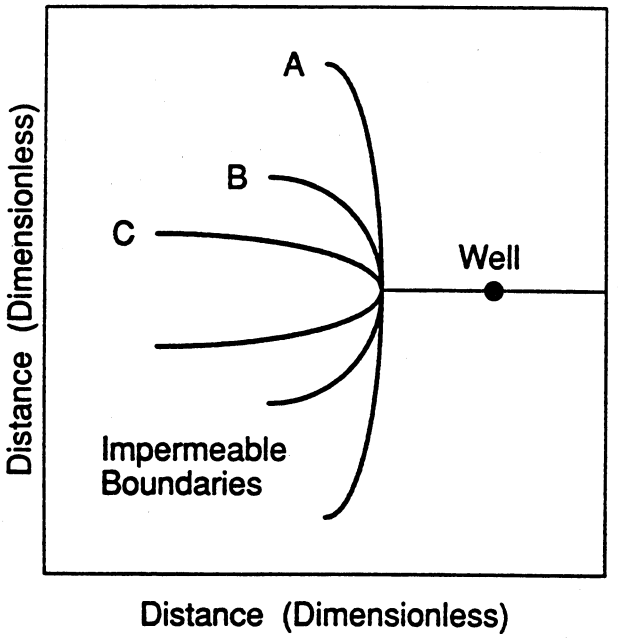

Fig. 5.2-14 Schematic diagram for a well near impermeable fractures; r_{min} = 100; Ellipses with a = 200, and b = 50; Circle with R = 100.

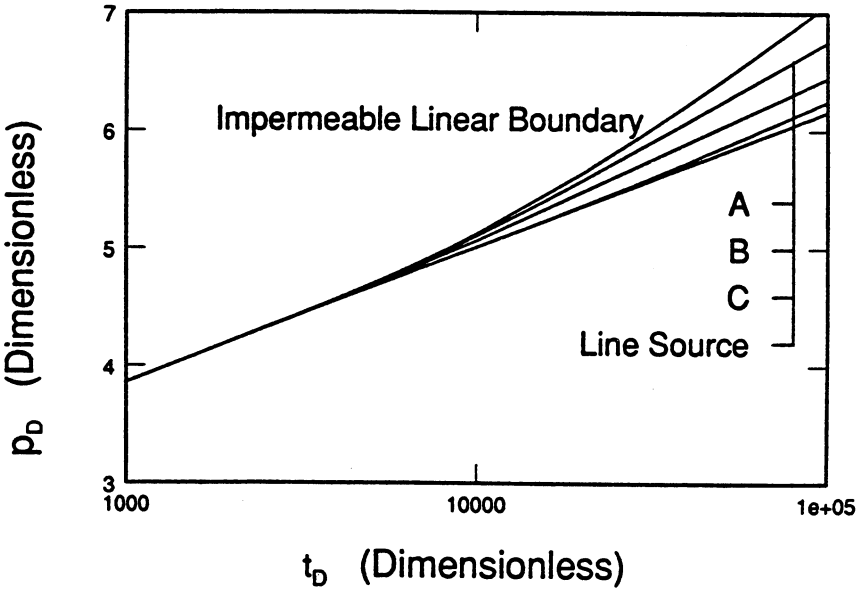

Fig. 5.2-15 Semilog pressure response for a well near impermeable fractures; r_{min} = 100; Ellipses with a = 200, and b = 50; Circle with R = 100.

impermeable region so that its pressure declines with time as in the actual case. Hence, there is a net production out of the boundary wells that accounts for the decompression of the boundary volume that in our model is part of the reservoir.

The above observations are valid for finite volumetric boundaries, and not valid for infinite volumetric boundaries. We have applied the new model for a case of a single well in the center of a closed outer boundary reservoir. In this case, most of the reservoir volume is not connected to the production well. The boundary wells produce at an ever increasing rate, and the new method fails at late time. However, the early time portion of the pseudosteady state flow period was generated by the new model.

There is a fundamental error in application of this new model to finite length impermeable line boundaries such as fractures. Since the line boundary has no volume associated with it, the boundary wells have no volume to deplete, hence, the excess production of the boundary wells does not relate to the real reservoir configuration. For infinitely long fractures, like an impermeable linear boundary, the application of the new model is reasonable, but as in the closed outer boundary case, it fails at late time. For finite length fractures, such as presented in Section 5.2.3, the new model is applicable only for the early time boundary effects where the reservoir area on the side of the boundary not containing the well is not allowed to expand toward the production well. The late time pressure response is affected by the net over production at the boundary wells, and is not correct. However, the early time pressure deviation from the line source curve allows determination of the minimum distance between the well and the impermeable fracture.

The effectiveness of the new model is sensitive to the density of the boundary wells and their distance from the actual location of the impermeable boundary. We have found, by matching the results from the new model to analytical solutions, that an average dimensionless distance between adjacent boundary wells of 10 yielded good pressure responses. The dimensionless distance between the line of boundary wells and the actual location of the impermeable boundary varied between 1 and 10, with an average value of 5 yielding good pressure responses. In general, boundary sections with large curvature required a high density of boundary wells. Also, the portions of the boundary facing the production well required a high density of boundary wells.

The model presented here can be extended to interference testing in the presence of large scale impermeable boundaries. However, interference wells must not be close to the impermeable boundary where the local discretization of the boundary affects interference responses in an unrealistic manner. The new model can also be applied to reservoir-well configurations that contain two or more large scale impermeable subregions, and to study isopressure finite fractures. Also, the new model can be used to study the effects of constant pressure regions on the response of a production well.

5.2.5 Conclusions

An algorithm is presented to study the effects of internal impermeable boundaries on the transient pressure response of a well producing with constant flow rate. The effects of the impermeable boundary are generated by replacing the boundary by a set of line source wells producing with variable flow rates, and then applying the method of superposition. Use of the method for sample problems yields the following conclusions.

(1) With other factors constant, the greater the size of the impermeable region the more the pressure response deviates from the line source homogeneous response. Also, impermeable regions must be relatively large with respect to their distance from the production well in order to be detected.

(2) An impermeable region whose shape causes a disturbance to the radial stream lines yields a significant deviation of the pressure response from the line source solution. The more the boundary resembles a linear impermeable barrier, the greater the deviation.

(3) From a practical point of view, there is essentially no difference in the early time transient responses of impermeable regions with volume, and impermeable fractures without volume. It would be necessary to extend a drawdown test for several log-cycles of time in order to distinguish between a volumetric and a nonvolumetric impermeable region.

(4) The orientation of an impermeable region with respect to the production well has a great influence on the transient pressure response. Together with the shortest distance between the production well and the boundary, orientation is the most significant characteristic parameter that affects the transient pressure response.

(5) In practice, the combined effects of size, shape, and orientation, and the distance to the production well are so intermingled that it is difficult to evaluate the effect of each parameter independently. However, those configurations that significantly disturb the radial stream lines produce the largest deviations from the homogeneous line source solution.

(6) The model can also be used to study the effect of different external geometries, the effects of multiple heterogeneous regions, isopressure finite fractures, and constant pressure regions on transient pressure responses of a production well. Its main drawback is its sensitivity to the number and distribution of line source wells used to simulated the heterogeneous region under study.

5.3 Effects of a Partially Communicating Fault in a Composite Reservoir on Transient Pressure Testing

Anil K. Ambastha and Abraham S. Grader

Many reservoirs are faulted, and the hydraulic characterization of these faults is essential for the design of field scale developments. In addition to the effects that a fault has on fluid flow in the reservoir, it may separate two reservoir regions with distinctly different properties. The detection of the properties on both sides of the fault, in addition to the detection of the distance to the fault, is important to reservoir characterization.

In this study, a linear fault is modeled as a skin boundary with infinitesimal thickness. Analytical solutions for pressure transient behavior for a line-source constant-rate well in a composite reservoir are obtained using one Fourier transform in space and time-space Laplace transforms. The solutions are presented for strip and infinite reservoirs.

This study examines drawdown pressure and pressure derivative behavior, and extends and generalizes many studies presented in the past. Correlating parameters for pressure transient responses are presented. The possibilities of boundary detections are considered, and interference pressure responses in a composite, strip reservoir are discussed briefly.

5.3.1 Introduction

In conventional well test analysis, faults have been treated as sealing boundaries. The method of images has been used to study drawdown, buildup or interference pressure transient behavior for a well in a homogeneous reservoir, containing single or multiple linear, sealing boundaries. The "doubling of slope" is used to indicate the presence of a linear, sealing boundary. The intersection time of the two semilog straight lines is used to calculate the distance to a barrier (Horner 1951, Davis and Hawkins 1963, and Gray 1965). Also, the deviation time at which the pressure response departs from the line-source solution can be used to calculate the

distance to a barrier. Log-log (Stallman 1952) and semilog (Horner 1951) type-curve matching methods have been developed to calculate the distance to a barrier. The pressure transient behavior of a well in a long narrow reservoir has been studied (Tiab and Kumar 1980, Ehlig-Economides and Economides 1982, Nutakki and Mattar 1982, and Ehlig-Economides and Economides 1985). Streltsova and McKinley (1984) discuss the pressure transient behavior for a well in a reservoir limited by one or more linear boundaries. They consider both closed and constant-pressure boundaries and discontinuities in reservoir properties. Prasad (1975) and Wong et al. (1986) used a Green's function approach to generate solutions for flow with multiple sealing boundaries.

Fig. 5.3-1 presents a number of homogeneous reservoir configurations with single or multiple linear, sealing boundaries considered in the literature. Recently, the effects of a partially communicating fault in an infinite, homogeneous reservoir have been considered numerically (Stewart et al. 1984) and analytically (Yaxley 1985). Pressure derivative techniques have been used to analyze pressure transient data for fault detection (Clark 1985). The pressure transient behavior of an infinitely large composite reservoir with a linear discontinuity in reservoir properties was considered by Bixel et al. (1963) and Streltsova and McKinley (1984). The effects of a partially communicating fault (or a linear leaky discontinuity) in a composite reservoir (Fig. 5.3-2a) on transient pressure testing have not been considered, however. The upper part of Fig. 5.3-2a shows a side view of two reservoir regions separated by a fault. Also, the fault may be partially communicating, depending on its characteristics. The reservoir configuration of the upper part of Fig. 5.3-2a is simplified by removing the vertical discontinuity caused by the fault, making the two reservoir parts horizontal, and by making the fault discontinuity vertical as described in the lower part of Fig. 5.3-2a. Figs. 5.3-2b and 5.3-2c are top views of the simplified reservoir configurations considered in this section. Fig. 5.3-2b represents a strip reservoir with two parallel no-flow boundaries and Fig. 5.3-2c represents an infinite reservoir with a linear discontinuity. The two reservoir regions on both sides of the fault (discontinuity) may have different diffusivities and transmissivities, and the resistance to flow at the fault is modeled as a thin skin, using the concepts of van Everdingen (1953) and Hurst (1953). The active well is located in region I and is considered as a constant rate line source. The problem is solved along the approach taken by Bixel et al. (1963), and Yaxley (1985), using one Fourier space transformation and two Laplace time-space transformations. The solutions for the pressure responses for the active and observation wells and drawdown pressure and pressure derivative behaviors are presented. Interference pressure behavior is also discussed.

5.3.2 Theory

The mathematical model and a solution technique for the strip reservoir configuration of Fig. 5.3-2b are detailed in Ambastha et al. (1987). In the development of the mathematical model, we analyze the flow of a single-phase, slightly compressible fluid of constant compressibility in a homogeneous and isotropic reservoir on each side of the partially communicating fault. We also assume constant formation thickness and a line-source well. Diffusivity equations for both regions along with the appropriate outer and skin boundary conditions result. The Laplace transformation with respect to the time variable and the Fourier transformation with respect to the y variable reduce the two partial differential equations to two ordinary differential equations. The ordinary differential equation for region II is readily solved. However, the ordinary differential equation for region I (the region containing the well) is solved by taking the Laplace transformation with respect to the x variable, and inverting the resulting solution analytically with respect to the x variable. Thus, the dimensionless pressure drops in the Laplace-Fourier space at any location in regions I and II at any time are given by Eqs. (5.3-1) and (5.3-2) respectively.

$$\hat{p}_{D1} = -\frac{\alpha_3}{2\sqrt{\alpha_1}}\left[e^{-|x_D - a_D|\sqrt{\alpha_1}} + \frac{\sqrt{\alpha_1} + S\lambda\sqrt{\alpha_1\alpha_2} - \lambda\sqrt{\alpha_2}}{\sqrt{\alpha_1} + S\lambda\sqrt{\alpha_1\alpha_2} + \lambda\sqrt{\alpha_2}}\ e^{-(x_D + a_D)\sqrt{\alpha_1}}\right] \quad \text{for } x_D \geq 0 \quad (5.3\text{-}1)$$

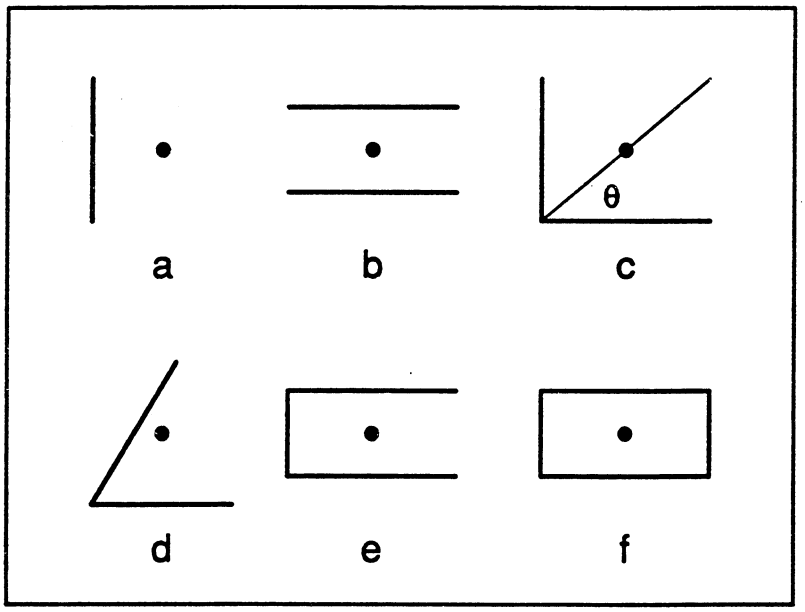

Fig. 5.3-1 Homogeneous reservoir configurations studied in the literature.

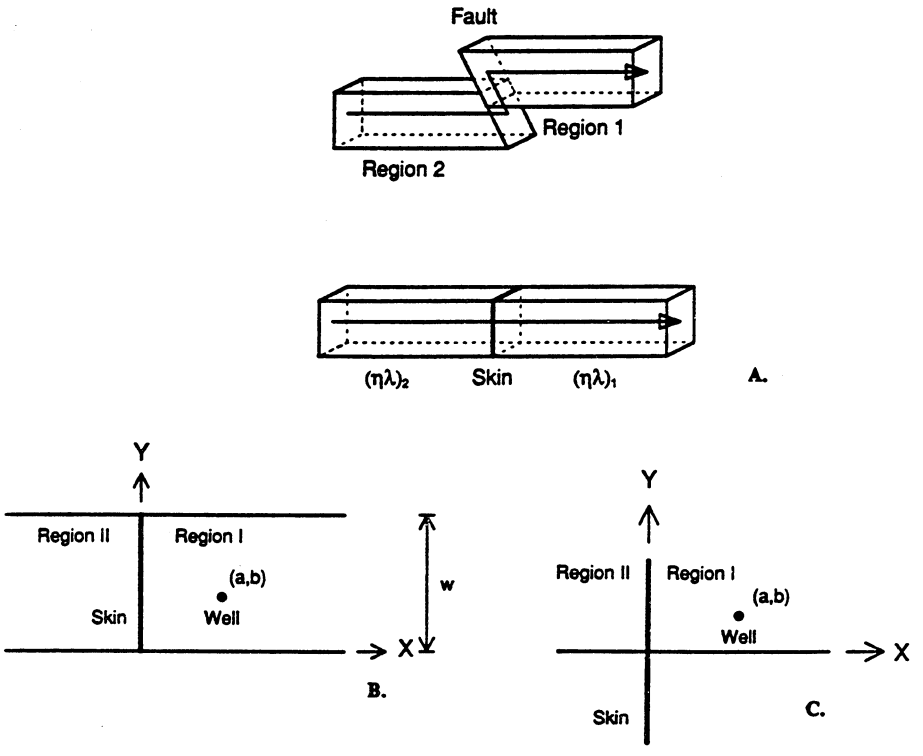

Fig. 5.3-2 Schematic diagram of a composite reservoir with a partially communicating fault; A: modeling fault as a skin boundary; B: idealized composite strip reservoir, and C: idealized composite infinite reservoir, top view.

$$\hat{\bar{p}}_{D2} = - \frac{\alpha_3 \, e^{x_D \sqrt{\alpha_2} - a_D \sqrt{\alpha_1}}}{\sqrt{\alpha_1} + S\lambda\sqrt{\alpha_1\alpha_2} + \lambda\sqrt{\alpha_2}} \quad \text{for } x_D \le 0 \qquad (5.3\text{-}2)$$

where

$\hat{\bar{p}}_{D1}$ = Laplace-Fourier dimensionless pressure drop in region I
$\hat{\bar{p}}_{D2}$ = Laplace-Fourier dimensionless pressure drop in region II
λ = Mobility ratio, $(k/\mu)_2 / (k/\mu)_1$
S = Skin effect at the discontinuity
x_D = Dimensionless distance, x/r_w
a_D = Distance between the well and the fault
α_1 = $\nu^2 m^2 + 1$
α_2 = $\nu^2 m^2 + \frac{1}{\eta}$
α_3 = $\frac{-2\pi\nu \cos(m\tilde{b}_D)}{1}$
b = y co-ordinate of well location
ν = Constant = π/w_D
m = Fourier variable
l = Laplace variable with respect to time

Eqs. (5.3-1) and (5.3-2) are of an exponential form in the x variable, and the Laplace time variable and the Fourier y variable are in the α terms. The variable S denotes the van Everdingen (1953) and Hurst (1953) skin assigned to the fault and the variable λ represents the mobility ratio between region II and region I. All the variables are defined in Ambastha et al. (1987). The numerical inversion technique of the Laplace-Fourier solutions is also described by Ambastha et al. (1987). Eqs. (5.3-1) and (5.3-2) also represent the dimensionless pressure drops in the Laplace-Fourier space at any location in regions I and II respectively for an infinitely large composite reservoir shown in Fig. 5.3-2c with the modified definitions of α_1, α_2 and α_3 as presented in Ambastha et al. (1987). The solution to the infinite reservoir case follows the solution for the strip reservoir case, except for the y direction Fourier transformation. In the strip case, we use a finite cosine Fourier transformation and in the infinite case, we use a complex infinite Fourier transformation. The numerical inversion technique of the solutions for an infinitely large composite reservoir and some computational experiences are discussed by Ambastha et al. (1987).

5.3.3 Validation

There are several special cases in the literature against which the model developed in this study can be validated. Fig. 5.3-3 presents a number of pressure responses in semilog co-ordinates for infinite reservoirs generated using the solution presented here. The wellbore pressure is computed at $x_D = a_D - 1$. In Fig. 5.3-3, the dimensionless distance between the well and the boundary, a_D, and the diffusivity ratio, η, are 400 and 1, respectively. The values of mobility ratio, λ, and skin at the boundary, S, used to generate the different curves are shown on Fig. 5.3-3. Computation of the dimensionless wellbore pressure drop in real space involves successive numerical inversions of the Fourier and Laplace transformations. The linearity of the Fourier and Laplace transformations is shown by curve E, where the solution represented by the solid line is obtained by a numerical inversion of the Fourier transformation first. The circles represent the solution obtained by a numerical inversion of the Laplace transformation first. The different curves in Fig. 5.3-3 represent the following reservoir configurations:

- Curves A and B: A well near a sealing fault (Horner 1951, Stallman 1952, Tiab and Kumar 1980, Yaxley 1985, and Bixel et al. 1963, Fig. 5.3-1a).

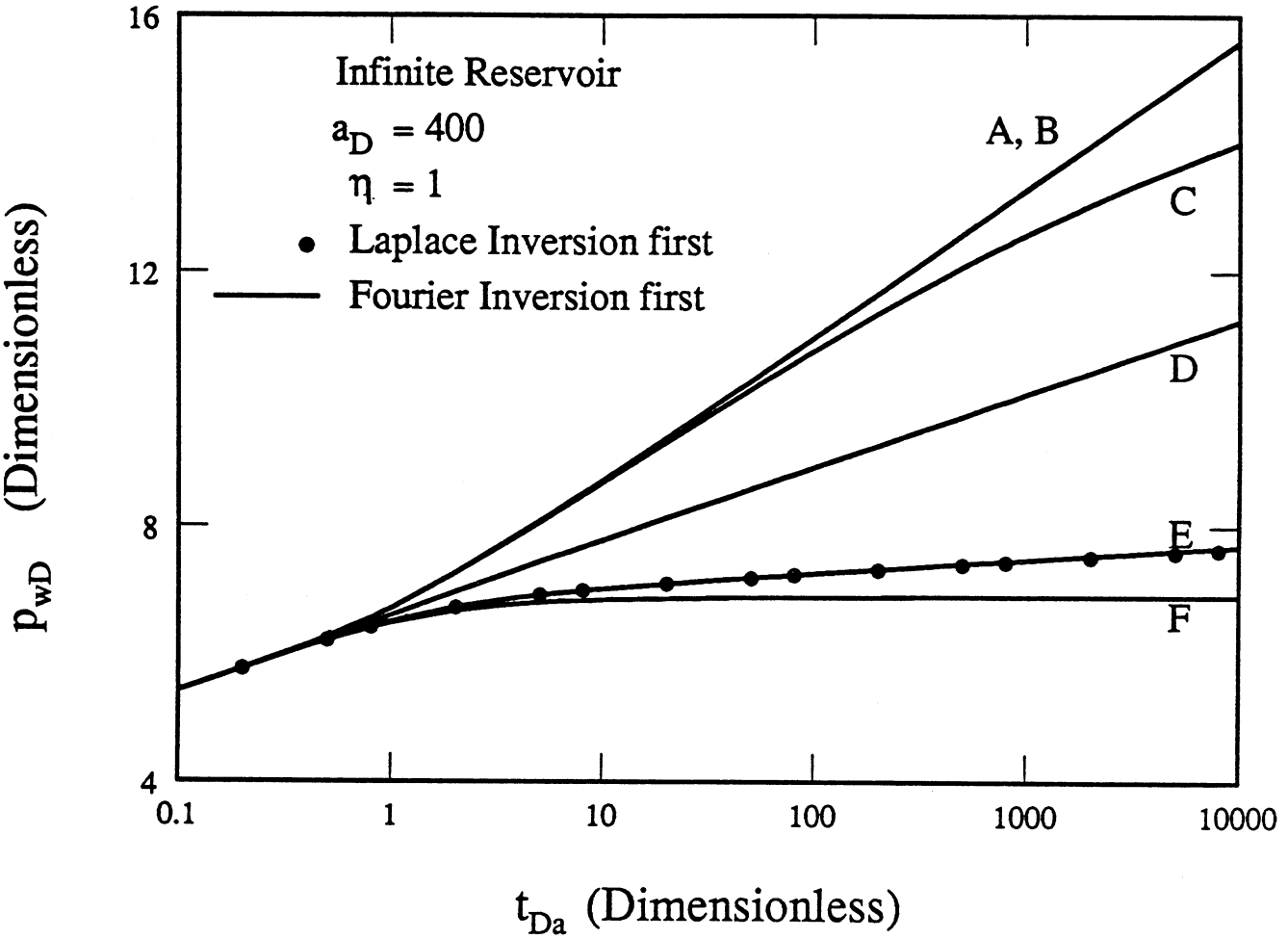

Fig. 5.3-3 Drawdown pressure responses for a well in an infinite reservoir A: $\lambda = 1$, $S = 10^6$, B: $\lambda = 10^{-4}$, $S = 0$, C: $\lambda = 1$, $S = 100$, D: $\lambda = 1$, $S = 0$ (Line-source solution), E: $\lambda = 10$, $S = 0$, and F: $\lambda = 10^{-4}$, $S = 0$.

- Curve C: A well near a partially communicating fault in a homogeneous reservoir (Yaxley 1985).
- Curve D: A line-source well in an infinite, homogeneous reservoir (Theis 1935).
- Curve E: A well in an infinite, composite reservoir (Streltsova and McKinley 1984, Bixel et al. 1963).
- Curve F: A well near a constant-pressure boundary (Tiab and Kumar 1980, Yaxley 1985, and Bixel et al. 1963).

A small mobility ratio or a large skin (curves A and B) results in the pressure drawdown behavior that follows the line-source solution until the boundary effects become significant. Then, the pressure response exhibits the doubling of slope, indicating the presence of a linear sealing boundary. However, if the boundary is leaky, as in curve C, the pressure transient behavior follows the double slope line after departing from the line-source solution for some time, and then depending on the magnitude of boundary skin, the pressure response becomes parallel to the line-source solution at late time. The pressure drawdown response for a well in an infinitely large homogeneous reservoir ($\lambda = 1$, $\eta = 1$, $S = 0$) is the same as the line-source solution (curve D). However, if there is a property contrast, such as shown in curve E, the pressure transient behavior departs from the line-source solution and lies closer to the constant-pressure boundary solution (curve F) for $\lambda > 1$. The pressure response remains bounded between the line-source solution (curve D) and the constant-pressure boundary solution (curve F), depending upon the mobility ratio.

Fig. 5.3-4 presents the dimensionless wellbore pressure responses for several strip reservoir cases generated using the solution developed in this study. The different curves represent the following configurations:

- Curve A: A well in the center of a strip reservoir (Ramey and Cobb 1971, Tiab and Kumar 1980, Ehlig-Economides and Economides 1982, Nutakki and Mattar 1982, Ehlig-Economides and Economides 1985, Streltsova and McKinley 1984, Fig. 5.3-1b)
- Curve B: A well located arbitrarily between parallel sealing faults (Tiab and Kumar 1980, Streltsova and McKinley 1984, Fig. 5.3-1b)
- Curve C: A well between two perpendicular intersecting faults (Tiab and Crichlow 1979 and Van Poolen 1965, Fig. 5.3-1c)
- Curve D: A well in a three fault system (Tiab and Crichlow 1979, Fig. 5.3-1e)

The pressure transient response of a line-source well is also shown in Fig. 5.3-4. The wellbore pressure is computed at $x_D = a_D - 1$. Fig. 5.3-5 shows the semilog pressure derivatives corresponding to the cases shown in Fig. 5.3-4. The semilog pressure derivative is computed as:

$$p'_D = \frac{dp_{wD}}{d \ln t_D} = t_D \frac{dp_{wD}}{dt_D} \tag{5.3-3}$$

where p_{wD} = dimensionless wellbore pressure, t_D = dimensionless time and $dp_{wD}/dt_D = L^{-1}[l\ \bar{p}_{wD}]$. Figs. 5.3-4 and 5.3-5 are for $\lambda = 1$, $\eta = 1$, and $a_D = 5$. Curves A and B are for $w_D = 100$ and $S = 0$ with $b_D = 50$ and 10, respectively. Curves C and D are for $S = 10^6$ to generate the effects of a sealing skin boundary. Curve C is for $b_D = 0.88$ and $w_D = 200$, while curve D is for $b_D = 5$ and $w_D = 10$. The distance $b_D = 0.88$ for curve C corresponds to $\theta = 10°$ (Fig. 5.3-1c) for a well between two perpendicular intersecting faults. The distance $b_D = 0.88$ was selected to display the behavior of the reservoir configuration shown in Fig. 5.3-1c for most of the pressure response shown in Fig. 5.3-4. For curves A and B, the value of a_D is irrelevant because the solution is for a homogeneous reservoir with $S = 0$. Curve A follows the line-source solution before the effects of two parallel boundaries are felt concurrently. After the departure of the pressure response of curve A from the line-source solution, the late time linear flow behavior is illustrated by half slope lines on the log-log

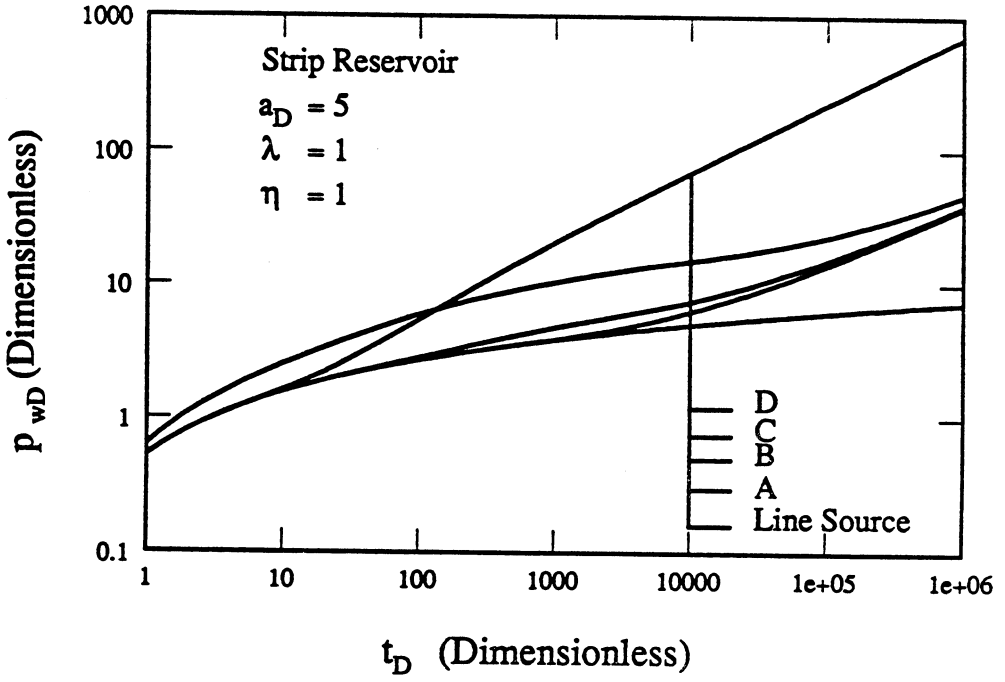

Fig. 5.3-4 Drawdown pressure responses for a well in a strip reservoir A: $b_D = 50$, $w_D = 100$, $S = 0$, B: $b_D = 10$, $w_D = 100$, $S = 0$, C: $b_D = 0.88$, $w_D = 200$, $S = 10^6$, and D: $b_D = 5$, $w_D = 10$, $S = 10^6$.

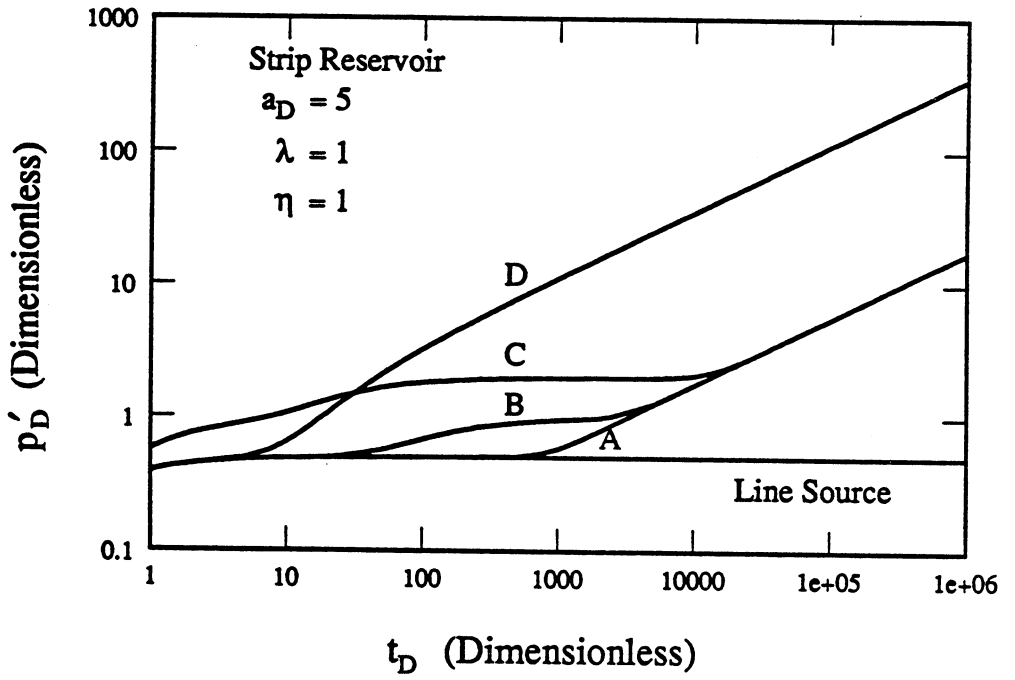

Fig. 5.3-5 Drawdown pressure derivative responses for a well in a strip reservoir A: $b_D = 50$, $w_D = 100$, $S = 0$, B: $b_D = 10$, $w_D = 100$, $S = 0$, C: $b_D = 0.88$, $w_D = 200$, $S = 100^6$, and D: $b_D = 5$, $w_D = 10$, $S = 10^6$.

graphs of the pressure (Fig. 5.3-4) and the pressure derivative (Fig. 5.3-5) responses. However, for curve B, the effect of one boundary at a distance of $b_D = 10$ is felt first, and then at late time, the transient response on curve B approaches the linear flow behavior, as in curve A. For curve B, the doubling of the semilog slope is also evident in Fig. 5.3-5 for a short duration. For curve C, the effect of the boundary at a distance of $b_D = 0.88$ has been felt even before $t_D = 1$, and therefore, the dimensionless wellbore pressure drop is always above the line source solution. However, before curve C may double the slope, the effects of the skin boundary (that is a sealing fault because of large skin value) are felt, and the semilog pressure derivative rises to 2 at $t_D \approx 100$, and lasts up to $t_D \approx 9000$. The quadrupling of the semilog slope to 2 is the same as the pressure transient behavior for a well between two perpendicular intersecting faults. At late time, the effects of the third boundary at a distance of $w_D - b_D = (200 - 0.88)$ from the wellbore is felt, and the linear flow in a semi-infinite strip reservoir is observed as half slope lines on Figs. 5.3-4 and 5.3-5 for the curve C. For curve D, the effects of three boundaries at distances of $a_D = 5$, $b_D = 5$, and $w_D - b_D = 5$ are felt simultaneously at $t_D \approx 10$. At late time, half slope lines on the log-log graphs of Figs. 5.3-4 and 5.3-5 depict the linear flow in a semi-infinite strip system. A more detailed analysis of the linear flow in a semi-infinite system appears in Ambastha and Sageev (1987). The departure of the pressure response from the line-source solution, the doubling or quadrupling of semilog slopes, and the late time linear flow is discussed in detail later.

5.3.4 Drawdown Behavior of Infinite Reservoirs

Bixel et al. (1963) presented the pressure transient behavior for a well in an infinitely large composite reservoir. The two reservoir regions are separated by a linear discontinuity. Bixel et al. (1963) stated that such a configuration may represent a well in a relatively thin reservoir near a fluid-fluid contact, or a well in a reservoir exhibiting a sudden change in rock and fluid characteristics because of clay fill, facies changes, buried shore lines, and channel deposits. Bixel et al. (1963) presented semilog graphs of the dimensionless wellbore pressure vs. dimensionless time based on the distance to the discontinuity, a, with the mobility and storativity ratios as the parameters. They defined the storativity ratio, F, as $(\phi c_t)_{II} / (\phi c_t)_I = \lambda/\eta$. They presented the results only for $a_D = 400$. They observed that if $t_D > 25$ (i.e., if the log approximation of exponential-integral solution is valid), the effect of a change in a or x is the addition or subtraction of a constant to the dimensionless wellbore pressure drops for any given a_D (in their case, $a_D = 400$). This additive constant is ln (400/bD), if the dimensionless wellbore pressure drops for any a_D are correlated with the pressure response for $a_D = 400$. A similar pressure scale shift has been used by Sageev et al. (1985) to develop a semilog type-curve for a well near a linear boundary. Yaxley (1985) considered the effects of a partially communicating fault on the transient pressure behavior of a well in an infinite, homogeneous reservoir. He treated a partially communicating fault as an infinitely long, vertical semipermeable barrier. He presented the drawdown pressure and pressure derivative behavior vs. t_{Da} as semilog graphs with the specific transmissivity ratio, α_A, as a parameter. α_A is defined as:

$$\alpha_A = \frac{k_S / \Delta X}{k / a} \tag{5.3-4}$$

for uniform viscosity and thickness in the reservoir and the fault regions. k_S and ΔX are the permeability and horizontal thickness of the fault zone, respectively, k is the reservoir permeability, and *a* is the distance between the fault and the active well. Since we model a partially communicating fault as an infinitesimally thin skin, a relationship between α_A and S can be derived using Darcy's law for steady-state flow across the fault zone. This relationship is

$$S = \frac{2\pi a}{\alpha_A} \tag{5.3-5}$$

per unit of reservoir width. In Eq. (5.3-5), a is in centimeters. The consideration of an example with a = 10 cm., and α_A = 0.001 shows that S = 10000 π. A relationship among the variables S, k_S/k, and ΔX is

$$S = \frac{2\pi}{k_S/k}\,\Delta X \tag{5.3-6}$$

Eq. (5.3-6) yields S = 200 π for k_S/k = 0.1 and ΔX = 10 cm. Thus, large skin values generate the effects of a sealing fault.

The parameters for the pressure drawdown behavior of a well in an infinite composite reservoir with a partially communicating fault are λ, η, and S, when the pressure and the pressure derivative responses are graphed as a function of the dimensionless time based on the distance between the fault and the well, t_{Da}, given by

$$t_{Da} = \left[\frac{k}{\phi\mu c_t}\right]_I \frac{t}{a^2} \tag{5.3-7}$$

where

- t = Time, hour
- t_{Da} = Dimensionless time, normalized by the distance a.
- k = Permeability, md
- μ = Viscosity, cp
- ϕ = Porosity, fraction
- c_t = Total system compressibility, psi $^{-1}$

Fig. 5.3-6 presents the effects of mobility ratio on the pressure drawdown behavior for a_D = 400, η = 1, and S = 0. The circles for λ = 0.1 are the results for a_D = 100. This shows that graphing p_{wD} + ln (400/a_D) vs. t_{Da} correlates the pressure transient responses for all a_D to an arbitrarily selected a_D of 400. The curve representing $\lambda \leq 0.01$ shows the transient pressure response for a well near a sealing fault in an infinite, homogeneous reservoir. The transient pressure responses for the cases where $\lambda \leq 0.01$ are similar to the pressure responses of a well near a constant-pressure boundary in an infinite, homogeneous reservoir. Also, the presence of a discontinuity causes the pressure response to depart from the homogeneous line-source response (λ =1, η =1, S =0) at $t_{Da} \approx 0.4$. Bixel et al. (1963) also report the departure to occur at $t_{Da} \approx 0.4$.

Fig. 5.3-7 shows the effects of the diffusivity ratio on the pressure drawdown behavior for λ = 1, S = 0, and a_D = 400. Since λ = 1, η = 1/F (see Bixel et al. 1963). Thus, Fig. 5.3-7 shows the effects of the storativity ratio, F. The curve for η = 1 represents the line-source solution. The pressure response departs from the line-source solution at $t_{Da} \approx 0.4$ for all η. For small η (or large F), the pressure response resembles that of a well near a constant-pressure boundary in an infinite, homogeneous reservoir. This is because region II has a large amount of fluid stored in comparison to the amount of fluid stored in region I. Also, since the fluid in region II has the same mobility as that of the fluid in region I, region II can supply the fluid across the boundary as fast as the well can produce. However, for large η (or small F), the pressure response departs from the line-source solution and the slope doubles, resembling a sealing boundary effect, but then becomes parallel to the line-source solution (solution for λ = 1) at late time. This occurs because for large values of η (or small F), most of the fluid is

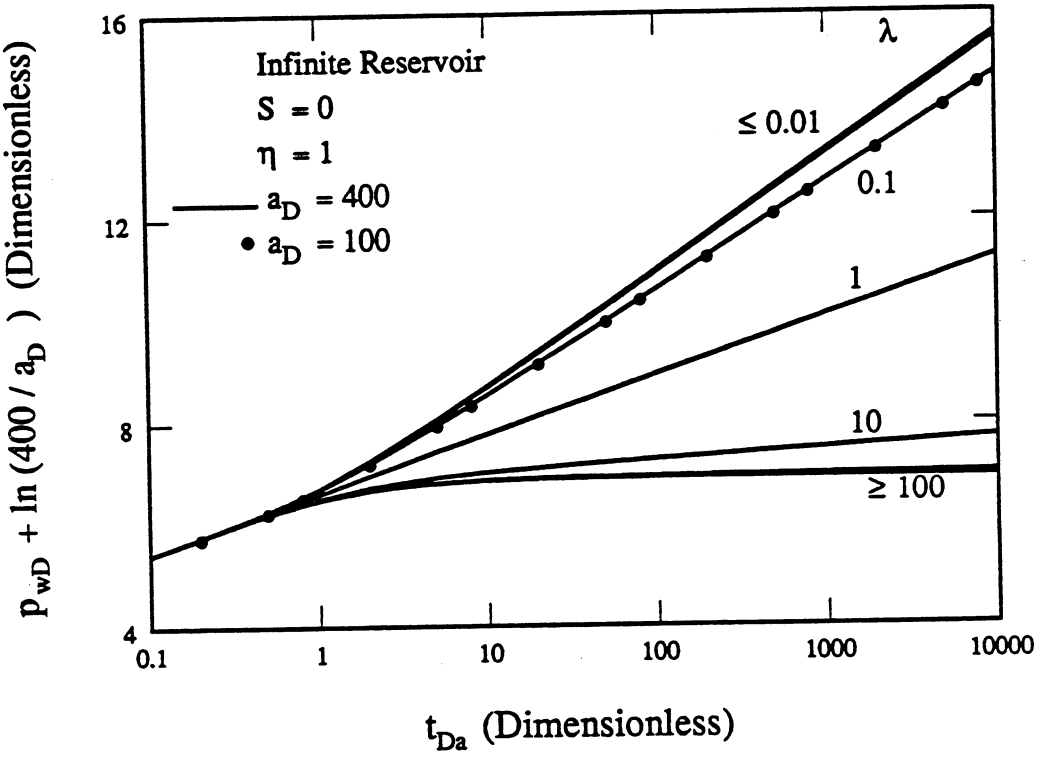

Fig. 5.3-6 Effect of mobility ratio on pressure drawdown responses for a well in an infinite reservoir.

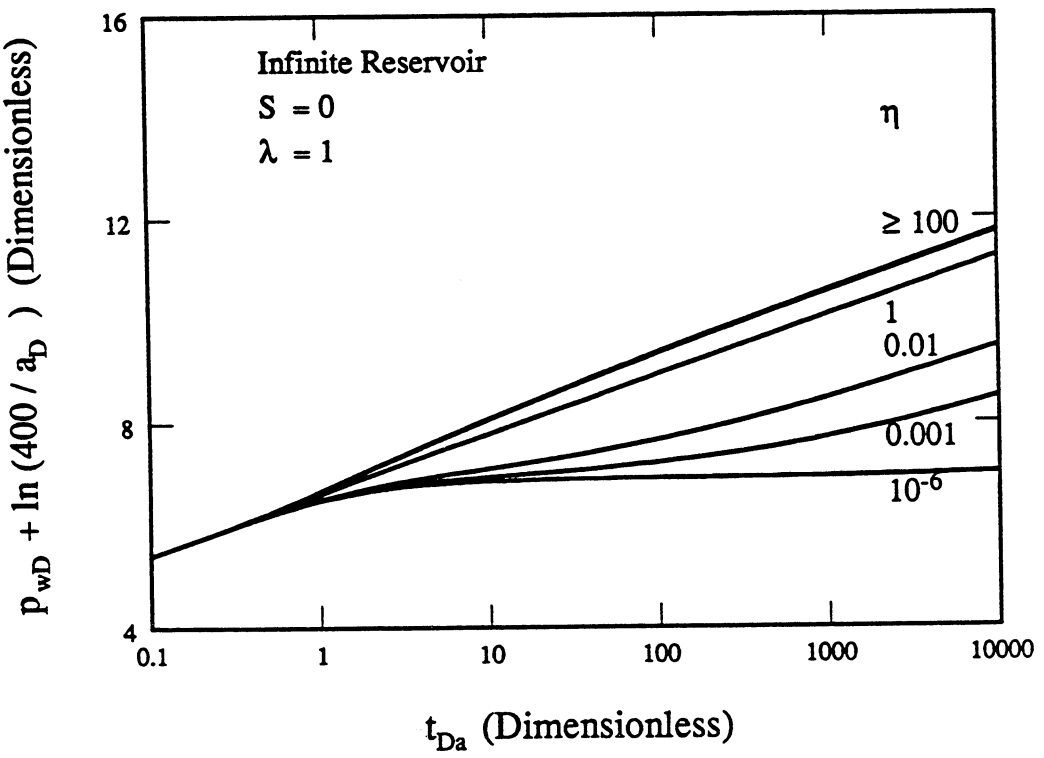

Fig. 5.3-7 Effect of diffusivity ratio on pressure drawdown responses for a well in an infinite reservoir.

stored in region I containing the well, and only a small fraction in region II. Therefore, the boundary is felt as a sealing boundary first. However, later on, since the fluids in the two regions have the same mobilities, the well produces mostly from region I and only a small fraction from region II. Thus, the pressure response becomes parallel to the line-source solution (solution for $\lambda = 1$). A low storativity in region II appears as a constant pressure difference on a semilog graph, which can be interpreted as a late time skin. The pressure responses shown in Figs. 5.3-6 and 5.3-7 agree with those obtained by Bixel et al. (1963) for the corresponding cases.

Fig. 5.3-8 shows the effects of storativity ratio for mobility ratios of 0.1 and 10. Again, for a given mobility ratio, the effects of a low storativity in region II (i.e., a small F) appear as a constant pressure difference on a semilog graph of the pressure behavior for that particular mobility ratio, but with $F = 1$. For large mobility and storativity ratios (see the case for $\lambda = 10$, $F = 10^6$), the pressure response resembles that for a well near a constant-pressure boundary. This is caused by less resistance for the flow of fluid stored in region II into region I, as $\lambda > 1$. A large amount of fluid flow from region II may equal the well production rate, causing the pressure transient behavior to resemble that for a well near a constant-pressure boundary. However, if the mobility ratio is less than unity, there is greater resistance to the flow of fluid from region II across the boundary. This causes the wellbore pressure behavior to resemble that of a well near a sealing boundary. However, if $F > 1$, there is a possibility of enough fluid flow from region II across the boundary, despite the greater resistance to flow as $\lambda < 1$, and the wellbore pressure behavior may resemble that for a well near a constant-pressure boundary. The relative magnitudes of λ and F determine the resulting pressure drawdown behavior. For $\lambda = 0.1$ and $F = 10^6$, Fig. 5.3-8 shows that the wellbore pressure drop follows the behavior for a well near a constant-pressure boundary to $t_{Da} \approx 200$. Thus, for a given mobility ratio and $S = 0$, the pressure drawdown behavior resembles that for a well near a constant-pressure boundary for a large storativity ratio. However, the effect of a small storativity ratio is exhibited as an additive late time skin to the pressure response for the specified λ with $F = 1$.

Fig. 5.3-9 shows the semilog pressure drawdown behavior for a well in an infinite, homogeneous reservoir for several values of skin at the discontinuity. Again, the pressure response departs from the homogeneous reservoir behavior at $t_{Da} \approx 0.4$. For large values of skin ($S \geq 10^4$), the pressure drawdown response resembles that for a well near a sealing fault. For moderate values of skin, however, the pressure response departs from the line-source solution, and then follows the double slope behavior for some time. Later, the pressure response reverts back to a semilog line parallel to the line-source solution as flow occurs across the partially communicating fault.

5.3.5 Drawdown Behavior of Strip Reservoirs

The pressure transient behavior of a well in a homogeneous strip reservoir (or a reservoir with parallel sealing boundaries) has been considered in the literature. A strip reservoir is shown in Fig. 5.3-1b. Such a reservoir approaches linear flow behavior at late time. But due to the convergence of the flow lines near the wellbore, there is an additional pressure drop. This additional pressure drop is termed "pseudoskin", σ, and the late time dimensionless wellbore pressure drop is given by:

$$p_{wD} = \frac{2\sqrt{\pi t_D}}{w_D} + \sigma \qquad (5.3\text{-}8)$$

where w_D = dimensionless reservoir width.

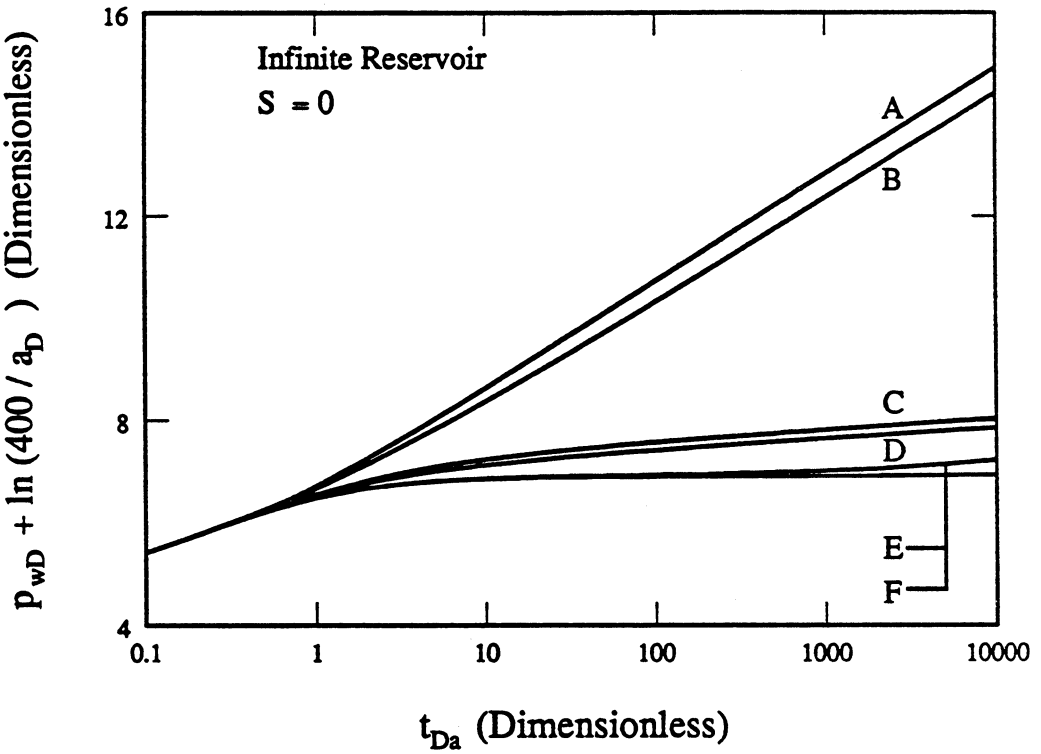

Fig. 5.3-8 Effect of storativity ratio on pressure drawdown responses for a well in an infinite reservoir A: λ = 0.1, F = 10^{-6}, B: λ= 0.1, F = 1, C: λ = 10, F = 10^{-6}, D: λ = 10, F = 1, E: λ = 0.1, F = 10^{6}, and F: λ = 10, F = 10^{6}.

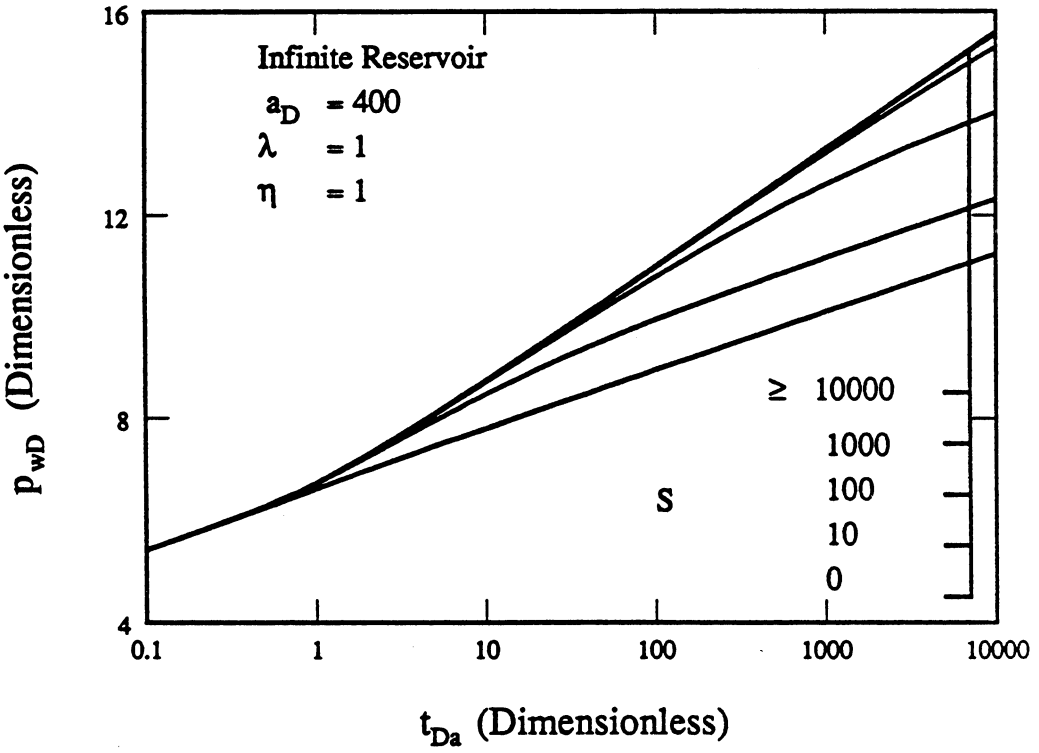

Fig. 5.3-9 Effect of skin on pressure drawdown responses for a well in a homogeneous infinite reservoir.

Fig. 5.3-10 presents σ vs. w_D for several well locations in a strip reservoir shown in Fig. 5.3-1b. This extends the study presented by Nutakki and Mattar (1982). The various curves in Fig. 5.3-10 are approximately semilog straight lines. Ehlig-Economides and Economides (1985) reported type-curves for a well in the center of a strip reservoir, shown in Fig. 5.3-1b, with the dimensionless reservoir width, w_D, as a parameter. Streltsova and McKinley (1984) and Tiab and Kumar (1980) studied the pressure transient behavior for an arbitrarily located well in a strip reservoir. They presented the pressure responses in terms of dimensionless well location, b/w. Tiab and Kumar (1980) also presented the pressure derivative behavior for an arbitrarily located well in a strip reservoir.

Since the model presented here includes the effects of a skin boundary (Fig. 5.3-2b) in a strip reservoir, it can be used to study the cases such as shown in Figs. 5.3-1c and 5.3-1e. The drawdown behavior for a well located between two intersecting faults (which includes the case of Fig. 5.3-1c) in a homogeneous reservoir was studied by van Poollen (1965) and Prasad (1975). Drawdown behaviors for a well in multiple-sealing fault systems (including the cases of Figs. 5.3-1c and 5.3-1e) were studied by Tiab and Crichlow (1979). However, the effects of a partially communicating skin boundary (or fault) in a homogeneous strip reservoir have not been treated. The pressure drawdown response of an arbitrarily located well in a homogeneous strip reservoir with a partially communicating fault is described by three parameters: a/w, b/w, and S. However, as Fig. 5.3-11 shows, the responses do not correlate exactly at intermediate times. Figs. 5.3-11 through 5.3-13 present the effects of a/w, b/w, and S, respectively, on the pressure transient behavior for a well in a homogeneous strip reservoir with a partially communicating fault. Figs. 5.3-11 through 5.3-13 are presented in terms of the semilog pressure derivatives computed as per Eq. (5.3-3). The line-source or exponential-integral solution exhibits a semilog slope of 0.5 for $t_D \geq 25$. Also, if the effects of one sealing boundary are felt, the semilog pressure derivative should double its value to 1. If the effects of two perpendicular intersecting sealing boundaries are simultaneously felt, the semilog slope should quadruple to 2. The quadrupling of the semilog derivative should also be observed, if the effects of two perpendicular sealing boundaries are felt in succession. However, the parallel sealing boundaries of a strip reservoir cause the late time flow configuration to resemble Fig. 5.3-1b or 1e for homogeneous reservoirs, depending on the magnitude of boundary skin. The late time dimensionless wellbore pressure drop is given by Eq. (5.3-8) for the configuration of Fig. 5.3-1b, and the semilog pressure derivative is

$$\frac{dp_{wD}}{d \ln t_D} = \frac{\sqrt{\pi\, t_D}}{w_D} \tag{5.3-9}$$

From Eq. (5.3-9), a log-log graph of the semilog pressure derivative vs. t_D yields a half slope line at late time. Similarly, the dimensionless wellbore pressure drop and the semilog pressure derivative at late time for the configuration of Fig. 5.3-1e are

$$p_{wD} = \frac{4\sqrt{\pi\, t_D}}{w_D} + \sigma_s \tag{5.3-10}$$

$$\frac{dp_{wD}}{d \ln t_D} = \frac{2\sqrt{\pi\, t_D}}{w_D} \tag{5.3-11}$$

where σ_s is the late time pseudoskin for a semi-infinite reservoir configuration of Fig. 5.3-1e, and is different from σ of Eq. (5.3-8). Eq. (5.3-11) shows that a log-log graph of the semilog pressure derivative vs. t_D yields a half slope line. Thus, the late time linear flow for the

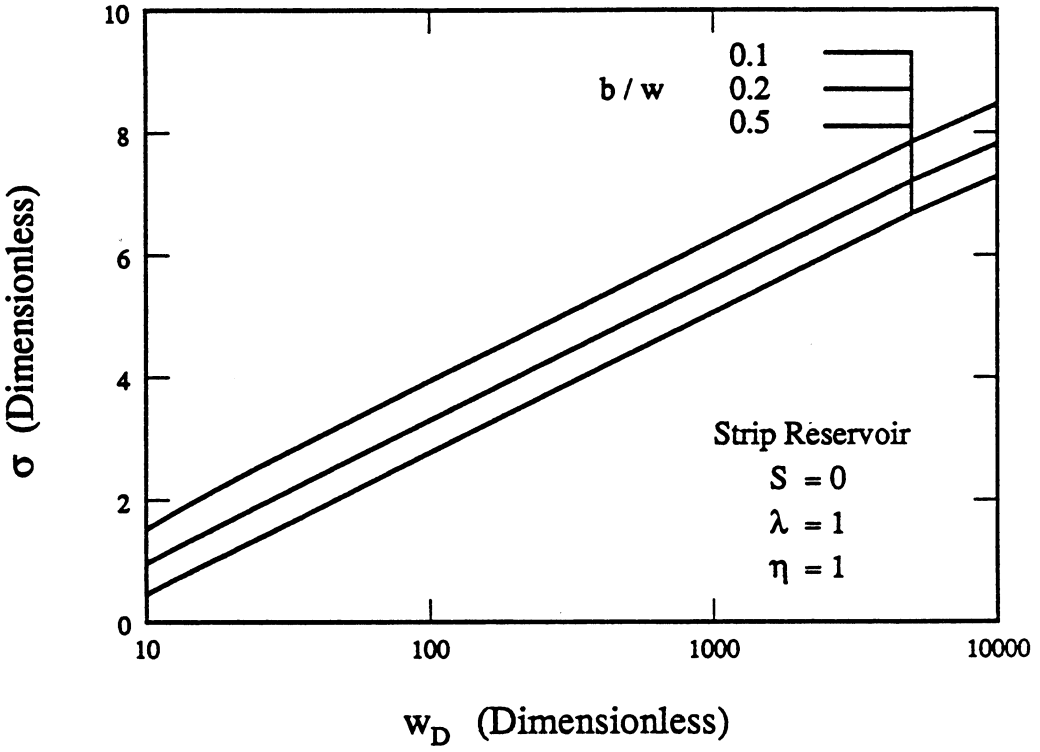

Fig. 5.3-10 Late time pseudoskin for several well locations in a homogeneous strip reservoir.

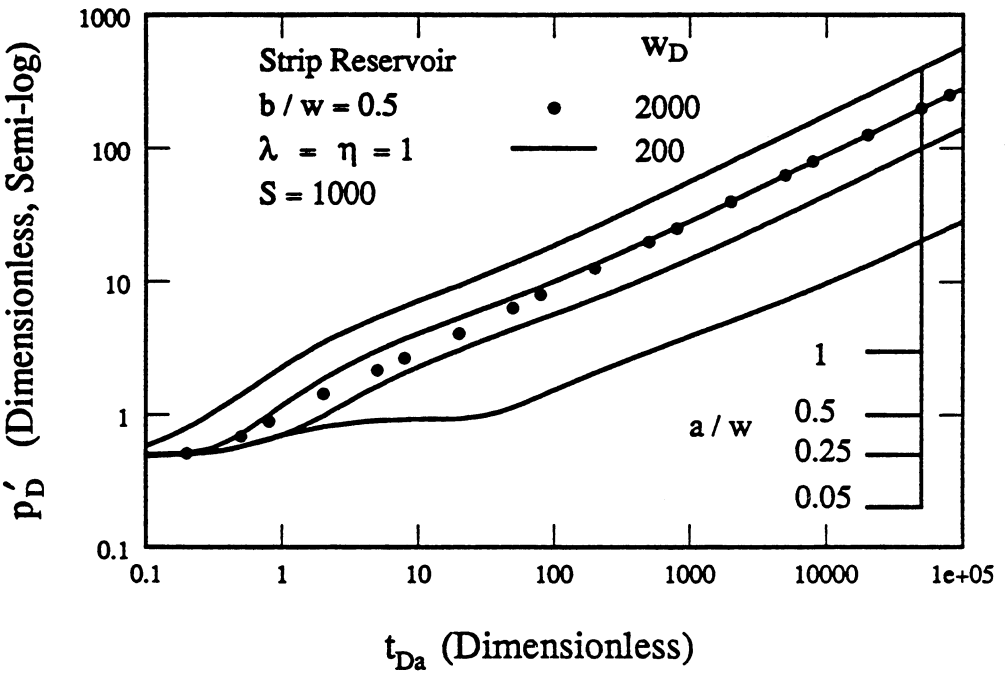

Fig. 5.3-11 Effect of a/w on drawdown pressure derivatives for a well in a homogeneous strip reservoir.

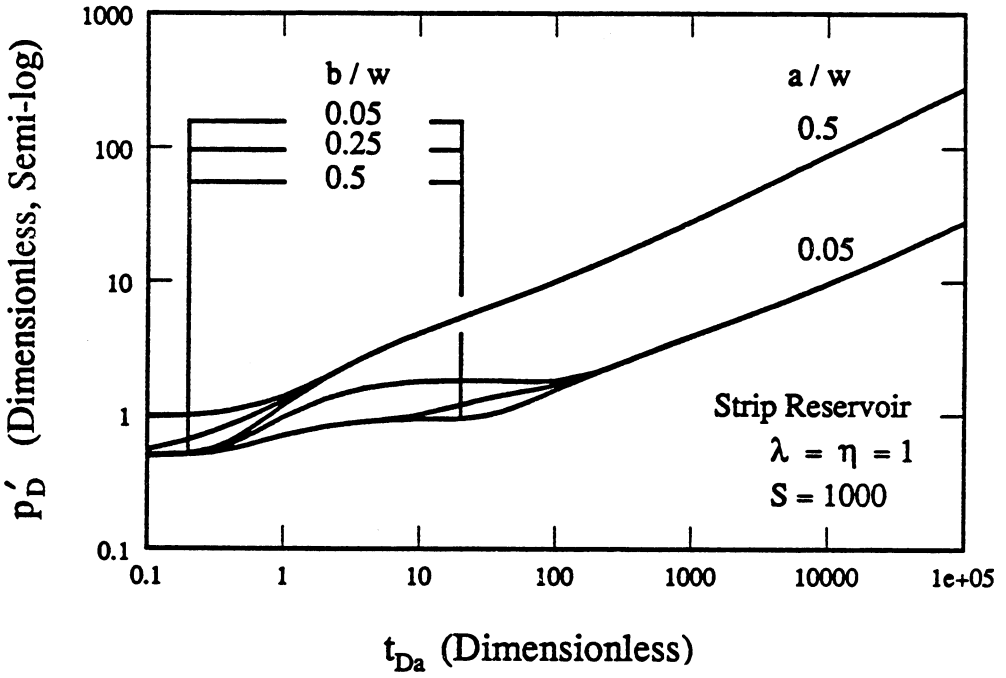

Fig. 5.3-12 Effect of b/w on drawdown pressure derivatives for a well in a homogeneous strip reservoir.

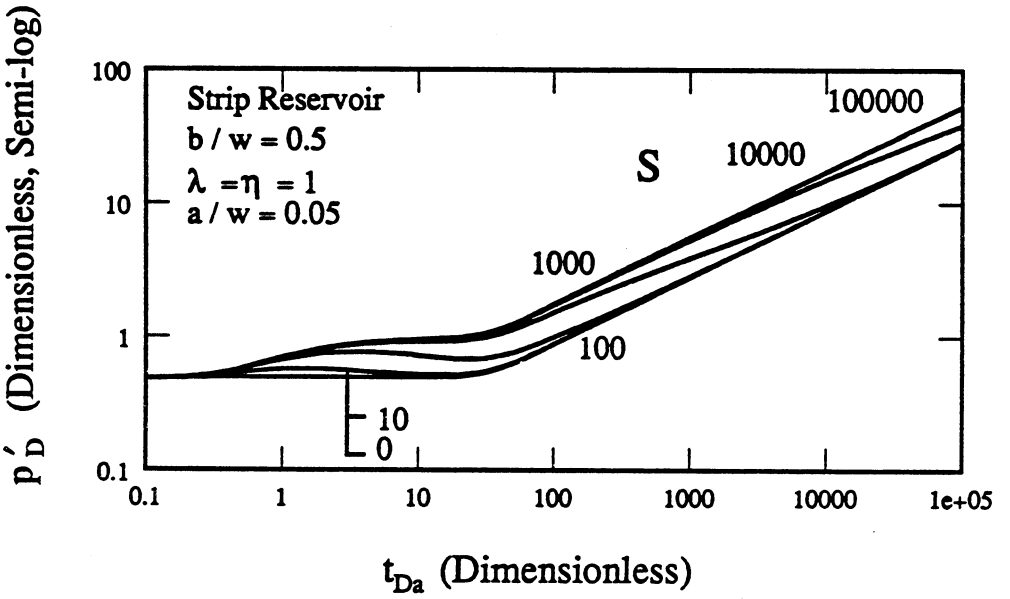

Fig. 5.3-13 Effect of S on drawdown pressure derivatives for a well in a homogeneous strip reservoir (well close to skin boundary).

reservoir configurations of both Figs. 5.3-1c and 5.3-1e are characterized by half slope lines on a log-log graph of the semilog derivative.

All the three boundaries (two parallel boundaries, and one skin boundary) are felt concurrently at $t_{Da} \approx 0.4$ for the case of $a/w = 0.5$ as shown in Fig. 5.3-11. However, for $a/w = 0.25$, the skin boundary is felt first at $t_{Da} \approx 0.4$, and the two parallel boundaries later at $t_{Da} \approx 1.6$ (which is $t_{Db} \approx 0.4$). The time, $t_{Da} \approx 1.6$, is the time at which the response for $a/w = 0.25$ departs from the response for $a/w = 0.05$. For the case of $a/w = 1$, the effects of the two parallel boundaries are felt first at $t_{Db} \approx 0.4$ or $t_{Da} \approx 0.1$. Then, the effects of the skin boundary cause an inflection point in the case of $a/w = 1$. The inflections in the responses for $a/w = 0.5$ and 0.25 are also due to the effects of skin. In the case of $a/w = 0.05$, the skin boundary is felt at $t_{Da} \approx 0.4$, and the semilog derivative doubles to 1. Then, at $t_{Da} \approx 40$ or $t_{Db} \approx 0.4$, the effects of the two parallel sealing boundaries are felt. All the curves approach a linear flow behavior at late time. The doubling of the slope is observed only for $a/w = 0.05$, suggesting that a well should be relatively close to one sealing boundary compared to the other boundaries of the reservoir for the semilog derivative to stabilize at 1. This observation is consistent with the work presented by Tiab and Crichlow (1979).

Fig. 5.3-12 shows the effects of different well locations in the y direction on the pressure derivative response for two different a/w values of 0.05 and 0.5. Again, the departures of the pressure transient responses, whenever one or more boundaries are felt, occur at $t_{DL} \approx 0.4$, where L is the distance between the well and the boundary first felt. For example, for the case of a/w and b/w both equal to 0.5, all the three boundaries are felt concurrently at $t_{Da} \approx 0.4$. For the case of a/w and b/w both equal to 0.05, the two perpendicular intersecting boundaries are felt at $t_{Da} \approx 0.4$, and thus, the semilog derivative quadruples to 2. At $t_{DL} \approx 0.4$ (where t_{DL} is based on the distance $w - b$) or $t_{Da} \approx 145$, the effects of the upper parallel boundary of the strip reservoir (Fig. 5.3-2b) are felt, and the derivative behavior changes from a constant slope of two to the late time linear flow behavior. The doubling of the semilog derivative to 1 for the cases of $b/w = 0.05$ and $a/w = 0.5$, and for $a/w = 0.05$ and $b/w = 0.5$ is observed. This again suggests that the doubling or quadrupling of slope is observed, if the well is relatively close to one sealing boundary or two equidistant perpendicular intersecting sealing boundaries compared to other reservoir boundaries.

Fig. 5.3-13 shows the effects of the magnitude of boundary skin on the semilog pressure derivatives for a homogeneous strip reservoir with $a/w = 0.05$ and $b/w = 0.5$. The skin boundary is felt first at $t_{Da} \approx 0.4$, and causes the doubling of the semilog derivative to 1 for large skin values ($S \geq 1000$). For low values of skin ($S \leq 10$), the semilog derivative reverts back to 0.5 producing a local maximum of the derivative. Again, the effects of the two parallel boundaries of the strip reservoir are felt at $t_{Db} \approx 0.4$ or $t_{Da} \approx 40$. Fig. 5.3-13 shows that the effects of the parallel boundaries are felt at $t_{Da} \approx 40$ for small skin values as the departure from a semilog slope of 0.5, and for large skin values as the departure from the semilog derivative of one. However, for moderate skin values (in this case, $10 < S < 1000$), the characteristic departure of the derivative response from a slope of 0.5 or 1 is not evident. The semilog derivative behavior merges to the behavior described by Eq. (5.3-9) for linear flow in a strip reservoir at late time, depending on the value of skin. The larger the skin, the longer is the transition time before the onset of the response described by Eq. (5.3-9). The duration of the transition for a large skin shows the behavior described by Eq. (5.3-11) for linear flow in a semi-infinite strip reservoir, before finally exhibiting the linear flow behavior of an infinite strip reservoir.

Fig. 5.3-14 shows the effects of the magnitude of boundary skin on the semilog pressure derivative for a homogeneous strip reservoir with $a/w = 1$ and $b/w = 0.5$. In this case, the effects of the two parallel boundaries are felt at $t_{Db} \approx 0.4$ or $t_{Da} \approx 0.1$, and the semilog derivative behavior tries to exhibit linear flow behavior in an infinite strip reservoir as per Eq. (5.3-9). But depending on the value of skin, the derivative behavior departs from that of $S = 0$ at $t_{Da} \approx 0.4$. However, as the distance between the well and the skin boundary is twice the distance between the well and the parallel boundaries, the departure at $t_{Da} \approx 0.4$ cannot be detected unless the skin is large ($S \geq 100$). In Fig. 5.3-13, the effects of the skin boundary

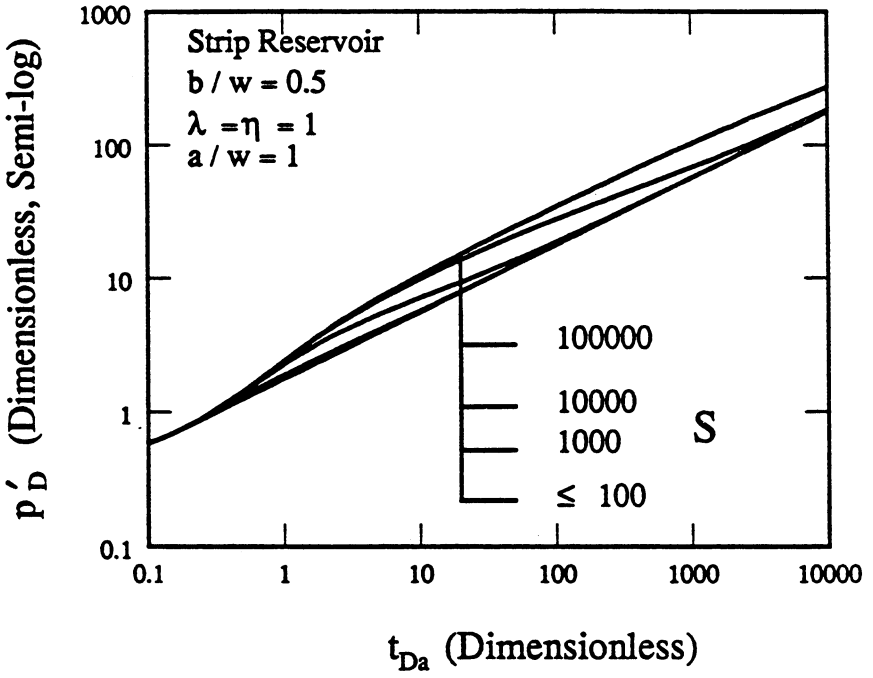

Fig. 5.3-14 Effect of S on drawdown pressure derivatives for a well in a homogeneous strip reservoir (well close to parallel strip boundaries).

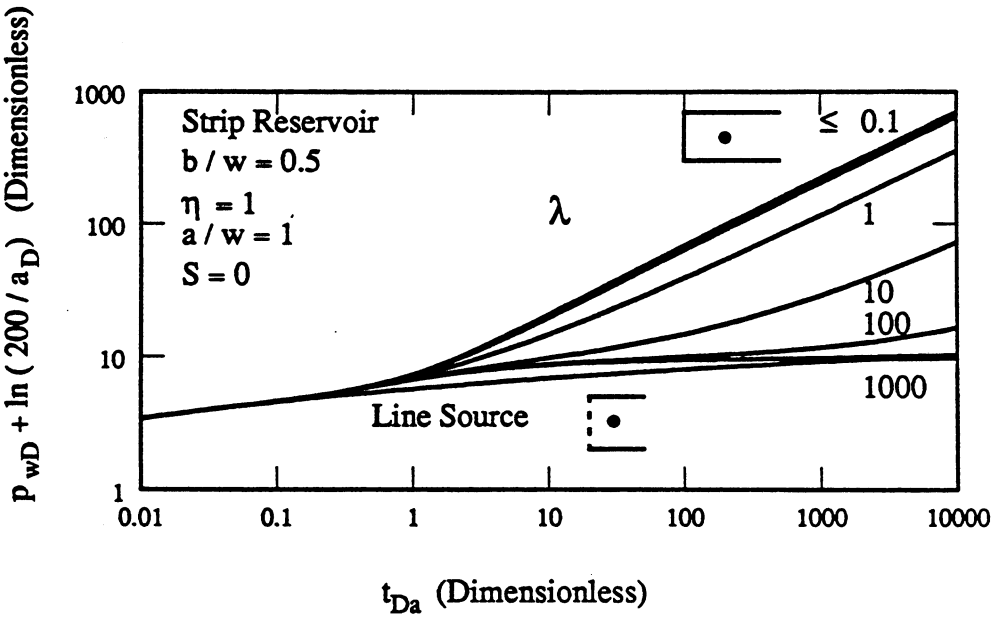

Fig. 5.3-15 Effect of mobility ratio on pressure drawdown responses for a well in a composite strip reservoir.

could be felt for $S \geq 10$, as the distance between the well and the skin boundary was 1/10th the distance between the well and the parallel boundaries. Thus, the farther the well is from the skin boundary, the larger the skin must be to have a significant effect on the pressure derivative. Again, the larger the skin, the longer is the duration of the transition, before the derivative behavior is described by Eq. (5.3-9). Also, for large skin values, the duration of the transition exhibits the behavior described by Eq. (5.3-11) for some time.

The pressure drawdown response of an arbitrarily located well in a composite strip reservoir with a partially communicating fault is described by five parameters: a/w, b/w, S, λ, and η. The responses for a well in the center (b/w = 0.5) of a strip reservoir with a/w = 1 and S = 0 are presented in Figs. 5.3-15 through 5.3-18. Figs. 5.3-15 and 5.3-17 show the effects of mobility and diffusivity ratios, respectively, on the wellbore pressure behavior. Figs. 5.3-16 and 5.3-18 show the effects of mobility and diffusivity ratios, respectively, on the semilog pressure derivative behavior. Figs. 5.3-15 and 5.3-16 are for $\eta = 1$, and Figs. 5.3-17 and 5.3-18 are for $\lambda = 1$. The effects of a constant-pressure or closed boundary perpendicular to the two parallel boundaries of a strip reservoir (Fig. 5.3-19) on the wellbore pressure behavior are also shown in Figs. 5.3-15 through 5.3-18.

The pressure and the pressure derivative responses for the cases in Fig. 5.3-19 were generated using the method of images. The wellbore pressure response is the sum of the pressure contributions of the two lines of image wells and the real well. The case of Fig. 5.3-19b has been analyzed by Tiab and Crichlow (1979). In the case of a constant-pressure boundary intersecting parallel strip boundaries (Fig. 5.3-19a), one line of image wells consists of injectors, and the other line consists of producers. The pressure drawdown response of a line-source well is also shown on Figs. 5.3-15 and 5.3-17. For the cases of Figs. 5.3-19a and 5.3-19b, the effects of parallel strip boundaries are felt simultaneously at $t_{Db} \approx 0.4$ or $t_{Da} \approx 0.1$, as the departure of the pressure transient response from the line-source solution. However, at $t_{Da} \approx 0.4$, the effects of a closed (Fig. 5.3-19b) or a constant-pressure (Fig. 5.3-19a) boundary perpendicular to parallel strip boundaries are felt. For the case of Fig. 5.3-19b, the pressure transient response shows linear flow behavior in a semi-infinite system (Fig. 5.3-1e) as per Eq. (5.3-10).

For the case of Fig. 5.3-19a, the pressure response tends to stabilize and the pressure derivative falls due to the supply of fluid across the constant-pressure boundary. The local maximum of the pressure derivative (Figs. 5.3-16 and 5.3-18) for the case of Fig. 5.3-19a occurs since the effects of the strip boundaries are felt before the effects of the constant-pressure boundary. The effects of the parallel strip boundaries are felt at $t_{Db} \approx 0.4$ or $t_{Da} \approx 0.1$ as the departure of the pressure transient responses for different cases from the line-source solution. At $t_{Da} \approx 0.4$, the effects of the boundary, representing a discontinuity in rock and/or fluid properties on both sides of the boundary, are felt. For small mobility ratios (Figs. 5.3-15 and 5.3-16) or large diffusivity ratios (Figs. 5.3-17 and 5.3-18), the pressure transient behavior resembles that for the case of Fig. 5.3-19b. For large mobility ratios or small diffusivity ratios, the pressure transient behavior resembles that for the case of Fig. 5.3-19a. For intermediate values of mobility and diffusivity ratios, the responses lie between the two limiting cases. However, at late time, the behavior approaches a linear flow condition illustrated by the half slope lines on the log-log graphs of the semilog derivatives in Figs. 5.3-16 and 5.3-18.

Fig. 5.3-20 shows the effects of the boundary skin on the dimensionless wellbore pressure derivative response for b/w = 0.5, a/w = 1, $\lambda = 10$ and $\eta = 1$. The effects of the parallel strip boundaries are felt at $t_{Db} \approx 0.4$ or $t_{Da} \approx 0.1$ as the departure of the semilog derivative from the value of 0.5. Then, the effects of the boundary representing the discontinuity in fluid and/or rock properties are felt at $t_{Da} \approx 0.4$. If there is a small skin at the boundary (in this case, $S \leq 10$), then fluid flows easily from region II across the boundary and the pressure derivative flattens. For large values of skin, the fluid from region II cannot flow easily across the boundary, despite a value of $\lambda = 10$, and therefore, the pressure derivative continues to rise. As the flow from region II occurs in larger amounts, the pressure derivative shows a tendency to stabilize. At late time, the semilog pressure derivative shows the linear flow behavior

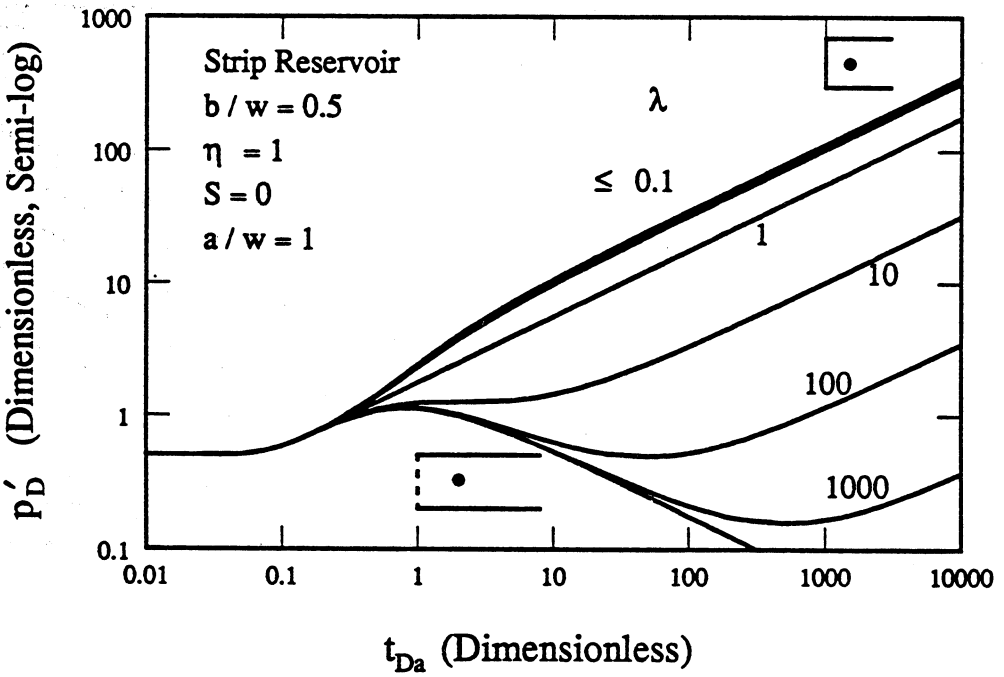

Fig. 5.3-16 Effect of mobility ratio on drawdown pressure derivatives for a well in a composite strip reservoir.

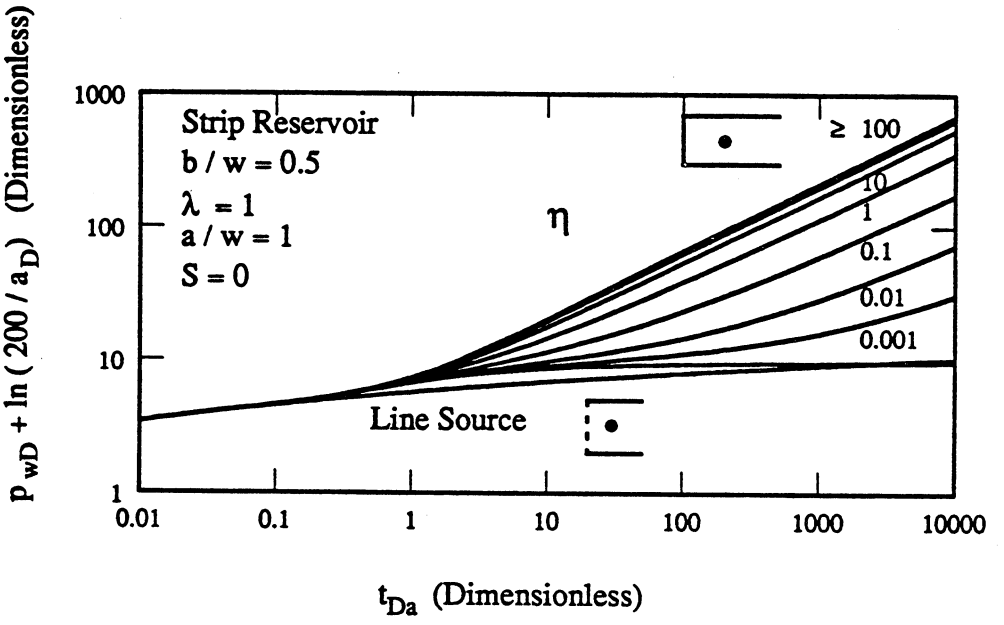

Fig. 5.3-17 Effect of diffusivity ratio on pressure drawdown responses for a well in a composite strip reservoir.

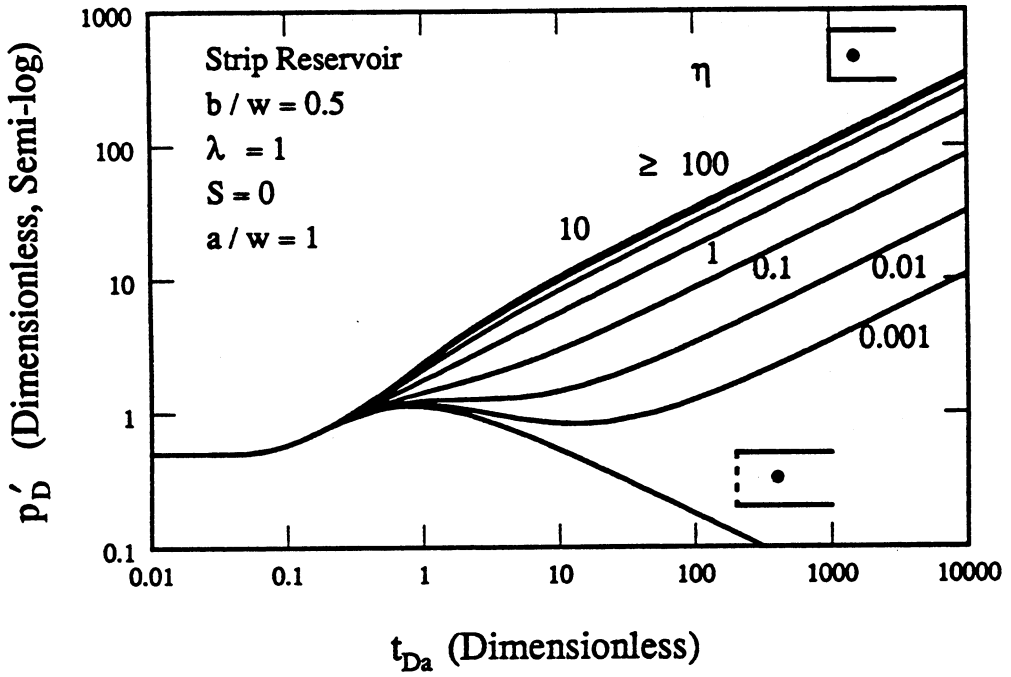

Fig. 5.3-18 Effect of diffusivity ratio on drawdown pressure derivatives for a well in a composite strip reservoir.

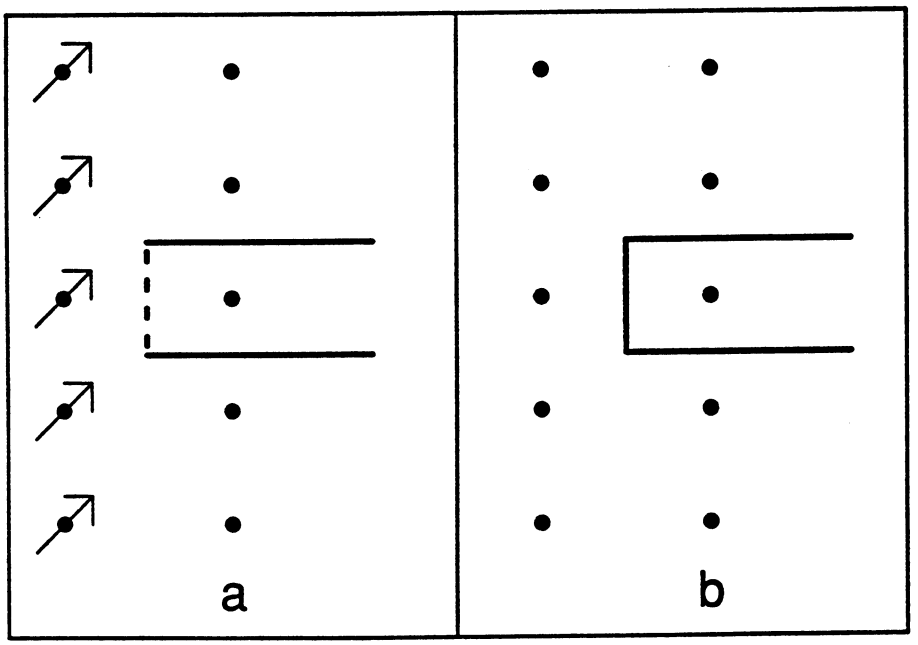

Fig. 5.3-19 Method of images for a well in a homogeneous strip reservoir with a perpendicular intersecting boundary A: constant-pressure intersecting boundary, and B: closed intersecting boundary.

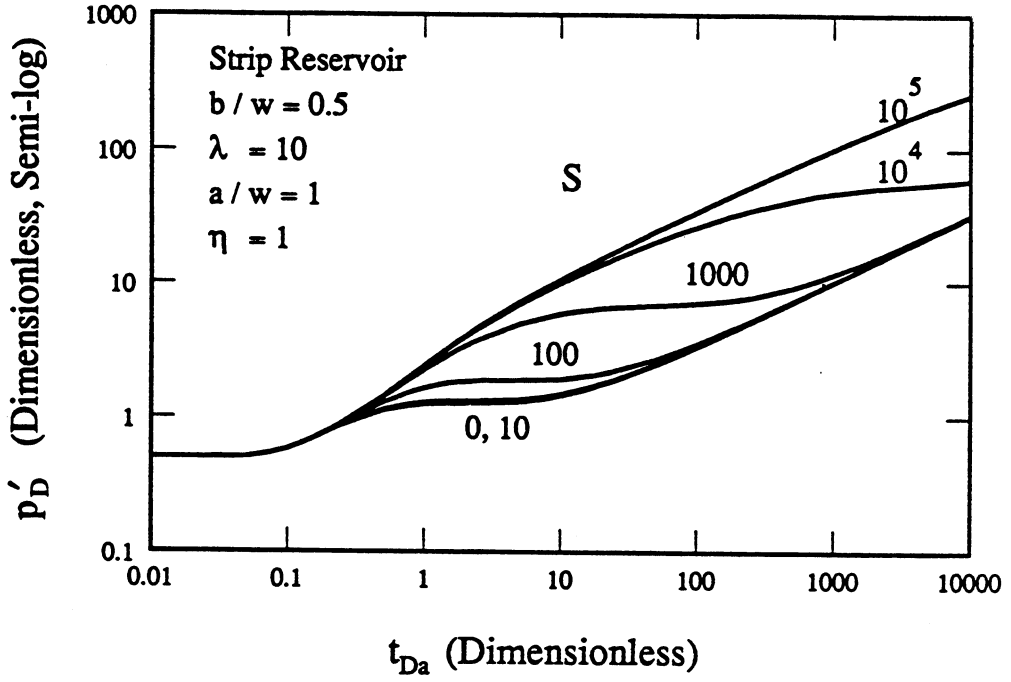

Fig. 5.3-20 Effect of skin on drawdown pressure derivatives for a well in a composite strip reservoir.

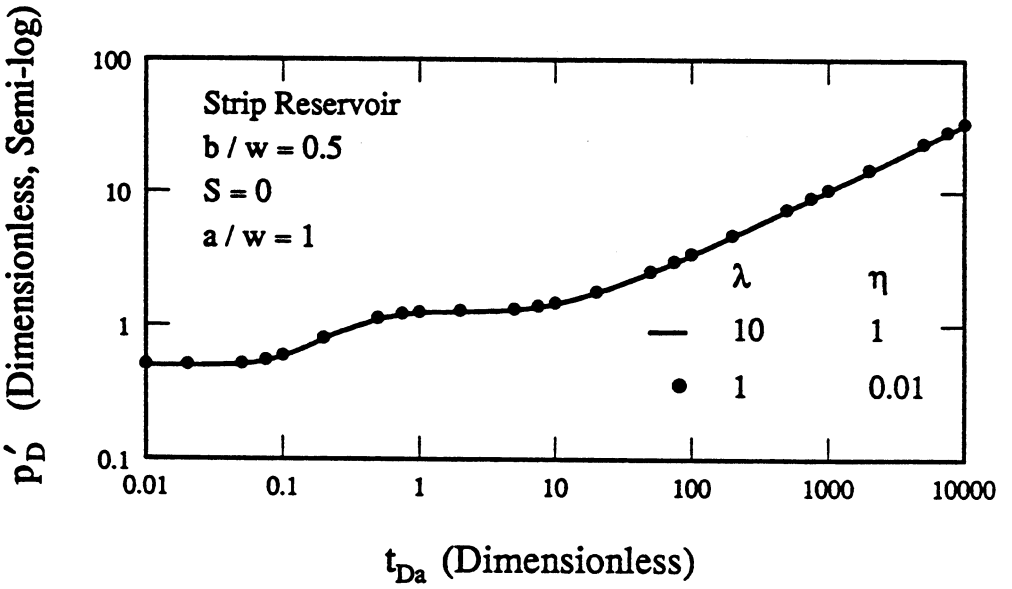

Fig. 5.3-21 Establishing $\lambda/\sqrt{\eta}$ as a correlating parameter for transient pressure responses for a well in a composite strip reservoir.

in a composite strip reservoir, irrespective of the magnitude of the skin. This is characterized by a half slope line on a log-log graph of the semilog pressure derivative in Fig. 5.3-20. Though the pressure derivative responses for $S = 10^4$ and 10^5 have not merged with the response for $S = 0$ on Fig. 5.3-20, these responses also show the late time linear flow at times beyond $t_{Da} = 10000$.

Fig. 5.3-21 illustrates the use of a correlating parameter $\lambda / \sqrt{\eta}$ for drawdown pressure derivative behavior for a well in a strip reservoir. The solid line shows the pressure derivative behavior for $\lambda = 10$ and $\eta = 1$. The circles are for $\lambda = 1$ and $\eta = 0.01$. For both cases, $\lambda / \sqrt{\eta} = 10$. Both responses are generated for $b/w = 0.5$, $a/w = 1$ and $S = 0$. Identical responses for the two cases establish $\lambda / \sqrt{\eta}$ as a correlating parameter. Ambastha and Sageev (1987) have established $\lambda / \sqrt{\eta}$ as a correlating parameter for the pressure responses in a linear semi-infinite system while considering linear water influx through a partially communicating fault.

5.3.6 Interference Behavior of Strip Reservoirs

The effects of a partially communicating fault in an infinite homogeneous reservoir on interference testing have been considered by Stewart et al. (1984) and Yaxley (1985). Interference testing in an infinite or strip composite reservoir with a partially communicating fault has not been considered. The solutions presented in this paper make such studies possible. An example presents the difficulties involved in interpreting interference responses, however.

Fig. 5.3-22 shows a strip composite reservoir with several wells located in regions I and II. The dimensionless reservoir width, w_D, is 4000. The producing well is marked P on Fig. 5.3-22, and A through G represent various observation wells. The observation wells A, B, and C are in region I containing the active production well, and D through G are in region II. The distances represented on Fig. 5.3-22 are the dimensionless distances with respect to the well radius. Such a reservoir situation may represent a well close to a sealing boundary and a fluid-fluid contact.

Fig. 5.3-23 shows the interference pressure responses at the locations A through G. The pressure drawdown response at the active well P, and the line-source solution are also graphed on Fig. 5.3-23. We use $\lambda = 0.1$, $\eta = 0.1$ and $S = 0$ to generate pressure transient responses. Since $\lambda = \eta$, $F = 1$. Thus, the storativities of the two regions are the same, and the mobility of region I is 10 times larger than the mobility of region II. Fig. 5.3-23 presents p_D vs. t_{DL}, where t_{DL} is the dimensionless time with respect to the distances, L, between the active well and the observation wells. The interference pressure responses of the observation wells in region I follow the line-source solution to $t_{DL} \approx 0.3 - 0.4$, exhibiting a homogeneous reservoir behavior. The interference response then departs from the line-source solution representing the effects of the upper sealing boundary. The larger pressure drops for the observation wells in region I compared to those in region II represent the larger mobility of region I with respect to region II and hence, the larger contribution of region I to the production from the wellbore. The half slope lines at late time for the observation well responses characterize the late time linear flow in a strip reservoir.

The early and the late time spreading of the interference pressure responses for the observation wells in region II, and the late time spreading of the interference pressure responses for the observation wells in region I show that the resultant response depends on the properties of the two regions and the location of an observation well with respect to the active well. This complicates interference test analysis in a composite reservoir. For example, the interference response of the observation well D is matched to the line-source solution by shifting the time scale to the left by a factor of 9 and by shifting the pressure scale upward by a factor of 1.9. The shifted response is shown by the solid circles on Fig. 5.3-23. The upward shift causes an overestimation of the mobility of region II by a factor of 1.9. The horizontal shift to the left causes an underestimation of the diffusivity of region II by a factor of 9. The combined effect

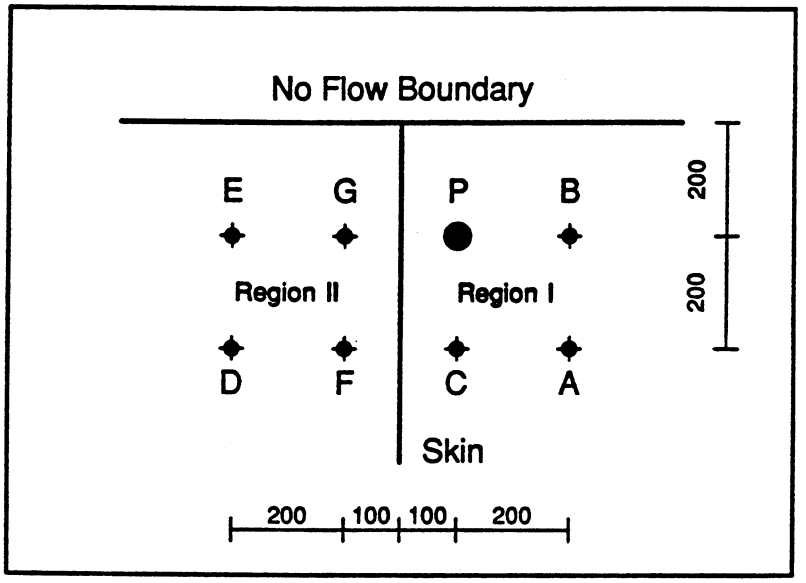

Fig. 5.3-22 Well locations for interference example.

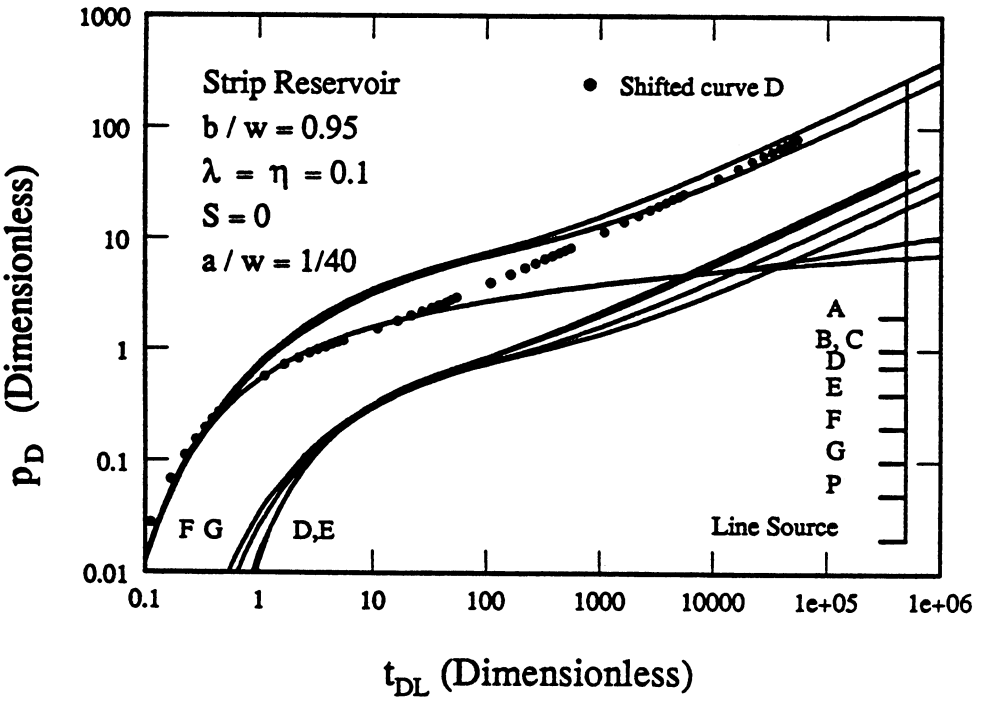

Fig. 5.3-23 Interference pressure responses.

is to produce a storativity, $(\phi c_t)_{II}$, which is $9 \times 1.9 = 17.1$ times the correct storativity of region II. Similar difficulties in the interpretation of interference tests near a steam cap are reported by Sageev (1985).

5.3.7 Conclusions

(1) A new analytical solution is presented for the pressure transient behavior of a line-source well producing at a constant rate in a strip or infinitely large reservoir with skin at the linear discontinuity and property contrasts on both sides of the discontinuity. The solution for the dimensionless pressure drop is in Laplace-Fourier space.

(2) The pressure drawdown behavior in an infinitely large homogeneous reservoir shows the behavior of a well near a sealing fault for large values of skin. However, for moderate values of skin, the pressure response departs from the line-source solution, follows the double slope behavior for some time, and then reverts back to a semilog linear pressure response parallel to the line-source solution at late time.

(3) The pressure drawdown behavior in an infinitely large composite reservoir shows the behavior of a well near a constant-pressure boundary for large mobility ratio or small diffusivity ratio (large storativity ratio). However, the effects of a small storativity in region II for a given mobility ratio appear as a constant-pressure difference on a semilog pressure graph compared to the pressure behavior for the same mobility ratio, but with $F = 1$.

(4) A correlation for pseudoskin vs. reservoir width is presented for various well locations in a homogeneous strip reservoir. This extends the study by Nutakki and Mattar (1982).

(5) The effects of the boundaries are felt at $t_{DL} \approx 0.4$, where L is the distance between the well and the boundary felt. If several boundaries are at the same distance from the well, their effects are still felt at $t_{DL} \approx 0.4$. However, the detection of the boundary effects is not possible in all cases.

(6) The doubling or quadrupling of semilog derivative is observed, if the well is relatively close to one sealing boundary or two equidistant perpendicular intersecting sealing boundaries, compared to the other reservoir boundaries in a homogeneous reservoir.

(7) The pressure drawdown behavior in a composite strip reservoir is bounded by the behavior for the cases in Figs. 5.3-19a and 19b. The late time linear flow characteristic of strip reservoirs is observed, irrespective of mobility ratio, diffusivity ratio or skin.

(8) Analysis of interference tests in a composite reservoir is not straightforward as the response depends on the property contrasts and the location of the observation well. A simple match of the observed interference response to the line-source solution may yield inaccurate results.

5.4 Summary

In this chapter, results that bear on the question of detection of reservoir heterogeneities are presented. Heterogeneities of permeability and porosity are important primarily because they determine flow performance. Tests that measure permeability directly, therefore, inevitably involve flow. Thus, we consider tracer and pressure transient tests because they depend directly on permeability. Permeability and porosity values measured are also averages over some flow domain, as are relative permeability functions. The results presented in this chapter are aimed at understanding how variations in those parameters affect flow performance at field scale and therefore, how significant heterogeneities can be detected.

Computations of the performance of well-to-well tracer tests showed that early breakthrough of injected fluid is likely if the permeability field has a significant variance and a

correlation length that is also large. On average, if either the variance or the correlation length is small, then the performance of the test can be described by a single dispersion coefficient. Thus, the probability that a particular realization of a permeability field can be described well by a dispersion coefficient correlates with a heterogeneity index, defined as the product of the variance $ln\ (k)$ and a dimensionless correlation length, the same parameter that proved so useful in the characterization of the interaction of viscous fingering with permeability heterogeneity. Comparison of calculated well test performance for the same permeability fields indicated that the heterogeneity index can be estimated using a dimensionless permeability difference determined from well tests in injection and production wells in a five-spot.

Detection of heterogeneities close to a producing well was also considered. Calculations of transient pressure response for flow in the neighborhood of an impermeable region indicated that impermeable regions of large size produced greater deviations from homogeneous behavior. Thus, large regions can be detected while small ones cannot, and the size of the region must be relatively large compared to the distance from the production well. While the presence of the low permeability zone can be detected, independent determination of parameters such as size, shape and distance from the well is difficult.

Detection of the presence of a fault separating zones with different flow properties was also considered. Again, effects of the heterogeneity can be detected, but the response depends on the property contrasts and the location of the observation well, and hence, determination of the composite reservoir parameters from the well test response is not straightforward.

6. Representation of the Effects of Reservoir Heterogeneity

Reservoir rock properties vary with many length scales. There are microscopic variations in pore sizes, layer variations in porosity and permeability with thicknesses that differ widely, and large-scale areal variations. If finite difference reservoir simulations are undertaken for any displacement process, the grid blocks used will inevitably be large enough that rock properties vary within the grid block. In this chapter, we consider how the effects of such variations can be represented. We begin in Section 6.1 with a simple scheme for generation of pseudorelativity permeability curves for layered systems. Then in Section 6.2 a more sophisticated tensor scaling algorithm is developed. Finally in Section 6.3 we examine the effects on scaling of capillary and viscous crossflow in heterogeneous systems and apply again the technique of Section 6.1 to determine relative permeability curves averaged according to the flow at a given scale.

6.1 Fractional Flow Representations of the Effects of Reservoir Heterogeneity

Kiran K. Pande

Experiments to determine the flow properties of a porous medium are inevitably interpreted in terms of some model representation of the flow. For example, if a miscible displacement is performed in a laboratory core, or in a field-scale experiment, the resulting effluent composition data are fit to the convection-dispersion equation to determine a dispersion coefficient. That model, with the dispersion coefficient so determined, can always be used to predict displacement performance for another miscible displacement in the same porous medium at the same scale, and it may or may not be useful for predictions of different scales or for different types of displacement. Another example is the use of the Buckley-Leverett equations to determine relative permeability data. In that case, it is assumed that the measured fractional flow can be interpreted as the result of variations of relative permeabilities with changes in phase saturations. There is, of course, no guarantee that the relative permeability description captures all the detail of the mechanisms that influence the transport of the phases. Thus, any model of a displacement is a compromise between detailed representation of physical mechanisms and tractability of the calculation scheme, and availability of data required to support the model.

In this section, we consider the advantages and limitations of fractional flow models for representation of the effects of heterogeneity. Given their simplicity, such models are attractive for some design calculations, but it is important to recognize the limitations of the approach, particularly those that involve application of displacement data measured at one scale to the prediction of displacement performance at other scales.

6.1.1 Fractional Flow Theory

A fractional flow representation of a displacement is based on the idea that the local flux of a component is a function only of its local concentration. If the local flux is the result of convection only, then a material balance yields

$$\frac{\partial}{\partial t}(\rho_D C_D) + \nabla \cdot (\rho_D f_D \vec{v}) = 0 \qquad (6.1\text{-}1)$$

where C_D is the local bulk concentration of fluid D, $\vec{v}$ is the total velocity, ρ_D is the density and f_D is the volume fraction of D in the flowing stream. If the fluid is incompressible (ρ_D is constant) and $\vec{v}$ is at most a function of time in one space dimension,

$$\frac{\partial C_D}{\partial t} + v \frac{\partial f_D}{\partial x} = 0 \tag{6.1-2}$$

If f_D is a function of C_D only, then

$$\frac{\partial f_D}{\partial x} = \frac{df_D}{dC_D} \frac{\partial C_D}{\partial x} \tag{6.1-3}$$

and hence Eq. (6.1-2) becomes

$$\frac{\partial C_D}{\partial t} + v \frac{df_D}{dC_D} \frac{\partial C_D}{\partial x} = 0 \tag{6.1-4}$$

Because C_D is a function of x and t

$$dC_D = \left[\frac{\partial C_D}{\partial t} \right] dt + \quad + \left[\frac{\partial C_D}{\partial x} \right] dx \tag{6.1-5}$$

If C_D is taken as constant, $dC_D = 0$, and hence

$$\left[\frac{dx}{dt} \right]_{C_D} = - \frac{\left[\frac{\partial C_D}{\partial t} \right]_x}{\left[\frac{\partial C_D}{\partial x} \right]_t} \tag{6.1-6}$$

and substitution of Eq. (6.1-4) into Eq. (6.1-6) gives

$$\left[\frac{dx}{dt} \right]_{C_D} = v \frac{df_D}{dC_D} \tag{6.1-7}$$

If the local concentration is taken to be the water saturation, for example, then Eq. (6.1-7) is the familiar Buckley-Leverett (1942) frontal advance equation

$$\left[\frac{dx}{dt} \right]_{S_w} = v \frac{df_w}{dS_w} \tag{6.1-8}$$

The derivation so far requires only that the flow be incompressible and purely convective in one-dimension, and that f_D be a function of C_D only. Any specification of the details of flow mechanisms is contained in the relationship between f_D and C_D. In the Buckley-Leverett case, the fractional flow is a function of water saturation through the relative permeabilities

$$f_w = \frac{1}{1 + \frac{k_{ro}}{k_{rw}} \frac{\mu_w}{\mu_D}} \tag{6.1-9}$$

Oil recovery calculations can be made using the graphical material balance relationship developed by Welge (1952). Determination of relative permeabilities from dynamic displacement experiments has been discussed by Johnson, Bossler and Naumann (1959) and Jones and Roszelle (1978). A simple graphical procedure was proposed by Jones and Roszelle to determine relative permeability curves from plots of oil recovery versus pore volumes water injected and reduced pressure drop versus pore volumes water injected. Both the Welge analysis for performance prediction and the Jones-Roszelle analysis for interpretation of process performance have been applied primarily to the problem of water displacing oil in a homogeneous porous medium. However, these graphical material balance procedures are general and can be applied to other problems described by Eq. (6.1-7). The simplest example of application of Eq. (6.1-7) to a more complicated system is the description of displacement in a reservoir composed of noncommunicating layers.

6.1.2 Displacement in Stratified Reservoir

Waterflooding in a stratified porous medium was described by Dykstra and Parsons (1950). This model is based on the assumption that the reservoir is composed of a number of layers that communicate only at the wellbores. Each layer is individually homogeneous, but may have properties different from that of other layers. Dykstra and Parsons considered piston-like displacement of oil by water where the initial saturations, porosity, and relative permeabilities were the same for each layer, and fluids were considered to be incompressible. Based on the relationship between bed flood-front positions at any given time, Dykstra and Parsons derived the following analytical expression for average coverage or oil recovery at breakthrough of successive layers

$$\overline{C}_D = \frac{1}{n} \left[j + \frac{(n-j)M}{M-1} - \frac{1}{M-1} \sum_{i=j+1}^{n} \left[M^2 + \frac{k_i}{k_j}(1-M^2) \right]^{1/2} \right] \tag{6.1-10}$$

where M is the mobility ratio $(k_{rw}/\mu_w) / (/k_{ro}/\mu_o)$, n is the number of layers and j is the number of layers that have broken through. This result is valid for all mobility ratios and any type of permeability distribution. Dykstra and Parsons used this result to produce design charts for log-normal permeability distributions between layers.

In this case, however, the porous medium is assumed to be one-dimensional, with the effects of the heterogeneity represented in the fractional flow function. Results similar to those of Dykstra and Parsons can be derived using a general frontal advance approach. The relationship between f_D and C_D is known. For this case, the outflow saturation or outflow coverage is defined as

$$C_D = \frac{j}{n} \tag{6.1-11}$$

where the fractional flow expression may be defined in terms of the producing water-oil ratio (WOR)

$$f_D = \frac{WOR}{WOR+1} \tag{6.1-12}$$

The producing water-oil ratio at breakthrough of successive layers is given by

$$WOR = \frac{\sum_{i=1}^{j} k_i}{\sum_{i=j+1}^{n} \frac{k_i}{\left[M^2+\frac{k_i}{k_j}(1-M^2)\right]^{1/2}}} \tag{6.1-13}$$

The individual layer permeabilities may be determined from some cumulative probability distribution. In this example, we use

$$P(k) = \frac{1}{2}\left[1+\text{erf}\left[\frac{\ln\frac{k}{k_m}}{k_\sigma\sqrt{2}}\right]\right] \tag{6.1-14}$$

which applies to a log-normal distribution with a permeability variation V given by

$$V = \frac{k_m - k_\sigma}{k_m} \tag{6.1-15}$$

where k_m is the mean permeability and k_σ the permeability at one standard deviation above the mean. The permeability, k, of layer j is given by Eq. (6.1-14) with $P(k) = j/(N + 1)$.

Welge's graphical material balance analysis can now be applied to determine the average coverage for a given outflow saturation. Since the Dykstra-Parsons model is actually a discrete model for layers of finite thickness, a large number of layers was used to approximate a continuous permeability distribution. The results shown here are based on 1000 layers with equal thickness. The permeability distributions used were symmetric and log normal. Fractional flow curves, determined from Eqs. (6.1-12) to (6.1-13) with permeability variation and mobility ratio as parameters are shown in Figs. 6.1-1 to 6.1-4. The Welge graphical analysis was performed on these fractional flow curves to obtain average coverage as a function of volume injected as shown in Figs. 6.1-5 to 6.1-8. In this case, since the initial water saturation is zero, the average water saturation is equal to the fraction of oil recovered. A time scale may be attached to the displacement process by relating time to pore volumes water injected and water injection rate. Also, the recovery curves are valid for constant pressure injection, constant rate injection or variable rate injection. Thus, given the relationship between local fractional flow and concentration derived from the model of the reservoir as noncommunicating layers, one-dimensional frontal advance formalism can be used in a straightforward way to calculate displacement performance.

The waterflood performance predictions of the Dykstra-Parsons model can be put in the form of oil recovery as a function of volume injected and dimensionless pressure drop as a function of volume injected. Performance curves were generated for different permeability variations and mobility ratios using the analytical results of Reznik et al. (1984). Their model extends the Dykstra-Parsons solution to a continuous time basis. The curves for oil recovery versus volume injected are shown in Figs. 6.1-9 to 6.1-12, since oil recovery in pore volumes

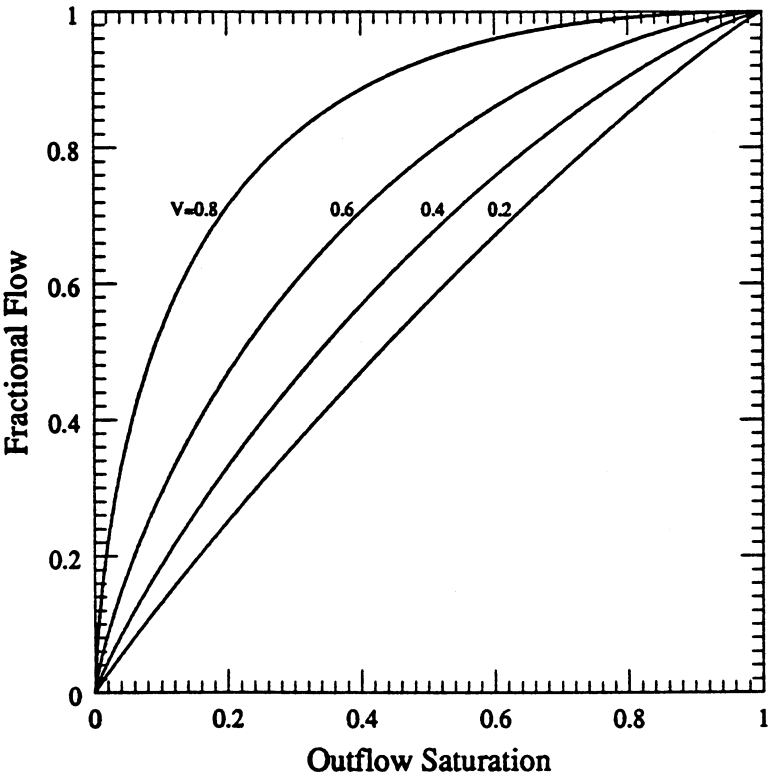

Fig. 6.1-1 Fractional flow curves for mobility ratio of 0.5.

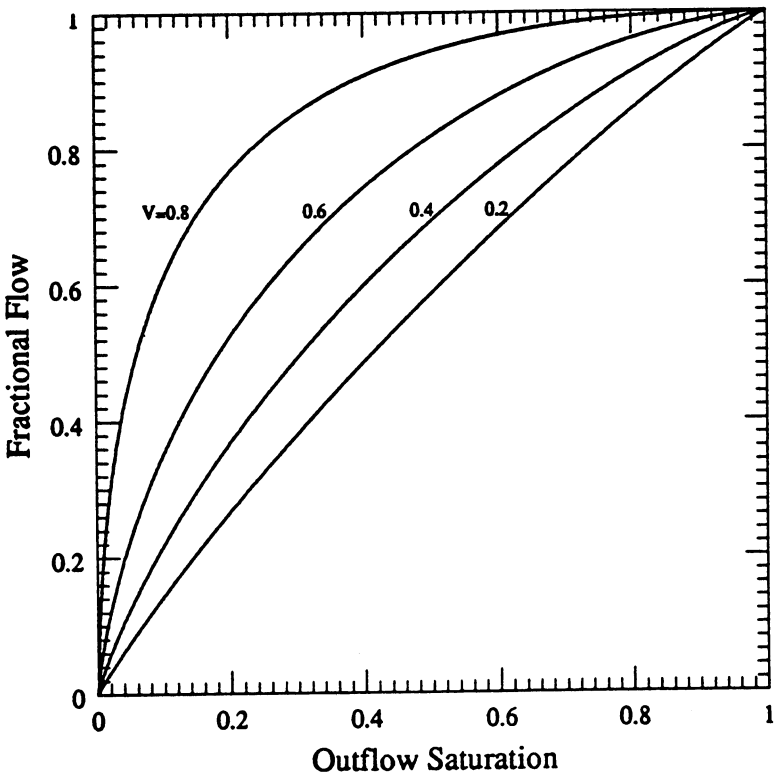

Fig. 6.1-2 Fractional flow curves for mobility ratio of 1.0.

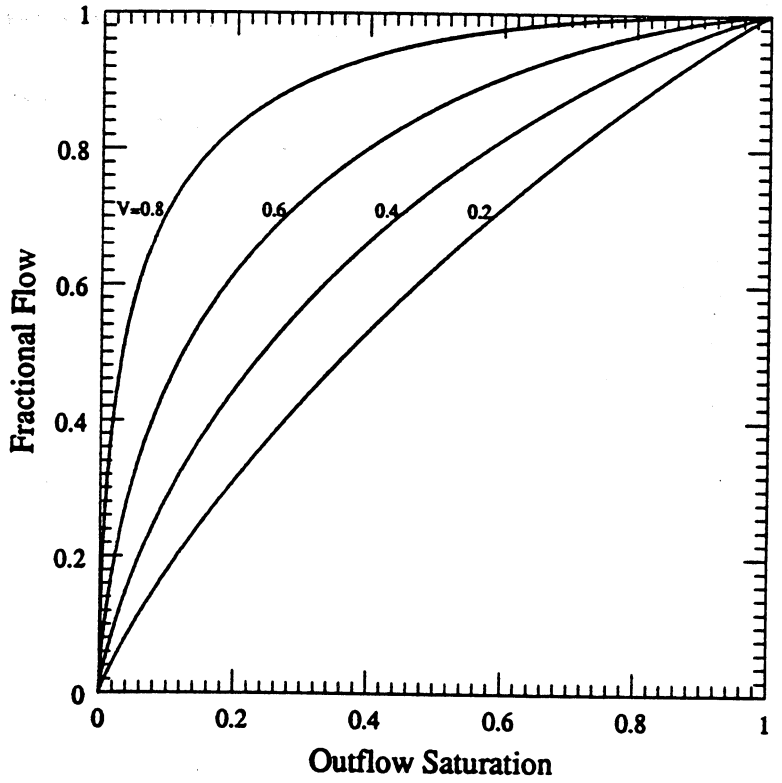

Fig. 6.1-3 Fractional flow curves for mobility ratio of 2.0.

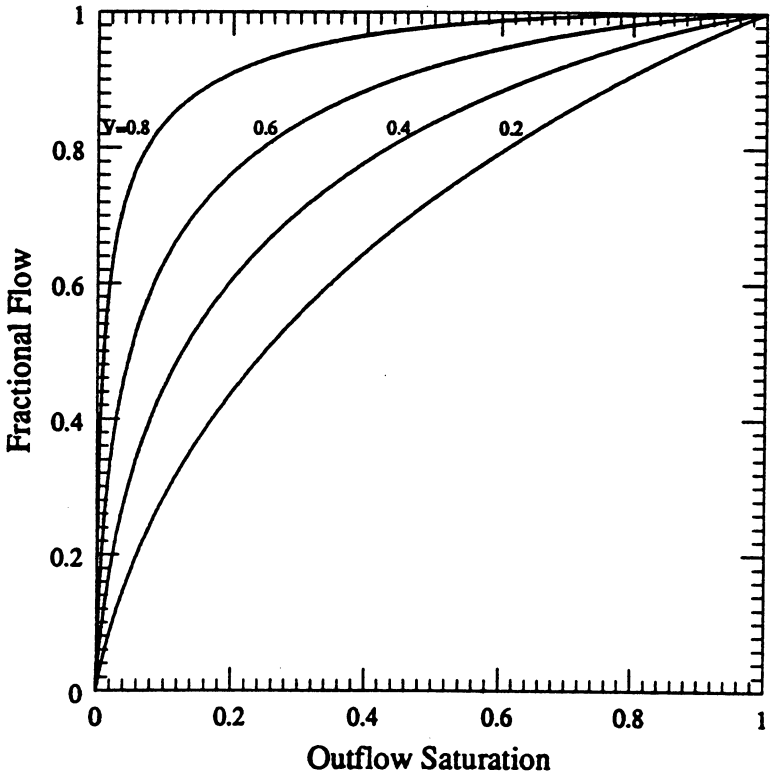

Fig. 6.1-4 Fractional flow curves for mobility ratio of 5.0.

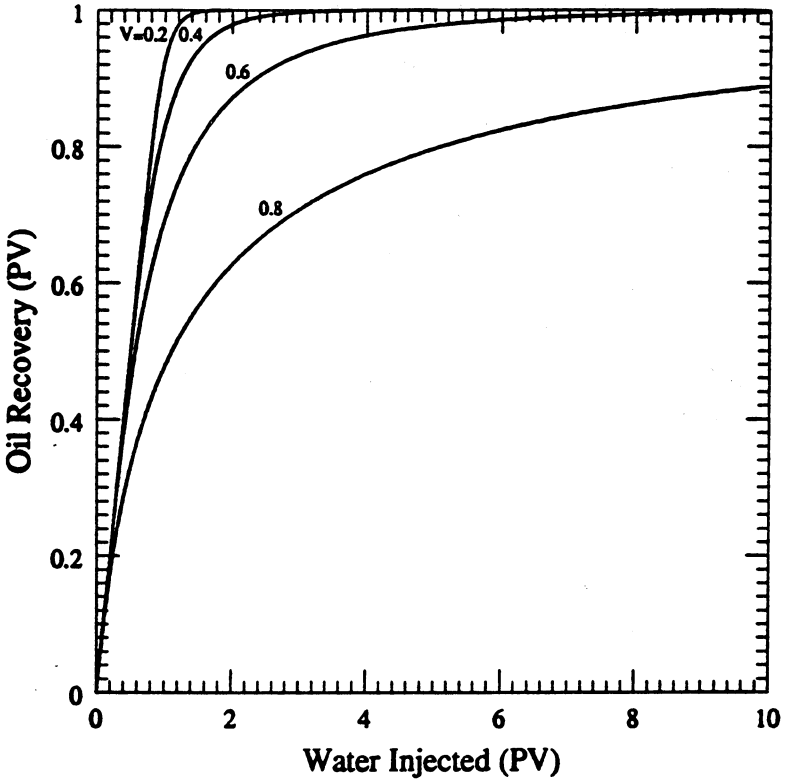

Fig. 6.1-5 Oil recovery curves for mobility ratio of 0.5 based on frontal advance method.

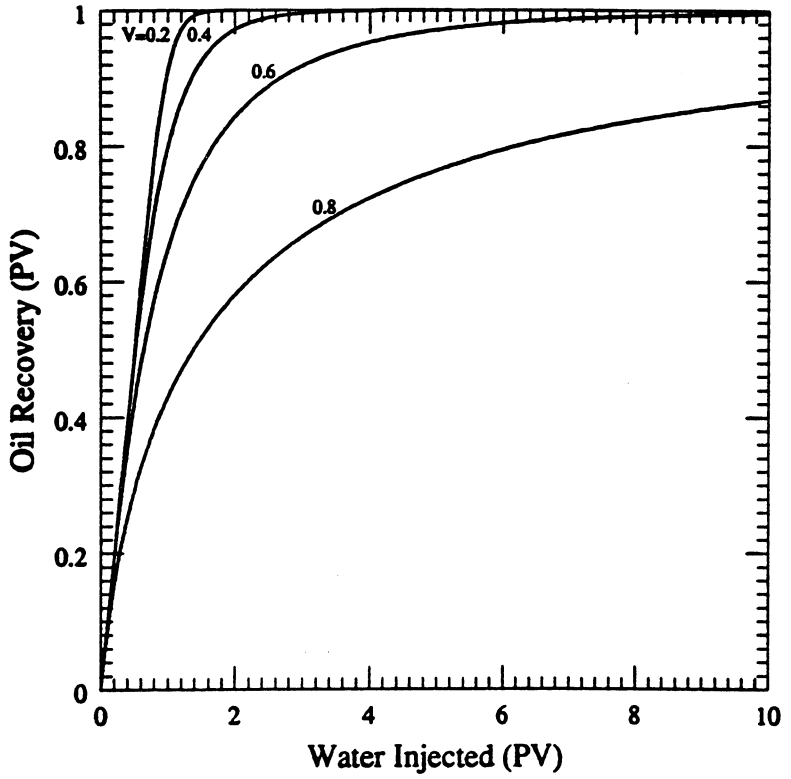

Fig. 6.1-6 Oil recovery curves for mobility ratio of 1.0 based on frontal advance method.

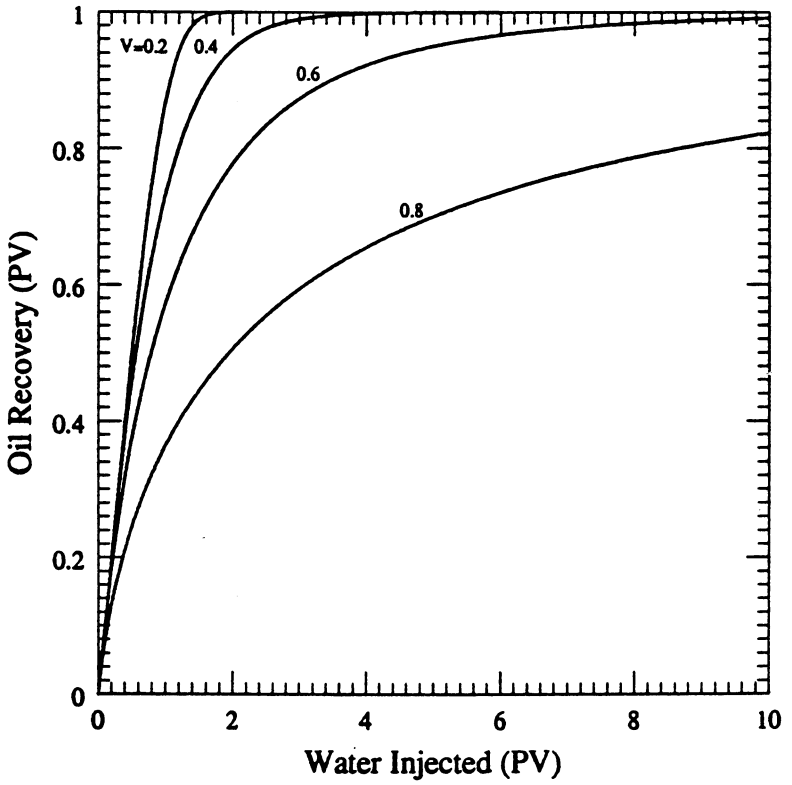

Fig. 6.1-7 Oil recovery curves for mobility ratio of 2.0 based on frontal advance method.

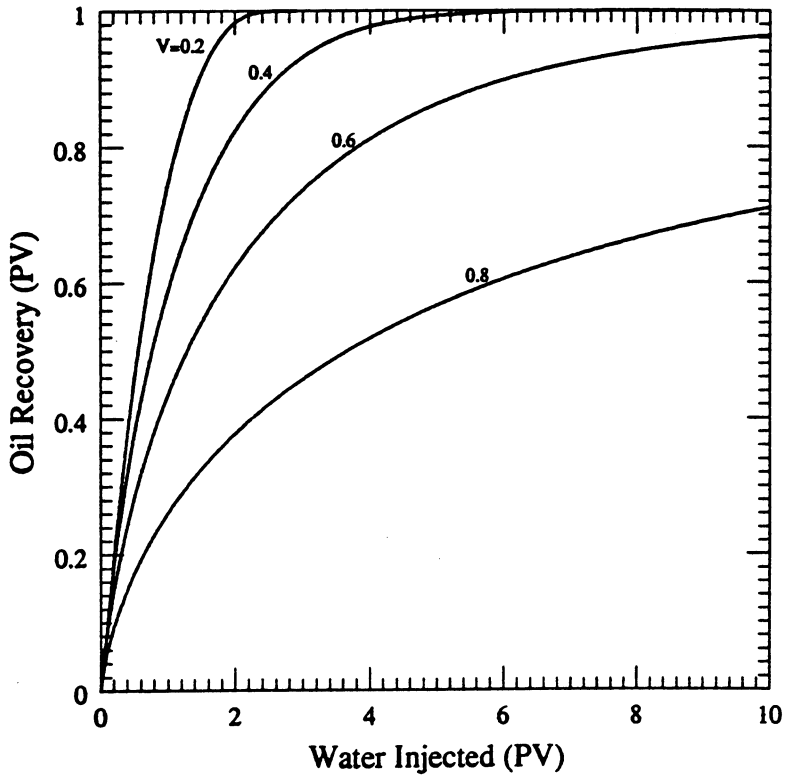

Fig. 6.1-8 Oil recovery curves for mobility ratio of 5.0 based on frontal advance method.

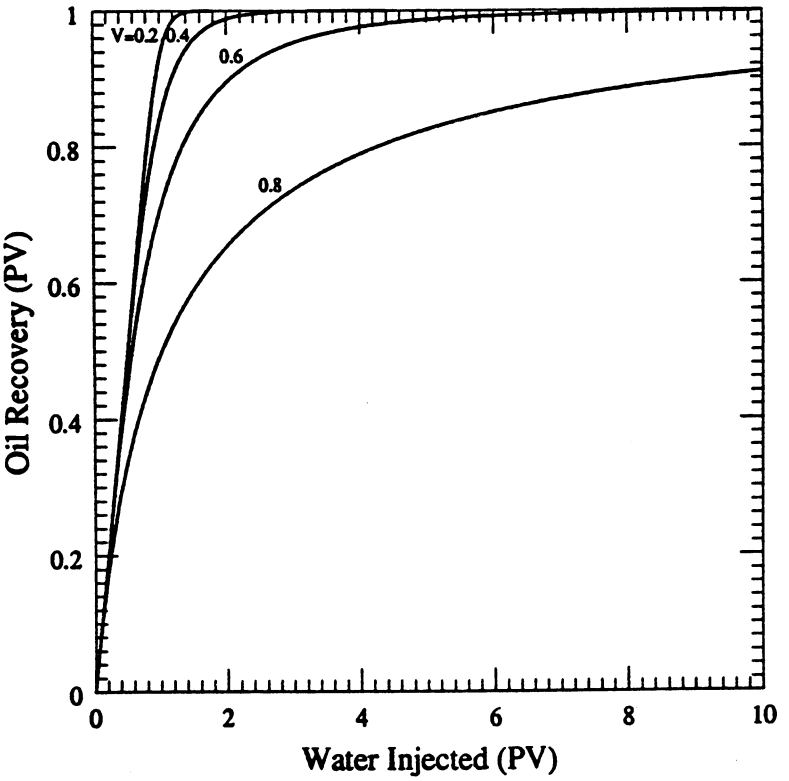

Fig. 6.1-9 Oil recovery curves for mobility ratio of 0.5 based on Dykstra-Parsons method.

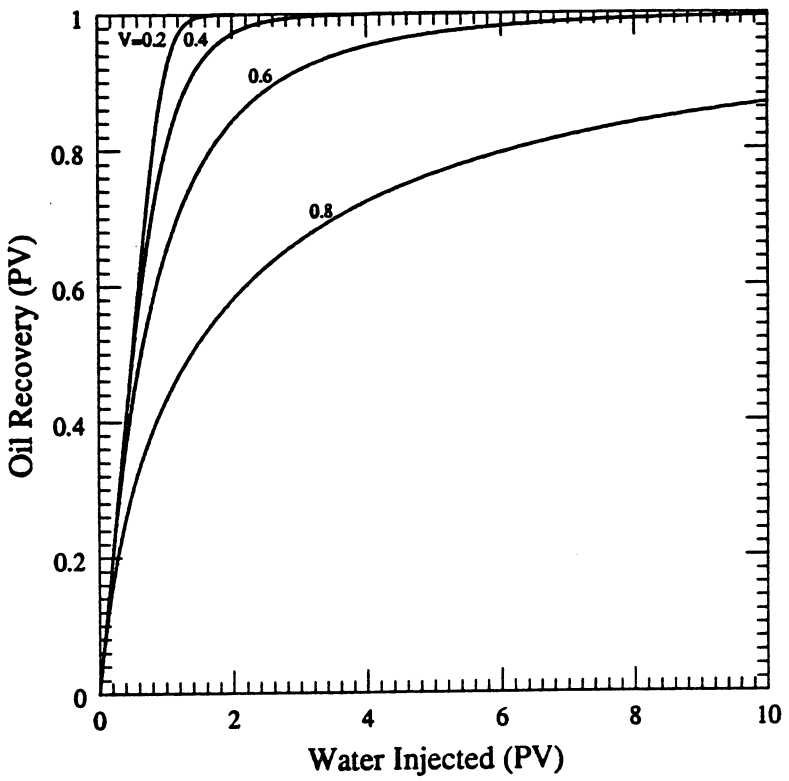

Fig. 6.1-10 Oil recovery curves for mobility ratio of 1.0 based on Dykstra-Parsons method.

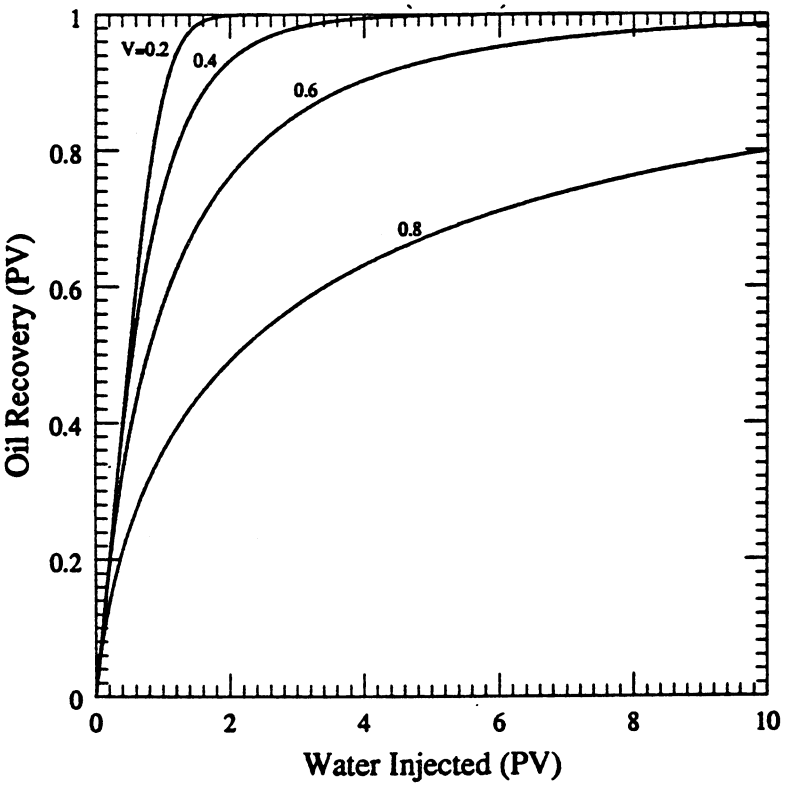

Fig. 6.1-11 Oil recovery curves for mobility ratio of 2.0 based on Dykstra-Parsons method.

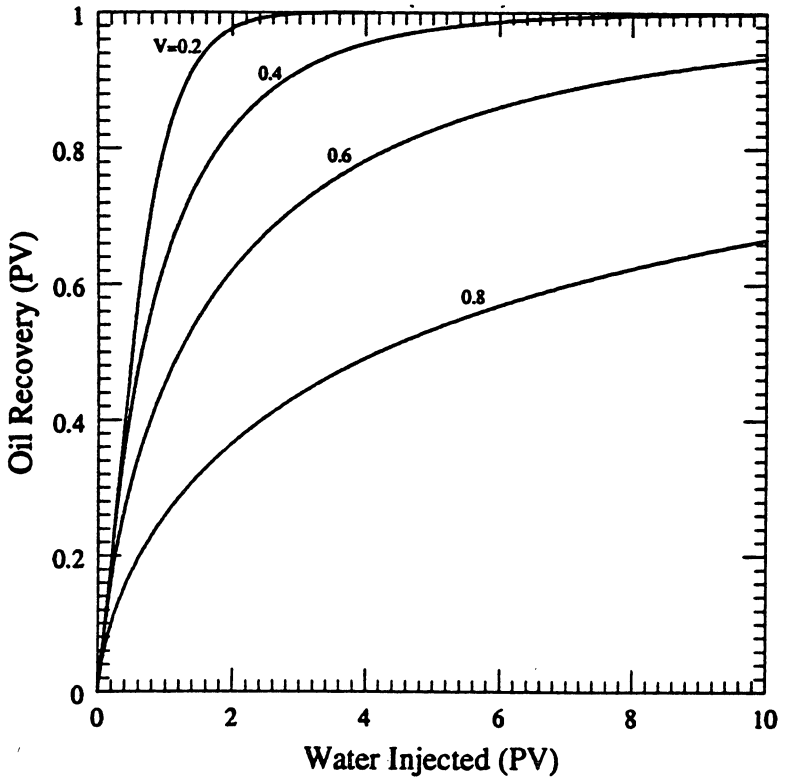

Fig. 6.1-12 Oil recovery curves for mobility ratio of 5.0 based on Dykstra-Parsons method.

is equal to average coverage. Similar plots have been generated by Enick et al. (1988). If the predictions of the frontal advance formulation were completely consistent with the behavior of the layered system, Figs. 6.1-5 to 6.1-8 would be identical to Figs. 6.1-9 to 6.1-12. However, comparison of the corresponding plots shows that performance prediction using the frontal advance approach is identical only for unit mobility ratio. The difference between forecast performance using the frontal advance approach and the performance calculated using the two dimensional Dykstra-Parsons analysis increases as the mobility ratio deviates from unity and as the permeability variation increases. The difference occurs because the assumption that local flux depends only on concentration is not strictly satisfied when $M \neq 1$. Instead, the local flux is a function of local velocity, which varies from layer to layer as injected fluid replaces original fluid with a different viscosity. Thus, the frontal advance approach, which assumes flow in only one dimension, cannot be expected to reproduce the full detail of the more complex two-dimensional flow. As comparison of Figs. 6.1-9 to 6.1-12 with Figs. 6.1-5 to 6.1-8 indicates, however, the qualitative performance of the frontal advance form is good, and for many applications, the simplified form may be acceptably accurate.

If pressure data are also available, then pseudorelative permeabilities can be determined from the fractional flow model of the displacement. Figs. 6.1-13 - 6.1-16 show dimensionless pressure drop, defined as $(\Delta P/q)/(\Delta P_i / q_i)$ where i refers to the initial values, for the various values of V and M. The use of pseudorelative permeability curves to model a stratified reservoir has been discussed by Hearn (1971). Hearn derived pseudorelative permeability curves assuming knowledge of layer properties. For example, layer permeabilities, porosity, saturations, and thicknesses must be known to derive appropriate pseudorelative permeability curves based on Hearn's method. Hearn also states that the vertical equilibrium assumption, as discussed by Coats et al. (1971) and Martin (1968), must be satisfied to use the pseudorelative permeability concept. Interpretation of displacement performance by the Jones-Roszelle method, on the other hand, can yield pseudorelative permeability curves without knowledge of the specific layer properties or any assumption about vertical equilibrium. Fig. 6.1-17 shows the pseudorelative permeability curves obtained by applying the Jones-Roszelle method to the production curves for a permeability variation of 0.6 and mobility ratios from 0.5 to 5. Use of those curves in a fractional flow model reproduces the oil recovery shown in Figs. 6.1-9 to 6.1-12 exactly. Such curves might be used, for example, to represent the effects of layering smaller than the scale of a grid block. It should be noted that the pseudorelative permeability curves obtained from this approach depend on mobility ratio and permeability variation for the displacement that generated the oil recovery data used. Thus, the pseudorelative permeabilities obtained are not properties of the porous medium alone.

The dependence of the pseudorelative permeabilities on the details of the displacement process, in this case M and V, is the price paid for the simplicity of the fractional flow model. The data used to determine parameters (or functions) used in the model must be obtained for displacement conditions very similar to those for which predictions are required. Thus, such models are useful for repeated calculations involving variables such as flow rate and pressure, but have little utility if the dependence of performance on other variables is to be explored. A related question concerns the use of fractional flow models when the displacement scale varies. If, for example, the scale of a layered system is increased, all of the analysis given above applies without change if the flow is still linear and the layer structure is identical. In addition, the flow process must be truly convective. To the extent that other transport mechanisms, such as crossflow, dispersion or viscous instability, for example, influence performance, measurements at one scale will have limited value at another scale if a fractional flow model is the basis for the scaling. Thus the principal limitation of such models is the need for displacement data at the scale and under the conditions of interest.

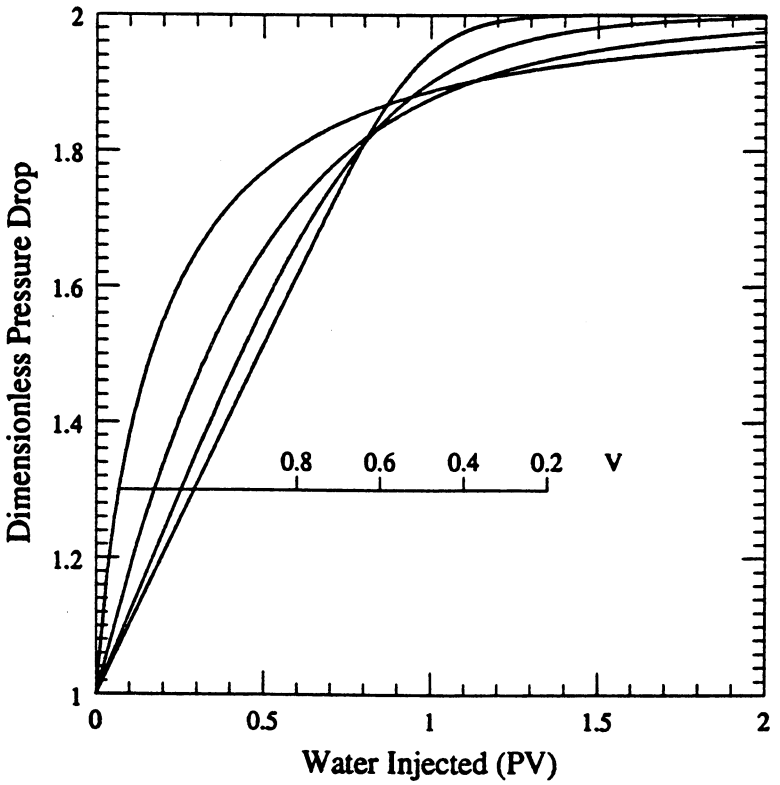

Fig. 6.1-13 Dimensionless pressure drop curves for mobility ratio of 0.5.

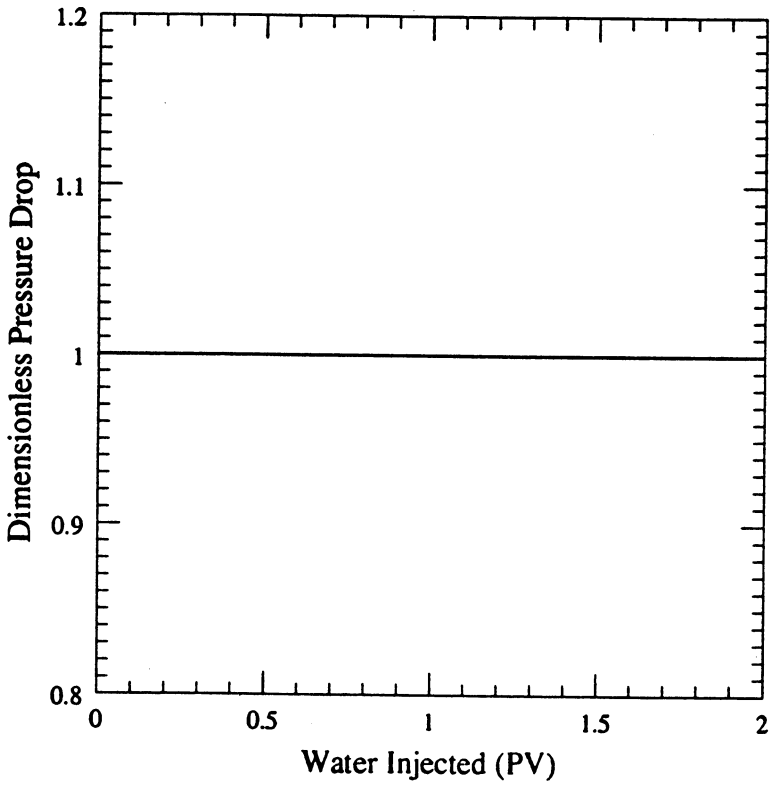

Fig. 6.1-14 Dimensionless pressure drop curves for mobility ratio of 1.0.

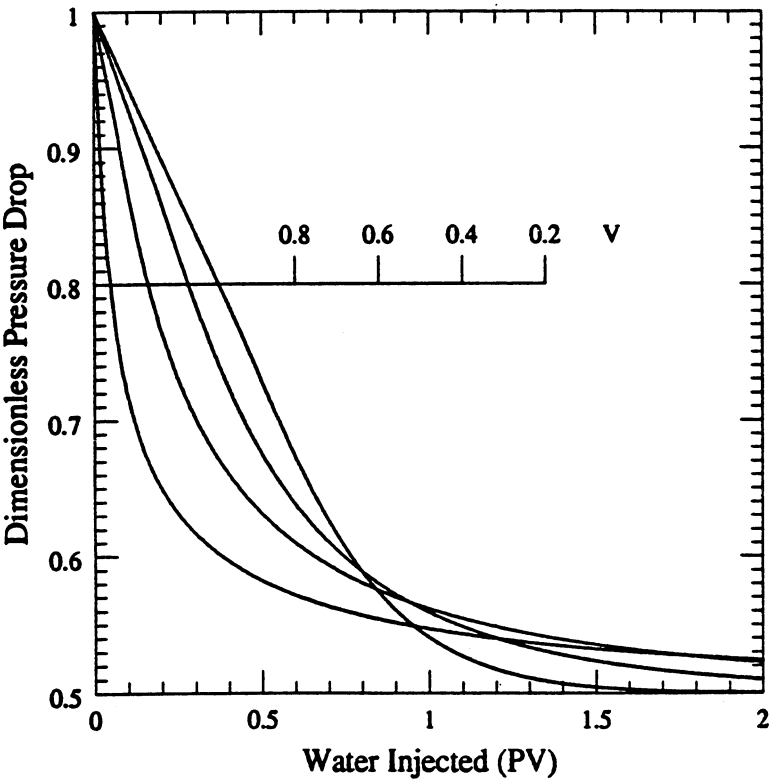

Fig. 6.1-15 Dimensionless pressure drop curves for mobility ratio of 2.0.

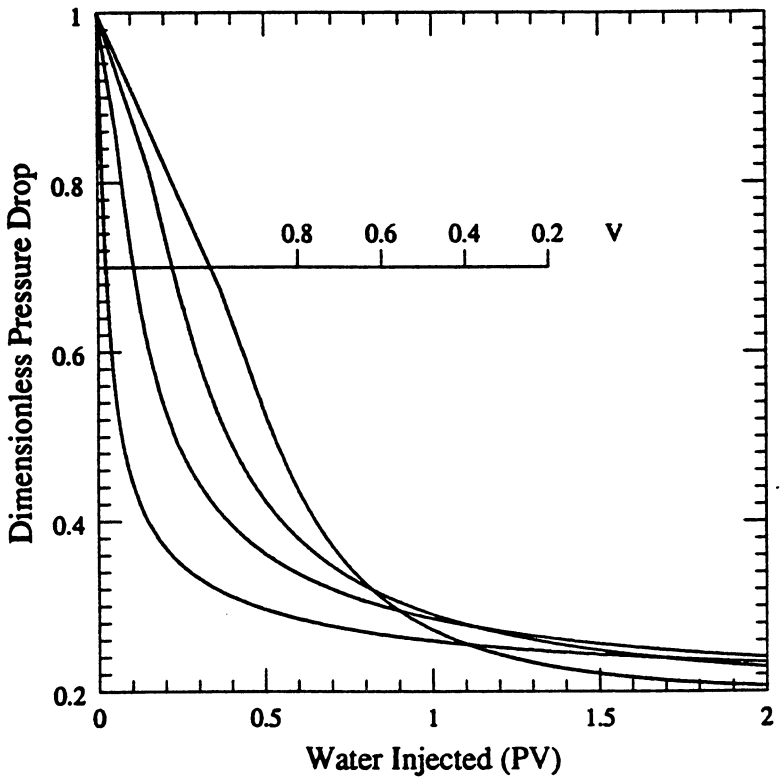

Fig. 6.1-16 Dimensionless pressure drop curves for mobility ratio of 5.0.

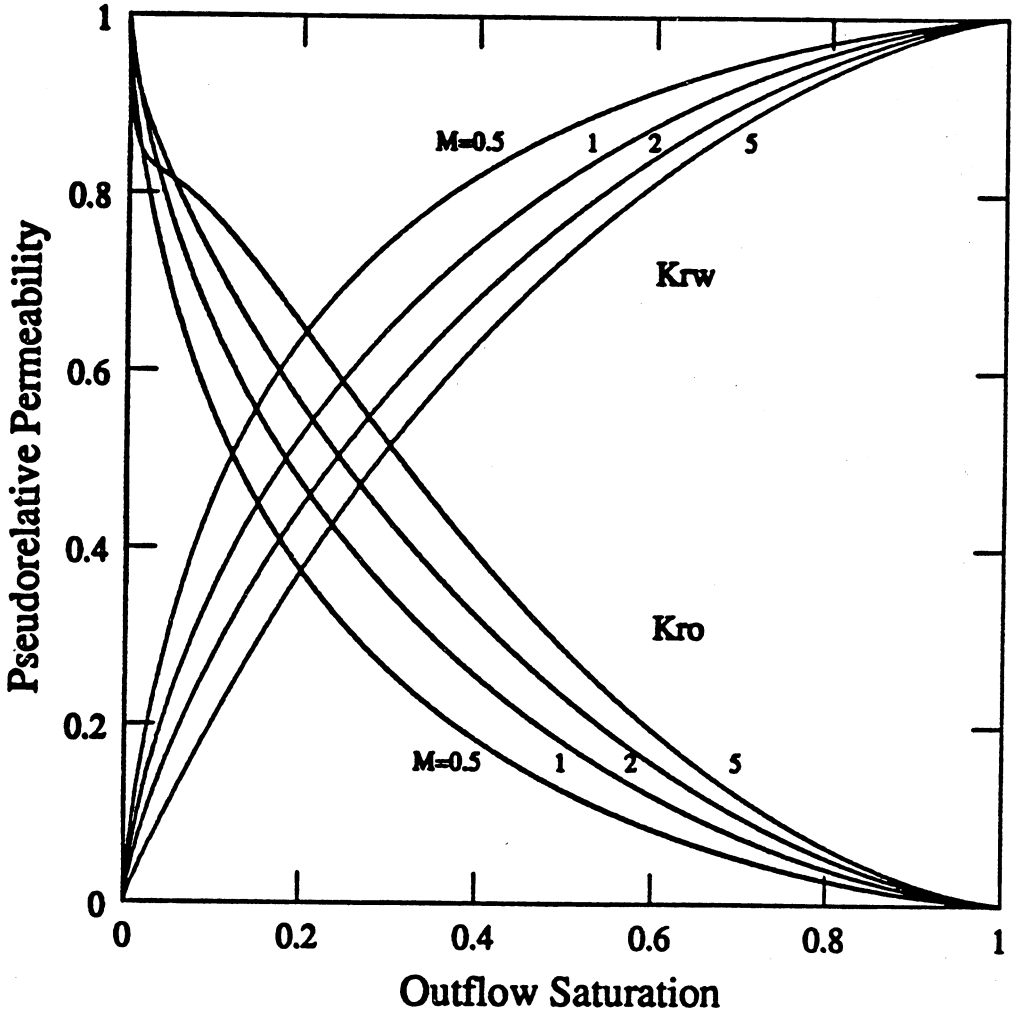

Fig. 6.1-17 Pseudorelative permeability functions for displacement in a system of noncommunicating layers for a permeability variance of 0.6.

6.1.3 Conclusions

Analysis of the use of one-dimensional fractional flow theory to represent the effects of more complex flows leads to the following conclusions:

(1) The two-dimensional Dykstra-Parsons model of flow in a layered system can be modeled using one-dimensional frontal advance theory with the effects of the heterogeneity represented in the fractional flow expression. Exact agreement between the two-dimensional and one-dimensional representations is obtained for the case of unit mobility ratio where the characteristics are linear. For nonunit mobility ratio, agreement is qualitative but not quantitative.

(2) Pseudorelative permeability functions can be determined that reproduce exactly the oil recovery calculated for a system of noncommunicating layers as represented by the Dykstra-Parsons model. The resulting pseudorelative permeability functions depend on the permeability variation, V, and the mobility ratio, M. While oil recovery calculations for the one and two-dimensional models agree exactly, local saturation distributions do not.

(3) Psudorelative permeability functions determined at one scale from the Dykstra-Parsons model can be used to caluclate displacement performance at another scale, as long as the layer structure and mobility ratio are unchanged, because the flow process is purely convective. For processes in which displacement mechanisms other than convection are important, pseudorelative permeability functions determined at one scale are applicable only at that scale.

6.2 Representation of Small-Scale Heterogeneity for Reservoir Simulation

Christopher D. White

All petroleum reservoirs contain variations in permeability and porosity at length scales that are smaller than the smallest grid blocks used in reservoir simulations. Thus any simulation of displacements at the reservoir scale must utilize some sort of averaging of the local variations, so that properties such as permeability and porosity may be assigned to the grid blocks. In most simulations, however, only the most rudimentary of averaging techniques are applied. Typically, the reservoir is divided into a small number of layers that are assigned uniform properties, even though logs and core data show significant variation within these layers. To obtain effective permeabilities for the layers, the core or log data might be averaged arithmetically, geometrically or harmonically. Similar techniques are used for areal variations, though data characterizing areal variations are usually sparse. Because computation costs climb rapidly as the number of grid blocks increases, there is considerable incentive to use the coarsest grid possible.

Representation of the effects of small scale permeability variations is made more difficult by the variety of variations that are possible. Most of the attempts to represent such effects have focused on specific types of variations. For example, the the methods of Haldorsen and Lake (1984) and Begg and King (1985) apply only to horizontal (or parallel), impermeable shale lenses. The single phase simulations of Warren and Price (1961) dealt with spatially random (uncorrelated) permeability distributions. They used a log-normal probability density function for permeability, and found that for distributions with moderate variability, effective permeability for a grid block (macropermeability) could be estimated as the geometric mean of the permeabilities of all the small scale blocks (microblocks) within the larger block. Weber (1982) used repetitive symmetry elements and Darcy flow analysis to estimate the effective permeability and anisotropy ratio for festoon cross-bed sets and sandstone with low-

permeability intercalations. Martin and Cooper (1984) extended Darcy flow analysis to stochastically generated sand/shale sequences, and considered two-phase flow. They found that the harmonic mean is a poor predictor of vertical permeability. Kortekaas (1983) performed very fine scale two-phase simulations on repetitive arrays intended to mimic cross-bedded sandstone geometry. He generated pseudofunction relations for relative permeability and capillary pressure, and noted that the pseudofunctions were anisotropic with respect to the sedimentary structure. Equally important, Kortekaas (1983) stated that neglecting the cross-bedding results in production predictions which are invariably optimistic. Lasseter et al. (1986) performed multiphase simulations to assess the effects of different scales of variability on displacement behavior. They found that the results depended strongly on the boundary conditions used in the microscale simulation. Also, they observed that repeated multiphase simulations are expensive and their interpretation is laborious.

None of the previous investigations considered the tensor aspects of permeability anisotropy, though macrolevel permeability anisotropy is likely to be present when large grid blocks are used to simulate displacements with smaller scale heterogeneities present. It is clear, for example, that anisotropy can be induced by heterogeneities such as lamination, burrows or cross-bedding (Pryor 1972, LeBlanc 1977a and 1977b, Weber 1982). The presence of such heterogeneities distorts the local streamlines, and that distortion is reflected in the local pressure field. When such a flow is modeled using a macrolevel representation, however, the local pressure field is represented by a single grid-block pressure. Since the pressure gradient between grid blocks is necessarily directed from block center to block center, the distortion in the flow directions can only be reproduced if the flux between blocks is not aligned with the macrolevel pressure gradient. That effect can be seen from a manipulation of Darcy's Law (Heller, 1963).

$$\nabla p + \frac{\phi \mu}{k} \vec{v} = 0 \tag{6.2-1}$$

where p is the pressure, ϕ is the porosity, k is the permeability, μ the viscosity and $\vec{v}$ is the superficial velocity vector. If the porosity and viscosity are taken to be constant, but the permeability is allowed to vary, the curl of Eq. (6.2-1) is

$$\nabla \times \vec{v} = \nabla \left[\ln k \right] \times \vec{v} \tag{6.2-2}$$

The term involving the gradient of pressure disappears because the curl of the gradient of a scalar is zero. Eq. (6.2-2) demonstrates that local variations in permeability induce vorticity (rotation), which indicates that the local flow in a linear system with constant pressure at each end must have a component perpendicular to the average (or macrolevel) pressure gradient. Thus, if the flow is represented only in terms of the macrolevel pressures, the local flow nonuniformities cannot be reproduced unless the macrolevel permeability is neither isotropic nor diagonal. Furthermore, if the details of the permeability distribution are different in different regions of the flow field, the magnitudes of the various components of the macrolevel permeability tensor will also vary with position. As a result, it will not be possible, in general, to align the macroscopic grid with the principal directions of permeability. Therefore, if the effects of microscale heterogeneity are to be represented with a macroscale grid, macroscale transmissibility must be a nondiagonal tensor quantity. The tensor equation for Darcy velocity is

$$\begin{bmatrix} \lambda^{xx} & \lambda^{xy} & \lambda^{xz} \\ \lambda^{yx} & \lambda^{yy} & \lambda^{yz} \\ \lambda^{zx} & \lambda^{zy} & \lambda^{zz} \end{bmatrix} \begin{bmatrix} \frac{\partial p}{\partial x} \\ \frac{\partial p}{\partial y} \\ \frac{\partial p}{\partial z} \end{bmatrix} = \begin{bmatrix} u^x \\ u^y \\ u^z \end{bmatrix} \tag{6.2-3}$$

where λ^{ij} is the mobility, $\frac{k^{ij}}{\mu}$. λ^{ij} is the constant of proportionality relating velocity in the i-direction to the gradient in the j-direction; k^{ij} is element (i,j) of the permeability tensor. Throughout this section, λ^{xx}, λ^{yy}, λ^{zz} and their associated fluxes are referred to as normal terms; λ^{xy}, λ^{xz}, etc., are referred to as cross terms. The normal or diagonal elements of the mobility tensor appear in **bold** typeface in Eq. (6.2-3). From Eq. (6.2-3), the velocity in the x-direction is

$$u^x = \lambda^{xx} \frac{\partial p}{\partial x} + \lambda^{xy} \frac{\partial p}{\partial y} + \lambda^{xz} \frac{\partial p}{\partial z} \tag{6.2-4a}$$

Or, in two dimensions,

$$u^x = \lambda^{xx} \frac{\partial p}{\partial x} + \lambda^{xy} \frac{\partial p}{\partial y} \tag{6.2-4b}$$

The simulation methods developed in this report are based on the finite-difference form of Eq. (6.2-4b).

In this section we describe a technique for the representation of the effects of heterogeneities smaller than the grid-block scale based on single phase flow simulations on a fine grid. Results of the fine grid calculations are used to estimate appropriate transmissibilities for the coarse grid. No restrictions are placed on the variability, geometry, or correlation of the permeability distribution. The tensor character of macroscale transmissibility is modeled, and the permeability anisotropy and contrasts are preserved.

6.2.1 Description of the Algorithm

The scaling process begins with a fine-scale reservoir description, assumed to be derived from a combination of measurements, inference and statistics. The reservoir is discretized into a microgrid, such that the size of the microblocks is near the scale on which the measurements and interpolation were performed.

A microscale simulation is performed on this grid. The governing partial differential equation for steady-state incompressible flow through an anisotropic medium is a tensor divergence expression analogous to the equation for heat flow presented by Carslaw and Jaeger (1959)

$$\nabla \cdot \Lambda \nabla p = \left[\lambda^{xx} + \lambda^{yx} + \lambda^{zx}\right] \frac{\partial p}{\partial x} + \left[\lambda^{xy} + \lambda^{yy} + \lambda^{zy}\right] \frac{\partial p}{\partial y} + \left[\lambda^{xz} + \lambda^{yz} + \lambda^{zz}\right] \frac{\partial p}{\partial z}$$

$$= 0 \tag{6.2-5}$$

where Λ is the mobility tensor and λ^{xy} is the element giving the proportionality between velocity in the x direction and pressure gradients in the y direction. Terms like $\lambda^{xy}\, \partial p / \partial y$ account for the flux due to anisotropy. The two-dimensional finite difference form of the divergence equation, Eq. (6.2-5), was derived by a surface integral (White 1987). Additional details are given by White (1987) and by White and Horne (1987). The operator is second-order and uses a nine-point stencil.

In order to pose the problem completely, boundary conditions must be specified. Given boundary conditions, the system of fine-grid equations may be solved for the microscale pressure. The unknowns are permuted using the Cuthill-McKee ordering algorithm, then the matrix equation is solved by a variable-bandwidth Choleski decomposition (Jennings 1977).

The permeability contrasts make the set of equations quite stiff, so that double precision is necessary. Even for uniform systems, if the number of unknowns is greater than about 500, rounding error makes single precision calculations inaccurate. The micropressure is used to

(1) Calculate the macropressure. The macropressure is defined as the storage-weighted mean of the pressures of all the microblocks composing the macroblock.

(2) Calculate the macrofluxes. The flux between two macroblocks is simply the sum of all the fluxes between microblocks on their mutual boundary.

Given the macrofluxes and macropressures, the macroscale transmissibilities can be estimated. For a two-dimensional, x – y simulation, the equation for the flux across the +x face of macroblock (i, j) is

$$q_{i+\frac{1}{2},j} = - \left[T^{xx}_{i+\frac{1}{2},j} \, \Delta^{x}_{i+\frac{1}{2},j} \, p + T^{xy}_{i+\frac{1}{2},j} \, \Delta^{y}_{i+\frac{1}{2},j} \, p \right] \tag{6.2-6}$$

where $\Delta^x p$ and $\Delta^y p$ are the the finite differences in pressure for the x and y directions, respectively. The expression for flux across a y-face is precisely analogous. Solutions with at least two distinct boundary conditions are necessary in order to determine both the normal and the cross transmissibility, T^{xx} and T^{xy}, for each face. Given two or more solutions, the macrotransmissibilities may be determined by linear least squares regression to minimize the error in flux assuming the pressure differences are exact. The normal equations based on Eq. (6.2-6) are

$$T^{xx}_{i+\frac{1}{2},j} \sum_{k=1}^{n} \left[\Delta^{x}_{i+\frac{1}{2},j;k} \, p \right]^2 + T^{xy}_{i+\frac{1}{2},j} \sum_{k=1}^{n} \left[\Delta^{x}_{i+\frac{1}{2},j;k} \, p \, \Delta^{y}_{i+\frac{1}{2},j;k} \, p \right] = \sum_{k=1}^{n} \left[\Delta^{x}_{i+\frac{1}{2},j;k} \, p \, q_{i+\frac{1}{2},j;k} \right] \tag{6.2-7a}$$

and

$$T^{xx}_{i+\frac{1}{2},j} \sum_{k=1}^{n} \left[\Delta^{x}_{i+\frac{1}{2},j;k} \, p \, \Delta^{y}_{i+\frac{1}{2},j;k} \, p \right] + T^{xy}_{i+\frac{1}{2},j} \sum_{k=1}^{n} \left[\Delta^{y}_{i+\frac{1}{2},j;k} \, p \right]^2 = \sum_{k=1}^{n} \left[\Delta^{y}_{i+\frac{1}{2},j;k} \, p \, q_{i+\frac{1}{2},j;k} \right] \tag{6.2-7b}$$

where n is the number of microsimulations performed, and the subscript k refers to the simulations, not the spatial location or phase. The normal equations Eqs. (6.2-7a) and (6.2-7b) form a system of two equations in the two unknowns T^{xx} and T^{xy} (or, for a y-face, T^{yy} and T^{yx}). The system will be well-posed for any $n \geq 2$.

From two to forty sets of boundary conditions have been used to determine macrotransmissibilities. Usually, three sets of boundary conditions were used:

(1) A pressure difference is imposed between the x-edges of the of the grid, with zero gradient normal to the y-edges,

(2) A pressure difference is imposed between the y-edges of the grid, with zero gradient normal to the x-edges,

(3) Sources and sinks were placed at the well locations, with zero gradient normal to the entire external boundary of the grid.

The x and y macrogradients (conditions 1 and 2 above) provide the well-distinguished flow geometries necessary for robust estimation, and the third boundary condition couples the well to the system, and to yield transmissibilities that correctly "weight" the nonuniformities in the permeability field. The well to well-block transmissibility is determined from the relation

$$Q_m = T_m \left[p_m - p_{i,j} \right] . \tag{6.2-8}$$

Here, Q_m is the injection rate of the mth well, located in macroblock (i,j), T_m is the (unknown) transmissibility, p_m is the imposed well pressure, and $p_{i,j}$ is the pressure in macroblock (i, j). If multiple well boundary conditions are used, Eq. (6.2-8) may be solved using least-squares. Again, minimization of the error in flux with the assumption that pressure differences are exact yields

$$T_m = \frac{\sum_{k=1}^{n} Q_{m;k} \left[p_{m;k} - p_{i,j;k} \right]}{\sum_{k=1}^{n} \left[p_{m;k} - p_{i,j;k} \right]^2} \tag{6.2-9}$$

Eq. (6.2-9) for well transmissibility is valid for $n \geq 1$. The tensor scaling method, as currently formulated, fails to couple wells correctly to heterogeneous blocks. This may be due to the fact that well-block pressure is not equal to the average block pressure, as noted by Peaceman (1978). As a result, the scaling formulation based on average block pressure (macropressure) is in error for the well block, with resulting flux errors up to 10%. This error is perhaps acceptable when predicting injectivity and breakthrough time, but it results in excessive material balance errors. To avoid this error in the example simulations, injection and production rates were specified, rather than well pressures.

A simple example demonstrates empirically the need to treat the macrotransmissibility as a tensor. Fig. 6.2-1 shows a heterogeneous permeability distribution and two grids: a 4-by-4 microgrid and a 2-by-2 macrogrid. The various boundary conditions are shown as well. The transmissibilities are estimated as a quotient of the total flux between macroblocks, and the difference of the mean pressure of the adjoining macroblocks,

$$T^{xx}_{i+\frac{1}{2},j} = \frac{q_{i+\frac{1}{2},j}}{\overline{p}_{i,j} - \overline{p}_{i+1,j}} \tag{6.2-10}$$

where $\overline{p}_{i,j}$ is the mean pressure of macroblock (i,j). As the entries of Table 6.2-1 indicate, the transmissibilities computed neglecting cross-terms are very sensitive to the macrogradient direction, and, worse, may be negative. However, if the transmissibility is treated as a tensor, the computed transmissibilities are less sensitive to the macrolevel pressure gradient direction and the diagonals of the tensor are strictly positive.

In summary, the pressures and fluxes from several microsimulations with different boundary conditions are averaged and summed to obtain macropressures and macrofluxes. The macropressures and fluxes are then used in the least-squares equations, Eqs. (6.2-7a), (6.2-7b) and (6.2-9), to obtain estimates for the macrotransmissibilities.

6.2.2 Validation of the Algorithm

The performance of the tensor scaling algorithm was evaluated with several simple test cases. First, a 30-by-30 microgrid with a uniform permeability of 1.0 Darcy was scaled to a 6-by-6 macrogrid. The boundary conditions for the macrogrid were no flux on the external boundary, while the injector was held at 1500 psi and the producing well was at 500 psi. The macropressures obtained from the microsimulation (averaging the pressures of the component blocks in a 900 block model) and the macrosimulation are compared in Figs. 6.2-2 and 6.2-3. There are minor differences in the pressure field, and the symmetry is slightly distorted, but the macropressures obtained by the 900-block and the tensor-scaled 36-block simulation agree to within 0.10 psi ($\approx$ 0.01% error).

Table 6.2-1 Transmissibility Calculations, 4-by-4 Grid

Connection	Method	Boundary Conditions	Result
A to B	Simple Quotient	1	$T^{xx} = 0.5251$
		2	$T^{xx} = 0.2088$
		3	$T^{xx} = 0.6185$
		4	$T^{xx} = 0.8229$
	Tensor/Least Squares	1,2,3,4	$T^{xx} = 0.4505$ $T^{xy} = -0.0988$
		1,2	$T^{xx} = 0.5353$ $T^{xy} = -0.1187$
		3,4	$T^{xx} = 0.6792$ $T^{xy} = -0.0977$
A to C	Simple Quotient	1	$T^{yy} = -6.3409$
		2	$T^{yy} = 0.6600$
		3	$T^{yy} = 0.6696$
		4	$T^{yy} = 0.9112$
	Tensor/Least Squares	1,2,3,4	$T^{yy} = 0.7483$ $T^{yx} = 0.0622$
		1,2	$T^{yy} = 0.8787$ $T^{yx} = -0.6152$
		3,4	$T^{yy} = 0.7325$ $T^{yx} = 0.4128$
B to D	Simple Quotient	1	$T^{yy} = 0.4839$
		2	$T^{yy} = 0.2722$
		3	$T^{yy} = 0.3143$
		4	$T^{yy} = 0.2697$
	Tensor/Least Squares	1,2,3,4	$T^{yy} = 0.2981$ $T^{yx} = -0.2157$
		1,2	$T^{yy} = 0.2704$ $T^{yx} = -0.1701$
		3,4	$T^{yy} = 0.2900$ $T^{yx} = -0.1119$
C to D	Simple Quotient	1	$T^{xx} = 1.2951$
		2	$T^{xx} = -3.3253$
		3	$T^{xx} = 1.3731$
		4	$T^{xx} = 2.1047$
	Tensor/Least Squares	1,2,3,4	$T^{xx} = 1.2251$ $T^{xy} = 0.4445$
		1,2	$T^{xx} = 1.3245$ $T^{xy} = 0.2290$
		3,4	$T^{xx} = 1.8056$ $T^{xy} = 0.2491$

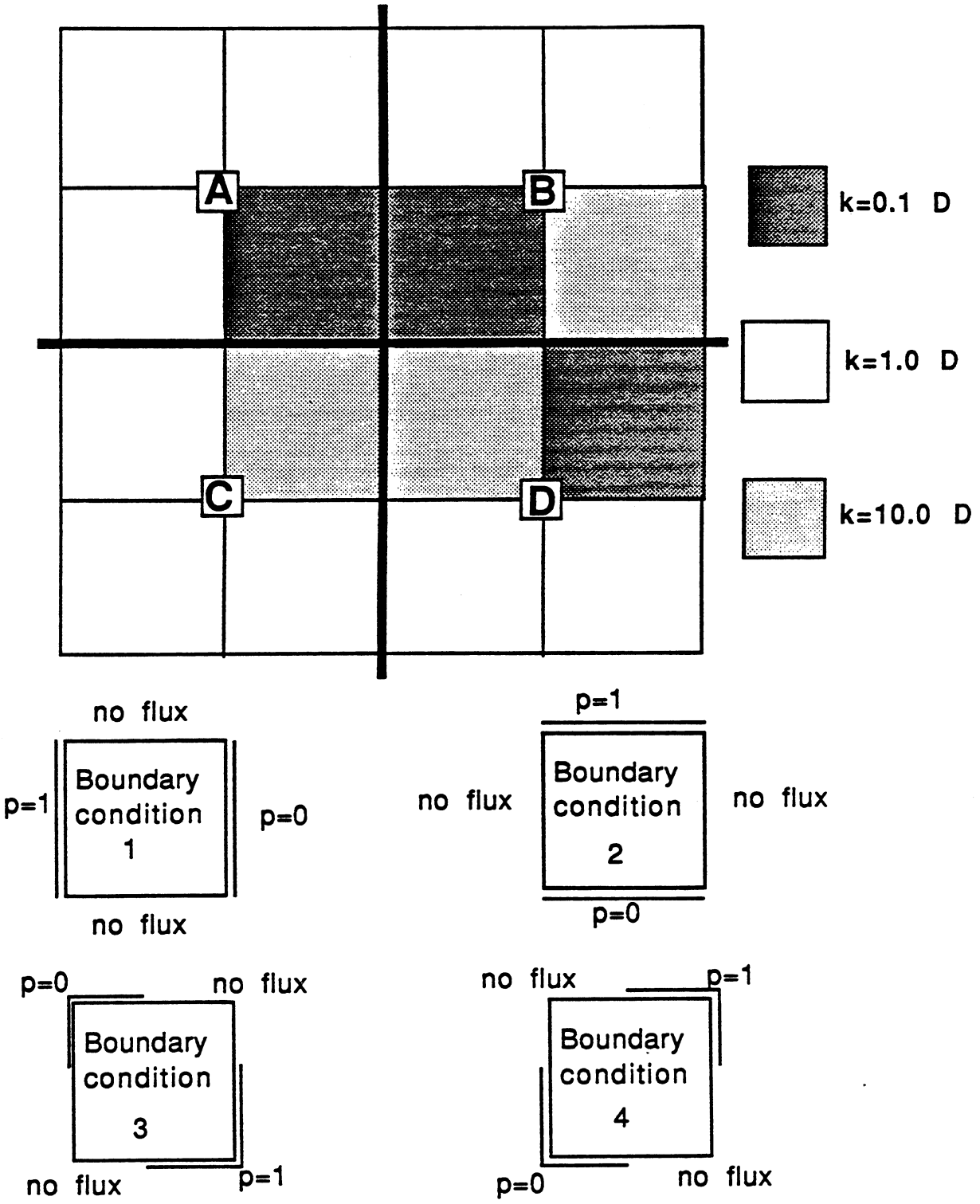

Fig. 6.2-1 Heterogeneous permeability distribution for scaling example. The macroblock boundaries (2-by-2) are indicated by bold black lines; microblock boundaries (4-by-4) are represented by fine lines.

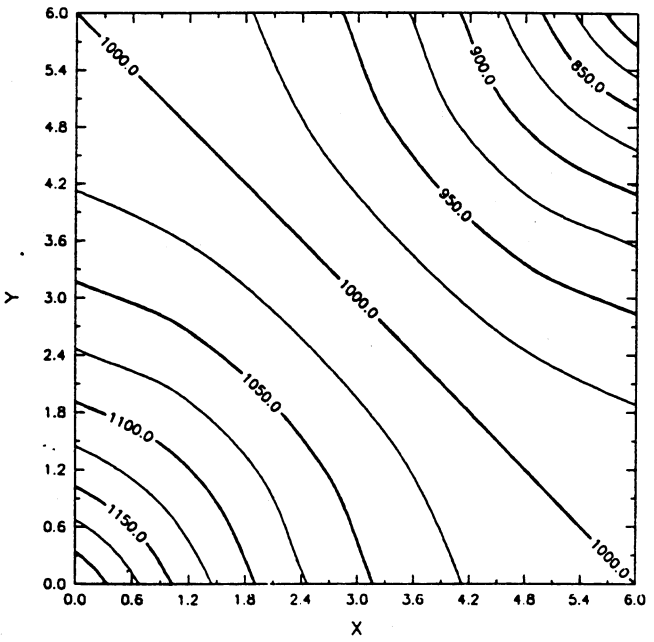

Fig. 6.2-2 Pressure contours from the microlevel simulations (900 blocks), five-spot geometry. Note the symmetry about the diagonals.

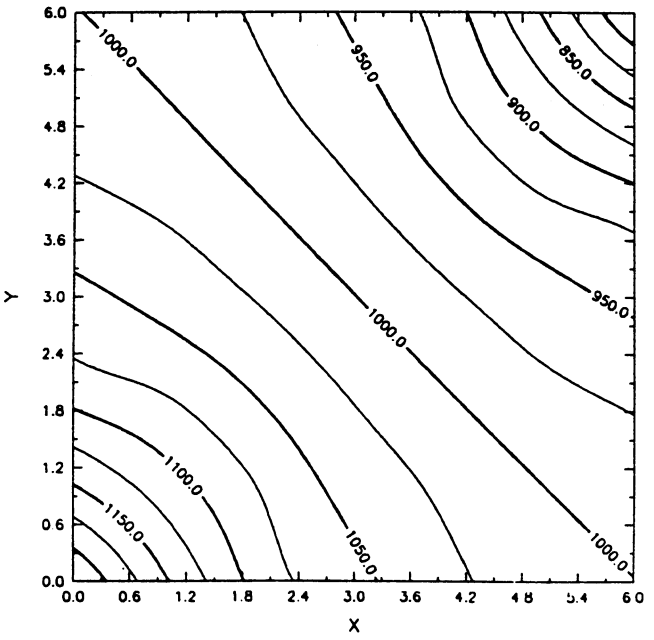

Fig. 6.2-3 Pressure contours from the macrolevel simulation (36 blocks), five-spot geometry. The symmetry is slightly distorted.

The next test was scaling of a heterogeneous 30-by-30 microgrid to a 6-by-6 macrogrid. The spatial distribution of permeability was obtained by drawing randomly from a log-normal permeability distribution (Dykstra-Parsons coefficient $V_{DP} = 0.852$ (Craig 1971) and median M = 1.0 D) and introducing anisotropic correlation via a moving average of the logarithm of permeability, with an x-range of 2 and a y-range of 1. The use of this correlation algorithm reduces the variability and may alter the median value slightly. The resulting permeability field is shown in Fig. 6.2-4. The macrofluxes and macropressures obtained from three different boundary conditions were then used to estimate macrotransmissibility. Both diagonal tensor (that is, all cross terms equal to zero) and general tensor transmissibility were considered; the resulting x-face transmissibilities T^{xx} are contoured in Figs. 6.2-5 and 6.2-6, respectively. The simple diagonal tensor method yielded negative transmissibilities. Negative transmissibilities are physically unrealistic, and hence this method was not considered further. On the other hand, the tensor scaling algorithm gave physically acceptable estimates for transmissibility. While this algorithm does not explicitly constrain the diagonal elements of the transmissibility tensor to be nonnegative, it has not yet yielded a negative normal transmissibility. This indicates that the transmissibilities being estimated are well constrained physically, and need no further mathematical constraint. The pressure results from a microlevel simulation of steady-state flow in a five-spot are contoured in Fig. 6.2-7. The macrolevel simulation, contoured in Fig. 6.2-8, agrees reasonably well. It is not surprising that the correspondence between macrolevel and microlevel results is poorer for the heterogeneous case than for the uniform case. While errors in macropressure now range up to about 10 psi, errors in flux are less than 10%. These results are probably acceptable for most applications. In any case, the results are superior to those that could be obtained if the heterogeneity were neglected.

6.2.3 Discussion

The general tensor scaling procedure may be applied to cross-sections, areal permeability distributions, or three-dimensional domains. This section discusses two-dimensional applications, for both single-phase and two-phase flow.

First, the problem of calculating effective single-phase vertical permeability for a sandstone reservoir interlayered with shale lenses is addressed. Haldorsen and Lake (1984), Begg and King (1985), Weber (1982), and Martin and Cooper (1984) have all studied this system or a variation of it. General tensor scaling may be applied instead of using the stream-tube/Darcy analysis or probabilistic approaches that these authors proposed.

A random map generated by the method of Haldorsen and Lake (1984) is shown as Fig. 6.2-9. The shale fraction is 0.30; no conditioning data were used. The results of the general tensor scaling calculations are shown in Table 6.2-2. Several of the results are easily anticipated: for all blocks $T^{xx} > T^{zz}$, and the macrotransmissibility values are bounded below and above by the intrinsic permeability of the shale and sandstone, respectively. More interesting, though, is the importance of the cross terms: the ratio of cross terms to normal terms may be much greater than one. The need for the cross terms is made yet clearer if normal transmissibilities are calculated, ignoring the tensor character of macrotransmissibility. Negative transmissibilities are calculated, and the transmissibility is no longer bounded by the intrinsic shale and sandstone properties. These results indicate that an anisotropy ratio (or, equivalently, $k_{x,\,eff}$ and $k_{z,\,eff}$) cannot adequately characterize porous media of the class considered.

The tensor scaling method has been demonstrated to perform satisfactorily in modeling single-phase flow. In order to be useful for petroleum reservoir simulation, it must work for two-phase flow as well. The following example verifies that general tensor scaling captures many features of fine-grid permeability variation that impact waterflood performance.

One-quarter of a five-spot was also considered as an example problem. A permeability distribution was generated by a method similar to that of Haldorsen and Lake (1984). Rather

Table 6.2-2 Cross Section Scaling Results

Parameter	Maximum*	Minimum*
T^{xx}	0.9392 D-ft/cp	0.1001 D-ft/cp
T^{zz}	0.7954	0.0006
T^{xz}	0.1237	-0.0009
T^{zx}	0.2745	0.0006
$\frac{T^{xz}}{T^{xx}}$	0.4677	0.0032
$\frac{T^{zx}}{T^{zz}}$	3.2876	0.0468
* in absolute value		

Table 6.2-3 Simulation Input

Parameter	Input Value
Injection Rate	100 BBL water/day
Production Rate	100 BBL total fluid/day
Oil Viscosity, μ_o	1.0 cp
Water Viscosity, μ_w	1.0 cp
Irreducible oil saturation, S_{or}	0.20
Initial/irreducible water saturation, S_{wc}	0.20
Porosity, ϕ	0.20
Thickness, Δz	10 ft.
Areal dimensions, Δx by Δy	600 ft. by 600 ft.
Initial pressure	1000 psi

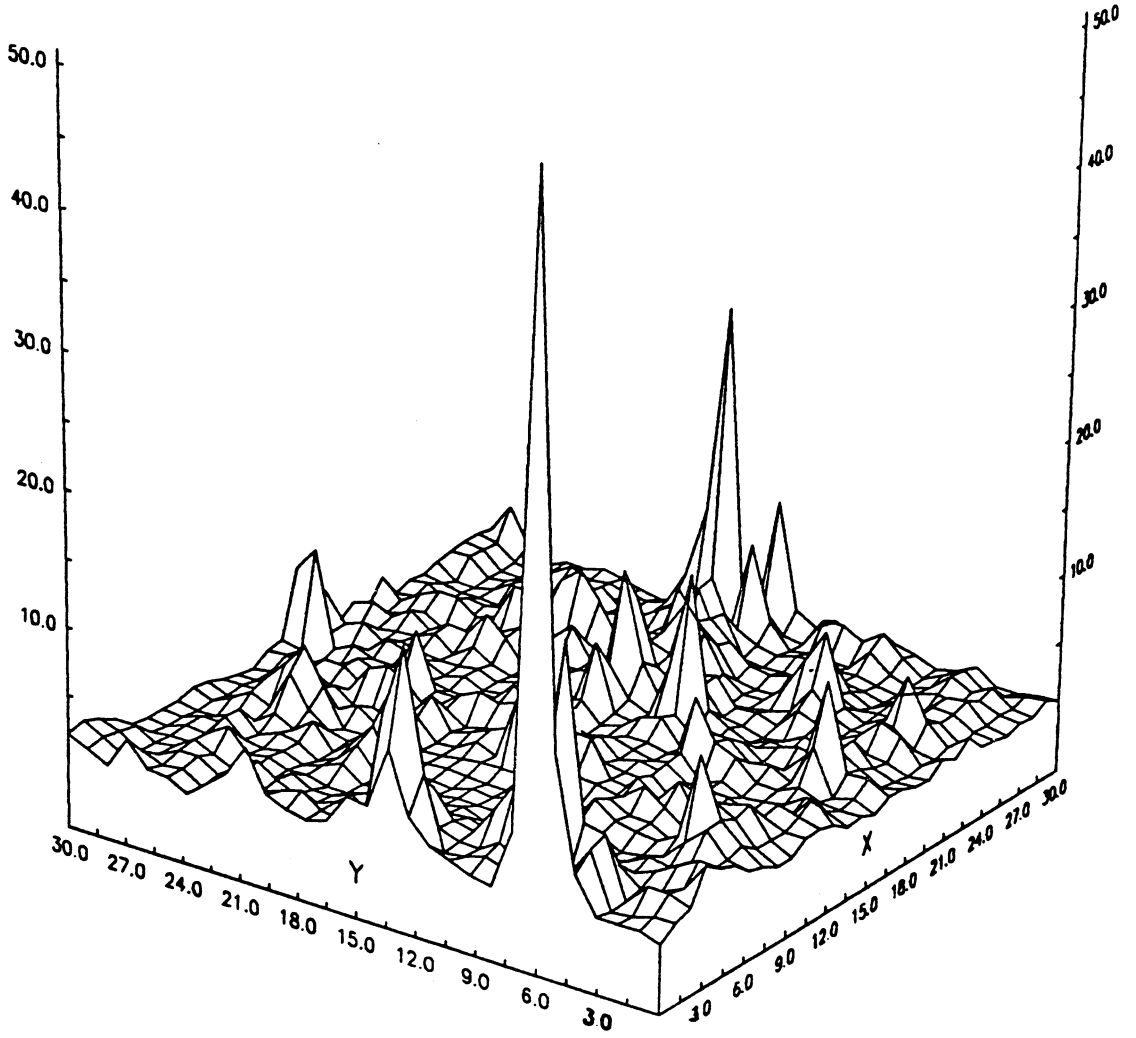

Fig. 6.2-4 Nonuniform permeability distribution created stochastically, and smoothed with an anisotropic moving average.

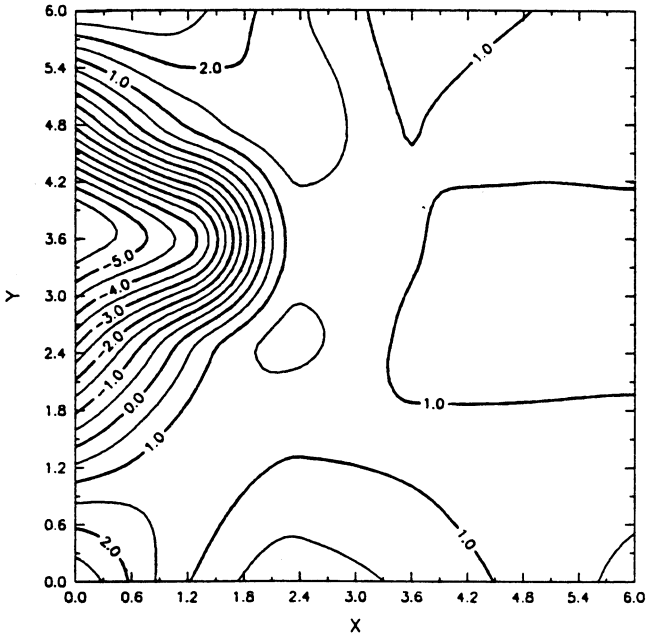

Fig. 6.2-5 Contours on the normal x-face transmissibility for normal scaling. Contour interval is 0.5 D-ft/cp. Note negative values in left-center of grid.

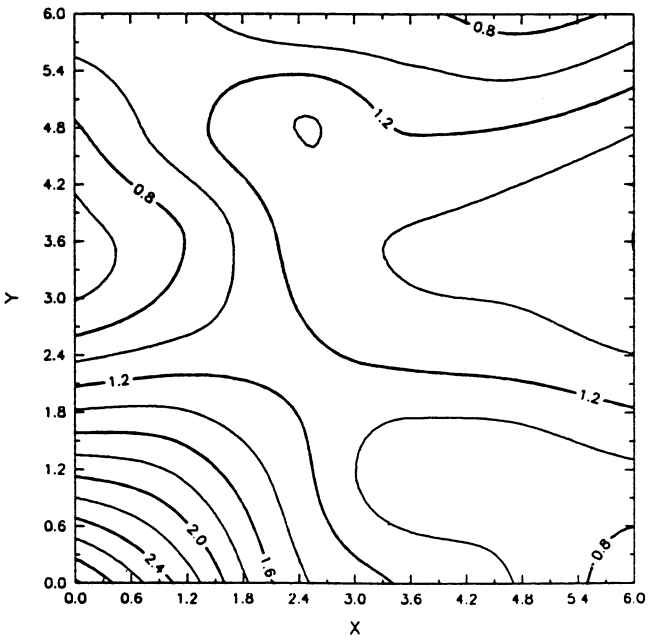

Fig. 6.2-6 Contours on the normal x-face transmissibility for general tensor scaling. Contour interval is 0.25 D-ft/cp.

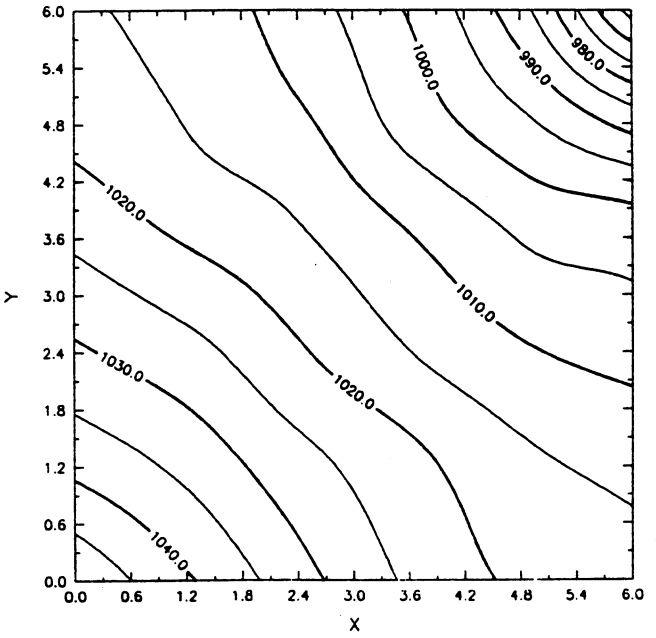

Fig. 6.2-7 Pressure contours for microsimulation (900 blocks) with the random permeability distribution of Fig. 6.2-4.

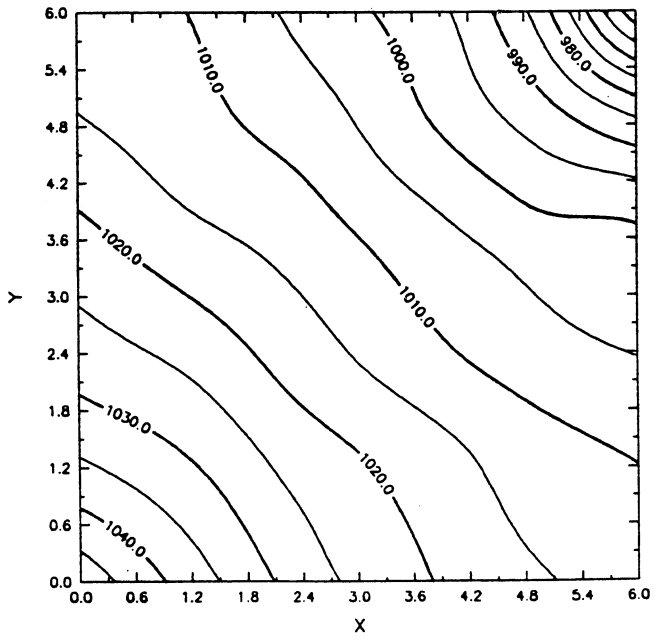

Fig. 6.2-8 Pressure contours for macrosimulation (36 blocks) with the random permeability distribution of Fig. 6.2-4.

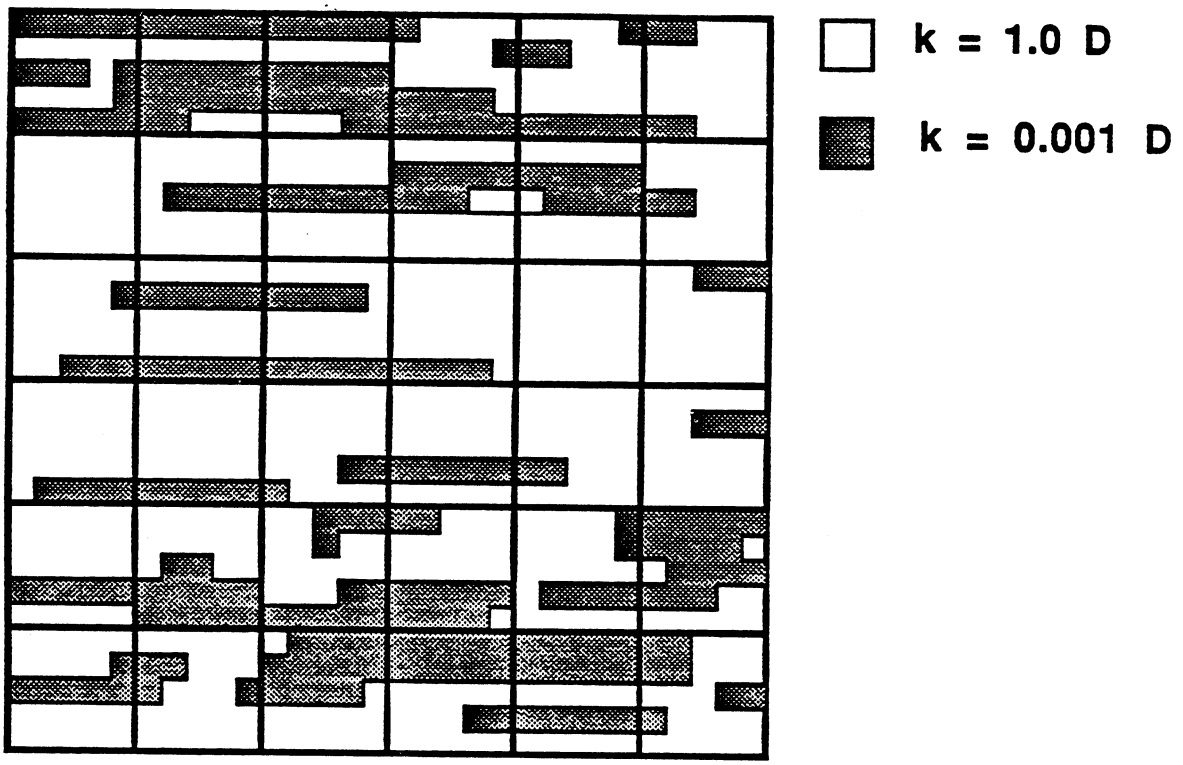

Fig. 6.2-9 Stochastic cross section generated by the procedure of Haldorsen and Lake (1984).

than drawing from a distribution of regularly oriented rectangles, the algorithm used here drew randomly oriented sinusoids, to emulate channel structures. The orientation, period, amplitude and width of the structures were all generated from probability density functions. This mapping algorithm was chosen because it yields high-contrast, well-correlated, geometrically complex permeability fields that are (1) reminiscent of fluvial geological environments, (2) particularly difficult to scale and (3) continuous enough that they tend to exhibit preferential flow paths. A map generated by this method, and used throughout this discussion, is shown in Fig. 6.2-10. The underlying microgrid is 30-by-30; it will be scaled to a 6-by-6 macrogrid.

Several scaling algorithms were applied to the microgrid shown in Fig. 6.2-10: (1) general tensor scaling; (2) geometric mean, on a macroblock-by-macroblock basis; and (3) geometric mean, applied to the entire grid. All averaging methods were compared to the microlevel results. Again, the diagonal tensor algorithm was rejected because it generates negative transmissibilities. Each of the scaling procedures was performed only once, before the two-phase simulation was performed. Thus, the tensor scaling algorithm performs a total of only three fine-grid pressure solutions, while a microlevel simulation requires a fine-grid pressure solution at each timestep.

Once the transmissibilities had been scaled to the macrolevel, a waterflood was simulated. Water was injected into macroblock (1,1) [microblock (3,3)] and displaced fluids were produced from macroblock (6,6) [microblock (28,28)]. The parameters of the simulation are summarized in Table 6.2-3, and the relative permeabilities are plotted in Fig. 6.2-11; note that the viscosities were matched and the oil and water relative permeabilities are symmetric about $S_w = 0.50$. Any nonuniformities in the flow field were therefore primarily due to the permeability heterogeneity. The system was assumed to be incompressible, and capillary pressure effects were neglected. As a result, a particularly simple pressure implicit, saturation explicit (IMPES) solution (Aziz and Settari 1979) may be obtained. The effects of compressibility and capillary pressure are important in many systems; they were neglected here in order to isolate the effects of transmissibility scaling. The two-phase simulator used in this study uses the general tensor finite-difference equations derived by White (1987). This simulator is similar to conventional models, except that it uses the tensor divergence expression for both the pressure and saturation solutions. The matrix equation for pressure was solved by line successive over-relaxation (LSOR).

Results of the simulations are shown in Figs. 6.2-12 to 6.2-17, and results are also summarized in Table 6.2-4. One of the most sensitive measures of the accuracy of a scaling algorithm is the producing water cut, plotted versus time in Fig. 6.2-12. Both geometric mean and uniform permeability predicted breakthrough times that are nearly 50% later than in the microscale simulation. This is due to "smearing" of high permeability channels that caused early breakthrough in the microsimulation. The tensor scaling algorithm delayed breakthrough slightly. The error was about 20 days, one-tenth the error for the other methods. Perhaps the most important result to match is cumulative oil production. As Table 6.2-4 and Fig. 6.2-13 show, the tensor scaling algorithm was the only procedure that gave reasonable estimates on a coarse grid. It is worth noting that the use of the block-by-block geometric mean scarcely affected the production prediction. Fig. 6.2-14 demonstrates that the differences between the production curves in Fig. 6.2-13 are the result of the averaging schemes and are not due to truncation error in the solution of the differential equations (Lantz 1971). It compares a uniform permeability microsimulation and a uniform permeability macrosimulation. The effects of truncation error were clearly small compared to the effects of the differences in averaging procedure.

The variations in displacement efficiency for the various simulations, implicit in the different production histories discussed above, are made explicit in contour plots of saturation. The results of the microsimulation, tensor scaling, and geometric mean simulations have been contoured at 400 days; these plots are included as Figs. 6.2-15, 6.2-16 and 6.2-17, respectively. The hatched contours indicate closed lows in water saturation. The uniform permeability macrosimulation is not included, as the front geometry was not at all unusual.

Table 6.2-4 Summary of Simulation Results

Case	Breakthrough		% Error, ε_{BT}	Cum. BBL Oil, $N_p(t$=1000 *days*)	% Error ε_N
	Pore volumes	Days			
Microsimulation	0.275	353	------	55.1	-----
Tensor Scaling	0.288	369	4.5	53.6	-2.7
Geometric Mean	0.381	489	38.5	64.0	16.2
Uniform Permeability	0.481	527	49.3	64.0	16.2

Table 6.2-5 Execution Times for Simulations

Method	Scaling*	Simulation*	Total*	Relative to Microsimulation
Microsimulation	0.0	193:31.3	193:31.3	1.0000
Tensor Scaling	0:08.1	0:15.3	0:23.4	0.0020
Geometric Mean	0:00.3	0:15.7	0:16.0	0.0014
Uniform Permeability	0.00.1	3:48.2	3:48.3	0.0197

* CPU time required, MIN:SEC.tenths, Gould 9080 (10 MIPS, 64-bit word)

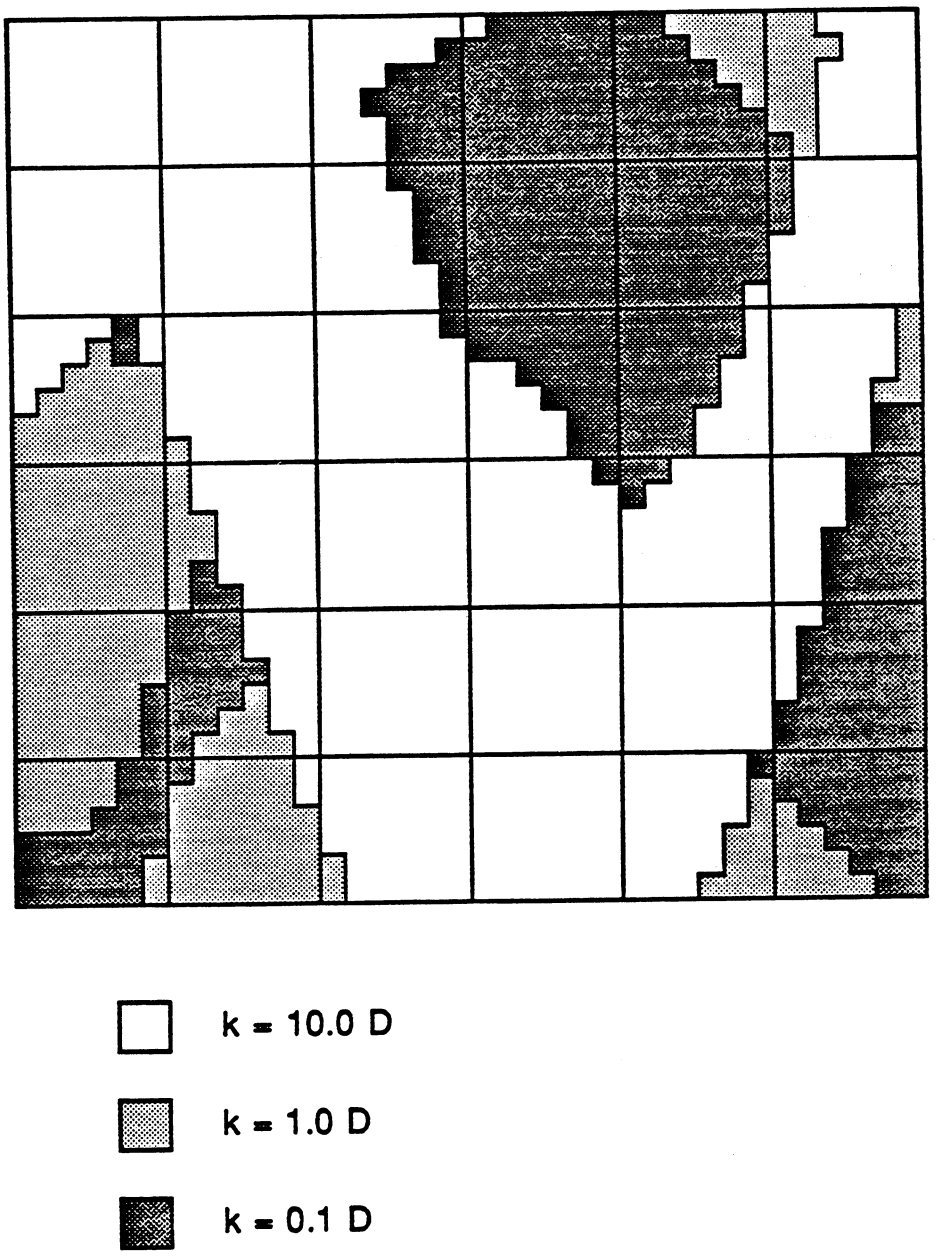

Fig. 6.2-10 Map of heterogeneous permeability distribution used for the two-phase waterflood simulation. Bold lines are macroblock boundaries.

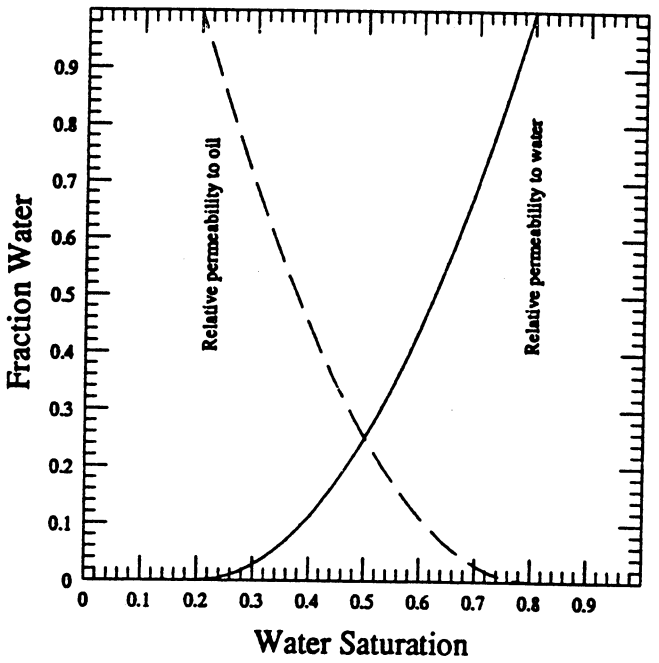

Fig. 6.2-11 Relative permeability curves used for waterflood simulation.

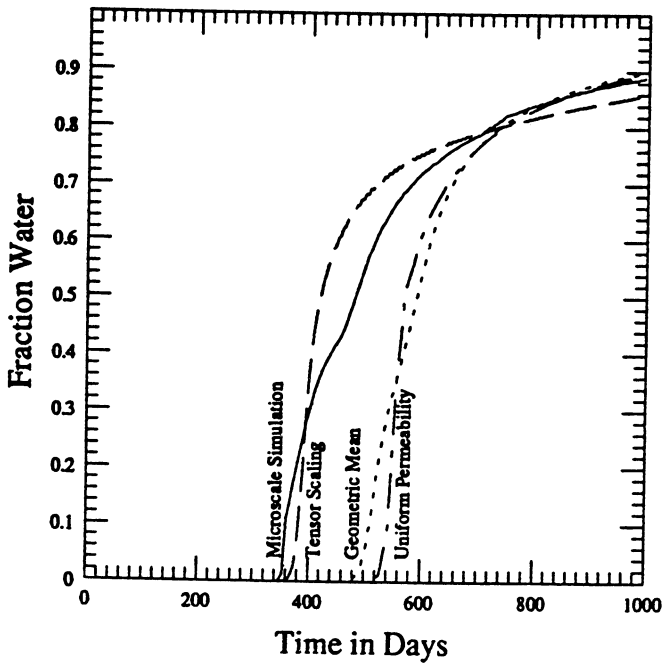

Fig. 6.2-12 Producing water cut vs. time in days for the waterflood simulation.

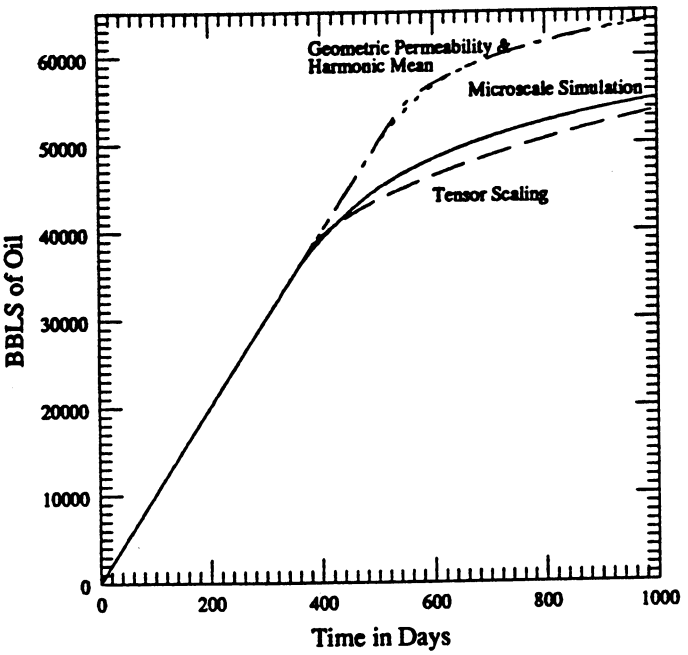

Fig. 6.2-13 Cumulative Oil Production vs. time in days for the waterflood simulation.

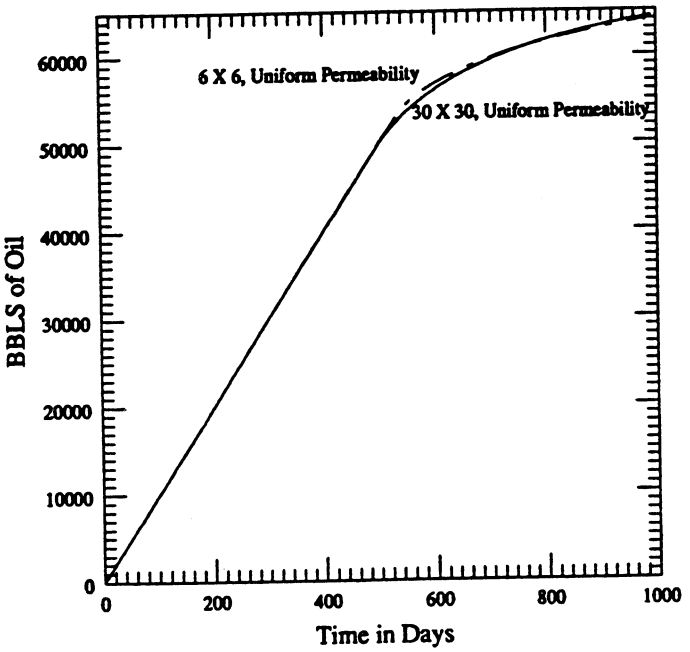

Fig. 6.2-14 Cumulative Oil Production vs. time in days for the waterflood simulation, homogeneous permeability. Truncation error does not affect the production prediction significantly.

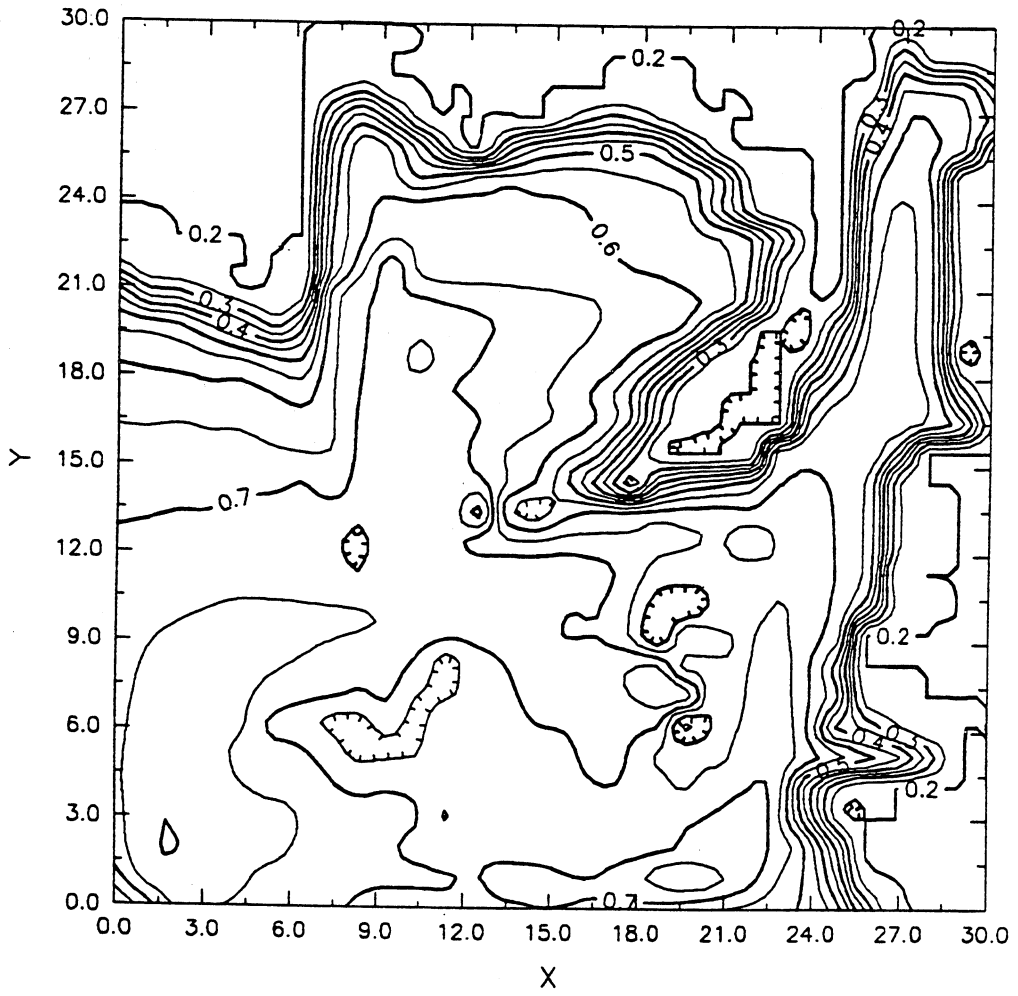

Fig. 6.2-15 Saturation contours for the 900-block microsimulation at 400 days.

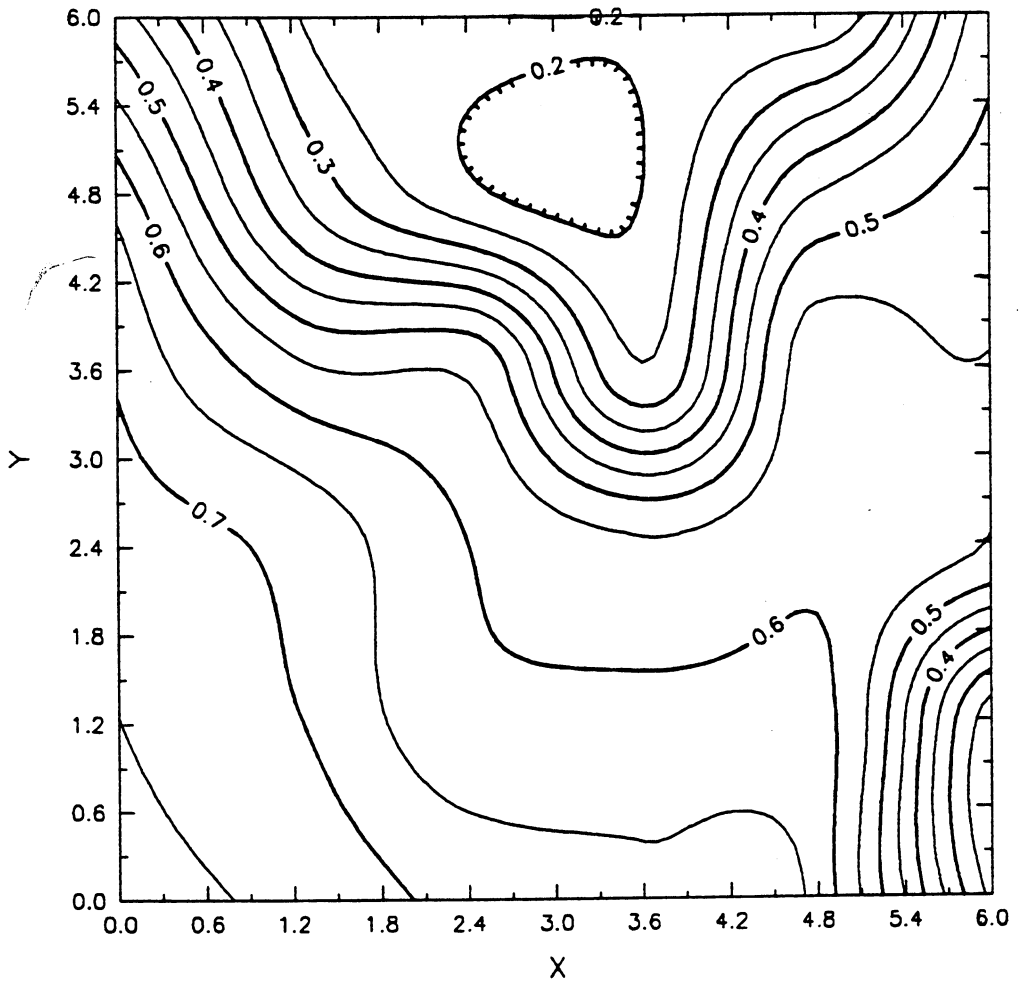

Fig. 6.2-16 Saturation contours for the 36-block tensor-scaled macrosimulation at 400 days.

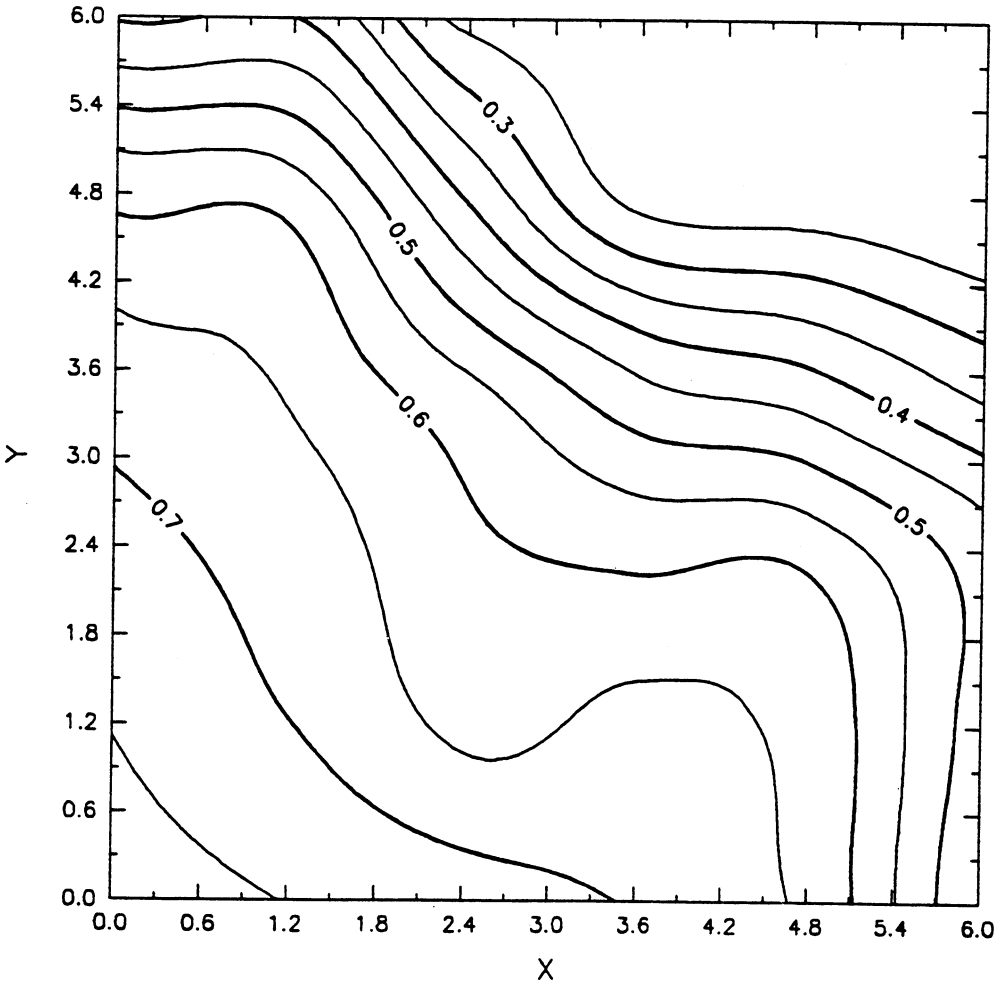

Fig. 6.2-17 Saturation contours for the 36-block geometrically averaged macrosimulation at 400 days.

It is, of course, impossible to capture the tortuous, detailed saturation distribution evident in the 900-block microsimulation (Fig. 6.2-15) using only 36 grid blocks. Nonetheless, the tensor method (Fig. 6.2-16) did succeed in reproducing the prominent cusp towards the well through the high-permeability zone along the right side of the grid, and also reproduced the initial water saturation that remained in the low-permeability regions behind the front (compare with Fig. 6.2-10). The saturations predicted by geometrically averaged permeability (Fig. 6.2-17) are smoother and fail to capture the destabilizing effects of the permeability heterogeneity.

The execution times for the four simulations are given in Table 6.2-5. Due to both block count and IMPES stability limitations (Todd et al. 1972) the microsimulation was about 500 times more expensive than the general tensor scaling algorithm. The uniform permeability simulation was slower than the general tensor scaling two phase simulation because (1) the uniform front had lower velocities, thus longer timesteps are taken and the total number of LSOR iterations was greater; and (2) saturations were changing in more blocks each time step for the uniform displacement, so that the effective transmissibility and pressure change more each time step. The simple geometric mean was some 30% faster that the general tensor scaling method. The main feature to note, however, is that the tensor scaling algorithm, which was shown to give good production predictions, was very efficient. Also, the scaling algorithm is only applied once, while the two-phase simulation may need to be repeated many times for a given micropermeability distribution — further increasing the savings of the scaling algorithm and coarse grid simulation relative to the fine grid simulation.

6.2.4 Conclusions

The simulation algorithm and results presented in this section lead to the following conclusions:

(1) Both mathematical results and numerical examples demonstrate that microscale permeability heterogeneity results in macroscale transmissibility anisotropy, which can be modeled by resorting to a tensor treatment of transmissibility.

(2) The arithmetic complications and numerical work associated with a tensor treatment of transmissibility are not excessive. Both single-phase and two-phase simulators using tensor permeability have been implemented.

(3) Least-squares regression may be applied to microscale fluxes and pressures to estimate the macroscale transmissibility tensors. The results are not overly sensitive to the boundary conditions imposed by the simulation.

(4) The macrotransmissibilities are estimated within the scaling algorithm, based on a user-specified micropermeability map. The use of tensor transmissibilities is entirely internal. Aside from the specification of the microscale permeability distribution, the mechanics of history-matching and production prediction are fundamentally unchanged from conventional simulation methods.

(5) Methods that compute effective vertical permeability in sand/shale sequences without considering the off-diagonal elements of the permeability tensor fail to characterize these media accurately and fully.

(6) The tensor scaling algorithm requires only three fine-grid pressure solutions, while a microlevel multiphase simulation requires a new fine-grid pressure solution at each time step. As a result, the computational savings due to the decrease in block count far outweigh the computational cost of the tensor scaling algorithm, for the level of scaling considered.

(7) Use of simple averaging methods, such as the geometric mean, usually results in optimistic recovery predictions. The destabilizing effects of permeability variation are suppressed, and water breakthrough is artificially delayed.

(8) The tensor scaling algorithm yields predictions that are close to the fine-grid results, and far superior to any other coarse-grid method.

6.3 Immiscible Displacements through Heterogeneous Porous Media: Capillarity, Convection and Scale Dependence

Christopher D. White

The efficiency of immiscible displacements is controlled by rock-fluid properties, boundary conditions, gross system dimensions and the correlation and variability of rock properties. The length and time scales of laboratory and field displacements are very different: laboratory measurements must be systematically averaged or scaled if they are to be used to model field-scale displacements. The scaling problem is complicated by the variability of reservoir properties; porous medium transport properties vary over distances as fine as centimeters (Giordano et al. 1985) and as long as kilometers (Hoeksema and Kitanidis 1985). Methods to compute large-scale properties must account for spatially correlated properties and for differences in the effects of rock-fluid properties at the laboratory and interwell scales.

In this study, the effects of hetrogeneity and scale upon displacement behavior was investigated by (1) examining the governing partial differential equations to define scaling groups and (2) performing a suite of numerical simulations to determine the values of the various scaling groups for which capillary or viscous forces are dominant. The different flow regimes which the dimensionless numbers and simulations delineate should scale differently: a convection dominated system may require that viscous fingering be considered, a capillary-dominated system might be modeled by a transversely uniform front, and intermediate cases could be treated in yet another way. Simulation results can also be used to compute average (or pseudo) relative permeabilities; examples are presented later in this section.

6.3.1 Partial Differential Equations and Dimensionless Groups

The conservation equation for the water phase in a water-oil system is

$$\frac{\partial}{\partial x}\left[\frac{k_w^x}{\mu_w}\left[\frac{\partial p_o}{\partial x}-\frac{\partial P_c}{\partial x}\right]\right]+\frac{\partial}{\partial y}\left[\frac{k_w^y}{\mu_w}\left[\frac{\partial p_o}{\partial y}-\frac{\partial P_c}{\partial y}\right]\right]=\phi\,\frac{\partial S_w}{\partial t}\,. \qquad (6.3\text{-}1)$$

where k, μ and ϕ are permeability, viscosity and porosity, P is pressure, P_c is capillary pressure and S is saturation. Subscripts o and w refer to oil and water and superscripts refer to coordinate directions.

In Eq. (6.3-1) the fluids and rock are assumed to be incompressible. Oil pressure and water saturation are taken as the primary unknowns. Rewriting Eq. (6.3-1) in dimensionless form gives

$$\frac{\partial}{\partial x_D}\left[\lambda_{wD}^x\frac{\partial p_D}{\partial x_D}\right]-N_{CL}\frac{\partial}{\partial x_D}\left[\lambda_{wD}^x\frac{\partial P_{cD}}{\partial x_D}\right]+R_L^2\frac{\partial}{\partial y_D}\left[\lambda_{wD}^y\frac{\partial p_D}{\partial y_D}\right]-N_{CT}\frac{\partial}{\partial y_D}\left[\lambda_{wD}^y\frac{\partial P_{cD}}{\partial y_D}\right]=\frac{\partial S_w}{\partial t_D} \qquad (6.3\text{-}2)$$

The dimensionless variables in Eq. (6.3-2) are defined as follows:

$$x_D = \frac{x}{L} \; ; \; L = \text{system length} \tag{6.3-3a}$$

$$y_D = \frac{y}{H} \; ; \; H = \text{system thickness} \tag{6.3-3b}$$

$$\lambda^x_{wD} = \frac{k^x k^x_{rw} \mu_{w,ref}}{k^x_{ref} \, \mu_w} \tag{6.3-3c}$$

$$\lambda^y_{wD} = \frac{k^y k^y_{rw} \mu_{w,ref}}{k^y_{ref} \, \mu_w} \tag{6.3-3d}$$

$$t_D = \frac{u_T t}{L\phi} \; ; \; u_T = u_o + u_w = \text{superficial total fluid velocity} \tag{6.3-3e}$$

The dimensionless dependent variables are

$$p_D = \frac{k^x_{ref}}{u_T \, \mu_{w,ref} \, L} \left[p_o(x,t) - p_L \right]$$

$$p_o(x,t) = \text{oil phase pressure}$$

$$p_L = p_o(L,0)$$

$$P_{cD} = \frac{P_c}{P_c^*} \tag{6.3-4b}$$

In these definitions, the subscript ref indicates a reference or average value to be used in scaling the equation. P_c^* is a reference capillary pressure or capillary pressure difference; here, $P_c^* = P_c(S_{wc})$.

The dimensionless longitudinal capillary number increases as capillary pressure exerts a greater smoothing influence in the direction parallel to the mean flow

$$N_{CL} = \frac{k^x_{ref}}{u_T \, \mu_{w,ref} \, L} \, P_c^* \tag{6.3-5a}$$

Physically, N_{CL} is the ratio of capillary pressure difference to viscous pressure difference. N_{CL} varies inversely with system length, even when the rock-fluid properties and flow velocity are constant. For systems with identical properties and aspect ratio, capillary pressure will tend to be more important in short systems (small L).

The transverse capillary number is a measure of the capillary-induced flux in the direction transverse to the mean flow,

$$N_{CT} = N_{CL} \left[\frac{L}{H} \right]^2 \frac{k^y_{ref}}{k^x_{ref}} = N_{CL} \, R_L{}^2 \, . \tag{6.3-5b}$$

$$R_L = \frac{L}{H}\sqrt{\frac{k^y_{ref}}{k^x_{ref}}} \qquad (6.3\text{-}5c)$$

R_L can be thought of as a hydraulic aspect ratio, where the geometric aspect ratio L/H has been corrected by the permeability anisotropy ratio. As the aspect ratio increases (at constant L), N_{CT} increases since the distance over which the transverse flow must occur is decreased; as L increases at constant L/H, N_{CT} decreases and the larger value of H impedes transverse capillary equilibrium. The dimensionless groups defined above are similar to those formulated by Yokoyama and Lake (1981), except for their use of the Leverett (1941) j-function rather than P_c^*, which was used here.

6.3.2 Behavior of Layered Systems

Many petroleum reservoirs are composed of several horizontal layers with distinct transport properties. The forces that drive crossflow and stabilize displacements through layered media can be studied analytically for some particular cases: no crossflow (Dykstra and Parsons 1950, Pande et al. 1987), viscous dominated (Zapata and Lake 1981), and capillary dominated (Yokoyama and Lake 1981). The current study requires that viscous, capillary, and gravity crossflow be investigated simultaneously; thus, a numerical simulation procedure was used. The understanding gained from the dimensionless groups defined above can be used to analyze and categorize displacements through layered systems.

Simulation of Layered Systems

To illustrate the interplay of heterogeneity and viscous and capillary crossflow, numerical simulations of displacements in a two-layer system were performed using the parameters summarized in Table 6.3-1. The simulations included uniform systems, systems with no crossflow, with viscous crossflow only, and systems with viscous and capillary crossflow. The capillary number, aspect ratio, and some results are given in Table 6.3-2. Runs 1 and 0 were performed for a uniform permeability field with mobility ratios M=1 and M=10. Runs 2 and 3 were for the two-layer system with a permeability ratio of 10 but no crossflow. Runs 5-7 included viscous crossflow but no capillary crossflow. Runs 8-16 simulated combined capillary and viscous crossflow. In runs 17-20 effects of gravity segregation were also present.

As comparison of runs 1 and 0 with runs 2 and 3 in Table 6.3-2 shows, a 10-to-1 permeability contrast with no crossflow resulted in a reduction in cumulative recovery of up to 0.25 movable hydrocarbon pore volumes (MHCPV) in cumulative recovery at 1.67 MHCPV injected. Water breakthrough, reported as τ_{BT} in Table 6.3-2, occurred up to 0.32 MHCPV earlier. In the absence of crossflow, therefore, layering affects production behavior significantly, as has long been known. However, if capillary pressure or other crossflow-inducing forces are large, the effect of layering may be smaller. Therefore, some knowledge of individual layer thicknesses and permeabilities is needed in order to predict production accurately. Techniques to obtain layer properties include tracer tests (Abbaszadeh-Dehghani and Brigham 1982) or pressure transient tests.

For the parameters considered here, capillary pressure stabilizes the immiscible displacement to a much greater degree than viscous forces do. Fig. 6.3-1 shows recovery curves for a uniform system, a layered system with no crossflow, a layered system with viscous crossflow, and a layered system with viscous and capillary crossflow. The recovery for the capillary crossflow case (Run 8, $N_{CT} = 11.52$) is nearly the same as the uniform case recovery (Run 1), while the viscous crossflow recovery (Run 5) is only a little higher than the no crossflow recovery (Run 2).

As the longitudinal capillary number increases, recovery falls slightly due to imbibition near the front — that is, the saturation behind the front is decreased, and breakthrough occurs earlier. Yokoyama and Lake (1981) estimate that longitudinal capillary dispersion is significant for $N_{CL} \geq 0.01$. The results obtained in this study (see Table 6.3-2) confirm their result.

Table 6.3-1 Simulation Description

Two-dimensional, 50-by-20, N_x-by-N_z.

Symmetric, parabolic, isotropic k_{rw} and k_{ro}.

Exponentially decaying P_c, $P_c^* = 0.0 - 4.0$

Incompressible flow, constant viscosity.

Uniform pressure at $x = 0$ and $x = L$, $0 \leq z \leq L$.

Constant rate, $u_T = 1\frac{\text{ft}}{\text{day}}$.

Isotropic intrinsic permeability.

Two equal-thickness layers.

Ten-to-one contrast in layer permeabilities.

Block centered, fully implicit simulation.

Table 6.3-2 Summary of Simulation Results

Run	M	$\frac{L}{H}\sqrt{\frac{k_z}{k_x}}$	N_{CL}	N_{CT}	N_{GT}[1]	τ_{BT}, MHCPV[2]	Q_o $\tau = 1.67$, MHCPV[2]
1	1.0					0.77	0.91
0	10.0					0.35	0.65
2	1.0	0.0				0.45	0.66
3	10.0	0.0				0.19	0.44
5	1.0	28.76				0.47	0.70
6	1.0	5.75				0.46	0.70
7	10.0	28.76				0.19	0.45
8	1.0	28.76	0.014	11.52		0.71	0.89
9	1.0	5.75	0.014	0.46		0.51	0.80
10	10.0	28.76	0.0014	1.152		0.25	0.63
11	10.0	28.76	0.00028	0.230		0.22	0.59
12	10.0	5.75	0.00028	0.009		0.19	0.47
13	1.0	28.76	0.0028	2.30		0.62	0.86
14	1.0	5.75	0.0028	0.09		0.49	0.74
15	1.0	28.76	0.00056	0.46		0.53	0.80
16	1.0	28.76	0.070	2.30		0.58	0.85
17	1.0	5.75	0.014	0.46	0.205	0.65	0.999
18	1.0	28.76	0.014	11.52	1.026	0.84	0.98
19	1.0	5.75	0.014	0.46	-0.205	0.42	0.89
20	1.0	28.76	0.014	11.52	-1.026	0.56	0.78

1. Negative sign indicates gravity flow into high k layer
2. MHCPV--Mobile Hydrocarbon Pore Volume = $\phi AL(S_{oi}-S_{or})$

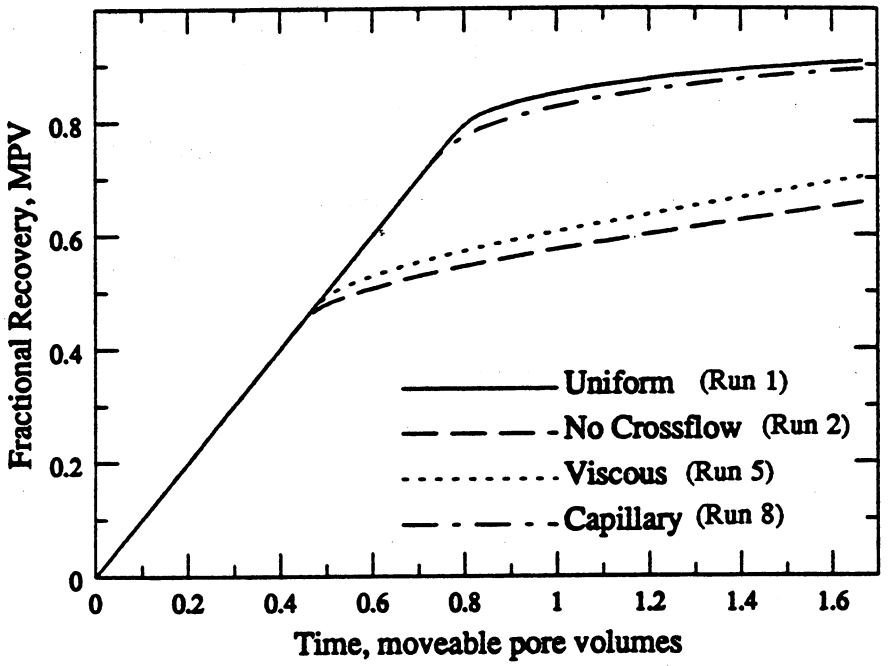

Fig. 6.3-1 Effects of viscous and capillary crossflow on recovery in displacements through layered systems with M=1.

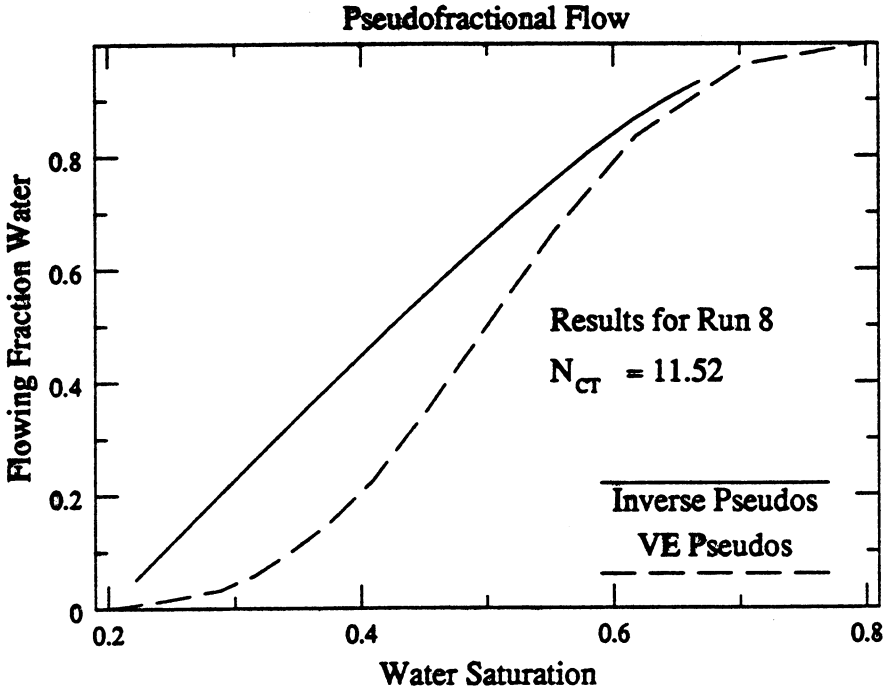

Fig. 6.3-2 Pseudofractional flow for a layered system in vertical equilibrium (Run 8).

Increasing the transverse capillary number increases recovery. Higher N_{CT} indicates that more water flows from the high- to the low-permeability region due to capillary pressure. The crossflow equalizes the front velocity in the two layers, retarding breakthrough and increasing sweep efficiency. For $N_{CT} > 1$, the displacement can be reasonably approximated as uniform. For $N_{CT} < 0.10$, the production behavior is much nearer the segregated flow than the uniform flow case. Yokoyama and Lake state that the displacement should be capillary dominated for $N_{CT} > 0.10$. This study confirms the order of magnitude of their estimate, though $N_{CT} > 0.25 - 0.50$ might be more appropriate (see discussion of pseudofunctions, below). Thus, the capillary crossflow can have a significant effect on process efficiency in layered systems.

Pseudofunctions for Layered Systems

Besides delineating flow regimes, simulation results may be used to estimate pseudorelative permeabilities (Jones and Rozelle 1978, Johnson et al. 1959, Pande et al. 1987). The results for two cases, Run 8 with $N_{CT} = 11.52$ and Run 14 with $N_{CT} = 0.09$, are shown in Figs. 6.3-2 and 6.3-3, respectively. The pseudofractional flows were estimated by both the vertical equilibrium (VE) method (Coats et al. 1971) and the inverse method of Pande et al. (1987) described in Section 6.1.

There are several reasons for studying pseudofractional flow, $\hat{f}_w$, rather than pseudorelative permeability. First, $\hat{f}_w$, incorporates the ratio of pseudorelative permeabilities, $\hat{k}_{rw}/\hat{k}_{ro}$. Subtle changes in $\hat{k}_r$ are magnified in $\hat{f}_w$. Also, the shock velocity (and thereby the breakthrough time) can be read from a simple tangent construction on the $\hat{f}_w$ vs. S_w graph (Welge 1952). Production behavior is therefore more explicit on the $\hat{f}_w$ curve than on the $\hat{k}_r$ curves. Finally, fractional flow, not relative permeability, is used to solve the saturation equations. (It is also necessary to know the total mobility as a function of saturation to solve the pressure equations; $\hat{\lambda}_T(S_w)$ and $\hat{f}_w(S_w)$ must both be tabulated.)

For high transverse capillary number displacements (Fig. 6.3-2), the VE and inverse method are nearly equivalent — the portion of the fractional flow curve before the tangent point has no effect on the shock velocity or saturation profile (Welge 1952). For Run 14 (Fig. 6.3-3), however, the capillary number ($N_{CT} = 0.09$) is too low for vertical equilibrium to apply, and pseudofunctions based on VE yield an incorrect shock velocity. The failure of the VE method in this case suggests that the critical value of $N_{CT} = 0.10$ given by Yokoyama and Lake (1981) may be a bit too low. The inverse pseudofunction method will, by construction, estimate the correct shock velocity and production history (Pande et al. 1987).

The frontal advance formalism used to derive the inverse pseudofunctions is strictly valid only if the velocity of a given concentration is a function of local concentration only — $d\hat{f}_w/dS_w$ cannot be a function of x or t (Pande et al. 1987). In other words, the characteristic curves, curves that give the spatial positions of given saturations as a function of time, must be straight lines in the x–t plane. Of course, the same restriction applies to both VE and inverse pseudofunctions. As shown in Fig. 6.3-4, the characteristic curves for Run 14 are not quite straight. Thus, the inverse pseudofunctions cannot be expected to reconstruct the longitudinal saturation distribution exactly. However, as shown in Fig. 6.3-5 for Run 9 with $N_{CT} = 0.46$, the errors in prediction using the frontal advance formalism will be small except in the capillary transition region near the front if the characteristic curves are nearly linear.

Some effects of gravity were also investigated. In particular, the arrangement of the layers (low-k above high-k, or vice versa) was found to be important. Fig. 6.3-6 shows the pseudofractional flow curve for the case with high permeability above low (Run 17, favorable g) and the low over high case (Run 19, unfavorable g). The two fractional flow curves are quite different, even though the capillary number, system size, and average permeabilities are identical. Furthermore, for the favorable gravity case the VE method yields a fractional flow curve which predicts the wrong shock velocity (in fact, it predicts no shock at all). Thus, while both displacements ostensibly meet the capillary domination criterion of Yokoyama and Lake (1981) ($N_{CT} = 0.46 \gg 0.01$),

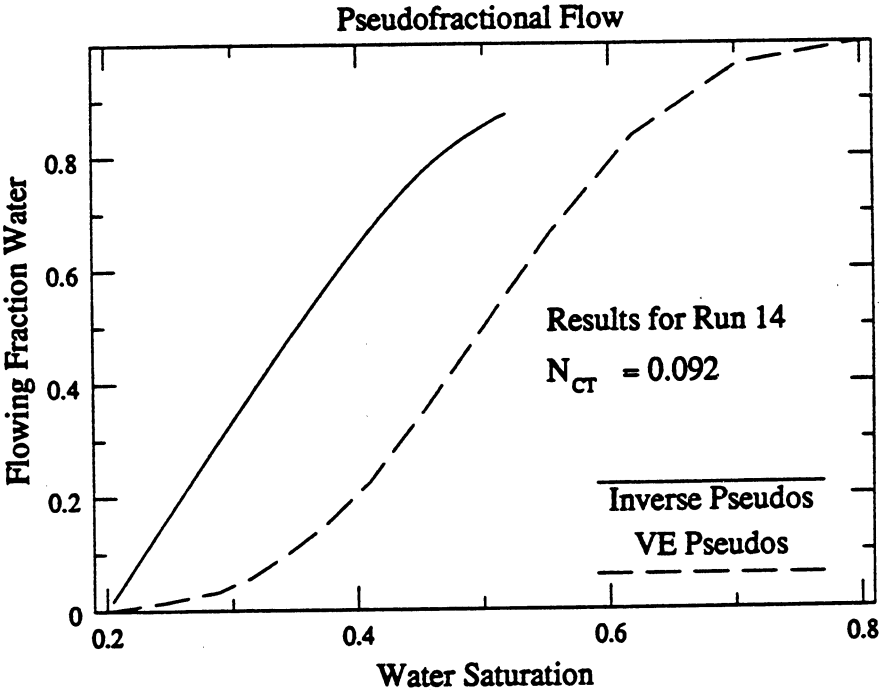

Fig. 6.3-3 Pseudofractional flow for a layered system not in vertical equilibrium (Run 14).

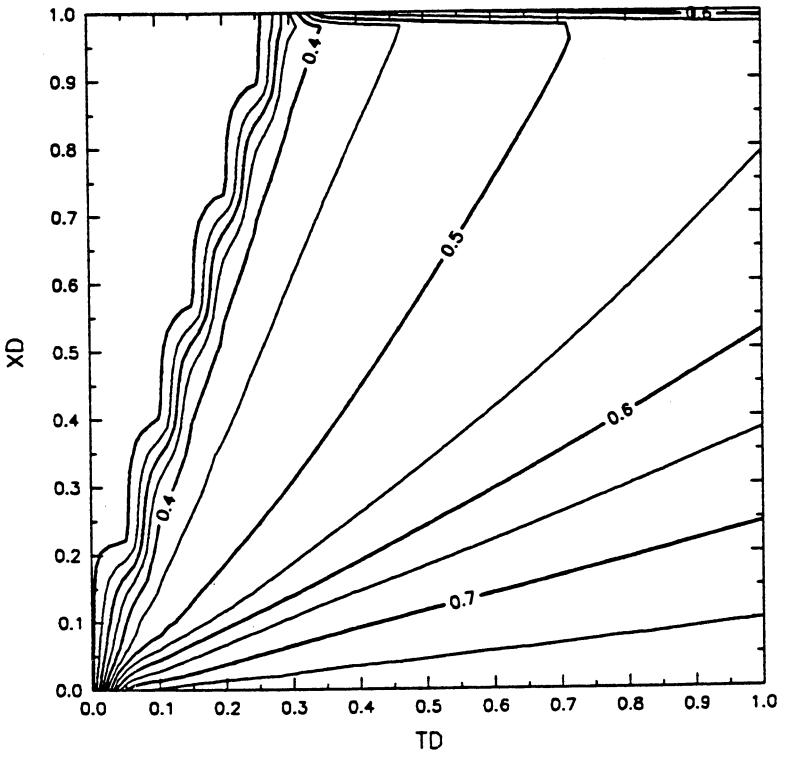

Fig. 6.3-4 Characteristics diagram for a non-VE layered system (Run 14, N_{CT} = 0.092).

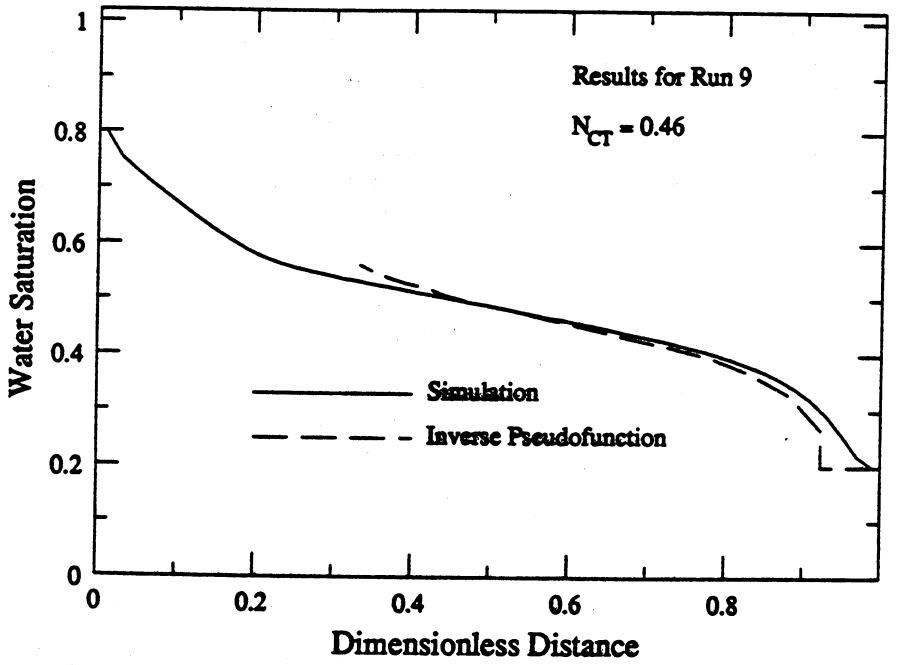

Fig. 6.3-5 Saturation profile for a layered system.

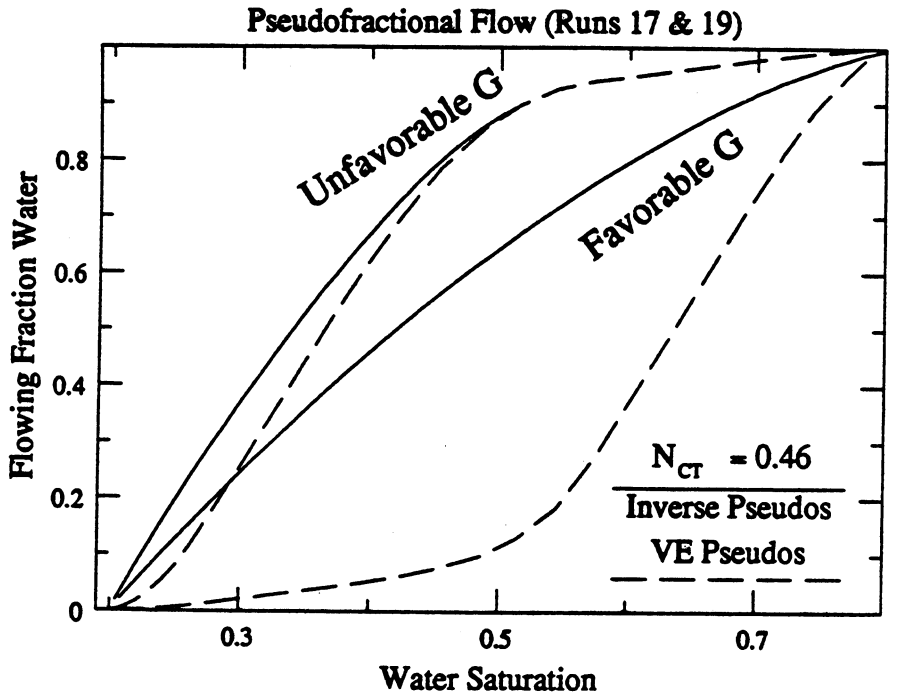

Fig. 6.3-6 Pseudofractional flow for layered systems with gravity crossflow.

only the unfavorable gravity case can be modeled approximately by the VE method. The favorable gravity case has the larger amount of stabilizing crossflow. Since VE implies maximum crossflow (Zapata and Lake 1981), it does not make sense that the favorable case should be less in vertical equilibrium than the unfavorable case. It is possible that gravity-stabilized displacements should be modeled using a permanent-form solution (Marle 1981) rather than the Buckley-Leverett shock theory (Buckley and Leverett 1942). Clearly, further examination of these displacements is needed, so that the interplay of viscous, gravity and capillary forces can be evaluated and more broadly applicable criteria for VE can be established. Finally, these examples emphasize the importance of geometry: a histogram of permeability and/or layer thicknesses is not sufficient. The spatial arrangement of the layers of contrasting permeability must be known also.

6.3.3 Systems with Areal Permeability Variations

Permeability varies areally as well as vertically. Areal variations tend to be more gradual and of smaller magnitude; the scale of variations may be much different in the vertical and horizontal directions. Thus, the coupling of heterogeneity and fluid properties to production behavior will be different. In the following paragraphs, methods to study the permeability distribution and model production behavior are discussed.

Geostatistical Analysis of an Areal Permeability Map

Data concerning areal variations of permeability are not abundant, and hence the horizontal variation of rock properties is more difficult to quantify. One of the simplest means of describing correlation and variation is the semivariogram function, which has been described and exploited by Journel and Huijbregts (1978), Desbarats (1987), Stalkup (1986), White (1987), and Mishra (1987), among others.

Variography and nonspatial statistical analysis have been applied to the permeability data obtained by Giordano et al. (1985). Giordano et al. measured the permeability at 1600 points on 2 two-by-two foot slabs of Berea sandstone using a minipermeameter (Eijpe and Weber 1971).

The probability density functions (pdf's) for both slabs are approximately normal — not log-normal as is commonly assumed. The statistics are summarized in Table 6.3-3.

Contour plots of the permeability fields of the two cores are shown in Figs. 6.3-7 and 6.3-8. Smoothing the data with a moving window (radius of five grid points or 0.25 feet) makes the trends more obvious (See Figs. 6.3-7b and 6.3-8b). Visual inspection suggests that Slab 1 is the most continuous in the (+x,+y) direction (SW to NE); Slab 2 displays the most correlation along the (+x,−y) direction (NW to SE). Giordano et al. (1985) noted that Slab 2 is microlaminated. The lower permeability of Slab 2 is partly due to the laminations, which are visible in the contour plots.

Variograms were computed for both cores; the results are shown in Figs. 6.3-9 and 6.3-10. Because of boundary effects, the variograms are not reliable at separation distances greater than 20 (one-half the total field size). Several features of the variograms merit discussion:

(1) The principal directions of variability may be deduced from the variograms. For Slab 1, the maximum variability is NW-SE; for Slab 2, the maximum variability occurs in the NE-SW direction. The direction of maximum continuity is perpendicular to the direction of maximum variability; thus, the variograms confirm the results of the inspection of the permeability contour plots.

(2) In the principal directions, the range of correlation (i.e., the distance at which the semivariogram assumes its sill or maximum stable value) is about 10 lags or 0.5 feet. These data show that this areal permeability distribution is not spatially random, even at the 0.5 ft scale.

Table 6.3-3 Permeability Distribution Statistics

Statistic	Core 1	Core 2
mean, $\bar{k}$ (md)	430.	245.
k_{min} (md)	220.	86.0
k_{max} (md)	604.	492.
variance, σ_k^2 (md^2)	28,280.	84,810.
coefficient of variation, $\frac{\sigma_k}{\bar{k}}$	0.133	0.284
confidence for χ^2 test of normal distribution	95%	90%

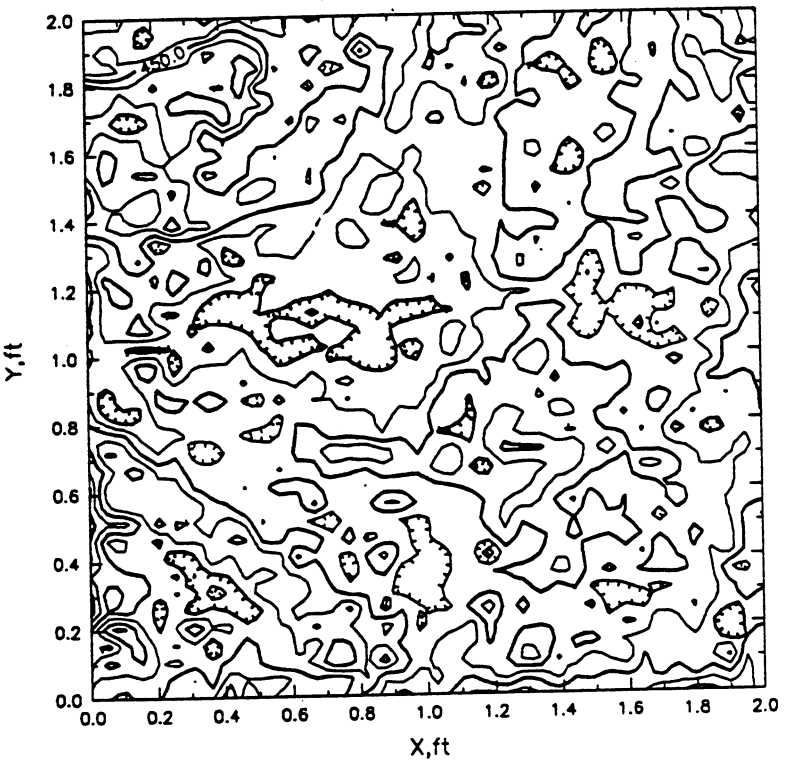

Fig. 6.3-7a Unsmoothed contour plot for Slab 1.

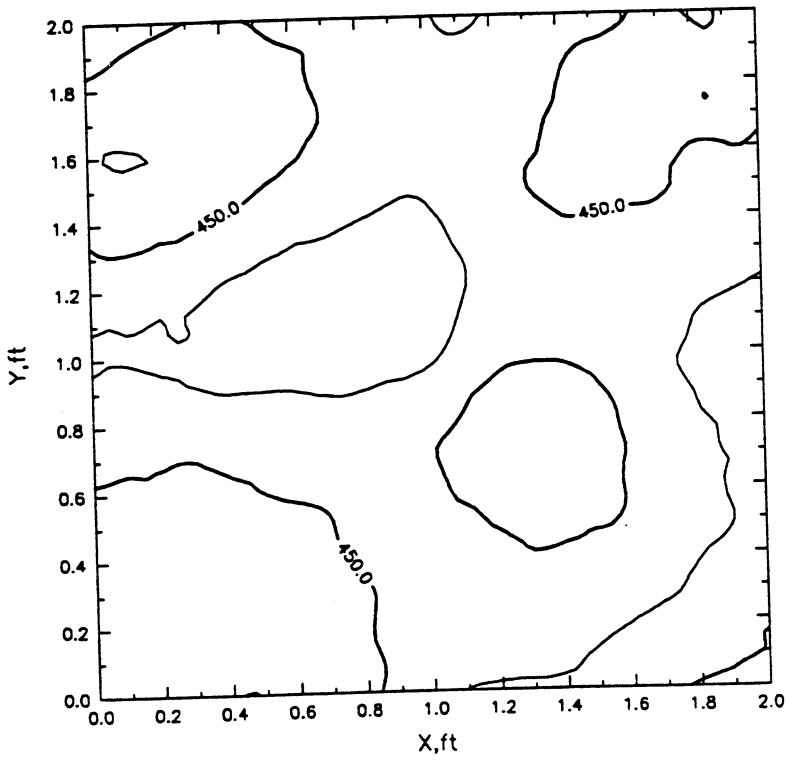

Fig. 6.3-7b Contour plots of permeability for Slab 1.

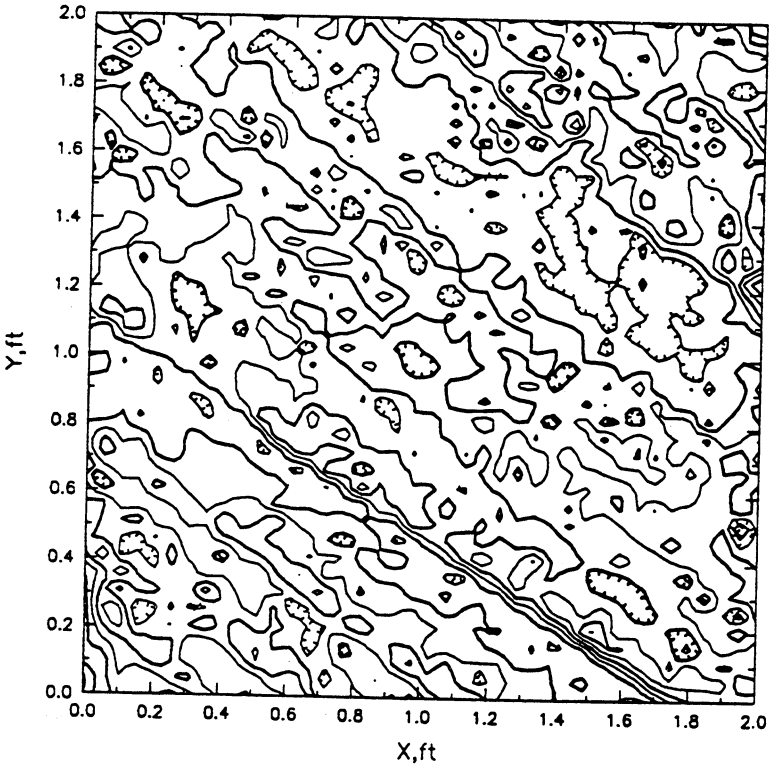

Fig. 6.3-8a Unsmoothed contour plot for Slab 2.

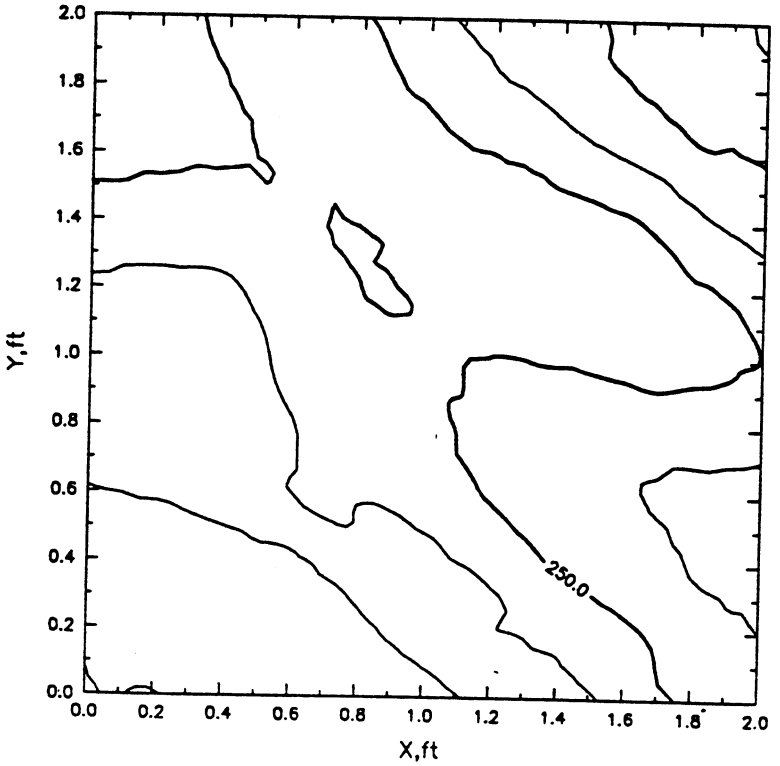

Fig. 6.3-8b Smoothed contour plot for Slab 2.

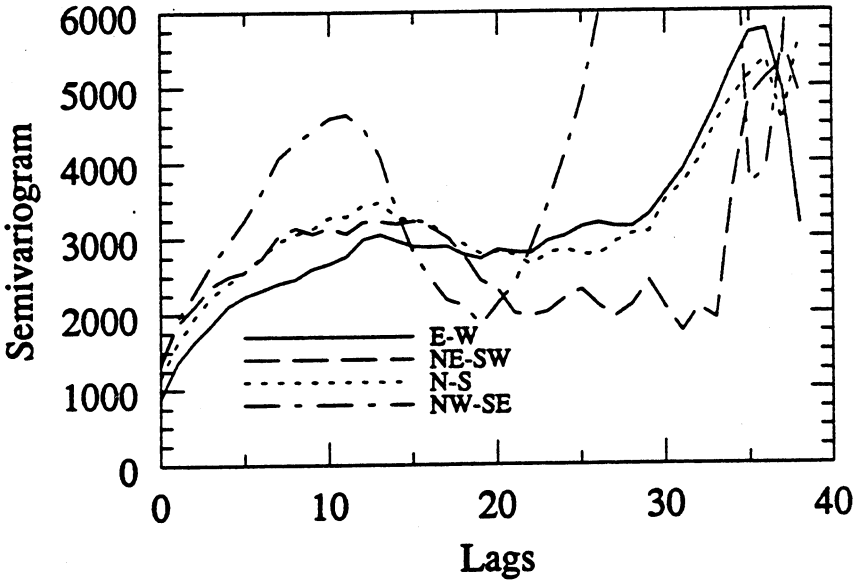

Fig. 6.3-9 Directional permeability variograms for Slab 1.

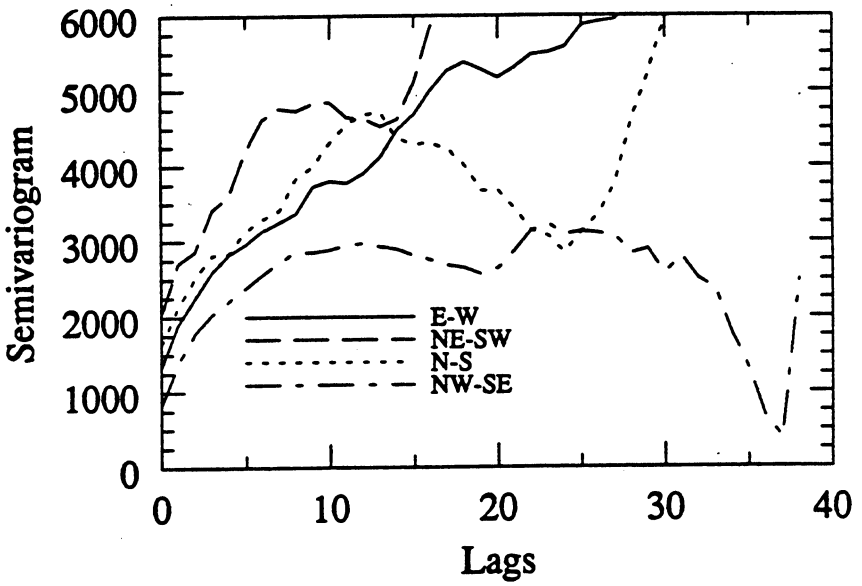

Fig. 6.3-10 Directional permeability variograms for Slab 2.

(3) Both slabs exhibit zonal anisotropy. That is, the magnitude of the sill depends upon the direction. This correlation structure is more difficult to model than geometric anisotropy. In geometric anisotropy, the range may depend on direction but the height of the sill is invariant.

(4) The NW-SE variogram for Slab 1 oscillates around its sill value. The oscillation is due to the laminations whose axes are roughly perpendicular to the NW-SE direction (see Figs. 6.3-7 and 6.3-9)

(5) In Slab 2, the NE-SW variogram increases at separation distances $h \geq 15$ lags. The parabolic increase in the variogram is caused by a linear trend (or drift) in the permeability along this direction (see Figs. 6.3-8 and 6.3-10).

Immiscible Flow Through Small-Scale Areally Heterogeneous Systems

Numerical simulation was used to study the effects of the above-described small-scale permeability distributions upon immiscible flow. The analysis was quite simple: the simulations results (cumulative oil production, instantaneous water cut, and pressure drop) were used to estimate the pseudofractional flow by the method of Section 6.1 (Pande et al. 1987). The sensitivity of the pseudofunctions to flow conditions was then examined.

Fig. 6.3-11 shows several (pseudo)fractional flow curves: (1) the rock curve which was input to the simulator in the relative permeability functions used, (2) low flow rate with capillary pressure (q_T = 1 PV/day, $N_{CT} = N_{CL} = 0.303$), (3) high flow rate with capillary pressure (q_T = 10 PV/day, $N_{CT} = N_{CL} = 0.0303$) and (4) no capillary pressure ($N_{CT} \rightarrow 0$, numerical dispersion only). None of the resulting fractional flow curves matches the rock curve. The shock velocities and average saturations behind the front depend upon the capillary number. The dependence of fractional flow upon the capillary number is not an end effect, but rather reflects the effects of longitudinal (and, to a lesser extent, transverse) imbibition. The length scale in the slab is small, so that capillary pressure is significant even at high rates (10 PV/day). When $P_c^* = 0$, the rate dependence vanishes — the capillary numbers are nearly zero regardless of the rate.

In order to investigate the effects of scale dependence, displacements with $N_{CT} \rightarrow 0$ ($P_c^* = 0$) were simulated using different subregions of Slab 2. Fig. 6.3-12 shows the results of the pseudofunction analysis. The "half slab" runs were displacements through either the upper or lower half of Slab 2 (N_x = 40, N_y = 20); the "quarter slabs" are defined analogously (N_x = 40, N_y = 10). All of the results are identical, even though the permeability fields are slightly different and the stabilizing effects of capillarity are small (numerical dispersion only). In this case, the contrasts in permeability are not large enough to cause significant differences in the multiphase flow behavior at the scale considered. The ratio k_{max}/k_{min} is only about 6 (versus 10 for the layered case), and, more importantly, the limited range of correlation further mitigates the effects of the permeability contrasts. Because no new correlation lengths are sampled as the scale of the displacement is increased from quarter to half to whole slabs, no change in the displacement behavior is observed. In systems with high mobility ratios or low dispersion, however, the permeability contrasts may affect the displacement more significantly (Giordano et al. 1985).

6.3.4 Summary and Conclusions

By casting the differential equations for immiscible flow in dimensionless form, important aspects of the scaling behavior for these systems can be encapsulated in dimensionless groups. For example, systems with identical aspect ratios and physical properties, but different lengths, will have different capillary numbers and different production behavior. As a result, attempts to lump or scale the systems via a pseudofunction approach must respect the differences in physical behavior, as reflected in the dimensionless groups (N_{CL}, N_{CT}, R_L).

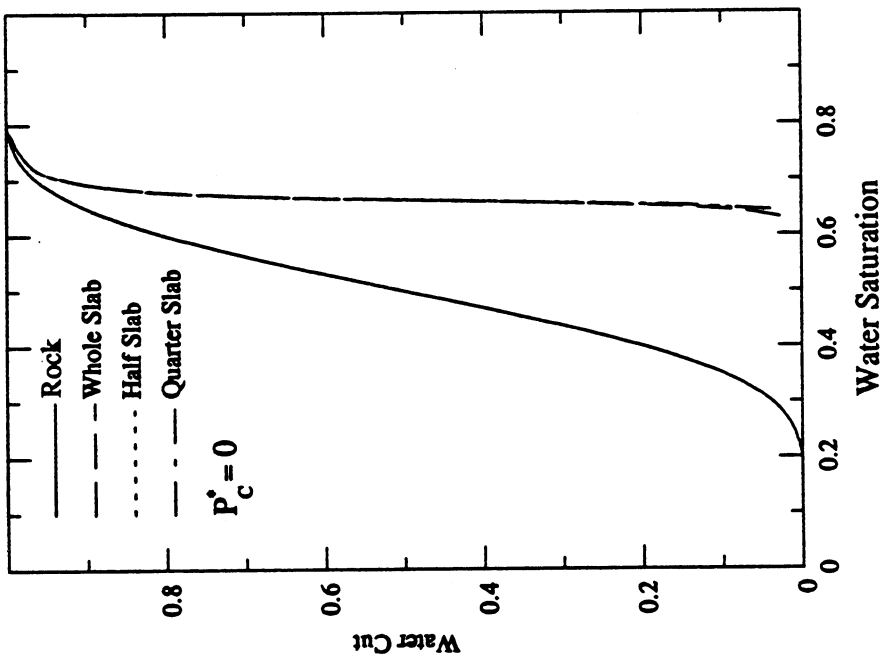

Fig. 6.3-12 Pseudofunctions for displacements through subregions of Slab 2.

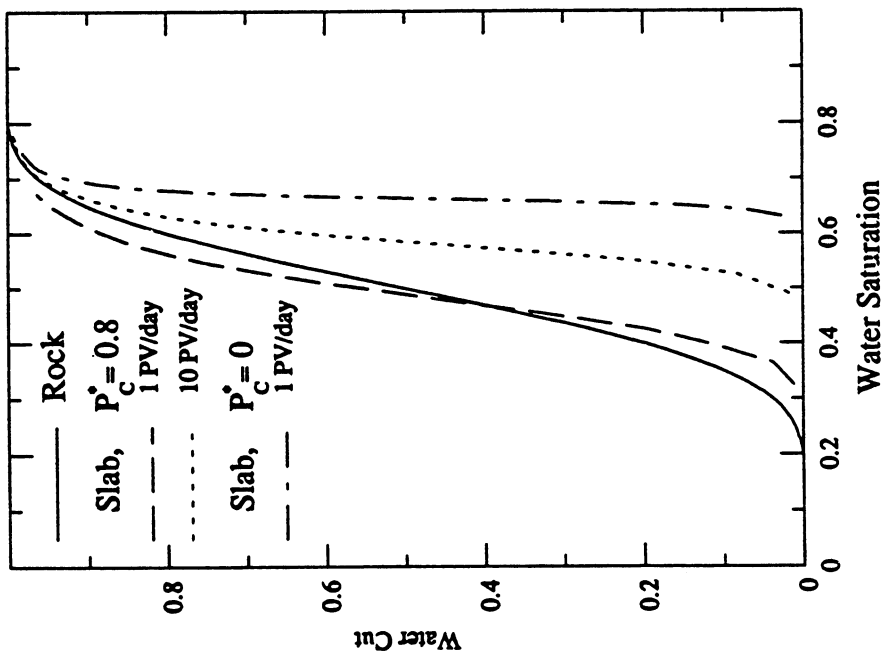

Fig. 6.3-11 Pseudofunctions showing rate effects for displacements through Slab 2.

The importance of permeability contrasts in determining production behavior depends upon rock-fluid properties, system size, and the spatial correlation of the permeability. For layers, permeability contrasts are high and longitudinal correlation is nearly perfect. At low capillary numbers, the flow behavior of the composite system is very sensitive to the layering. At high capillary numbers, crossflow equalizes the saturation in the high- and low-permeability regions, and the effects of layering become less pronounced. Heterogeneity and scale effects are both important for the layered systems. The core-level areal simulations showed less sensitivity to the permeability variations. The permeability contrasts were relatively low, and the correlation length scales were short enough that capillary effects stabilized the flow very quickly. Thus, the simulations indicate that if the permeability variation is mild enough and the correlation length of permeability variations is small enough compared to the flow length, the effect of permeability variation on displacement performance can be ignored, and fractional flow representations of the flow behavior are adequate for estimation of recovery performance.

6.4 Summary

The results reported in this chapter reinforce the idea that it is the combination of (1) permeability variation (with sufficient permeability contrast) with (2) correlation lengths that are a significant fraction of the displacement length that is the most important characteristic of heterogeneity. If the contrast is mild and the correlation length is small compared to the flow length, as it was in the Berea slab, then effects of heterogeneity are small. If the correlation length is long, as it was in the layered system of Section 6.1 and in the areal variations and cross-sections of Section 6.2, then some representations of heterogeneity is required. Those results are consistent with the results presented in Section 5.1 for tracer flow at unit mobility ratio and with those of Sections 4.1 and 4.2 for unstable flow in heterogeneous systems.

In such cases, the permeability heterogeneity can be represented explicitly in fine grid simulations, or some averaging technique can be employed. Two techniques were demonstrated in this chapter. The fractional flow approach of Section 6.1 can always be employed, though it cannot reproduce all the details of local saturation distributions, and the fractional flow functions appropriate to the fluid properties and scale of the displacement must be determined. The tensor scaling approach of Section 6.2 can capture significantly more detail, though at the cost of additional complexity in the scaling calculations.

Flows in which both capillary and viscous crossflow operate are complex, but the net effect of the crossflow is to provide a cutoff of length scales of permeability variations that have significant effect on displacement performance. Variations with short length scales are wiped out by the crossflow. How that cutoff works when phase behavior is also important remains to be worked out, but the results presented in Section 6.3 suggest that for a given displacement process there is some scale below which permeability variations do not matter. Future work should be aimed at more precise quantification of that scale.

7. Summary and Conclusions

This report summarizes progress in a research effort to quantify the effects of nonuniform flow on displacement performance in miscible floods. Results are reported in five areas:

(1) Phase behavior and fluid property measurements.

(2) Interaction of phase behavior and multiphase flow.

(3) Interaction of viscous instability and flow in heterogeneous porous media.

(4) Detection of reservoir heterogeneity.

(5) Representation of the effects of reservoir heterogeneity.

In the first area, results of experiments that compare the efficiency of supercritical extraction by CO_2, C_1 and N_2 are described. Experimental conditions were selected at which the solvent molar density, which is a measure of the number of solvent molecules per unit volume, was the same (at constant temperature). Composition measurements of samples of solvent-rich phases indicated that CO_2 extracted greater amounts of hydrocarbons and also much heavier hydrocarbons than did C_1 or N_2. Those results indicate that physical solvency alone does not control extraction by CO_2, C_1 or N_2, and that the presence of volatile, light hydrocarbons will be much more important for C_1 and N_2 flooding than for CO_2 flooding, where extraction of relatively heavy hydrocarbons is observed.

Also reported in the first area are results of the application of two analytical techniques to the characterization of oils for miscible flooding. The use of supercritical fluid chromatography (SFC) with CO_2 as a carrier was demonstrated. The results reported indicate that simulated distillations can be performed rapidly and without the addition of an internal standard by SFC. Similar analyses by more standard gas chromatography take more than twice as long and require use of an internal standard. Also described are results of a detailed analysis of a crude oil by mass spectrometry. More than 300 compounds present in an oil were identified. The techniques demonstrated will permit direct determination of which hydrocarbons are extracted most efficiently by CO_2 or other miscible flood solvents. In addition, the data obtained will allow assessment of the adequacy of techniques used to lump hydrocarbon components present in a crude oil for calculations with an equation of state. Thus, the analytical techniques demonstrated should lead to improved understanding of fundamental aspects of supercritical extraction by miscible flood solvents and also to improved characterization of oils for miscible flood processes.

In the second area, calculations of the compositional behavior of displacements are described. The method of characteristics (MOC) was applied to the theory of multiphase flow of multicomponent mixtures. The analytical solutions obtained extend significantly the range of problems for which detailed theory is available. For example, a MOC solution for four-component, two-phase flow with volume change on mixing was developed. That calculation resolves a long-standing inconsistency between theoretical descriptions of the development of miscibility, based on analysis of ternary diagrams, and experimental observations that addition of methane to the oil has little effect on the minimum miscibility pressure unless the bubblepoint of the recombined oil exceeds the MMP of the dead oil. The calculated results show that the MMP is insensitive to the amount of methane present in the oil because the methane partitions so strongly into the vapor phase that all the methane has been displaced before the CO_2 arrives. Thus, the CO_2 displaces dead oil, and if the pressure exceeds the dead oil MMP, that displacement is efficient. The entire displacement does, however, take place in the two-phase region. Hence, the absence of two-phase flow is not required for efficient displacement, contrary to the standard assumption made in descriptions of multiple contact miscibility. Analysis of the resulting compositions paths also indicates that as long as the flow is one-dimensional, a displacement of a live oil at a pressure below its bubblepoint pressure can also yield very high recovery.

The method of characteristics was also applied to the flow of steam/oil/water mixtures with temperature variation. The calculations demonstrate the dependence of fluid flow velocities on the volume change that accompanies condensation of steam. The analytical solutions show that shocks must occur when the number of phases changes. Solutions obtained show a water/oil region followed by a three-phase steam/oil/water zone. That zone, in turn, is followed by a steam/oil region. The solutions described indicate that the steam saturation, where steam is present, are sensitive to the oil viscosity and its temperature dependence.

MOC and finite difference solutions are also reported for flow of two- and three-component mixtures in a two-layer porous medium. Solutions for flow with viscous crossflow between layers are reported and compared with solutions for flow when crossflow is absent. Those solutions show that crossflow lengthens significantly the region in which two-phase flow occurs. They also show that crossflow can induce two-phase flow in systems that would be multicontact miscible if crossflow were absent. If the layer permeability ratio is 3.0 or higher, however, the negative effects of two-phase flow are more than offset by the benefits of moving oil from the slow layer to the high velocity layer. The calculations reported give some indication of the type of interactions that can be expected to result from capillary crossflow or gravity segregation for displacements in heterogeneous reservoirs or in reservoirs in which significant viscous fingering occurs.

Also reported is an analysis of the effect of dispersion on composition paths. That analysis complements those based on the method of characteristics, which do not include effects of dispersion (or any other nonlocal mixing). Direct computations did not confirm a previously reported difference in calculated results between explicit representation of dispersion and use of numerical dispersion. The computations reported here showed clearly, however, that the impact of dispersion is sensitive to the size and shape of the two-phase region. Thus, control of numerical dispersion may be more important for some fluid systems than for others.

In the third area, two approaches are being used to study the effects of viscous instability in the presence of variations in permeability. The first is a set of partly scaled flow visualization experiments in which the length associated with the permeability variation is controlled and the dimensions of the resulting viscous fingers are measured. The second is a set of calculations of the growth of fingers in two-dimensional flows based on a probabilistic representation of the flow. Calculations of the growth of fingers were performed by adding random perturbations of position to account for the effects of dispersion of tracer particles being carried by convection. Calculated recovery data agreed very well with experimental observations for a full range of mobility ratios. No history matching or other adjustment of simulation parameters was required. Additional calculations of the growth of fingers in heterogeneous porous media indicated that the permeability field dominates finger formation when the permeability is sufficiently variable and sufficiently correlated that preferential flow paths aligned with the flow direction exist. When the permeability field is variable but uncorrelated, or when it is homogeneous, however, finger growth shows complex patterns that include shielding of some fingers by faster growing ones, broadening of finger tips, compression of finger tails, and coalescence of fingers by viscous crossflow.

The fourth area recognizes that even if the impact of reservoir heterogeneity on displacement performance were completely understood, the problem of detection and representation of the relevant scales of heterogeneity would still be significant. Several aspects of the detection problem are considered. The first is the use of tracers to detect the presence of areal heterogeneities. Calculated response to injection into a five-spot at unit mobility ratio indicates that when the permeability is variable, spatial correlation leads to preferential flow paths. Thus, spatial correlation over a significant fraction of the displacement length causes early breakthrough and an effluent composition history that cannot be modeled using a dispersion coefficient alone. Calculations of tracer response for permeability fields described by a variance of ln k and a correlation length indicated that a heterogeneity index, defined as the product of the variance and correlation length, gives a good indication of the type of flow

behavior to be expected. For low values of the index, which result from permeability fields with small variance or little correlation, flow is likely to be described by a single dispersion coefficient. For high values of the index, the specific permeability realization has an important impact on displacement performance. Analysis of pressure transient tests for the same flow systems indicated that the heterogeneity index can be estimated from well test data.

The extent to which pressure transient tests can be used to detect the presence of heterogeneities is also considered. A technique is presented with which the transient response to large-scale heterogeneities can be calculated easily. It makes use of discrete constant pressure and impermeable flow boundary conditions to represent heterogeneities of arbitrary shape. That calculation scheme was used to examine the response to variations in the length and orientation of regions of different flow properties. In addition, the pressure response of one- and two-dimensional composite reservoirs is described. That analysis is useful because it describes either a reservoir with regions of different permeability or regions containing fluids with different viscosity. The calculated responses indicate that if the contrasts between properties in the two regions are large enough, the presence of the heterogeneities can be detected.

In the fifth area, techniques for representation of the effects of heterogeneity in flow calculations were considered. First, a straightforward technique for calculation of pseudorelative permeability functions was demonstrated for layered systems. The calculations presented show that reasonable, but not exact, representations of flow behavior can be obtained from fractional flow theory, even when assumptions made in the analysis are not strictly satisfied. A simple test for the adequacy of pseudorelative permeability curves was also demonstrated. If characteristic curves that show the position vs. time of a given concentration or saturation are approximately linear, a fractional flow representation will be reasonably accurate.

Representation of more complex heterogeneities was also demonstrated. The technique developed is based on the use of tensor transmissibilities to reproduce the effects of local variations in permeability at scales smaller than that of a grid block. Any but the simplest of permeability variations will induce local rotation that cannot be reproduced with a course grid unless the macroscopic permeability is not isotropic. Instead, a tensor version of the transmissibility is derived that permits a macroscopic representation of the flow effects of the small-scale variation. Comparison of simulations using the tensor transmissibility with those performed using simpler average permeabilities show that the more complex tensor form does a much better job of reproducing the details of the flow.

Also as part of the fifth area, the use of simplified representations of the flow effects of reservoir heterogeneities is considered. In any reservoir simulation, for example, flow properties will be assigned to large grid blocks, even though the reservoir rocks will be heterogeneous at smaller scales. To examine that behavior, calculations of the effects of heterogeneity, and capillary and viscous crossflow were undertaken. They showed that for relatively mild permeability variations, crossflow can mitigate the effects of permeability variation sufficiently that representation of the flow in terms of pseudorelative permeability functions is reasonable.

The descriptions of the effects of phase behavior, viscous instability and heterogeneity given here are not, of course, a complete description of all of the interactions of those mechanisms, particularly at field scale. Instead, the individual investigations are an attempt to simplify the analysis enough that progress can be made toward the overall goal of more accurate predictions of miscible flood performance at field scale. Thus, subsequent work will be needed to integrate the predictions made for the individual physical mechanisms into a more comprehensive picture of the scales on which they act.

References

Abbaszadeh-Dehghani, M. and Brigham, W.E., 1982, "Analysis of Unit-Mobility Ratio Well-to-Well Tracer Flow to Determine Reservoir Heterogeneity," SUPRI-TR-36, Stanford University, Stanford, CA.

Abou-Kassem, J.H. and Aziz, K, 1985, "Analytical Well Models for Reservoir Simulation," *Soc. Pet. Eng. J.*, **25**, 573-579.

Ambastha, A.K., McLeroy, P.G., and Grader, A., 1987, "Effects of a Partially Communicating Fault in a Composite Reservoir on Transient Pressure Testing," paper SPE 16764 presented at the SPE 62nd Annual Technical Conference, Dallas, September 27-30.

Ambastha, A.K. and Sageev, A., 1987, "Linear Water Influx of an Infinite Aquifer through a Partially Communicating Fault," *Proc.*, 12th Geothermal Reservoir Engineering Workshop, Stanford, CA, January 20-22.

Araktingi, U.G., 1988, "Viscous Fingering in Heterogeneous Porous Media," PhD dissertation, Stanford U., Stanford, CA.

Aris, R. and Amundson, N.R., 1957, "Some Remarks on Longitudinal Mixing or Diffusion in Fixed Beds," *AIChE J.*, **3**, 280-282.

Arya, A., Hewett, T., Larson, R.G., and Lake, L.W., 1985, "Dispersion and Reservoir Heterogeneity," paper SPE 14364 presented at the SPE 60th Annual Technical Conference, Las Vegas, September 24-27.

Arya, A., Hewett, T.A., Larson, R.G., and Lake, L.W., 1988, "Dispersion and Reservoir Heterogeneity," *SPE Reservoir Engineering J.*, 140-148, February.

ASTM D2887, 1976, "Standard Test Method for Boiling Range Distribution of Petroleum Fractions by Gas Chromatography," *Annual Book of ASTM Standards*, American Society for Testing and Materials, Philadelphia, 658-667.

Aziz, K. and Settari, A., 1979, *Petroleum Reservoir Simulation*, Applied Science Publishers Ltd., London.

Bear, J., 1972, *Dynamics of Fluids in Porous Media*, American Elsevier Publishing Company, New York.

Begg, S.H. and King, P.R., 1985, "Modelling the Effects of Shales on Reservoir Performance, Calculation of Effective Permeability," paper SPE 13529 presented at the Reservoir Simulation Symposium, Dallas, February 10-13.

Bette, S. and Heinemann, R.F., 1986, "The Utility of Compositional Simulators in the Analysis of Rich Gas Condensate Reservoirs," *Proc.*, First Wyoming Symposium on Enhanced Oil Recovery, Laramie, March.

Bixel, H.C., Larkin, B.K., and Van Poollen, H.K., 1963, "Effect of Linear Discontinuities on Pressure Buildup and Drawdown Behavior," *J. Pet. Tech.*, **13**, 885-895.

Blackwell, R.J., Rayne, J.R., and Terry, W.M., 1959, "Factors Influencing the Efficiency of Miscible Displacement," *Trans.*, AIME, **216**, 1-8.

Brigham, W.E. and Abbaszadeh-Dehghani, M., 1987, "Tracer Testing for Reservoir Description," *J. Pet. Tech.*, 519-527, May.

Buckley, S.E. and Leverett, M.C., 1942, "Mechanism of Fluid Displacement in Sands," *Trans.*, AIME, **146**, 107.

Carslaw, H.S. and Jaeger, J.C., 1959, *Conduction of Heat in Solids*, 2nd ed. Oxford University Press.

Christie, M.A., 1987, "Numerical Techniques for High Resolution Simulation of Instabilities," paper SPE 16005 presented at the SPE 9th Symposium on Reservoir Simulation, San Antonio, February 1-4.

Christie, M.A. and Bond, D.J., 1987, "Detailed Simulation of Unstable Processes in Miscible Flooding," *SPE Reservoir Engineering J.*, 514-522, November.

Cinco, H., Samaniego, V., and Dominguez, A., 1976, "Unsteady-State Flow Behavior for a Well Near a Natural Fracture," paper SPE 6019 presented at the SPE 51st Annual Technical Conference, New Orleans, October.

Clark, D.G. and Van Golf-Racht, T.D., 1985, "Pressure Derivative Approach to Transient Test Analysis: A High-Permeability North Sea Reservoir Example," *J. Pet. Tech.*, 2023-2029, November.

Coats, K.H., Dempsey, J.R., and Henderson, J.H., 1971, "The Use of Vertical Equilibrium in Two-dimensional Simulation of Three-dimensional Reservoir Performance," *Trans.*, AIME **251**, 63-71.

Coats, K.H., Nielson, R.L., Terhune, M.H., and Weber, A.G., 1967, "Simulation of Three Dimensional Two-Phase Flow in Oil and Gas Reservoirs," *Soc. Pet. Eng. J.*, **7**, 377-388.

Craig, F.F., 1971, *The Reservoir Engineering Aspects of Waterflooding*, Monograph 3, Soc. of Pet. Eng. of AIME, Dallas, 62-68.

Da Costa e Silva, A.J., 1985, "A New Approach to the Characterization of Reservoir Heterogeneity based on the Geomathematical Model and Kriging Technique," paper SPE 14275 presented at the SPE 60th Annual Technical Conference, Las Vegas, September 22-25.

Davis, E.G. and Hawkins, M.F., 1963, "Linear Fluid-Barrier Detection by Well Pressure Measurements," *J. Pet. Tech.*, 1077-1079, October.

Deffrenne, P., Jeantet, M., Marle, C., and Pacsirszki, J., 1961, "The Determination of Pressures of Miscibility," paper SPE 116 presented at the SPE 36th Annual Meeting, Dallas, October.

DeGregoria, A.J., 1985, "A Predictive Monte-Carlo Simulation of Two-Fluid Flow through Porous Media at Finite Mobility Ratio," *Phys. Fluids*, **28**, 1216-1220.

Desbarats, A.J., 1987, "Numerical Estimation of Effective Permeability in Sand-Shale Formations," *Water Resources Res.*, **23**, 273-286.

Dougherty, E.L., 1963, "Mathematical Model of an Unstable Displacement," *Trans.*, AIME, **222**, 155-163.

Dumoré, J.M., Hagoort, J., and Risseeuw, A.S., 1984, "An Analytical Model for One Dimensional Three Component and Vaporizing Gas Drives," *Soc. Pet. Eng. J* **24**, 169-179.

Dykstra, H. and Parsons, R.L., 1950, "The Prediction of Oil Recovery by Waterflooding," *Secondary Recovery of Oil in the United States*, 2nd ed., American Petroleum Institute, Washington, D.C., 160-174.

Earlougher, R.C., Jr. and Ramey, H.J., Jr., 1973, "Interference Analysis in Bounded Systems," *J. Can: Pet. Tech.*, 33-45, October-December.

Ehlig-Economides, C. and Economides, M.J., 1982, "Analysis of a Geothermal Well Test in a Predominantly Linear Flow System," *Trans.*, Intl. Conf. on Geothermal Energy, Florence, Italy, 281-292, May 11-14.

Ehlig-Economides, C. and Economides, M.J., 1985, "Pressure Transient Analysis in an Elongated Linear Flow System," *Soc. Pet. Eng. J.*, 839-847, December.

Eijpe, R. and Weber, K.J., 1971, "Minipermeameters for Rock and Unconsolidated Sand," *Bull.*, AAPG, **55**, 307-309.

Enick, R.M., Reznik, A.A., and Miller, R.A., 1988, "The Statistical and Dimensionless-Time Analog to the Generalized Dykstra-Parsons Method, *SPE Reservoir Engineering J.*, 313-319, February.

Fayers, F.J., 1984, "An Approximate Model with Physically Interpretable Parameters for Representing Miscible Viscous Fingering," paper SPE 13166, presented at SPE 59th Annual Technical Conference, Houston, September 16-19.

Fayers, F.J., 1988, "An Approximate Model with Physically Interpretable Parameters for Representing Miscible Viscous Fingering," *paper SPE Reservoir Engineering J.*, 551-558, May.

Fayers, F.J. and Newley, T.M.J., 1988, "Detailed Validation of an Empirical Model for Viscous Fingering with Gravity Effects," *SPE Reservoir Engineering J.*, 542-550, May.

Flory, D.A., Rubenstein, A.E., Lichtenstein, A., Koons, C.B., Rogers, M.A., and Mercer, J.N., 1978, "Sophisticated Equipment Fingerprints Crude Oils," *Oil Gas J.*, **76**, 102.

Fried, J.J., 1975, *Groundwater Pollution*, Elsevier Scientific Publishing Company, Amsterdam, 330 p.

Garder, A.O., Peaceman, D.W., and Pozzi, A.L., Jr., 1964, "Numerical Calculation of Multidimensional Miscible Displacement by the Method of Characteristics," *Soc. Pet. Eng. J.*, **4**, 26-36.

Gardner, J.W., Orr, F.M., Jr., and Patel, P.D., 1981, "The Effect of Phase Behavior on CO_2-Flood Displacement Efficiency," *Soc. Pet. Eng. J.*, **21**, 2067-2081.

Gardner, J.W. and Ypma, J.G.J., 1984, "An Investigation of Phase Behavior - Macroscopic Bypassing Interaction in CO_2 Flooding," *Soc. Pet. Eng. J.*, **24**, 508-520.

Geertsma, J., Croes, G.A., and Schwarz, N., 1956, "Theory of Dimensionally Scaled Models of Petroleum Reservoirs," *Trans.*, AIME, **207**, 118-127.

Gelhar, L.W., 1986, "Stochastic Subsurface Hydrology: From Theory to Applications," *Water Resources Res.*, **22**, 135S-145S.

Gelhar, L.W. and Axness, C.L., 1981, "Stochastic Analysis of Macrodispersion in Three Dimensionally Heterogeneous Aquifers," Geophysical Research Center, Hydrology Research Program, Rep. No. H8, New Mexico Inst. of Mining and Technology, Socorro, New Mexico.

Gelhar, L.W. and Axness, C.L., 1983, "Three-dimensional Stochastic Analysis of Macrodispersion in Aquifers, *Water Resour. Res.*, **19**, 160-180.

Gelhar, L.W., Mantoglou, A., Welty, C., and Rehfelt, K.R., 1985, "A Review of Field Scale Solute Transport Processes in Saturated and Unsaturated Porous Media," Electrical Power Research Institute Report RP-2485-05, Palo Alto.

Giordano, R.M., Salter, S.J., and Mohanty, K.K., 1985, "The Effects of Permeability Variations on Flow in Porous Media," paper SPE 14365 presented at the SPE 60th Annual Technical Conference, Las Vegas, September 22-25.

Gray, K.E., 1965, "Approximating Well-to-Fault Distance from Pressure Buildup Tests," *J. Pet. Tech.*, 761-767, July.

Habermann, B., 1960, "The Efficiency of Miscible Displacement As A Function of Mobility Ratio," *Trans.*, AIME, **219**, 264-272.

Haldorsen, H.H. and Lake, L.W., 1984, "A New Approach to Shale Management in Field Scale Simulation Models," *Soc. Pet. Eng. J.*, **24**, 447-457.

Hatziavramidis, D.T., 1987, "A New Computational Approach to the Miscible Displacement Problem," paper SPE 16004, presented at Symposium on Reservoir Simulation, San Antonio, February 1-4.

Hearn, C. L., 1971, "Simulation of Stratified Waterflooding by Pseudo Relative Permeability Curves," *J. Pet. Tech.*, 805-813, July.

Helfferich, F.G., 1981, "General Theory of Multicomponent, Multiphase Displacement in Porous Media," *Soc. Pet. Eng. J.* **21**, 51-62.

Helfferich, F.G., 1982, "Generalized Welge Construction for Two-Phase Flow in Porous Media in System with Limited Miscibility," SPE 9730 presented at SPE 57th Annual Technical Conference, Dallas, September 26-29.

Heller, J.P., 1963, "The Interpretation of Model Experiments for the Displacement of Fluids Through Porous Media," *AIChE J.*, 452-459, July.

Heller, J.P., 1966, "Onset of Instability Patterns Between Miscible Fluids in Porous Media," *J. Appl. Phys.*, **37**, 1566-1579.

Heller, J.P., 1972, "Observations of Mixing and Diffusion in Porous Media," *Proc.*, Second International Symposium on Fundamentals of Transport Phenomena in Porous Media, Guelph, Canada, 1-26.

Heller, S.R. and Milne, G.W.A., 1978, EPA/NIH Mass Spectral Data Base, Volumes 1-4, NSRDS-NBS 63, Washington.

Hirasaki, George J., 1981, "Application of the Theory of Multicomponent, Multiphase Displacement to Three-Component, Two-Phase Surfactant Flooding," *Soc. Pet. Eng. J.*, **21**, 191-204.

Hoeksema, R.J. and Kitanidis, P.K., 1985, "Analysis of the Spatial Structure of Properties of Selected Aquifers," *Water Resources Res.*, **21**, No. 4, 563-572.

Holm, L.W. and Josendal, V.A., 1982, "Effect of Oil Composition on Miscible-Type Displacement by Carbon Dioxide," *Soc. Pet. Eng. J.*, **22**, 87-98.

Homsy, G.M., 1987, "Viscous Fingering in Porous Media," *Ann. Rev. Fluid Mech.*, **19**, 271-311.

Horner, D.R., 1951, "Pressure Buildup in Wells," *Proc.*, Third World Pet. Congress, The Hague, Sec. II, 503-23.

Hurst, W., 1953, "Establishment of the Skin Effect and Its Impediment to Fluid Flow into a Well Bore," *Pet. Eng.*, B-6 - B-16, October.

Hutchinson, C.A., Jr. and Braun, P.H., 1961, "Phase Relations of Miscible Displacement and Oil Recovery," *AIChE J.*, **7**, 64-72.

Jap, J., Khawaja, B., Taggart, I., and Pinczewski, W.V., 1985, "Modelling of Phase Behaviour and Displacement Performance for the Miscible Gas Flooding EOR Process," *Proc.*, Chemeca 1985, 13th Australian Chemical Engineering Conference, Perth, Australia, 89-93, August.

Jeffrey, Alan, 1976, *Quasilinear Hyperbolic Systems and Waves*, Pitman Publishing, London.

Jennings, A., 1977, *Matrix Computations for Engineers and Scientists*, John Wiley and Sons, New York, 100-166.

Jensen, J.L., Lake, L.W., and Hinkley, D.V., 1985, "A Statistical Study of Reservoir Permeability: Distributions, Correlations and Averages," paper SPE 14270 presented at the SPE 60th Annual Technical Conference, Las Vegas, September 22-25.

Johnson, E.F., Bossler, D.P., and Naumann, V.O., 1959, "Calculation of Relative Permeability from Displacement Experiments," *Trans.*, AIME, **216**, 370-372.

Jones, S.C. and Roszelle, W.O., 1978, "Graphical Techniques for Determining Relative Permeability From Displacement Experiments," *J. Pet. Tech.*, 807-817, May.

Jossi, J.A., Stiel, L.I., and Thodos, G., 1962, "The Viscosity of Pure Substances in the Dense Gaseous and Liquid Phases," *A.I.Ch.E. J.*, **8**, No. 1, 59-62.

Journel, A.G. and Huijbregts, C.J., 1978, *Mining Geostatistics*, Academic Press, London.

King, M. and Scher, H., 1985, "Probabilistic Stability Analysis of Multiphase Flow in Porous Media," paper SPE 14366 presented at SPE 60th Annual Technical Conference, Las Vegas, September 22-25.

King, M., and Scher, H., 1986, "A Probability Approach to Multiphase and Multi-component Fluid Flow in Porous Media," *Phys. Rev. A.*. (In press)

Klins, M.A., 1984, *Carbon Dioxide Flooding: Basic Mechanisms and Project Design,* International Human Resources Development Corporation, Boston, 267 pp.

Konikow, L.W. and Bredehoeft, J.D., 1978, *Computer Model of Two-Dimensional Solute Transport and Dispersion in Ground Water,* U.S. Geological Survey Techniques of Water Resources Investigation, Book 7, Chapter C2.

Kortekaas, T.F.M., 1983, "Water/Oil Displacement Characteristics in Cross-Bedded Reservoir Zones," paper SPE 12112, presented at SPE 58th Annual Technical Conference, San Francisco, October 5-8.

Koval, E.J., 1963, "A Method for Predicting the Performance of Unstable Miscible Displacement in Heterogeneous Media," *Trans.*, AIME, **228**, 145-154.

Lallemand-Barres and Peaudecerf, 1978, "Recherche des Relations entre la Valeur de la Dersivite Macroscopique d'un Milieu Aquifere ses autre Caracteristiques et les Conditions de Mesure," *Bulletin du BRGM 2e Serie*, Section III, No. 4.

Lantz, R.B., 1971, "Quantitative Evaluation of Numerical Diffusion (Truncation Error)," *Soc. of Pet. Eng. J.* **11**, 315-319.

Larsen, L.L., 1984, "Prediction of Phase Behavior of CO_2-Hydrocarbon Mixtures." MS thesis, New Mexico Institute of Mining and Technology, Socorro, New Mexico.

Larson, R.G., 1979, "The Influence of Phase Behavior on Surfactant Flooding," *Soc. Pet. Eng. J.*, **19**, 411-422, December.

Lasseter, T.J., Waggoner, J.R., and Lake, L.W., 1986, "Reservoir Heterogeneities and Their Influence on Ultimate Recovery," *Reservoir Characterization*, L.W. Lake and H.B. Carroll, Jr., Eds., Academic Press, New York, 545-560.

Law, J., 1944, "A Statistical Approach to the Interstitial Heterogeneity of Sand Reservoirs," *Trans.*, AIME, **155**, 202-222.

LeBlanc, R.J., Sr., 1977a, "Distribution and Continuity of Sandstone Reservoirs--Part I," *J. Pet. Tech.*, **29**, 776-792.

LeBlanc, R.J., Sr., 1977b, "Distribution and Continuity of Sandstone Reservoirs-- Part 2," *J. Pet. Tech.*, **29**, 793-804.

Lee, S., Li, K.M.G., and Culham, W.E., 1984, "Stability Analysis of Miscible Displacement Processes, paper SPE/DOE 12631 presented at Fourth Symposium on Enhanced Oil Recovery, Tulsa, April 15-18.

Leverett, M. C., 1941, "Capillary Behavior in Porous Solids," *Trans.*, AIME, **142**, 341.

Lohrenz, John, Bray, B.C., and Clark, C.R., 1964, "Calculation Viscosities of Reservoir Fluids from their Compositions," *J. Pet. Tech.*, **6**, 1171-1176.

Luster, G.R., 1984, "Practical Conditional Simulation of Coregionalization, I: Basic Methods and Formations," Progress Report 3, for Exxon Minerals Company Research Grant, Geostatistical Estimation and Simulation of Ore Deposits."

Luster, G.R., 1985, "Raw Materials for Portland Cement: Applications of Conditional Simulation," Ph.D. Dissertation, Stanford University, Stanford.

Marle, C.M., 1981, *Multiphase Flow in Porous Media*, Gulf Publishing Co., Houston, 39-49.

Martin, J.C., 1968, "Partial Integration of Equations of Multiphase Flow," *Trans.*, AIME, **243**, 370-380.

Martin, J.H. and Cooper, J.A., 1984, "An Integrated Approach to the Modeling of Permeability Barrier Distribution in a Sedimentologically Complex Reservoir," paper SPE 13051 presented at the SPE 59th Annual Technical Conference, Houston, September 16-19.

Metcalfe, R.S. and Yarborough, L., 1979, "The Effect of Phase Equilibria on the CO_2 Displacement Mechanism," *Soc. Pet. Eng. J.*, **19**, 242-252.

Mishra, S., 1987, "On the Use of Pressure and Tracer Test Data for Reservoir Description," PhD dissertation, Stanford University, Stanford, CA.

Mishra, S. and Ramey, H.J., Jr., 1985, "A Comparison of Pressure Transient and Tracer Concentration-Time Data for Layered Reservoirs Under Injection," paper SPE 14170 presented at SPE 60th Annual Technical Conference, Las Vegas, Sept. 22-25.

Moldowan, J.M., et al., 1985, "Relationship between Petroleum Composition and Depositional Environment of Petroleum Source Rocks," *Amer. Assn. Pet. Geo. Bull.*, **69**, 1255-1268.

Moler, C.B. and Stewart, G. W., 1973, "An Algorithm for Generalized Matrix Eigenvalue Problems," *SIAM Journal of Numerical Analysis*, **10**, 241-256.

Monroe, W.W., 1986, "The Effect of Dissolved Methane on Composition Paths in Quaternary CO_2-Hydrocarbon Systems," Master's Thesis, Stanford University, Stanford, CA, September.

Monroe, W.W., Silva, M.K., Larsen, L.L., and Orr, F.M., Jr., 1987, "Composition Paths in Four-Component Systems: The Effect of Dissolved Methane on CO_2 Flood Performance in One Dimension," paper SPE 16712 presented at the Fall Meeting of SPE of AIME, Dallas, Sept. 27-30.

Nutakki, R., Wong, T., Firoozabadi, A., and Aziz, K., 1985, "Development of General Purpose Simulators. Part 1: Vapor-Liquid Equilibrium Calculations Using Three Equations of State and Accelerated Successive Substitution," Department of Petroleum Engineering, School of Earth Sciences, Stanford University.

Nutakki, R. and Mattar, L., 1982, "Pressure Transient Analysis of Wells in Very Long Narrow Reservoirs," paper SPE 11221 presented at the 57th Annual Technical Conference, New Orleans, September 26-29.

Odeh, A.S., 1987, "A Proposed Technique for Simulation of Viscous Fingering in One-Dimensional Immiscible Flow," paper SPE 17087 presented at the SPE 62nd Annual Technical Conference, Dallas, September 27-30.

Offeringa, J. and Van der Poel, C., 1954, "Displacement of Oil from Porous Media by Miscible Liquids," *Trans.*, AIME, **201**, 310-316.

Orr, F.M., Jr., 1980, "Simulation of the One-Dimensional Convection of Four-Phase, Four-Component Mixtures," US DOE Rep. No. DOE/ET/12082-8.

Orr, F.M., Jr. and Grader, A., 1987, "Reservoir Characterization for the CO_2 Enhanced Oil Recovery Process, Annual Report," DOE Contract No. DE-AC21-22042, 255 pp., November

Orr, F.M., Jr. and Jensen, C.M., 1984, "Interpretation of Pressure-Composition Phase Diagrams for CO_2-Crude Oil Systems," *Soc. Pet. Eng. J.*, October, 485-497.

Orr, F.M., Jr. and Sageev, A., 1986, "Reservoir Characterization for CO_2 Flooding, Annual Report," DOE Contract No. DE-AC21-22042, 139 pp., November.

Orr, F.M. Jr. and Silva, M.K., 1985, "Effect of Oil Composition on Minimum Miscibility Pressure—Part 2: Correlation," paper SPE 14150 presented at the SPE 60th Annual Technical Conference, Las Vegas, September 22-25.

Orr, F.M., Jr., Silva, M.K., Lien, C.L., and Pelletier, M.T., 1982, "Laboratory Experiments to Evaluate Field Prospects for Carbon Dioxide Flooding," *J. Pet. Tech.* **34**, 888-898.

Orr, F.M., Jr., Yu, A.D., and Lien, C.L., 1981, "Phase Behavior of Carbon Dioxide and Crude Oil in Low Temperature Reservoirs," *Soc. Pet. Eng. J.*, **21**, 480-492.

Pande, K.K., 1989, "Interaction of Phase Behavior with Nonuniform Flow," PhD dissertation, Stanford U., Stanford, CA.

Pande, K.K., Ramey, H.J., Jr., Brigham. W.E., and Orr, F.M., Jr., 1987, "Frontal Advance Theory for Flow in Heterogeneous Porous Media," paper SPE 16344 presented at the SPE California Regional Meeting, Ventura, April 2-10.

Peaceman, D.W., 1978, "Interpretation of Well-Block Pressures in Numerical Reservoir Simulation," *Soc. Pet. Eng. J.*, 183-184, June.

Peaceman, D.W. and Rachford, H.H., Jr., 1962, "Numerical Calculation of Multidimensional Miscible Displacement," *Soc. Pet. Eng. J*, 301-317, May.

Peng, D-Y and Robinson, D.B., 1976, "A New Two-Constant Equation of State," *Ind. Eng. Chem.*, **15**, 59-64.

Perkins, T.K. and Johnston, O.C., 1963, "A Review of Dispersion in Porous Media," *Soc. Pet. Eng. J.*, **3**, 70-80, March.

Perrine, R.L., 1963, "A Unified Theory for Stable and Unstable Miscible Displacement," *Soc. Pet. Eng. J.*, **3**, 205, March.

Peters, E.J., Broman, W.H., and Broman, J.A., 1984, "A Stability Theory for Miscible Displacement," paper SPE 13167 presented at SPE 59th Annual Technical Conference, Houston, September 16-19.

Pope, G.A. and Nelson, R.C., 1978, "A Chemical Flooding Compositional Simulator," *Soc. Pet. Eng. J.*, 339-354, October.

Pozzi, A.L. and Blackwell, R.J., 1963, "Design of Laboratory Models for Study of Miscible Displacement," *Soc. Pet. Eng. J*, 28-40, March.

Prasad, R.K., 1975, "Pressure Transient Analysis in the Presence of Two Intersecting Boundaries," *J. Pet. Tech.*, **27**, 89-96.

Prickett, T.A., Naymik, T.G., and Lonnquist, C.G., 1981, "A Random-Walk Solute Transport Model for Selected Groundwater Quality Evaluations," *Illinois State Water Survey Bulletin*, **65**, 66 p.

Pryor, W. A., 1972, "Reservoir Inhomogeneities of Some Recent Sand Bodies," *Soc. Pet. Eng. J.* **12** 229-245, June.

Ramey, H.J., Jr., 1982, "Pressure Transient Testing," Distinguished Author Series, *J. Pet Tech.*, 1407-1413.

Ramey, H.J., Jr. and Cobb, W.M., 1971, "A General Buildup Theory for a Well in a Closed Drainage Area," *J. Pet. Tech.*, 1493-1505, December.

Rathmell, J.J., Stalkup, F.I., and Hassinger, R.C., 1971, "A Laboratory Investigation of Miscible Displacement by Carbon Dioxide," paper SPE 3483 presented at the SPE 46th Annual Meeting, New Orleans, October 4-8.

Reamer, H.H. and Sage, B.H., 1963, "Phase Equilibria in Hydrocarbon Systems. Volumetric and Phase Behavior of the n-Decane-CO_2 System," *J. Chem. Eng. Data*, **8**, 508-513.

Reid, R.C., Prausnitz, J.M., and Sherwood, T.K., 1977, *The Properties of Gases and Liquids*, McGraw Hill, New York, Third Edition.

Reynolds, W.C., 1979, *Thermodynamic Properties in SI*, Department of Mechanical Engineering at Stanford University, Stanford, CA.

Reznik, A.A., Enick. R.M., and Panvelker, S.B., 1984, "An Analytical Extension of the Dykstra-Parsons Vertical Stratification Discrete Solution to a Continuous, Real-Time Basis," *Soc. Pet. Eng. J.*, **24**, 643-656.

Sageev, A. 1985, "Interference Testing Near a Steam Cap," *Trans.*, Geothermal Resources Council, **9**, Part 2, October.

Sageev, A. and Horne, R.N., 1983a, "Pressure Transient Analysis of Reservoirs with Linear or Internal Circular Boundaries," paper SPE 12076 presented at the SPE 58th Annual Technical Conference, San Francisco, October 5-8.

Sageev, A. and Horne, R.N., 1983b, "Drawdown Pressure Transient Analysis of a Well Near a Steam Cap," *Trans.*, Geothermal Resources Council, **7**, October.

Sageev, A. and Horne, R. N., 1986, "Interference Testing: Detecting an Impermeable or Compressible Region," paper SPE 15585 presented at the SPE 61st Annual Technical Conference, New Orleans, October 5-8.

Sageev, A., Horne, R.N., and Ramey, H.J., Jr., 1985, "Detection of Linear Boundaries by Drawdown Tests: A Semilog Type Curve Matching Approach," *Water Resources Research*, **21**, No. 3, 305-310, March.

Schowalter, W.R., 1965, "Stability Criteria for Miscible Displacement of Fluids from a Porous Medium," *AIChE. J.*, **11**, 99-105.

Schwartz, H.E., 1988, "Simulated Distillation by Packed Column Supercritical Fluid Chromatography," *Journal of Chromatographic Science*, **26**, 275-279.

Sigmund, P., Sharma, H., Sheldon, D., and Aziz, K., 1988, "Rate Dependence of Unstable Waterfloods, *SPE Reservoir Engineering J.*, 401-409, May.

Silva, M.K. and Orr, F.M., Jr., 1987, "Effect of Oil Composition on Minimum Miscibility Pressure-Part 1: Solubility of Hydrocarbons in Dense CO_2," *SPE Reservoir Engineering J.*, **27**, 468-476.

Slobod, R.L. and Koch, H.A., Jr., 1953, High-pressure Gas Injection - Mechanism of Recovery Increase," *Drill and Prod. Prac.*, API, 82-96.

Slobod, R.L. and Thomas, R.A., 1963, "Effect of Transverse Diffusion on Fingering in Miscible-Phase Displacement," *Soc. Pet. Eng. J.*, **3**, p. 9.

Smith, P.J. and Brown, C.E., 1984, "The Interpretation of Tracer Test Response from Heterogeneous Reservoirs," paper SPE 13262 presented at SPE 59th Annual Technical Conference, Houston, September 16-19.

Stalkup, F.I., Jr., 1983, *Miscible Displacement*, Monograph 8, Society of Petroleum Engineers of AIME, New York.

Stalkup, F.I., Jr., 1986, "Permeability Variations Observed at the Faces of Crossbedded Sandstone Outcrops," *Reservoir Characterization*, L.W. Lake and H.B. Carroll, Jr. Eds. Academic Press, Inc., Orlando, 141-180.

Stalkup, F.I., 1988, "Effect of Gas Enrichment and Numerical Dispersion on Compositional Simulator Predictions of Oil Recovery in Reservoir Condensing and Condensing/Vaporizing Gas Drives," paper SPE 18060 presented at the 1988 Fall Meeting of SPE of AIME, Houston, October 2-5.

Stallman, R.W., 1952, "Nonequilibrium Type Curves Modified for Two-Well Systems," U.S. Geological Survey Groundwater Note 3.

Stewart, G., Gupta, A., and Westaway, P., 1984, "The Interpretation of Interference Tests in a Reservoir with Sealing and Partially Communicating Faults," paper SPE 12967 presented at the 1984 European Petroleum Conf. in London, England, October 25-28.

Stone, H.L., 1970, "Probability Model for Estimating Three-Phase Relative Permeability," *J. Pet. Tech.*, **22**, 214-218.

Streltsova, T.D. and McKinley, R.M., 1984, "Effect of Flow Time Duration on Buildup Pattern for Reservoirs with Heterogeneous Properties," *Soc. Pet. Eng. J.*, 294-306, June.

Tan, C.T., 1988, "Stability of Miscible Displacements in Porous Media", Ph.D. Dissertation, Stanford University, Stanford, CA.

Tan, C.T. and Homsy, G.M., 1988, "Simulation of Nonlinear Viscous Fingering in Miscible Displacement," *Phys. Fluids*, **31**, 1330-1338.

Theis, C.V., 1935, "Relation Between the Lowering of the Piezometric Surface and the Rate and Duration of Discharge of a Well Using Ground-Water Storage," *Trans.*, EOS, AGU, **16**, No. 2, 519-524.

Tiab, D. and Crichlow, H.B., 1979, "Pressure Analysis of Multiple-Sealing Fault Systems and Bounded Reservoirs by Type-Curve Matching," *Soc. Pet. Eng. J.*, 379-392, December.

Tiab, D. and Kumar, A., 1980, "Detection and Location of Two Parallel Sealing Faults Around a Well," *J. Pet. Tech.*, 1701-1708, October.

Todd, M.R., and Longstaff, W.J., 1972, "The Development, Testing, and Application of a Numerical Simulator for Predicting Miscible Flood Performance," *Trans.*, AIME, **253**, 874-882.

Todd, M.R., O'Dell, P.M., and Hirasaki, G.J., 1972, "Methods for Increased Accuracy in Numerical Reservoir Simulators", *Soc. Pet. Eng. J.*, 515-530, December.

Van Everdingen, A.F., 1953, "The Skin Effect and Its Influence on the Productive Capacity of a Well," *Trans.*, AIME, **198**, 171-176.

Van Everdingen, A.F. and Hurst, W., 1949, "The Application of the Laplace Transformation to Flow Problems in Reservoirs," *Trans.*, AIME, **186**, 305-324.

Van Poollen, H.K., 1965, "Drawdown Curves Give Angle Between Intersecting Faults," *Oil and Gas Journal*, 71-75, December.

Vargaftik, N.B., 1975, *Handbook of Physical Properties of Liquids and Gases: Pure Substances and Mixtures*, Hemisphere Publishing Corporation, Washington, 758 pp.

Warren, J.E. and Price, H.S., 1961, "Flow in Heterogeneous Porous Media," *Soc. Pet. Eng. J.* **1**, 153-169.

Warren, J.E. and Skiba, F.F., 1964, "Macroscopic Dispersion," *Soc. Pet. Eng. J.*, 215-230, September.

Weber, J., 1982, "Influence of Common Sedimentary Structures of Fluid Flow in Reservoir Models," *J. Pet. Tech.*, **34**, 665-672.

Welge, H.J., 1952, "A Simplified Method for Computing Oil Recovery by Gas or Water Drive," *Trans.*, AIME, **195**, 91-98.

Welge, H.J., Johnson, E.F., Ewing, S.P., Jr., and Brinkman, F.H., 1961, "The Linear Displacement of Oil from Porous Media by Enriched Gas," *J. Pet. Tech.*, **3**, 787-796.

White, C.D., 1987, "Representation of Heterogeneity for Numerical Reservoir Simulation," PhD dissertation, Stanford University, Stanford, CA.

White, C.D. and Horne, R.N., 1987, "Computing Absolute Miscibility in the Presence of Fine-Scale Heterogeneity," paper SPE 16011 presented at the 9th SPE Simulation Symposium, San Antonio, February 1-4.

Wingard, J.S., 1989, "Multicomponent, Multiphase Flow in Porous Media with Temperature Variation," PhD dissertation, Stanford University, Stanford, CA.

Withjack, E.M., 1987, "Computed Tomography for Rock-Property Determination and Fluid-Flow Visualization," paper SPE 16951 presented at the SPE 62th Annual Technical Conference, Dallas, September 27-30.

Wong, W.D., Mothersele, C.D., Harrington, A.G., and Cinco-Ley, H., 1986, "Pressure Transient Analysis in Finite Linear Reservoirs Using Derivative and Conventional Techniques: Field Examples," SPE 15421 presented at the 61st Annual Meeting, New Orleans, October 5-8.

Yaxley, L.M., 1985, "The Effect of a Partially Communicating Fault on Transient Pressure Behavior," paper SPE 14311 presented at 60th Annual Technical Conference, Las Vegas, September 22-25.

Yellig, W.F. and Metcalfe, R.S., 1980, "Determination and Prediction of CO_2 Minimum Miscibility Pressures," *J. Pet. Tech.*, **32**, 160-168.

Yokoyama, Y. and Lake, L.W., 1981, "The Effects of Capillary Pressure on Miscible Displacements in Stratified Porous Media," paper SPE 10109 presented at the SPE 56th Annual Technical Conference, San Antonio, October 5-7.

Young, L.C., 1988, "Full-Field Compositional Modeling on Vector Processors," *Proc.*, Fourth Wyoming Enhanced Oil Recovery Symposium, Casper, 115-134, May 16-18.

Ypma, J.G.J., 1985, "Compositional Effects in Gravity-Dominated Nitrogen Displacements," paper SPE 14416 presented at the 60th Annual Technical Conference, Las Vegas, September 22-25.

Zadro, S., Haken, J.K., and Pinczewski, W.V., 1985, "Analysis of Australian Crude by High-Resolution Capillary Gas Chromatography—Mass Spectrometry," *J. Chromatography*, **323**, 305-322.

Zapata, V.J., 1981, "A Theoretical Analysis of Viscous Crossflow," PhD dissertation, University of Texas, Austin. TX.

Zapata, V.J. and Lake, L.W., 1981, "A Theoretical Analysis of Viscous Crossflow," paper SPE 10111 presented at the SPE 56th Annual Technical Conference, San Antonio, October 5-7.

☆U.S. GOVERNMENT PRINTING OFFICE: 1989-671-030/00054